UC Santa Cruz
UC Santa Cruz Electronic Theses and Dissertations

Title

Design and construction of biocompatible theranostic carbon monoxide and silver delivery systems for anticancer and antibacterial photochemotherapy

Permalink

https://escholarship.org/uc/item/09n1394g

Author

Pinto, Miguel Nicolás

Publication Date

2019

Peer reviewed|Thesis/dissertation

UNIVERSITY OF CALIFORNIA

SANTA CRUZ

**DESIGN AND CONSTRUCTION OF BIOCOMPATIBLE THERANOSTIC
CARBON MONOXIDE AND SILVER DELIVERY SYSTEMS FOR
ANTICANCER AND ANTIBACTERIAL PHOTOCHEMOTHERAPY**

A dissertation submitted in partial satisfaction
of the requirements for the degree of

DOCTOR OF PHILOSOPHY

in

CHEMISTRY

by

Miguel Nicolás Pinto

December 2019

The dissertation of Miguel Nicolás Pinto
is approved:

_____
Professor Pradip K. Mascharak, Chair

_____
Professor Scott R. J. Oliver

_____
Professor Yat Li

_____
Quentin Williams
Acting Vice Provost and Dean of Graduate Studies

Table of Contents

xi

List of Figures

xxv

List of Tables

DESIGN AND CONSTRUCTION OF BIOCOMPATIBLE THERANOSTIC CARBON MONOXIDE AND SILVER DELIVERY SYSTEMS FOR ANTICANCER AND ANTIBACTERIAL PHOTOCHEMOTHERAPY

Miguel Nicolás Pinto

ABSTRACT

Theranostic systems are materials or processes that combine modalities of diagnostic imaging with the delivery of therapeutics. The information obtained from theranostic drug-delivery systems can be used to make decisions in real time in efforts to optimize the treatment. This combination of therapy and diagnostics in a single treatment is a viable method for improving drug efficacy, patient safety, and therapeutic outcomes. The theranostic delivery of carbon monoxide (CO) as a chemotherapeutic and silver (Ag^+) as an antibacterial agent is discussed in detail in the following chapters.

The gaseous signaling molecule carbon monoxide has been recently recognized for its wide range of physiological activity as well as its antineoplastic properties. Endogenously produced CO directly regulates heme protein activity and indirectly modulates a variety of biochemical processes. Exogenous delivery of CO is also a viable strategy for influencing cellular biochemical responses in efforts to elicit desired salutary therapeutic effects. However, the main technical challenge is the delivery of this noxious and potentially hazardous gas in a controlled and dependable manner.

Several elegant strategies have been designed and implemented for the delivery of this gaseous signaling molecule to cells, including photo-triggered CO releasing systems (molecules, materials, carriers). Light can be used as a benign remote trigger for the on-demand release of CO from photoactivatable CO-releasing systems (photoCORs). However, the delivery of CO to light inaccessible cavities/tissues with spatiotemporal control is a considerable challenge.

The delivery of CO to remote parts of the body through the use of an optical fiber-based CO-releasing device is discussed in Chapter 2.I. The CO-releasing polymeric material described in this chapter can be used as a solid-state source of CO triggered through external light illumination. In addition, this material exhibits a color change upon CO release, indicating qualitatively the extent of CO delivered to cells and therefore has promising *in vivo* applications. Chapter 2.II describes the use of luminescent rhenium complexes that can also be covalently attached within polymeric matrices for the theranostic remote delivery of CO.

Strategies for tracking photoCORMs within cellular matrices and increasing their internalization are discussed in chapter 3. The cellular penetration rates of photoCORMs with distinct solubilities are investigated through confocal microscopy using a luminescent tag. Chapter 3.II focuses on investigating the luminescence quenching of fluorophores conjugated to a manganese metal center. The use of fluorescent tags allows for the convenient tracking photoCORMs and therefore theranostic delivery of CO to cellular targets *in vitro* .

Chapter 4 examines the theranostic delivery of silver for antimicrobial chemotherapy. Silver has been used as an antimicrobial agent since ancient times and it continues to be used in a variety of biomedical devices and consumer products. Silver exerts its antimicrobial properties by binding functional groups of amino acids, disrupting biochemical processes. Chapter 4.I discusses two antimicrobial silver complexes that exhibit a luminescence enhancement upon release of Ag^+. The increase in luminescence observed can be used to track the extent of Ag^+ delivered to microbial cells *in vitro*. Chapter 4.II describes the incorporation of luminescent silver complexes into a soft agar hydrogel for the treatment of skin and soft tissue infections. In this case, the complexes exhibit a change in luminescence upon silver release. Finally, chapter 4.III discusses the synthesis of a helical dinuclear silver complex and its antimicrobial efficacy in a skin and soft tissue infection model. The luminescence of the tridentate ligand is quenched, similarly to what was observed with the complexes described in chapter 4.I, which can be used to monitor the delivery of Ag^+ through "turn on" luminescence.

The theranostic drug-delivery systems described here aim to monitor the delivery of anticancer and antimicrobial therapeutics to cellular targets. This emerging science provides a unique opportunity to tailor and adjust drug-releasing events in real time to achieve the desired therapeutic effects. The change in luminescence in these systems can be extrapolated to determine the extent of drug delivered and/or the amount of prodrug remaining in the delivery system.

Acknowledgements

  I would first like to start by acknowledging my P. I. Prof. Pradip K. Mascharak for all his help, support, and training. His mentorship and advice have had very profound implications in my development as a scientist. I really admire his dedication and passion towards doing excellent science, and he is one of my biggest role models. I believe that completing my PhD under the supervision of Pradip really helped me sharpen my skills and grow as a scientist. Thanks to the training that I received from him I was able to surpass my goals and receive numerous accolades. I have received great advice from Pradip over the years which I am also deeply grateful for. I consider myself very lucky to have had him as my advisor because I can tell he truly cares for my success.

  I would like to thank my thesis members Prof. Scott R. J. Oliver and Prof. Yat Li for all their advice and mentorship throughout the years. It was a pleasure to have worked with them throughout my PhD at UC Santa Cruz. Scott has also been a great mentor and friend. I really enjoyed teaching along his side, allowing me the freedom to plan certain lectures and laboratory experiments. Prof. Li has also been a great mentor and friend. I am very thankful for his keen insight and deep research questions in particular during my presentations.

  Two other mentors that have also played an important role in my development as a scientist are Prof. Jevgenij Raskatov and Prof. Timothy Johnstone. I came to meet Jevgenij after multiple times of running into each other at odd hours of the night in the Physical Science Building. Since then, Jevgenij has become my mentor and good

friend. I truly admire Jevgenij's dedication to science and all of the fantastic knowledge and insight he has in various science and non-science fields. Tim Johnstone has also been a great friend always giving me solid advice. Since the first day I met Tim during his faculty interview I could tell that he is a great scientist. I really admire the vast knowledge and dedication that Tim has towards numerous fields of science.

I would really like to acknowledge my laboratory members that I have worked with throughout the years. First of all, the person who has helped me the most and has essentially trained me since day one is Dr. Indranil Chakraborty. He has been a great friend and a mentor who always give me great advice. Thanks to Indranil's help I was able to complete a substantial amount of publications while at UC Santa Cruz. I owe a great deal of my success to his advice and all his help. Another great friend in the Mascharak lab was Dr. Jorge Jimenez. Jorge became like a brother to me while I was in Santa Cruz and became one of my closest friends. I would really like to thank him for all his scientific discussions we had throughout the years and advice he gave me towards applying to postdoctoral positions. I truly enjoyed my time in the Mascharak lab hanging out with both Jorge Jimenez and Jorge Martinez-Gonzalez. It became very easy to stay and work in the lab until very late at night because besides working I was hanging out with great friends. Two other important graduate students and friends in my lab were Jenny Stenger-Smith and Brian Kawahara. Jenny was a very fun person to be around, always enthusiastic about research and overall a great friend. Brian is definitely one of the smarter graduate students that I have had the pleasure to work with. Having Jenny and Brian in the lab made it easy for me to be in there, and I am

extremely thankful for their friendship and scientific discussions. Last but not least I am very happy to have had the chance to work closely with John Wenger. He came into the lab with great enthusiasm and a really strong work ethic. We almost immediately became friends inside the lab and right away I was able to tell that he was a high-quality researcher. I am glad that I spent the time training John because I can tell he will make good use of it and will be very successful. Throughout the years I have had quite a few undergraduates working with me and along-side me including Jorge Martinez-Gonzalez, Sachin Deepak, Cosme Sandoval, Jesus Valdez, Addican Hatch, Jennifer Tena, Anthony Del Cid, Annmarie Dominguez, and Katelyn Murphy. Each one of them was great help and became great friends to me. A special mention to Jorge, Sachin, and Cosme since they were the ones who made the biggest impact on my life. Jorge is probably one of the only people who has earned a lot of respect from me as a researcher. By far he has one of the strongest work ethics that I have ever seen. I clearly remember that if I needed a task completed, I could just pass it onto him and consider it done. Sachin and Cosme were really good friends to me, provided me with a lot of help, and it was fun having them around.

I am very grateful to have had so many great friends throughout my time at UCSC. I would like to acknowledge some of my best friends from "The CREW" which consisted of Dr. Tianyi Kou, Dr. Michael Roders, and Evan Vickers. First and foremost, I would like to thank Dr. Tianyi Kou, one of my best friends. I quickly became friends with Tianyi during our first year at UCSC. Tianyi is a very smart and caring, and I am proud to call him one of my best friends. Dr. Michael Roders and Evan Vickers were

also really great friends and we often did a lot of things together. I would also like to acknowledge quite a few friends including Dr. Dominik Safranek, Alejandro Rodriguez, David Delgadillo, Brent Linquist, Jerah Barnet, Dr. Ian Colinas, Graham Rosemann, Dr. Chad Higa, and Dr. Mauricio Rojas.

Finally, I would like to acknowledge my family, who with their love and support made it possible for me to complete my PhD. I would like to thank my mother Rosa Maria Peralta for teaching me a very strong work ethic, dedication, passion, and excellence with everything that I do. Thanks to her sacrifice and support I was able to complete my studies very comfortably. She is truly my inspiration and my all-time hero. Along with my mother, my grandmother Rosa Garcia has also helped and supported me all this time. My father Miguel Pinto has also supported me in every way that he can, and he is also one of my heroes. I also want to thank my brothers John Pinto and Franky Lopez for their friendship, emotional support, great advice and being there whenever I needed them. Last but not least, I would like to thank my beautiful fiancé and soon to be wife Ashley Calderon. I am not sure how she managed to put up with me this whole time, but I am sure glad she did. Over the years she has provided me with a lot of love and support that also made it possible for me to complete my PhD and will always be grateful for that. She is my best friend and I am extremely happy to have her in my life. I consider myself fortunate to be surrounded by so many people who care for me. It is impossible for me to imagine me being able to complete such difficult task on my own and I am very grateful for everyone that has had a part in my life and development.

Dedication

I dedicate this thesis and all my work to my mother Rosa Maria Peralta and my grandmother Rosa Garcia de Peralta. Thank you for believing in me! I love you so much!

Chapter 1. Introduction.

1.1. Theranostic Drug Delivery.

The fusion of therapy and diagnostics 'theranostics' allows for the optimization of drug-delivery and drug-efficacy in real time during the course of treatment regimens. The information obtained through the use of theranostics delivery systems may then allow physicians to take treatment decisions in efforts to improve on patient safety, therapeutic outcomes, and/or identify patients that do not respond to the treatment. The use of light as a remote-triggering mechanism for drug delivery is growing at a rapid pace throughout a variety of fields in efforts to control drug delivery, leading to the personalized treatments and medicine. Photo-triggered theranostics facilitate the guided delivery of therapeutics for a variety of personalized solutions through imaging modalities (Figure 1.1). In addition, the diagnostic properties of these systems may also be used to determine the extent of drug delivered to a target tissue. The use of theranostic systems for the delivery of carbon monoxide (CO) and silver will be discussed in sections 1.2 and 1.3 respectively.

1.2. Carbon Monoxide, Remote Release, and Theranostic Delivery.

1.2.1 Background on Gasotransmitters.

Gasotransmitters are small gaseous signaling molecules characterized by their endogenous production, having specific cellular/molecular targets and well-defined physiological functions.[1] Some of the gasotransmitters identified include nitric oxide
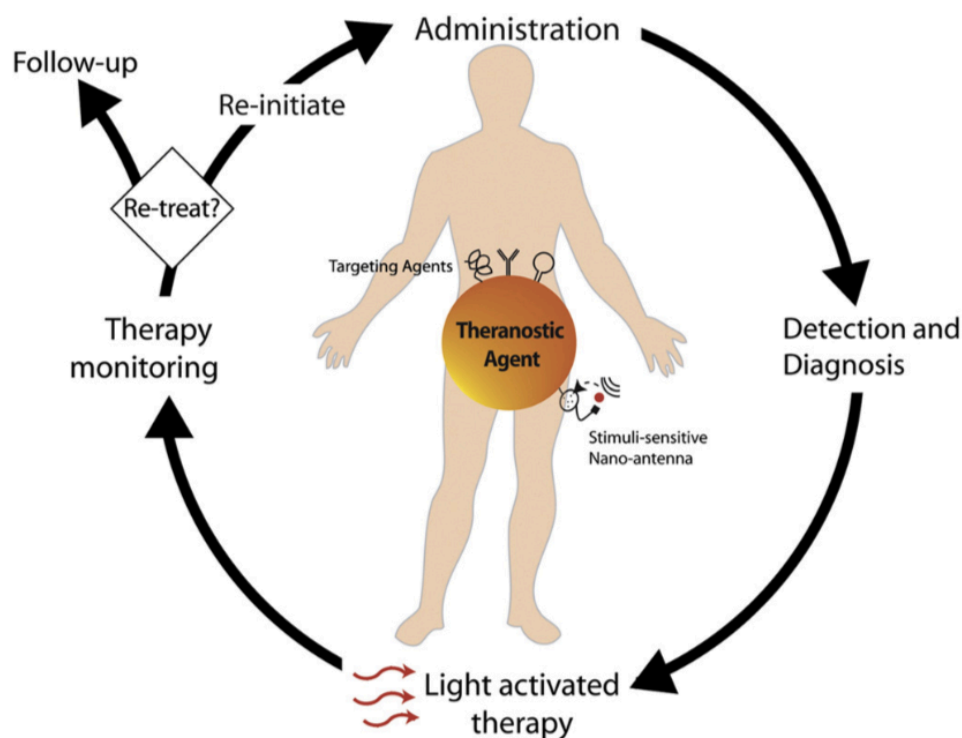
Figure 1.1. Photo-triggered theranostic chemotherapy. Figure reproduced with permission from *Advanced Drug Delivery Reviews* **2010**, *62*, 1094-1124.

(NO), carbon monoxide (CO), hydrogen sulfide (H_2S), carbonyl sulfide (COS), and sulfur dioxide (SO_2).[1-8] A wide variety of biological response can be stimulated through precise administration of these molecules within specific targets in efforts to mimic their natural roles. In addition, exogenous administration of gasotransmitters may serves as a viable method for eliciting desired biochemical responses. However, gasotransmitter therapeutic application is limited by their physiochemical nature, reactivity, half-life, and/or toxicity. Therefore, their precise and localized delivery is the predominant challenge surrounding their clinical use. Several passive and active methods have been developed for the local delivery of these noxious agents to cellular

2

targets or tissues. Targets of these biodynamic gases are often constitutively expressed throughout the mammalian body. Systemic administration of therapeutics is burdened by problems associated with poor selectivity. Often, pharmacological targets are constitutively expressed in both healthy and diseased tissues,[9] creating difficulties in achieving the selectivity required for a successful treatment. The affinity of a drug towards unintended targets may result in the manifestation of potentially severe side effects and toxicity. Decreasing therapeutic doses to non-toxic/tolerable levels often narrows the therapeutic window, reducing the drug's efficacy at the intended target site.[10] Delivery of therapeutics with spatial and temporal control allows for the minimization of systemic toxicity and non-specificity of conventional systemic administration routes.[11,12] Attractive approaches for controlling drug activity include the utilization of external stimuli to 'trigger' the release of the therapeutic from a biocompatible molecular-switch, device, or carrier. Remotely-triggerable delivery systems can be used for the precise modulation of drug doses in real time, tailoring the treatment to an individual patient.[12-14] Regulating the release of bioactive compounds at the desired site through the use of *photoactivatable* delivery systems is one attractive method for reducing off-target activity. Light offers a "great degree of orthogonality" towards most chemical and biological components and can be used as a minimally invasive stimulus for the delivery/release of therapeutics with spatiotemporal resolution.[15] Methods that incorporate the use of light for medical treatment include photopharmacology,[15-17] photodynamic therapy,[18-20] optogenetics,[21-23] and photorelease of small molecules.[23-27] Therefore, the delivery of these molecules in

3

small and moderate doses at the precise location is required for eliciting desired therapeutic effects.

1.2.2 Carbon Monoxide.

Carbon monoxide is a signaling molecule with well-defined biological functions, produced throughout the mammalian body by degradation of heme by heme-oxygenase.[28] Unlike the other gasotransmitters, CO is physically and chemically inert and can essentially diffuse into all compartments of the cell and has exclusive affinity towards low-valent 'soft' metal centers in heme proteins.[2] Endogenously produced CO regulates heme protein activity, eliciting biochemical responses and promoting signaling cascades that can influence the modulation of other non-heme proteins.[29,30] Besides its natural roles, CO has implications in neurodegeneration, hypertension, inflammation, oxidative stress, organ transplantation, apoptosis, and cellular proliferation.[2,31] Exogenous delivery of CO is a viable method for the modulation of a variety of biochemical responses (Figure 1.2).

1.2.3 Carbon Monoxide and Cancer.

In addition to its natural roles, moderate doses of exogenous CO can produce salutary effects on normal cells. However, at these same concentrations, delivery of exogenous CO at moderate local doses has shown to decrease chemotherapeutic resistance[32-35] and/or produce pro-apoptotic/anti-proliferative effects on several cancer cell lines[25,26,36-38] by expediting their metabolic exhaustion through an "anti-Warburg"

effect.[35] A variety of studies have demonstrated that cancer cell treatment with exogenous CO results in increased intracellular reactive oxygen species (ROS). Glutathione (GSH) and its disulfide-oxidize form (GSSG) are the most abundant and ubiquitous redox couples inside the cell.[39] Their ratio (GSH/GSSG) is often used as a measure of cellular antioxidant capacity and redox homeostasis.[39,40] An increased GSH/GSSG ratio can protect cells from apoptosis[39] and promotes resistance against chemotherapeutics that induce ROS as their mechanism of action, such as doxorubicin and paclitaxel.[41-43] In addition, GSH and metallothionine (MT) react readily with platinum drugs to form stable complexes such as cisplatin, decreasing its efficacy and leads to drug resistance.[44] GSH and MT biosynthesis in cancer cells is highly dependent on cystathionine β-synthase (CBS). Experiments have demonstrated that CO inhibits CBS bioactivity in certain cancer cells, leading to a decrease of intracellular GSH and MT. Overall, inhibition of CBS bioactivity through exogenous CO delivery leads to a reduction cellular antioxidant capacity. A reduction in antioxidant capacity hinders the ability of cancer cells to cope with increasing levels of intracellular ROS and potentiates chemotherapeutics that rely in the generation of ROS as their mechanism of action.[33,34] It is also understood that exogenous delivery of CO also results in the inhibition of cytochrome c oxidase (CCOx) and leads to the production of mitochondrial ROS.[45,46] Disruption of the sensitive balance between antioxidant proteins and ROS in cancer cells is a viable and common chemotherapeutic strategy.[39,46-48] Nonetheless, all hemeproteins are potential targets for CO. It is therefore
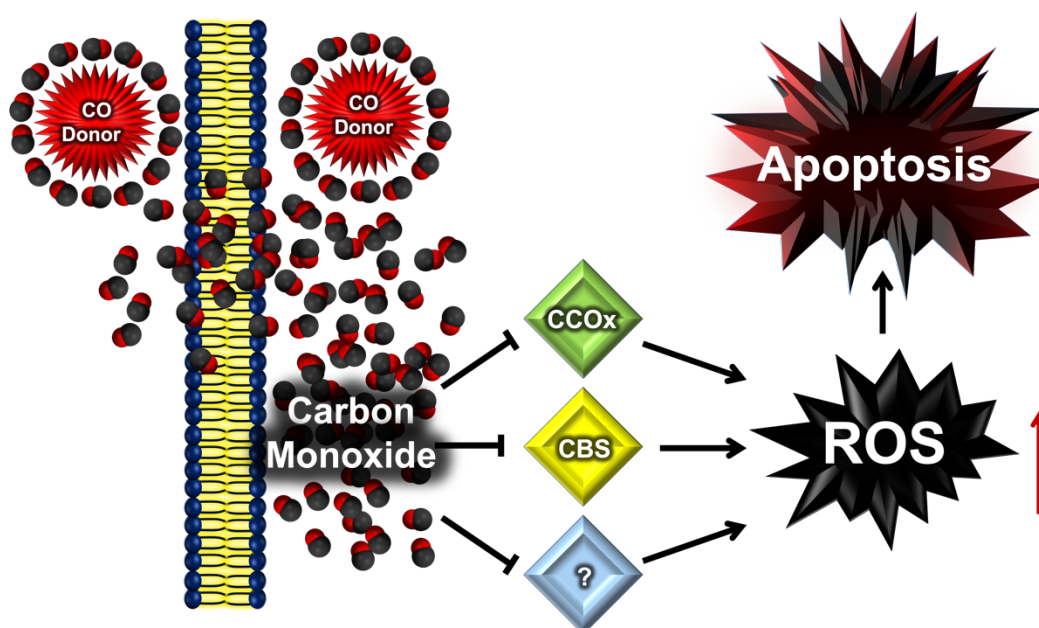
Figure 1.2. Schematic representation of CO-induced inhibition of cytochrome.

difficult to attribute the observed chemotherapeutic effects to the modulation of a single biochemical pathway. It is necessary to determine the individual/isolated contributions from CO-induced inhibition of oxidase (CCOx), cystathionine β-synthase (CBS) and/or other hemeproteins that result in increased levels of reactive oxygen species (ROS) and lead to apoptosis.

1.2.4 Controlled Delivery of Carbon Monoxide Cancer Cells.

The problem one encounters when using CO for its therapeutic effects it's the site-specific delivery of this gas in a controlled and dependable manner. Exposures to high levels of CO gas for prolonged periods of time may accentuate its negative effects and toxicity. Inhalation is not a viable method for increasing concentrations of CO at a

specific site due to its widespread interactions throughout the body. Controlling the delivery of CO can be achieved through a variety of passive and active methods including the use of CO-releasing molecules (CORMs). First-generation metallic CORMs passively release CO into their surrounding medium through ligand exchange with organic solvents.[49] Other passive CO-delivery methods include a wide variety of elegant prodrugs that release CO through enrichment[50] or endogenous triggers and do not-require any external inputs.[38,51-53] Passive delivery of CO using these systems is attractive due to the minimum involvement required for treatment, increasing patient compliance. However, certain CO therapies may require precise delivery of this gas in a deliberate and quantitative manner. On-demand and localized release of CO with spatiotemporal control requires the use of remotely controlled stimulus, such as electromagnetic irradiation. Generally, light is the trigger most extensively for the release of CO due to its precise modulation and low toxicity.

1.2.5 Photoactivated CO Releasers.

Photoactivatable CO-releasers (photoCORs) utilize light as the external trigger for the activation of the CO-releasing event.[27,54-57] PhotoCORs systems based on molecules, nanocarriers, or materials have been used for the delivery of CO to biological targets with spatial, temporal, and dosage control (Figure 1.3). The precise delivery of CO can be achieved by modulation of photoCORM concentration, irradiation time/intensity, and area illuminated. Each CO-donor is sensitive to a specific set of wavelengths with ranges between the ultraviolet to near-infrared regions. The

first set of photoCORMs identified consisted of metal-carbonyl complexes that required high-intensity ultraviolet (UV) irradiation for CO photo-uncaging.[51] However, the poor tissue penetration and toxicity associated with the use of UV-light renders these photoCORMs unsuitable for *in vivo* applications. Biocompatible photoCORMs that can be activated using lower-energy wavelengths are highly desirable. A considerable amount of visible-light active CO-donors have been reported and used for diverse biological experiments. The chemotherapeutic effects, mechanisms of action, and biological functions of CO have been extensively studied using visible-light active CO-donors. However, the limited tissue penetration of visible light also restricts their therapeutic use to light accessible surfaces. CO delivery to deeper tissues requires the
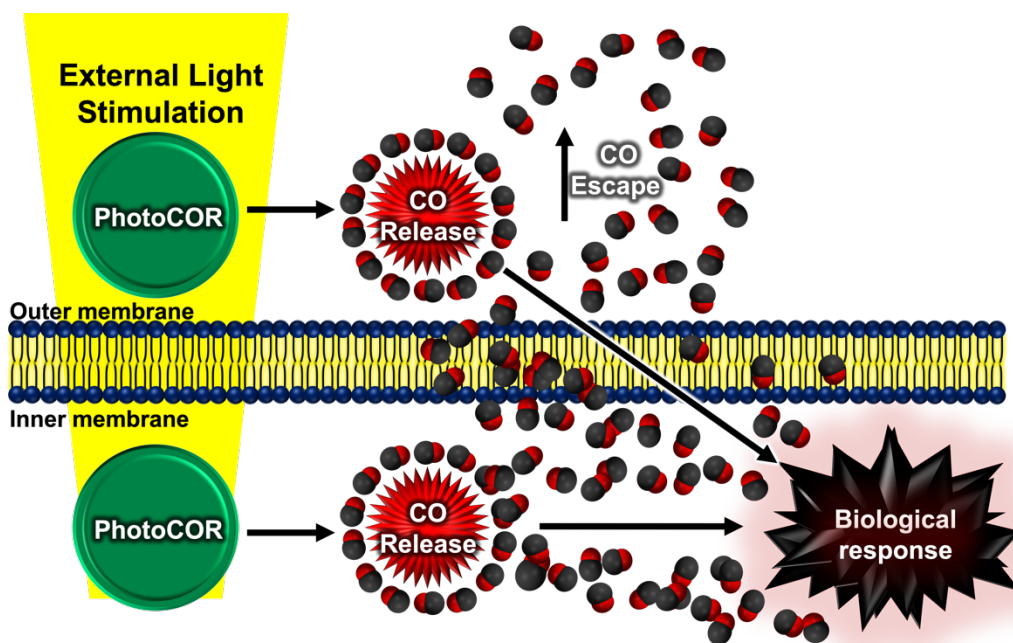
Figure 1.3. Schematic representation photoactivated delivery of CO from a photoCOR system inducing biochemical responses.

photo-release of CO using wavelengths in the NIR optical window (700 nm – 1100 nm).[37] NIR light is able to reach tissue depths of up to ~10 cm.[58] However, NIR-light intensity decreases as a function of depth due to tissue absorption and scattering. Therefore, the photo-uncaging of CO within deep tissues would require the use of photoCORMs possessing exquisite NIR-sensitivity. Other options for deep tissue CO-release include the use of carrier materials with large NIR-absorption or two-photon cross sections. These materials can then serve 'antennas', redirecting the absorbed energy to the photoCORM in the form of upconverted emission or heat, resulting in CO release.[27] NIR-responsive nanomaterials coupled to CO or CO-donors have been used for heat-induced hyperthermia and CO-release *in vivo*. Alternatively, the photorelease of CO in NIR-light inaccessible cavities/tissues can be controlled remotely with optical fibers using minimally invasive procedures. The chemotherapeutic effects of photodelivered CO to cancer cells/tissues using photoCORMs and CO-releasing materials are discussed in detail in the following sections.

1.2.5.1 UV-Light Active PhotoCORM Systems.

CO can be released using ultraviolet irradiation from essentially any photoCOR system. However, a large number of photoCORs can only be activated using UV irradiation (200 – 400 nm). A wide variety of UV-light active photoCOR molecules (photoCORMs) with a broad range of structural and metal variation have been used for delivery of CO for biological applications. Metallacycle-based manganese

photoCORMs **1 – 5** (Figure 1.4) have been used extensively for the eradication of various cancer cells *in vitro* and for studying the chemotherapeutic effects of CO.[59-64] Some of these complexes possess potent antineoplastic effects and are promising CO-releasing systems for the delivery of CO in vitro. A dinuclear metallacyclophane carbonyl complex **2**[60] was used to investigate in detail some of the effects that photodelivered CO exerts on cancer cells.[61] The cytotoxicity profile of this complex was first evaluated against lung (A549), colon (HCT-15), cervical (HeLa), and breast (MDA-MB-231) cancer cells using MTT assay. The IC_{50} values obtained were 24.12±1.03, 21.89±0.59, 21.37±1.72, and 13.69±0.91μM for A549, HCT-15, HeLa, and MDA-MB-231 respectively. CO-photodelivery produced morphological changes in the cancer cells indicative of apoptosis, including cell shrinkage/deformation, condensation of chromatin, and blebbing. The condensation and fragmentation of chromatin was observed in confocal micrographs using AO/EB stains. Increased levels of superoxide and reactive oxygen species (ROS) were detected *via* confocal microscopy and flow cytometry respectively. A decrease in mitochondrial membrane potential was determined using rhodamine 123 *via* flow cytometry and the expression of specific apoptotic protein markers were quantified using Western blotting techniques. The collective findings suggest that treatment of these cancer cell lines with photoreleased CO results in the accumulation/increase of intracellular superoxide/ROS, resulting in the decrease of the mitochondrial membrane potential, and ultimately culminating in apoptosis (Figure 1.5).[61] Other noteworthy light-

triggerable CO-donors based on bridged dinuclear-manganese (complexes **3**[62] and **4**[63])

or -rhenium (complex **5**[64]) metallastirrups have also been investigated as anticancer

agents against a variety of cancer cell lines.
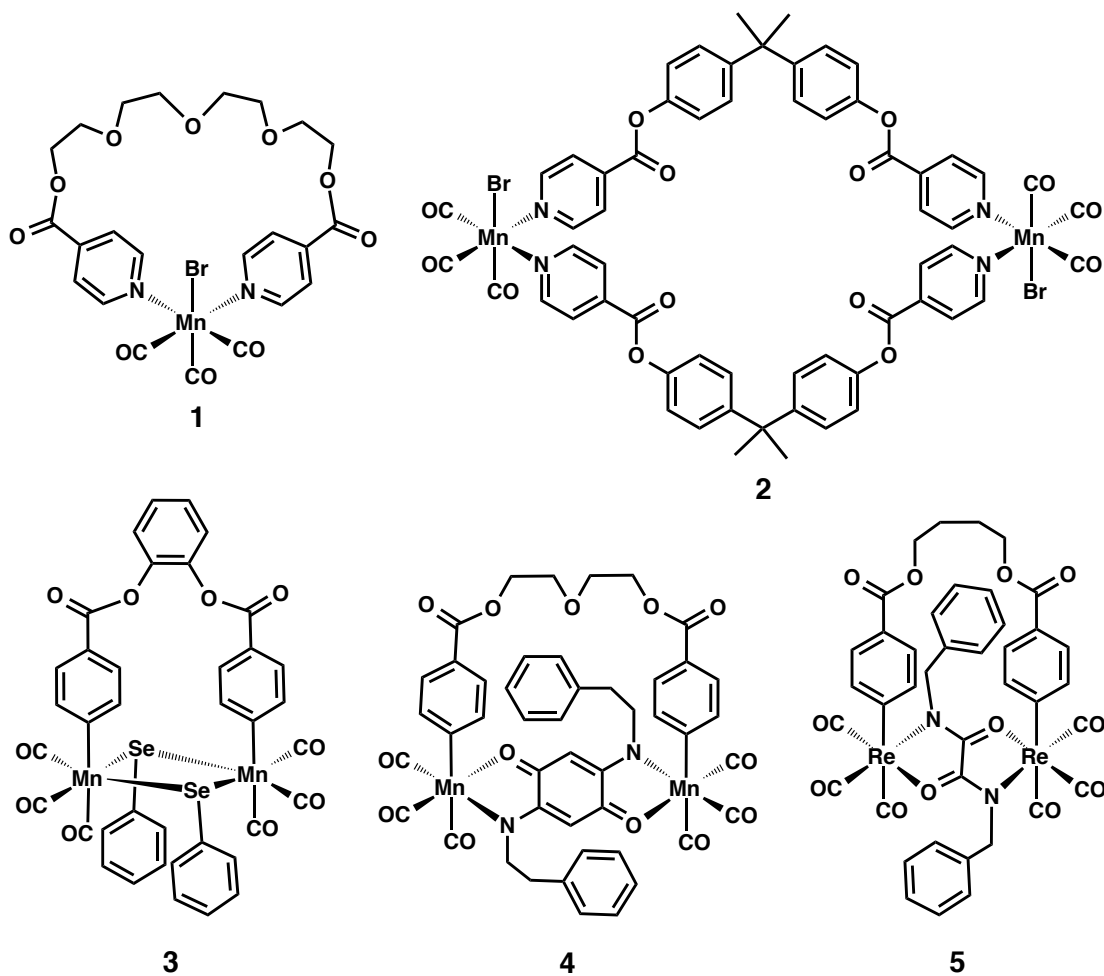
Figure 1.4. Examples of UV-active metalacyclic photoCORMs used CO-delivery to

cancer cells.
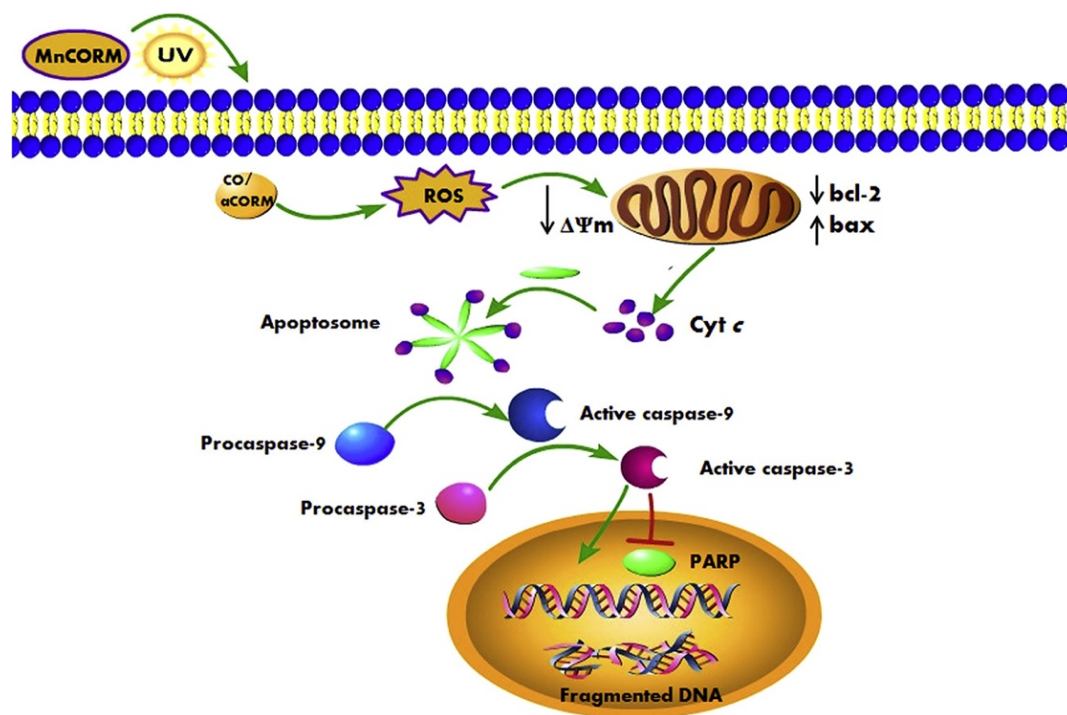
Figure 1.5. Schematic representation of action of photoCORMs. Figure reproduced with permissions from *J. Photochem. Photobiol. B Biol.* **2018**, *188*, 28-41.

1.2.5.2 Visible-Light Active PhotoCORM Systems.

Facially disposed carbonyl manganese complexes bearing conjugated bidentate ligands have low lying LF states that can be populated using wavelengths in the visible range, promoting CO-labilization.[27] One of the first visible active photoCORMs used to deliver CO to cancer cell lines was derived from 2-phenylazopyridine, a non-luminescent ligand.[65] The resulting complex **6** (Figure 1.6) exhibited a strong metal to ligand charge transfer (MLCT) band centered at 586 nm. Studies were performed using a 525 nm filter that blocked shorter light wavelengths, indicating that excitation of this MLCT band resulted in CO-labilization. The phototoxicity of this complex was

investigated against cervical (HeLa) and breast (MDA-MB-231) cancer cells. Treatment of cells with photoreleased CO produced a dose-dependent reduction in metabolic activity and the reduction in cell viability at 75 μM (~42%) was comparable to that of the 5-fluorouracil (5-FU; 10 μM) control. CO-treatment induced morphological changes indicative of apoptosis in both cell lines, detected *via* confocal microscopy. Dark control experiments did not exhibit significant reduction in metabolic activity at the highest concentration tested (120 μM, ~14%). This indicates that visible light active photoCORMs are promising tools for monitoring the effects of CO *in vitro*.

1.2.5.3 NIR-Light Active PhotoCORM Systems.

Several elegant photoCORMs have been synthesized with activation wavelengths in the near-infrared (NIR) optical window (~700 nm – 1100 nm).[66-70] The low absorbance of hemoglobin and water in this region allows NIR-light to penetrate deep into soft tissue (up to 10 cm).[58] Nevertheless, tissues indeed absorb and scatter photons with energies in the NIR optical window and therefore the intensity of the incident light decreases as a function of depth. In addition, exposure to prolong and/or high levels of NIR irradiation may cause ulcerations in tissues.[13] Hence, deep-tissue CO photodelivery using NIR light requires the use of exceptionally sensitive photoCORMs with strong absorption in the NIR range. Deep tissue CO-release may also be accomplished using systems where the CO-donors are conjugated to a NIR photosensitizing antenna.[27,71-74] A variety of NIR sensitive photoCORMs **7** – **10** (Figure

1.6) have been reported in the literature,[66-70] but none have been used for the delivery of CO to cancer cells.
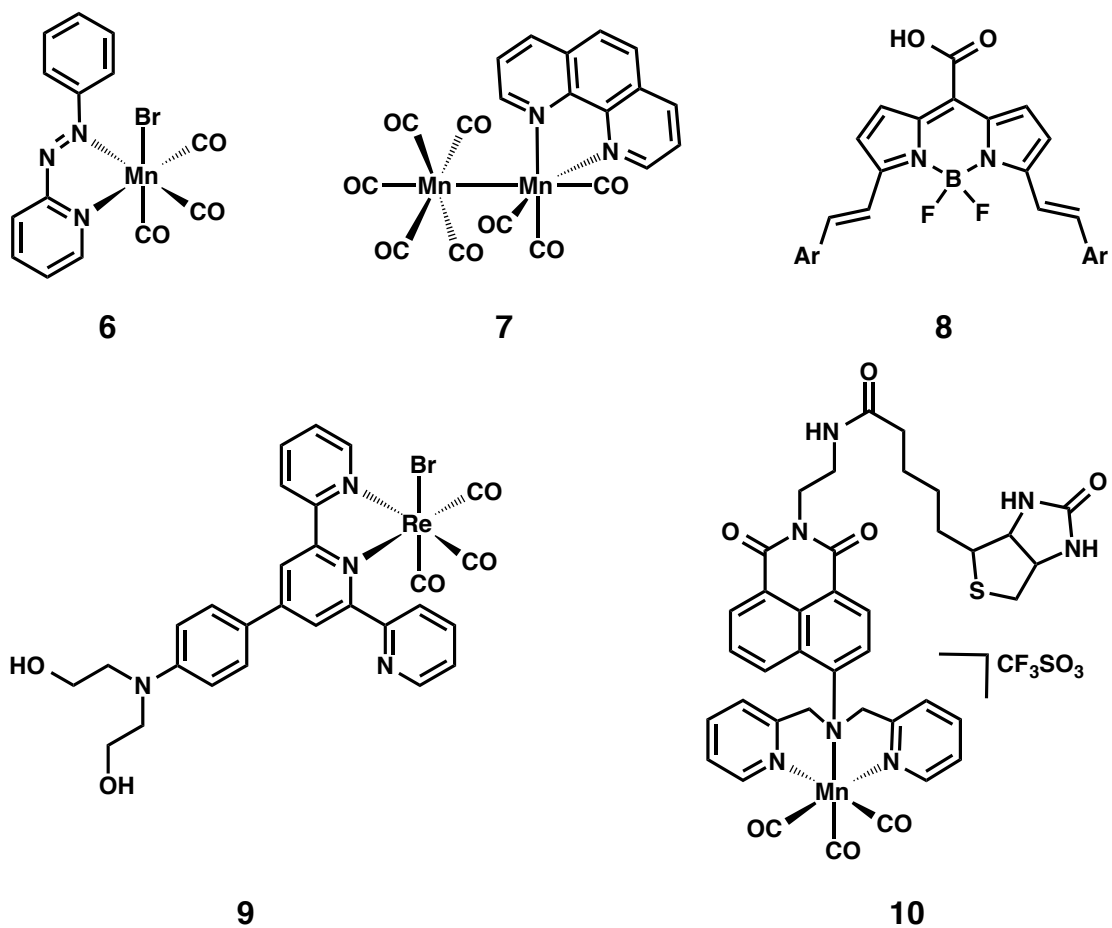
Figure 1.6. Visible light active photoCORM **6** and NIR-active photoCORMs **7 – 10**.

1.2.5.4 Non-Metal photoCORMs.

Non-metal photoCORMs are attractive systems to delivery CO to biological targets (Figure 1.7).[57,75,76] Visible light active photoCORMs derivatives of 3-hydroxyflavone (3-HflH) were used to deliver CO to a variety of human cancer cell

lines.[77] The naturally occurring parent structure 3-HflH possess anti- inflammatory, antioxidant, and anticancer activity,[76,78] therefore an excellent candidate for biological applications. Extending the conjugation of these derivatives red-shifted their absorbance with respect to the parent compound, allowing for the CO-release under visible-light illumination. The CO-donors **11** and **12** (Figure 1.7) were selected for biological experiments due to its low toxicity, its bright luminescence and non-emissive photoproduct. Treatment of A549 photoCORMs **11** and **12** produced an IC_{50} values of 76.1 $\pm$ 5.2 μM and 4.6$\pm$3.6 μM respectively under illumination. The photoproduct(s) of these compounds did not produce significant toxicity on A549 cells or normal human umbilical vein endothelial cell (HUVECs) controls. On a subsequent account, the photoCORMs **13** and **14** derived from the 3-hydroxybenzo[*g*]quinolone was used for CO-delivery to a panel of cancer cell lines *in vitro*.[76] The absorption band of these molecules were centered well within the visible range at 449 nm and CO-release was readily achieved upon visible light illumination (465 nm). A549 cancer cells treated with these photoCORMs resulted in a strong reduction of metabolic activity with IC_{50} values of 24 μM and 50 μM for **13** and **14** respectively. It is noteworthy to mention that the photoproducts did not produce detectable toxicity when tested at the IC_{50} concentrations of their respective fresh CO-donors in all of the conditions tested. Taken together these results suggest that the non-metal photoCORM are excellent CO-donors.
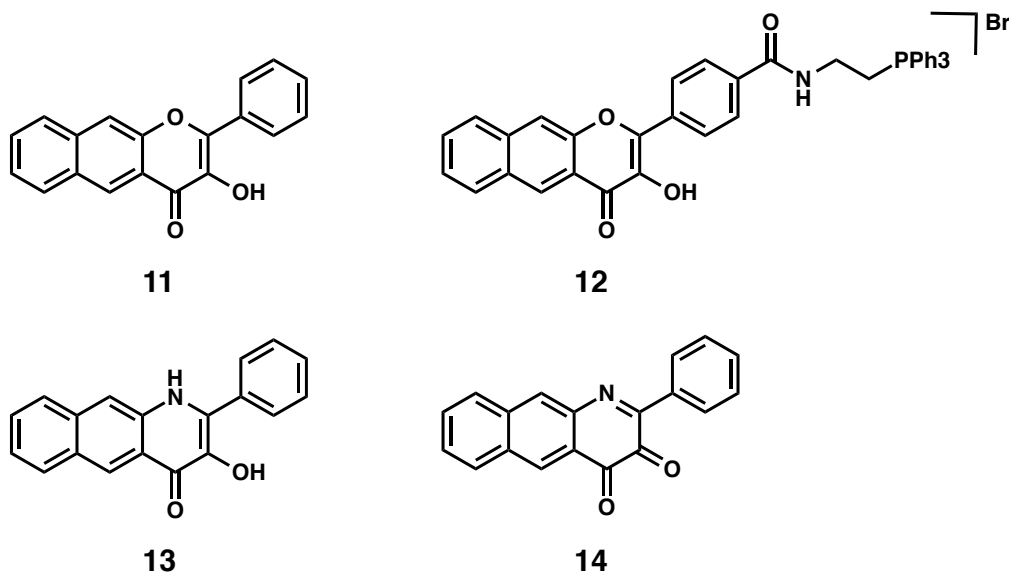
Figure 1.7. Representative example of metal-free CO-donors used for CO-delivery to cancer cells.

1.2.6 Theranostic CO Delivery.

Tracking CO-release within cancer cells can be achieved in a number of ways including monitoring the changes in luminescence of the photoCORM itself,[77,79-81] and/or its photoproduct(s)[82-84] (Figure 1.8). The ability to photorelease CO while simultaneously tracking the CO-prodrug and/or photoproduct(s) classifies these types of photoCORMs as theranostic (therapeutic and diagnostic) delivery systems. The non-metal photoCORMs described above (Figure 1.7) possessed inherent fluorescence which decreased upon photolysis. These properties allowed for tracking the CO-prodrug within the cancer cells and subsequent CO release was monitored through "turn-off" luminescence (Fig. 1.8, green arrow). Facially disposed tricarbonyl

rhenium(I) complexes are attractive CO-donors systems due to the inherent luminescence arising from the excitation of their metal-to-ligand charge transfer
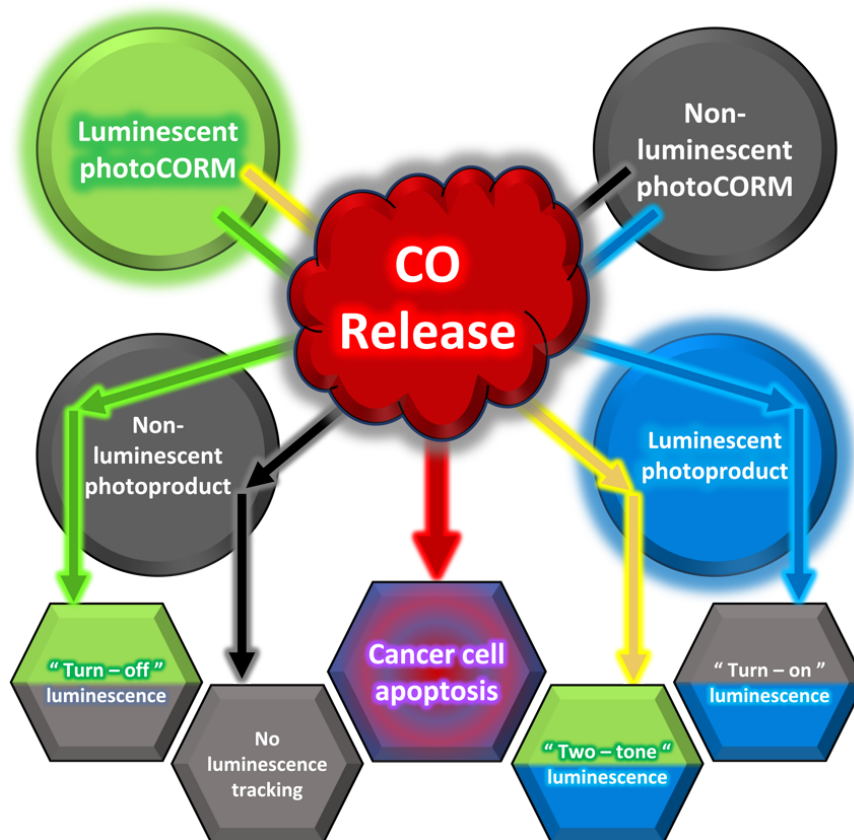
Figure 1.8. Theranostic luminescence tracking of CO-delivery. Turn off luminescence (green arrow); "Two-tone" luminescence (yellow arrow); "Turn-off" luminescence (Blue arrow); No luminescence tracking (black arrow).

(MLCT) bands. When coupled to fluorescent ligands, only the luminescence of the Re- complex is observed. However, an increase in luminescence corresponding to the chelating ligand can be realized after CO-photodissociation. This "two-tone" luminescence (Figure 1.8, yellow arrow), observed between a Re-complex and its

photoproduct, can be used to visualize the internalization of the photoCORM and subsequent CO-release within cellular matrices. A Re(I)-based photoCORM **15** (Figure 1.9) bearing a luminescent 2-(pyridine-2-yl)-benzothiazole (pbt) bidentate ligand was used to monitor CO-delivery to breast cancer (MDA-MB-231) cells *in vitro*.[80] Breast (MDA-MB-231) cancer cells were treated with **15** (50 μM) for 3 h and irradiated for 0 to 28 min (302 nm; 0.35 mW cm^{-2}) or 0 to 20 min (302 nm; 0.12 mW cm^{-2}) for confocal microscopy and flow cytometry respectively. Confocal micrographs and flow cytometry measurements were recorded at each time points. The results indicated that the luminescence intensity of the photoCORM decreased while the intensity of photoproduct(s) increased in an irradiation-time dependent manner. The CO-induced toxicity on the breast cancer cells was assessed after CO delivery *via* MTT assay. The results indicated that the cells exhibited CO-induced toxicity in an irradiation-time dependent manner, with over 47% reduction in viability when illuminated for 28 min. Control experiments exhibited insignificant reduction in viabilities under dark conditions. The nature of CO-induced cell death was then investigated *via* flow cytometry using Annexin V-fluorophore conjugate. Breast cancer cell populations treated with photoreleased CO exhibited an increase in annexin V binding, suggesting CO-induced apoptotic cell death. It is worth noting that Re(I)-based photoCORMs require high energy wavelengths (UV or near-UV) to populate the metal centered ligand field (LF) states that lead to CO-photodissociation.[27] The high photostability of Re(I)-based photoCORMs allow for their tracking within cellular matrices, but often result in a slow CO-release rate. Structurally analogous manganese complexes have

been used to carry out the CO-delivery task under the control of visible light, and at a much faster rate than their rhenium counterparts. On the other hand, manganese complexes have poor inherent luminescence, and therefore luminescent rhenium structural analogs were used to evaluate their internalization within cellular matrices.

Mn(I)-based photoCORMs generally do not exhibit inherent luminescence and often partially quench the fluorescence of the chelating ligands.[82,83] Upon illumination, however, the release of CO may be accompanied with an increase in luminescence that corresponds to the fluorescent ligand. The location of the photoproduct(s), and therefore the CO-releasing event, can then be determined using this "turn-on" luminescence (Figure 1.8, blue arrow).[82,83] Monitoring the delivery of CO to MDA-MB-231 cells *in vitro* through "turn-on" luminescence was accomplished using the Mn(I) carbonyl complex **16**, a structural analog of **15** (Figure 1.9) with the exception of the metal center.[82] The fluorescence of pbt was dramatically quenched upon complexation to Mn but subsequently restored upon photolysis, allowing for the visualization of the photoproduct(s) *via* confocal microscopy. CO-induced toxicity was investigated by treating the cells with the complex **16** (Figure 1.8) and irradiated with low-power visible-light (15 mW cm^{-2}) for 45 min. The results of the MTT assay indicated a dose dependent reduction in viability upon treatment. Using "turn-on" luminescence to monitor the delivery of CO to cancer cells was also demonstrated using a manganese photoCORM **18** (Figure 1.8) bearing a tridentate fluorescent ligand.[83] In a similar fashion, the fluorescence of the chelating ligand was partially quenched upon complexation to the Mn metal center and returned after CO photo-uncaging. CO-

induced phototoxicity of this complex was investigated against a panel of malignant

cell lines and viabilities were assessed using a sulforhodamine B (SRB) assay.
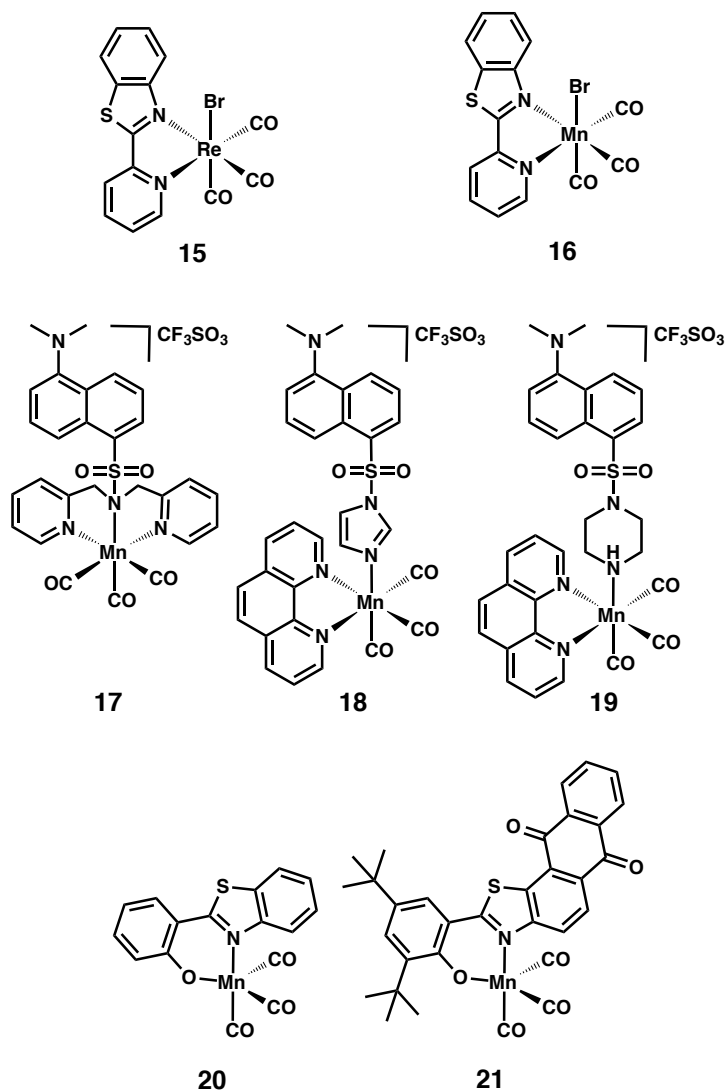
Figure 1.9. Luminescent rhenium (**15**) and manganese (**15 – 21**) metal complexes for

theranostic delivery of CO to cancer cells in vitro.

In general, cancer cells exhibited a decrease in viability upon treatment with

photoreleased CO when compared to their respective dark control experiments. It is

important to note, that the non-cancerous MRC-5 and HepaRG cell controls exhibited relatively low toxicity upon treatment with the complex under any of the conditions tested. Overall, these types of photoCORMs are attractive systems for elucidating the effects of CO in cancer cell lines *in vitro*.

Attachment of fluorescent chelating ligands at the axial position of the manganese complex through the use of spacers is one method used to decrease the observed quenching. Two visible-light active and luminescent photoCORMs were synthesized by axially coordinating the fluorophore to the metal center through conjugated **18**[85] or unconjugated **19**[86] linkers (Figure 1.9). The CO-donors were tracked within cellular matrices through luminescence and CO was delivered to colorectal adenocarcinoma (HT-29) cells under the control of visible light. The cells were treated with photoreleased CO from these complexes and viabilities were assessed using MTT assay. The IC_{50} values for these luminescent CO-donors were found between 80 and 100 μM and cell viabilities of ~47% at the highest concentrations tested (100 μM). Control experiments exhibited reduction in viabilities $\leq$ 7%, suggesting the complexes or their photoproduct(s) were non-toxic in the timeframe of these experiments. No significant toxicity (<10%) was observed in normal human embryonic kidney (HEK-293) cell controls under any of the conditions tested. The luminescence of these complexes allowed for the visual tracking of the CO-donors within cancer cells *via* confocal microscopy. However, subsequent release of CO could not be determined due to the lack of luminescence change upon CO photodissociation. Taken together these results indicate that these types of complexes are useful to visualize the cellular

internalization of manganese photoCORMs, whereas previously a Re-analog had to be employed.

A family of penta-coordinated manganese carbonyl complexes that exhibit interesting changes in luminescence upon CO photorelease was recently described.[84] The complexes consisted of a luminescent benzothiazole or benzimidazole bidentate ligand and three facial CO molecules in a calculated trigonal bipyramidal coordination geometry (Figure 1.9). Complex **20** exhibited "turn-on" luminescence centered at 420 nm upon photolysis in a similar manner as previous reports.[82,83] However, complex **21** exhibited inherent luminescence with emissions centered at ~410 nm and ~600 nm, unlike previous reports. In addition, photolysis of **21** resulted in a decrease of the emission intensity centered at 410 nm and a moderate increase in the emission centered at 600 nm. Visual discrimination between the intact complex and its photoproduct(s) allowed for the qualitative tracking of CO-release through "two-tone" luminescence (Fig. 1.7, yellow arrow). The phototoxicity of the reported complexes was investigated against HeLa cells *in vitro*. The cells were incubated with the complexes for 4 h and then exposed to visible light to induce CO release and viabilities were assessed using MTT assay. The complexes exhibited a decrease in viability in both dose- and irradiation-time dependent manner. IC_{50} values for these complexes were ~32.39 µM whereas control experiments exhibited values of >50 µM. The "two-tone" luminescence between **21** and its photoproduct were analogous to what was only observed using rhenium complexes **15** (Figure 1.9).[80] Unlike rhenium complexes, however, **21** releases CO under the control of visible light. Collectively these results

suggest that these type of trigonal bipyramidal Mn-based photoCORMs may be useful for the visual tracking and delivery of CO to cellular targets.

1.2.7 Water Soluble PhotoCORMs.

The vast majority of reported cellular treatments involving photoCORMs require the use of organic co-solvents to solubilize the CO-donor. Increasing the water-solubility of CO-donors circumvents the need for organic solvents, thus making the delivery system more biocompatible. Approaches to increases photoCORM hydrophylicity include the use of ligands bearing functional groups with hydrogen bonding capabilities.[87-90] A family of luminescent rhenium complexes bearing water-soluble phosphine ligands (Figure 1.10) were used for the delivery of CO to cervical cancer (HeLa) cells under the control of UV-light.[91] Several of the Re photoCORMs described were able to photosensitize the formation singlet oxygen ($^1O_2$) in addition to CO-release, augmenting the photochemotherapeutic effect. HeLa cells were incubated with PBS solutions (0.01 – 200 μM) of the Re(I) complexes for 4 h and irradiated at 365 nm for 1 h (photon flux = $2.38\pm0.31 \times 10^{-10}$ einstein s^{-1}). MTT assay results indicated that most of the Re(I) complexes displayed strong photoinduced toxicity and IC$_{50}$ values ranged between 5.9 ± 1.4 μM and 68.0 ± 4.3 μM. The phototoxicity of the most potent complex **22** was further investigated against A2780 (ovarian) and A2780CP70 (cisplatin-resistant ovarian) cancer cell lines using the same protocol. MTT assay results indicated that **22** produced IC$_{50}$ values of 2.2 ± 1.1 μM and 3.2 ± 0.7 μM under UV-illumination for A2780 and A2780CP70 respectively. The negligible difference in IC$_{50}$ in the resistant cell line suggests that the toxicity induced by CO

circumvents the cisplatin-resistance pathways. The composition of the photoproduct **23** of complex **22** was carefully determined and its isolated cytotoxic contribution was independently investigated. HeLa cells treated with **23** exhibited similar reductions in viability under dark and illumination conditions, comparable to the cytotoxic responses obtained while using photolysed solutions of **22** ($IC_{50} > 50$ μM). HeLa cells were also treated with **22** under hypoxic conditions in efforts to isolate the cytotoxic contributions of photoreleased CO. A decrease in $^1O_2$ generation was expected under these conditions due to the lack of oxygen availability. The cervical cancer cells were incubated with **22** in a hypoxia chamber (95% N_2 + 5% CO_2) for 4 h and irradiated with UV-light for 1 h (365 nm). The cells were allowed to recover for 16 h under hypoxic conditions and viabilities were assessed using MTT assay. The IC_{50} produced by **22** was found to be 20 ± 1.5 μM, suggesting that indeed $^1O_2$ contributed towards the overall chemotherapeutic effect. No observable toxicity was detected in any of the cell lines treated with **22** under dark conditions making it an excellent chemotherapeutic system.
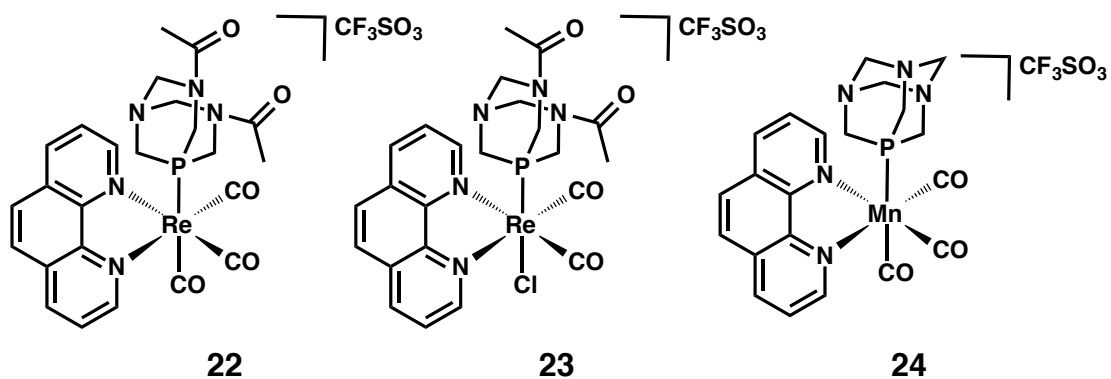
Figure 1.10. Luminescent rhenium complexes bearing water-soluble phosphine ligands for CO delivery and photodynamic therapy of cancer cells.

The anticancer effect can be attributed primarily to intracellular delivery of CO and to a lesser yet considerable extent to $^1O_2$ generation plus the release of a toxic photoproduct. Overall these findings suggest that the photochemotherapeutic effects of Re(I)-based photoCORMs may be a combination of singlet oxygen generation in addition to the photoreleased CO.

1.2.8 Photoactivatable CO Releasing Materials.

Advances in material science have led to the development of responsive macro,[92-94] micro,[95] and nano-carrier[96,97] drug delivery systems. Some materials can deliver drugs with precise spatial, temporal, and dosage-control upon activation from an external stimulus.[12,98-101] Remotely controlled drug releasing events can be triggered by temperature,[94,102-105] ultrasound,[106-109] light,[110-112] magnetic,[113-114] and electric field.[115-117] A large majority of these carriers become thermally excited upon application of the external stimulus, resulting in the release of the drug. In some cases, however, application of the external trigger results in a chemical, or physical change that results in drug release. PhotoCORMs have been incorporated into a wide variety of carriers such as peptides,[118-120] polymers,[121,122] nanoparticles,[123-129] metallodendrimers,[130] protein crystals,[131,132] micelles,[133] non-wovens,[134-136] MOFs,[137-138] polysaccharides,[139] vesicles,[140] and nanocarriers.[71-74] PhotoCORM carrier systems can be used to overcome several problems associated with CO-phototherapy, such as increasing photoCORM solubility and trapping photoproduct(s) after CO delivery reducing their toxicity. A large number of nanocarrier systems can be used to take

advantage of the enhanced permeability and retention (EPR) effect for the passive accumulation inside tumor tissues. Some of these materials can also be functionalized to target specific sites or can act as antennas that stimulate the release of CO.

A wide variety of polymers carriers have been used for the transport of CO-donors[141,142] and delivery of CO to cancer cells under the control of light.[121] One approach to assemble a polymer-photoCORM conjugate is to construct a coordination site within the polymeric matrix and subsequently complexing a carbonyl metal center. An early report described the use of a tridentate chelating ligand (bpmea; bis(pyridinemethyl)ethanolamine) tethered to a polylactide backbone which was then copolymerized with monomers of 2-hydroxypropyl methacrylamide to produce a polymeric carrier P2. Reaction between the manganese carbonyl center and the tridentate-bpma appendage afforded the adduct $MnCO_3$@P2 **25** (Figure 1.11) with 2.8% loading with respect to (w. r. t.) Mn. This carrier system was then used to deliver CO to human colon carcinoma Hct116 under the control of UV-light and the resulting CO-induced cytotoxicity was assessed *via* MTT assay. Cells were incubated with a range of concentrations of $MnCO_3$@P2 in the dark for 24 h and irradiated for 40 min with UV-light (365 nm). Cells treated with **25** exhibited IC_{50} values of 50 ± 21 µg mL^{-1} under illumination and almost identical toxicity under dark conditions. Interestingly, neither P2 nor the $Mn(CO)_3$-loaded bpmea fragment exhibited any significant cytotoxicity to the cancer cells under any conditions tested. Although the results appear less than optimal, this work provided a viable method for the incorporation of photoCORMs into polymeric materials.

Another method for producing a photoCORM-polymer conjugates is by reacting available functional groups between the photoCORM and the polymeric carrier. Polysaccharides are biocompatible polymeric carriers used as drug delivery systems in a variety of biomedical applications.[143] Carboxymethyl chitosan (CMC) is
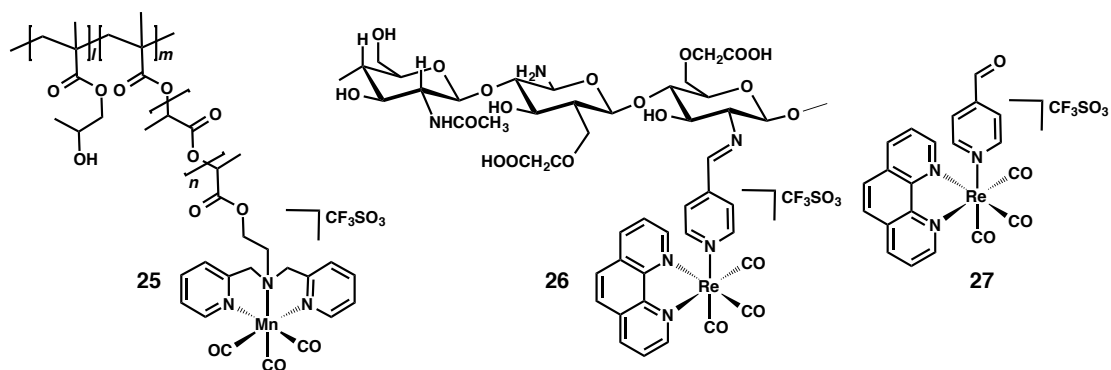
Figure 1.11. PhotoCOR systems based on polymers (28, 29).

a water-soluble polysaccharide widely used as a drug delivery system in a variety of biomedical applications for its excellent solubility, biocompatibility, and biodegradability.[144] A photoCORM-CMC composite material **26** was fabricated through a condensation reaction between free secondary amines of CMC and the aldehyde from an ancillary ligand of a rhenium carbonyl complex **27**.[139] The condensation reaction was carried out under extended reflux conditions to achieve a 12 wt. % loading of Re w. r. t. CMC. Light triggered CO-induced cytotoxicity of this material was investigated against human colorectal adenocarcinoma (HT-29) cells using MTT assay. HT-29 cells were incubated with 150 or 300 $\mu g \ mL^{-1}$ of ReCMC **26** for 2 h and then irradiated for 20 min using UV light (305 nm, 5 mW cm^{-2}). MTT assay

results indicated a 49% decrease in HT-29 cell viability under illumination (300 mg mL^{-1}), whereas control groups exhibited marginal cytotoxicity ($\leq$ 6%). Under similar conditions, HT-29 cells treated with the free rhenium complex **27** exhibited a decrease in viability of 48% (100 μM). HEK 293 normal cell controls treated under the identical conditions did not exhibit significant toxicity ($\leq$ 6%) under any of the conditions tested. The activation of caspase-3/7 in HT-29 cells was also detected *via* confocal microscopy after CO photodelivery from **27** (300 μg mL^{-1}) in an irradiation-time dependent manner. CMC is a flexible and biocompatible carrier system for the delivery of CO to cells in vitro. However, the delivery of CO to malignant tissues *in vivo* would require conjugation of CMC with visible- or NIR-active CO-donors. Nonetheless, the expected biodegradation of CMC within cellular matrices suggests that the cytotoxicity of CO-spent products must be taken into consideration.

Mesoporous silica nanoparticles (MSNs) are attractive biocompatible vehicles for the delivery of gasotransmitters to cellular targets due to their rapid internalization and minor alterations to cellular metabolism.[145,146] MSNs doped with negatively charged aluminum sites (Al-MCM-41) can be used to encapsulate photoCORMs and their photodegradation products through electrostatic interactions.[126-128] The utility and CO-donating ability of photoCORM loaded Al-MCM-41 was first investigated in rat aorta muscle rings using the UV-active Mn-photoCORM **28** (Figure 1.12).[126] After the therapeutic potential of these CO-releasers was established, Al-MCM-41 particles loaded with a cationic rhenium carbonyl complex **29** (Figure 1.12) were used to deliver CO to breast cancer cells *in vitro*.[127] The strong electrostatic interactions between the

luminescent complex and Al-MCM-41 afforded the adduct {Re-CO}@Al-MCM-41 with a 0.97±0.10 wt. % loading w. r. t. Re. MDA-MB-231 human breast cancer cells were incubated with 0.25 mg mL^{-1} of {Re-CO}@Al-MCM-41 for 3 h and irradiated with UV-light (305 nm, 5 mW cm^{-2}) for 15 min. The cells were allowed to recuperate for 4 h after treatment and then cell viabilities were investigated using MTT assay. MDA-
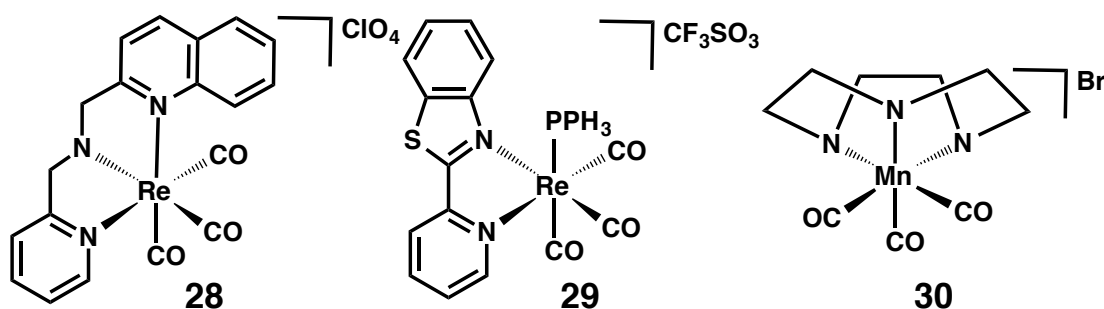
Figure 1.12. UV-active photoCORMs incorporated into Al-MCM-41 for light triggered CO release.

MB-231 cell viability decreased drastically (~80%) upon CO treatment from {Re-CO}@Al-MCM-41, whereas control groups produced marginal decreases in viability ($\leq$ 13%). The internalization of the photoCORM-loaded particles within the breast cancer cells was investigated *via* confocal microscopy by monitoring the luminescence of **29**, and CO-delivery was visualized through "turn-off" luminescence. The high photoCORM loading and efficient CO release from this material suggests that Al-MCM-41 is another promising vehicle for the delivery of CO to cellular targets. The versatility of mesoporous silica materials allows for the facile incorporation of almost

any visible- or NIR-active photoCORMs that would be required for the delivery of CO *in vivo*. Complex **30** was also incorporated into Al-MCM-41 nanoparticles along with cisplatin for their dual delivery under the control of light,[128] however their chemotherapeutic effects were not investigated.

Other interesting CO-delivery vehicles include gas-permeable bulk/macro materials. Some of these reservoir-based systems have little restrictions for the types of CO-donors used and often retain CO-spent products. Non-wovens are polymeric bulk materials commonly used in a variety of biomedical applications[147] and have also been used for the delivery of CO to cancer cells *in vitro*.[134] Manganese(0) carbonyl (Mn_2CO_{10}) **31** (Figure 1.13)was incorporated into poly(*L*-lactide-co-*D/L*-lactide) (70:30, PLA) non-wovens *via* electrospinning to afford fibers with photoCORM loading of 1 – 20 wt.% (with respect to PLA). Mouse fibroblasts (3T3) cells were incubated in the dark with the resulting CO-loaded materials for 24 h and subsequently irradiated for 15 – 60 min (365 nm, 4 mW cm^{-2}). The cells were allowed to recuperate for 1 h after treatment and viabilities were determined using GelRed® (viable-cell impermeable nuclear-stain). Confocal micrographs of CO-treated cells (60 min) exhibited pronounced changes in morphology and GelRed® nuclear staining, indicative of cell death. No significant morphological change was observed after incubation of the cells with photoCORM-loaded materials under dark conditions during the course of 4 days. On a subsequent report, **31** was incorporated into PLA non-wovens in combination with a triplet-state photosensitizer, allowing for CO-release under the control of visible light.[135] Pd(II)tetraphenyltetrabenzoporphyrin **32** (Fig. 12)
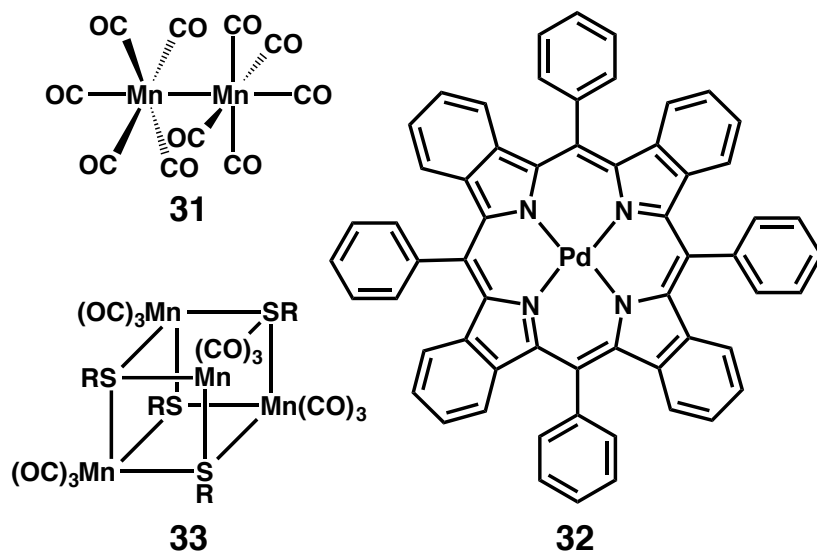
Figure 1.13. Schematic representations of UV-active photoCORMs (34, 35) and photosensitizer (35) incorporated into non-woven materials.

absorbs low-energy photons (635 nm) and reaches a singlet excited state which undergoes fast intersystem crossing to a triplet excited state. The triplet energy from this excited state can then be transferred to **31** through collisions, photosensitizing the decomposition of the Mn complex and releasing the CO. More importantly, the use of triplet-state photosensitizers is a viable approach for shifting the CO-photorelease of **31** from near UV to the visible range in solutions or solid-state devices. The high loading capacity, light sensitivity, and biocompatibility of electrospun poly(*L*-lactide-co-*D/L*-lactide) suggest this material can be used as an implantable reservoir for the delivery of CO to tissues.

1.2.8.1 NIR-Active PhotoCOR Materials for the Eradication of Cancer *In Vivo*.

The delivery of CO to deep tissues with spatial and temporal control is a challenging feat. UV- and visible-light active photoCORMs are excellent tools for studying the effects of exogenously delivered CO *in vitro.* However, their clinical applications are limited to light accessible surfaces due to poor tissue penetration of UV-visible light. Several elegant photoCORMs have been synthesized with activation wavelengths in the near-infrared (NIR) optical window (~700 nm – 1100 nm).[66-70] The low absorbance of hemoglobin and water in this region allows NIR-light to penetrate deep into soft tissue (up to 10 cm).[58] Nevertheless, tissues indeed absorb and scatter photons with energies in the NIR optical window and therefore the intensity of the incident light decreases as a function of depth. In addition, exposure to prolong and/or high levels of NIR irradiation may cause ulcerations in tissues.[13] Hence, deep-tissue CO photodelivery using NIR light requires the use of exceptionally sensitive photoCORMs with strong absorption in the NIR range. Deep tissue CO-release may also be accomplished using systems where the CO-donors are conjugated to a NIR photosensitizing antenna.[27,71-74] A variety of NIR sensitive photoCORMs[66-70] and photoCORM-nanocarriers conjugates[129,71-74] have been reported in the literature, but only a few materials have been used for the delivery of CO to cancer cells.[72,129] Mesoporous Prussian blue nanoparticles (PBNPs) conjugated to iron pentacarbonyl CO-donors were used for NIR-triggered CO-release and photothermal ablation of tumors *in vivo*.[129] HeLa cells were subcutaneously implanted into the thighs of mice

and the tumors were allowed to develop for 7 days. CO-loaded PBNPs (m-PB-**CO**/PEG; 5 mg[Fe] kg^{-1}) or bare PBNPs (m-PB-PEG; 5 mg[Fe] kg^{-1}) were suspended in 10 mL of PBS and injected directly into the developed tumor. Groups receiving laser treatment were irradiated at the tumor site with an 808 nm diode laser for 5 min (800 mW cm^{-2}) or 15 min (300 mW cm^{-2}), and tumor sizes were monitored every 2 days for 20 days. Interestingly, the group treated with m-PB-**CO**/PEG (800 mW cm^{-2}) exhibited complete eradication of the tumors as a result of the synergistic chemotherapeutic effect between photoinduced hyperthermia and CO delivery. Groups treated with m-PB-PEG (5 min, 800 mW cm^{-2}) and m-PB-**CO**/PEG (300 mW cm^{-2}) displayed strong tumor-growth suppression but no eradication. Other control groups observed consistent tumor growth throughout the length of the experiment. The biodistribution of the of the conjugate system was carefully monitored for 7 days, indicating predominant accumulation in the liver and spleen. Another example of a materials used *in vivo* for NIR-triggered CO-delivery and photothermal ablation of subcutaneous tumors are CO-carrying palladium nanosheets (CO-PdNS).[72] PdNS fabricated under a high-pressure CO-confinement method adsorb considerable amounts of CO on their surfaces during their synthesis. CO molecules bind through the carbon atom to the basal planes of the PdNS and can be ejected through thermal excitation driven by NIR light, circumventing the need for additional photoCORMs. A549 cells were incubated with 0 - 20 μg mL^{-1} of CO-PdNS for 4 h and irradiated for 12 min using an 808 nm diode laser (250 mW). The photothermally induced cytotoxicity of this material was investigated *via* MTT assay, indicating a significantly decreased cell viability in a concentration dependent

manner. NIR-light exposure decreased cell viabilities over 80% at the highest concentration tested, whereas controls did not produce significant toxicity (> 10%). The effectiveness of PdNS-CO at eradicating malignant tissue was investigated in a xenograft tumor-bearing mouse model. In contrast to the previous account, fresh PdNS-CO (10 mg kg^{-1}) were systemically administered through the tail vein every 2 days and tumors were irradiated (808 nm, 250 mW, 8 min) 6 h after each injection. Groups treated with PdNS-CO + 808 nm laser exhibited strong tumor-growth suppression whereas control groups exhibited consistent increases in tumor volumes during the 14-day treatment. Systemically administered nanocarriers accumulate within malignant tissues through the enhanced permeability and retention (EPR) effect. However, local administration and/or targeted delivery may be an effective method to increase their concentrations at the target site and therefore improve their efficacy. Overall, NIR-driven CO release combined with photothermal ablation appears to be an effective method for the suppression and/or eradication of subcutaneous tumors.

1.2.9 Factors Affecting CO-Induced Cancer Cell Toxicity.

The observed cancer cell cytotoxicity during photoCOR treatment is affected by a wide variety of factors. CO may affect certain cells more than others due to differences in their biochemical composition and it is therefore misleading to compare results between different cell lines. The CO-releaser itself may also carry inherent toxicity that will not necessarily be specific towards cancer cells, possibly resulting in the damage of inadvertent targets. CO-releasers that are *not inherently toxic* or include

agents that increase their accumulation within target tissues (decreasing their systemic toxicity) are highly desirable. The toxicity of CO-spent products must also be carefully investigated to determine its isolated contributions. The release of toxic photoproduct(s) along with CO may be a viable chemotherapeutic strategy, especially if the prodrug is non-toxic. However, highly toxic photoproducts may cause systemic toxicity if delivered in high-enough concentrations and/or through repeated applications. Metallic photoCORMs based on Mn do not possess inherent systemic toxicity at doses required for treatment. Mn is a micronutrient used in a variety of metalloproteins constitutively expressed throughout the mammalian body including manganese superoxide dismutase, pyruvate carboxylase, glutamate synthetase, and arginase.[148,149] The daily intake of manganese of a normal diet on average is between 2 mg to 9 mg day^{-1} for a 70 kg person[149] and its acute oral toxicity (LD_{50}) is 9 g kg^{-1} in rats as per safety and data sheets available online. This suggests that the mammalian body has a relatively high tolerance for µM concentrations of this metal.

The rate by which photoCORMs accumulate within cancer cells also plays an important role in the observed CO-induced cytotoxicity. Higher accumulation rates of the CO-donors within cells may result in higher observed toxicity. Active transport of CO-donors into cellular targets include their conjugation to a nanocarrier systems that are internalized through endocytic pathways.[146,150] CO-releasing efficiency of the photoCOR system may be another factor that influences CO-induced toxicity. The sensitivity of a releasing-system towards a particular wavelength dictates its release rate and therefore its irradiation time/intensity. Nonetheless, excessively rapid release

of CO may result in the escape of this noxious gas into the surrounding medium before it reaches it intended targets. Time must also be allotted for the cells to exhibit toxicity after CO treatment. However, extensive incubation times may allow cells to recuperate metabolically and/or proliferate. Other factors that affect the metabolic activity of cells and eschew MTT results include culture conditions, confluency, depletion of nutrients, altered pH, excessive use and prolonged incubation times with MTT reagent.[151]

1.3 Silver and Theranostic Delivery.

1.3.1 Background on Silver.

Coinage metals have been used for their antimicrobial properties since ancient times. In particular, silver was consistently used in a variety of medical treatments until the first half of the 20th century.[152,153] Currently, silver is incorporated into a variety of consumer products, healthcare applications, and medical devices due to its antimicrobial properties. Silver is a broad-spectrum antibiotic with high toxicity against microbial cells and low toxicity to mammalian cells.[152,154] Silver antimicrobials (metal, salts, nanoparticles, complexes) exert their bactericidal activity by continuously releasing trace amounts of reactive cations (Ag^+), which are toxic to microorganisms.[155] Silver cations (Ag^+) are highly reactive and interact strongly with functional groups such as thiols, amines, and carboxylic acids on amino acid residues in proteins, nucleic acids, and cell membranes. These interactions result in the disruption of protein activity which then disturbs key biochemical processes in bacterial cells (Figure 1.14).[153,156]
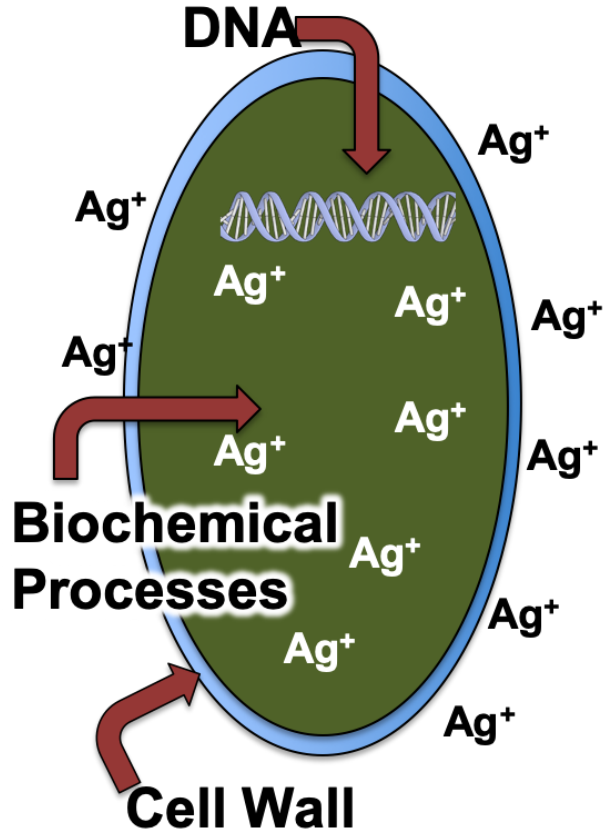
Figure 1.14. Antimicrobial mechanism of action of silver ions (Ag^+). Silver interacts strongly with soft Lewis bases in proteins and nucleic acids resulting in the disruption of biochemical processes.

Silver ions may also generate reactive oxygen species toxicity by releasing iron from iron-sulfur (4Fe-4S) clusters, which participates in Fenton reactions.[157] Finally, it has been determined that silver killed microorganisms can serve as a reservoir of silver and slowly release Ag^+ cations which can then again exert their bactericidal activity, known as the "zombie effect" (Figure 1.15.).[158,159]
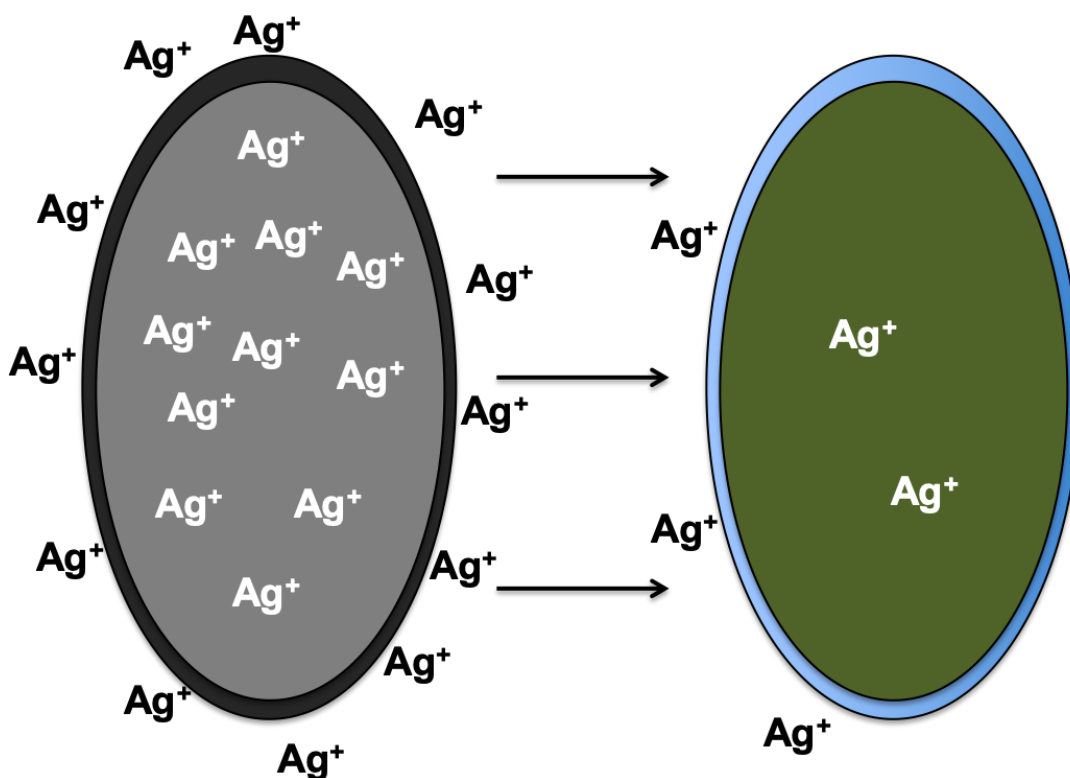
Figure 1.15. "Zombies effect".[Wakshlak] Silver killed microbes (left) may serve as a reservoir for Ag^+ ions. These ions then may be released from the dead microbe and kill other microbial cells (right).

The antimicrobial applications of silver diminished with the introduction of β-lactam antibiotics in the 1940s. However, the treatment and prevention of infections caused by multidrug resistant organisms (MDROs) is a serious threat to global health,[160] and a challenge to the pharmaceutical industry.[161] The spread of antimicrobial resistance is expedited by the misuse and overuse of organic antibiotics, rising population densities, and increased international travel.[162] In addition, the development of antimicrobials is becoming increasingly unattractive to pharmaceutical companies

due to short drug lifecycles, acuteness of antibacterial therapies, low market growth, high generic penetration, and restricted sales.[161] All of these factors decrease our current antimicrobial arsenal. In addition, recent reports of bacterial resistance to "last resort" antibiotics, such as colistin (polymyxin E), have been reported in China,[162] and the United States.[163] The plasmid-mediated resistance to polymyxins, MCR-1, has the potential of spreading resistance to microbes through horizontal gene transfer leading to global resistance.[162]

1.3.2 Skin and Soft Tissue Infections.

Microbial invasion and colonization of the skin and underlying soft tissues are among the most common types of infections. In particular, nosocomial infections caused by multidrug resistant strains are becoming increasingly prevalent. Systemic antibiotic chemotherapies are also becoming extremely limited due to emergence of multidrug-resistant Gram-positive and Gram-negative bacterial strains. Infections caused by drug-resistant pathogens are a considerable cause of global morbidity and mortality, leading to major clinical and economic burden.[164-166] In particular, nosocomial infections caused by the notoriously pathogenic *Enterococcus faecium, Staphylococcus aureus, Klebsiella pneumoniae, Acinetobacter baumannii, Pseudomonas aeruginosa, and Enterobacter spp. (ESKAPE)* bacteria present a major therapeutic challenge due to their resistance to conventional antibiotics.[167-169] Skin and soft tissue infections (SSTIs) caused by the *ESKAPE* pathogens result in growing rates of hospitalization with severities ranging from mild to lethal.[170,171] Damage and breaks

to the structural barrier of the skin allow for the infection and colonization by a variety of pathogens.[171,172] Microbial invasion of the skin and underlying soft tissues are caused predominantly by *S. aureus*, and to a lesser yet considerable extent by *A. Baumannii* and *P. aeuroginosa*. Treatment of SSTIs caused by these pathogens is becoming increasingly difficult due to the emergence and rapid dissemination of drug-resistant strains in hospital settings.[174-176] *S. aureus* is a Gram-positive bacteria that breaks down tissue for nutrition during the course of infection by employing a variety of extracellular proteins such as hemolysins, proteases, and collagenases. Over 95% of *S. aureus* strains are resistant to penicillin, and more than 50% are resistant to methicillin.[175,177] On the other hand chronic wound infections are caused primarily by *P. aeruginosa* and *A. baumannii*,[167,178] particularly in hospital settings.[154,168-170,178] *P. aeuroginosa* is one of the most common Gram-negative drug-resistant pathogens encountered in SSTIs.[179] Strains of *P. aeruginosa* can be highly resistant against most or almost all current antibiotic chemotherapeutics and are often classified as "panresistant".[180] *A. baumannii* is another opportunistic and problematic Gram-negative bacteria found in hospital environments affecting immunocompromised individuals.[181] Resistant *A. baumannii* infections have also been reported by military service members injured in combat in Iraq and Afghanistan[182-184] exemplifying its persistence in dry inanimate environments for extended periods of time.[185] *A. baumannii* is of particular interest due to its inherent resistance to some Gram-negative antibiotics as well as rapid development of drug resistance to others.[186]

1.3.3 Topical Antimicrobial Chemotherapy and SSTIs.

Systemic therapeutic options for SSTIs caused by resistant strains of bacteria are also becoming limited.[169,187] Accounts of resistance toward other "last-resort" antibiotics such as Carbapanem have already been reported globally.[162,163,166] Thus, development of new, safe, and effective antibiotic treatments for SSTIs is of paramount importance. Topical administration of antimicrobials provides an effective route for the treatment of skin and soft tissue infections (SSTIs) compared to systemic antibiotic therapy.[170] High antimicrobial doses can be administered directly to the site of infection avoiding clearance by the gastrointestinal tract, enzymatic and metabolic degradation (with associated side effects), as well as possible drug-drug interactions. Therefore, it is recommended to treat SSTI's topically using effective antimicrobial delivery systems for these agents. Topical delivery of antibiotics also increases patient compliance, convenience, and reduces treatment costs.

1.3.4 Current Antimicrobial Silver Treatments.

The use of silver as an antimicrobial agent is once again gaining interest due to its effectiveness against multidrug resistant organisms (MDROs) that withstand conventional antibiotic regiments. However, ingestion of large amounts of silver can produce adverse effects such as argyria. As a consequence most silver based therapies are applied topically for the treatment of SSTIs and prophylactic treatment of burn wound infections.[153,154,188-190] Because of its reactive nature, silver tends to precipitate as an insoluble salt (AgCl) in the presence of chloride ions (blood plasma chloride

concentration: 95−110 mM).[153] Thus, silver therapies require multiple applications and irrigations to maintain the infected area sterile. Topical application of silver sulfadiazine (Ag-SD) cream is another attractive way to treat SSTIs and burn wound infections. However, it also tends to adhere to the wound and leads to damage to newly epithelized surfaces during dressings and delay in wound healing.[189,191] Excessive topical use of silver may result in hypersensitivity, allergic contact dermatitis, erythema multiforme, and permanent undesirable aesthetic outcomes such as localized argyria.[192]

1.3.5 Theranostic Delivery of Silver to Wounds.

A desirable wound dressing therefore needs to deliver the minimum yet effective dose of silver to an affected area while allowing painless application and easy removal of the bandage. Current silver-based antibiotics lack the ability to indicate if enough silver has been applied or when it is necessary to administer more. Having a way to quantify the amount of active silver still present in the wound would be advantageous in determining how regularly the topical antibiotic should be administered to keep the wound sterile. Currently, efforts to develop theranostic silver antibiotic chemotherapies are still at its infancy. Nonetheless, a variety of silver complexes,[193-194] nanoparticles,[196-198] and materials[199-201] have been developed for the tracking of silver delivery and/or theranostic applications.

1.4 Direction of Present Research.

Carbon monoxide is an attractive bioactive agent with a degree of systemic tolerability arising from its endogenous production which regulates heme protein activity and indirectly modulate other biochemical processes. Exogenous administration of CO may serve as a viable method for the modulation of certain biochemical responses in efforts to elicit desired therapeutic outcomes. Precise and localized delivery of this gaseous molecule within biological systems, however, remains as the predominant challenge surrounding such implementation. Systemic administration of this biodynamic gas is generally an inadequate method for promoting an explicit response from a specific target due to the possible interaction with inadvertent targets. The deliberate introduction of CO at the intended site increases its efficacy and decreases its potential negative systemic effects. Light triggered CO-release from photoactivatable CO releasers (photoCORs) allow for the quantitative and on-demand delivery of CO to targets cells and tissues. Each photoCOR is sensitive to a specific range of light wavelengths, often dictating the depth at which they can be activated within tissues. UV- and visible-light active photoCORMs are excellent tools for studying the effects of exogenously delivered CO *in vitro.* However, their clinical applications are limited to light accessible surfaces due to poor tissue penetration of UV and visible light. The delivery of CO to deep tissues with spatial and temporal control is still a challenging feat. NIR-light sensitive photoCOR systems can be used to deliver CO into deep tissue due to their sensitivity towards tissue-penetrating ability of NIR of light. Viable therapeutic options for the delivery of CO to tissues inaccessible

by NIR light include the release of CO through enrichment or using internal triggers that do not require external inputs. In addition, controlled doses of CO can be delivered to deep tissues with spatiotemporal control through the use of fiberoptic technology (Figure 1.16).
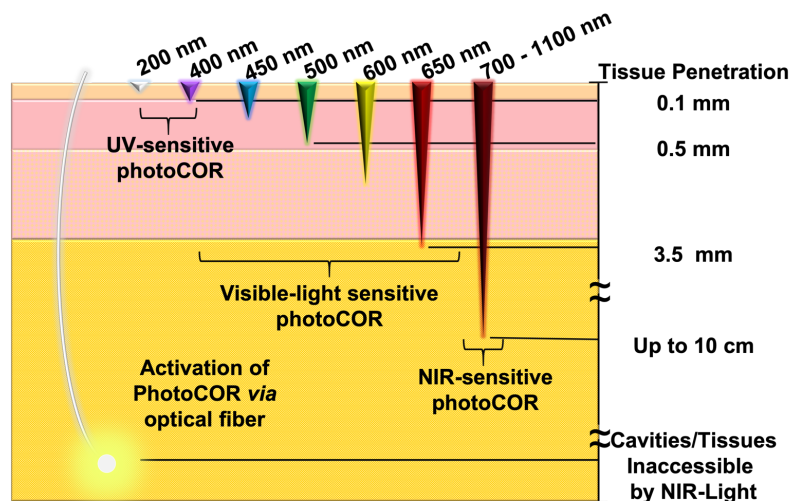
Figure 1.16. Activation depth of photoactivatable CO-releasing (photoCOR) systems. UV-light active ~0.1-0.5 mm; Visible-light active up to 3.5 cm; NIR-light active up to 10 cm in soft tissue, 7 cm muscle, 4 cm of skull/brain tissue. Optical fiber activation may reach any depth desired to illuminate molecules, implantable devices, or photoCOR reservoirs but requires invasive procedures. Figure adapted with permission from *Dalton Trans.* **2016**, *45*, 13012-13020.

The design and construction of a fiberoptic based device for the remote delivery of CO to deep tissues and organs is described in detail in Chapter 2.I. The resulting CO-releasing construct was composed of a photoactivated CO releasing molecule co-polymerized into a gas permeable polymeric hydrogel. The optical fiber was introduced

into the prepolymer mixture before the polymerization was carried to produce a CO-releasing catheter (Figure 4.17). The CO-donating abilities of this device by direct illumination through the optical fiber were investigated against a suspension of colorectal adenocarcinoma (HT-29) cells. In addition, the photoCORM-loaded polymer was also used as a is a suitable device for the delivery of CO to light inaccessible cavities or tissues using minimally invasive procedures. The polymeric
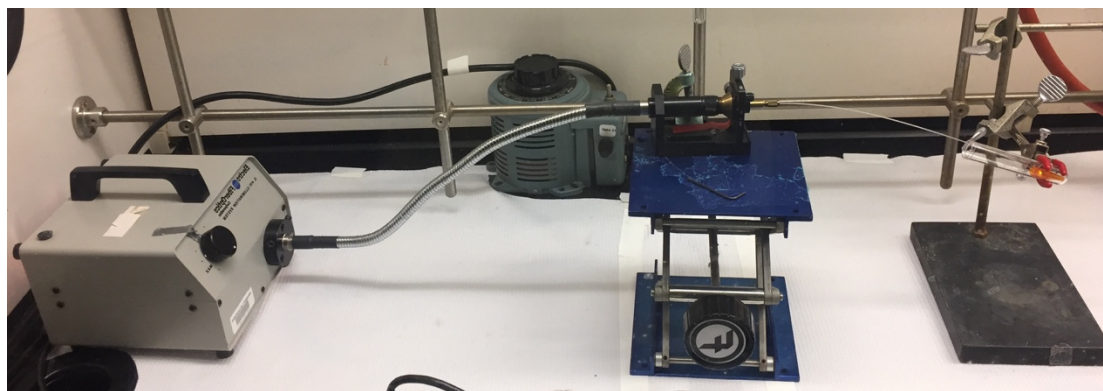
Figure 1.17. Picture of carbon monoxide releasing catheter. Light source (right), coupled to an optical fiber containing a polymeric tip for the remote delivery of CO to cancer cells. Image reproduced with permission of *J. Control. Release* **2017**, *264*, 192-202.

 matrix permitted the escape of CO into its surrounding medium while retaining the photoproduct(s), thus serving as a convenient solid-state source of CO. Chapter 2.II discusses the design and synthesis of various luminescent rhenium complexes bearing a vinyl polymeric tether (Figure 1.18) for their incorporation into similar gas permeable polymers for the remote delivery of CO.
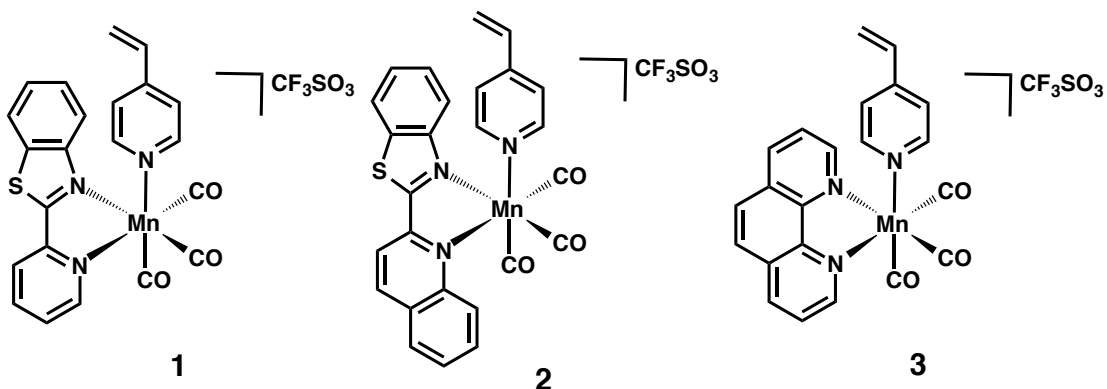
Figure 1.18. Schematic representation of complexes discussed in chapter 2.II.

Chapter 3 focuses on addressing various important factors and improvements for the tracking and internalization of photoCORMs. Chapter 3.I discusses in detail the synthesis of luminescent manganese photoCORMs with minimal quenching (complexes **1** and **2**; Figure 1.19). Direct complexation of fluorophores to the manganese metal center (no spacer molecule between metal center and fluorophore) results in quenching of the observed luminescence. The quenching can be minimized by attaching the fluorophore using spacer ligands. In the present work it was determined that using non-conjugated ligands result in less quenching of the luminescence compared to fully conjugated spacer ligands. The CO-induced totoxicity of these complexes were investigated in vitro and the internalization of the complexes was confirmed by confocal microscopy. Chapter 3.II Focuses on the improvement of cellular uptake of photoCORMs. Hydrophilic photoCOR systems may exhibit difficulties in penetrating cellular membranes and therefore require prolonged incubation times to increase their concentrations within cells. On the other hand,

lipophilic CO-releasers may diffuse through cellular membranes with ease and accumulate within subcellular structures. In
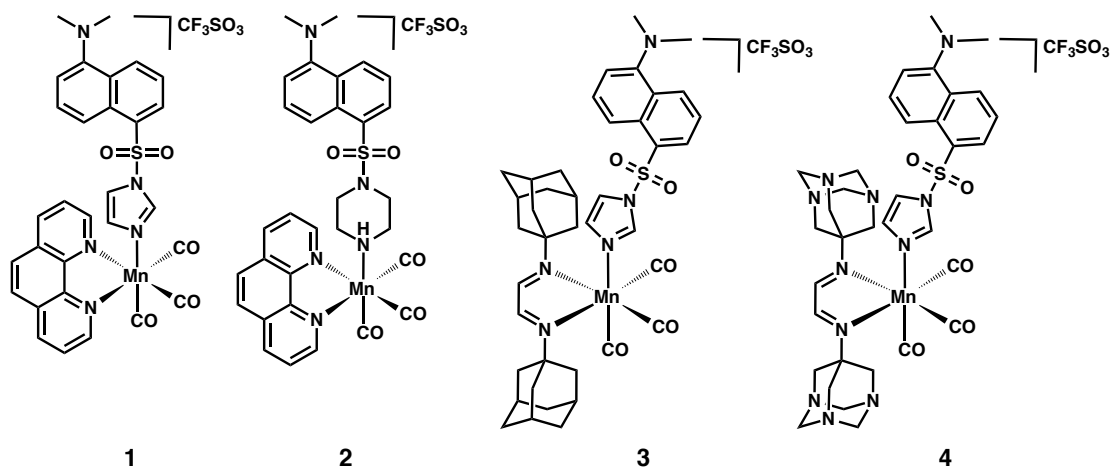
Figure 1.19. Complexes **1** and **2** discussed in chapter 3.I; complexes **3** and **4** discussed in chapter 3.II.

this chapter we report two complexes with identical structures but different solubility arising from the substitution of 6 carbon atoms for 6 nitrogens as hydrogen bond acceptors. The highly lipophilic photoCORM (complex **3**; Figure 1.19) based on adamantane showed enhanced permeation into cells and produced a low IC_{50} value (high toxicity). In contrast, the amphiphilic CO-donor analog based on triazaadamantane (complex **4**; Figure 1.19) was found to also efficiently permeate cancer cell membranes, but at a slower rate compared to the lipophilic photoCORM. The internalization rates of both of these CO-donors was investigated through confocal microscopy by conjugating them to a fluorophore. The intracellular localization,

cytotoxicity and the nature of cancer cell death resulting from treatment with these photoCORs were also investigated in detail.

Chapter 4 discusses theranostic delivery systems for bioactive silver for the treatment of bacterial infections. Preliminary approaches to develop silver delivery systems that exhibit fluorescence increase upon Ag^+ release is discussed in chapter 4.I. The theranostic silver complexes (Figure 1.20) consist of a fluorescent ligand that
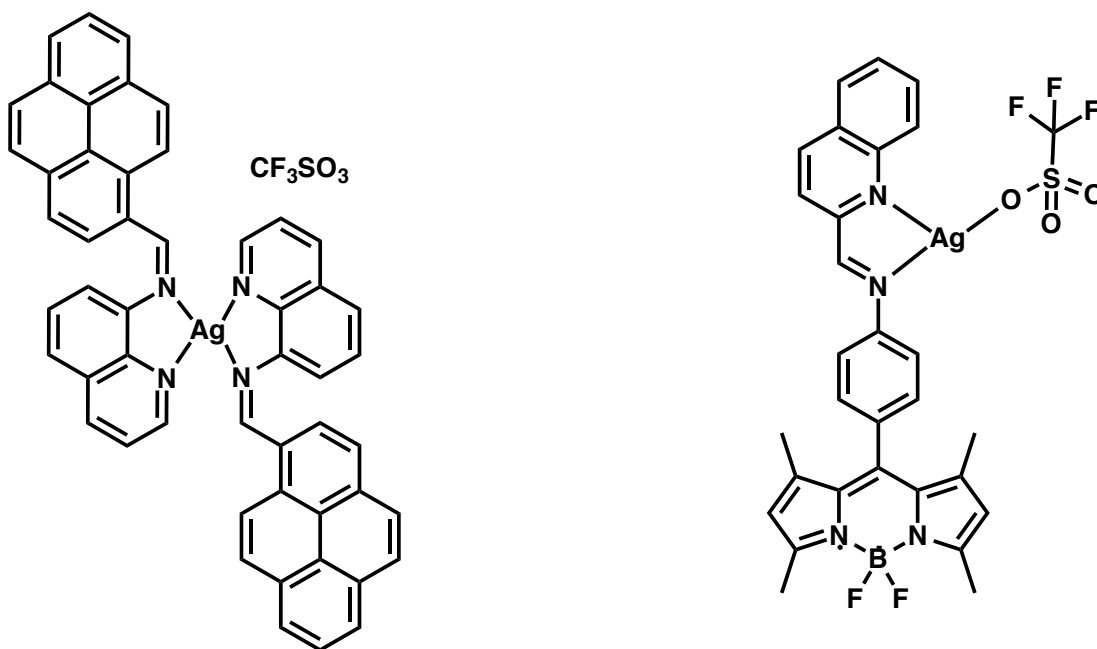
Figure 1.20. Theranostic silver complexes utilized in chapter 4.I.

observes quenching of fluorescence upon chelation to the silver metal center. The luminescence is restored upon release of Ag^+ ("turn-on" luminescence), exerting its bactericidal activity. Chapter 4.II focuses on the incorporation of a theranostic "two-tone" luminescent silver complex into a biocompatible hydrogel (Figure 1.21) for the

treatment of infections in a skin and soft tissue infection model. This material exhibited

excellent theranostic properties and was used to eradicate a panel of multidrug resistant

microbes. Chapter 4.III utilizes a tridentate fluorescent ligand that also quenches in
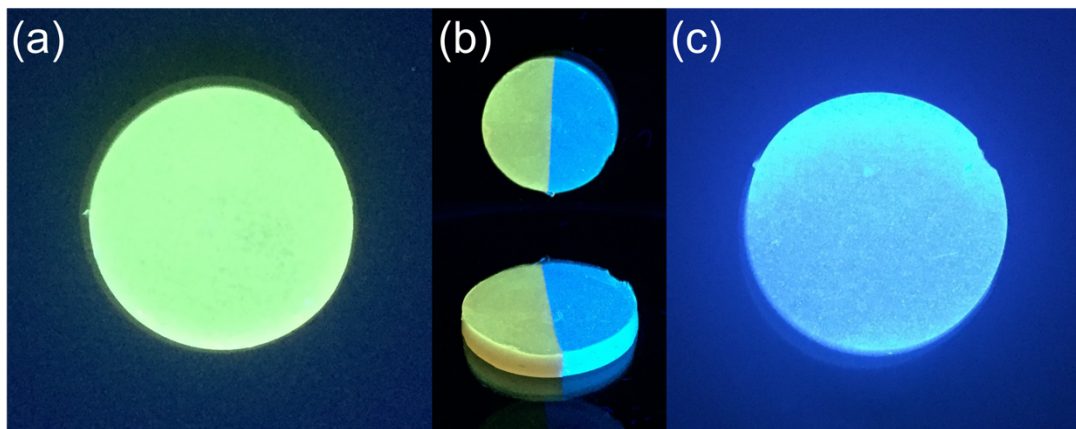
Figure 1.21. Theranostic luminescent silver delivery system described in chapter 4.II.

luminescence upon binding coinage metals such as silver and copper. The bactericidal

activity of both silver and copper complexes of this tridentate ligand in a KBr matrix

was investigated in a skin and soft tissue infection model.

1.5 References.

1. Quian, Y.; Matson, J. B. Gasotransmitter delivery via self-assembling peptides: treating diseases with natural signaling gases. *Adv. Drug Deliv. Rev.* **2017**, *110-111*, 137-156.

2. Motterlini, R.; Otterbein, L. E. The therapeutic potential of carbon monoxide. *Nat. Rev. Drug Discov.* **2010**, *9*, 422-428.

3. Lundberg, J. O.; Weitzberg, E.; Gladwin, M. The nitrate-nitrite-nitric oxide pathway in physiology and therapeutics. *Nat. Rev. Drug Discov*. **2008**, *7*, 156-167.

4. Wang, R. Physiological implications of hydrogen sulfide: A whiff exploration that blossomed. *Physiol. Rev.* **2012**, *92*, 791-896.

5. Wang, W.; Wang, B. SO_2 donors and prodrugs, and their possible applications: A review. *Front. Chem.* **2018**, *6*, 559.

6. Wallace, J. L.; Wang, R. Hydrogen sulfide-based therapeutics: exploiting a unique but ubiquitous gasotransmitter. *Nat. Rev. Drug Discov*. **2015**, *14*, 329-345.

7. Huang, Y.; Tang, C.; Du, J.; Jin, H. Endogenous sulfur dioxide: a new member of gasotransmitter family in the cardiovascular system. *Oxid. Med. Cell. Longevity* **2016**, 8961951.

8. Steiger, A. K.; Zhao, Y.; Pluth, M. D. Emerging toles of carbonyl sulfide in chemical biology: sulfide transporter or gasotransmitter? *Antiox. Redox Signal.* **2018**, *28*, 1516-1532.

9. Hanahan, D.; Weinberg, R. A. Hallmarks of cancer: the next generation. *Cell* **2011**, *144*, 646-647.

10. Edwards, I. R.; Aronson, J. K. Adverse drug reactions: definitions, diagnosis, and management. *Lancet* **2000**, *356*, 1255-1259.

11. Mirnezami, R.; Nicholson, J.; Darzi, A. Preparing for precision medicine. *N. Engl. J. Med.* **2012**, *366*, 489-491.

12. Wang, Y.; Kohane, D. S. External triggering and triggered targeting strategies for drug delivery. *Nat. Rev. Mater.* **2017**, *2*, 17020.

13. Timko, B. P.; Arruebo, M.; Shankarappa, S. A.; McAlvin, J. B.; Okonkwo, O. S.; Mizrahi, B.; Stefanescu, C. F.; Gomez, L.; Zhu, J.; Zhu, A.; Santamaria, J.; Langer, R.; Kohane, D. S. Near-infrared-actuated devices for remotely controlled drug delivery. *Proc. Natl. Acad. Sci.* **2014**, *111*, 1349-1354.

14. Murdan, S. Electro-responsive drug delivery from hydrogels. *J. Control. Release* **2003**, *92*, 1-17.

15. Velema, W. A.; Szymanski, W.; Feringa, B. L. Photopharmacology: beyond proof of principle. *J. Am. Chem. Soc.* **2014**, *136*, 2178-2191.

16. Lerch, M. M.; Hansen, M. J.; van Dam, G. M.; Szymanski, W.; Feringa, B. L. Emerging targets in photopharmacology. *Angew. Chem. Int. Ed.* **2016**, *55*, 10978-10999.

17. Broichhagen, J.; Frank, J. A.; Trauner, D. A roadmap to success in photopharmacology. *Acc. Chem. Res.* **2015**, *48*, 1947-1960.

18. Robertson, C. A.; Evans, D. H.; Abrahamse, H. Photodynamic therapy (PDT): a short review on cellular mechanisms and cancer research applications for PDT. *J. Photochem. Photobiol. B Biol.* **2009**, *1*, 1-8.

19. Yano, S.; Hirohara, S.; Obata, M.; Hagiya, Y.; Ogura, S.-I.; Ikeda, A.; Kataoka, H.; Tanaka, M.; Joh, T. Current states and future reviews in photodynamic therapy. *J. Photochem. Photobiol. C Photochem. Rev.* **2011**, *12*, 46-67.

20. Shibu, E. S.; Hamada, M.; Murase, N.; Biju, V. Nanomaterials formulations for photothermal and photodynamic therapy of cancer. *J. Photochem. Photobiol. C Photochem. Rev.* **2013**, *15*, 53-72.

21. Endo, M.; Ozawa, T. Strategies for development of optogenetic systems and their applications. *J. Photochem. Photobiol. C Photochem. Rev.* **2017**, *30*, 10-23.

22. Fenno, L.; Yizhar, O.; Deisseroth, K. The development and application of optogenetics. *Annu. Rev. Neurosci.* **2011**, *34*, 389-412.

23. Beaute, L.; McClenaghan, N.; Lecommandoux, S. Photo-triggered polymer nanomedicines: from molecular mechanisms to therapeutic applications. *Adv. Drug Deliv. Rev.* **2019**, *138*, 148-166.

24. Zhu, D.; Roy, S.; Liu, Z.; Weller, H.; Parak, W. J. Feliu, N. Remotely controlled opening of delivery vehicles and release of cargo by external triggers. *Adv. Drug Deliv. Rev.* **2019**, *138*, 117-132.

25. Faizan, M.; Muhammad, N.; Niazi, K. U. K.; Hu, Y.; Wang, Y.; Wu, Y.; Sun, H.; Liu, R.; Dong, W.; Zhang, W.; Gao, Z. CO-releasing materials: an emphasis on therapeutic implications, as release and subsequent cytotoxicity are the part of therapy. *Materials* **2019**, *12*, 1643.

26. Kottelat, E.; Zobi, F. Visible light-activated photoCORMs. *Inorganics* **2017**, *5*, 24.

27. Ford, P. C. Metal complex strategies for photo-uncaging the small molecule bioregulators nitric oxide and carbon monoxide. *Coord. Chem. Rev.* **2018**, *376*, 548-564.

28. Kikuchi, G.; Yoshida, T.; Noguchi, M. Heme oxygenase and heme degradation. *Biochem. Biophys. Res. Commun.* **2005**, *338*, 558-567.

29. Zuckerbraun, B. S.; Billiar, T. R.; Otterbein, S. L.; Kim, P. K.; Liu, F.; Choi, A. M. K. Otterbein, L. E. Carbon monoxide protects against liver failure through nitric oxide-induced heme oxygenase 1. *J. Exp. Med.* **2003**, *198*, 1707-1716.

30. Otterbein, L. E.; Bach, F. H.; Alam, J.; Soares, M.; Lu, H. T.; Wysk, M.; Davis, R. J.; Flavell, R. A.; Choi, A. M. K. Carbon monoxide ha anti-inflammatory effects involving the mitogen-activated protein kinase pathway. *Nat. Med.* **2000**, *6*, 422-428.

31. Wu, L.; Wang, R. Carbon monoxide: Endogenous production, physiological functions, and pharmacological applications. *Pharmacol. Rev.* **2005**, *57*, 585-630.

32. Yamamoto, T.; Takano, N.; Ishiwata, K.; Ohmura, M.; Nagahata, Y.; Matsuura, T.; Kamata, A.; Sakamoto, K.; Nakanishi, T.; Kubo, A.; Hishiki, T.; Suematsu, M. Reduced methylation of PFKFB3 in cancer cells shunts glucose towards the pentose phosphate pathway. *Nat. Commun.* **2014**, *5*, 3480.

33. Kawahara, B.; Ramadoss, S.; Chaudhuri, G.; Janzen, C.; Sen, S.; Mascharak, P. K. Carbon monoxide sensitizes cisplatin-resistant ovarian cancer cell lines toward cisplatin *via* attenuation of levels of glutathione and nuclear metallothionein. *J. Inorg. Biochem.* **2019**, *191*, 29-39.

34. Kawahara, B.; Moller, T.; Hu-Moore, K.; Carrington, S.; Faull, K. F.; Sen, S.; Mascharak, P. K. Attenuation of antioxidant capacity in human breast cancer cells by carbon monoxide through inhibition of cystathionine β-synthase activity: Implications in chemotherapeutic drug sensitivity. *J. Med. Chem.* **2017**, *60*, 8000-8010.

35. Wegiel, B.; Gallo, D.; Csizmadia, E.; Harris, C.; Belcher, J.; Vercellotti, G. M.; Penacho, N.; Seth, P.; Sukatme, V.; Ahmed, A.; Pandolfi, P. P.; Helczynski, L.; Bjartell, A.; Persson, J. L.; Otterbein, L. E. Carbon monoxide expedites metabolic exhaustion to inhibit tumor growth. *Cancer Res.* **2013**, *73*, 7009-7021.

36. Vitek, L.; Gbelcova, H.; Muchova, L.; Vanova, K.; Zelenka, J.; Konickova, R.; Suk, J.; Zadinova, M.; Knejzlik, Z.; Ahmad, S.; Fujisawa, T.; Ahmed, A.; Ruml, T. Antiproliferative effects of carbon monoxide on pancreatic cancer. *Dig. Liver Dis.* **2014**, *46*, 369-375.

37. Lee, L., C.-C.; Leung, L.-K.; Lo, K. K.-W. Recent development of luminescent rhenium(I) tricarbonyl polypyridine complexes as cellular imaging reagents, anticancer drugs, and antibacterial agents. *Dalton Trans.* **2017**, *46*, 16357-16380.

38. Ji, X.; Damera, K.; Zheng, Y.; Yu, B.; Otterbein, L. E.; Wang, B. Toward carbon monoxide-based therapeutics: critical drug delivery and developability issues. *J. Pharm. Sci.* **2016**, *105*, 406-416.

39. Gorrini, C.; Harris, I. S.; Mak, T. W. Modulation of oxidative stress as an anticancer strategy. *Nat. Rev. Drug Discov.* **2013**, *12*, 931-947.

40. Lu, S. C. Regulation of glutathione synthesis. *Mol. Aspects Med.* **2009**, *30*, 42-59.

41. Diehn, M.; Cho, R. W.; Lobo, N. A.; Kalisky, T.; Dorie, M. J.; Kulp, A. N.; Quian, D. L.; Lam, J. S.; Allies, L. E.; Wong, M. Z.; Joshua, B.; Kaplan, M. J.; Wapnir, I.; Dirbas, F. M.; Somlo, G.; Garberoglio, C.; Paz, B.; Shen, J.; Lau, S. K.; Quake, S. R.; Brown, J. M.; Weissman, I. L.; Clarke, M. F. Association of reactive oxygen species levels and radioresistance in cancer stem cells. Nature 2009, 458, 780-783.

42. Scarborough, P. M.; Mapuskar, K. A.; Mattson, D. M.; Gius, D.; Watson, W. H.; Spitz, D. R. Simultaneous inhibition of glutathione- and thioredoxin-dependent metabolism is necessary to potentiate 17AAG-induced cancer cell killing via oxidative stress. *Free Radic. Biol. Med.* **2012**, *52*, 436-443.

43. Tai, D. J.; Jin, W. S.; Wu, C. S.; Si, H. W.; Cao, X. D.; Guo, A. J.; Chang, J. C. Changes in intracellular redox status influence multidrug resistance in gastric adenocarcinoma cells. *Exp. Ther. Med*. **2012**, *4*, 291-296.

44. Reedijk, J. Why does cisplatin reach guanine-N7 with competing S-donor ligands available in the cell? *Chem. Rev.* **1999**, *99*, 2499-2510.

45. Zuckerbraun, B. S.; Chin, B, Y,; Bilban, M.; d'Avila, J. C.; Rao, T.; Billiar, T. R.; Otterbein, L. E. Carbon monoxide signals via inhibition of cytochrome c oxidase and generation of mitochondrial reactive oxygen species. *FASEB J*. **2007**, *21*, 1099-1106.

46. Pintadosi, C. A. Carbon monoxide, reactive oxygen signaling and oxidative stress. *Free Radic. Biol. Med.* **2008**, *45*, 562-569.

47. Li, X.; Fang, P.; Mai, J.; Choi, E. T.; Wang, H.; Yang, X. F. Targeting mitochondrial reactive oxygen species as a novel therapy for inflammatory diseases and cancers. *J. Hematol. Oncol.* **2013**, *6*, 19;

48. Liou, G. Y.; Storz, P. Reactive oxygen species in cancer. *Free Radic. Res.* **2010**, *44*, 479-496.

49. Motterlini, R.; Clark, J. E.; Foresti, R.; Saratchandra, P.; Mann, B. E.; Green, C. J. Carbon monoxide-releasing molecules characterization of biochemical and vascular activities. *Circ. Res.* **2002**, *90*, e17-e24.

50. Zheng, Y.; Ji, X.; Yu, B.; Ji, K.; Gallo, D.; Csizmadia, E.; Zhu, M.; Choudhury, M. R.; De La Cruz, L. K. C.; Chittavong, V.; Pan, Z.; Yuan, Z.; Otterbein, L. E.; Wang, B. Enrichment-triggered prodrug activation demonstrated through mitochondria-targeted delivery of doxorubicin and carbon monoxide. *Nat. Chem.* **2018**, *10*, 787-794.

51. Ji, X.; De La Cruz, L. K. C.; Pan, Z.; Chittavong, V.; Wang, B. pH-sensitive metal free carbon monoxide prodrugs with tunable and predictable release rates. *Chem. Commun.* **2017**, *53*, 9628-9631.

52. Ji, X.; Pan, Z.; Li, C.; Kang, T.; De La Cruz, L. K. C.; Yang, L.; Yuan, Z.; Ke, B.; Wang, B. Esterase-sensitive and pH-controlled carbon monoxide prodrugs for treating systemic inflammation. *J. Med. Chem*. **2019**, *62*, 3163-3168.

53. Ji, X.; Wang, B. Strategies toward organic carbon monoxide prodrugs. *Acc. Chem. Res.* **2018**, *51*, 1377-1385.

54. Chakraborty, I.; Carrington, S. J.; Mascharak, P. K. Design strategies to improve sensitivity of photoactive metal carbonyl complexes (photoCORMs) to visible light and their potential as CO-donors to biological targets. *Acc. Chem. Res.* **2014**, *47*, 2603-2611.

55. Garcia-Gallego, S.; Bernardes, G. J. L. Carbon monoxide-releasing molecules for the delivery of therapeutic CO in vivo. *Angew. Chem. Int. Ed*. **2014**, *53*, 9712-9721.

56. Romao, C. C.; Blatter, W. A.; Seixas, J. D.; Bernardes, G. J. Developing drug molecules for therapy with carbon monoxide. *Chem. Soc. Rev.* **2012**, *41*, 3571-3583.

57. Anthony, L. A.; Slanian, T.; Sebej, P.; Solomek, T.; Klan, P. Fluorescein analogue xanthene-9-carboxylic acid: a transition-metal-free CO releasing molecule activated by green light. *Org. Lett*. **2013**, *15*, 4552-4555.

58. Weissleder, R. A clearer vision for in vivo imaging. *Nat. Biotechnol.* **2001**, *19*, 316-317.

59. Kumar, C. A.; Nagarajaprakash, R.; Victoria, W.; Veena, V.; Sakthivel, N.; Manimaran, B. Synthesis, characterization and cytotoxicity studies on Manganese(I) and Rhenium(I) based metallacrown ethers. *Inorg. Chem. Commun*. **2016**, *64*, 39-44.

60. Kumar, C. A.; Divya, D.; Nagarajaprakash, R.; Veena, V.; Vidhyapriya, P.; Sakthivel, N.; Manimaran, B. Self-assembly of manganese(I) and rhenium(I) based semi-rigid ester functionalized M2L2-type metallacyclophanes: synthesis,

characterization, and cytotoxicity evaluation. *J. Organomet. Chem.* **2017**, *846*, 152-160.

61. Vidhyapriya, P.; Divya, D.; Manimara, B.; Sakthivel, N. Photoactivated [Mn(CO)$_3$(Br(μ-bpcpd)]$_2$ induces apoptosis in cancer cells via intrinsic pathway. *J. Photochem. Photobiol. B, Biol.* **2018**, *188*, 28-41.

62. Kumar, U.; Roy, S.; Jha, R. K.; Vidhyapriya, P.; Sakthivel, N.; Manimaran, B. Selenolato-bridged manganese(I)-based dinuclear metallacycles as potential anticancer agents and photo-CORMs. *ACS Omega* **2019**, *4*, 1923-1930.

63. Divya, D.; Nagarajaprakash, R.; Vidhyapriya, P.; Sakthivel, N.; Manimaran, B. Single-pot self-assembly of heteroleptic Mn(I)-based aminoquinonato-bridged ester/amide-functionalized dinuclear metallastirrups: potential anticancer and visible light triggered CORMs. *ACS Omega* **2019**, *4*, 12790-12802.

64. Ramakrishna, B.; Nagarajaprakash, R.; Veena, V.; Sakthivel, N.; Manimaran B. Self-assembly of oxamidato bridged ester functionalized dirhenium metallastirrups: synthesis, characterization and cytotoxicity studies. *Dalton Trans.* **2015**, *44*, 17629-17638.

65. Carrington, S. J.; Chakraborty, I.; Mascharak, P. K. Rapid CO release from a Mn(I) carbonyl complex derived from azopyridine upon exposure to visible light and its phototoxicity toward malignant cells. *Chem. Commun.* **2013**, *49*, 11254-11256.

66. Li, Z.; Pierri, A. E.; Huang, P. J.; Wu, G.; Ford, P. C. Dinuclear photoCORMs: dioxygen-assisted carbon monoxide uncaging from long-wavelength-absorbing metal-metal-bonded carbonyl complexes, *Inorg. Chem.* **2017**, *56*, 6094-6104.

67. Nakae, T.; Hirotsu, M.; Nakajima H. CO release from N,C,S-pincer iron(III) carbonyl complexes induced by visible-to-NIR irradiation: mechanistic insight into effects of axial phosphorous ligands. *Inorg. Chem.* **2018**, *57*, 8615-8626.

68. Palao, E.; Slanian, T.; Muchova, L.; Solomek, T.; Vitek, L.; Klan, P. Transition-metal-free CO-releasing BODIPY derivatives activatable by visible to NIR light as promising bioactive molecules. *J. Am. Chem. Soc.* **2016**, *138*, 126-133.

69. Jiang, Q.; Xia, Y.; Barrett, J.; Mikhailovsky, A.; Wu, G.; Wang, D.; Shi, P.; Ford, P. C. Near-infrared and visible photoactivation to uncage carbon monoxide from an aqueous-soluble photoCORM. *Inorg. Chem.* **2019**, 58, 11066-11075.

70. Ramu, V.; Reddy, G. U.; Liu, J.; Hoffmann, P.; Sollapur, R.; Wyrwa, R.; Kupfer, S.; Spielmann, C.; Bonnet, S.; Neugebauer, U.; Schiller, A. Two-photon-induced CO-releasing molecules as molecular logic systems in solution, polymers, and cells. *Chem. Eur. J.* **2019**, *25*, 8453-8458.

71. Pierri, A. E.; Huang, P.-J.; Garcia, J. V.; Stanfill, J. G.; Chui, M.; Wu, G.; Zheng, N.; Ford, P. C. A photoCORM nanocarrier for CO release using NIR light. *Chem. Commun.* **2015**, *51*, 2072-2075.

72. Wang, C.; Li, Y.; Shi, X.; Zhou, J.; Wei, S. Use of a NIR-light-responsive CO nanodonor to improve the EPR effect in photothermal cancer treatment. *Chem. Commun*. **2018**, *54*, 13403-13406.

73. He, Q.; Kiesewetter, D. O.; Qu, Y.; Fu, X.; Fan, J.; Huang, P.; Liu, Y.; Zhu, G.; Liu, Y.; Quian, Z.; Chen, X. NIR-responsive on-demand release of CO from metal carbonyl-caged graphene oxide nanomedicine. *Adv. Mater.* **2015**, *27*, 6741-6746.

74. Ou, J.; Zheng, W.; Xiao, Z.; Yan, Y.; Jiang, X.; Dou, Y.; Jiang, R.; Liu, X. Core-shell materials bearing iron(II) carbonyl units and their CO-release via an upconversion process. *J. Mater. Chem. B* **2017**, *5*, 8161-8168.

75. Soboleva, T,; Berreau, L. M. 3-Hydroxyflavones and 3-hydroxy-4-oxoquinolines as carbon monoxide-releasing molecules. *Molecules* **2019**, *24*, 1252.

76. Popova, M.; Soboleva, T.; Ayad, S.; Benninghoff, A.; Berreau, L. Visible-light-activated quinolone carbon-monoxide-releasing molecule: prodrug and albumin-assisted delivery enables anticancer and potent anti-inflammatory effects. *J. Am. Chem. Soc.* **2018**, *140*, 9721-9729.

77. Anderson, S. N.; Richards, J. M.; Esquer, H. J.; Benninghoff, A. D.; Arif, A. M.; Berreau, L. M. A structurally-tunable 3-hydroxyflavone motif for visible light-induced carbon monoxide-releasing molecules (CORMs). *ChemistryOpen* **2015**, *4*, 590-594.

78. Romano, B.; Pagano, E.; Montanaro, V.; Fortunato, A. L.; Milic, N.; Borrelli, F. Novel insights into the pharmacology of flavonoids. *Phytother. Res.* **2013**, *27*, 1588-1596.

79. Pierri, A. E.; Pallaoro, A.; Wu, G.; Ford, P. C. A luminescent and biocompatible photoCORM. *J. Am. Chem. Soc.* **2012**, *134*, 18197-181200.

80. Carrington, S. J.; Chakraborty, I.; Bernard, J. M. L.; Mascharak, P. K. A theranostic two-tone luminescent photoCORM derived from Re(I) and 2-(pyridyl)-benzothiazole: Trackable CO delivery to malignant cells. *Inorg. Chem.* **2016**, *55*, 7852-7858.

81. Soboleva, T.; Esquer, H. J.; Benninghoff, A. D.; Berreau, L. M. Sense and release: a thiol responsive flavonol-based photonically driven carbon monoxide-releasing molecule that operates via a multiple input AND logic gate. *J. Am. Chem. Soc.* **2017**, *139*, 9435-9438.

82. Carrington, S. J.; Chakraborty, I.; Bernard, J. M. L. Mascharak, P. K. Synthesis and characterization of a "turn-on" photoCORM for trackable CO delivery to biological targets. *ACS Med. Chem. Lett.* **2014**, *4*, 1324-1328.

83. G, U. R.; Axthelm, J.; Hoffmann, P.; Taye, N.; Glaser, S.; Gorls, H.; Hopkins, S. L.; Plass, W.; Neugebauer, U.; Bonnet, S.; Schiller, A. Co-registered molecular logic gate with a CO-releasing molecule triggered by light and peroxide. *J. Am. Chem. Soc.* **2017**, *139*, 4991-4994.

84. Musib, D.; Raza, M. K.; Martina, K.; Roy, M. Mn(I)-based photoCORMs for trackable visible light-induced CO release and phototoxicity to cancer cells. *Polyhedron* **2019**, In press, Corrected Proof.

85. Jimenez, J.; Chakraborty, I.; Dominguez, A.; Martinez-Gonzalez, J.; Sameera, W. M. C.; Mascharak, P. K. A luminescent manganese photoCORM for CO delivery to cellular targets under the control of visible light. *Inorg. Chem.* **2018**, *57*, 1766-1773.

86. Jimenez, J.; Pinto, M. N.; Martinez-Gonzalez, J.; Mascharak, P. K. Photo-induced eradication of human colorectal adenocarcinoma HT-29 cells by carbon monoxide (CO) delivery from a Mn-based green luminescent photoCORM. *Inorg. Chim. Acta* **2019**, *485*, 113-117.

87. Romanski, S.; Rucker, H.; Stamellou, E.; Guttentag, M.; Neudorfl, J.-M.; Alberto, R.; Amslinger, S.; Yard, B.; Schmalz, H.-G. Iron dienylphosphate tricarbonyl complexes as water-soluble enzyme-triggered CO-releasing molecules (ET-CORMs). *Organometallics* **2012**, *31*, 5800-5809.

88. Poh, H. T.; Sim, B. T.; Chwee, T. S.; Leong, W. K.; Fan, W. Y. The dithiolate-bridged diiron hexacarbonyl complex $Na_2[(\mu\text{-}SCH_2CH_2COO)Fe(CO)_3]_2$ as a water-soluble photoCORM. *Organometallics* **2014**, *33*, 959-963.

89. Mede, R.; Klein, M.; Claus, R. A.; Krieck, S.; Quickert, S.; Gorls, H.; Neugebauer, U.; Schmitt, M.; Gessner, G.; Heinemann, S. H.; Popp, J.; Bauer, M.; Westerhausen, M. CORM-EDE1: A highly water soluble and nontoxic manganese-based photoCORM with a biogenic ligand sphere. *Inorg. Chem.* **2016**, *55*, 104-113.

90. Jimenez, J.; Chakraborty, I.; Carrington, S. J.; Mascharak, P. K. Light-triggered CO delivery by a water-soluble and biocompatible manganese photoCORM. *Dalton Trans.* **2016**, *45*, 13204-13213.

91. Marker, S. C.; MacMillan, S. N.; Zipfel, W. R.; Li, Z.; Ford, P. C.; Wilson, J. J. Photoactivated in vitro anticancer activity of Rhenium(I) tricarbonyl complexes bearing water-soluble phosphines. *Inorg. Chem.* **2018**, *57*, 1311-1331.

92. Zhang, Y.; Yu, J.; Bomba, H. N.; Zhu, Y.; Gu, Z. Mechanical force-triggered drug delivery. *Chem. Rev*. **2016**, *116*, 12536-12563.

93. Kanamala, M.; Wilson, W. R.; Yand, M.; Palmer, B. D.; Wu, Z. Mechanisms and biomaterials in pH responsive tumor targeted drug delivery: A review. *Biomaterials* **2016**, *85*, 152-167.

94. Schmaljohann, D. Thermo- and pH-responsive polymers in drug delivery. *Adv. Drug Deliv. Rev.* **2006**, *58*, 1655-1670.

95. Brun-Graeppi, A. K. A. S.; Richard, C.; Bessodes, M.; Scherman, D.; Merten, O.-W. Cell microcarriers and microcapsules of stimuli-responsive polymers. *J. Control. Release*. **2011**, *149*, 209-224.

96. Gu, M.; Wang, X.; Toh, T. B.; Chow, E. K. H. Applications of stimuli-responsive nanoscale drug delivery systems in translational research. *Drug Discov. Today* **2018**, *23*, 1043-1052.

97. Li, Z.; Ye, E.; David; Rajamani, L.; Loh, X, J. Recent advances of using hybrid nanocarriers in remotely controlled therapeutic delivery. *Small* **2016**, *12*, 4782-4806.

98. Timko, B. P.; Kohane, D. S. Drug-delivery systems for tunable and localized drug release. *Isr. J. Chem.* **2013**, *53*, 728-736.

99. Timko, B. P.; Dvir, T.; Kohane, D. S. Remotely triggerable drug delivery systems. *Adv. Mater.* **2010**, *22*, 4925-4943.

100. Mura, S.; Nicolas, J.; Couvreur, P. Stimuli-responsive nanocarriers for drug delivery. *Nat. Mater.* **2013**, *12*, 991-1003.

101. Rapoport, N. Physical stimuli-responsive polymeric micelles for anti-cancer drug delivery. *Prog. Polym. Sci.* **2007**, *32*, 962-990.

102. Al-Ahmady, Z. S.; Al-Jamal, W. T.; Bossche, J. V.; Bui, T. T.; Drake, A. F.; Mason, A. J. Lipid-peptide vesicle nanoscale hybrids for triggered drug release by mild hyperthermia *in vitro* and *in vivo*. *ACS Nano* **2012**, *6*, 9335-9346.

103. Brazel, C. S.; Peppas, N. A. Pulsatile local delivery of thrombolytic and antithrombotic agents using poly(*N*-isopropylacrylamide-co-methacrylic acid) hydrogels. *J. Control. Release* **1996**, *38*, 57-64.

104. Chung, J. E.; Yokoyama, M.; Okano, T. Inner core segment design for drug delivery control of thermo-responsive polymeric micelles. *J. Control. Release* **2000**, *65*, 93-103.

105. Chung, J. E.; Yokoyama, M.; Yamamoto, M.; Aoyagi, T.; Sakurai, Y.; Okano, T. Thermo-responsive drug delivery from polymeric micelles constructed using block copolymers of poly(N-isopropylacrylamide) and poly(butylmethacrylate). *J. Control. Release* **1999**, *62*, 115-127.

106. Paris, J. L.; Cabañas, V.; Manzano, M.; Vallet-Regi, M. Polymer-grafted mesoporous silica nanoparticles as ultrasound responsive drug carriers. *ACS Nano* **2015**, *11*, 11023-11033.

107. Chen, W.; Du, J. Ultrasound and pH dually responsive polymer vesicles for anticancer drug delivery. *Sci. Rep*. **2013**, *2*, 2162.

108. Sirsi, S. R.; Borden, M. A. State-of-the-art materials for ultrasound triggered drug delivery. *Adv. Drug Deliv. Rev*. **2014**, *72*, 3-14.

109. Manzano, M.; Vallet-Regi, M. Ultrasound responsive mesoporous silica nanoparticles for biomedical applications. *Chem. Commun*. **2019**, *55*, 2731-2740.

110. Gao, G.; Jiang, Y.-W.; Jia, H.-R.; Wu, F.-G. Near-infrared light-controllable on-demand antibiotics release using thermo-sensitive hydrogel-based drug reservoir for combating bacterial infection. *Biomaterials* **2019**, *188*, 83-95.

111.   Zhao, Y.; Wei, C.; Chen, X.; Liu, J.; Yu, Q.; Liu, Y.; Liu, J. Drug delivery systems based on near-infrared light-responsive molybdenum disulfide nanosheets controls the high efficacy release of dexamethasone to inhibit inflammation to treat osteoarthritis. *ACS Appl. Mater. Interfaces* **2019**, *11*, 11586-11601.

112.   Jia, S.; Fong, W.-K.; Graham, B.; Boyd, B. J. Photoswitchable molecules in long wavelength light-responsive drug delivery: From molecular design to applications. *Chem. Mater.* **2018**, *30*, 2873-2887.

113.   Amiri, M.; Akbari, A.; Ahmadi, M.; Pardakthi, A.; Salvati-Niasari, M. Synthesis and in vitro evaluation of a novel magnetic drug delivery system; proecological method for the preparation of $CoFe_2O_4$ nanostructures. *J. Mol. Liq*. **2018**, *249*, 1151-1160.

114.   Neuberger, T.; Schopf, B.; Hofmann, H.; Hofmann, M.; von Rechenberg, B. Superparamagnetic nanoparticles for biomedical applications: Possibilities and limitations of a new drug delivery system. *J. Magn. Magn. Mater.* **2005**, *293*, 483-496.

115.   Puiggali-Jou, A.; Cejudo, A.; del Valle, L. J.; Aleman, C. Smart drug delivery from electrospun fibers though electroresponsive polymeric nanoparticles. *ACS Appl. Bio Mater*. **2018**, *1*, 1594-1605.

116.   Samantha, D.; Hosseini-Nassab, N.; McCarthy, A. D.; Zare, R. N. Ultra-low voltage triggered release of an anticancer drug from polypyrrole nanoparticles. *Nanoscale* **2018**, *10*, 9773-9779.

117.   Neumann, S. E.; Chamberlayne, C. F.; Zare, R. N. Electrically controlled drug release using pH-sensitive polymer film. *Nanoscale* **2018**, *10*, 10087-10093.

118.   Pfeiffer, H.; Rojas, A, R.; Niesel, J.; Schatzschneider, U. Sonogashira and "click" reactions for the N-terminal and side-chain functionalization of peptides with [Mn(CO)$_3$(tpm)]$^+$ -based CO releasing molecules (tpm = tris(pyrazolyl)methane). *Dalton Trans.* **2009**, *22*, 4292-4298.

119.   Matson, J. B.; Webber, M. J.; Tamboli, V. K.; Weber, B.; Stupp, S. I. A peptide-based material for therapeutic carbon monoxide delivery. *Soft. Mater.* **2012**, *8*, 2689-2692.

120.   Leonidova, A.; Pierroz, V.; Adams, L. A.; Barlow, N.; Ferrari, S.; Graham, B.; Gasser, G. Enhanced cytotoxicity through conjugation of a "clickable" luminescent Re(I) complex to a cell-penetrating lipopeptide. *ACS Med. Chem. Lett.* **2014**, *5*, 809-814.

121.   Bruckmann, N. E.; Wahl, M.; Reib, G. J.; Kohns, M.; Watjen, W.; Kunz, P. C. Polymer conjugates of photoinducible CO-releasing molecules. *Eur. J. Inorg. Chem.* **2011**, *29*, 4571-4577.

122.   Pinto, M. N.; Chakraborty, I.; Sandoval, C.; Mascharak, P. K.; Eradication of HT-29 colorectal adenocarcinoma cells by controlled photorelease of CO from a CO-releasing polymer (photoCORP-1) triggered by visible light through an optical fiber-based device. *J. Control. Release* **2017**, *264*, 192-202.

123. Dordelmann, G.; Pfeiffer, H.; Birkner, A.; Schatzschneider, U. Silicium dioxide nanoparticles as carriers for photoactivatable CO-releasing molecules (photoCORMs). *Inorg. Chem.* **2011**, *50*, 4362-4367.

124. Dordelmann, G.; Meinhardt, T.; Sowik, T.; Krueger, A.; Schatzschneider, U. CuAAC click functionalization of azide-modified nanodiamond with a photoactivatable CO-releasing molecule (photoCORM) based on [Mn(CO)$_3$(tpm)]. *Chem. Commun.* **2012**, *48*, 11528-11530.

125. Kunz, P. C.; Meyer, H.; Barthel, J.; Sollazzo, S.; Schmidt, A. M.; Janiak, C. Metal carbonyls supported on iron oxide nanoparticles to trigger the CO-gasotransmitter release by magnetic heating. *Chem. Commun.* **2013**, *49*, 4896-4898.

126. Gonzales, M.; Han, H.; Moyes, A.; Radinos, A.; Hobbs, A. J.; Coombs, N.; Oliver, S. R. J.; Mascharak, P. K. Light-triggered carbon monoxide delivery with Al-MAM-41-based nanoparticles bearing a designed manganese carbonyl complex. *J. Mater. Chem. B* **2014**, *2*, 2107-2113.

127. Chakraborty, I.; Carrington, S. J.; Hauser, J.; Oliver, S. R. J.; Mascharak, P. K. Rapid eradication of human breast cancer cells trough trackable light-triggered CO delivery by mesoporous silica nanoparticles packed with a designed photoCORM. *Chem. Matter.* **2015**, *27*, 8387-8397.

128. Carmona, F. J.; Jimenez-Amezcia, I.; Rojas, S.; Romao, C. C.; Navarro, J. A. R.; Maldonado, C. R.; Barea, E. Aluminum doped MCM-41 nanoparticles as

platforms for the dual encapsulation of a CO-releasing molecule and cisplatin. *Inorg. Chem.* **2017**, *56*, 10474-10480.

129. Li, W.-P.; Su, C.-H.; Tsao, L.-C.; Chang, C.-T.; Hsu, Y.-P.; Yeh, C.-S. Infrared light-induced cleavage of iron carbonyl derivatized Prussian blue nanoparticles for CO-assisted synergistic treatment. *ACS Nano* **2016**, *10*, 11027-11036.

130. Govender, P.; Pai, S.; Schatzschneider, U.; Smith, G. S. Next generation photoCORMs: polynuclear tricarbonylmanganese(I)-functionalized polypyridyl metallodendrimers. *Inorg. Chem.* **2013**, *52*, 5470-5478.

131. Fujita, K.; Yanaka, Y.; Abe, S.; Ueno, T. A photoactive carbon-monoxide-releasing protein cage for dose-regulated deliver in living cells. *Angew. Chem. Int. Ed.* **2016**, *55*, 1056-1060.

132. Tabe, H.; Shimoi, T.; Boudes, M.; Abe, S.; Coulibaly, F.; Kitagawa, S.; Mori, H.; Ueno, T. Photoactivatable CO release from engineered protein crystal to modulate NF-kB activation. *Chem. Commun.* **2016**, *50*, 4545-4548.

133. Hasegawa, U.; van der Viles, A. J.; Simeoni, E.; Wandrey, C.; Hubbell, J. A. Carbon monoxide-releasing micelles for immunotherapy. *J. Am. Chem. Soc.* **2010**, *132*, 18273-18280.

134. Bohlender, C.; Glaser, S.; Klein, M.; Weisser, J.; Susanne, T.; Neugebauer, U.; Popp, J.; Wyrwa, R.; Schiller, A. Light-triggered CO release from nanoporous non-wovens. *J. Mater. Chem. B* **2014**, *2*, 1454-1463.

135. Askes, S. H. C.; Reddy, G. U.; Wyrwa, R.; Bonnet, S.; Schiller, A. Red light-triggered CO release from $Mn_2(CO)_{10}$ using triplet sensitization in polymer nonwoven fabrics. *J. Am. Chem. Soc.* **2017**, *139*, 14292-15295.

136. Glaser, S.; Mede, R.; Gorls, H.; Seupel, S.; Bohlender, C.; Wyrwa, R.; Schirmer, S.; Dochow, S.; Reddy, G. U.; Popp, J.; Westernhausen, M.; Schiller, A. Remote-controlled delivery of CO *via* photoactive CO-releasing materials on a fiber optical device. *Dalton Trans.* **2016**, *45*, 13222-13233.

137. Diring, S.; Carne-Sanchez, A.; Zhang, J.C.; Ikemura, S.; Kim, C.; Inaba, H.; Kitagawa, S.; Furukawa, S. Light responsive metal-organic frameworks as controllable CO-releasing cell culture substrates. *Chem. Sci.* **2017**, *8*, 2381-2386.

138. Carmona, F. J.; Maldonado, C. R.; Ikemura, S.; Romao, C. C.; Huang, Z.; Xu, H.; Zou, X.; Kitagawa, S.; Furukawa, S.; Barea, E. Coordination modulation method to prepare new metal-organic framework-based CO-releasing materials. *ACS Appl. Mater. Interfaces* **2018**, *10*, 31158-31167.

139. Chakraborty, I.; Jimenez, J.; Mascharak, P. K. CO-induced apoptotic death of colorectal cancer cells by a luminescent photoCORM grafted on biocompatible carboxymethyl chitosan. *Chem. Commun.* **2017**, *53*, 5519-5522.

140. Sakla, R.; Jose, A. Vesicles functionalized with a CO-releasing molecule for light-induced CO delivery. *ACS Appl. Mater. Interfaces* **2018**, *10*, 14214-14220.

141. Nguyen, D.; Nguyen, T. K.; Rice, S. A.; Cyrille B. CO-releasing polymers exert antimicrobial activity. *Biomacromolecules* **2015**, *16*, 2776-2786.

142.   Nguyen, D.; Adnan, N. N. M.; Oliver, S.; Boyer, C. The interaction of CORM-2 with block copolymers containing poly(4-vinylpyridine): macromolecular scaffolds for carbon monoxide delivery in biological systems. *Macromol. Rapid Commun.* **2016**, *37*, 739-744.

143.   Bernkop-Schnurch, A.; Dunnhaupt, S. Chitosan-based drug delivery systems. *Eur. J. Pharm. Biopharm.* **2012**, *81*, 463-469.

144.   Upadhyay, L.; Singh, J.; Agarwal, V.; Tewari, R. P. The implication of recent advances in carboxymethyl chitosan based targeted drug delivery and tissue engineering applications. *J. Control. Release* **2014**, *186*, 54-87.

145.   Chakraborty, I.; Mascharak, P. K. Mesoporous silica materials and nanoparticles as carriers for the controlled and site-specific delivery of gaseous signaling molecules. *Microporous Mesoporous Mater.* **2016**, *234*, 409-419.

146.   Zhang, S.; Gao, H.; Bao, G. Physical principles of nanoparticle cellular endocytosis. *ACS Nano* **2015**, *9*, 8655-8671.

147.   Repanas, A.; Andriopoulou, S.; Glasmacher, B. The significance of electrospinning as a method to create fibrous scaffolds for biomedical engineering and drug delivery applications. *J. Drug Deliv. Sci. Technol.* **2016**, *31*, 137-146.

148.   Fraga, C. G. Relevance, essentiality and toxicity of trace elements in human health. *Molec. Aspects Med.* **2005**, *26*, 235-244.

149.   Aschner, M. Manganese: Brain transport and emerging research needs. *Environ. Health Perspect.* **2000**, *109*, 429-432.

150.   de Jesus, M. B.; Kapila, Y. L. (2013) Cellular mechanisms in nanomaterial internalization, intracellular trafficking and toxicity. In: Duran, N.; Guterres, S.; Alves, O. (eds) Nanotoxicology. Nanomedicine and Nanotoxicology. Springer, New York. NY.

151.   T. L. Riss, R. A. Moravec, A. L. Niles, H. A. Benink, T. J. Worzella, L. Minor, Cell viability assays, in: Assay guidance manual (Internet). Eli Lilly & Company and the National Center for Advancing Translational Sciences, 2016.

152.   Lemire, J. A.; Harrison, J. J.; Turner, R. J. Antimicrobial Activity of Metals: Mechanism, Molecular Targets and Applications. *Nat. Rev. Microbiol*. **2013**, *11*, 371-384.

153.   Chernousova, S.; Epple, M. Silver as antibacterial agent: Ion, nanoparticle, and metal. *Angew. Chem. Int. Ed.* **2013**, *52*, 1636-1653.

154.   Klasen, H. J. Historical review of the use of silver in the treatment of burns. I. Early uses. *Burns* **2000**, *26*, 117-130.

155.   Chopra, I. The increasing use of silver-based products as antimicrobial agents: a useful development or a cause for concern? *J. Antimicrob. Chemother.* **2007**, *59*, 587-590.

156.   Liu, J.; Sonshine, D. A.; Shervani, S.; Hurt, R. H. Controlled release of biologically active silver from nanosilver surfaces. *ACS Nano* **2010**, *4*, 6903-6913.

157.   Neissa, J.; Perez-Arnaiz, C.; Porto, V.; Busto, N.; Borrajo, E.; Leal, J. M.; Lopez-Quintela, M. A.; Garcia, B.; Dominguez, F. Interaction of silver atomic quantum clusters with living organisms: Bactericidal effect of Ag$_3$ clusters

mediated by disruption of topoisomerase-DNA complexes. *Chem. Sci*. **2015**, *4*, 6717-6724.

158.	Wakshlak, W. B-K.; Pedahzur, R.; Anvir, D. Antibacterial activity of silver-killed bacteria: The "zombies" effect. *Sci. Rep*. **2015**, *5*, 9555.

159.	Glisic, B. D.; Senerovic, L.; Comba, P.; Wadepohl, H.; Veselinovic, A.; Milivojevic, D. R.; Djuran, M. I.; Nikodinovic-Runic, J. Silver(I) complexes with phthalazine and quinazoline as effective agents against pathogenic *Pseudomonas aeruginosa* strains. *J. Inorg. Biochem.* **2016**, *155*, 115-129.

160.	Wright, P. M.; Seiple, I. B.; Myers, A. G. The evolving role of chemical synthesis in antibacterial drug discovery. *Angew. Chem. Int. Ed*. **2014**, *53*, 8840-8869.

161.	Kresse H.; Beasley, M. J.; Rovini, H. The antibacterial drugs market. *Nat. Rev. Drug Discovery* **2007**, *6*, 19-20.

162.	Liu, Y. Y.; Wang, Y.; Walsh, T. R.; Yi, L. X.; Zhang, R.; Spencer, J.; Doi, Y.; Tian, G.; Dong, B.; Huang, X.; Yu, L. F.; Gu, D.; Ren, H.; Chen, X.; Lv, L.; He, D.; Zhou, H.; Liang, Z.; Liu, J. H.; Shen, J. Emergence of plasmid-mediated colistin resistance mechanism MCR-1 in animals and human beings in China: A microbiological and molecular biological study. *Lancet Infect. Dis*. **2016**, *16*, 161-168.

163.	McGann, P.; Snesrud, E.; Maybank, R.; Corey, B.; Ong, A. C.; Clifford, R.; Hinkle, M.; Whitman, T.; Lesho, E.; Schaecher, K. E. Escherichia coli harboring

mcr-1 and blaCTX-M on a novel IncF plasmid: First report of mcr-1 in the United States. *Antimicrob. Agents Chemother*. **2016**, *60*, 4420-4421.

164.   Kaye, K. S.;   Pogue, J. M. Infections caused by resistant Gram-negative bacteria: epidemiology and management. *Pharmacotherapy* **2015**, *35*, 949-962.

165.   Barrasa-Villar, J. I.; Aibar-Remon, C.; Prieto-Andres, P.; Mareca-Doñate, R.; Moliner-Lahoz, J. Impact on morbidity, mortality, and length of stay of hospital-acquired infections by resistant microorganisms. *Clin. Infect. Dis.* **2017**, *65*, 644-652.

166.   Ventola, C. L. The antibiotic resistance crisis. *P. T.* **2015**, *40*, 277-283.

167.   Cardona, A. F.; Wilson, S. E. Skin and soft-Tissue infections: A critical review and the role of telavancin in their treatment. *Clin. Infect. Dis*. **2015**, *61*, S69-S78.

168.   Pendleton, J. N.; Gorman, S. P.; Gilmore, B. F. Clinical relevance of the *ESKAPE* pathogens. *Expert Rev. Anti Infect. Ther.* **2013**, *11*, 297-308.

169.   Boucher, H. W.; Talbot, G. H.; Bradley, J. S.; Edwards, J. E.; Gilbert, D.; Rice, L. B.; Scheld, M.; Spellberg, B.; Bartlett, J. Bad bugs, no drugs: No *ESKAPE*! An update from the infectious diseases society of America. *Clin. Infect. Dis*. **2009**, *48*, 1-12.

170.   Lam, P. L.; Lee, K. K. H.; Wong, R. S. M.; Cheng, G. Y. M.; Bian, Z. X.; Chui, C. H.; Gambari, R. Recent advances on topical antimicrobials for skin and soft tissue infections and their safety concerns. *Crit. Rev. Microbiol*. **2018**, *44*, 40-78.

171.   Eckmann, C.; Dreyden, M. S. Treatment of complicated skin and soft-tissue infections caused by resistant bacteria: Value of Linezolid, Tigecycline, Daptomycin and Vancomycin. *Eur. J. Med. Res*. **2010**, *15*, 554-563.

172.   Dryden, M. S. Complicated skin and soft tissue infection. *J. Antimicrob. Chemother*. **2010**, *65*, iii35-44.

173.   Ray, G. T.; Suaya, J. A.; Baxter, R. Incidence, microbiology, and patient characteristics of skin and soft-tissue infections in a U.S. population: A retrospective population-based study. *BMC Infect. Dis*. **2013**, *13*, 252.

174.   Ki, V.; Rotstein, C. Bacterial skin and soft tissue infections in adults: A review of their epidemiology, pathogenesis, diagnosis, treatment and site of care. *Can. J. Infect. Dis. Microbiol*. **2008**, *19*, 173-184.

175.   Gulick, A. M. Nonribosomal peptide synthetase biosynthetic clusters of ESKAPE pathogens. *Nat. Prod. Rev*. **2017**, *34*, 981-1009.

176.   Dryden, M. S. Skin and soft tissue infection: Microbiology and epidemiology. *Int. J. Antimicrob. Agents* **2009**, *34*, S2-S7.

177.   Lyon, B. R.; Skurray, R. Antimicrobial resistance of *Staphylococcus aureus*: genetic basis. *Microbiol. Rev*. **1987**, *51*, 88-134.

178.   Sommer, R.; Wagner, S.; Varrot, A.; Nycholat, C. M.; Khaledi, A.; Häussler, S.; Paulson, J. C.; Imberty, A.; Titz, A. The virulence factor LecB varies in clinical isolates: Consequences for ligand binding and drug discovery. *Chem. Sci*. **2016**, *7*, 4990-5001.

179. Viera, A.; Silva, Y. J.; Cunha, A.; Gomes, N. M. C.; Ackermann, H. W.; Almeida, A. Phage therapy to control multidrug-resistant *Pseudomonas aeruginosa* skin infections: In vitro and ex vivo experiments. *Eur. J. Clin. Microbiol Infect. Dis*. **2012**, *31*, 3241-3249.

180. Paterson, D. L. The epidemiological profile of infections with multidrug-resistant *Pseudomonas aeruginosa* and *Acinetobacter* species. *Clin. Infect. Dis*. **2006**, *43*, S43-S48.

181. Howard, A.; O'Donoghue, M.; Feeny, A.; Sleator, R. D. *Acinetobacter baumannii*. *Virulence*, **2012**, *3*, 243-250.

182. Calhoun, J. H.; Murray, C. K.; Manring, M. M. Multidrug-resistant organisms in military wounds from Iraq and Afghanistan. *Clin. Orthop. Relat. Res*. **2008**, *466*, 1356-1362.

183. Scott, P. T. et al. *Acinetobacter baumannii* infections among patients at military medical facilities treating injured U.S. service members, 2002-2004. *MMRW*, **2004**, *292*, 2964-2966.

184. Scott, P.; Deye, G.; Srinivasan, A.; Murray, C.; Moran, K.; Hulten, E.; Fishbain, J.; Craft, D.; Riddell, S.; Lindler, L.; Mancusi, J.; Milstrey, E.; Bautista, C. T.; Patel, J.; Ewel, A.; Hamilton, T.; Gaddy, C.; Tenney, M.; Christopher, G.; Petersen, K.; Endy, T.; Petruccelli, B. An outbreak of multidrug-resistant *Acinetobacter baumannii-calcoaceticus* complex infection in the US military health care system associated with military operations in Iraq. *Clin. Infect. Dis.* **2007**, *44*, 1577-1584.

185. Wendt, C.; Dietze, B.; Dietz, E.; Rüden, H. Survival of *Acinetobacter baumannii* on dry surfaces. *J. Clin. Microbiol*. **1997**, *35*, 1394-1397.

186. Fair, R. J.; Tor, Y. Antibiotics and bacterial resistance in the 21st century. *Perspect. Medicin. Chem*. **2014**, *6*, 25-64.

187. Falagas, M. E.; Kasiakou, S. K. Colistin: The revival of polymyxins for the management of multidrug-resistant gram-negative bacterial infections. *Clin. Infect. Dis*. **2005**, *40*, 1333-1341.

188. Lansdown, A. B. G. Silver in health care: antimicrobial effects and safety in use. *Curr. Probl. Dermatol*. **2006**, *33*, 17-34.

189. Aziz, Z.; Abu, S. F.; Chong, N. J. A Systematic Review of Silver-Containing Dressings and Topical Silver Agents (Used with Dressings) for Burn Wounds. *Burns*, **2012**, *38*, 307-318.

190. Nherera, L. M.; Trueman, P.; Roberts, C. D.; Berg, L. A systematic review and meta-analysis of clinical outcomes associated with nanocrystalline silver use compared to alternative silver delivery systems in the management of superficial and deep partial thickness burns. *Burns* **2017**, *43*, 939-948.

191. Thomas, S. S.; Lawrence, J.; Thomas, A. Evaluation of hydrocolloids and topical medication in minor burns. *J. Wound Care* **1995**, *4*, 218-220.

192. Fisher, N. M.; Marsh, E.; Lazoca, R. Scar-localized argyria secondary to silver sulfadiazine cream. *J. Am. Acad. Dermatol*. **2003**, *49*, 730-732.

193.   Pinto, M.; Chakraborty, I.; Mascharak P. Synthesis and crystal structure of bis(1{[(quinoline-8-yk)imino]methyl}pyrene-K2N,N')Silver(I) trifluoromethanesulfonate. *Acta Cryst.* **2016**, *E72*, 1495-1498,

194.   Chakraborty, I.; Pinto, M.; Stenger-Smith, J.; Martinez-Gonzalez, J. Mascharak, P. K. Synthesis, structures and antibacterial properties of Cu(II) and Ag(I) complexes derived from 2,6-bis(benzothiazole)-pyridine. *Polyhedron* **2019**, In Press, Corrected Proof.

195.   Pinto, M. N.; Chakraborty, I.; Schultz-Simonton, W.; Rojas-Andrade, M.; Braslau, R.; Mascharak, P. K. Tracking silver delivery to bacteria using turn-on fluorescence. *Chem. Commun.* **2017**, *53*, 1459-1462.

196.   Soica, C.; Pinzaru, L.; Trandafirescu, C.; Andrica, F.; Canicu, C.; Moic, M.; Coricovc, D.; Sitaru, C.; Dehelean, C. Silver-, gold-, and iron-based metallic nanoparticles: biomedical applications as theranostic agents for cancer. Design of nanostructures for theranostic applications **2018**, [Online] 161-242.

197.   Pietro, P. D.; Strano, G.; Zuccarello, L.; Satriano, C. Gold and silver nanoparticles for applications in theranostics, *Curr. Top Med. Chem.* **2016**, *16*, 3069-3102.

198.   Li, Y.; Chang, Y.; Lian, X.; Zhou, L.; Yu, Z.; Wang, H.; An, F. Silver nanoparticles for enhanced cancer theranostics: in vitro and in vivo perspectives. *J. Biomed. Nanotechnol.* **2018**, *14*, 1515-1542.

199. Barabadi, H.; Saravanan, M. Emerging theranostic silver and gold nanomaterials to combat prostate cancer: a systematic review. *J. Cluster Sci*. **2019**, 1-8.

200. De Matteis, V.; Cascione, M.; Toma, C. C.; Leporatti, S. Silver nanoparticles: synthetic routes, in vitro toxicity and theranostic applications for cancer disease. *Nanomaterials* **2018**, *8*, 319-328.

201. Pinto, M. N.; Martinez-Gonzalez, J.; Chakraborty, I.; Mascharak, P. K. Incorporation of a theranostic "two-tone" luminescent silver complex into biocompatible agar hydrogel composite for the eradication of *ESKAPE* pathogens in a skin and soft tissue infection model. *Inorg. Chem.* **2018**, *57*, 6692-67012.

1.6 Copyright

Order Completed

Thank you for your order.

This Agreement between University of California, Santa Cruz -- Miguel Pinto ("You") and Elsevier ("Elsevier") consists of your license details and the terms and conditions provided by Elsevier and Copyright Clearance Center.

Your confirmation email will contain your order number for future reference.

printable details

License Number	4674540833303
License date	Sep 22, 2019
Licensed Content Publisher	Elsevier
Licensed Content Publication	Advanced Drug Delivery Reviews
Licensed Content Title	Development and applications of photo-triggered theranostic agents
Licensed Content Author	Prakash Rai,Srivalleesha Mallidi,Xiang Zheng,Ramtin Rahmanzadeh,Youssef Mir,Stefan Elrington,Ahmat Khurshid,Tayyaba Hasan
Licensed Content Date	Aug 30, 2010
Licensed Content Volume	62
Licensed Content Issue	11
Licensed Content Pages	31
Type of Use	reuse in a thesis/dissertation
Portion	figures/tables/illustrations
Number of figures/tables/illustrations	1
Format	both print and electronic
Are you the author of this Elsevier article?	No
Will you be translating?	No
Original figure numbers	Figure 1.
Title of your thesis/dissertation	DESIGN AND CONSTRUCTION OF BIOCOMPATIBLE THERANOSTIC CARBON MONOXIDE AND SILVER DELIVERY SYSTEMS FOR ANTICANCER AND ANTIBACTERIAL PHOTOCHEMOTHERAPY
Expected completion date	Jan 2020
Estimated size (number of pages)	470
Requestor Location	University of California, Santa Cruz 1156 High Street SANTA CRUZ, CA 95064 United States Attn: University of California, Santa Cruz

Title: Photoactivated [Mn(CO)3Br(μ-bpcpd)]2 induces apoptosis in cancer cells via intrinsic pathway

Author: Vidhyapriya P.,Divya D.,Manimaran Bala,Sakthivel N.

Publication: Journal of Photochemistry and Photobiology B: Biology

Publisher: Elsevier

Date: November 2018

© 2018 Elsevier B.V. All rights reserved.

Order Completed

Thank you for your order.

This Agreement between University of California, Santa Cruz -- Miguel Pinto ("You") and Elsevier ("Elsevier") consists of your license details and the terms and conditions provided by Elsevier and Copyright Clearance Center.

Your confirmation email will contain your order number for future reference.

printable details

License Number	4674541218606
License date	Sep 22, 2019
Licensed Content Publisher	Elsevier
Licensed Content Publication	Journal of Photochemistry and Photobiology B: Biology
Licensed Content Title	Photoactivated [Mn(CO)3Br(μ-bpcpd)]2 induces apoptosis in cancer cells via intrinsic pathway
Licensed Content Author	Vidhyapriya P.,Divya D.,Manimaran Bala,Sakthivel N.
Licensed Content Date	Nov 1, 2018
Licensed Content Volume	188
Licensed Content Issue	n/a
Licensed Content Pages	14
Type of Use	reuse in a thesis/dissertation
Portion	figures/tables/illustrations
Number of figures/tables/illustrations	1
Format	both print and electronic
Are you the author of this Elsevier article?	No
Will you be translating?	No
Original figure numbers	Figure 14
Title of your thesis/dissertation	DESIGN AND CONSTRUCTION OF BIOCOMPATIBLE THERANOSTIC CARBON MONOXIDE AND SILVER DELIVERY SYSTEMS FOR ANTICANCER AND ANTIBACTERIAL PHOTOCHEMOTHERAPY
Expected completion date	Jan 2020
Estimated size (number of pages)	470
Requestor Location	University of California, Santa Cruz 1156 High Street SANTA CRUZ, CA 95064 United States Attn: University of California, Santa Cruz
Publisher Tax ID	98-0397604

Upconverting nanoparticles for the near infrared photoactivation of transition metal complexes: new opportunities and challenges in medicinal inorganic photochemistry

Title: Photo-induced eradication of human colorectal adenocarcinoma HT-29 cells by carbon monoxide (CO) delivery from a Mn-based green luminescent photoCORM

Author: Jorge Jimenez,Miguel N. Pinto,Jorge Martinez-Gonzalez,Pradip K. Mascharak

Publication: Inorganica Chimica Acta

Publisher: Elsevier

Date: 24 January 2019

Published by Elsevier B.V.

BACK   CLOSE WINDOW

Tracking silver delivery to bacteria using turn-on fluorescence

Title: Eradication of HT-29 colorectal adenocarcinoma cells by controlled photorelease of CO from a CO-releasing polymer (photoCORP-1) triggered by visible light through an optical fiber-based device

Author: Miguel N. Pinto,Indranil Chakraborty,Cosme Sandoval,Pradip K. Mascharak

Publication: Journal of Controlled Release

Publisher: Elsevier

Date: 28 October 2017

BACK | CLOSE WINDOW

ACS Publications
Most Trusted. Most Cited. Most Read.

Title:	Incorporation of a Theranostic "Two-Tone" Luminescent Silver Complex into Biocompatible Agar Hydrogel Composite for the Eradication of ESKAPE Pathogens in a Skin and Soft Tissue Infection Model
Author:	Miguel N. Pinto, Jorge Martinez-Gonzalez, Indranil Chakraborty, et al
Publication:	Inorganic Chemistry
Publisher:	American Chemical Society
Date:	Jun 1, 2018

Copyright © 2018, American Chemical Society

Chapter 2.I: Eradication of HT-29 Colorectal Adenocarcinoma Cells by Controlled Photorelease of CO from a CO-Releasing Polymer (photoCORP-1) Triggered by Visible Light Through an Optical Fiber-Based Device.

2.I.1 Background.

Carbon monoxide (CO) is a colorless, odorless, tasteless, and poisonous gas produced by the incomplete combustion/oxidation of carbon containing compounds.[1] The inhalation of large amounts of CO is one of the leading causes of unintentional poisoning around the world.[2] However, this gas is produced endogenously within mammals through the degradation of heme by the enzyme heme oxygenase (inducible HO-1 or constitutive HO-2).[3-5] Interest in the biochemical effects of CO continues to increase due to its role as a 'gasotransmitter' (gaseous signaling molecule) in mammalian pathophysiology.[6,7] In addition, CO is implicated in neurodegeneration,[8-10] hypertension,[11–13] inflammation,[14–17] oxidative stress,[7,18–21] cell proliferation,[22] and apoptosis.[23,24] Administration of low/moderate doses of CO has been shown to induce proapoptotic/anti-proliferative effects on a number of malignant cell lines[6,25–27] and can sensitize cancer cells to conventional anticancer drugs.[28-31] As a consequence, use of CO in direct and/or adjuvant chemotherapy appears to be a reasonable option for the treatment of malignancy. Unlike other gasotransmitters, CO does not undergo physical or chemical alterations inside the cell, and it can essentially diffuse into all cellular compartments. CO primarily interacts with 'soft' metal centers in heme proteins.[6] However, the molecular targets of CO remain somewhat unclear since not all heme proteins

are present in every cell or they may vary in their levels of expression.[29] Upon CO

binding, the function of a heme protein can be enhanced[32-34] or blocked,[35] promoting

signaling cascades. The effect of these signaling pathways can then influence the

modulation of many other non-heme proteins such as mitogen activated protein

kinases,[14,35] nuclear factor erythroid 2-related factor (Nrf2),[37] heat shock proteins,[38] and

others.[39-41] Another common target is the mitochondria, which is also present in

different numbers depending on the cell type. In general, most cancer cells exhibit

elevated levels of reactive oxygen species (ROS) as well as antioxidants proteins,

suggesting a relatively fragile balance of intracellular ROS when compared to normal

cells.[42-44] The treatment of cancer cells with CO leads to increased mitochondrial ROS

production,[18,35] which then may tip the balance toward ROS-induced apoptotic

signaling.[43,44] The main technical difficulty one encounters in using CO as a

chemotherapeutic is its site-specific administration in a controlled and sustainable

manner. For example, direct inhalation therapy requires sustained exposure to

relatively high amounts of CO to elicit an observable response.[43] Systemic

administration of CO gas lacks specificity and results in increased CO concentrations

throughout the body, accentuating its negative side effects.[46] CO releasing molecules

(CORMs) present an alternative way to deliver controlled amounts CO to target tissues.

Use of the first-generation CORMs (such as $[Ru(Cl)_2(CO)_3]_2$ and $Mn_2(CO)_{10}$) in

clinical settings has however been quite difficult due to problems related to their low

solubility in water, toxicity, short lifetime, and requirements of organic solvents to

trigger CO release through ligand exchange.[47] Photoactive carbon monoxide releasing

molecules (photoCORMs), with some exceptions, are metal carbonyl complexes that release CO upon illumination. These CO donors present a way to deliver CO to a specific site with spatial and temporal control.[48-54] Recent efforts from our group have been made to impart desirable characteristics such as sensitivity toward visible light, solubility and stability in water, and low toxicity to make photoCORMs more appropriate for CO delivery *in vivo*.

PhotoCORMs conjugated to a large variety of carriers such as dendrimers,[55] polymers,[56-58] peptides,[59] protein cages,[60] micelles,[61] and nanocarriers,[62,63] have been reported. These materials transport and deliver the photoCORMs to biological targets and often retain the CO-spent products within the polymer matrices thus avoiding adverse side effects. Among such delivery vehicles, only the example reported by the Schiller group delivers CO from a bulk material source which is removed following CO delivery.[60-64] In this case, the photoCORM is non-covalently encapsulated into electrospun fibers of poly(L-lactide-co-D/L-lactide). This non-woven fabric when stretched and wrapped around an optical fiber allows for remote triggering of the encapsulated photoCORM with the aid of a 405 nm laser (14 mW cm^{-2}). We have previously used composite materials for re- mote delivery of a different gasotransmitter, nitric oxide (NO).[65-68] In such research, we have reported a silica-based sol-gel material that non-covalently encapsulated a photoactive NO-releasing molecule.[65] The material was triggered remotely using an optical fiber, and the photoreleased NO was used for the eradication of pathogenic bacteria.[65] In a separate

case, a photoactive NO-donor was covalently attached to a polyHEMA hydrogel and the material was employed to deliver NO to myoglobin.[69]

In the present work, we report a novel polyHEMA-based CO-re- leasing polymer (photoCORP-**1**) in which a manganese photoCORM $[Mn(CO)_3(qbt)(4-vpy)](CF_3SO_3)$ (**1**) bearing a 4-vinylpyridine (4-vpy) ancillary ligand has been covalently attached to 2-hydroxyethyl methacrylate (HEMA) polymer backbone. This robust yet flexible photoCOR hydrogel rapidly releases CO upon illumination with low power (> 1 mW cm^{-2}) visible light. The HEMA-based hydrogel was selected because of its extensive use in biomedical applications, gas permeability, low toxicity, biocompatibility, softness, chemical stability, and transparency.[70-72] Indeed photoCORP-1 allows controlled escape of CO from the entire HEMA hydrogel monolith as evidenced by loss of the original orange color (arising from **1**). We also report the construction of a fiber optic-based catheter with photoCORP-**1** tip that allows remote triggering of CO photorelease by visible light. The catheter has been successfully used to promote CO-induced apoptosis in human colorectal adenocarcinoma HT-29 cells. The extent of apoptotic death of the cancer cells has been investigated with the aid of flow cytometry using propidium iodide (PI)/Annexin V stain. To the best of our knowledge, photoCORP-**1** is the first example of a CO-releasing hydrogel that could be remotely triggered by low power visible light and used to eradicate cancer cells. The easy removal of the CO-releasing catheter from the malignant site also allows one to circumvent toxicity arising from any CO-spent products at the targeted site.

2.I.2 Results and Discussion.

2.I.2.1 Synthesis and characterization of [Mn(CO)$_3$(qbt)(4-vpy)](CF$_3$SO$_3$) 1.

Complex **1** was synthesized in a stepwise manner, intermediates were isolated and purified, and all manipulations were performed in the dark to avoid the decomposition of the CO donor. First, manganese pentacarbonyl bromide ([Mn(CO)$_5$Br]) reacted with the ligand qbt in a chloroform/ methanol mixture (1:3 v/v) for 10 h at room temperature to afford [Mn (CO)$_3$(qbt)Br]. The Br$^-$ ligand was replaced with CF$_3$SO$_3^-$ by treating the complex [Mn(CO)$_3$(qbt)Br] with silver triflate (Ag(CF$_3$SO$_3$) in dichloromethane. Then, the weakly coordinating CF$_3$SO$_3^-$ ligand of the resulting complex ([Mn(CO)$_3$(qbt)(CF$_3$SO$_3$)] complex was replaced with 4-vinylpyridine (4-vpy) to afford **1** in good yield. This photoCORMs was selected for the present study for a variety of reasons. Much like other manganese-containing photoCORMs,[49] **1** exhibits rapid release of CO upon exposure to low power visible light, suitable for phototherapy. The dark orange coloration of this photoCORM becomes colorless upon CO release, a characteristic that allows visualization of the overall photorelease process. The 4-vpy unit allowed us to covalently attach this photoCORM to the polyHEMA framework; the radical-derived polymerization step does not decompose complex **1** and allows its easy incorporation. Finally, the resulting photoCORP-**1** composite retains the CO-spent products quite tightly (as evidenced by leaching experiments) while CO readily diffuses out of the polymeric matrix upon illumination.

Complex **1** exhibits FTIR stretching frequencies (2040, 1955, and 1929 cm^{-1}) typical of metal carbonyl complexes with three facially coordinated CO ligands (*fac*-[Mn(CO)$_3$] moiety (Figure 2.I.1).[25] It dissolves in organic solvents like chloroform, dichloromethane and acetone. A solution of **1** in dichloromethane displays two absorption bands at 445 and 382 nm, resulting in an orange red coloration.
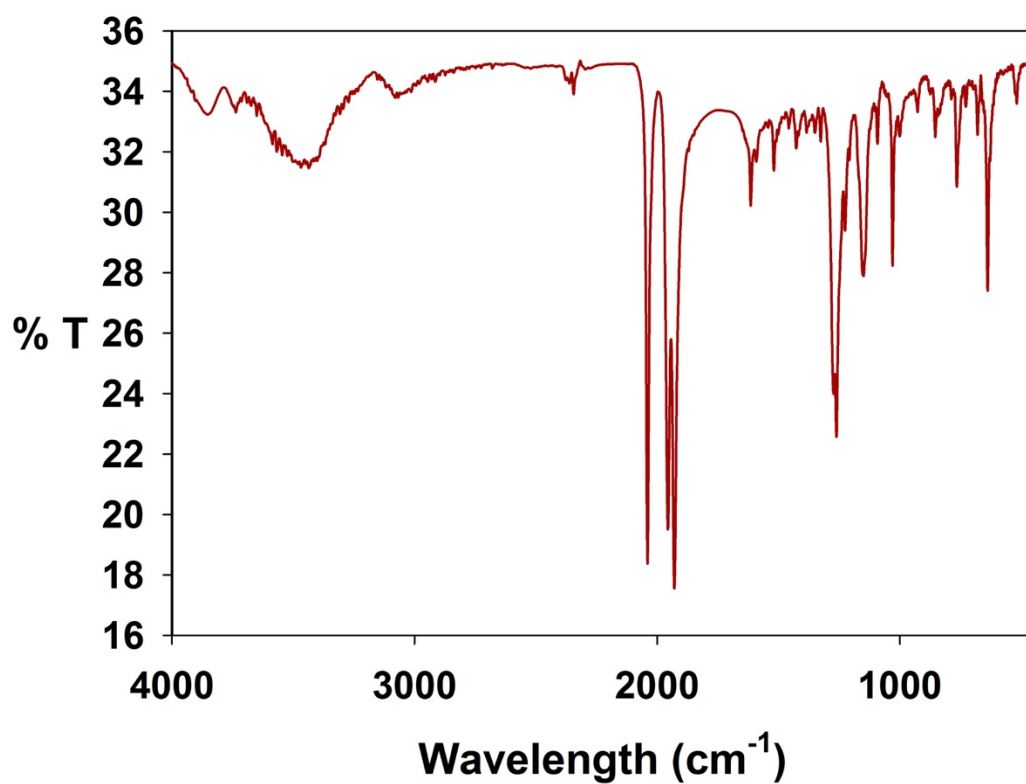
Figure 2.I.1. FT-IR spectrum of complex **1** in KBr matrix.

*2.I.2.2 X-ray Structure Analysis of **1***.

X-ray quality crystals were obtained by layering hexanes over a dichloromethane solution of **1**. The molecular structure of **1** is shown in Figure 2.I.2
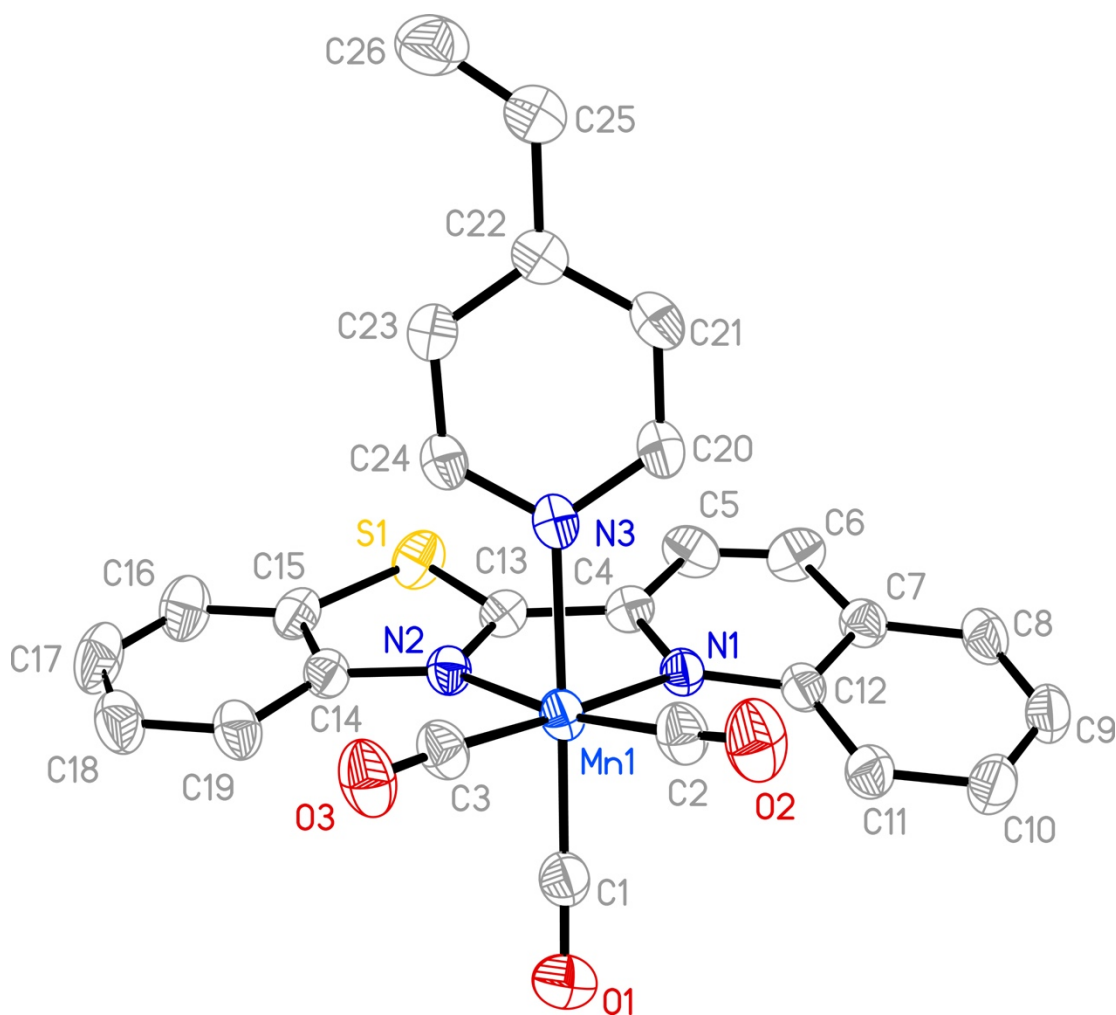
Figure 2.I.2. Molecular structure of the cation of complex **1** with atom labeling scheme. The thermal ellipsoids are shown at 50%0 probability level. Selected bond distances (Å): Mn1-C1 1.818(5), Mn1-C2 1.800(5), Mn1-C3 1.823(6), Mn1-N1 2.113(4), Mn1-N2 2.062(4), and Mn1-N3 2.0094(4).

and selected matrix parameters are listed in the figure caption. The coordination geometry surrounding the Mn(I) metal center is distorted octahedral. The equatorial plane is composed of two CO ligands (in cis conformation) and two N atoms from the bidentate ligand qbt, while the third CO occupies an axial position trans to the 4-vinyl pyridine ligand (Figure 2.I.2). Crystal data and structure refinement parameters are listed in Table 2.I.1.

Although the equatorial plane comprised of C2, C3, N1 and N2 atoms in **1** is satisfactorily planar (mean deviation of 0.050(5) Å), the Mn atom is deviated from this plane by 0.110(4) Å toward the N3 atom of the vinyl pyridine fragment. In addition, the chelate ring composed of Mn1, N1, C4, C13, and N2 atoms significantly deviates from planarity (mean deviation, 0.110(3) Å). As a consequence, the entire qbt ligand frame is tilted toward the 4-vpy moiety (dihedral angle 12.7°). The average the Mn-C bond distances in complex **1** (1.814(6) Å) is quite similar to that observed with analogous [Mn(CO)$_3$(qbt)Cl] complex (1.800(6) Å).[76] The crystal packing of **1** reveals no π-π stacking interactions. However, non-classical hydrogen bonding of types C-H···O (2.547(5) and 2.542(5) Å) and C-H···F (2.466(6) Å) is present in the solid state.

2.I.2.3 Photochemical Characteristics and CO Release Rate of 1.

The deep orange color of solutions of **1** is lost upon exposure to visible light. Systematic exposure of such solutions to small intervals of broadband visible light (10 mW cm^{-2}) results in sequential changes in the electronic absorption spectrum (Figure 2.I.3). Myoglobin assay (*vide infra*) reveals that the spectral changes are due to

Table 2.I.1. Crystal data and structure refinement parameters for **1**.

	1 CH_2Cl_2
Empirical formula	$C_{27}H_{17}N_3O_6F_3S_2Mn$
T(K)	298
λ (Å)	0.71073
Crystal system	Monoclinic
Space group	$P2(1)/n$
a (Å)	12.6789(6)
b (Å)	11.9823(6)
c (Å)	18.3284(9)
α (°)	90
β (°)	93.982(1)
γ (°)	90
V (Å^3)	2777.8(2)
Z	4
D_{calc} (Mg m^{-3})	1.567
Absorption Coeff (mm^{-1})	0.69
No. of unique reflections	3367
Goodness-of-fit[a] on F^2	1.06
R_1[b]	0.070
wR_2[c]	0.222
largest diff peak and hole	0.90, -0.51

[a]GOF = $[\Sigma[\omega(F_o^2-F_c^2)^2]/(N_o-N_v)]^{1/2}$ (N_o = number of observations, N_v = number of variables).
[b]$R_1 = \Sigma||F_o|-|F_c||/\Sigma|F_o|$. [c]w$R_2 = [(\Sigma\omega(F_o^2-F_c^2)^2/\Sigma|F_o|^2)]^{1/2}$

photorelease of CO from **1** upon illumination. In order to determine the apparent CO-release rate (k_{CO}), a 0.067 mM solution of **1** in dichloromethane was exposed to broadband visible light (10 mW cm^{-2}) for 20 s intervals and the value of k_{CO} was determined from the ln(C) (C = concentration of **1**) vs. time (t) plot. The k_{CO} value for **1** (0.96 min^{-1}) clearly indicated that this photoCORM is very sensitive to low power visible light.
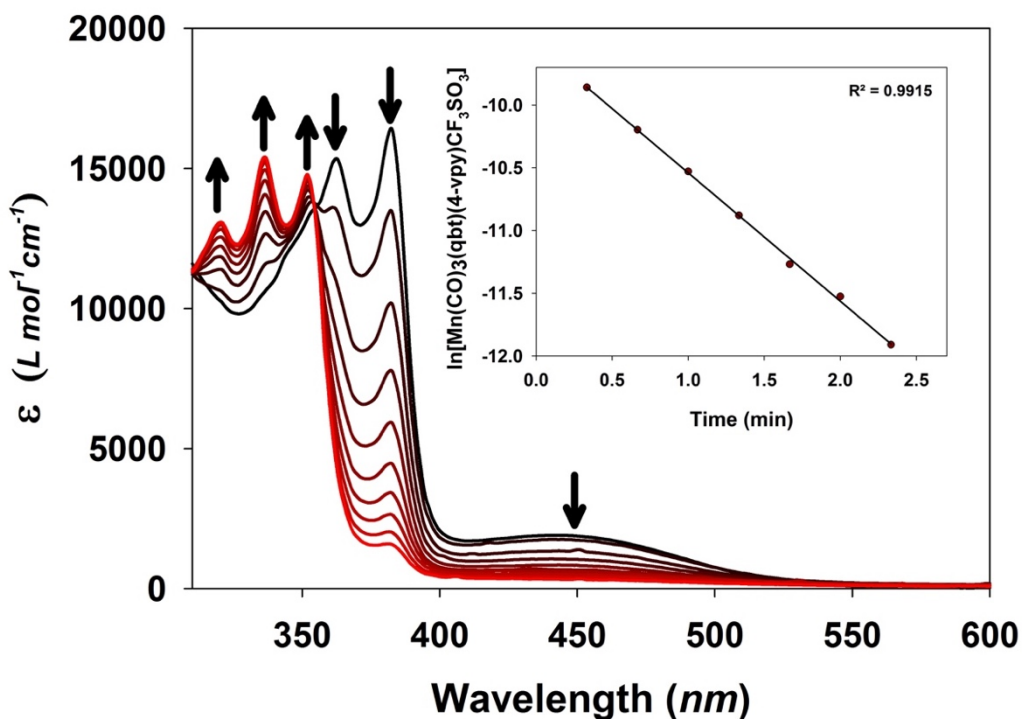
Figure 2.I.3. Systematic changes in the electronic absorption spectrum of **1** in dichloromethane upon exposure to intervals of broadband visible light (10 mW cm^{-2}, 20 s intervals, 298 K) leading to CO photorelease (Inset: apparent CO release rate k_{CO} = 0.96 min^{-1} as determined by the ln(C) vs. time plot).

2.1.2.4 Synthesis and Characteristics of photoCORP-1 and CO Releasing Experiments.

The HEMA/EGDMA polymer was chosen for its well-studied biocompatibility, transparency, gas permeability, chemical/physical stability, and porosity characteristics.[70-72] PhotoCORP-**1** was synthesized by mixing a solution of **1** in acetone with a pre-polymer mixture containing the HEMA monomer, EGDMA cross-linker, water, and VA-044 (temperature sensitive initiator). A final 0.1 mM concentration of **1** in such mixture was necessary to isolate photoCORP-**1** suitable for absorption spectroscopy, while a higher final concentration of **1** (4 mM) was employed to isolate composite materials suitable for CO delivery required in the cellular experiments. No dichloromethane was employed in the polymerization reactions to avoid any toxicity due to residual solvent in the final photoCORP-**1** samples. The polymerization temperature conditions allowed us to use acetone as the solvent for preparing the solutions of **1**. The temperature of the polymerization reaction was carefully controlled to avoid reaching boiling points of any solvent component during the synthesis of photoCORP-**1** and hence problems associated with formation of bubbles leading to irregular/brittle polymeric product(s) were absent. VA-044 was selected as the radical initiator in our experiments due to its decomposition/activation at relatively mild temperatures. Conventional initiators requiring UV irradiation were not considered in order to prevent any premature decomposition of the manganese photoCORM.

Once cured for 48 h, photoCORP-**1** is a photosensitive and malleable orange solid that has a shelf life of over 3 months if kept at 0 °C in a moist sealed container in the dark. The malleability of the solid samples is slowly lost when the material is left out of a sealed package and results in a hard solid within 5 days. Fresh samples of photoCORP-**1** can be cast into any shape or form if a mold is available. However, if the size of the mold is large, it is often difficult to control the temperature of the polymerization step because the radical polymerization reaction is highly exothermic and may reach temperatures higher than the boiling point of the solvents used. This causes the solvent to boil and create bubbles within the bulk of the polymer. When freshly prepared, photoCORP-**1** is relatively flexible and can easily be cut into different shapes using a razor blade.

The covalent binding of **1** to the polymer frame (Figure 2.I.4) ensures retention of both 1 and its photoproduct(s) within the polymer matrix. The high hydrophobicity of these species could also be responsible for effective retention. No detectable leaching of complex/ligands was observed when photoCORP-**1** was submerged in aqueous buffer for over 2 months (before and/or after photolysis) as determined UV–Vis spectrophotometry and EPR spectrometry.

In order to examine the CO-releasing parameters of photoCORP-**1**, the pre-polymer mixture containing the initiator, monomer, cross linker, solvents and complex **1** (0.1 mM w.r.t. **1**) was poured into a polystyrene cuvette and heated for 30 min in a water bath carefully kept right below 50 °C to initiate the radical polymerization. The heat was then turned off and the cuvette was allowed to cool slowly to room

PhotoCORM

Covalent Attachment to Polymer

HEMA (Monomer)

EGDMA (Crosslinker)
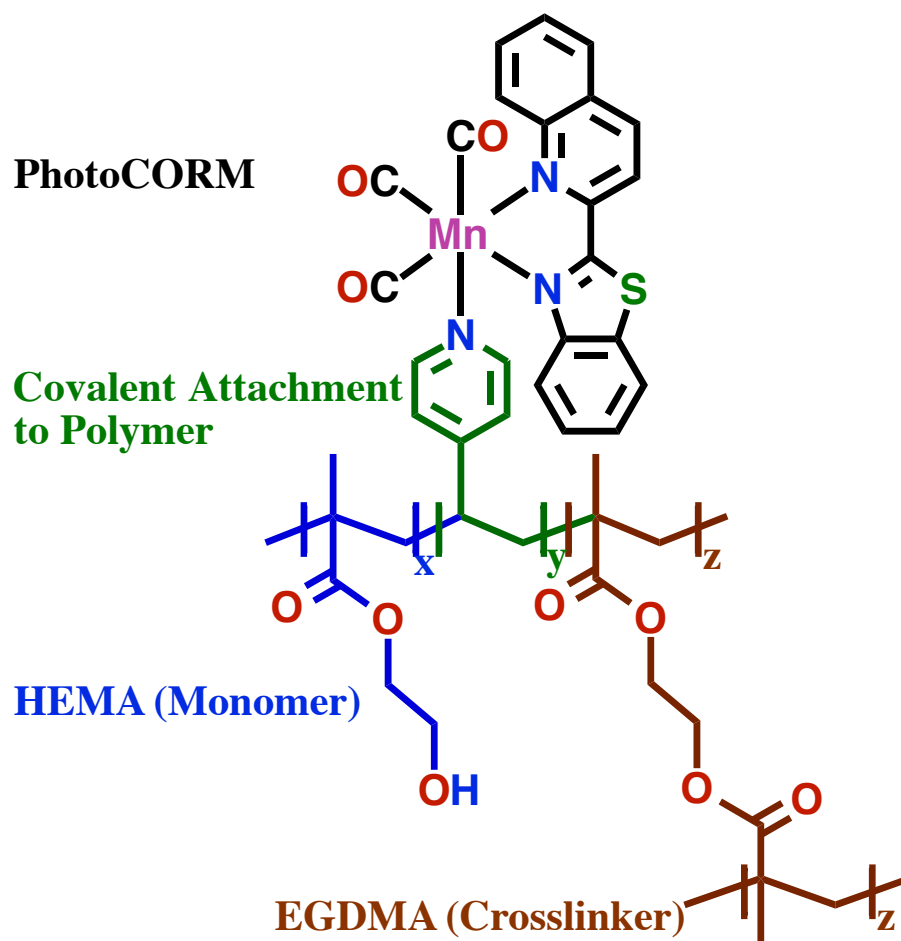
Figure 2.I.4. Schematic representation of photoCORP-**1** co-polymerized within HEMA/EGDMA hydrogel.

temperature to control the exothermic polymerization. A blank polymer containing everything except the manganese photoCORM was used as a blank (Figure 2.I.5a) for baseline correction. The cuvettes were then kept in the dark at room temperature for 48 h to ensure curing. The cuvette containing photoCORP-**1** was then exposed to 10 mW cm^{-2} broadband visible light and the changes in the electronic absorption spectrum were recorded as before. As shown in Figure 2.I.6, the spectral traces clearly indicate that
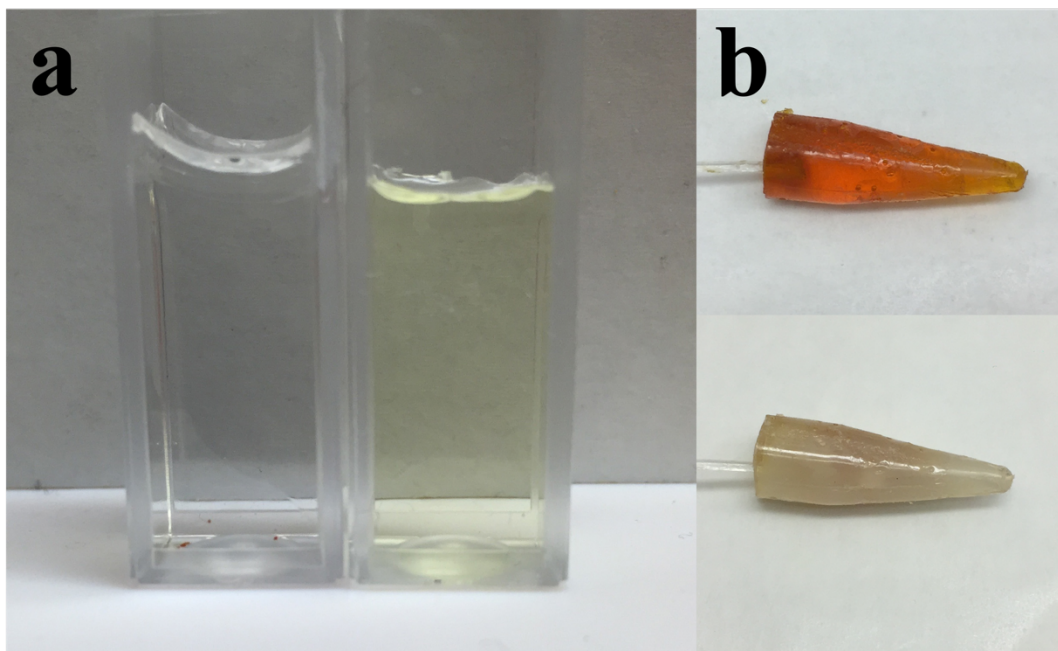
Figure 2.I.5. Images of photoCORP-**1** polymerized (a) inside polystyrene cuvettes for UV-vis spectrophotometry, blank (left) and photoCORP-**1** (0.1 mM w.r.t. 1, right); (b) inside Eppendorf^{TM} tubes to afford the tip of the optical fiber-based CO-catheter, before use (top) and after extensive photolysis (bottom).

photoCORP-**1** releases CO upon illumination. Kinetic analysis of the spectral changes afforded an apparent CO release rate k^{CO} of 0.40 min^{-1}, a value slower than the k_{CO} value of free complex **1**. This slow-down of CO photorelease is expected since the porosity (and extent of hydration) of the polymer matrix does attenuate the diffusion rate of CO from the bulk of the photoCORM-**1** monolith. In addition, the intensity of the incident light may also be attenuated while passing through the polymeric matrix.
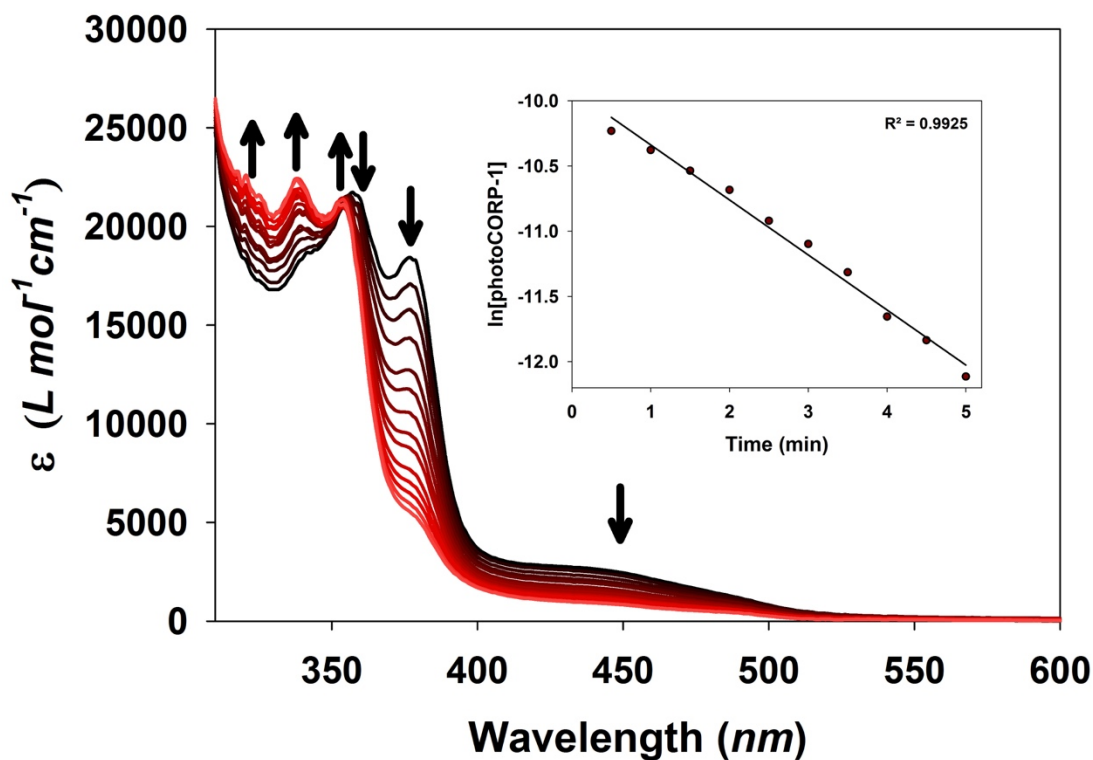
Figure 2.I.6. Systematic changes in the electronic absorption spectrum of a monolith of photoCORP-**1** (within a polystyrene cuvette) upon exposure to small intervals of visible light (10 mW cm^{-2}, 30 s intervals, 298 K) due to CO photorelease (inset: apparent CO release rate kCO = 0.40 min-1 as determined by the ln(C) vs. time plot).

The tips of the CO-catheters were cast in Eppendorf^{TM} tubes. In this case, the pre-polymer mixture containing the initiator, monomer, cross linker, solvents and complex **1** (4 mM) was poured into Eppendorf^{TM} tubes with the optical fiber dipped in it and the assemblies were heated at 50 °C for 30 min in a water bath. After slow cooling to room temperature, the assemblies were kept in the dark for 48 h. The tubes were then carefully broken apart with a hammer and the CO-catheters were taken out and rinsed

with water. As shown in Figure 2.I.5b (top), the high concentration of **1** in the tip is indicated by the dark orange color. The CO release rate from the tip of the CO-catheter was determined by myoglobin assay (*vide infra*). Extensive illumination of such tips results in loss of the color (Figure 2.1.5b, bottom) due to complete loss of CO from the composite material. It is important to note here that a much higher concentration of **1** was used to prepare the tips of the CO-catheters (compared to that in the polystyrene cuvettes used in the previous step) to ensure delivery of enough CO to elicit apoptotic response in malignant targets.

2.I.2.5 Determination of Coupling Efficiency of Our Fiberoptic-Based Device.

The coupling efficiency of our set-up was tuned to deliver low-power light to the polymer tip to release sustained and moderate amounts of CO. With a 30 cm optical fiber attached to the 10 mW cm^{-2} broadband visible light source through our F-915 T
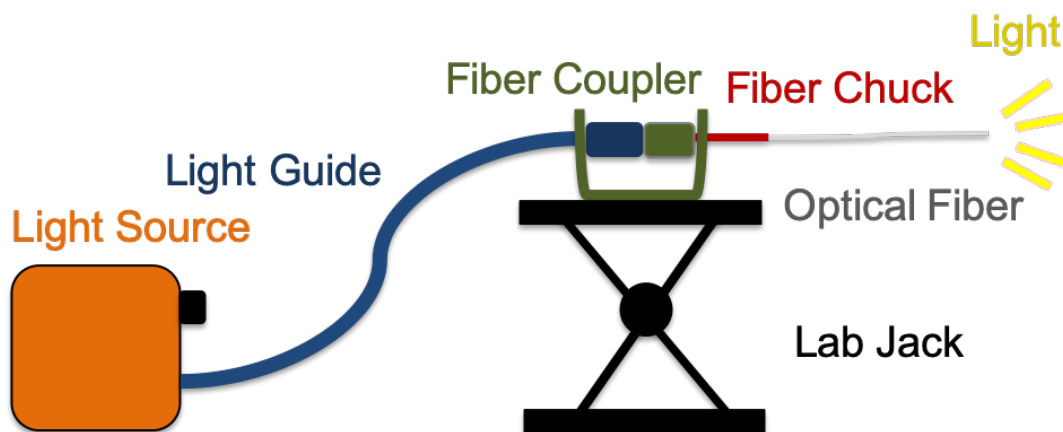
Figure 2.I.7. Schematic representation of the fiberoptic based assembly.

multimode fiber coupler (Figure 2.I.7), we recorded an output of 2.31 mW cm^{-2} at the end of the fiber (coupling efficiency 23%). However, when the tip was directly illuminated with light of this intensity, most of the CO was released from the polymer within 30 min. Since the solubility of CO in aqueous media is very low, such rapid expulsion of CO from the catheter would result in escape of a major part of the photoreleased CO from the target tissues before it causes the desired physiological effect. Therefore, to achieve a more controlled and sustained levels of CO, the power of the incidence light was adjusted to 2.5 mW cm^{-2} to bring down the output to 0.58 mW cm^{-2} at the end of the optical fiber. All experiments with CO-catheters were therefore performed with an incident light intensity of 2.5 mW cm^{-2}.

2.I.2.6 Controlled Delivery of CO to Myoglobin from CO-Catheter.

Myoglobin assay was used to confirm the release of CO from the polymer tip of the CO-catheter. In this assay, the rate of CO release was measured by tracking the formation of carbonmonoxymyoglobin (MbCO) with a polymer tip which was made from pre-polymer mixture with 4 mM concentration of **1**. Analytical data indicated that this composite contained a total of 1.018 mg of **1** covalently bound to 260 mg of the final tip material (0.39 wt. %). The power of the incident light was set to 2.5 mW cm^{-2} to expose the tip to visible light intensity of 0.58 mW cm^{-2}. The tip of the CO-catheter used in the assay comprised of 0.26 g of photoCORP-**1**. It was dipped directly into a reduced myoglobin solution and was triggered with the visible light source for **1** min intervals. To keep oxygen from interacting with the solution, a current of dry nitrogen

was placed directly over the quartz cuvette. Following each min of illumination, the CO-catheter was taken out, rinsed with water, dried and kept in the dark. The absorption spectra were recorded after each illumination period. As shown in Figure 2.I.8, the delivery of CO from the CO-catheter results in the rapid formation of MbCO evidenced by shift of the Soret band of reduced Mb (435 nm) to 424 nm. A device capable of CO delivery to myoglobin by remote light triggering has recently been reported by Schiller and coworkers.[64] In this work, a hydrophobic tetranuclear tricarbonyl manganese complex was non-covalently imbedded inside electrospun non-woven fibers of poly(L-lactide-co-D/L-lactide) 70/30. Unlike the present system consisting of photoCORP-**1** covalently embedded within the bulk of a solid polymer tip, the porous fibers were wrapped around a spherical glass head at the tip of an optical fiber to achieve the CO-donating unit. This system also requires a 405 nm laser (14 mW cm^{-2}) for CO release. Although Schiller and co-workers presented an excellent portable illumination device, the CO release was observed "only from the sample areas in direct contact with the glass sphere exposed to light whereas salient areas remained unaffected". Consequently, CO release from the Schiller device is expected to be somewhat slow compared to the present device in which CO is released from the entire tip as evidenced by complete bleaching of the orange color upon exhaustive illumination (Figure 2.I.5b, bottom panel). Also, the light intensity required for rapid CO release from the photoCORP-**1** tip is considerably low compared to the requirement for the Schiller device. Finally, the Schiller material contained 10 wt. % complex "according to the amount of theoretically embedded photoCORM" compared to photoCORP-**1**
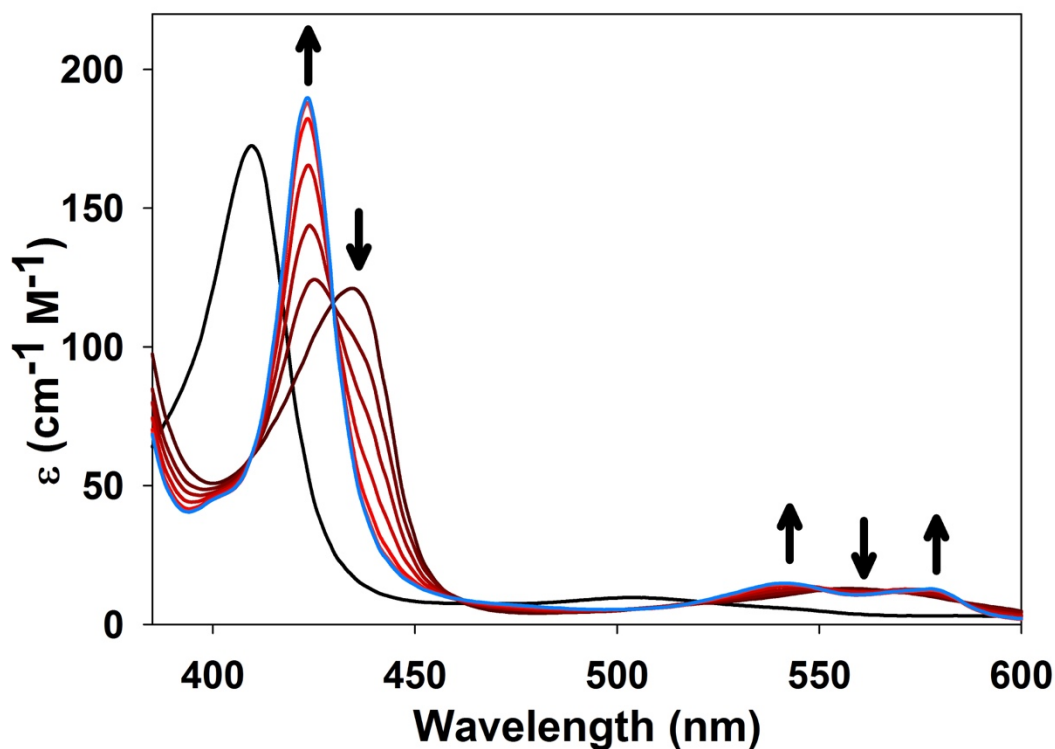
Figure 2.I.8. Myoglobin assay performed by submerging the tip of the CO-catheter directly into the reduced Mb solution. The catheter was triggered by visible light (0.58 mW cm^{-2}) for 1 min intervals and the changes in the spectrum were recorded. Shift of the Soret band from 435 nm to 424 nm indicates the formation of Mn$_{CO}$ by CO release from the tip of the catheter. The black trace is the absorption spectrum of the starting oxidized Mb.

containing 0.39 wt. % of **1**. Nevertheless photoCORP-**1** released 12.78 μM CO in 30min upon exposure to 0.58 mW cm^{-2} visible light while equivalent amount of the Schiller material released 1.2 μmol of CO in 30 min with a 14 mW cm^{-2} laser.[64]

*2.I.2.7 Variations in CO Delivery Capacity of PhotoCORP-**1** with Light Intensity and Extent of Drying.*

To study the effect of hydration on the CO-release rate of photoCORP-**1**, one block of cured polymer was removed from its mold and cut into smaller blocks (0.9 × 0.4 × 0.4 cm, 0.26 g, 0.39 wt. % of **1**) which were then air dried in the dark for different amounts of time (0 days, 5 days, 10 days) before myoglobin assays were performed to determine their capacity of CO delivery. In all assays, the polymer block was submerged inside the reduced Mb solution and the quartz cuvette was stoppered. The polymer block inside the cuvette was then directly exposed to the external visible light source (10 mW cm^{-2}), inverted multiple times, and the absorption spectra were recorded. The fresh polymer (0 day) exhibited full conversion from Mb to MbCO within 40 s (4 × 10 s exposures). To ensure full conversion of MbCO, the polymer was illuminated for a total of 3 min and the absorption spectrum was recorded again. The rate of CO release from the photoCORP-1 piece was 0.074 μM s^{-1} mg^{-1} (Figure 2.I.9, T_{30} = 133.20 μM mg^{-1}).

When the power of the incident light was sequentially changed from 10 mW cm^{-2} to 1.6 mW cm^{-2}, 0.58 mW cm^{-2}, and 0.50 mW cm^{-2}, the k_{CO} value dropped down from 0.074 μM s^{-1} mg^{-1} (T_{30} = 133.20 μM mg^{-1}) to 0.0094 μM s^{-1} mg^{-1} (T_{30} =16.92 μM mg^{-1}), 0.0071 μM s^{-1} mg^{-1} (T_{30} =12.78 μM mg^{-1}), and 0.0065 μM s^{-1} mg^{-1} (T_{30} = 11.70 μM mg^{-1}), respectively (Figure 2.I.9). These results confirm that the CO release capacity of photoCORP-**1** depends on the intensity of the incident light (in addition to

the concentration of **1**). The nonlinearity in the variation of CO release rates from photoCORP-**1** with the power of the incident light appears to arise from the fact that
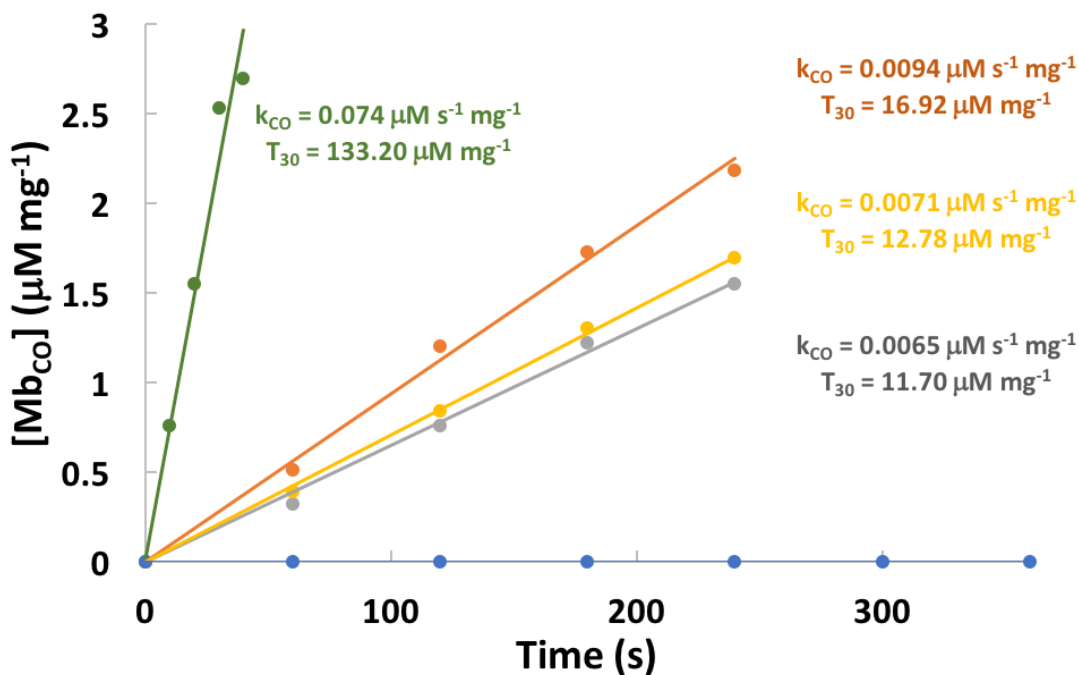
Figure 2.I.9. Plot of conversion of Mb to Mb$_{CO}$ by fresh photoCORP-**1** under different light intensity. Green trace: Light intensity: 10 mW cm^{-2}; k$_{CO}$: 0.074 μM s^{-1} mg^{-1}; Orange trace: light intensity: 1.6 mW cm^{-2}; k$_{CO}$: 0.0094 μM s^{-1} mg^{-1}; Yellow trace: light intensity: 0.58 mW cm^{-2}; k$_{CO}$: 0.0071 μM s^{-1} mg^{-1}; Grey trace: light intensity: 0.50 mW cm^{-2}; k$_{CO}$: 0.0065 μM s^{-1} mg^{-1}; Blue trace: No light.

when the polymer is illuminated with high power light, the CO molecules closest to the surface exit the polymer rather fast, whereas CO molecules that are released deep inside the polymer block are not able to exit the polymer as quickly.

When an identical polymer block ($0.9 \times 0.4 \times 0.4$ cm, 0.26 g, 4 mM w.r.t. **1**) was air dried in dark for 5 days, the weight of the material decreased from 0.26 g to 0.21 g, indicating a loss of about 20% of its initial weight presumably due to loss of solvent molecules from the polymer matrix. The composite lost its compressibility and became hard after such loss of solvent. When we subjected this 5-day old polymer block to the same myoglobin assay under the same direct illumination (10 mW cm^{-2}), conversion of Mb to MbCO was complete within 40s (4 exposures of 10s each). The CO release rate was 0.058 μM s^{-1} mg^{-1} (Figure 2.I.10, $T_{30} = 104.4$ μM mg^{-1}), somewhat slower than that obtained with a fresh identical sample of photoCORP-**1**. Air drying (in dark) for 10 days did not lead to much reduction in weight of the polymer blocks (changed from 0.26 g to 0.20 g). However, the CO release rate dropped to 0.044 μM s^{-1} mg^{-1} (Figure 2.I.10, $T_{30} = 79.2$ μM mg^{-1}), as evidenced by the myoglobin assay. Collectively, these results indicate that despite loss of flexibility, the polymer remains useful for CO delivery even after it becomes relatively dry.

2.I.2.8 Controlled Delivery of CO to Human Colorectal Adenocarcinoma Cells and Human Embryonic Kidney Cells (as Normal Control).

The pro-apoptotic effects of CO on hyperproliferative and dysregulated cells such as cancer cells[6] has prompted us to assemble this CO-catheter to deliver controlled doses of CO to colorectal adenocarcinoma cells. The onset of apoptosis in cells is regularly detected by Annexin V assay where a dye-tethered phospholipid-binding protein binds to phosphatidylserine translocated on the outer leaflet of the

plasma membrane at the beginning of apoptosis and identifies cells that have entered

the apoptotic cycle. Propidium iodide (PI) is also used in such measurement to detect

cells with heavily compromised membranes in which PI intercalates between the base

pairs of the nucleic acids and exhibits enhanced fluorescence. In the present study, we

Figure 2.I.10. Plot conversion of Mb to Mb_{CO} by photoCORP-**1** following different

extent of drying. Blue trace: fresh polymer, CO release rate 0.074 $\mu M\ s^{-1}\ mg^{-1}$; Orange

trace: polymer after 5 days of drying, CO release rate 0.058 $\mu M\ s^{-1}\ mg^{-1}$; Green trace:

polymer after 10 days of drying, CO release rate 0.044 $\mu M\ s^{-1}\ mg^{-1}$.

performed this assay to detect the pro-apoptotic effects of CO in the cancer cells and

analyzed the extent of cell apoptosis/death by FACS analysis.

Prior the start of the cellular treatment, freshly prepared CO-catheters were

removed from their sealed container, checked for their integrity and weight, washed,

and sterilized using 70% ethanol. They were then air dried for 30 min and kept in the dark inside a sealed sterile container until the beginning of the treatment. A fresh CO-catheter was used for each cell treatment and the weight of the tip (0.50 g, 0.39 wt. % of **1**) was carefully controlled to ensure similar amounts of CO delivery to the cells. Human colon cancer cells (HT-29) were cultured in their appropriate media, harvested, and counted manually using a hemocytometer. The cells were diluted to a concentration of 10^6 cells mL^{-1} using the growth medium, and 2 mL portions of this solution were split into FACS tubes. The cells were then subjected to CO by submerging the tips of the catheters directly into the cell suspension and triggering the CO-catheter for 5, 10, 20 and 40 min (Figure 2.I.11 and Figure 2.I.12). Following exposure to CO the cells were centrifuged and the cell pellets were resuspended in 900 μL of PBS buffer. Finally, 100 μL of Annexin binding buffer was added to each FACS tube along with 2 μL of Annexin V. After 15 min of incubation at room temperature, the cells were treated with 2 μL of propidium iodide and subjected to FACS analysis.

Results of the FACS analysis (Figure 2.I.13) reveal that exposure to CO led to the onset of apoptosis (Annexin V binding) to the cancer cells soon after the CO-catheter was triggered with visible light (0.58 mW cm^{-2}). The extent of apoptotic response was dose-dependent as evidenced by the illumination-time dependent increase of the apoptotic cells. Annexin V binding to the cancer cells increased with time of CO exposure (Figure 2.I.13., top panel) as evidenced by shift of the cell population toward the Annexin V axis. In addition, a considerable number of doubly-stained cells were also detected (Figure 2.I.13d), indicating the beginning of cell

destruction. Cells without any CO treatment (Figure 2.I.13e, bottom panel) were used

as blanks to determine the amount of apoptosis induced by the handling steps alone.

For accuracy, the control cells were kept under conditions identical to those of the

treated samples. In our hand, the various handling steps (trypsinization, centrifugation,

resuspension) led to a background apoptotic cell count of ~10% (Figure 2.I.14.).
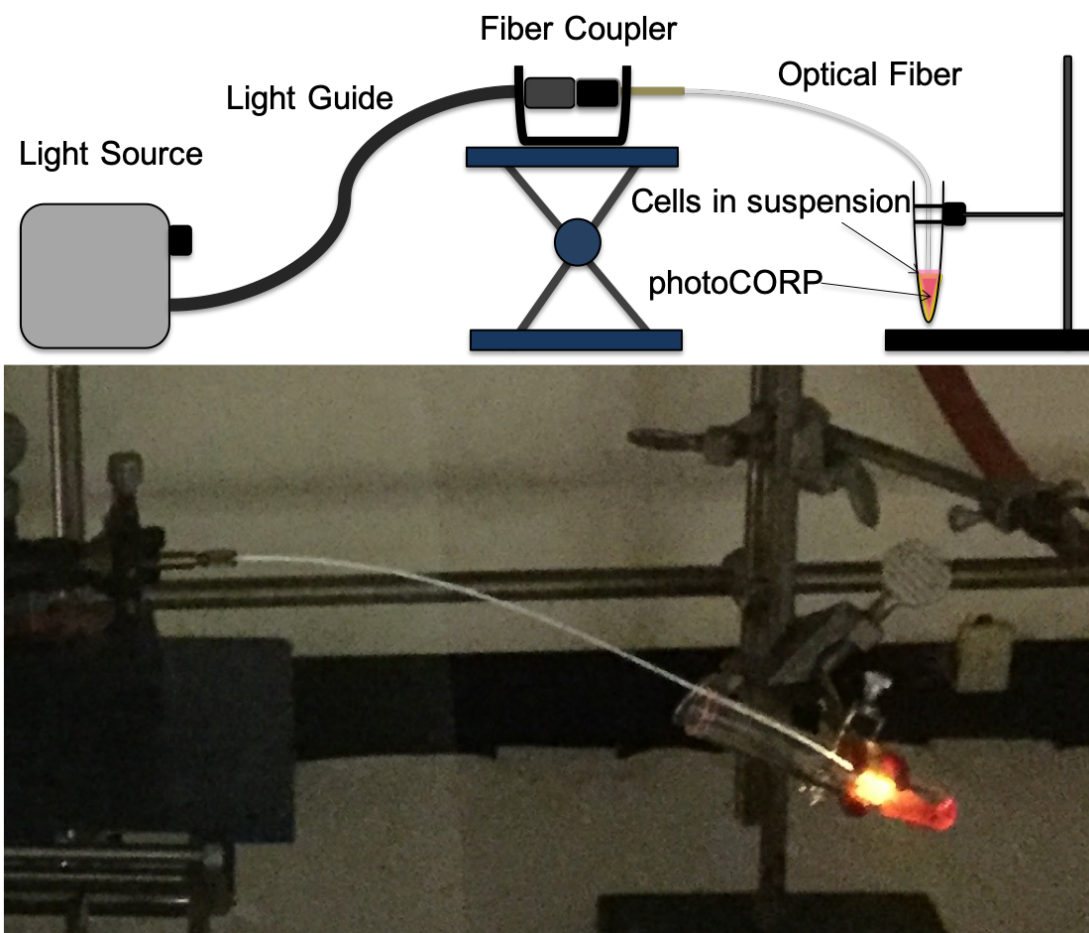
Figure 2.I.11. Top panel: Schematic representation of the CO-delivery set up. Bottom

panel: photograph of the actual set up.

Controls also included cytometry of cells treated with a CO-spent catheter (Figure 2.I.13f, bottom panel) and cells treated with a fresh CO-catheter but no light (Figure 2.I.13g, bottom panel). Collectively these results demonstrate that the CO-catheter delivers CO to the cell suspension (total volume 2 mL) to cause onset of CO-induced apoptosis within a short time and such onset of apoptosis occurs only when the CO-catheter is triggered with light. The slow and sustained effects of CO also demonstrate
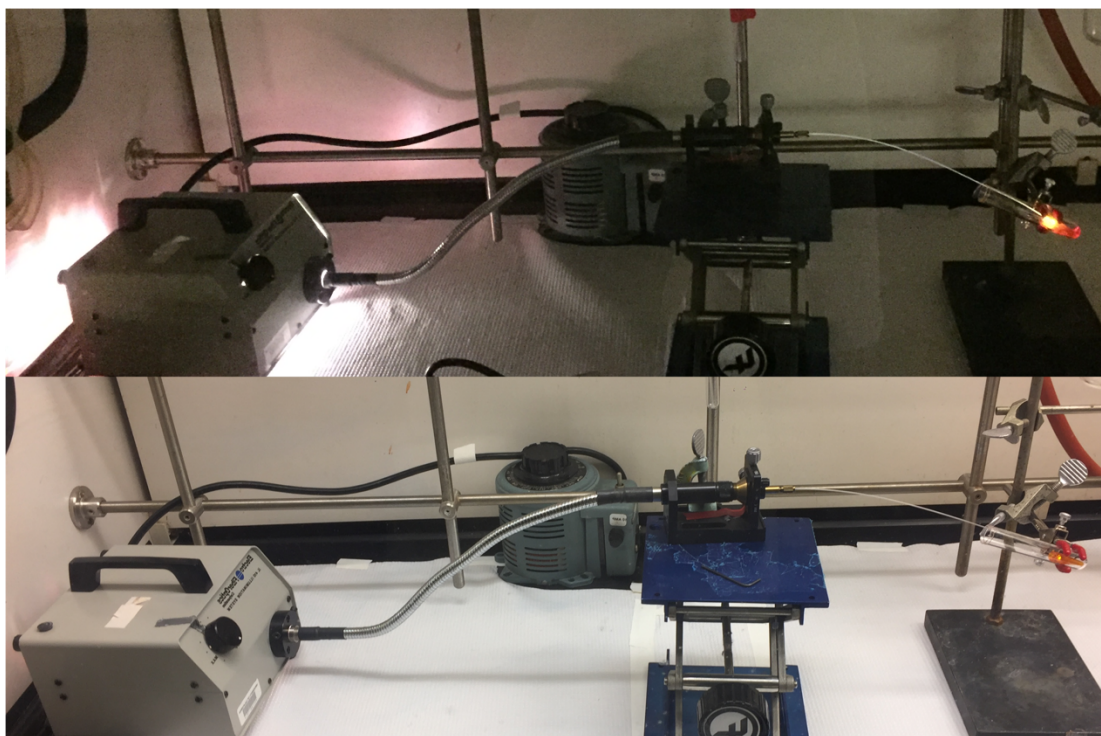
Figure 2.I.12. Photographs of CO delivery set up using CO-catheter.

that controlled delivery of CO is indeed possible with photoCORP-**1** and this composite material can be employed in a light-triggering device to carry out CO delivery to remote targets. Interestingly, the tip of the CO-catheter lost most of its dark orange color

(Figure 2.I.5b) after 40 min of illumination. The CO-spent catheter that we employed was irradiated with visible light for a long time and therefore was completely colorless (Figure 2.I.5b).

The results of FACS analysis are better represented in a bar plot as shown in Figure 2.I.14. In case of HT-29 cells, the induction of apoptotic death increases with the time of CO exposure. As shown in Figure 2.I.14, remote illumination by the CO-
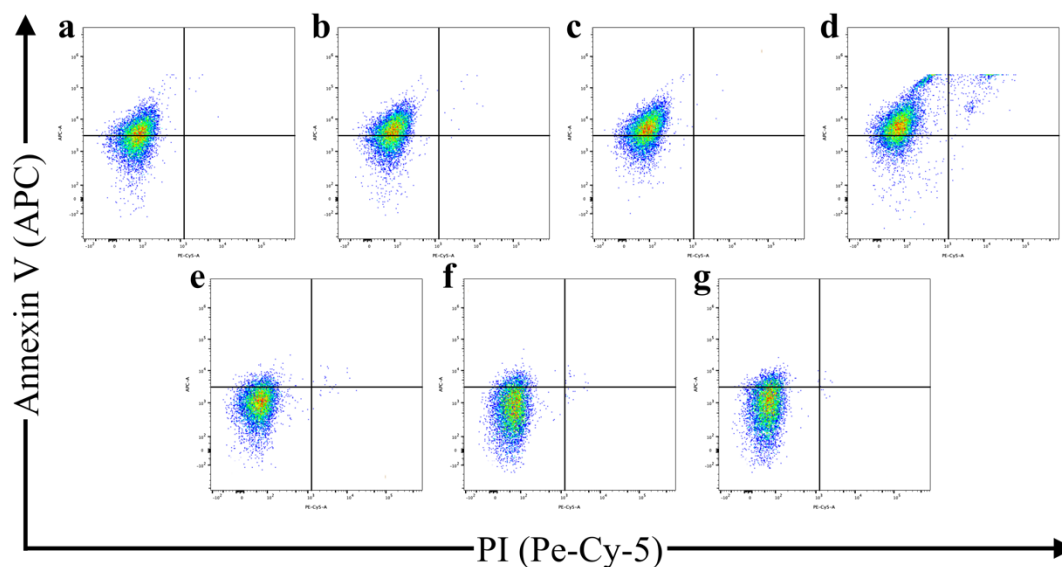
Figure 2.I.13. (Top panel) Flow cytometry analysis (plots of Annexin V-Alexafluor647/Propidium iodide staining of HT-29 cells) after CO exposure (from the CO-catheter) of (a) 5 min, (b) 10 min, (c) 20 min, (d) 40 min. (Bottom panel) plots of Annexin V-Alexafluor647/Propidium iodide staining of HT-29 cells with (e) no CO treatment, (f) treatment with a CO-spent catheter and (g) treatment with a fresh CO-catheter but no light.

catheter for 5 min resulted in Annexin binding by 48% of the cell population (blue bars). The number of apoptotic cells thereafter increased to 60% upon 10 min exposure and to 75% at the end of 40 min. In contrast, when human embryonic kidney cells (HEK 293) were exposed to CO by similar technique, no induction of apoptosis was observed (orange bars). The last observation confirms that exposure to CO (as available from the tips of the catheter) does not result in any cytotoxic effects in normal cells.
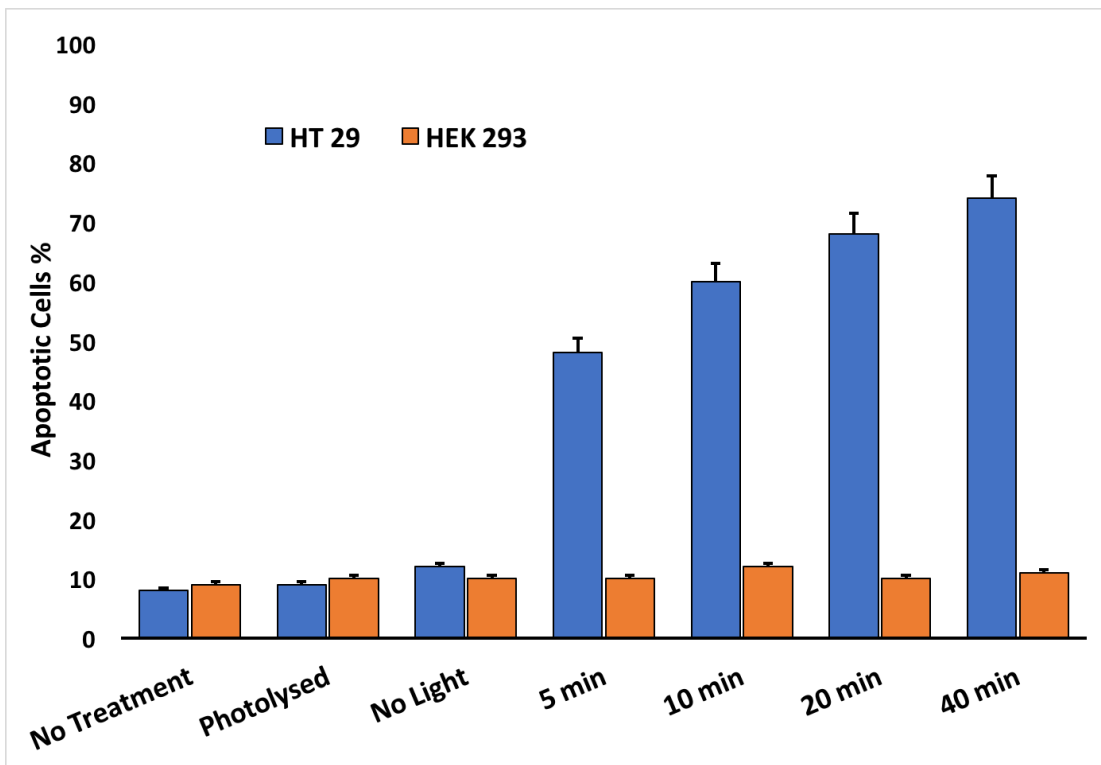
Figure 2.I.14. Bar plot representation of the flow cytometry results shown in Figure 2.I.13 showing the progression of apoptosis in HT-29 cells upon exposure to CO (blue bars). The absence of apoptosis upon exposure of HEK 293 cells to CO is shown by the orange bars.

Repeat experiments with CO-catheter containing a lower concentration of **1** (made from pre-polymer mixture with 0.1 mM of **1**) led to much smaller extent of CO-induced apoptosis in HT-29 cells. It is therefore evident that the tip of the CO-catheter must contain a high concentration of the CO-donating complex **1** to achieve rapid onset of apoptosis in the cell culture. This is somewhat expected since a major portion of CO photoreleased from the tip of the CO-catheter escapes the suspension containing the cancer cells (due to the low solubility of CO in aqueous media) before reaching to its target. Important is to note that photoCORP-**1** is very sensitive to light and hence we used low-power (0.58 mW cm^{-2}) broadband visible light to trigger CO release to achieve a sustained and moderate levels of CO at the target site in all these experiments. For the very same reason, the con- centration of **1** in the tip material must be raised to 0.30 – 0.40 wt. % to deliver a steady release of CO for hours. Finally, the rate of CO release from the CO-catheter with a certain concentration of **1** can be accelerated or decelerated substantially by changing the power of the light used to trigger the device.

2.I.3 Conclusions.

The proapoptotic and chemosensitizing properties of CO make it a potential therapeutic for certain types of cancer. However, precise delivery of controlled doses of this noxious gas to the malignant site poses as major challenge to CO therapy. In this work, we report a biocompatible CO-donating polymer composite photoCORP-**1** that releases CO when triggered with low-power (mW levels) broadband visible light. The gas permeable HEMA/EGDMA hydrogel allows rapid release of CO from the polymer monolith but retains the photoproducts tightly bound to the organic framework through

covalent bond (Figure 2.I.4). Synthesis of photoCORP-**1** involves two steps and requires 48 h of curing time to afford a malleable composite that can be molded or cut into any size and shape. The CO-releasing capacity of photoCORP-**1** does not change considerably upon drying of the hydrogel. Because the polymer matrix traps all products but CO upon illumination, photoCORP-**1** can be utilized as a convenient CO source for experiments such as delivery of controlled doses of CO to biological samples like proteins (as in the myoglobin experiments reported here). Indeed, we have
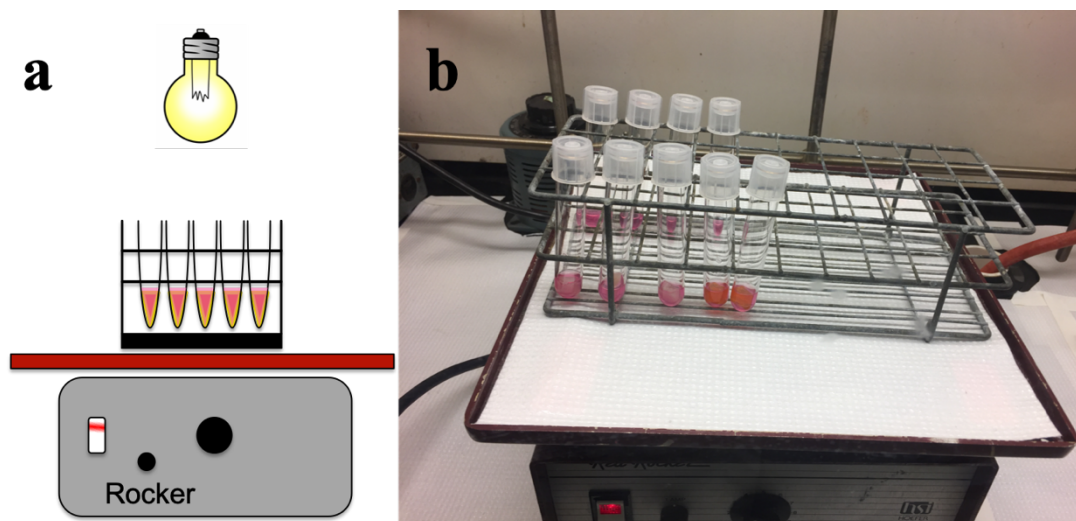
Figure 2.I.15. (a) Schematic representation of the CO delivery set up under ambient light. (b) photograph of the actual treatment.

performed the CO delivery experiments with the HT-29 cells by using small blocks of photoCORP-**1** and external illumination by the room light (Figure 2.I.15). In such attempts, CO-induced apoptosis was readily achieved much like the experiments described above (Figure 2.I.16 and Figure 2.I.17).

The most important result of this study is the assembly of the CO-catheter that allows delivery of controlled and sustained doses of CO to a target consisting of HT-29 (human colorectal adenocarcinoma) cells under the total control of light. The success in this mode of CO delivery demonstrates that it is possible to deliver controlled doses of CO to malignant targets in inaccessible cavity and promote CO-induced
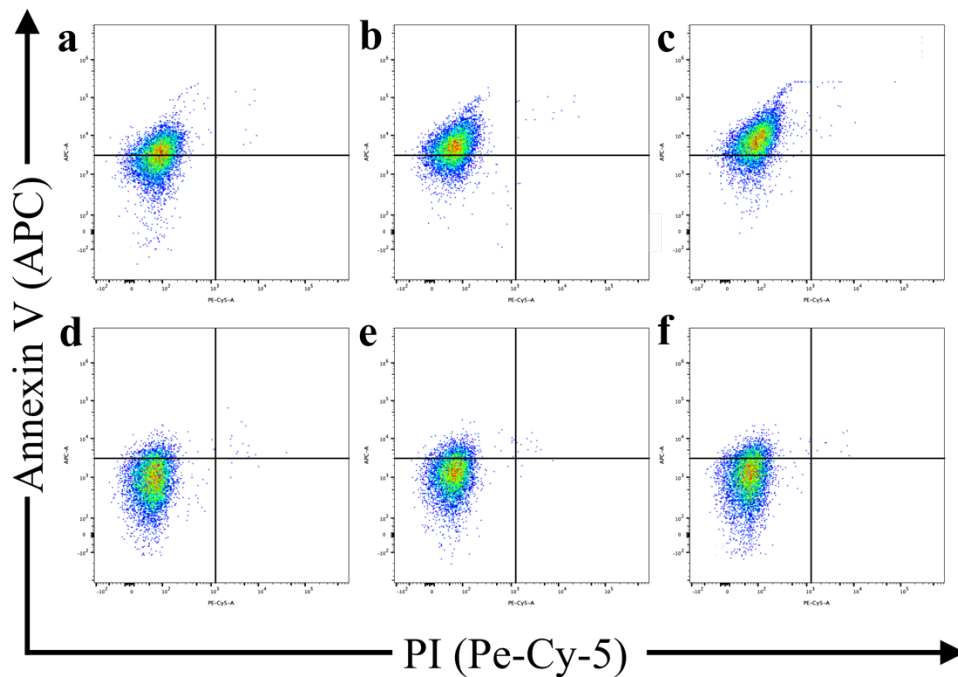
Figure 2.I.16. (Top panel) Flow cytometry analysis (plots of Annexin V-Alexafluor647/propidium iodide staining of HT-29 cells) after CO exposure (from 0.50 g block of photoCORP-**1**) of (a) 5 min, (b) 20 min and (c) 40 min. (Bottom panel) Plots of Annexin V- Alexafluor647/propidium iodide staining of HT-29 cells with (d) no CO treatment, (e) treatment with a CO-spent photoCORP-**1** block, and (f) treatment with a fresh photoCORP-**1** but no light.

apoptosis in cancer cells. For example, it is possible to employ this CO-catheter to deliver CO to malignant sites in adjuvant chemotherapy of colon cancer. Because CO is known to enhance chemosensitivity, one expects to use lower doses of conventional chemotherapeutics and avoid their toxic side effects. The relatively recent Endoscopic Fiber Optic Shape Tracker (EFOST) technology has emerged as a minimally invasive
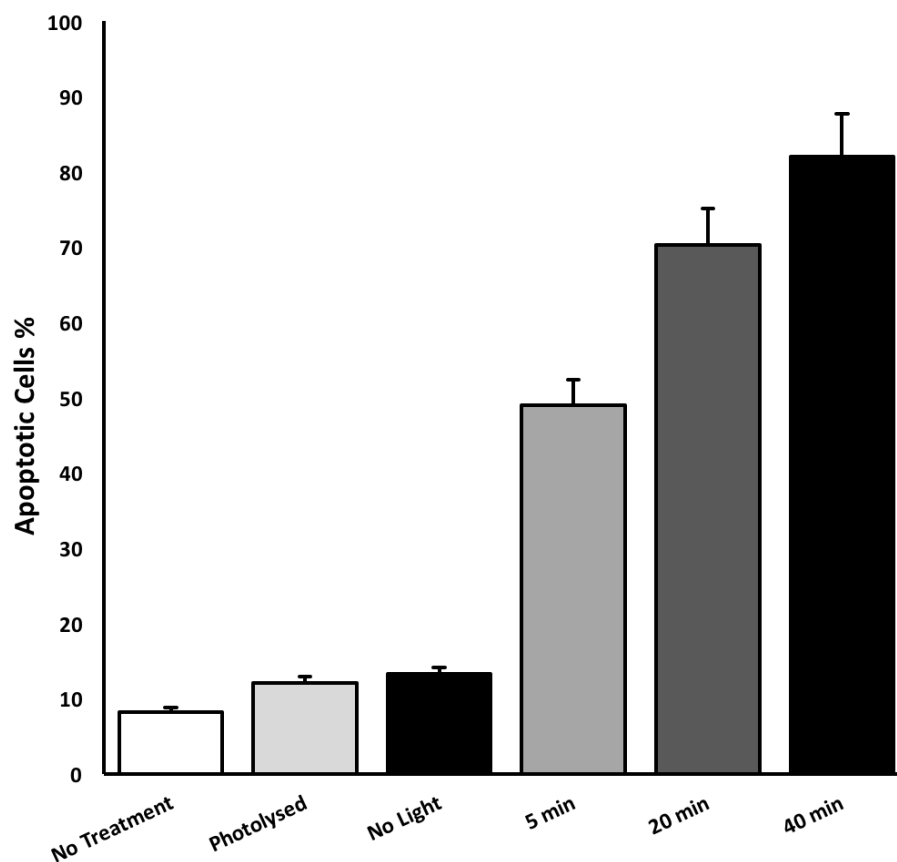
Figure 2.I.17. Bar plot representation of the flow cytometry results shown in Figure 2.I.16 indicating the progression of apoptosis in HT-29 cells upon exposure to CO triggered by ambient light.

means for application toward endovascular space.[76] In fact, the newly developed fiberoptic illumination sources can deliver sufficient light through very thin optical fiber to activate CO release from photoactive materials such as photoCORP-**1** and deliver required doses of CO to a colonic target.

2.I.4 Experiential Section.

2.I.4.1 General Methods and Instrumentation.

Bromopentacarbonylmanganese (I) was purchased from Strem Chemicals. 2,2′-azobis[2-(2-imidazolin-2-yl)propane] dihydrochloride (VA-044) was purchased from Wako Pure Chemical Industries Ltd. The cell growth medium McCoy's 5A 1 × (Iwakata & Grace Modification) with L-glutamine was obtained from Corning. Annexin V (Alexa Fluor™ 647 conjugate, Invitrogen™) and Dulbecco's Modified Eagle medium (DMEM) were purchased from ThermoFisher Scientific™. The human colon cancer cell line HT-29 was purchased from ATCC™. All other chemicals, solvents and reagents were purchased from Sigma-Aldrich™ and used as received, unless otherwise noted. The optical fiber (poly(methylmethacrylate), 1.5mm core diameter) was obtained from South Coast Fiber Optics, Inc™. The FPH-DJ fiber chuck and the F- 915T multimode fiber coupler were procured from Newport Corp™. UV–Vis spectra were obtained with Varian Cary 50 UV–Vis spectrophotometer. IR spectra were recorded using a Perkin-Elmer Spectrum One FT-IR spectrometer. 1H-NMR spectra were obtained using a Varian 500 (500MHz) spectrometer. Fluorescence-activated cell sorting (FACS) experiments were carried out in a BD FACS LSRII

instrument equipped with 488 nm and 640 nm lasers (BD Biosciences, Franklin Lakes, N. J.). The flow cytometry data were collected using FACSDIVA software v8.0.1 (BD Biosciences, Franklin Lakes, N. J.) and the raw data were analyzed using FlowJo software v10.2 (FlowJo, LLC). The power of the incident light source (Electro Fiber Optics Corp. IL 410 illumination system) was recorded using a Field MaxII-TO laser power meter (Coherent, Portland, OR).

2.I.4.2 Synthesis of 2-(2-quinolyl)-benzothiazole (qbt).

A mixture of quinoline-2-carboxaldehyde (1.25 g, 8.0 mmol) and 2-aminothiophenol (1.00 g, 8.0 mmol) was refluxed in xylenes (30 mL) for 20 h. The orange solution thus obtained was cooled and the solvent was removed under reduced pressure. The dark orange residue was recrystallized several times from methanol to obtain 1.81 g (86% yield) of 2-(2-quinolyl)-benzothiazole as a microcrystalline white powder. ^{1}H NMR (500 MHz, CDCl$_3$): δ 8.50 (d, J = 8.5 Hz, 1H), 8.31 (d, J = 8.5 Hz, 1H), 8.21 (d, J = 8.5Hz, 1H), 8.14 (d, J = 8.1Hz, 1H), 7.99 (d, J = 7.9 Hz, 1H), 7.88 (d, J = 8.1 Hz, 1H), 7.78 (t, J = 7.7 Hz, 1H), 7.60 (t, J = 7.5Hz, 1H), 7.53 (t, J =7.7Hz, 1H), 7.45 (t, J = 7.5Hz, 1H). Selected IR (KBr, cm^{-1}): 3056, 1594, 1559, 1500, 1453, 1427, 1326, 1117, 996, 939, 829, 753, 727 cm^{-1}.

*2.I.4.3 Synthesis of [Mn(CO)$_3$(qbt)(4-vpy)](CF$_3$SO$_3$) **1**.*

A solution of 2-(2-quinolyl)-benzothiazole (0.100 g, 0.38 mmol, 1 equiv) in 10 mL of dichloromethane was added to a flask containing [Mn(CO)$_5$Br] (0.105 g, 0.38

mmol, 1 equiv) in 20 mL of methanol. The mixture was magnetically stirred at room temperature for 20 h resulting in a brownish-red colored solution. The volume of the solution was reduced under low pressure until microcrystals of [Mn(CO)$_3$(qbt)Br] were observed. After being stored at room temperature for 1 h, the microcrystalline material was collected by decantation of the mother liquor, washed several times with hexanes and dried under vacuum to obtain [Mn(CO)$_3$(qbt)Br] as a brownish-red powder (150 mg, 82% yield). Next, a solution of silver trifluoromethanesulfonate (AgCF$_3$SO$_3$, 100 mg, 0.38 mmol, 1.2 equiv) in 30 mL of dichloromethane was added to microcrystalline [Mn(CO)$_3$(qbt)Br] (140 mg, 0.31 mmol, 1 equiv) residue and the mixture was magnetically stirred for 12 h at room temperature. The solution was then filtered using a fritted funnel with Celite to remove excess silver trifluoromethanesulfonate and silver bromide (AgBr) precipitate and the clear red filtrate was collected. The solvent was removed at reduced pressure to collect [Mn(CO)$_3$(qbt)(CF$_3$SO$_3$)] (125 mg, 73% yield) as a red powder. The resulting [Mn(CO)$_3$(qbt)(CF$_3$SO$_3$)] (125 mg, 0.23 mmol, 1 equiv) was then dissolved in 20 mL of chloroform, followed by the addition of 4-vinylpyridine (245 µL, 2.3 mmol, 10 equiv). The reaction mixture was magnetically stirred at room temperature for 16 h when a cloudy red solution was obtained. The mixture was filtered using a fritted funnel and Celite and the solvent was removed under reduced pressure. The resulting solid was recrystallized by layering hexanes over a solution of the complex in dichloromethane to afford 121 mg (0.18 mmol, 80% yield) of [Mn(CO)$_3$(qbt)(4-vpy)](CF$_3$SO$_3$) **1** as dark red crystals. Selected IR (KBr, cm^{-1}): 3066(w), 2040(s), 1955(s), 1929(s), 1615(w), 1519(w), 1273(s), 1261(s), 1151(m),

1030(m), 765(w), 639(m), 518(w). UV–vis (dichloromethane, ε, M^{-1} cm^{-1}): 445 (1900), 382 (16,400).

2.I.4.4 X-Ray Structure Determination.

Single crystals of complex **1** were grown by layering hexanes over its dichloromethane solution. One suitable crystal was selected and fixed on top of MiTiGen micromount using Paratone N-Oil (Hampton Research) and transferred to the diffractometer. Data were collected on a Bruker APEX II single-crystal X-ray diffractometer with graphite monochromated Mo-Kα-radiation (λ = 0.71073 Å) using ω-scan technique in the range of $3 \leq 2\theta \leq 50°$. Multi-scan absorption corrections[73] were applied to the data set using SADABS. The structure was generated using SHELXT (intrinsic phasing) and subsequently refined by full-matrix least squares procedures on F2 with SHELXL.[74] All non-hydrogen atoms were refined anisotropically. All hydrogen atoms were included in calculated positions on the C atoms to which they are bonded, with C-H = 0.93 Å and $U_{iso}(H) = 1.2U_{eq}(C)$. Calculations and molecular graphics were preformed using SHELXTL 2014 and Olex2 programs.[75] Crystal data and structure refinement parameters are listed in Table 2.I.1.

*2.I.4.5 Incorporation of [Mn(CO)$_3$(qbt)(4-vpy)](CF$_3$SO$_3$) **1** into pHEMA/EGDMA Hydrogel.*

The preparation, polymerization, and curing of polymer samples was carried out in the dark to avoid decomposition of the CO-donating complex. The water-soluble

initiator 2,2′-azobis[2-(2-imidazolin-2-yl) propane] dihydrochloride (VA-044) (0.015 g, 0.045 mmol) was dissolved in milliQ water (2.85 g, 158 mmol) aided by sonication. This solution was mixed with 2-hydroxyethyl methacrylate (HEMA) (5.00 g, 41 mmol) and ethylene glycol dimethacrylate (EGDMA) (0.250 g, 1.3 mmol). The pre-polymer mixture was combined with a dilute solution of 1 in acetone (0.60 mL, 0.00145 M) to afford photoCORP-**1** which was 0.1 mM w.r.t **1** for UV–vis analysis. In a similar manner, a second pre-polymer mixture (4 mM w.r.t. **1**) was prepared by adding a concentrated solution of **1** in acetone (0.60 mL, 0.058 M) to make photoCORP-**1** for myoglobin/cell treatment. Blank polymer samples (without **1**) were prepared by combining a third pre-polymer batch with acetone (0.6 mL). The mixtures were degassed for 20 min by bubbling dry nitrogen gas and placed into polystyrene cuvettes or Eppendorf™ tubes. Once the solutions were placed in their respective mold, they were heated for 30 min at 50 °C using a water bath. The heat was then turned off and the water-bath was allowed to cool slowly, and the polymers were then cured at room temperature for 48 h in the dark. Microanalytical data (from Galbraith Laboratories Inc.) indicated that the photoCORP-**1** tip material contained 0.0328% of Mn corresponding to 0.39 wt. % incorporation of the photoCORM in the hydrogel.

Photolysed polymer samples were prepared by irradiating photoCORP-**1** (sealed within its mold) with visible light. The samples were then removed from their containers, washed, sterilized, and air- dried for 30 min before use. Dilute polymer samples (0.1 mM) were kept inside their polystyrene cuvette mold and used as blank for UV–vis absorption studies.

2.1.4.6 Assembly of the Optical Fiber-Based Catheter.

Four optical fiber lines were cut into 30 cm segments and one end of each line was manually polished into a cone to increase the illumination area as well as to remove rough surface from the polymer interface. If the rough edges were not removed from the optical fiber line, polymerization nucleated at such sites resulting in cracked and frail polymer tips. The polished end of each line was then placed 0.5 ± 0.15 cm into a 1.5mL Eppendorf™ tube and the fibers were secured in the Eppendorf™ tube using clamps and clear tape. A batch of 1.5 mL of the pre-polymer mixture containing **1** was added in each tube and the tubes were heated at 50 °C (in a water bath) for 30 min. The resulting photoCORP-**1** cones thus obtained remained securely attached to the optical fibers after polymerization. Batches of photoCORP-**1** were also polymerized in polystyrene cuvettes (with 0.1 mM of **1**) for spectroscopic measurements. The cones (with optical fiber attached) and rectangular prisms of solid photoCORP-**1** were taken out of their mold by carefully breaking the container using a hammer, washed with milliQ water, sterilized using 70% ethanol, and air dried for 30 min before use. The fiber-photoCORP-**1** assembly is abbreviated as CO-catheter here- after. The weight of the polymer piece attached to the optical fiber was regularly adjusted to 0.26 g for myoglobin assays or 0.50 g for cellular studies.

2.1.4.7 Coupling of the CO-Catheters with Visible Light Source.

The light guide of a visible light source (Electro Fiber Optics Corp. IL 410 illumination system, 10 mW cm^{-2}) was coupled to the open end of the optical fiber

using a F-915 T multimode fiber coupler (Newport Corp.) attached to a lab jack. The fiber was connected to the fiber coupler with a pre-adjusted FPH-DJ fiber chuck (Newport Corp.) to obtain ~ 6% coupling efficiency (0.58 mW cm^{-2}).

*2.I.4.8 Photolysis experiments with **1** and photoCORP-**1**.*

The CO release rates (k$_{CO}$) from complex **1** and photoCORP-**1** were measured by using polystyrene cuvettes (1 cm × 1 cm × 4.5 cm) and a broadband visible light source (Electro Fiber Optics Corp. IL 410 illumination system, 10 mW cm^{-1}) to induce CO photorelease. The cuvettes containing either solution of complex **1** or photoCORP-**1** were placed 1 cm away from the light source, irradiated for 20 or 30 s intervals respectively, and the electronic absorption spectra were sequentially recorded. A blank polymer sample was used for the baseline correction for the studies using photoCORP-**1**. The changes in absorption spectra upon light exposure were monitored and the CO release rates (k$_{CO}$) were determined from a ln(C) versus time (t) plot at an appropriate wavelength.

2.I.4.9 Myoglobin Assays.

Myoglobin (Mb) assays were performed in quartz cuvettes (1 cm × 1 cm × 4.5 cm) by dissolving horse heart myoglobin in phosphate buffer saline (PBS, 100 mM, pH 7.4) and reducing it with sodium dithionite. The Soret band of deoxymyoglobin at 435nm (ε = 121 mM^{-1} cm^{-1}) or the band at 540 nm (ε = 15.4 mM^{-1} cm^{-1}) were used to calculate the concentration of myoglobin used. All assays were conducted in one

cuvette system by placing and illuminating photoCORP-**1** directly inside the myoglobin solution.

The CO release rate of CO-catheter (photoCORP-**1** concentration 4 mM) was investigated using low-power broadband visible light. The tip of the CO-catheter was placed inside the reduced myoglobin solution and illuminated internally using broadband visible light (power of light at the tip: 0.58 mW cm^{-2}). The cuvette was kept under a dry nitrogen current to keep oxygen out of the solution while the treatment was in progress. The CO-treated myoglobin solution was then mixed thoroughly by inverting the cuvette several times and the absorption spectra were recorded. The polymer used was kept in the dark, rinsed with milliQ water, and carefully dried in between UV–vis analysis of the myoglobin solution. Since sodium dithionite itself may induce CO release, a control cuvette containing myoglobin, sodium dithionite and photoCORP-**1** was kept in the dark and scanned at 1 min time intervals for 15 min.

2.I.4.10 Leaching Experiments from PhotoCORP-1 into Aqueous Solutions.

To determine whether complex **1** or its photoproduct(s) following CO release leach out of the polymer matrix, rectangular blocks of photoCORP-**1** (4 mM, weight: 0.50 g) were submerged in 2 mL of PBS and each sample was sealed in its container and kept under ambient light or dark conditions at room temperature for different number (0, 2, 4, 8 and 10) of weeks. The polymer blocks were then removed from their containers and the solutions were analyzed by spectrophotometry. No absorption due to complex **1** or the free ligand was observed in any sample thus prepared. These

solutions were also subjected to electron spin resonance (ESR) spectrometry to determine any presence of Mn^{2+} ion. No EPR signal due to Mn^{2+} ion was detected.

*2.I.4.11 Shelf Life of PhotoCORP-**1***.

The effect of the extent of hydration of the polymer on its performance as a CO donor was investigated by using small rectangular blocks of photoCORP-**1**. First, samples of photoCORP-**1** (4 mM w.r.t. **1**) were polymerized inside polystyrene cuvettes and then cut (using a razor blade) into smaller rectangular blocks (~0.9 × 0.4 × 0.4 cm, weight: 0.26 g). These blocks were then dried for different number of days (0, 5, and 10 days). Each CO-donating polymer block was used for myoglobin assay to determine their capacity as CO donor. The polymer blocks were submerged and sealed in a quartz cuvette containing a PBS solution of myoglobin, and sodium dithionite. These samples were then irradiated externally using the above-mentioned light source (10 mW cm^{-2}) for 10 s intervals, mixed thoroughly, and their absorption spectra were recorded. The k_{CO} values were then calculated from the [MbCO] versus time (t) plot to determine any changes in efficacy of the polymer as CO donor with time.

2.I.4.12 Delivery of CO to HT-29 Cancer Cell Line and HEK 293 Normal Embryonic Cell Line by the CO-Catheter and Flow Cytometry Analysis.

The human colorectal adenocarcinoma cell line (HT-29) was cultured using McCoy's 5A medium with L-glutamine (Corning), supplemented with 20% fetal bovine serum (FBS). The cells were then washed, harvested, counted, and diluted to a

concentration of 1×10^6 cells mL^{-1} using the culture growth medium. Several 2-mL portions of this solution were separated into round-bottom Falcon^{TM} tubes (12×75 mm, polystyrene) with snap caps (Corning^{TM}) and treated with CO released from the polymer irradiated for various time intervals as follows.

The HT-29 cell suspensions were taken in four different Falcon^{TM} tubes and one fresh CO-catheter (tip weight: 0.50 g, 4 mM concentration of **1**) was dipped into each of the tubes kept under dark condition. The cells were then treated with CO released from CO-catheters upon remote triggering with visible light (0.58 mW cm^{-2}). The time of illumination was 5, 10, 20, and 40 min for tubes numbered 1 to 4. Control experiments were carried out using one CO-catheter without light irradiation, and another CO-catheter with light but carrying an extensively photolysed tip. After treatment, the cells were centrifuged and re-suspended in 900 μL of PBS buffer and transported to the flow cytometer (BD FACS LSR II). Next the cells were treated with 100 μL of annexin-binding buffer (10 mM HEPES, 140 mM NaCl, 2.5 mM CaCl2, pH 7.4), 2 μL of annexin V Alex FluorTM 647 conjugate, and incubated for 15 min at room temperature. The cells were then treated with propidium iodide (PI, 2 μL, 300 nM), and analyzed using flow cytometry (BD FACS LSRII).

The normal human embryonic kidney cells (HEK 293) were grown in DMEM supplemented with 10% FBS. The cells were then washed, harvested, counted, and diluted to a concentration of 10^6 cells mL^{-1} using DMEM. Samples (2 mL) of these cells were then treated with CO by following the same procedure as described above and the extent of apoptosis was measured by flow cytometry.

2.I.5 References.

1. Carbon Monoxide Poisoning, National Center for Environmental Health, Centers for Disease Control and Prevention (CCDC), https://www.cdc.gov/co/, (2015) (accessed 01.09.19).

2. Sykes, O. T.; Walker, E. The neurotoxicology of carbon monoxide – historical perspective and review. *Cortex* **2016**, *74*, 440–448.

3. Yoshida, T.; Migita, C.T. Mechanism of heme degradation by heme oxygenase. *J. Inorg. Biochem.* **2000**, *82*, 33–41.

4. Kikuchi, G.; Yoshida, T.; Noguchi, M. Heme oxygenase and heme degradation. *Biochem. Biophys. Res. Commun.* **2005**, *338*, 558–567.

5. Roderique, J. D.; Josef, C. S.; Feldman, M. J.; Spiess, B. D. A modern literature review of carbon monoxide poisoning, theories, therapies, and potential targets for therapy advancement. *Toxicology* **2015**, *334*, 45–58.

6. Motterlini, R.; Otterbein, L. E. The therapeutic potential of carbon monoxide. *Nat. Rev. Drug Discov.* **2010**, *9*, 728–743.

7. Wu, L.; Wang, R. Carbon monoxide: endogenous production, physiological functions, and pharmacological applications. *Pharmacol. Rev.* **2005**, *57*, 585–630.

8. Chen, Z.; Wang, R.; Wu, J.; Xia, F.; Sun, Q.; Xu, J.; Liu, L. Low-dose carbon monoxide inhalation protects neuronal cells from apoptosis after optic nerve crush. *Biochem. Biophys. Res. Comm.* 2016, *269*, 809–815.

9. Wang, B.; Cao, W.; Biswal, S.; Dore, S. Carbon monoxide-activated Nrf2 pathway leads to protection against permanent focal cerebral ischemia. *Stroke* 2010, *42*, 2605–2610.

10. Queiroga, C. S. F.; Tomasi, S.; Widerøe, M.; Alves, P. M.; Vercelli, A.; Vieira, H. L. A. Preconditioning triggered by carbon monoxide (CO) provides neuronal protection following perinatal hypoxia-ischemia. *PLoS One* **2012**, *7*, e42632.

11. Ndisang, J. F.; Tabien, H. E. N.; Wang, R. Carbon monoxide and hypertension. *J. Hypertens.* **2004**, *22*, 1057–1074.

12. Stec, D. E.; Drummond, H. A.; Vera, T. Role of carbon monoxide in blood pressure regulation. *Hypertension* **2008**, *51*, 597–604.

13. Kobayashi, A.; Ishikawa, K.; Matsumoto, H.; Kimura, S.; Kamiyama, Y.; Maruyama, Y. Synergetic antioxidant and vasodilatory action of carbon monoxide in angiotensin II-induced cardiac hypertrophy. *Hypertension* **2007**, *50*, 1040–1048.

14. Otterbein, L. E.; Bach, F. H.; Alam, J.; Soares, M.; Lu, H. T.; Wysk, M.; Davis, R. J.; Flavell, R. A.; Choi, A. M. K. Carbon monoxide has anti-inflammatory effects involving the mitogen-activated protein kinase pathway. *Nat. Med.* **2000**, *6*, 422–428.

15. Naito, Y.; Uchiyama, K.; Takagi, T.; Yoshikawa, T. Therapeutic potential of carbon monoxide (CO) for intestinal inflammation. *Curr. Med. Chem.* **2012**, *19*, 70–76.

16. Ryter, S. W.; Choi, A. M. K. Targeting heme oxygenase-1 and carbon monoxide for therapeutic modulation of inflammation. *Transl. Res.* **2016**, *167*, 7–34.

17. Otterbein, L. E. Carbon monoxide: innovative anti-inflammatory properties of an age-old gas molecule. *Antioxid. Redox Signal.* **2002**, *4*, 309–319.

18. Pintadosi, C. A. Carbon monoxide, reactive oxygen signaling and oxidative stress. *Free Radic. Biol. Med.* **2008**, *45*, 562–569.

19. Rhodes, M. A.; Carraway, M. S.; Pintadosi, C. A.; Reynolds, C. M.; Cherry, A. D.; Wester, T. E.; Natoli, M. J.; Massey, E. W.; Moon, R. E.; Suliman, H. B. Carbon monoxide, skeletal muscle oxidative stress, and mitochondrial biogenesis in humans. *Am. J. Physiol. Heart Circ. Physiol.* **2009**, *297*, H392–H399.

20. Conde de la Rosa, L.; Vrenken, T. E.; Hannivoort, R.A.; Buist-Homan, M.; Havinga, R.; Slebos, D. J.; Kauffman, H. F.; Faber, K. N.; Jansen, P. L. M.; Moshage, H. Carbon mon- oxide blocks oxidative stress-induced hepatocyte apoptosis via inhibition of the p54 JNK isoform. *Free Radic. Biol. Med*. **2008**, *44*, 1323–1333.

21. Pintadosi, C. A.; Carraway, M. S.; Suliman, H. B. Carbon monoxide, oxidative stress, and mitochondrial permeability pore transition. *Free Radic. Biol. Med*. **2006**, 40 (2006) 1332–1339.

22. Wegiel, B.; Chin, B. Y.; Otterbein, L. E. Carbon monoxide, cellular proliferation. *Cell Cycle* **2008**, *7*, 1379–1384.

23. Almeida, S. S.; Queiroga, C. S. F.; Sousa, M. F.; Alves, P. M.; Vieira, H. L. A. Carbon monoxide modulates apoptosis by reinforcing oxidative metabolism in astrocytes: role of BCL-2. *J. Biol. Chem.* **2012**, *30*, 10761–10770.

24. Brouard, S.; Otterbein, L. E.; Anrather, J.; Tobiasch, E.; Bach, F. H.; Choi, A. M. K.; Soares, M. P. Carbon monoxide generated by heme oxygenase 1 suppresses endothelial cell apoptosis. *J. Exp. Med.* **2000**, *192*, 1015–1026.

25. Chakraborty, I.; Carrington, S. J.; Roseman, G.; Mascharak, P. K. Synthesis, structures, and CO release capacity of a family of water soluble photoCORMs: assessment of the biocompatibility and their phototoxicity toward human breast cancer cells. *Inorg. Chem.* **2017**, *56*, 1534–1545.

26. Carrington, S. J.; Chakraborty, I.; Bernard, J. M. L.; Mascharak, P.K. A theranostic two-tone luminescent photoCORM derived from Re(I) and (2-pyridyl)-benzothiazole: trackable CO delivery to malignant cells. *Inorg. Chem.* **2016**, *55*, 7752–7858.

27. Carrington, S. J.; Chakraborty, I.; Mascharak, P.K. Rapid CO release from a Mn(I) carbonyl complex derived from azopyridine upon exposure to visible light and its phototoxicity toward malignant cells. *Chem. Commun.* **2013**, *49*, 11254–11256.

28. Wegiel, B.; Gallo, D.; Csizmadia, E.; Harris, C.; Belcher, J.; Vercellotti, G. M.; Penacho, N.; Seth, P.; Sukatme, V.; Ahmed, A.; Pandolfi, P. P.; Helczynski, L.; Bjartell, A.; Persson, J. L.; Otterbein, L. E. Carbon monoxide expedites metabolic exhaustion to inhibit tumor growth. *Cancer Res.* **2013**, *73*, 7009–7021.

29. Otterbein, L. E.; Foresti, R.; Motterlini, R. Heme Oxygenase-1 and carbon monoxide in the heart: the balancing act between danger signaling and pro-survival. *Circ. Res.* **2016**, *118*, 1940–1959.

30. Kawahara, B.; Ramadoss, S.; Chaudhuri, G.; Janzen, C.; Sen, S.; Mascharak, P. K. Carbon monoxide sensitizes cisplatin-resistant ovarian cancer cell lines toward cisplatin via attenuation of levels of glutathione and nuclear metallothionein. *J. Inorg. Biochem.* **2019**, *191*, 29-39.

31. Kawahara, B.; Moller, T.; Hu-Moore, K.; Carrington, S.; Faull, K. F.; Sen, S.; Mascharak, P. K. Attenuation of antioxidant capacity in human breast cancer cells by carbon monoxide through inhibition of cystathionine b-synthase activity: Implications in chemotherapeutic drug sensitivity. *J. Med. Chem.* **2017**, *60*, 8000-8010.

32. Morita, T.; Perrella, M. A.; Lee, M. E.; Kourembanas, S. Smooth muscle cell-derived carbon monoxide is a regulator of vascular cGMP. *Proc. Natl. Acad. Sci. U. S. A.* **1995**, *92*, 1475–1479.

33. Sarady, J. K.; Zuckerbraun, B. S.; Bilban, M.; Wagner, O.; Usheva, A.; Liu, F.; Ifedigbo, E.; Zamora, R.; Choi, A. M. K.; Otterbein, L. E. Carbon monoxide protection against endotoxic shock involves reciprocal effects on iNOS in the lung and liver. *FASEB J.* **2004**, *18*, 854–856.

34. Zuckerbraun, B. S.; Billiar, T. R.; Otterbein, S. L.; Kim, P. K.; Liu, F.; Choi, A. M. K.; Otterbein, L. E. Carbon monoxide protects against liver failure through nitric oxide-induced heme oxygenase 1. *J. Exp. Med.* **2003**, *198*, 1707–1716.

35. Chin, B. Y.; Jiang, G.; Wegiel, B.; Wang, H. J.; MacDonald, T.; Zhang, X. C.; Gallo, D.; Cszimadia, E.; Bach, F. H.; Lee, P. J.; Otterbein, L. E. Hypoxia-inducible

factor 1α stabilization by carbon monoxide results in cytoprotective preconditioning. *Proc. Natl. Acad. Sci. U. S. A*. **2007**, *104*, 5109–5114.

36. Peers, C.; Steele, D. S. Carbon monoxide: a vital signaling molecule and potent toxin in the myocardium. *J. Mol. Cell. Cardiol*. **2012**, *52*, 359–365.

37. Pintadosi, C.A.; Carraway, M. S.; Babiker, A.; Suliman, H. B. Heme oxygenase-1 regulates cardiac mitochondrial biogenesis via Nrf2-mediated transcriptional control of nuclear respiratory factor-1. *Circ. Res.* **2008**, *103*, 1232–1240.

38. Kim, H. P.; Wang, X.; Zhang, J.; Suh, G. Y.; Benjamin, I. J.; Ryter, S. W.; Choi, A. M. K. Heat shock protein-70 mediates the cytoprotective effect of carbon monoxide: involvement of p38B MAPK and heat shock factor-1. *J. Immunol*. **2005**, *165*, 2622–2629.

39. Haschemi, A.; Wagner, O.; Marculescu, R.; Wegiel, B.; Robinson, S. C.; Gagliani, N.; Gallo, D.; Chen, J. F.; Bach, F. H.; Otterbein, L. E. Cross regulation of carbon monoxide and the adenosine A2a receptor in macrophages. *J. Immunol*. **2007**, *178*, 5921–5929.

40. Suliman, H. B.; Carraway, M. S.; Tatro, L. G.; Pintadosi, C. A. A new activating role for CO in cardiac mitochondrial biogenesis. *J. Cell Sci.* **2007**, *120*, 299–308.

41. Nakao, A.; Huang, C. S.; Stolz, D. B.; Wang, Y.; Franks, J. M.; Tochigi, N.; Billiar, T. R.; Toyoda, Y.; Tzeng, E.; McCurry, K. Ex vivo carbon monoxide delivery inhibits intima hyperplasia in arterialized vein grafts. *Cardiovasc. Res*. **2011**, *89*, 457–463.

42. Liou, G. Y.; Storz, P. Reactive oxygen species in cancer. *Free Radic. Res*. **2010**, *44*, 479–496.

43. Li, X.; Fang, P.; Mai, J.; Choi, E. T.; Wang, H.; Yang, X. F. Targeting mitochondrial reactive oxygen species as novel therapy for inflammatory diseases and cancers. *J. Hematol. Oncol*. **2013**, *6*, 19.

44. Gorrini, C.; Harris, I. S.; Mak, T. W. Modulation of oxidative stress as an anticancer strategy. *Nat. Rev. Drug Discov.* **2013**, *12*, 931–947.

45. Nakao, A.; Kimizuka, K.; Stolz, D. B.; Neto, J. S.; Kaizu, T.; Choi, A. M. K.; Uchiyama, T.; Zuckerbraun, B. S.; Nalesnik, M. A.; Otterbein, L. E.; Murase, N. Carbon monoxide inhalation protects rat intestinal grafts from ischemia/reperfusion injury. *Am. J. Pathol*. **2003**, *163*, 1587–1598.

46. Foresti, R.; Bani-Hani, M. G.; Motterlini, R. Use of carbon monoxide as therapeutic agent: promises and challenges. *Intensive Care Med*. **2008**, *34*, 649–658.

47. Motterlini, R.; Clark, J. E.; Foresti, R.; Sarathchandra, P.; Mann, B. E.; Green, C. J. Carbon monoxide-releasing molecules characterization of biochemical and vascular activities. *Circ. Res.* **2002**, *90*, e17–e24.

48. Schatzschneider, U. Novel lead structures and activation mechanisms for CO-releasing molecules (CORMs). *Br. J. Pharmacol*. **2015**, *172*, 1638–1650.

49. Chakraborty, I.; Carrington, S. J.; Mascharak, P. K. Design strategies to improve the sensitivity of photoactive metal carbonyl complexes (photoCORMs) to visible light and their potential as CO-donors to biological targets. *Acc. Chem. Res*. **2014**, *47*, 2603–2611.

50. Garcia-Gallego, S.; Bernardes, G. J. L. Carbon monoxide-releasing molecules for the delivery of therapeutic CO in vivo. *Angew. Chem. Int. Ed*. **2014**, *53*, 9712–9721.

51. Heinemann, S. H.; Hoshi, T.; Westerhausen, M.; Schiller, A. Carbon monoxide – physiology, detection and controlled release. *Chem. Commun.* **2014**, *50*, 3644–3660.

52. Romao, C. C.; Blatter, W. A.; Seixas, J. D.; Bernardes, G. J. Developing drug molecules for therapy with carbon monoxide. *Chem. Soc. Rev*. **2012**, *41*, 3571–3583.

53. Rimmer, R. D.; Pierri, A. E.; Ford, P. C. Photochemically activated carbon monoxide release for biological targets. Toward developing air-stable photoCORMs labilized by visible light. *Coord. Chem. Rev*. **2012**, *256*, 1509–1519.

54. Schatzschneider, U. PhotoCORMs: light-triggered release of carbon monoxide from the coordination sphere of transition metal complexes for biological applications. *Inorg. Chim. Acta* **2011**, *374*, 19–23.

55. Govender, P.; Pai, S.; Schatzschneider, U.; Smith, G. S. Next generation photoCORMs: polynuclear tricarbonylmanganese (I)-functionalized polypyridyl metallodendrimers. *Inorg. Chem*. **2013**, *52*, 5470–5478.

56. Nguyen, D.; Adan, N. N. M.; Oliver, S.; Boyer, C. The interaction of CORM-2 with block copolymers containing poly(4-vinylpyridine): macromolecular scaffolds for carbon monoxide delivery in biological systems. *Macromol. Rapid Commun.* **2016**, *37*, 739–744.
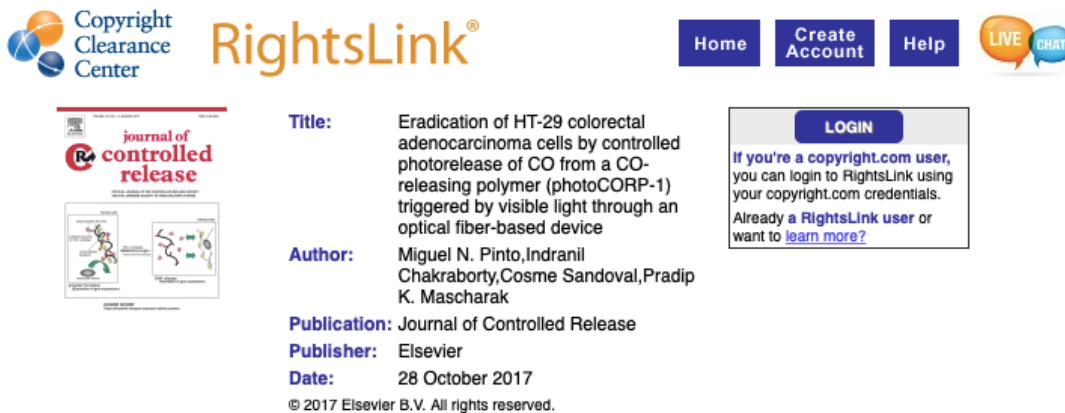
57. Brückmann, N. E.; Wahl, M.; Reiß, G. J.; Kohns, M.; Wätjen, W.; Kunz, P. C. Polymer conjugates of photoinducible CO-releasing molecules. *Eur. J. Inorg. Chem*. **2011**, *29*, 4571–4577.

58. Bohlender, C.; Gläser, S.; Klein, M.; Weisser, J.; Thein, S.; Neugebauer, U.; Popp, J.; Wyrwa, R.; Schiller, A. Light-triggered CO release from nanoporous non-wovens. *J. Matter. Chem. B* **2014**, *2*, 1454–1463.

59. Pfeiffer, H.; Rojas, A.; Niesel, J.; Schatzschneider, U. Sonogashira and click: reactions for the N-terminal and side-chain functionalization of peptides with [Mn (CO)3(TPM)]$^+$-based CO releasing molecules (tpm = tris(pyrazolyl)methane). *Dalton Trans*. **2009**, *22*, 4292–4298.

60. Fujita, K.; Tanaka, Y.; Abe, S.; Ueno, T. A photoactive carbon-monoxide-releasing protein cage for dose regulated delivery in living cells. *Angew. Chem. Int. Ed*. **2016**, *55*, 1056–1060.

61. Hasegawa, U.; van der Vlies, A. J.; Simeoni, E.; Wandrey, C.; Hubbell, J. A. Carbon monoxide-releasing micelles for immunotherapy. *J. Am. Chem. Soc*. **2010**, *132*, 18273–18280.

62. Pierri, A. E.; Huang, P. J.; Garcia, J. V.; Stanfill, J. G.; Chui, M.; Wu, G.; Zheng, N.; Ford, P. C. A photoCORM nanocarrier for CO release using NIR light. *Chem. Comm*. **2015**, *51*, 2072–2075.

63. Chakraborty, I.; Carrington, S. J.; Hauser, J.; Oliver, S. R. J.; Mascharak, P. K. Rapid eradication of human breast cancer cells through trackable light triggered CO

delivery by mesoporous silica nanoparticles packed with a designed photoCORM. *Chem. Matter*. **2015**, *27*, 8387–8397.

64. Glasser, S.; Mede, R.; Görls, H.; Seupel, S.; Bohlender, C.; Wyrwa, R.; Schurmer, S.; Dochow, S.; Reddy, G. U.; Popp, J.; Westernhausen, M.; Schiller, A. Remote-controlled delivery of CO via photoactive CO-releasing materials on a fiber optical device. *Dalton Trans*. **2016**, *45*, 13222–13233.

65. Halpenny, G. M.; Gandhi, K. R.; Mascharak, P. K. Eradication of pathogenic bacteria by remote delivery of NO via light triggering of nitrosyl-containing materials. *ACS Med. Chem. Lett*. **2010**, *1*, 180–183.

66. Halpenny, G. M.; Heilman, B.; Mascharak, P. K. Nitric oxide(NO)-induced death of Gram-negative bacteria from a light-controlled NO-releasing platform. *Chem. Biodivers*. **2012**, *9*, 1829–1839.

67. Heilman, B.; Halpenny, G. M.; Mascharak, P. K. Synthesis, characterization, and light-controlled antibiotic application of a composite material derived from polyurethane and silica xerogel with embedded photoactive manganese nitrosyl. *J. Biomed. Mater. Res. B* **2011**, *99B*, 328–337.

68. Halpenny, G. M.; Steinhardt, R.C.; Okialda, K. A.; Mascharak, P. K. Characterization of pHEMA-based hydrogels that exhibit light-induced bactericidal effect via release of NO. *J. Mater. Sci. Mater. Med*. **2009**, *20*, 2353–2360.

69. Halpenny, G. M.; Olmstead, M. M.; Mascharak, P. K. Incorporation of a designed ruthenium nitrosyl in polyHEMA hydrogel and light-activated delivery of NO to myoglobin. *Inorg. Chem*. **2007**, *46*, 6601–6606.

70. Flynn, L.; Dalton, P. D.; Shoichet, M. S. Fiber templating of poly(2-hydroxyethyl methacrylate) for neural tissue engineering. *Biomaterials* **2003**, *24*, 4265–4272.

71. Sun, Y. M.; Huang, J. J.; Lin, F. C.; Lai, J. Y. Composite poly(2-hydroxyethyl methacrylate) membranes as rate controlling barriers for transdermal application. *Biomaterials* **1997**, *18*, 527–533.

72. Peppas, N. A. Hydrogels in Medicine and Pharmacy, Ed, Vol I-III, CRC Press, Boca Raton, 1987.

73. Blessing, R. H. An empirical correction for absorption anisotropy. *Acta Crystallogr. Sect. A* **1995**, *51*, 33–38.

74. Sheldrick, G. M. Crystal structure refinement with SHELXL. *Acta Crystallogr. C, Struct. Chem*. **2015**, *71*, 3–8.

75. Dolomanov, O. V.; Bourhis, L. J.; Gildea, R. J.; Howard, J. A. K.; Puschmann, H. OLEX2: a complete structure solution, refinement and analysis program. *J. Appl. Crystallogr*. **2009**, *42*, 339–341.

76. Cao, C. G. L.; Wong, P. Y.; Lilge, L.; Gavalis, R. M.; Xing, H.; Zamarripa, N. Advanced shape tracking to improve flexible endoscopic diagnostics. *Proc. of SPIE* **2008**, *6935*, http://dx.doi.org/10.1117/12.776276.

2.I.6 Reprints of Publications and Permissions

Reprinted with permissions from Pinto, M. N.; Chakraborty, I.; Sandoval, C.; Mascharak, P. K. Eradication of HT-29 colorectal adenocarcinoma cells by controlled photorelease of CO from a CO-releasing polymer (photoCORP-**1**) triggered by visible light through an optical fiber-based device. J. Control. Release **2017**, *264*, 192-202.

Eradication of HT-29 colorectal adenocarcinoma cells by controlled photorelease of CO from a CO-releasing polymer (photoCORP-**1**) triggered by visible light through an optical fiber-based device

Miguel N. Pinto, Indranil Chakraborty, Cosme Sandoval, Pradip K. Mascharak*

Department of Chemistry and Biochemistry, University of California, Santa Cruz, CA 95064, USA

ARTICLE INFO

ABSTRACT

The gaseous signaling molecule carbon monoxide (CO) has recently been recognized for its wide range of physiological activity as well as its antineoplastic properties. However, site-specific delivery of this noxious gas presents a major challenge in hospital settings. In this work, a visible light-sensitive CO-releasing molecule (photoCORM) derived from manganese(I) and 2-(quinolyl)benzothiazole (qbt) namely, [Mn(CO)$_3$(qbt)(4-vpy)] (CF$_3$SO$_3$) (**1**), has been *co*-polymerized within a gas-permeable HEMA/EGDMA hydrogel. The resulting photo-active CO-releasing polymer (photoCORP-1) incorporates **1** such that neither the carbonyl complex nor its photoproduct(s) exits the polymer at any time. The material can be triggered to photorelease CO remotely by low-power broadband visible light (< 1 mW cm^{-2}) with the aid of fiber optics technology. The CO photorelease rates of photoCORP-**1** (determined by spectrophotometry) can be modulated by both the concentration of **1** in the hydrogel and the intensity of the light. A CO-delivery device has been assembled to deliver CO to a sus-pension of human colorectal adenocarcinoma cells (HT-29) under the control of visible light and the extent of CO-induced apoptotic death of the cancer cells has been determined via Annexin V/Propidium iodide stain and flow cytometry. This photoactive CO-releasing polymer could find use in delivering controlled doses of CO to cellular targets such as malignant tissues in remote parts of the body.

1. Introduction

Carbon monoxide (CO), also known as "silent killer", is a colorless, odorless, tasteless, and poisonous gas produced primarily by the in-complete combustion/oxidation of carbon containing compounds [1]. Inhalation of large amounts of CO remains a leading cause of unin-tentional poisoning around the world [2]. Notably this gas is also produced endogenously within mammals, mainly from the degradation of heme by the enzyme heme oxygenase (inducible HO-1 or constitutive HO-2) [3–5]. Interest in the biochemical effects of CO has increased over the past decade due to its role as a gaseous signaling molecule (gasotransmitter) in mammalian pathophysiology [6,7]. CO has been implicated in neurodegeneration [8–10], hypertension [11–13], in-flammation [14–17], oxidative stress [7,18–21], cell proliferation [22], and apoptosis [23,24]. In addition, administration of moderate doses (~200 ppm) of CO has been shown to induce proapoptotic/anti-proliferative effects on malignant cells [6,25–27] and sensitize cancer cells to conventional anticancer drugs [28]. As a consequence, use of CO in direct and/or adjuvant chemotherapy appears to be a reasonable option for the treatment of malignancy. Unlike other gasotransmitters,

CO does not undergo physical or chemical alterations inside the cell, and it can essentially diffuse into all cellular compartments. CO pri-marily interacts with 'soft' metal centers in heme proteins [6]. How-ever, the molecular targets of CO remain somewhat unclear since not all heme proteins are present in every cell or they may vary in their levels of expression [29]. Upon CO binding, the function of a heme protein can be enhanced [30–32] or blocked [33], promoting signaling cas-cades. The effect of these signaling pathways can then influence the modulation of many other non-heme proteins such as mitogen activated protein kinases [14,34], nuclear factor erythroid 2-related factor (Nrf2) [35], heat shock proteins [36], and others [37–39]. Another common target is the mitochondria, also present in different numbers depending on the cell type. In general, most cancer cells exhibit elevated levels of reactive oxygen species (ROS) as well as antioxidants proteins, sug-gesting a relatively fragile balance of intracellular ROS when compared to normal cells [40–42]. The treatment of cancer cells with CO is be-lieved to lead to increased mitochondrial ROS production [18,33], which then may tip the balance toward ROS-induced apoptotic sig-naling [41,42].

The main technical difficulty one encounters in using CO as a

chemotherapeutic is its *site-specific administration in a controlled and sustainable manner*. For example, direct inhalation therapy requires sustained exposure to relatively high amounts of CO to elicit an observable response [43]. Such exposure to CO gas lacks specificity and results in increasing CO concentrations throughout the body, accentuating its negative side effects [44]. CO releasing molecules (CORMs) present an alternative way to deliver controlled amounts CO to target tissues. Use of the first-generation CORMs (such as [Ru(Cl)$_2$(CO)$_3$]$_2$ and Mn$_2$(CO)$_{10}$) in clinical settings has however been quite difficult due to problems related to their low solubility in water, toxicity, short lifetime, and requirements of organic solvents to trigger CO release through ligand exchange [45]. Photoactive carbon monoxide releasing molecules (photoCORMs), with few exceptions, are metal carbonyl complexes that release CO upon illumination. These CO donors present a way to deliver CO to a specific site with spatial and temporal control [46–52]. Recently, efforts have been made to impart desirable characteristics such as sensitivity toward visible light, solubility and stability in water, and low toxicity to make photoCORMs more appropriate for CO delivery.

PhotoCORMs conjugated to a large variety of carriers such as dendrimers [53], polymers [54–56], peptides [57], protein cages [58], micelles [59], and nanocarriers [60,61] have also been reported. These materials transport and deliver the photoCORMs to biological targets and often retain the *CO*-spent products within the polymer matrices thus avoiding adverse side effects. Among such delivery vehicles, only the example reported by Schiller and coworkers delivers CO from a bulk material source which is removed following CO delivery [58,62]. In this case, the photoCORM is *non-covalently encapsulated* into electrospun fibers of poly(L-lactide-*co*-D/L-lactide). This non-woven fabric when stretched and *wrapped around* an optical fiber allows for remote triggering of the encapsulated photoCORM with the aid of a 405 nm laser (14 mW cm^{-2}). We have previously used composite materials for remote delivery of a different gasotransmitter, nitric oxide (NO) [63–66]. In such research, we have reported a silica-based sol-gel material that non-covalently encapsulated a photoactive NO-releasing molecule [63]. The material was triggered remotely using an optical fiber, and the photoreleased NO was used for the eradication of pathogenic bacteria [63]. In a separate case, a photoactive NO-donor was covalently attached to a polyHEMA hydrogel and the material was employed to deliver NO to myoglobin [67].

In the present work, we report a novel polyHEMA-based CO-releasing polymer (photoCORP-**1**) in which a manganese photoCORM [Mn(CO)$_3$(qbt)(4-vpy)](CF$_3$SO$_3$) (**1**) bearing a 4-vinylpyridine (4-vpy) ancillary ligand has been *covalently attached* to 2-hydroxyethyl methacrylate (HEMA) polymer backbone. This robust yet flexible CO-releasing hydrogel releases CO upon illumination with low power (> 1 mW cm^{-2}) visible light. The HEMA-based hydrogel was selected because of its extensive use in biomedical applications, gas permeability, low toxicity, biocompatibility, softness, chemical stability, and transparency [68–70]. Indeed photoCORP-**1** allows *controlled escape of CO* from the entire HEMA hydrogel monolith as evidenced by loss of the original red color (arising from **1**). We also report the construction of a fiber optic-based catheter with photoCORP-**1** tip that allows remote triggering of CO photorelease by visible light. The catheter has been successfully used to promote CO-induced apoptosis in human colorectal adenocarcinoma HT-29 cells. The extent of apoptotic death of the cancer cells has been investigated with the aid of flow cytometry using propidium iodide (PI)/Annexin V stain. To the best of our knowledge, photoCORP-**1** is the first example of a *CO-releasing hydrogel* that could be remotely triggered by low power visible light and used to eradicate cancer cells. The easy removal of the CO-releasing catheter from the malignant site also allows one to circumvent toxicity arising from any CO-spent products at the targeted site.

2. Materials and methods

Bromopentacarbonylmanganese (I) was purchased from Strem

Chemicals. 2,2′-azobis[2-(2-imidazolin-2-yl)propane] dihydrochloride (VA-044) was purchased from Wako Pure Chemical Industries Ltd. The cell growth medium McCoy's 5A 1 × (Iwakata & Grace Modification) with L-glutamine was obtained from Corning. Annexin V (Alexa Fluor™ 647 conjugate, Invitrogen™) and Dulbecco's Modified Eagle medium (DMEM) were purchased from ThermoFisher Scientific™. The human colon cancer cell line HT-29 was purchased from ATCC™. All other chemicals, solvents and reagents were purchased from Sigma-Aldrich™ and used as received, unless otherwise noted. The optical fiber (poly (methyl methacrylate), 1.5 mm core diameter) was obtained from South Coast Fiber Optics, Inc™. Both the FPH-DJ fiber chuck and the F-915T multimode fiber coupler were procured from Newport Corp™.

UV–Vis spectra were obtained with Varian Cary 50 UV–Vis spectrophotometer. IR spectra were recorded using a Perkin-Elmer Spectrum One FT-IR spectrometer. ^{1}H NMR spectra were obtained using a Varian 500 (500 MHz) spectrometer. Fluorescence-activated cell sorting (FACS) experiments were carried out in a BD FACS LSRII instrument equipped with 488 nm and 640 nm lasers (BD Biosciences, Franklin Lakes, N. J.). The flow cytometry data were collected using FACSDIVA software v8.0.1 (BD Biosciences, Franklin Lakes, N. J.) and the raw data were analyzed using FlowJo software v10.2 (FlowJo, LLC). The power of the incident light source (Electro Fiber Optics Corp. IL 410 illumination system) was recorded using a Field MaxII-TO laser power meter (Coherent, Portland, OR).

2.1. Synthesis of 2-(2-quinolyl)-benzothiazole (qbt)

A mixture of quinoline-2-carboxaldehyde (1.25 g, 8.0 mmol) and 2-aminothiophenol (1.00 g, 8.0 mmol) was refluxed in xylenes (30 mL) for 20 h. The orange solution thus obtained was cooled and the solvent was removed under reduced pressure. The dark orange residue was recrystallized from methanol to obtain 1.81 g (86% yield) of 2-(2-quinolyl)-benzothiazole as a microcrystalline yellow powder. ^{1}H NMR (500 MHz, CDCl$_3$): δ 8.50 (d, $J = 8.5$ Hz, 1H), 8.31 (d, $J = 8.5$ Hz, 1H), 8.21 (d, $J = 8.5$ Hz, 1H), 8.14 (d, $J = 8.1$ Hz, 1H), 7.99 (d, $J = 7.9$ Hz, 1H), 7.88 (d, $J = 8.1$ Hz, 1H), 7.78 (t, $J = 7.7$ Hz, 1H), 7.60 (t, $J = 7.5$ Hz, 1H), 7.53 (t, $J = 7.7$ Hz, 1H), 7.45 (t, $J = 7.5$ Hz, 1H). Selected IR (KBr, cm^{-1}): 3056, 1594, 1559, 1500, 1453, 1427, 1326, 1117, 996, 939, 829, 753, 727 cm^{-1}.

2.2. Synthesis of [Mn(CO)$_3$(qbt)(4-vpy)](CF$_3$SO$_3$) (1)

A solution of 2-(2-quinolyl)-benzothiazole (0.100 g, 0.38 mmol, 1 equiv) in 10 mL of dichloromethane was added to a flask containing [Mn(CO)$_5$Br] (0.105 g, 0.38 mmol, 1 equiv) in 20 mL of methanol. The mixture was magnetically stirred at room temperature for 20 h resulting in a brownish-red colored solution. The volume of the solution was reduced under low pressure until microcrystals of [Mn(CO)$_3$(qbt)Br] were observed. After being stored at room temperature for 1 h, the microcrystalline material was collected by decantation of the mother liquor, washed several times with hexanes and dried under vacuum to obtain [Mn(CO)$_3$(qbt)Br] as a brownish-red powder (150 mg, 82% yield). Next, a solution of silver trifluoromethanesulfonate (AgCF$_3$SO$_3$, 100 mg, 0.38 mmol, 1.2 equiv) in 30 mL of dichloromethane was added to microcrystalline [Mn(CO)$_3$(qbt)Br] (140 mg, 0.31 mmol, 1 equiv) residue and the mixture was magnetically stirred for 12 h at room temperature. The solution was then filtered using a fritted funnel with Celite to remove excess silver trifluoromethanesulfonate and silver bromide (AgBr) precipitate and the clear red filtrate was collected. The solvent was removed at reduced pressure to collect [Mn(CO)$_3$(qbt) (CF$_3$SO$_3$)] (125 mg, 73% yield) as a red powder. The resulting [Mn (CO)$_3$(qbt) (CF$_3$SO$_3$)] (125 mg, 0.23 mmol, 1 equiv) was then dissolved in 20 mL of chloroform, followed by the addition of 4-vinylpyridine (245 μL, 2.3 mmol, 10 equiv). The reaction mixture was magnetically stirred at room temperature for 16 h when a cloudy red solution was obtained. The mixture was filtered using a fritted funnel and Celite and

143

the solvent was removed under reduced pressure. The resulting solid was recrystallized by layering hexanes over a solution of the complex in dichloromethane to afford 121 mg (0.18 mmol, 80% yield) of [Mn(CO)$_3$(qbt)(4-vpy)](CF$_3$SO$_3$) (1) as dark red crystals. Selected IR (KBr, cm^{-1}): 3066(w), 2040(s), 1955(s), 1929(s), 1615(w), 1519(w), 1273(s), 1261(s), 1151(m), 1030(m), 765(w), 639(m), 518(w). UV–vis (dichloromethane, ε, M^{-1} cm^{-1}): 445 (1900), 382 (16,400).

2.3. X-ray structure determination

Single crystals of complex 1 were grown by layering hexanes over its dichloromethane solution. One suitable crystal was selected and fixed on top of MiTiGen micromount using Paratone N-Oil (Hampton Research) and transferred to the diffractometer. Data were collected on a Bruker APEX II single-crystal X-ray diffractometer with graphite monochromated Mo-Kα-radiation (λ = 0.71073 Å) using ω-scan technique in the range of 3 ≤ 2θ ≤ 50°. Multi-scan absorption corrections [71] were applied to the data set using SADABS. The structure was generated using *SHELXT* (intrinsic phasing) and subsequently refined by full-matrix least squares procedures on F^2 with *SHELXL* [72]. All non-hydrogen atoms were refined anisotropically. All hydrogen atoms were included in calculated positions on the C atoms to which they are bonded, with C−H = 0.93 Å and U_{iso}(H) = 1.2U_{eq}(C). Calculations and molecular graphics were preformed using *SHELXTL* 2014 and *Olex2* programs [73]. Crystal data and structure refinement parameters are listed in Supporting Table S1.

2.4. Incorporation of [Mn(CO)$_3$(qbt)(4-vpy)](CF$_3$SO$_3$) into pHEMA/EGDMA hydrogel

The preparation, polymerization, and curing of polymer samples was carried out in the dark to avoid decomposition of the CO-donating complex. The water-soluble initiator 2,2′-azobis[2-(2-imidazolin-2-yl) propane] dihydrochloride (VA-044) (0.015 g, 0.045 mmol) was dissolved in milliQ water (2.85 g, 158 mmol) aided by sonication. This solution was mixed with 2-hydroxyethyl methacrylate (HEMA) (5.00 g, 41 mmol) and ethylene glycol dimethacrylate (EGDMA) (0.250 g, 1.3 mmol). The pre-polymer mixture was combined with a dilute solution of 1 in acetone (0.60 mL, 0.00145 M) to afford photoCORP-1 which was 0.1 mM with respect to (w.r.t.) 1 for UV–vis analysis. In a similar manner, a second pre-polymer mixture (4 mM w.r.t. 1) was prepared by adding a concentrated solution of 1 in acetone (0.60 mL, 0.058 M) to make photoCORP-1 for myoglobin/cell treatment. Blank polymer samples (without 1) were prepared by combining a third pre-polymer batch with acetone (0.6 mL). The mixtures were degassed for 20 min by bubbling dry nitrogen gas, and placed into polystyrene cuvettes or Eppendorf™ tubes. Once the solutions were placed in their respective mold they were heated for 30 min at 50 °C using a water bath. The heat was then turned off and the water-bath was allowed to cool slowly and the polymers were then cured at room temperature for 48 h in the dark. Microanalytical data (from Galbraith Laboratories Inc.) indicated that the photoCORP-1 tip material contained 0.0328% of Mn corresponding to 0.39 wt% incorporation of the photoCORM in the hydrogel.

Photolysed polymer samples were prepared by irradiating photoCORP-1 (sealed within its mold) with visible light. The samples were then removed from their containers, washed, sterilized, and air-dried for 30 min before use. Dilute polymer samples (0.1 mM) were kept inside their polystyrene cuvette mold and used as blank for UV–vis absorption studies.

2.5. Assembly of the optical fiber-based catheter

Four optical fiber lines were cut into 30 cm segments and one end of each line was manually polished into a cone to increase the illumination area as well as to remove rough surface from the polymer interface. If the rough edges were not removed from the optical fiber line, polymerization nucleated at such sites resulting in cracked and frail polymer tips. The polished end of each line was then placed 0.5 ± 0.15 cm into a 1.5 mL Eppendorf™ tube and the fibers were secured in the Eppendorf™ tube using clamps and clear tape. A batch of 1.5 mL of the pre-polymer mixture containing 1 was added in each tube and the tubes were heated at 50 °C (in a water bath) for 30 min. The resulting photoCORP-1 cones thus obtained remained securely attached to the optical fibers after polymerization. Batches of photoCORP-1 were also polymerized in polystyrene cuvettes (with 0.1 mM of 1) for spectroscopic measurements. The cones (with optical fiber attached) and rectangular prisms of solid photoCORP-1 were taken out of their mold by carefully breaking the container using a hammer, washed with milliQ water, sterilized using 70% ethanol, and air dried for 30 min before use. The fiber-photoCORP-1 assembly is abbreviated as CO-catheter hereafter. The weight of the polymer piece attached to the optical fiber was regularly adjusted to 0.26 g for myoglobin assays or 0.50 g for cellular studies.

2.6. Coupling of the CO-catheters with visible light source

The light guide of a visible light source (Electro Fiber Optics Corp. IL 410 illumination system, 10 mW cm^{-2}) was coupled to the open end of the optical fiber using a F-915 T multimode fiber coupler (Newport Corp.) attached to a lab jack. The fiber was connected to the fiber coupler with a pre-adjusted FPH-DJ fiber chuck (Newport Corp.) to obtain ~6% coupling efficiency (0.58 mW cm^{-2}).

2.7. Photolysis experiments with 1 and photoCORP-1

The CO release rates (k_{CO}) from complex 1 and photoCORP-1 were measured by using polystyrene cuvettes (1 cm × 1 cm × 4.5 cm) and a broadband visible light source (Electro Fiber Optics Corp. IL 410 illumination system, 10 mW cm^{-2}) to induce CO photorelease. The cuvettes containing either solution of complex 1 or photoCORP-1 were placed 1 cm away from the light source, irradiated for 20 or 30 s intervals respectively, and the electronic absorption spectra were sequentially recorded. A blank polymer sample was used for the baseline correction for the studies using photoCORP-1. The changes in absorption spectra upon light exposure were monitored and the CO release rates (k_{CO}) were determined from a ln(C) versus time (t) plot at an appropriate wavelength.

2.8. Myoglobin assay

Myoglobin (Mb) assays were performed in quartz cuvettes (1 cm × 1 cm × 4.5 cm) by dissolving horse heart myoglobin in phosphate buffer saline (PBS, 100 mM, pH 7.4) and reducing it with sodium dithionite. The Soret band of deoxymyoglobin at 435 nm (ε = 121 mM^{-1} cm^{-1}) or the band at 540 nm (ε = 15.4 mM^{-1} cm^{-1}) were used to calculate the concentration of myoglobin used. All assays were conducted in one cuvette system by placing and illuminating photoCORP-1 directly inside the myoglobin solution.

The CO release rate of CO-catheter (photoCORP-1 concentration 4 mM) was investigated using low-power broadband visible light. The tip of the CO-catheter was placed inside the reduced myoglobin solution and illuminated internally using broadband visible light (power of light at the tip: 0.58 mW cm^{-2}). The cuvette was kept under a dry nitrogen current to keep oxygen out of the solution while the treatment was in progress. The CO-treated myoglobin solution was then mixed thoroughly by inverting the cuvette several times and the absorption spectra were recorded. The polymer used was kept in the dark, rinsed with milliQ water, and carefully dried in between UV–vis analysis of the myoglobin solution. Since sodium dithionite itself may induce CO release, a control cuvette containing myoglobin, sodium dithionite and photoCORP-1 was kept in the dark and scanned at 1 min time intervals for 15 min.

2.9. Leaching experiments

In order to determine whether complex **1** or its photoproduct (s) following CO release leach out of the polymer matrix, rectangular blocks of photoCORP-**1** (4 mM, weight: 0.50 g) were submerged in 2 mL of PBS and each sample was sealed in its container and kept under ambient light or dark conditions at room temperature for different number (0, 2, 4, 8 and 10) of weeks. The polymer blocks were then removed from their containers and the solutions were analyzed by spectrophotometry. No absorption due to complex **1** or the free ligand was observed in any sample thus prepared. These solutions were also subjected to electron spin resonance (ESR) spectrometry to determine any presence of Mn^{2+} ion. No EPR signal due to Mn^{2+} ion was detected.

2.10. Shelf life of photoCORP-**1**

The effect of the extent of hydration of the polymer on its performance as a CO donor was investigated by using small rectangular blocks of photoCORP-**1**. First, samples of photoCORP-**1** (with 4 mM concentration of **1** in the starting mixture) were polymerized inside polystyrene cuvettes and then cut (using a razor blade) into smaller rectangular blocks ($\sim 0.9 \times 0.4 \times 0.4$ cm, weight: 0.26 g). These blocks were then dried for different number of days (0, 5, and 10 days). Each *CO*-donating polymer block was used for myoglobin assay to determine their capacity as CO donor. The polymer blocks were submerged and sealed in a quartz cuvette containing a PBS solution of myoglobin, and sodium dithionite. These samples were then irradiated externally using the above-mentioned light source (10 mW cm^{-2}) for 10 s intervals, mixed thoroughly, and their absorption spectra were recorded. The k_{CO} values were then calculated from the [Mb$_{CO}$] versus time (*t*) plot to determine any changes in efficacy of the polymer as CO donor with time.

2.11. Delivery of CO to HT-29 cancer cell line and HEK 293 normal embryonic cell line by the CO-catheter and flow cytometry analysis

The human colorectal adenocarcinoma cell line (HT-29) was cultured using McCoy's 5A medium with L-glutamine (Corning), supplemented with 20% fetal bovine serum (FBS). The cells were then washed, harvested, counted, and diluted to a concentration of 1×10^6 cells/mL using the culture growth medium. Several 2-mL portions of this solution were separated into round-bottom Falcon™ tubes (12×75 mm, polystyrene) with snap caps (Corning™) and treated with CO released from the polymer irradiated for various time intervals as follows.

The HT-29 cell suspensions were taken in four different Falcon™ tubes and one fresh CO-catheter (tip weight: 0.50 g, 4 mM concentration of **1**) was dipped into each of the tubes kept under dark condition. The cells were then treated with CO released from CO-catheters upon remote triggering with visible light (0.58 mW cm^{-2}). The time of illumination was 5, 10, 20, and 40 min for tubes numbered 1 to 4. Control experiments were carried out using one CO-catheter without light irradiation, and another CO-catheter with light but carrying an extensively photolysed tip. After treatment, the cells were centrifuged and re-suspended in 900 µL of PBS buffer and transported to the flow cytometer (BD FACS LSR II). Next the cells were treated with 100 µL of annexin-binding buffer (10 mM HEPES, 140 mM NaCl, 2.5 mM CaCl$_2$, pH 7.4), 2 µL of annexin V Alex Fluor™ 647 conjugate, and incubated for 15 min at room temperature. The cells were then treated with propidium iodide (PI, 2 µL, 300 nM), and analyzed using flow cytometry (BD FACS LSRII).

The normal human embryonic kidney cells (HEK 293) were grown in DMEM supplemented with 10% FBS. The cells were then washed, harvested, counted, and diluted to a concentration of 1×10^6 cells/mL using DMEM. Samples (2 mL) of these cells were then treated with CO

by following the same procedure as described above and the extent of apoptosis was measured by flow cytometry.

3. Results and discussion

3.1. Synthesis and characterization of [Mn(CO)₃(qbt)(4-vpy)](CF₃SO₃) (1)

Complex **1** was synthesized in a stepwise manner and all manipulations were performed in the dark to avoid the decomposition of the CO donor. First, [Mn(CO)₅Br] was stirred with qbt in a chloroform/methanol mixture (1:3 v/v) for 10 h at room temperature to afford [Mn(CO)₃(qbt)Br]. Next, the Br⁻ ligand was replaced with CF₃SO₃⁻ by treating [Mn(CO)₃(qbt)Br] with Ag(CF₃SO₃) in dichloromethane. Finally, the weakly coordinating CF₃SO₃⁻ ligand in [Mn(CO)₃(qbt)(CF₃SO₃)] complex was replaced with 4- vinylpyridine (4-vpy) to afford **1** in good yield. This photoCORMs was selected for the present study because of several reasons. Much like other manganese-containing photoCORMs [47], **1** exhibits rapid release of CO upon exposure to low power visible light, very suitable for phototherapy. This dark orange photoCORM also turns colorless upon CO release, a characteristic that allows visual observation of the overall photorelease process. The 4-vpy unit allowed us to covalently attach this photoCORM to the polyHEMA framework; the radical-derived polymerization step does not decompose complex **1** and allows its easy incorporation. And finally, the photoCORP-**1** composite retains the CO-spent products quite tightly (as evidenced by leaching experiments) while CO readily diffuses out of the robust polymer monoliths upon illumination.

Complex **1** exhibits FTIR stretching frequencies (2040, 1955, and 1929 cm^{-1}) typical of metal carbonyl complexes with three facially coordinated CO ligands (*fac*-[Mn(CO)₃] moiety, Fig. 1) [25]. It dissolves in organic solvents like chloroform, dichloromethane and acetone. A solution of **1** in dichloromethane displays two absorption bands at 445 and 382 nm, resulting in an orange red coloration.

3.2. X-ray structure analysis

The molecular structure of **1** is shown in Fig. 2 and selected matrix parameters are listed in the figure caption. The coordination geometry of Mn(I) is distorted octahedral. The equatorial plane is composed of two CO ligands (in *cis* conformation) and two N atoms from the bidentate ligand qbt, while the third CO occupies an axial position *trans* to the 4-vinyl pyridine ligand (Fig. 2).

Although the equatorial plane comprised of C2, C3, N1 and N2 atoms in **1** is satisfactorily planar (mean deviation of 0.050(5) Å), the Mn atom is deviated from this plane by 0.110(4) Å toward the N3 atom of the vinyl pyridine fragment. In addition, the chelate ring composed of Mn1, N1, C4, C13, and N2 atoms significantly deviates from planarity (mean deviation, 0.110(3) Å). As a consequence, the entire qbt
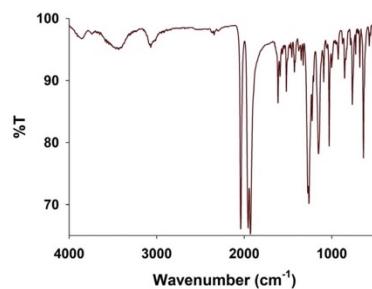
Fig. 1. FTIR spectrum of **1** in KBr matrix.
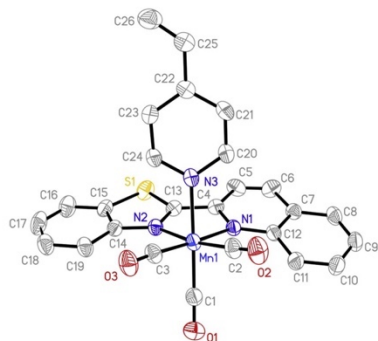
Fig. 2. Molecular structure of the cation of complex **1** with atom labeling scheme. The thermal ellipsoids are shown at 50% probability level. Selected bond distances (Å): Mn1-C1 1.818(5), Mn1-C2 1.800(5), Mn1-C3 1.823(6), Mn1-N1 2.113(4), Mn1-N2 2.062(4), and Mn1-N3 2.093(4).

ligand frame is tilted toward the 4-vpy moiety (dihedral angle 12.7°). The average the Mn—C bond distances in complex **1** (1.814(6) Å) is quite similar to that observed with analogous [Mn(CO)₃(qbt)Cl] complex (1.800(6) Å) [74]. The crystal packing of **1** reveals no π-π stacking interactions. However, non-classical hydrogen bonding of types C—H···O (2.547(5) and 2.542(5) Å) and C—H···F (2.466(6) Å) is present in the solid state.

3.3. Photochemical characteristics of 1

The deep orange color of solutions of **1** is lost upon exposure to visible light. Systematic exposure of such solutions to small intervals of broadband visible light (10 mW cm⁻²) results in sequential changes in the electronic absorption spectrum as shown in Fig. 3. Myoglobin assay (vide infra) reveals that the spectral changes are due to photorelease of CO from **1** upon illumination. In order to determine the apparent CO-release rate (k_{CO}), a 0.067 mM solution of **1** in dichloromethane was exposed to broadband visible light (10 mW cm⁻²) for 20 s intervals and the value of k_{CO} was determined from the ln(C) (C = concentration of **1**) vs. time (t) plot. The k_{CO} value for **1** (0.96 min⁻¹) clearly indicated that this photoCORM is very sensitive to low power visible light.

3.4. Characterization of photoCORP-1 and photolysis experiments

The HEMA/EGDMA polymer was chosen for its well-studied bio-compatibility, transparency, gas permeability, chemical/physical stability, and porosity characteristics [68–70]. PhotoCORP was synthesized by mixing a solution of **1** in acetone with a pre-polymer mixture containing the HEMA monomer, EGDMA cross-linker, water, and VA-044 initiator. A final 0.1 mM concentration of **1** in such mixture was necessary to isolate photoCORP-1 suitable for absorption spectroscopy, while a higher final concentration of **1** (4 mM) was employed to isolate composite materials suitable for CO delivery required in the cellular experiments. No dichloromethane was employed in the polymerization reactions to avoid any toxicity due to residual solvent in the final photoCORP-1 samples. The polymerization temperature conditions allowed us to use acetone as the solvent for preparing the solutions of **1**. No boiling of any solvent component occurred during the synthesis of photoCORP-1 and hence problems associated with formation of bubbles leading to irregular/brittle polymeric product(s) were absent. The initiator VA-044 was selected as the radical initiator in our experiments due to its decomposition/activation at relatively mild temperatures. Conventional initiators requiring UV irradiation were not considered in order to prevent any decomposition of the manganese photoCORM.

Once cured for 48 h, photoCORP-1 is a photosensitive and malleable orange solid that has a shelf life of over 3 months if kept at 0 °C in a moist sealed container in the dark. The malleability of the solid samples is slowly lost when the material is left out of a sealed package and results in a hard solid within 5 days. Fresh samples of photoCORP-1 can be cast into any shape or form if a mold is available. However, if the size of the mold is large, it is often difficult to control the temperature of the polymerization step because the radical polymerization reaction is highly exothermic and may reach temperatures higher than the boiling point of the solvents used. This causes the solvent to boil and create bubbles within the bulk of the polymer. When freshly prepared, photoCORP-1 is relatively flexible and can easily be cut into different shapes using a razor blade.

The covalent binding of **1** to the polymer frame (a schematic representation is shown in Fig. 4) ensures retention of both **1** and its photo-product(s) within the polymer matrix. The high hydrophobicity of these species could also be responsible for effective retention. No detectable leaching of complex/ligands was observed when photoCORP-1 was submerged in aqueous buffer for over 2 months (before and/or after photolysis) as determined UV–Vis spectrophotometry and EPR spectrometry.

Fig. 3. Systematic changes in the electronic absorption spectrum of **1** in dichloromethane upon exposure to small intervals of visible light (10 mW cm⁻², 20 s intervals, 298 K) leading to CO photorelease (inset: apparent CO release rate $k_{CO} = 0.96$ min⁻¹ as determined by the ln(C) vs. time plot).
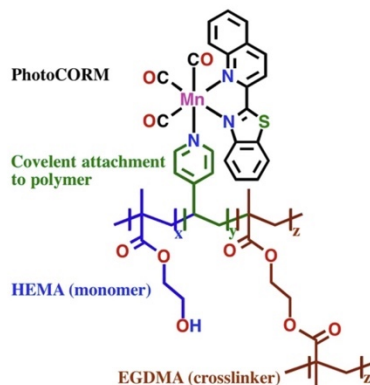
Fig. 4. Schematic representation of (photoCORP-1) with complex **1** *co*-polymerized within HEMA/EGDMA hydrogel.

146
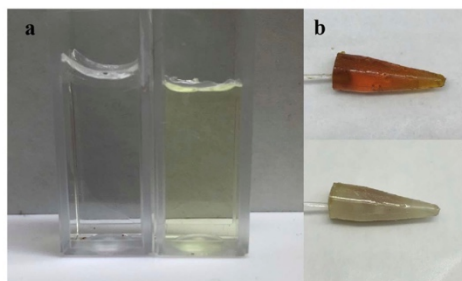
Fig. 5. Images of photoCORP-**1** polymerized (a) inside polystyrene cuvettes for UV–vis spectrophotometry, blank (left) and photoCORP-**1** (0.1 mM w.r.t. **1**, right); (b) inside Eppendorf™ tubes to afford the tip of the optical fiber-based CO-catheter, before use (top) and after extensive photolysis (bottom).

In order to examine the CO-releasing parameters of photoCORP-**1**, the pre-polymer mixture containing the initiator, monomer, cross linker, solvents and complex **1** (0.1 mM w.r.t. **1**) was poured into a polystyrene cuvette and heated for 30 min in a water bath carefully kept at 50 °C to initiate the radical polymerization. The heat was then turned off and the cuvette was allowed to cool slowly to room temperature to control any exothermic polymerization. A blank polymer containing everything except the manganese photoCORM was used as a blank (Fig. 5a) for baseline correction. The cuvettes were then kept in the dark for 48 h to ensure curing. The cuvette containing photoCORP-**1** was then exposed to 10 mW cm^{-2} broadband visible light and the changes in the electronic absorption spectrum were recorded as before. As shown in Fig. 6, the spectral traces clearly indicate that photoCORP-**1** does release CO upon illumination. Kinetic analysis of the spectral changes afforded an apparent CO release rate k_{CO} of 0.40 min^{-1}, a value slower than the k_{CO} value of free complex **1**. This slow-down of CO photorelease is expected since the porosity (and extent of hydration) of the polymer matrix does attenuate the diffusion rate of CO from the bulk of the photoCORM-**1** monolith.

The tips of the CO-catheters were cast in Eppendorf™ tubes. In this case, the pre-polymer mixture containing the initiator, monomer, cross linker, solvents and complex **1** (4 mM) was poured into Eppendorf™ tubes with the optical fiber dipped in it and the assemblies were heated at 50 °C for 30 min in a water bath. After slow cooling to room

temperature, the assemblies were kept in the dark for 48 h. The tubes were then carefully broken apart with a hammer and the CO-catheters were taken out and rinsed with water. As shown in Fig. 5b (top), the high concentration of **1** in the tip is indicated by the dark orange color. The CO release rate from the tip of the CO-catheter was determined by myoglobin assay (vide infra). Extensive illumination of such tips results in loss of the color (Fig. 5b, bottom) due to complete loss of CO from the composite material. It is important to note here that a much higher concentration of **1** was used to prepare the tips of the CO-catheters (compared to that in the polystyrene cuvettes used in the previous step) to ensure delivery of enough CO to elicit apoptotic response in malignant targets.

3.5. Determination of coupling efficiency of our visible light set-up

The coupling efficiency of our visible light set-up was tuned to deliver low-power light to the polymer tip to release sustained and moderate amounts of CO. With a 30 cm optical fiber attached to the 10 mW cm^{-2} broadband visible light source through our F-915 T multimode fiber coupler (Fig. 7), we recorded an output of 2.31 mW cm^{-2} at the end of the fiber (coupling efficiency 23%). However, when the tip was directly illuminated with light of this intensity, most of the CO was released from the polymer within 30 min. Since the solubility of CO in aqueous media is very low, such rapid expulsion of CO from the catheter would result in escape of a major part of the photoreleased CO from the target tissues before it causes the desired physiological effect. Therefore, to achieve a more controlled and sustained levels of CO, the power of the incidence light was adjusted to 2.5 mW cm^{-2} to bring down the output to 0.58 mW cm^{-2} at the end of the optical fiber. All experiments with CO-catheters were therefore performed with an incident light intensity of 2.5 mW cm^{-2}.

3.6. Controlled delivery of CO to myoglobin with CO-catheter

Myoglobin assay was used to confirm the release of CO from the polymer tip of the CO-catheter. In this assay, the rate of CO release was measured by tracking the formation of carboxymyoglobin (Mb$_{CO}$) with a polymer tip which was made from pre-polymer mixture with 4 mM concentration of **1**. Analytical data indicated that this composite contained a total of 1.018 mg of **1** covalently bound to 260 mg of the final tip material (0.39 wt%). The power of the incident light was set to 2.5 mW cm^{-2} to expose the tip to visible light intensity of 0.58 mW cm^{-2}. The tip of the CO-catheter used in the assay comprised of 0.26 g of photoCORP-**1**. It was dipped directly into a reduced myoglobin solution and was triggered with the visible light source for 1 min intervals. To keep oxygen from interacting with the solution, a current of dry nitrogen was placed directly over the quartz cuvette. Following each min of illumination, the CO-catheter was taken out, rinsed with water, dried and kept in the dark. The absorption spectra were recorded after each illumination period. As shown in Fig. 8, delivery of CO from the CO-catheter results in the rapid formation of Mb$_{CO}$ evidenced by shift of the Soret band of reduced Mb (435 nm) to 424 nm. A device capable of CO delivery to myoglobin by remote light triggering has recently been reported by Schiller and coworkers [62]. In this work, a hydrophobic tetranuclear tricarbonyl manganese complex was non-

Fig. 6. Systematic changes in the electronic absorption spectrum of a monolith of photoCORP-**1** (within a polystyrene cuvette) upon exposure to small intervals of visible light (10 mW cm^{-2}, 30 s intervals, 298 K) due to CO photorelease (inset: apparent CO release rate k_{CO} = 0.40 min^{-1} as determined by the ln(C) vs. time plot).
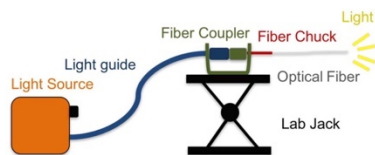
Fig. 7. The remote light-triggering assembly.

147

covalently imbedded inside electrospun non-woven fibers of poly(L-lactide-*co*-D/L-lactide) 70/30. Unlike the present system consisting of photoCORP-**1** *covalently embedded within the bulk of a solid polymer tip,* the porous fibers were wrapped around a spherical glass head at the tip of an optical fiber to achieve the CO-donating unit. This system also requires a 405 nm laser (14 mW cm^{-2}) for CO release. Although Schiller and co-workers presented an excellent portable illumination device, the CO release was observed "only from the sample areas in direct contact with the glass sphere exposed to light whereas salient areas remained unaffected". Consequently, CO release from the Schiller device is expected to be somewhat slow compared to the present device in which CO is released from the entire tip as evidenced by complete bleaching of the orange color upon exhaustive illumination (Fig. 5b, bottom panel). Also, the light intensity required for rapid CO release from the photoCORP-**1** tip is considerably low compared to the requirement for the Schiller device. Finally, the Schiller material contained 10 wt% complex "according to the amount of theoretically embedded photoCORM" compared to photoCORP-**1** containing 0.39 wt% of **1**. Nevertheless photoCORP-**1** released 12.78 μM CO in 30 min upon exposure to 0.58 mW cm^{-2} visible light while equivalent amount of the Schiller material released 1.2 μmol of CO in 30 min with a 14 mW cm^{-2} laser [62].

3.7. Variations in CO delivery capacity of photoCORP-**1** with light intensity and extent of drying

To study the effect of hydration on the CO-release rate of photoCORP-**1**, one block of cured polymer was removed from its mold and cut into smaller blocks (0.9 × 0.4 × 0.4 cm, 0.26 g, 0.39 wt% of **1**) which were then air dried in the dark for different amounts of time (0 days, 5 days, 10 days) before myoglobin assays were performed to determine their capacity of CO delivery. In all assays, the polymer block was submerged inside the reduced Mb solution and the quartz cuvette was stoppered. The polymer block inside the cuvette was then directly exposed to the external visible light source (10 mW cm^{-2}), inverted multiple times, and the absorption spectra were recorded. The fresh polymer (0 day) exhibited full conversion from Mb to Mb$_{CO}$ within 40 s (4 × 10 s exposures). To ensure full conversion of Mb$_{CO}$, the polymer was illuminated for a total of 3 min and the absorption spectrum was recorded again. The rate of CO release from the photoCORP-**1** piece was 0.074 μM s^{-1} mg^{-1} (Fig. 9, T$_{30}$ = 133.20 μM mg^{-1}).

When the power of the incident light was sequentially changed from 10 mW cm^{-2} to 1.6 mW cm^{-2}, 0.58 mW cm^{-2}, and 0.50 mW cm^{-2}, the k_{CO} value dropped down from 0.074 μM s^{-1} mg^{-1} (T$_{30}$ = 133.20 μM mg^{-1}) to 0.0094 μM s^{-1} mg^{-1} (T$_{30}$ = 16.92 μM mg^{-1}), 0.0071 μM s^{-1} mg^{-1} (T$_{30}$ = 12.78 μM mg^{-1}), and 0.0065 μM s^{-1} mg^{-1} (T$_{30}$ = 11.70 μM mg^{-1}), respectively (Fig. 9). These results confirm that the CO release capacity of photoCORP-**1** depends on the intensity of the incident light (in addition to the concentration of **1**). The nonlinearity in the variation of CO release rates from photoCORP-**1** with the power of the incident light appears to arise from the fact that when the polymer is illuminated with high power light, the CO molecules closest to the surface exit the polymer rather fast, whereas CO molecules that are released deep inside the polymer block are not able to exit the polymer as quickly.

When an identical polymer block (0.9 × 0.4 × 0.4 cm, 0.26 g, 4 mM concentration of **1**) was air dried in dark for 5 days, the weight of the material decreased from 0.26 g to 0.21 g, indicating a loss of about 20% of its initial weight presumably due to loss of solvent molecules from the polymer matrix. The composite lost its compressibility and became hard after such loss of solvent. When we subjected this 5-day old polymer block to the same myoglobin assay under the same direct illumination (10 mW cm^{-2}), conversion of Mb to Mb$_{CO}$ was complete within 40 s (4 exposures of 10 s each). The CO release rate was 0.058 μM s^{-1} mg^{-1} (Fig. 10, T$_{30}$ = 104.4 μM mg^{-1}), somewhat slower than that obtained with a fresh identical sample of photoCORP-

Fig. 8. Myoglobin assay performed in submerging the tip of the CO-catheter directly into the reduced Mb solution. The catheter was triggered by visible light (0.58 mW cm^{-2}) for 1 min intervals and the changes in the spectrum were recorded. Shift of the Soret band from 435 nm to 424 nm indicates the formation of Mb$_{CO}$ by CO released from the tip of the catheter. The black trace is the absorption spectrum of the starting oxidized Mb.
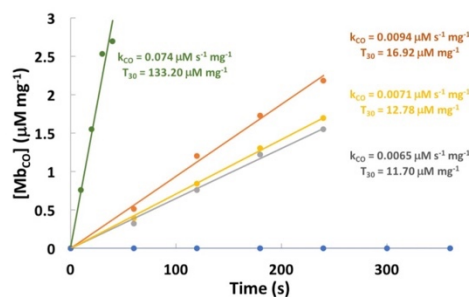
Fig. 9. Plot of conversion of Mb to Mb$_{CO}$ by fresh photoCORP-**1** under different light intensity. Greene trace: light intensity: 10 mW cm^{-2}; k_{CO}: 0.074 μM s^{-1} mg^{-1}; Orange trace: light intensity: 1.6 mW cm^{-2}; k_{CO}: 0.0094 μM s^{-1} mg^{-1}; Yellow trace: light intensity: 0.58 mW cm^{-2}; k_{CO}: 0.0071 μM s^{-1} mg^{-1}; Grey trace: light intensity: 0.50 mW cm^{-2}; k_{CO}: 0.0065 μM s^{-1} mg^{-1}; Blue trace: No light. (For interpretation of the references to color in this figure legend, the reader is referred to the web version of this article.)

1. Air drying (in dark) for 10 days did not lead to much reduction in weight of the polymer blocks (changed from 0.26 g to 0.20 g). However, the CO release rate dropped to 0.044 μM s^{-1} mg^{-1} (Fig. 10, T$_{30}$ = 79.2 μM mg^{-1}), as evidenced by the myoglobin assay. Collectively, these results indicate that despite loss of flexibility, the polymer remains useful for CO delivery even after it becomes relatively dry.

3.8. Controlled delivery of CO to human colorectal adenocarcinoma cells and human embryonic kidney cells (as normal control)

The pro-apoptotic effects of CO on hyperproliferative and dysregulated cells such as cancer cells [6] has prompted us to assemble this CO-catheter to deliver controlled doses of CO to colorectal adenocarcinoma cells. The onset of apoptosis in cells is regularly detected by Annexin V assay where a dye-tethered phospholipid-binding protein binds to phosphatidylserine translocated on the outer leaflet of the plasma membrane at the beginning of apoptosis and identifies cells that have entered the apoptotic cycle. Propidium iodide (PI) is also used in such measurement to detect cells with heavily compromised membranes in

which PI intercalates between the base pairs of the nucleic acids and exhibits enhanced fluorescence. In the present study, we performed this assay to detect the pro-apoptotic effects of CO in the cancer cells and analyzed the extent of cell apoptosis/death by FACS analysis.

Prior the start of the cellular treatment, freshly prepared CO-catheters were removed from their sealed container, checked for their integrity and weight, washed, and sterilized using 70% ethanol. They were then air dried for 30 min and kept in the dark inside a sealed sterile container until the beginning of the treatment. A fresh CO-catheter was used for each cell treatment and the weight of the tip (0.50 g, 0.39 wt% of **1**) was carefully controlled to ensure similar amounts of CO delivery to the cells. Human colon cancer cells (HT-29) were cultured in their appropriate media, harvested, and counted manually using a hemocytometer. The cells were diluted to a concentration of 10^6 cells/mL using the growth medium, and 2 mL portions of this solution were split into FACS tubes. The cells were then subjected to CO by submerging the tips of the catheters directly into the cell suspension and triggering the CO-catheter for 5, 10, 20 and 40 min (Fig. 11 and Fig. S1). Following exposure to CO the cells were centrifuged and the cell pellets were resuspended in 900 μL of PBS buffer. Finally, 100 μL of Annexin binding buffer was added to each FACS tube along with 2 μL of Annexin V. After 15 min of incubation at room temperature, the cells were treated with 2 μL of propidium iodide and subjected to FACS analysis.

Results of the FACS analysis (Fig. 12) reveal that exposure to CO led to the onset of apoptosis (Annexin V binding) to the cancer cells soon after the CO-catheter was triggered with visible light (0.58 mW cm^{-2}). The extent of apoptotic response was dose-dependent as evidenced by the illumination-time dependent increase of the apoptotic cells. Annexin V binding to the cancer cells increased with time of CO exposure (Fig. 12, top panel) as evidenced by shift of the cell population toward the Annexin V axis. In addition, a considerable number of doubly-stained cells were also detected (Fig. 12d), indicating the beginning of cell destruction. Cells without any CO treatment (Fig. 12e, bottom panel) were used as blanks to determine the amount of apoptosis induced by the handling steps alone. For accuracy, the control cells were kept under conditions identical to those of the treated samples. In our hand, the various handling steps (trypsinization, centrifugation, resuspension) led to a background apoptotic cell count of ~10% (Fig. 13). Controls also included cytometry of cells treated with a CO-spent catheter (Fig. 12f, bottom panel) and cells treated with a fresh CO-catheter but no light (Fig. 12g, bottom panel). Collectively these results demonstrate that the CO-catheter delivers CO to the cell suspension

Fig. 11. Top panel: schematics of the CO delivery set up. Bottom panel: photograph of the actual set up.

(total volume 2 mL) to cause onset of CO-induced apoptosis within a short time and such onset of apoptosis occurs only when the CO-catheter is triggered with light. The slow and sustained effects of CO also demonstrate that controlled delivery of CO is indeed possible with photoCORP-**1** and this composite material can be employed in a light-triggering device to carry out CO delivery to remote targets. Interestingly, the tip of the CO-catheter lost most of its dark orange color (Fig. 5b) after 40 min of illumination. The CO-spent catheter that we employed was irradiated with visible light for a long time and therefore was completely colorless (Fig. 5b).

The results of FACS analysis are better represented in a bar plot as shown in Fig. 13. In case of HT-29 cells, the induction of apoptotic death increases with the time of CO exposure. As shown in Fig. 13, remote illumination by the CO-catheter for 5 min resulted in Annexin binding by 48% of the cell population (blue bars). The number of apoptotic cells thereafter increased to 60% upon 10 min exposure and to 75% at the end of 40 min. In contrast, when human embryonic kidney cells (HEK 293) were exposed to CO by similar technique, no induction of apoptosis was observed (orange bars). The last observation confirms that exposure to CO (as available from the tips of the catheter) does not result in any cytotoxic effects in normal cells.

Repeat experiments with *CO*-catheter containing a lower concentration of **1** (made from pre-polymer mixture with 0.1 mM of **1**) led to much smaller extent of CO-induced apoptosis in HT-29 cells. It is therefore evident that the tip of the CO-catheter must contain a high concentration of the CO-donating complex **1** to achieve rapid onset of apoptosis in the cell culture. This is somewhat expected since a major portion of CO photoreleased from the tip of the CO-catheter escapes the suspension containing the cancer cells (due to the low solubility of CO in aqueous media) before reaching to its target. Important is to note that photoCORP-**1** is very sensitive to light and hence we used low-power (0.58 mW cm^{-2}) broadband visible light to trigger CO release to achieve a sustained and moderate levels of CO at the target site in all these experiments. For the very same reason, the concentration of **1** in the tip material must be raised to 0.30–0.40 wt% to deliver a steady release of CO for hours. Finally, the rate of CO release from the CO-catheter with a certain concentration of **1** can be accelerated or decelerated substantially by changing the power of the light used to trigger the device.

Fig. 10. Plot of conversion of Mb to Mb$_{CO}$ by photoCORP-**1** following different extent of drying. Blue trace: fresh polymer, CO release rate 0.074 μM s^{-1} mg^{-1}; Orange trace: polymer after 5 days of drying, CO release rate 0.058 μM s^{-1} mg^{-1}; Green trace: polymer after 10 days of drying, CO release rate 0.044 μM s^{-1} mg^{-1}. (For interpretation of the references to color in this figure legend, the reader is referred to the web version of this article.)

Fig. 12. (Top panel) Flow cytometry analysis (plots of Annexin V-Alexafluor647/propidium iodide staining of HT-29 cells) after CO exposure (from the CO-catheter) of (a) 5 min, (b) 10 min, (c) 20 min and (d) 40 min. (Bottom panel) Plots of Annexin V- Alexafluor647/propidium iodide staining of HT-29 cells with (e) no CO treatment, (f) treatment with a CO-spent catheter and (g) treatment with a CO-catheter but no light.
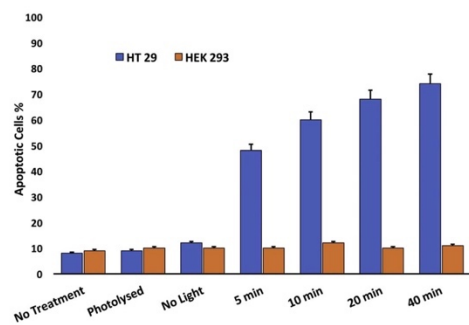
Fig. 13. Bar plot representation of the flow cytometry results shown in Fig. 12 showing the progression of apoptosis in HT-29 cells upon exposure to CO (blue bars). The absence of apoptosis upon exposure of HEK 293 cells to CO is shown by the orange bars. (For interpretation of the references to color in this figure legend, the reader is referred to the web version of this article.)

4. Conclusions

The proapoptotic and chemosensitizing properties of CO make it a potential therapeutic for certain types of cancer. However, precise delivery of controlled doses of this noxious gas to the malignant site poses as major challenge to CO therapy. In this work, we report a biocompatible CO-donating polymer composite photoCORP-**1** that releases CO when triggered with low-power (mW levels) broadband visible light. The gas permeable HEMA/EGDMA hydrogel allows rapid release of CO from the polymer monolith but retains the photoproducts tightly bound to the organic framework through covalent bond (Fig. 4). Synthesis of photoCORP-**1** involves two steps and requires 48 h of curing time to afford a malleable composite that can be molded or cut

into any size and shape. The CO-releasing capacity of photoCORP-**1** does not change considerably upon drying of the hydrogel. Because the polymer matrix traps all products but CO upon illumination, photoCORP-**1** can be utilized as a convenient CO source for experiments such as delivery of controlled doses of CO to biological samples like proteins (as in the myoglobin experiments reported here). Indeed, we have performed the CO delivery experiments with the HT-29 cells by using small blocks of photoCORP-**1** and external illumination by the room light (Fig. S2). In such attempts, CO-induced apoptosis was readily achieved much like the experiments described above (Figs. S3 and S4).

The most important result of this study is the assembly of the CO-catheter that allows delivery of *controlled and sustained* doses of CO to a target consisting of HT-29 (human colorectal adenocarcinoma) cells under the total control of light. The success in this mode of CO delivery demonstrates that it is possible to deliver controlled doses of CO to malignant targets in inaccessible cavity and promote CO-induced apoptosis in cancer cells. For example, it is possible to employ this CO-catheter to deliver CO to malignant sites in adjuvant chemotherapy of colon cancer. Because CO is known to enhance chemosensitivity, one expects to use lower doses of conventional chemotherapeutics and avoid their toxic side effects. The relatively recent Endoscopic Fiber Optic Shape Tracker (EFOST) technology has emerged as a minimally invasive means for application toward endovascular space [74]. In fact, the newly developed fiber-optic illumination sources can deliver sufficient light through very thin optical fiber to activate CO release from photoactive materials such as photoCORP-**1** and deliver required doses of CO to a colonic target.

Appendix A. Supplementary data

Crystal data and structure refinement parameters for **1** (Table S1), photograph of the CO delivery setup with the CO-catheter (Fig. S1), schematic representation and the actual photograph of the CO delivery setup using photoCORP-**1** blocks under ambient light (Fig. S2), FACS analysis of CO-induced apoptosis in HT-29 cells using photoCORP-**1** blocks under ambient light (Fig. S3) and bar plot representation of the FACS results showing progression of apoptosis in HT-29 cells upon exposure to CO using blocks of photoCORP-**1** and ambient light (Fig. S4). Supplementary data associated with this article can be found in the online version, at: http://dx.doi.org/10.1016/j.jconrel.2017.08.039

References

[1] Carbon Monoxide Poisoning, National Center for Environmental Health, Centers for Disease Control and Prevention (CCDC), https://www.cdc.gov/co/, (2015) (accessed 03.08.17).

[2] O.T. Sykes, E. Walker, The neurotoxicology of carbon monoxide – historical perspective and review, Cortex 74 (2016) 440–448.

[3] T. Yoshida, C.T. Migita, Mechanism of heme degradation by heme oxygenase, J. Inorg. Biochem. 82 (2000) 33–41.

[4] G. Kikuchi, T. Yoshida, M. Noguchi, Heme oxygenase and heme degradation, Biochem. Biophys. Res. Commun. 338 (2005) 558–567.

[5] J.D. Roderique, C.S. Josef, M.J. Feldman, B.D. Spiess, A modern literature review of carbon monoxide poisoning theories, therapies, and potential targets for therapy advancement, Toxicology 334 (2015) 45–58.

[6] R. Motterlini, L. Otterbein, The therapeutic potential of carbon monoxide, Nat. Rev. Drug Discov. 9 (2010) 728–743.

[7] L. Wu, R. Wang, Carbon monoxide: endogenous production, physiological functions, and pharmacological applications, Pharmacol. Rev. 57 (2005) 585–630.

[8] Z. Chen, R. Wang, J. Wu, F. Xia, Q. Sun, J. Xu, L. Liu, Low-dose carbon monoxide inhalation protects neuronal cells from apoptosis after optic nerve crush, Biochem. Biophys. Res. Comm. 269 (2016) 809–815.

[9] B. Wang, W. Cao, S. Biswal, S. Dore, Carbon monoxide-activated Nrf2 pathway leads to protection against permanent focal cerebral ischemia, Stroke 42 (2011) 2605–2610.

[10] C.S.F. Queiroga, S. Tomasi, M. Widerøe, P.M. Alves, A. Vercelli, H.L.A. Vieira, Preconditioning triggered by carbon monoxide (CO) provides neuronal protection following perinatal hypoxia-ischemia, PLoS One 7 (2012) e42632.

[11] J.F. Ndisang, H.E.N. Tabien, R. Wang, Carbon monoxide and hypertension, J. Hypertens. 22 (2004) 1057–1074.

[12] D.E. Stec, H.A. Drummond, T. Vera, Role of carbon monoxide in blood pressure regulation, Hypertension 51 (2008) 597–604.

[13] A. Kobayashi, K. Ishikawa, H. Matsumoto, S. Kimura, Y. Kamiyama, M. Maruyama, Synergetic antioxidant and vasodilatory action of carbon monoxide in angiotensin II-induced cardiac hypertrophy, Hypertension 50 (2007) 1040–1048.

[14] L.E. Otterbein, F.H. Bach, J. Alam, M. Soares, H.T. Lu, M. Wysk, R.J. Davis, R.A. Flavell, A.M.K. Choi, Carbon monoxide has anti-inflammatory effects involving the mitogen-activated protein kinase pathway, Nat. Med. 6 (2000) 422–428.

[15] Y. Naito, K. Uchiyama, T. Takagi, T. Yoshikawa, Therapeutic potential of carbon monoxide (CO) for intestinal inflammation, Curr. Med. Chem. 19 (2012) 70–76.

[16] S.W. Ryter, A.M.K. Choi, Targeting heme oxygenase-1 and carbon monoxide for therapeutic modulation of inflammation, Transl. Res. 167 (2016) 7–34.

[17] L.E. Otterbein, Carbon monoxide: innovative anti-inflammatory properties of an age-old gas molecule, Antioxid. Redox Signal. 4 (2002) 309–319.

[18] C.A. Pintadosi, Carbon monoxide, reactive oxygen signaling and oxidative stress, Free Radic. Biol. Med. 45 (2008) 562–569.

[19] M.A. Rhodes, M.S. Carraway, C.A. Pintadosi, C.M. Reynolds, A.D. Cherry, T.E. Wester, M.J. Natoli, E.W. Massey, R.E. Moon, H.B. Suliman, Carbon monoxide, skeletal muscle oxidative stress, and mitochondrial biogenesis in humans, Am. J. Physiol. Heart Circ. Physiol. 297 (2009) H392–H399.

[20] L. Conde de la Rosa, T.E. Vrenken, R.A. Hannivoort, M. Buist-Homan, R. Havinga, D.J. Slebos, H.F. Kauffman, K.N. Faber, P.L.M. Jansen, H. Moshage, Carbon monoxide blocks oxidative stress-induced hepatocyte apoptosis via inhibition of the p54 JNK isoform, Free Radic. Biol. Med. 44 (2008) 1323–1333.

[21] C.A. Pintadosi, M.S. Carraway, H.B. Suliman, Carbon monoxide, oxidative stress, and mitochondrial permeability pore transition, Free Radic. Biol. Med. 40 (2006) 1332–1339.

[22] B. Wegiel, B.Y. Chin, L.E. Otterbein, Carbon monoxide, cellular proliferation, Cell Cycle 7 (2008) 1379–1384.

[23] S.S. Almeida, C.S.F. Queiroga, M.F. Sousa, P.M. Alves, H.L.A. Vieira, Carbon monoxide modulates apoptosis by reinforcing oxidative metabolism in astrocytes: role of BCL-2, J. Biol. Chem. 30 (2012) 10761–10770.

[24] S. Brouard, L.E. Otterbein, J. Anrather, E. Tobiasch, F.H. Bach, A.M.K. Choi, M.P. Soares, Carbon monoxide generated by heme oxygenase 1 suppresses endothelial cell apoptosis, J. Exp. Med. 192 (2000) 1015–1026.

[25] I. Chakraborty, S.J. Carrington, G. Roseman, P.K. Mascharak, Synthesis, structures, and CO release capacity of a family of water soluble photoCORMs: assessment of the biocompatibility and their phototoxicity toward human breast cancer cells, Inorg. Chem. 56 (2017) 1534–1545.

[26] S.J. Carrington, I. Chakraborty, J.M.L. Bernard, P.K. Mascharak, A theranostic two-tone luminescent photoCORM derived from Re(I) and (2-pyridyl)-benzothiazole: trackable CO delivery to malignant cells, Inorg. Chem. 55 (2016) 7752–7858.

[27] S.J. Carrington, I. Chakraborty, P.K. Mascharak, Rapid CO release from a Mn(I) carbonyl complex derived from azopyridine upon exposure to visible light and its phototoxicity toward malignant cells, Chem. Commun. 49 (2013) 11254–11256.

[28] B. Wegiel, D. Gallo, E. Csizmadia, C. Harris, J. Belcher, G.M. Vercellotti, N. Penacho, P. Seth, V. Sukatme, A. Ahmed, P.P. Pandolfi, L. Helczynski, A. Bjartell, J.L. Persson, L.E. Otterbein, Carbon monoxide expedites metabolic exhaustion to inhibit tumor growth, Cancer Res. 73 (2013) 7009–7021.

[29] L.E. Otterbein, R. Foresti, R. Motterlini, Heme Oxygenase-1 and carbon monoxide in the heart: the balancing act between danger signaling and pro-survival, Circ. Res. 118 (2016) 1940–1959.

[30] T. Morita, M.A. Perrella, M.E. Lee, S. Kourembanas, Smooth muscle cell-derived carbon monoxide is a regulator of vascular cGMP, Proc. Natl. Acad. Sci. U. S. A. 92 (1995) 1475–1479.

[31] J.K. Sarady, B.S. Zuckerbraun, M. Bilban, O. Wagner, A. Usheva, F. Liu, E. Ifedigbo, R. Zamora, A.M.K. Choi, L.E. Otterbein, Carbon monoxide protection against endotoxic shock involves reciprocal effects on iNOS in the lung and liver, FASEB J. 18 (2004) 854–856.

[32] B.S. Zuckerbraun, T.R. Billiar, S.L. Otterbein, P.K. Kim, F. Liu, A.M.K. Choi, L.E. Otterbein, Carbon monoxide protects against liver failure through nitric oxide-induced heme oxygenase 1, J. Exp. Med. 198 (2003) 1707–1716.

[33] B.Y. Chin, G. Jiang, B. Wegiel, H.J. Wang, T. MacDonald, X.C. Zhang, D. Gallo, E. Csizmadia, F.H. Bach, P.J. Lee, L.E. Otterbein, Hypoxia-inducible factor 1α stabilization by carbon monoxide results in cytoprotective preconditioning, Proc. Natl. Acad. Sci. U. S. A. 104 (2007) 5109–5114.

[34] C. Peers, D.S. Steele, Carbon monoxide: a vital signaling molecule and potent toxin in the myocardium, J. Mol. Cell. Cardiol. 52 (2012) 359–365.

[35] C.A. Pintadosi, M.S. Carraway, A. Babiker, H.B. Suliman, Heme oxygenase-1 regulates cardiac mitochondrial biogenesis via Nrf2-mediated transcriptional control of nuclear respiratory factor-1, Circ. Res. 103 (2008) 1232–1240.

[36] H.P. Kim, X. Wang, J. Zhang, G.Y. Suh, I.J. Benjamin, S.W. Ryter, A.M.K. Choi, Heat shock protein-70 mediates the cytoprotective effect of carbon monoxide: involvement of p38B MAPK and heat shock factor-1, J. Immunol. 165 (2005) 2622–2629.

[37] A. Haschemi, O. Wagner, R. Marculescu, B. Wegiel, S.C. Robinson, N. Gagliani, D. Gallo, J.F. Chen, F.H. Bach, L.E. Otterbein, Cross regulation of carbon monoxide and the adenosine A2a receptor in macrophages, J. Immunol. 178 (2007) 5921–5929.

[38] H.B. Suliman, M.S. Carraway, L.G. Tatro, C.A. Pintadosi, A new activating role for CO in cardiac mitochondrial biogenesis, J. Cell Sci. 120 (2007) 299–308.

[39] A. Nakao, C.S. Huang, D.B. Stolz, Y. Wang, J.M. Franks, N. Tochigi, T.R. Billiar, Y. Toyoda, E. Tzeng, K. McCurry, Ex vivo carbon monoxide delivery inhibits intima hyperplasia in arterialized vein grafts, Cardiovasc. Res. 89 (2011) 457–463.

[40] G.Y. Liou, P. Storz, Reactive oxygen species in cancer, Free Radic. Res. 44 (2010) 479–496.

[41] X. Li, P. Fang, J. Mai, E.T. Choi, H. Wang, X.F. Yang, Targeting mitochondrial reactive oxygen species as novel therapy for inflammatory diseases and cancers, J. Hematol. Oncol. 6 (2013) 19.

[42] C. Gorrini, I.S. Harris, T.W. Mak, Modulation of oxidative stress as an anticancer strategy, Nat. Rev. Drug Discov. 12 (2013) 931–947.

[43] A. Nakao, K. Kimizuka, D.B. Stolz, J.S. Neto, T. Kaizu, A.M.K. Choi, T. Uchiyama, B.S. Zuckerbraun, M.A. Nalesnik, L.E. Otterbein, N. Murase, Carbon monoxide inhalation protects rat intestinal grafts from ischemia/reperfusion injury, Am. J. Pathol. 163 (2003) 1587–1594.

[44] R. Foresti, M.G. Bani-Hani, R. Motterlini, Use of carbon monoxide as therapeutic agent: promises and challenges, Intensive Care Med. 34 (2008) 649–658.

[45] R. Motterlini, J.E. Clark, R. Foresti, P. Sarathchandra, B.E. Mann, C.J. Green, Carbon monoxide-releasing molecules characterization of biochemical and vascular activities, Circ. Res. 90 (2002) e17–e24.

[46] U. Schatzschneider, Novel lead structures and activation mechanisms for CO-releasing molecules (CORMs), Br. J. Pharmacol. 172 (2015) 1638–1650.

[47] I. Chakraborty, S.J. Carrington, P.K. Mascharak, Design strategies to improve the sensitivity of photoactive metal carbonyl complexes (photoCORMs) to visible light and their potential as CO-donors to biological targets, Acc. Chem. Res. 47 (2014) 2603–2611.

[48] S. Garcia-Gallego, G.J.L. Bernardes, Carbon monoxide-releasing molecules for the delivery of therapeutic CO in vivo, Angew. Chem. Int. Ed. 53 (2014) 9712–9721.

[49] S.H. Heinemann, T. Hoshi, M. Westerhausen, A. Schiller, Carbon monoxide – physiology, detection and controlled release, Chem. Commun. 50 (2014) 3644–3660.

[50] C.C. Romao, W.A. Blatter, J.D. Seixas, G.J. Bernardes, Developing drug molecules for therapy with carbon monoxide, Chem. Soc. Rev. 41 (2012) 3571–3583.

[51] R.D. Rimmer, A.E. Pierri, P.C. Ford, Photochemically activated carbon monoxide release for biological targets. Toward developing air-stable photoCORMs labilized by visible light, Coord. Chem. Rev. 256 (2012) 1509–1519.

[52] U. Schatzschneider, PhotoCORMs: light-triggered release of carbon monoxide from the coordination sphere of transition metal complexes for biological applications, Inorg. Chim. Acta 374 (2011) 19–23.

[53] P. Govender, S. Pai, U. Schatzschneider, G.S. Smith, Next generation photoCORMs: polynuclear tricarbonylmanganese (I)-functionalized polypyridyl metallodendrimers, Inorg. Chem. 52 (2013) 5470–5478.

[54] D. Nguyen, N.N.M. Adan, S. Oliver, C. Boyer, The interaction of CORM-2 with block copolymers containing poly(4-vinylpyridine): macromolecular scaffolds for carbon monoxide delivery in biological systems, Macromol. Rapid Commun. 37 (2016) 739–744.

[55] N.E. Brückmann, M. Wahl, G.J. Reiß, M. Kohns, W. Wätjen, P.C. Kunz, Polymer conjugates of photoinducible CO-releasing molecules, Eur. J. Inorg. Chem. (29) (2011) 4571–4577.

[56] C. Bohlender, S. Gläser, M. Klein, J. Weisser, S. Thein, U. Neugebauer, J. Popp, R. Wyrwa, A. Schiller, Light-triggered CO release from nanoporous non-wovens, J. Matter. Chem. B 2 (2) (2014) 1454–1463.

[57] H. Pfeiffer, A. Rojas, J. Niesel, U. Schatzschneider, Sonogashira and click: reactions for the N-terminal and side-chain functionalization of peptides with [Mn (CO)$_3$(TPM)]$^+$-based CO releasing molecules (tpm = tris(pyrazolyl)methane), Dalton Trans. (2009) 4292–4298.

[58] K. Fujita, Y. Tanaka, S. Abe, T. Ueno, A photoactive carbon-monoxide-releasing protein cage for dose regulated delivery in living cells, Angew. Chem. Int. Ed. 55 (2016) 1056–1060.

[59] U. Hasegawa, A.J. van der Vlies, E. Simeoni, C. Wandrey, J.A. Hubbell, Carbon monoxide-releasing micelles for immunotherapy, J. Am. Chem. Soc. 132 (2010) 18273–18280.

[60] A.E. Pierri, P.J. Huang, J.V. Garcia, J.G. Stanfill, M. Chui, G. Wu, N. Zheng, P.C. Ford, A photoCORM nanocarrier for CO release using NIR light, Chem. Comm. 51 (2015) 2072–2075.

[61] I. Chakraborty, S.J. Carrington, J. Hauser, S.R.J. Oliver, P.K. Mascharak, Rapid eradication of human breast cancer cells through trackable light triggered CO delivery by mesoporous silica nanoparticles packed with a designed photoCORM, Chem. Matter. 27 (2015) 8387–8397.

[62] S. Glasser, R. Mede, H. Görls, S. Seupel, C. Bohlender, R. Wyrwa, S. Schurmer, S. Dochow, G.U. Reddy, J. Popp, M. Westernhausen, A. Schiller, Remote-controlled delivery of CO *via* photoactive CO-releasing materials on a fiber optical device, Dalton Trans. 45 (2016) 13222–13233.

[63] G.M. Halpenny, K.R. Gandhi, P.K. Mascharak, Eradication of pathogenic bacteria by remote delivery of NO via light triggering of nitrosyl-containing materials, ACS Med. Chem. Lett. 1 (2010) 180–183.

[64] G.M. Halpenny, B. Heilman, P.K. Mascharak, Nitric oxide(NO)-induced death of gram-negative bacteria from a light-controlled NO-releasing platform, Chem. Biodivers. 9 (2012) 1829–1839.

[65] B. Heilman, G.M. Halpenny, P.K. Mascharak, Synthesis, characterization, and light-controlled antibiotic application of a composite material derived from polyurethane and silica xerogel with embedded photoactive manganese nitrosyl, J. Biomed. Mater. Res. B 99B (2011) 328–337.

[66] G.M. Halpenny, R.C. Steinhardt, K.A. Okialda, P.K. Mascharak, Characterization of pHEMA-based hydrogels that exhibit light-induced bactericidal effect via release of NO, J. Mater. Sci. Mater. Med. 20 (2009) 2353–2360.

[67] G.M. Halpenny, M.M. Olmstead, P.K. Mascharak, Incorporation of a designed ruthenium nitrosyl in polyHEMA hydrogel and light-activated delivery of NO to myoglobin, Inorg. Chem. 46 (2007) 6601–6606.

[68] L. Flynn, P.D. Dalton, M.S. Shoichet, Fiber templating of poly(2-hydroxyethyl methacrylate) for neural tissue engineering, Biomaterials 24 (2003) 4265–4272.

[69] Y.M. Sun, J.J. Huang, F.C. Lin, J.Y. Lai, Composite poly(2-hydroxyethyl methacrylate) membranes as rate controlling barriers for transdermal application, Biomaterials 18 (1997) 527–533.

[70] N.A. Peppas, Hydrogels in Medicine and Pharmacy, Ed, Vol I-III, CRC Press, Boca Raton, 1987.

[71] R.H. Blessing, An empirical correction for absorption anisotropy, Acta Crystallogr. Sect. A 51 (1995) 33–38.

[72] G.M. Sheldrick, Crystal structure refinement with SHELXL, Acta Crystallogr. C, Struct. Chem. 71 (2015) 3–8.

[73] O.V. Dolomanov, L.J. Bourhis, R.J. Gildea, J.A.K. Howard, H. Puschmann, OLEX2: a complete structure solution, refinement and analysis program, J. Appl. Crystallogr. 42 (2009) 339–341.

[74] C.G.L. Cao, P.Y. Wong, L. Lilge, R.M. Gavalis, H. Xing, N. Zamarripa, Advanced shape tracking to improve flexible endoscopic diagnostics, Proc. of SPIE 6935 (2008), http://dx.doi.org/10.1117/12.776276.

152

Chapter 2.II: Synthesis, Characterization, and Structures of Photoactive Rhenium Carbonyl Complexes Derived from 2-(quinoline-2-yl)-1,3-benzothiazole, 2-(quinoline-2-yl)-1,3-benzothiazole and 1,10-phenanthroline Bearing a 4-vinylpyridine Polymeric Tether for Their Incorporation into Polymeric Hydrogels for Remote CO Delivery.

2.I.1 Background.

Carbon monoxide (CO), has recently been recognized as a gaseous signaling molecule 'gasotransmitter' responsible for a variety of physiological responses in mammalian physiology and pathology.[1,2] CO is endogenously throughout the mammalian body through heme catabolism.[2,3] Unlike other gasotransmitters, it does not undergo chemical alterations within cells and can essentially diffuse into all cellular compartments. CO primarily binds low-valent 'soft' metal centers of heme proteins,[1,2] blocking,[4,5] enhancing, or altering their functions.[6,7] This interaction results in signaling cascades responsible for the modulation of several processes, such as inflammation,[6,8] oxidative stress,[9-12] and hypertension.[13,14] Interestingly, moderate doses of CO (~200 ppm) have been shown to sensitize cancer cells to conventional chemotherapeutics,[15-17] as well as induce apoptosis in malignant cells.[18-21] The main challenge regarding the use of CO as a direct or adjuvant chemotherapeutic is to deliver this gaseous molecule in a site-specific manner. Systemic administration of this gasotransmitter requires continuous exposure to relatively high levels of CO, which lacks specificity and may cause negative effects. CO-releasing molecules (CORMs) offer an alternative way to

deliver controlled amounts of CO to a specific site of interest.[22-30] The difficulty in using first-generation CORMs in clinical settings arises from their short half-life, low solubility, and the requirement of organic solvents to trigger CO release.[13] Photoactivated carbon monoxide releasing molecules (photoCORMs) present a relatively facile way to trigger CO release with temporal and spatial control.[25,26,31-46] Enhancing the concentration of a therapeutic to the desired area is an effective way to increase its efficiency and to minimize the side effects due to systemic exposure. To achieve this, a logical design strategy is to couple the prodrug/drug to an appropriate drug-delivery vehicle. Photoactive metal carbonyl complexes (photoCORMs) are ideal exogenous candidates for more controllable and site-specific CO delivery compared to gaseous CO. Along this line, our group has been engaged for the past few years in developing group-7-based photoCORMs towards the efficient eradication of various malignant cells. Moreover, several such complexes can be tracked within cancerous cells by virtue of their luminescence. The inherent luminescent nature of some photoCORMs and the change in emission wavelength upon CO release also provide a convenient means to track the entry of the prodrug and, in some cases, both the entry and CO release from the prodrug. The development of trackable photoCORMs and also to graft such molecules covalently to conventional delivery vehicles. Fulfilling this goal requires suitable chemical functionalization within the photoCORM is necessary that can be subsequently utilized to couple the delivery vehicle. In such pursuits, we have synthesized three photoCORMs, bearing a vinylpyridine (4-vpy) group which can be potentially used to crosslink the metal complex into a polymeric drug delivery vehicle.

Three fluorogenic ligands, namely 2-(pyridin- 2-yl)-1,3-benzothiazole (pbt), 2-(quinolin-2-yl)-1,3-benzothiazole (qbt), and 1,10-phenanthroline (phen) have also been employed as bidentate ligands to derive luminescent rhenium photoCORMs, namely [Re(CO)$_3$(pbt)(4-vpy)](CF$_3$SO$_3$) **1**, [Re(CO)$_3$(qbt)(4-vpy)](CF$_3$SO$_3$) **2**, and [Re(CO)$_3$(phen)(4-vpy)](CF$_3$SO$_3$) **3** (Figure 2.II.1), that can be tracked within the cellular matrices. The described complexes have been characterized with conventional analytical techniques and single-crystal X-ray crystallography. In all three cases, the Re(I) metal center resides in a distorted octahedral coordination environment. These complexes exhibit CO release upon exposure to low-power UV light and the apparent CO release rates of the complexes have been measured to assess their comparative CO-donating capacity. These rhenium-based photoCORMs reveal variable CO release rates upon increasing the degree of conjugation within the bidentate ligand frame. The three complexes are highly luminescent and this in turn provides a convenient way to track
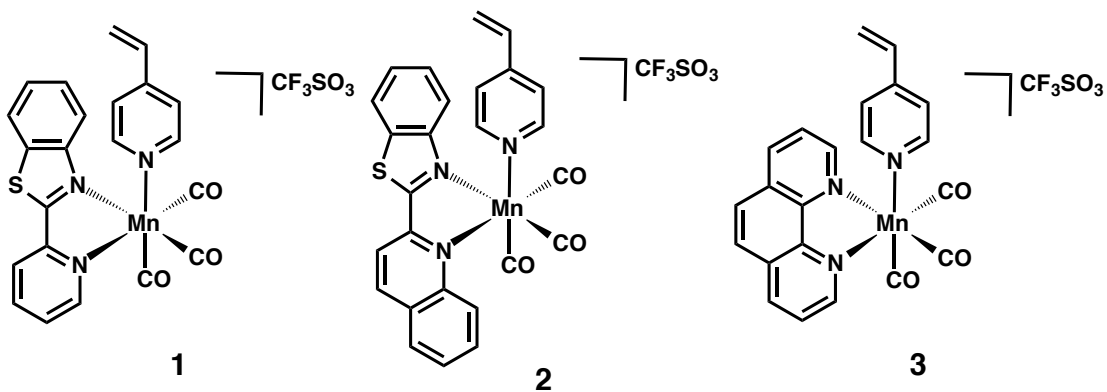
Figure 2.II.1. Schematic representation of complexes [Re(CO)$_3$(pbt)(4-vpy)](CF$_3$SO$_3$) **1**, [Re(CO)$_3$(qbt)(4-vpy)](CF$_3$SO$_3$) **2**, and [Re(CO)$_3$(phen)(4-vpy)](CF$_3$SO$_3$) **3**.

the entry of the prodrug molecules within biological targets. Moreover, the degree in conjugation produces substantial shifts in their emission profile. The photophysical behavior of all three complexes will be discussed in this chapter.

2.II.2 Results and Discussion.

2.II.2.1 Synthesis and characterization of [Re(CO)$_3$(pbt)(4-vpy)](CF$_3$SO$_3$) **1**, *[Re(CO)$_3$(qbt)(4-vpy)](CF$_3$SO$_3$)* **2**, *[Re(CO)$_3$(phen)(4-vpy)](CF$_3$SO$_3$)* **3**.

The synthesis of the complex was carried out under dark conditions to avoid premature decomposition of the photoCORMs. Initial reaction between the Re(CO)$_5$Cl and the bidentate ligands (pbt, qbt, or phen) refluxing conditions in chloroform:methanol (1:3) to produce the complex. Upon slow cooling of the reaction mixtures, the resulting complexes of the form [Re(CO)$_3$(L)Br] (where L is pbt, qbt, or phen) precipitated in a microcrystalline fashion and collected through filtration in a high yield. Reaction between the complex [Re(CO)$_3$(L)Br] and excess Ag(CF$_3$SO$_3$) was carried out in DCM since the triflate salt of silver is insoluble in that solvent while the resulting product of the form [Re(CO)$_3$(L)(CF$_3$SO$_3$)] is highly soluble. The reactions were usually completed within 6 – 12 h at room temperature. Prolonged reaction times results in the dark coloration of the solution possibly due to the decomposed/oxidized silver. However, this dark coloration doesn't affect the isolation or purity of the resulting complex since the decomposition products, AgCl, and excess Ag(CF$_3$SO$_3$) are filtered off using celite. Finally, the reaction between [Re(CO)$_3$(L)(CF$_3$SO$_3$)] and excess 4-vinylpyridine is carried out under reflux in

chloroform for 16 h resulting in the formation of a brownish black precipitate which is possibly some decomposition product. The reaction mixture is filtered off and the complexes are isolated from the mother liquor through crystallization by layering hexanes on top of a dichloromethane solution of the complex.

The IR spectra of the reported complexes display strong CO stretches indicative of a facial disposition of the three carbonyl groups (Figures 2.II.2 to 2.II.4). All the complexes exhibit well-resolved ^{1}H-NMR spectra, with no line broadening. This is consistent with the complexes being diamagnetic, as would be expected for low-spin d^6 Re(I) ions in an octahedral ligand field. Complexes **1**, **2**, and **3** display strong absorption bands centered around 340, 386, and 277 nm, respectively. These complexes are indefinitely stable in dichloromethane solutions under dark conditions.
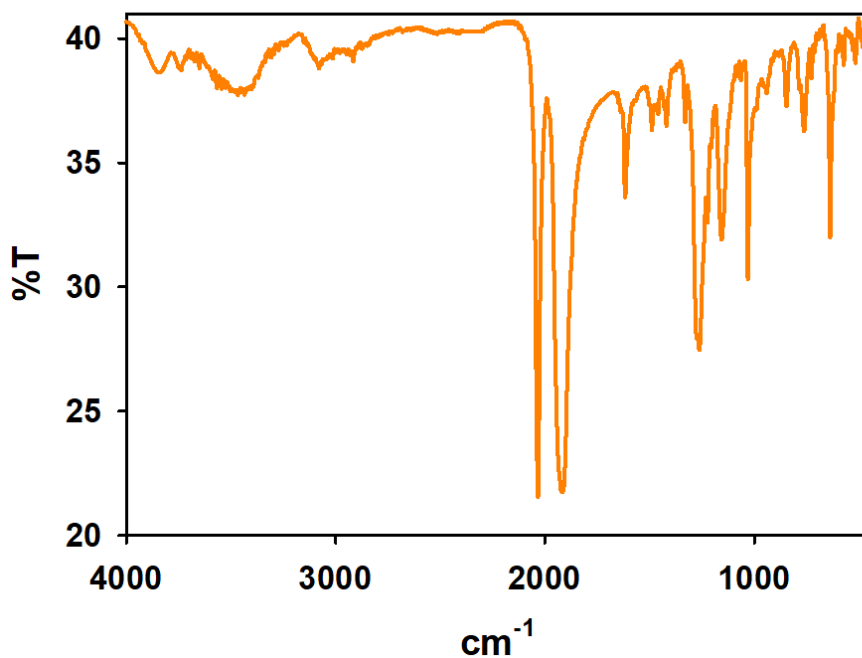
Figure 2.II.2. Infrared spectrum of complex **1** in KBr matrix.
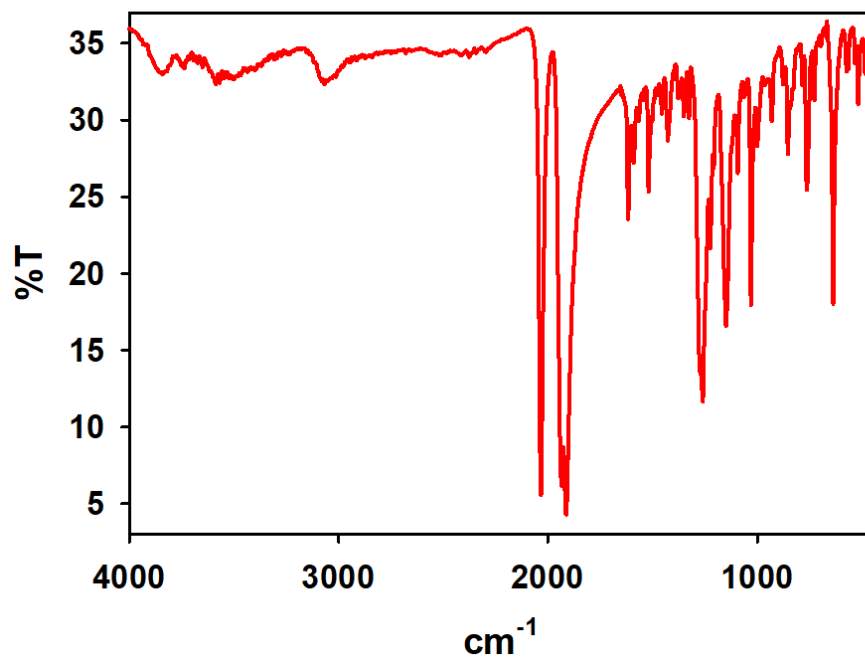
Figure 2.II.3. Infrared spectrum of complex **2** in KBr matrix.
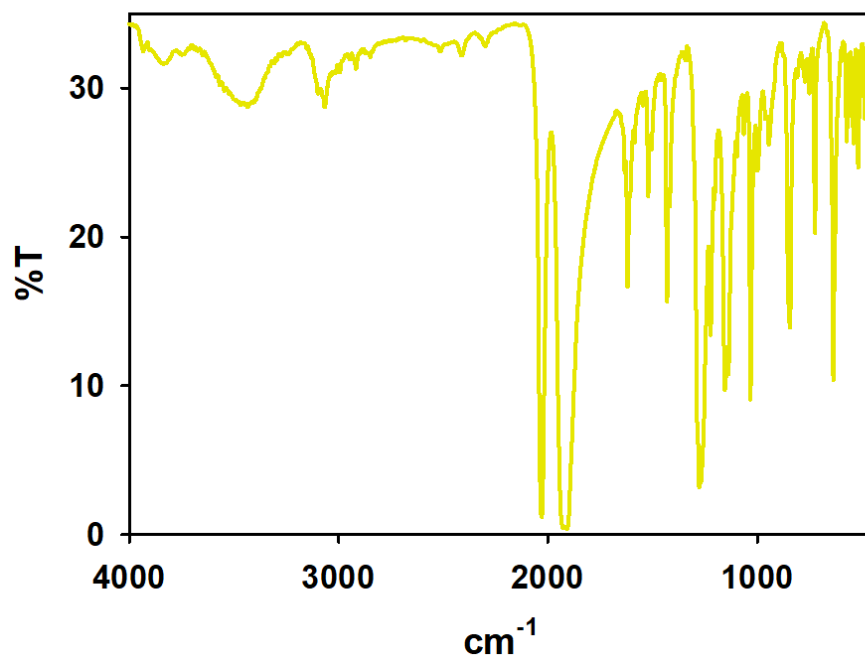
Figure 2.II.4. Infrared spectrum of complex **3** in KBr matrix.

159

2.II.2.2 Photochemical Characteristics and CO Release Rate of 1, 2, and 3.

Exposure to UV-A irradiation (λ = 365 nm), these complexes exhibit no changes in their electronic absorption spectra. However, upon exposure to UV-B irradiation (λ = 302 nm), the absorption bands of the complexes showed systematic changes. In addition, the coloration of the solutions of all three complexes are lost upon exposure to UV light. Systematic exposure of such solutions to small intervals of broadband visible light (10 mW cm^{-2}) results in sequential changes in the electronic absorption spectrum (Figure 2.II.5 to 2.II.7). These changes are associated with CO
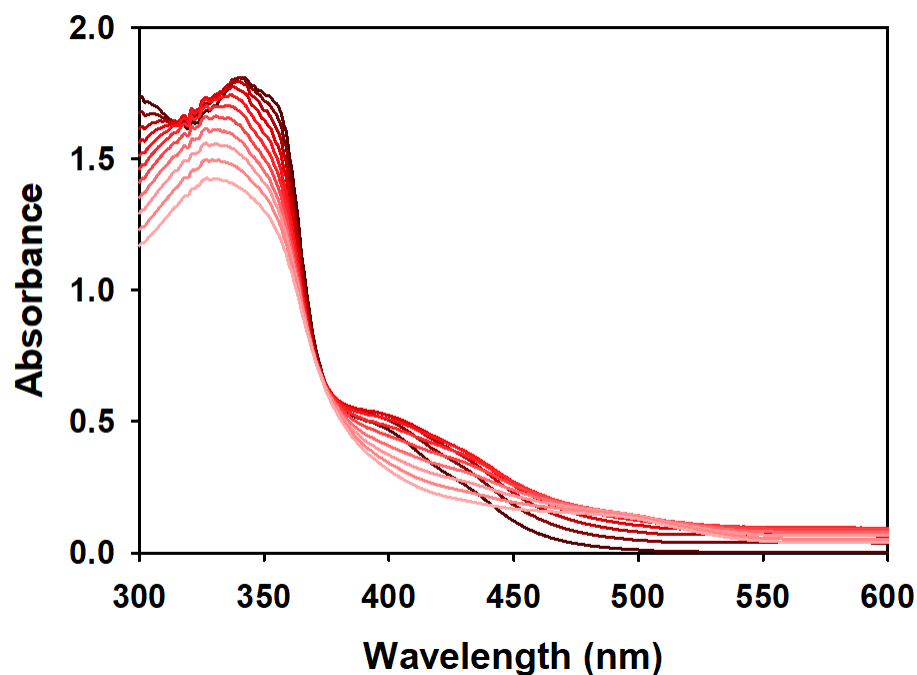
Figure 2.II.5. Systematic changes in the electronic absorption spectrum **1** upon exposure to small intervals of UV light (15 mW cm^{-2}, 1 min intervals, 298 K) due to CO photorelease.
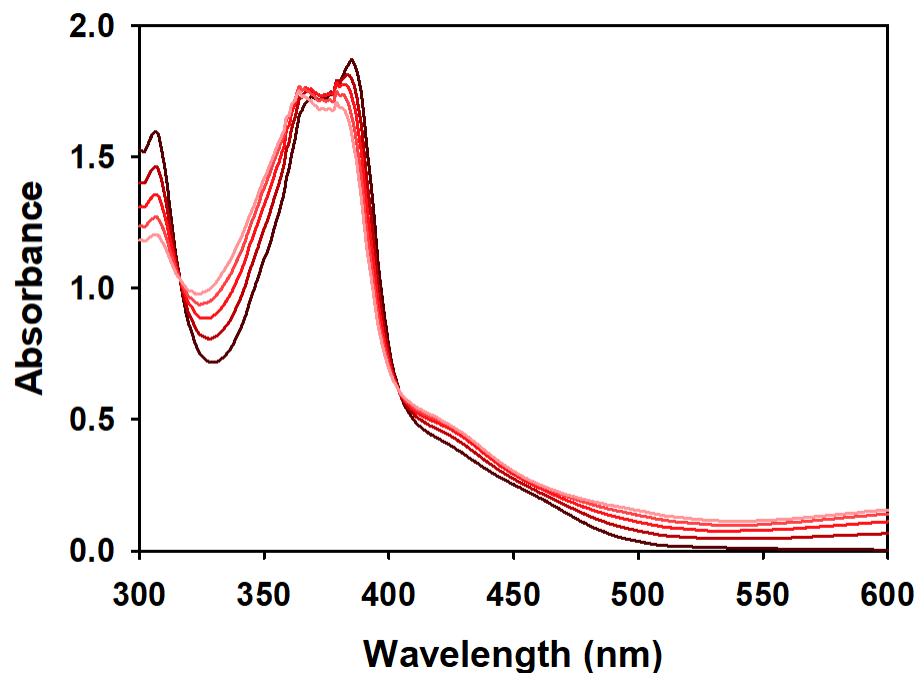
Figure 2.II.6. Systematic changes in the electronic absorption spectrum **2** upon exposure to small intervals of UV light (15 mW cm^{-2}, 1 min intervals, 298 K) due to CO photorelease.

photorelease, as was also evidenced by a standard myoglobin assay.[25] The Myoglobin assay (*vide infra*) reveals that the spectral changes are due to photorelease of CO from the complexes upon illumination (Representative example Figure 2.II.8). In order to determine the apparent CO-release rate (k_{CO}), a solution of each complex in dichloromethane was exposed to UV-B (15 mW cm^{-2}) for 1 min intervals and the value of k_{CO} was determined from the ln(C) (C = concentration of complex) vs. time (t) plot. The k_{CO} values obtained for complexes **1**, **2**, and **3** were 0.050 min^{-1}, 0.130 min^{-1}, and 0.0709 min^{-1}, indicated that complex **2** was the most sensitive to low power UV light.
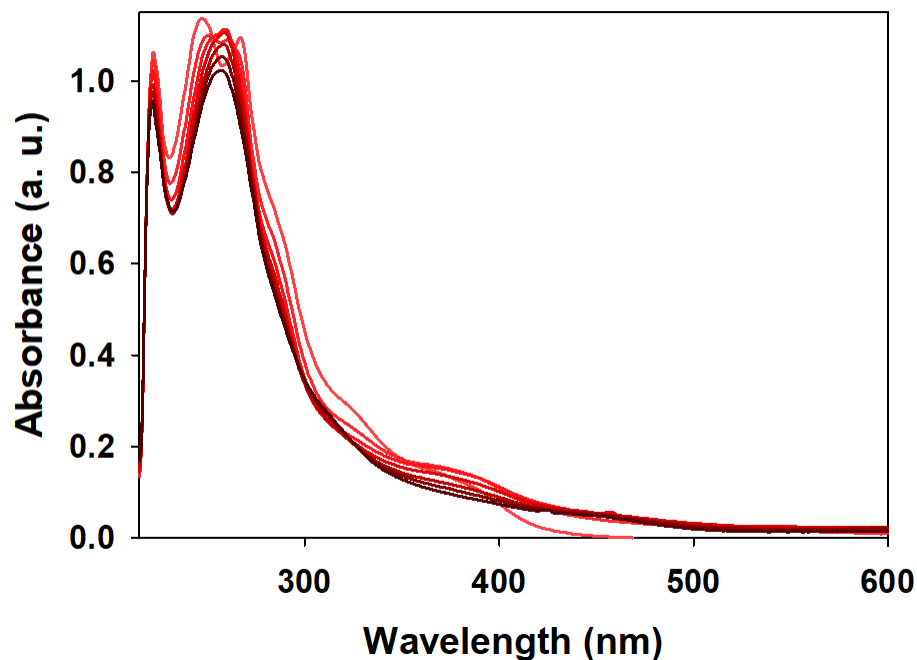
Figure 2.II.7. Systematic changes in the electronic absorption spectrum **3** upon exposure to small intervals of UV light (15 mW cm^{-2}, 1 min intervals, 298 K) due to CO photorelease.

The apparent rate of CO release (k_{CO}) have been determined spectrophotometrically by monitoring the changes in spectral traces upon UV-light irradiation at regular time intervals (2 min). The k_{CO} values, obtained from the plots of ln(C) versus time (t), are 0.050, 0.130, and 0.071 min^{-1} for complexes **1**, **2**, and **3**, respectively. Upon excitation of dichloromethane solutions of the complexes at 350 nm, **1**, **2**, and **3**, exhibit strong luminescence centered around 611, 652, and 542 nm, respectively (Figure 2.II.3). The change in luminescence upon CO release can be potentially utilized to track the delivery of CO to specific targets.
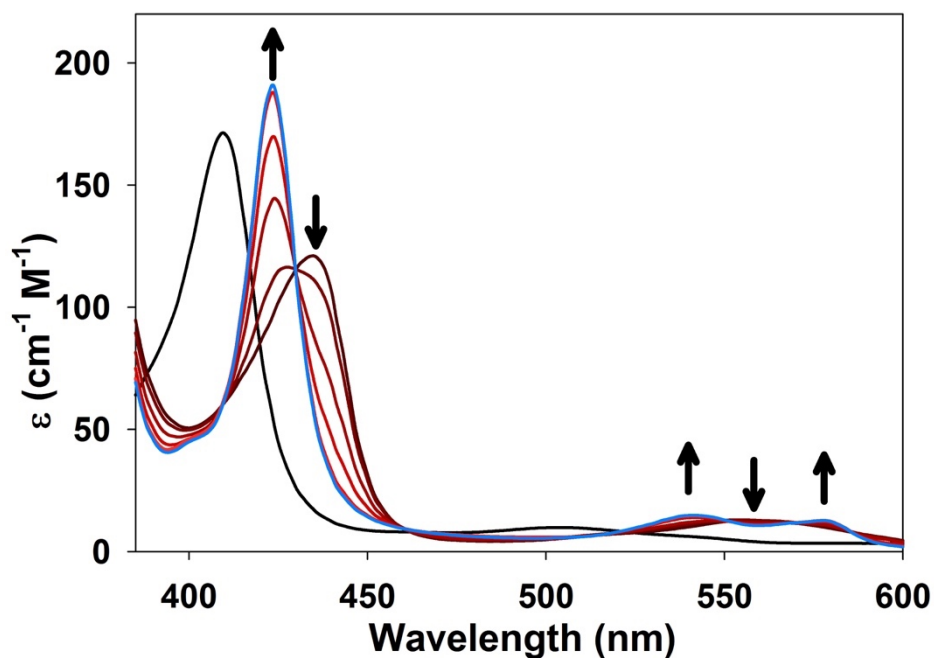
Figure 2.II.8. Myoglobin assay performed using complex **1**. The complex was triggered by UV light (15 mW cm^{-2}) for 5 min intervals and the changes in the spectrum were recorded. Shift of the Soret band from 435 nm to 424 nm indicates the formation of Mb$_{CO}$ by CO release. The black trace represents the absorbance of oxidized myoglobin.

Interestingly, complexes of the form [Re(CO)$_3$(L)Br] have very similar red luminescence with differences of ± 10 nm and therefore cannot be distinguished easily. However, upon coordination of the 4-vinylpyridine the luminescence difference between each complex is accentuated (differences in luminescence ± 50 nm). This allows for the clear qualitative discrimination between complexes (Figure 2.II.9).
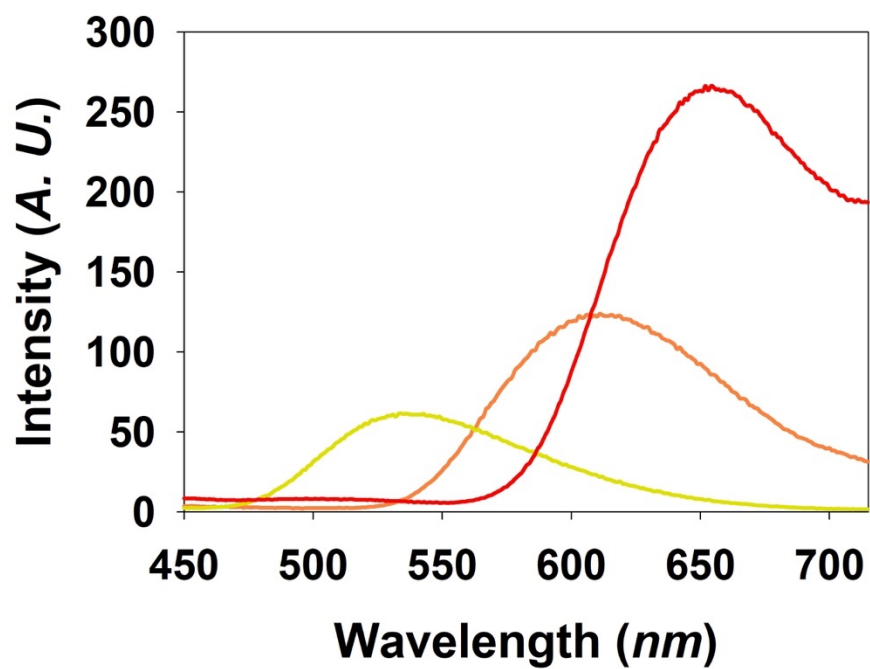
Figure 2.II.9. Luminescence spectra of complexes **1** (orange trace), **2** (red trace), and **3** (yellow trace) upon UV light (365 nm) excitation.
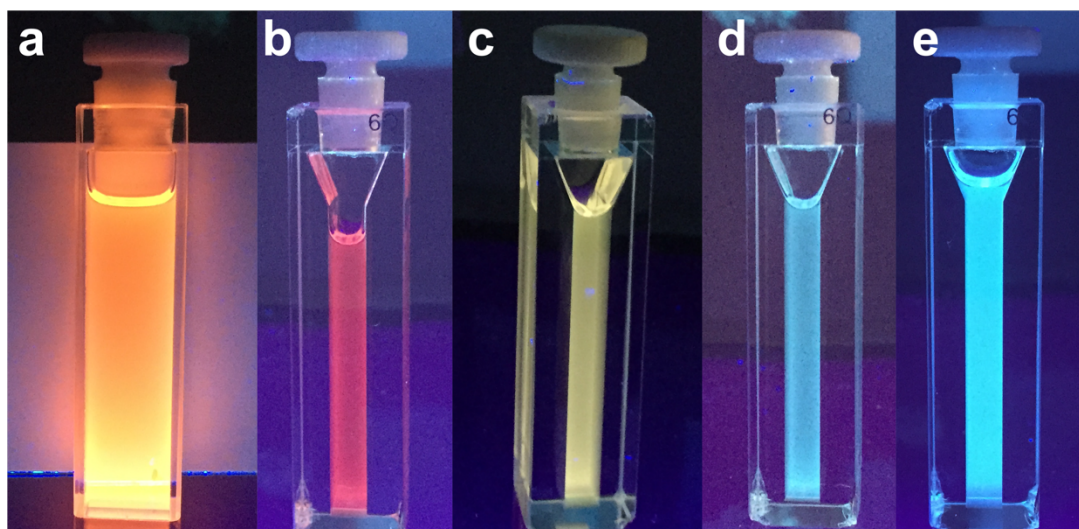
Figure 2.II.10. Luminescence of complexes **1** (a), **2** (b), **3** (c), photolysed sample of **1** (d), and photolysed sample of **2** (e).

Complex **1** appears orange, complex **2** is deep red, while complex **3** is light yellow (Figure 2.II.10a through 2.II.10c). The decomposition of each complex upon photolysis was then carefully monitored through luminescence by irradiating the complex for 1 min and monitoring its luminescence (Figures 2.II.11 through 2.II.13). Upon photolysis of complexes **1** or **2** result in the disappearance of the luminescence of the complex and the appearance of the of the fluorescent chelating ligand pbt or qbt respectively (Figure 2.II.10d - 2.II.10e and 2.II.11 - 2.II.12).
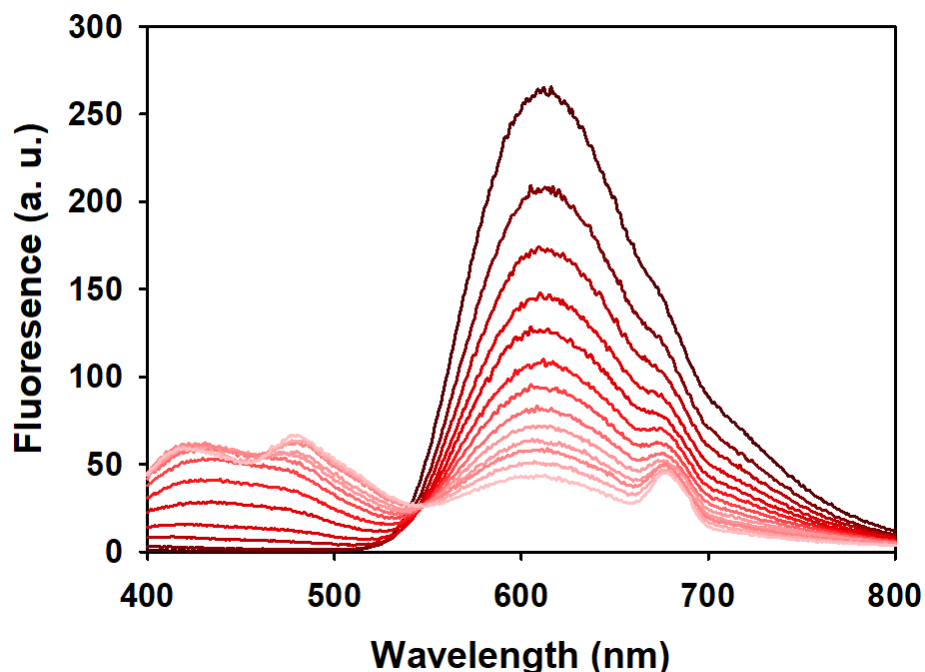
Figure 2.II.11. Luminescence spectra of complex **1** (darkest trace) decreasing upon exposure to UV-light (15 mW cm^{-2}) in 1 min intervals. As the complex decomposes the luminescence of the complex (centered at ~611 nm) decreases, while the luminescence of the photoproduct (centered at ~450 nm) increases.
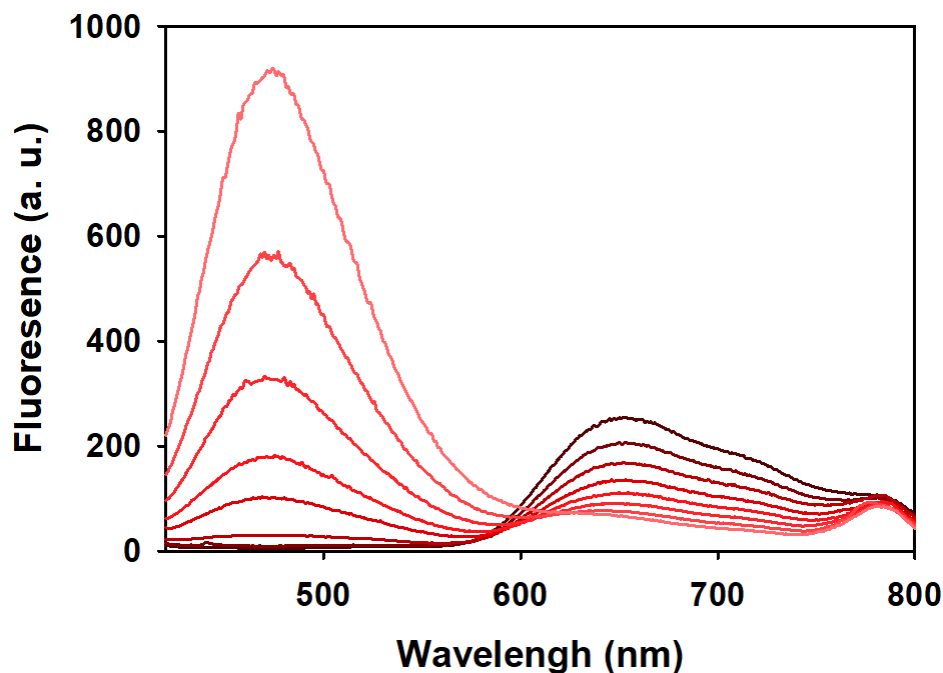
Figure 2.II.12. Luminescence spectra of complex **2** (darkest trace) decreasing upon exposure to UV-light (15 mW cm^{-2}) in 1 min intervals. As the complex decomposes the luminescence of the complex (centered at ~652 nm) decreases, while the luminescence of the photoproduct (centered at ~480 nm) increases.

*2.II.2.3 Incorporation of [Re(CO)$_3$(pbt)(4-vpy)](CF$_3$SO$_3$) **1**, [Re(CO)$_3$(qbt)(4-vpy)](CF$_3$SO$_3$) **2**, [Re(CO)$_3$(phen)(4-vpy)](CF$_3$SO$_3$) **3** into pHEMA/EGDMA Hydrogel.*

The preparation, polymerization, and curing of polymer samples was carried out in the dark to avoid decomposition of the CO-donating complex. The water-soluble initiator 2,2′-azobis[2-(2-imidazolin-2-yl)propane] dihydrochloride (VA-044) was

dissolved in milliQ water aided by sonication. This solution was mixed with 2-hydroxyethyl methacrylate (HEMA) (5.00 g, 41 mmol) and ethylene glycol
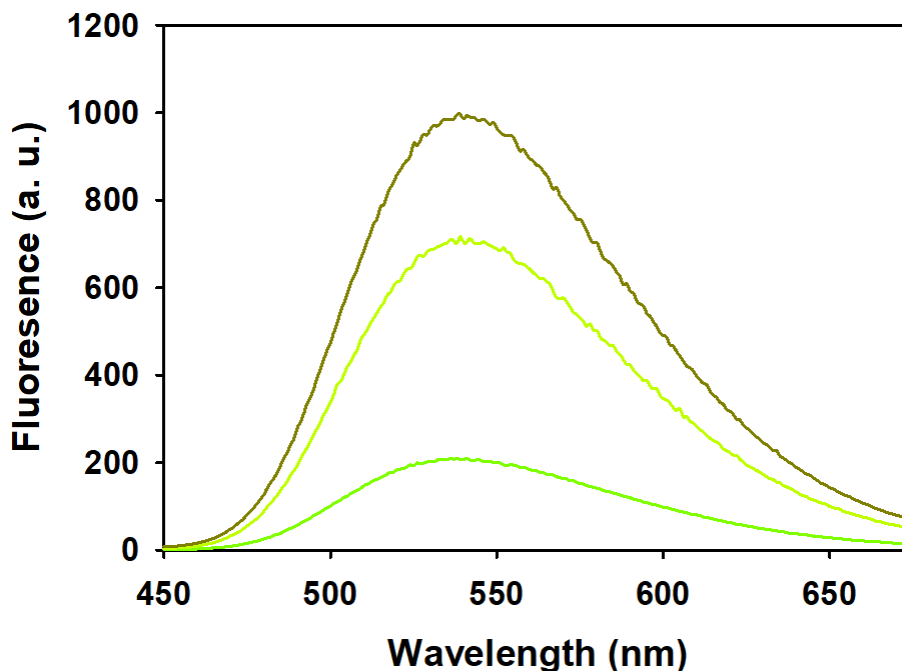
Figure 2.II.13. Luminescence spectra of complex **3** (dark yellow) decreasing upon exposure to UV-light (15 mW cm^{-2}) in 1 min intervals. As the complex decomposes the luminescence of the complex (centered at ~540 nm) decreases. No increase in luminescence corresponding to the photoproduct is observed.

dimethacrylate (EGDMA) (0.250 g, 1.3 mmol). Only complex **1** was incorporated into the polymeric matrix for the construction of a CO donating polymer. The pre-polymer mixture was combined with a dilute solution of **1** in acetone to afford their respective CO-releasing polymers which was 0.1 mM w.r.t **1** for UV–vis analysis. Blank polymer samples (without complex) were prepared by combining a third pre-polymer batch with

acetone. The mixtures were degassed for 20 min by bubbling dry nitrogen gas and placed into polystyrene cuvettes or various molds. Once the solutions were placed in their respective mold, they were heated for 30 min at 50 °C using a water bath. The heat was then turned off and the water-bath was allowed to cool slowly, and the polymers were then cured at room temperature for 48 h in the dark. The resulting polymers (Figure 2.II.14) were used for UV-vis CO-releasing studies (Figure 2.II.15),

Figure 2.II.14. (a) Images of the photoactivated CO-releasing polymer under visible light and (b) under UV light (365 nm). The polymer is composed of complex **1** covalently attached within polymeric matrix of pHEMA/EGDMA. The intense luminescence of **1** can be detected qualitatively indicating the amount of photoCORM remaining within the polymer.

indicating that the release of CO from the polymeric matrix was relatively slow. The consistency of the resulting polymers was soft and malleable and could easily be cut using a razorblade (Figure 2.II.14a). Upon drying however, the material becomes tough and difficult to cut. Complex **1** imbedded within the polymeric material luminesces brightly upon UV irradiation (Figure 2.II.14b).
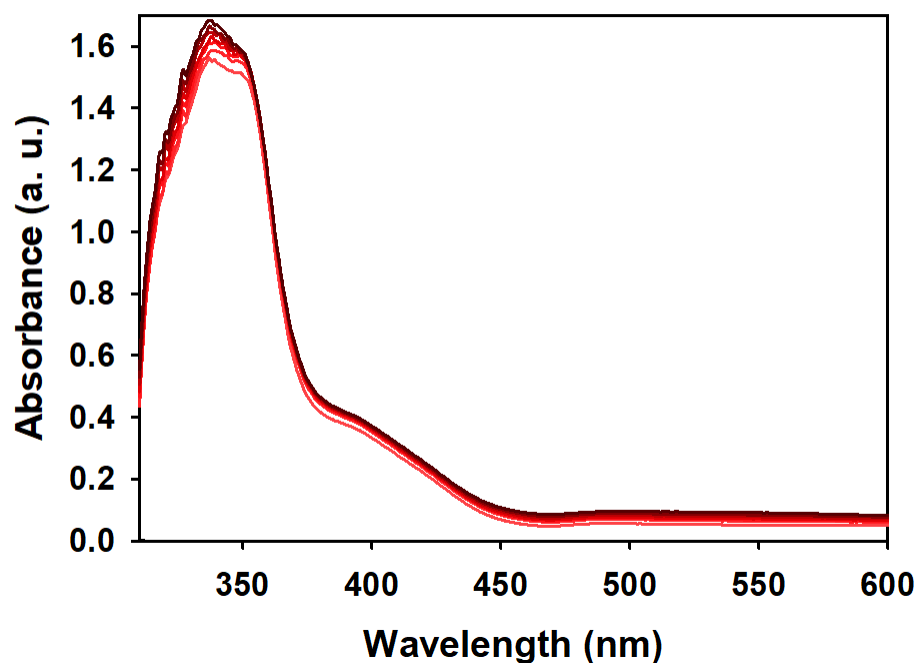
Figure 2.II.15. Systematic changes in the electronic absorption spectrum of complex **1** co-polymerized within pHEMA/EGDMA hydrogel upon exposure to small intervals of UV light (15 mW cm^{-2}, 1 min intervals, 298 K) due to CO photorelease.

2.II.2.4 X-Ray Structure Determination.

In all three title complexes, **1**–**3**, the coordination geometry around the Re(I) center is distorted octahedral (Tables 2.II.1 through 2.II.3). In all the structures, the

equatorial planes are composed of two *cis* CO ligands and two N atoms from the bidentate ligands (pbt, qbt or phen), while the axial positions are occupied by the third CO ligand and the N atom of the vinylpyridine group (Figures 2.II.16 – 2.II.18). In the

Table 2.II.1. Selected geometric parameters (Å,°) for **1**.

Re1—C2	1.900 (3)
Re1—C1	1.923 (3)
Re1—C3	1.924 (3)
Re1—N2	2.189 (2)
Re1—N1	2.193 (2)
Re1—N3	2.207 (2)
C2—Re1—C1	87.73 (14)
C2—Re1—C3	87.46 (14)
C1—Re1—C3	87.51 (14)
C2—Re1—N2	101.15 (11)
C1—Re1—N2	95.57 (12)
C3—Re1—N2	170.94 (11)
C2—Re1—N1	175.15 (11)
C1—Re1—N1	94.91 (12)
C3—Re1—N1	96.70 (11)
N2—Re1—N1	74.58 (9)
C2—Re1—N3	90.44 (12)
C1—Re1—N3	177.94 (11)
C3—Re1—N3	91.46 (12)

equatorial plane, comprising atoms Re1, C2, C3, N1, and N2, is almost planar, with a mean deviation of 0.018(3) Å; the corresponding planes in **2** deviates appreciably from planarity [Mean deviation = 0.080 (5) Å] and the planarity of the same plane in (3) lies between that of the other two compounds [mean deviation = 0.040 (3) Å]. In complex

Table 2.II.2. Selected geometric parameters (Å,°) for **2**.

Re1—C2	1.909 (5)
Re1—C1	1.910 (6)
Re1—C3	1.924 (6)
Re1—N2	2.176 (4)
Re1—N1	2.214 (4)
Re1—N3	2.222 (4)
C2—Re1—C1	87.9 (2)
C2—Re1—C3	85.7 (2)
C1—Re1—C3	91.2 (2)
C2—Re1—N2	100.42 (18)
C1—Re1—N2	97.63 (19)
C3—Re1—N2	169.40 (18)
C2—Re1—N1	91.92 (19)
C1—Re1—N1	179.21 (19)
C3—Re1—N1	89.5 (2)
N2—Re1—N1	81.63 (14)
C2—Re1—N3	174.73 (18)
C1—Re1—N3	94.45 (18)
C3—Re1—N3	98.97 (18)

1, the chelate ring composed of atoms Re1, N1, C8, C9, and N2 is highly planar, with

a mean deviation of 0.020 (5) Å. In contrast, in complex **2**, the chelate ring composed

of atoms Re1, N1, C12, C13, and N2 deviates appreciably from planarity [mean

deviation = 0.080 (5) Å]. In the case of complex **3**, the chelate ring composed of atoms

Table 2.II.3. Selected geometric parameters (Å,°) for **3**.

Re1—C2	1.917 (3)
Re1—C1	1.918 (3)
Re1—C3	1.923 (3)
Re1—N2	2.174 (2)
Re1—N1	2.185 (2)
Re1—N3	2.218 (2)
C2—Re1—C1	88.35 (14)
C2—Re1—C3	88.70 (13)
C1—Re1—C3	88.39 (14)
C2—Re1—N2	91.89 (11)
C1—Re1—N2	97.18 (12)
C3—Re1—N2	174.41 (11)
C2—Re1—N1	96.48 (11)
C1—Re1—N1	171.39 (11)
C3—Re1—N1	98.81 (11)
N2—Re1—N1	75.59 (8)
C2—Re1—N3	178.44 (11)
C1—Re1—N3	92.69 (12)
C3—Re1—N3	92.49 (11)
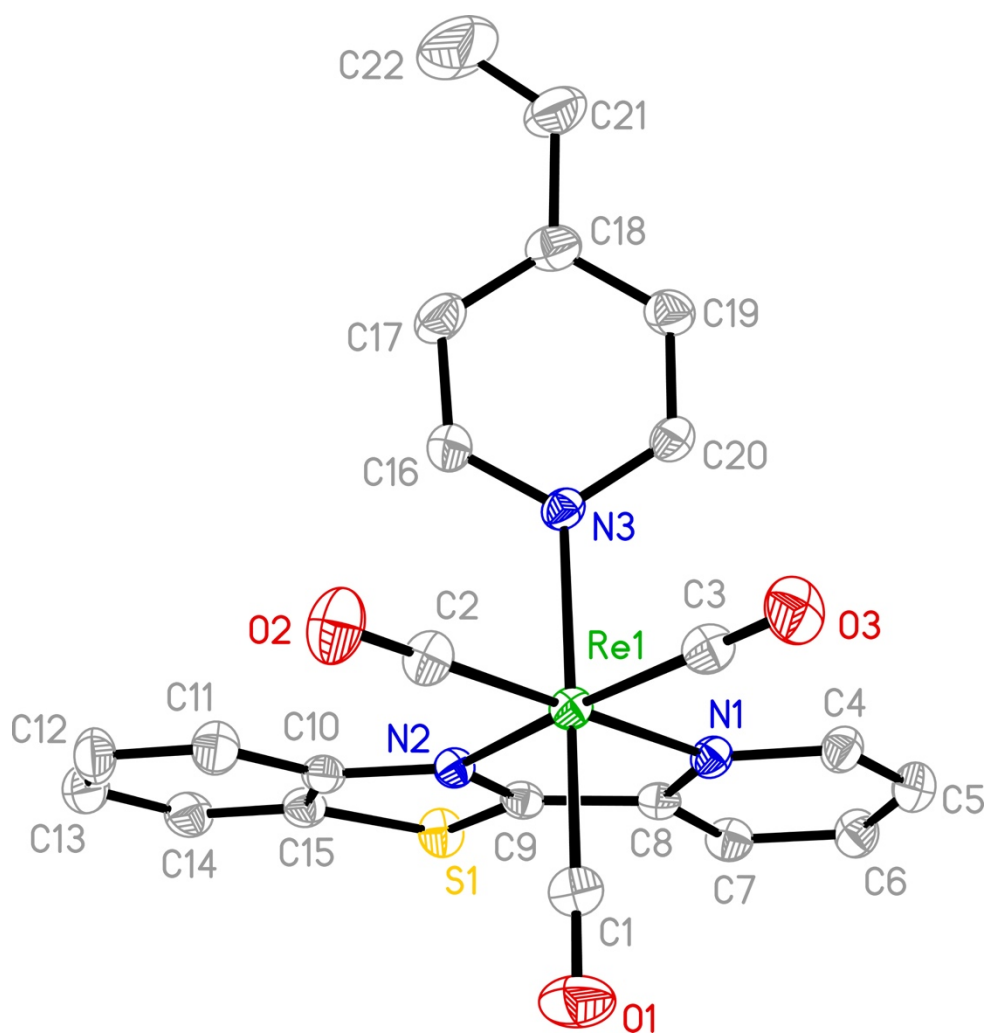
Figure 2.II.16. A perspective view of complex **1**, showing the atom-labeling scheme. Displacement ellipsoids are drawn at the 50% probability level.

Re1, N1, C14, C15, and N2 exhibits a small deviation from planarity [mean deviation = 0.029 (3) Å]. The dihedral angles between the planes of the pyridine ring and the benzothiazole moiety in (1) and (2) are 7.0 (5) and 10.1 (7)°, respectively.

In both cases, the benzo- thiazole frame is planar, with mean deviations of 0.013 (3) and 0.007 (3) Å for complexes **1** and **2**, respectively. The average Re—C bond
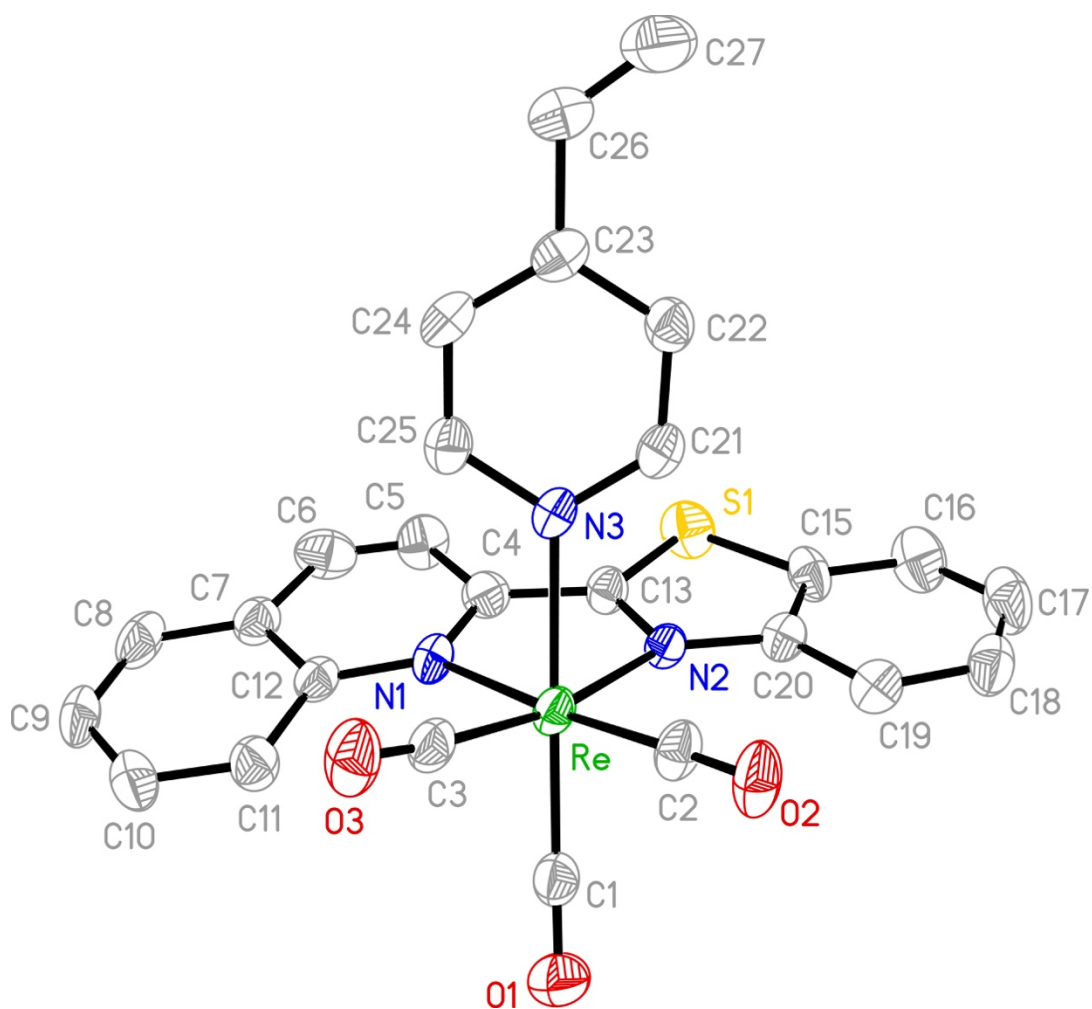
Figure 2.II.17. A perspective view of complex **2**, showing the atom-labeling scheme.

lengths in complexes **1** and **2** are statistically identical [1.915 (3) and 1.912 (7) Å, respectively] (Tables 2.II.1 and 2.II.2). The average Re—N bond lengths in complexes **1** and **2** display a similar trend [2.191 (2) and 2.195 (5) Å, respectively]. The average Re—C bond length in complex **3** (Table 2.II.3) is 1.921 (3) Å, while the average Re—N bond length is marginally shorter [2.179 (2) Å] compared to complexes **1** and **2**. In
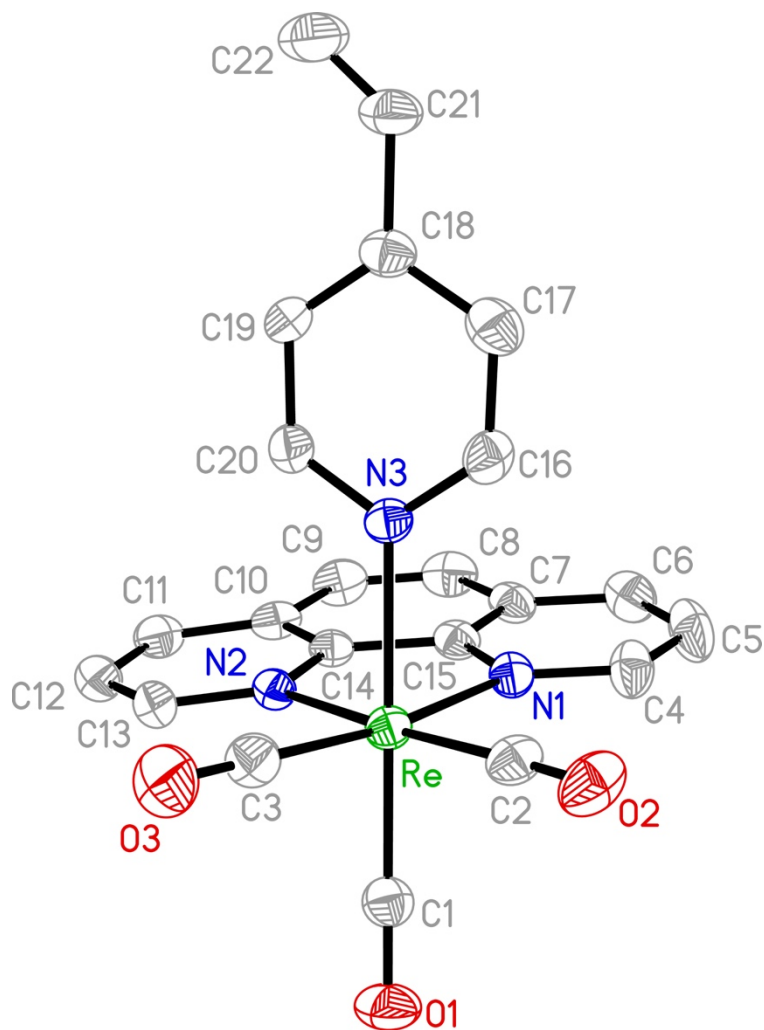
Figure 2.II.18. A perspective view of complex **2**, showing the atom-labeling scheme.

a structurally similar complex, namely $[Re(CO)_3(phen)(pyAl)](CF_3SO_3)$ (pyAl = pyridine-4- carbaldehyde), the average Re—C [1.919 (6) Å] and Re—N [2.178 (4) Å] bond lengths are statistically identical as those of complex **3**.[20]

The crystal packing of complex **1** reveals no intermolecular π–π stacking interactions. However, such interactions have been observed for complexes **2** and **3**. In
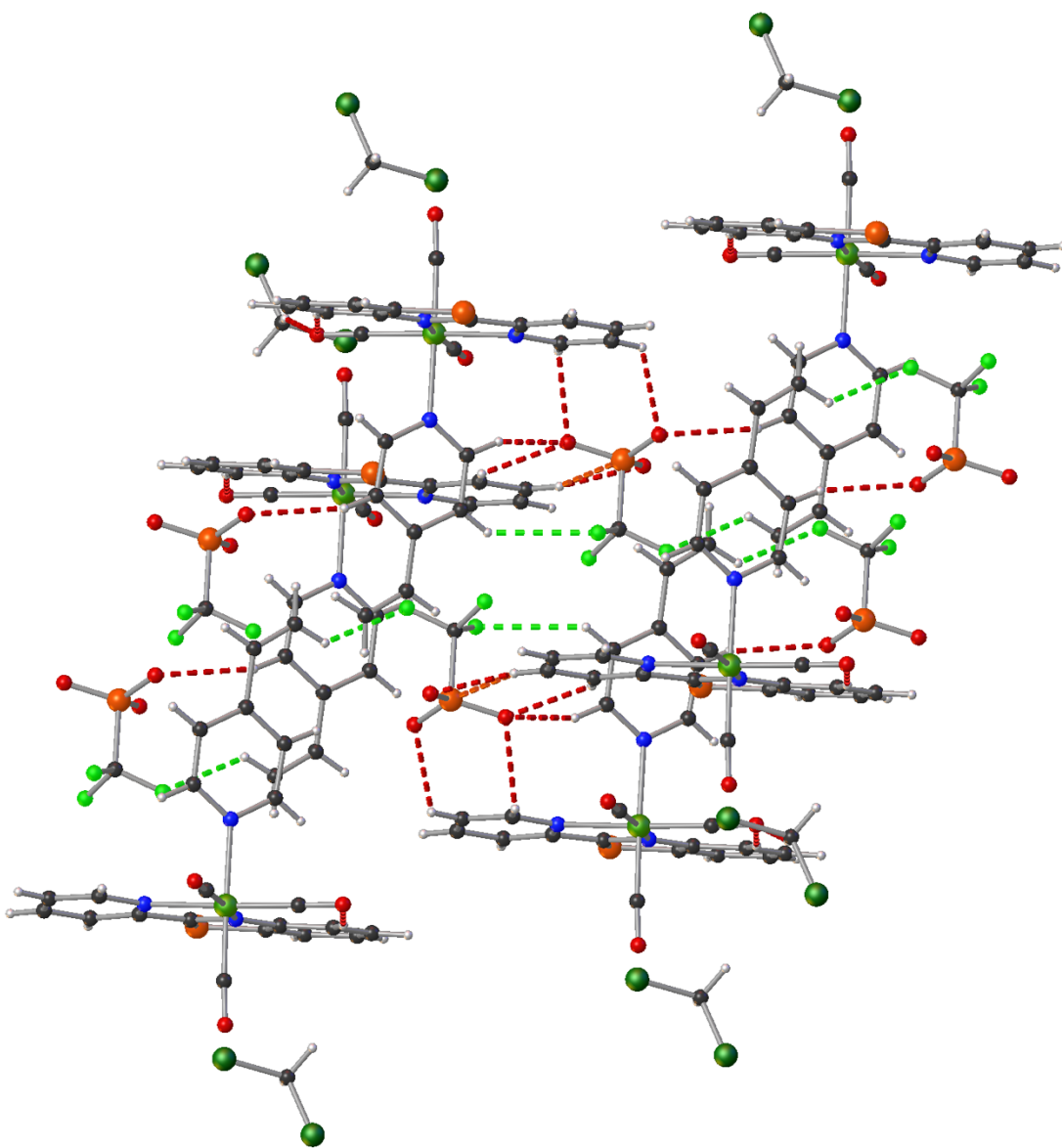
Figure 2.II.19. Crystal packing diagram for complex **1**, showing nonclassical contacts between the aromatic ligand and the triflate anion.

complex **2**, offset π– π stacking interactions have been noticed between the quinoline rings of two adjacent molecules [centroid-to-centroid distance = 3.852 (5) Å]. In
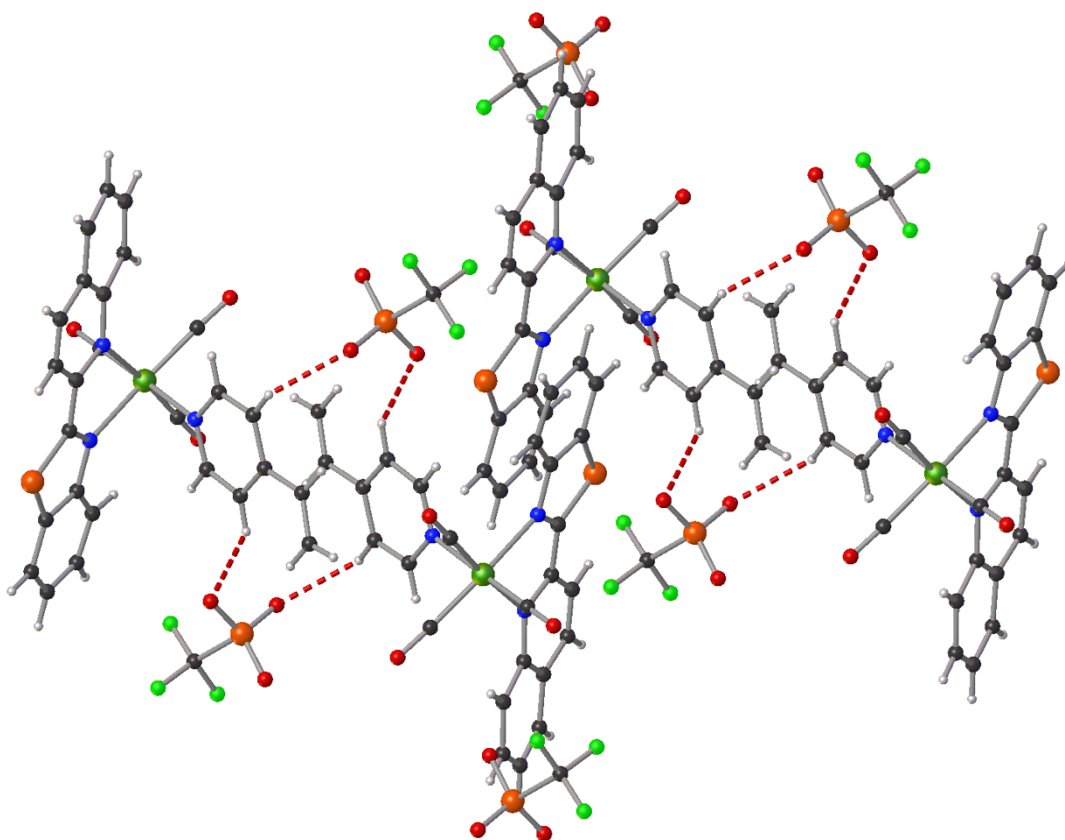
Figure 2.II.20. Crystal packing diagram for complex **2**, showing nonclassical hydrogen- bonding interactions.

complex **3**, considerable $\pi-\pi$ stacking interactions were apparent between the two phenanthroline rings of two adjacent molecules [centroid-to-centroid distance between the two central phenanthroline rings = 3.579 (5) Å]. In complex **1**, examination of the extended structure revealed a few nonclassical hydrogen-bonding contacts (Figure 2.II.19). These interactions result in a three-dimensional network of hydrogen-bonded molecules within the lattice. In complex **2**, analysis of the packing pattern revealed three nonclassical hydrogen-bonding interactions (Figure 2.II.20). Primarily, these

interactions are from the aromatic ligands to the triflate anions. Inspection of these contacts reveals that the ensemble is a three-dimensional hydrogen-bonded network. The extended lattice of complex **3** was consolidated by several nonclassical hydrogen-bonding contacts (Figure 2.II.21). As seen in complexes **1** and **2**, these interactions also result in a three-dimensional hydrogen-bonded network connected through the triflate anions.
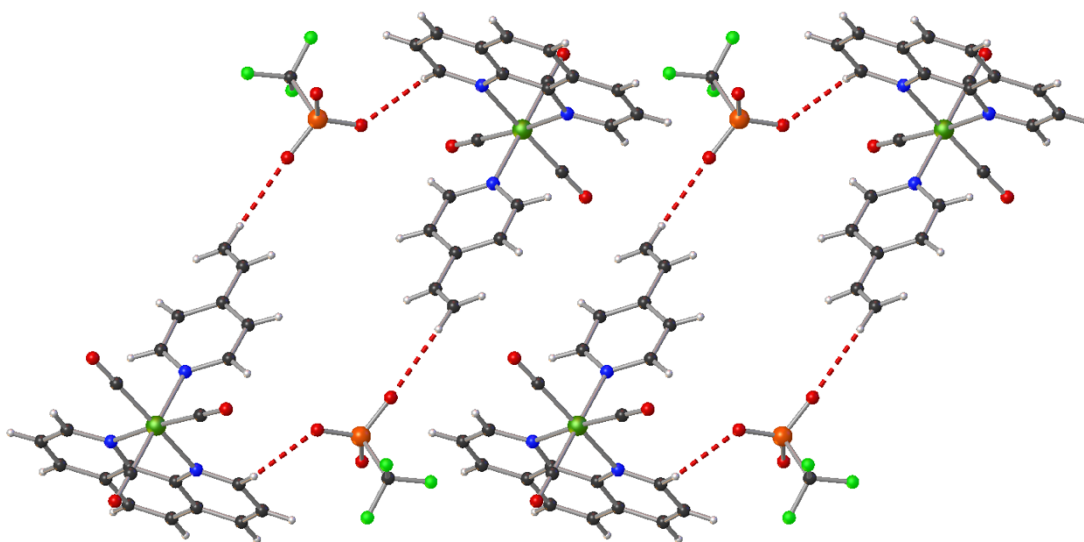
Figure 2.II.21. Crystal packing diagram for complex **3**, showing nonclassical hydrogen- bonding contacts.

2.II.2.5 X-Ray Structure Refinement.

Crystal data, data collection and structure refinement details are summarized in Tables 2.II.4 through 2.II.6. The non-H atoms were located through intrinsic phasing using SHELXT[47] integrated in the OLEX2 graphical user interface.[48] H atoms were included in calculated positions riding on the C atoms to which they are bonded, with

C—H = 0.93 A˚ and $U_{iso}(H) = 1.2U_{eq}(C)$. In **2** and **3**, the highest residual electron-density peak is located near the Re atom. No satisfactory disorder model could be found to resolve this. In complexes **2** and **3**, the triflate counter-anions exhibit disorder.

Table 2.II.4. Crystal data and structure refinement parameters for **1**.

	1
Empirical formula	$C_{22}H_{15}N_3O_3ReS \cdot CF_3O_3S$
T(K)	298
λ (Å)	0.71073
Crystal system	Triclinic
Space group	*P*-1
a (Å)	8.596 (2)
b (Å)	11.217 (3)
c (Å)	15.161 (3)
α (°)	92.88 (3)
β (°)	104.12 (2)
γ (°)	91.19 (3)
V (Å^3)	1415.1(6)
Z	2
D_{calc} (Mg m^{-3})	1.928
Absorption Coeff (mm^{-1})	4.695
No. of unique reflections	6442
Goodness-of-fit[a] on F^2	1.038
R_1[b]	0.0242
wR_2[c]	0.222
largest diff peak and hole	0.924, -0.793

The triflate anion in complex **2** is disordered over four positions. Two of the positions, with occupancies of 37.5 and 22.2%, have the same orientation of the anion, while the third position contains the anion rotated by 180° so that the –CF3 group is disordered with the –SO3 groups of the anions from the first two domains (12.5%).[49]

Table 2.II.5. Crystal data and structure refinement parameters for **2**.

	2
Empirical formula	$C_{26}H_{17}N_3O_3ReS \cdot CF_{2.21}O_3S$
T(K)	298
λ (Å)	0.71073
Crystal system	Monoclinic
Space group	$P2_1/n$
a (Å)	12.814 (3)
b (Å)	12.088 (2)
c (Å)	18.248 (3)
α (°)	90
β (°)	196.56 (3)
γ (°)	90
V (Å^3)	2808.0 (10)
Z	4
D_{calc} (Mg m^{-3})	1.826
Absorption Coeff (mm^{-1})	4.537
No. of unique reflections	5247
Goodness-of-fit[a] on F^2	1.062
R_1[b]	0.0672
wR_2[c]	0.1384
largest diff peak and hole	1.269, -0.780

The fourth position of the anion is almost perpendicular to the first three and, in this case, the free volume is filled by a partially occupied water molecule. Due to the low occupancy of the water molecule (27.8%) and the extensive disorder of the anion, the H atoms could not be located and are thus not included either in the model or within the sum formula.

Table 2.II.6. Crystal data and structure refinement parameters for **3**.

	3
Empirical formula	$C_{22}H_{15}N_3O_3Re \cdot CF_3O_3S$
T(K)	298
λ (Å)	0.71073
Crystal system	Monoclinic
Space group	$P2_1/n$
a (Å)	12.398 (2)
b (Å)	12.878 (3)
c (Å)	15.393 (3)
α (°)	90
β (°)	91.83 (3)
γ (°)	90
V (Å^3)	2456.5 (8)
Z	4
D_{calc} (Mg m^{-3})	1.513
Absorption Coeff (mm^{-1})	5.099
No. of unique reflections	5432
Goodness-of-fit^a on F^2	1.067
$R_1{}^b$	0.0213
w$R_2{}^c$	0.0519
largest diff peak and hole	1.513, -0.595

The triflate anion in complex **3** is disordered over three positions and the disorder was refined using geometry and U_{ij} similarity restraints.[49] Two of the positions, with occupancies of 33.8 and 31.8%, have the same orientation of the anion, while the third position contains the anion rotated by 180° so that the –CF3 group is disordered with the –SO3 groups of the anions from the first two domains. The sum of the occupancies of the three refined positions of the triflate anion was restrained to be 1.

2.II.3 Conclusions.

In conclusion, photoactive metal carbonyl complexes (photoCORMs) are ideal exogenous candidates for more controllable and site-specific CO delivery compared to the gaseous CO. Our group has been engaged for past few years in developing Group 7 based photoCORMs towards efficient eradication of various malignant cells. Moreover, several such complexes can be tracked within the cancerous cells by virtue of their luminescence. Three analogous UV-light sensitive Re(I)-based photoCORMs were synthesized and fully characterized. All three complexes exhibited relatively rapid release of CO upon exposure to low powered UV-irradiation. The first isolated intermediates (of the form [Re(CO)3(L)Br] where L = pbt, qbt, or phen) exhibited red luminescence with minor shifts (~20 nm) between complexes. Interestingly, upon coordination of the 4-vinylpyridine ligand, the shift in luminescence was much more pronounced (>50 nm). This change in luminescence allowed for visual discrimination between all three complexes. In addition, the photoproducts of **1** and **2** exhibited bright

blue luminescence upon excitation with UV light (365 nm). On the other hand, the photoproduct of complex **3** did not exhibit increase in luminescence upon extensive photolysis. The inherent luminescent nature of these photoCORMs and the change in emission wavelength upon CO release also provide a convenient means to track the entry of the prodrug and in some cases both the entry and CO release from the prodrug. In all complexes, the Re(I) center resides in a distorted octahedral coordination environment. These complexes exhibit CO release upon exposure to low power UV light. The apparent CO release rates of the complexes have been measured to assess their comparative CO donating capacity. The three complexes are highly luminescent and this in turn provide a convenient way to track the entry of the prodrug molecules within biological targets. In continuation of the research circumscribing the development of trackable photoCORMs and also to graft molecules covalently to conventional delivery vehicles. The vinyl polymeric tether would allow such covalent incorporation within polymeric matrices.

2.II.4 Experimental Section.

2.II.4.1 General Methods and Instrumentation.

All reagents were of commercial grade and were used without further purification unless stated otherwise. The ligand 2-(pyridin-2-yl)-1,3-benzothiazole (pbt)[50] and 2-(quinolin-2-yl)-1,3-benzothiazole (qbt)[51] were synthesized following reported literature procedures. 2,2′-azobis[2-(2-imidazolin-2-yl)propane] dihydrochloride (VA-044) was purchased from Wako Pure Chemical Industries Ltd.

1,10-phenanthroline (phen) was purchased from Sigma-Aldrich Inc. and was used as received. A PerkinElmer Spectrum-One FT—IR spectrometer was used to record IR spectra of the ligands and complexes. UV-vis spectra were obtained using a Varian Cary 50 UV-Vis spectrophotometer. Fluorescence data were recorded using a Cary-Eclipse Fluorescence Spectrophotometer. Microanalyses were obtained using a PerkinElmer Series II 2400 Elemental Analyzer. The 1H NMR spectra of the complexes were recorded at 298 K on a Varian Unity Inova 500 MHz instrument.

*2.II.4.2 Synthesis and Crystallization of [Re(CO)$_3$(pbt)(4-vpy)](CF$_3$SO$_3$) **1**.*

A solution of 2-(2-pyridyl)-benzothiazole (0.100 g, 0.47 mmol, 1 equiv.) in 10 mL of chloroform was added to [Re(CO)$_5$Cl] (0.170 g, 0.47 mmol, 1 equiv.) in 20 ml of methanol. The mixture was refluxed overnight resulting in a bright orange-red colored solution. The volume of the mixture was then reduced under low pressure until microcrystals of [Re(CO)$_3$(pbt)Cl] were observed. The reaction flask was then stored at 0 °C for 1 h. The microcrystalline material was collected by vacuum filtration, washed with 3 – 5 ml of hexanes and dried under vacuum to obtain [Re(CO)$_3$(pbt)Cl] as an orange-red powder (0.214 g, 88% yield). Next, a solution of silver trifluoromethanesulfonate (AgCF$_3$SO$_3$, 0.100 g, 0.39 mmol, 1.2 equiv) in 30 ml of dichloromethane was added to [Re(CO)$_3$(pbt)Cl] (0.168 g, 0.32 mmol, 1 equiv) and the mixture was stirred overnight. Next, the solution was filtered using a fritted funnel packed with Celite to remove unreacted silver trifluoromethanesulfonate and silver bromide (AgBr) precipitate. The resulting bright red filtrate was collected, and the

solvent volume was reduced under vacuum resulting in a bright red precipitate. The precipitate was then collected through vacuum filtration and washed with 3 – 5 ml portions of hexanes, furnishing 0.160 g (79% yield) of [Re(CO)$_3$(pbt)(CF$_3$SO$_3$)] as a red-orange powder. The complex [Re(CO)$_3$(pbt)(CF$_3$SO$_3$)] (0.100 g, 0.16 mmol, 1 equiv) was dissolved in 20 ml of chloroform, followed by the addition of 4-vinylpyridine (0.173 ml, 1.6 mmol, 10 equiv). The reaction mixture was refluxed overnight resulting in a cloudy orange solution. After this time, the reaction mixture was filtered using a fritted funnel and Celite bed to remove a brown residue. The filtrate was collected, and solvent was completely removed under reduced pressure. The resulting solid was recrystallized by layering hexanes over a solution of the complex in dichloromethane to afford 109 mg (93% yield) of [Re(CO)$_3$(pbt)(4-vpy)](CF$_3$SO$_3$) **1** as light-orange crystals. Elemental analysis (%) found: C 37.54, H 2.08, N 5.67; calculated for C$_{23}$H$_{15}$F$_3$N$_3$O$_6$ReS$_2$: C 37.50, H 2.05, N 5.70. IR (KBr, cm^{-1}): 3078 (*w*), 2031 (*s*), 1918 (*s*), 1617 (*w*), 1487 (*w*), 1418 (*w*), 1263 (*s*), 1223 (*w*), 1152 (*s*), 1030 (*s*), 944 (*w*), 847 (*w*), 763 (*w*), 724 (*w*), 637 (*s*), 517 (*w*); ^{1}H NMR (CDCl$_3$): δ 9.16 (d, 1H), 8.60 (d, 1H), 8.44 (d, 1H), 8.36 (t, 1H), 8.13 (d, 1H), 7.98 (d, 2H), 7.83 (m, 2H), 7.71 (t, 1H), 7.18 (d, 2H), 6.45 (m, 1H), 5.91 (d, 1H), 5.52 (d, 1H).

*2.II.4.3 Synthesis and Crystallization of [Re(CO)$_3$(qbt)(4-vpy)](CF$_3$SO$_3$) **2**.*

A solution of 2-(quinoline-2-yl)-benzothiazole (0.125 g, 0.47 mmol, 1 equiv.) in 10 mL of chloroform was added to [Re(CO)$_5$Cl] (0.170 g, 0.47 mmol, 1 equiv.) in 20 ml of methanol. The mixture was refluxed overnight resulting in a bright red colored

solution. The volume of the mixture was then reduced under low pressure until microcrystals of [Re(CO)$_3$(qbt)Cl] were observed. The reaction flask was then stored at 0 °C for 1 h. The microcrystalline material was collected by vacuum filtration, washed with 3 – 5 ml of hexanes and dried under vacuum to obtain [Re(CO)$_3$(qbt)Cl] as an orange-red powder (0.230 g, 86% yield). Next, a solution of silver trifluoromethanesulfonate (AgCF$_3$SO$_3$, 0.100 g, 0.39 mmol, 1.2 equiv) in 30 ml of dichloromethane was added to [Re(CO)$_3$(qbt)Cl] (0.178 g, 0.32 mmol, 1 equiv) and the mixture was stirred overnight. Next, the solution was filtered using a fritted funnel packed with Celite to remove unreacted silver trifluoromethanesulfonate and silver bromide (AgBr) precipitate. The resulting bright red filtrate was collected, and the solvent volume was reduced under vacuum resulting in a bright red precipitate. The precipitate was then collected through vacuum filtration and washed with 3 – 5 ml portions of hexanes, furnishing 0.180 g (80% yield) of [Re(CO)$_3$(qbt)(CF$_3$SO$_3$)] as a red-orange powder. The complex [Re(CO)$_3$(qbt)(CF$_3$SO$_3$)] (0.110 g, 0.16 mmol, 1 equiv) was dissolved in 20 ml of chloroform, followed by the addition of 4-vinylpyridine (0.173 ml, 1.6 mmol, 10 equiv). The reaction mixture was refluxed overnight resulting in a cloudy orange solution. After this time, the reaction mixture was filtered using a fritted funnel and Celite bed to remove a brown residue. The filtrate was collected, and solvent was completely removed under reduced pressure. The resulting solid was recrystallized by layering hexanes over a solution of the complex in dichloromethane to afford 122 mg (95% yield) of [Re(CO)$_3$(qbt)(4-vpy)](CF$_3$SO$_3$) **2** as light-red crystals. Elemental analysis (%) found: C 41.25, H 2.21, N 5.38; calculated

for $C_{27}H_{17}F_3N_3O_6ReS_2$: C 41.22, H 2.18, N 5.34. IR (KBr, cm-1): 3066 (*w*), 2033 (*s*), 1934 (*s*), 1913 (*s*), 1616 (*w*), 1590 (*w*), 1518 (*w*), 1427 (*w*), 1260 (*s*), 1148 (*s*), 1093 (*w*), 1029 (*s*), 999 (*w*), 930 (*w*), 853 (*w*), 762 (*w*), 727 (*w*), 636 (*s*), 517 (*w*); ^{1}H NMR (CDCl$_3$): δ 8.90 (d, 1H), 8.85 (d, 1H), 8.65 (d, 1H), 8.57 (d, 1H), 8.22 (d, 1H), 8.16 (d, 1H), 8.11 (t, 1H), 8.87 (t, 2H), 7.75 (t, 1H), 7.52 (d, 2H), 7.01 (d, 2H), 6.41 (m, 1H), 5.86 (d, 1H), 5.51 (d, 1H).

2.II.4.4 Synthesis and Crystallization of [Re(CO)$_3$(phen)(4-vpy)](CF$_3$SO$_3$) **3**.

A solution of 1,10-phenanthroline (0.090 g, 0.50 mmol, 1 equiv.) in 10 mL of chloroform was added to [Re(CO)$_5$Cl] (0.185 g, 0.50 mmol, 1 equiv.) in 20 ml of methanol. The mixture was refluxed overnight resulting in a bright orange-red colored solution. The volume of the mixture was then reduced under low pressure until microcrystals of [Re(CO)$_3$(phen)Cl] were observed. The reaction flask was then stored at 0 °C for 1 h. The microcrystalline material was collected by vacuum filtration, washed with 3 – 5 ml of hexanes and dried under vacuum to obtain [Re(CO)$_3$(phen)Cl] as an dark orange powder (0.224 g, 82% yield). Next, a solution of silver trifluoromethanesulfonate (AgCF$_3$SO$_3$, 0.100 g, 0.39 mmol, 1.2 equiv) in 30 ml of dichloromethane was added to [Re(CO)$_3$(phen)Cl] (0.165 g, 0.32 mmol, 1 equiv) and the mixture was stirred overnight. Next, the solution was filtered using a fritted funnel packed with Celite to remove unreacted silver trifluoromethanesulfonate and silver bromide (AgBr) precipitate. The resulting bright red filtrate was collected, and the solvent volume was reduced under vacuum resulting in a bright orange precipitate. The

precipitate was then collected through vacuum filtration and washed with 3 – 5 ml portions of hexanes, furnishing 0.140 g (78% yield) of [Re(CO)$_3$(phen)(CF$_3$SO$_3$)] as a red-orange powder. The complex [Re(CO)$_3$(pbt)(CF$_3$SO$_3$)] (0.105 g, 0.16 mmol, 1 equiv) was dissolved in 20 ml of chloroform, followed by the addition of 4-vinylpyridine (0.173 ml, 1.6 mmol, 10 equiv). The reaction mixture was refluxed overnight resulting in a cloudy orange solution. After this time, the reaction mixture was filtered using a fritted funnel and Celite bed to remove a brown residue. The filtrate was collected, and solvent was completely removed under reduced pressure. The resulting solid was recrystallized by layering hexanes over a solution of the complex in dichloromethane to afford 108 mg (92% yield) of [Re(CO)$_3$(phen)(4-vpy)](CF$_3$SO$_3$) **1** as light-orange crystals. Elemental analysis (%) found: C 39.24, H 2.17, N 5.92; calculated for C$_{23}$H$_{15}$F$_3$N$_3$O$_6$ReS: C 39.20, H 2.15, N 5.96. IR (KBr, cm^{-1}): 3065 (*w*), 2029 (*s*), 1910 (*s*), 1619 (*w*), 1520 (*w*), 1430 (*w*), 1276 (*s*), 1223 (*w*), 1154 (*s*), 1137 (*s*), 1032 (*s*), 998 (*w*), 944 (*w*), 844 (*w*), 724 (*w*), 636 (*s*); ^{1}H NMR (CDCl$_3$): δ 9.48 (d, 2H), 8.76 (d, 2H), 8.11 (m, 6H), 7.18 (d, 2H), 6.39 (m, 1H), 5.87 (d, 1H), 5.46 (d, 1H).

2.II.4.5 Incorporation of [Re(CO)$_3$(pbt)(4-vpy)](CF$_3$SO$_3$) **1**, *[Re(CO)$_3$(qbt)(4-vpy)](CF$_3$SO$_3$)* **2**, *[Re(CO)$_3$(phen)(4-vpy)](CF$_3$SO$_3$)* **3** *into pHEMA/EGDMA Hydrogel.*

The preparation, polymerization, and curing of polymer samples was carried out in the dark to avoid decomposition of the CO-donating complex. The water-soluble initiator 2,2′-azobis[2-(2-imidazolin-2-yl) propane] dihydrochloride (VA-044) (0.015

g, 0.045 mmol) was dissolved in milliQ water (2.85 g, 158 mmol) aided by sonication. This solution was mixed with 2-hydroxyethyl methacrylate (HEMA) (5.00 g, 41 mmol) and ethylene glycol dimethacrylate (EGDMA) (0.250 g, 1.3 mmol). The pre-polymer mixture was combined with a dilute solution of 1 in acetone (0.60 mL, 0.00145 M) to afford photoCORP-**1** which was 0.1 mM w.r.t **1** for UV–vis analysis. In a similar manner, a second pre-polymer mixture (4 mM w.r.t. **1**) was prepared by adding a concentrated solution of **1** in acetone (0.60 mL, 0.058 M) to make photoCORP-**1** for myoglobin/cell treatment. Blank polymer samples (without **1**) were prepared by combining a third pre-polymer batch with acetone (0.6 mL). The mixtures were degassed for 20 min by bubbling dry nitrogen gas and placed into polystyrene cuvettes or other molds tubes. Once the solutions were placed in their respective mold, they were heated for 30 min at 50 °C using a water bath. The heat was then turned off and the water-bath was allowed to cool slowly, and the polymers were then cured at room temperature for 48 h in the dark. Microanalytical data (from Galbraith Laboratories Inc.) indicated that the photoCORP-**1** tip material contained 0.0328% of Mn corresponding to 0.39 wt. % incorporation of the photoCORM in the hydrogel.

Photolysed polymer samples were prepared by irradiating photoCORP-**1** (sealed within its mold) with visible light. The samples were then removed from their containers, washed, sterilized, and air- dried for 30 min before use. Dilute polymer samples (0.1 mM) were kept inside their polystyrene cuvette mold and used as blank for UV–vis absorption studies.

*2.II.4.6 Photolysis Experiments with Complexes **1-3** and CO-Releasing Polymer Containing Complex **1**.*

The CO release rates (k_{CO}) from the complexes **1-3** and the CO-releasing polymer containing complex **1** were measured by using polystyrene cuvettes (1 cm × 1 cm × 4.5 cm) and a UV light source (15 mW cm^{-1}) to induce CO photorelease. The cuvettes containing either solution of the free complex in dichloromethane or the CO-loaded polymer were placed directly on top of the UV-light transilluminator, irradiated for 1 or 3 min intervals respectively, and the electronic absorption spectra were sequentially recorded. A blank polymer sample was used for the baseline correction for the studies using the photoCORM loaded polymer. The changes in absorption spectra upon light exposure were monitored and the CO release rates (k_{CO}) were determined from a ln(C) versus time (t) plot at an appropriate wavelength.

2.II.5 References.

1. Motterlini, R.; Otterbein, L. E. The therapeutic potential of carbon monoxide. *Nat. Rev. Drug Discov.* **2010**, *9*, 422-428.

2. Wu, L.; Wang, R. Carbon monoxide: Endogenous production, physiological functions, and pharmacological applications. *Pharmacol. Rev.* **2005**, *57*, 585-630.

3. Kikuchi, G.; Yoshida, T.; Noguchi, M. Heme oxygenase and heme degradation. *Biochem. Biophys. Res. Commun.* **2005**, *338*, 558-567.

4. Yoshida, T,; Migita, C. T. Mechanisms of heme degradation by heme oxygenase. J. Inorg. Biochem. 2000, 82, 33-41.

5. Zuckerbraun, B. S.; Billiar, T. R.; Otterbein, S. L.; Kim, P. K.; Liu, F.; Choi, A. M. K. Otterbein, L. E. Carbon monoxide protects against liver failure through nitric oxide-induced heme oxygenase 1. *J. Exp. Med.* **2003**, *198*, 1707-1716.

6. Otterbein, L. E.; Bach, F. H.; Alam, J.; Soares, M.; Lu, H. T.; Wysk, M.; Davis, R. J.; Flavell, R. A.; Choi, A. M. K. Carbon monoxide ha anti-inflammatory effects involving the mitogen-activated protein kinase pathway. *Nat. Med.* **2000**, *6*, 422-428.

7. Chin, B. Y.; Jiang, G.; Wegiel, B.; Wang, H. J.; MacDonald, T.; Zhang, X. C.; Gallo, D.; Cszimadia, E.; Bach, F. H.; Lee, P. J.; Otterbein, L. E. Hypoxia-inducible factor 1α stabilization by carbon monoxide results in cytoprotective preconditioning. *Proc. Natl. Acad. Sci. USA* **2007**, *104*, 5109-5144.

8. Haschemi, A.; Wagner, O.; Marculescu, R.; Wegiel, B.; Robson, S. C.; Gagliani, N.; Gallo, D.; Chen, J. F.; Bach, F. H.; Otterbein, L. E. Cross-regulation of carbon monoxide and the adenosine A2a receptor in macrophages. *J. Immunol.* **2007**, *178*, 5921–5929.

9. Pintadosi, C. A. Carbon monoxide, reactive oxygen signaling and oxidative stress. *Free Radic. Biol. Med.* **2008**, *45*, 562-569.

10. Zuckerbraun, B. S.; Chin, B, Y,; Bilban, M.; d'Avila, J. C.; Rao, T.; Billiar, T. R.; Otterbein, L. E. Carbon monoxide signals via inhibition of cytochrome c

oxidase and generation of mitochondrial reactive oxygen species. *FASEB J.* **2007**, *21*, 1099-1106.

11. Li, X.; Fang, P.; Mai, J.; Choi, E. T.; Wang, H.; Yang, X. F. Targeting mitochondrial reactive oxygen species as a novel therapy for inflammatory diseases and cancers. *J. Hematol. Oncol.* **2013**, *6*, 19;

12. Liou, G. Y.; Storz, P. Reactive oxygen species in cancer. *Free Radic. Res.* **2010**, *44*, 479-496.

13. Motterlini, R.; Clark, J. E.; Foresti, R.; Saratchandra, P.; Mann, B. E.; Green, C. J. Carbon monoxide-releasing molecules characterization of biochemical and vascular activities. *Circ. Res.* **2002**, *90*, e17-e24.

14. Stec, D. E.; Drummond, H. A.; Vera, T. Role of carbon monoxide in blood pressure regulation. *Hypertension* **2008**, *51*, 597–604.

15. Wegiel, B.; Gallo, D.; Csizmadia, E.; Harris, C.; Belcher, J.; Vercellotti, G. M.; Penacho, N.; Seth, P.; Sukatme, V.; Ahmed, A.; Pandolfi, P. P.; Helczynski, L.; Bjartell, A.; Persson, J. L.; Otterbein, L. E. Carbon monoxide expedites metabolic exhaustion to inhibit tumor growth. *Cancer Res.* **2013**, *73*, 7009-7021.

16. Kawahara, B.; Ramadoss, S.; Chaudhuri, G.; Janzen, C.; Sen, S.; Mascharak, P. K. Carbon monoxide sensitizes cisplatin-resistant ovarian cancer cell lines toward cisplatin via attenuation of levels of glutathione and nuclear metallothionein. *J. Inorg. Biochem.* **2019**, *191*, 29-39.

17. Kawahara, B.; Moller, T.; Hu-Moore, K.; Carrington, S.; Faull, K. F.; Sen, S.; Mascharak, P. K. Attenuation of antioxidant capacity in human breast cancer cells by carbon monoxide through inhibition of cystathionine b-synthase activity: Implications in chemotherapeutic drug sensitivity. *J. Med. Chem.* **2017**, *60*, 8000-8010.

18. Vidhyapriya, P.; Divya, D.; Manimara, B.; Sakthivel, N. Photoactivated [Mn(CO)$_3$(Br(μ-bpcpd)]$_2$ induces apoptosis in cancer cells via intrinsic pathway. *J. Photochem. Photobiol. B, Biol.* **2018**, *188*, 28-41.

19. Vidhyapriya, P.; Divya, D.; Manimara, B.; Sakthivel, N. Photoactivated [Mn(CO)$_3$(Br(μ-bpcpd)]$_2$ induces apoptosis in cancer cells via intrinsic pathway. *J. Photochem. Photobiol. B, Biol.* **2018**, *188*, 28-41.

20. Chakraborty, I.; Jimenez, J.; Mascharak, P. K. CO-induced apoptotic death of colorectal cancer cells by a luminescent photoCORM grafted on biocompatible carboxymethyl chitosan. *Chem. Commun.* **2017**, *53*, 5519-5522.

21. Pinto, M. N.; Chakraborty, I.; Sandoval, C.; Mascharak, P. K.; Eradication of HT-29 colorectal adenocarcinoma cells by controlled photorelease of CO from a CO-releasing polymer (photoCORP-**1**) triggered by visible light through an optical fiber-based device. *J. Control. Release* **2017**, *264*, 192-202.

22. Ji, X.; De La Cruz, L. K. C.; Pan, Z.; Chittavong, V.; Wang, B. pH-sensitive metal free carbon monoxide prodrugs with tunable and predictable release rates. *Chem. Commun.* **2017**, *53*, 9628-9631.

23. Ji, X.; Pan, Z.; Li, C.; Kang, T.; De La Cruz, L. K. C.; Yang, L.; Yuan, Z.; Ke, B.; Wang, B. Esterase-sensitive and pH-controlled carbon monoxide prodrugs for treating systemic inflammation. *J. Med. Chem*. **2019**, *62*, 3163-3168.

24. Ji, X.; Wang, B. Strategies toward organic carbon monoxide prodrugs. *Acc. Chem. Res.* **2018**, *51*, 1377-1385.

25. Chakraborty, I.; Carrington, S. J.; Mascharak, P. K. Design strategies to improve sensitivity of photoactive metal carbonyl complexes (photoCORMs) to visible light and their potential as CO-donors to biological targets. *Acc. Chem. Res.* **2014**, *47*, 2603-2611.

26. Garcia-Gallego, S.; Bernardes, G. J. L. Carbon monoxide-releasing molecules for the delivery of therapeutic CO in vivo. *Angew. Chem. Int. Ed*. **2014**, *53*, 9712-9721.

27. Romao, C. C.; Blatter, W. A.; Seixas, J. D.; Bernardes, G. J. Developing drug molecules for therapy with carbon monoxide. *Chem. Soc. Rev.* **2012**, *41*, 3571-3583.

28. Faizan, M.; Muhammad, N.; Niazi, K. U. K.; Hu, Y.; Wang, Y.; Wu, Y.; Sun, H.; Liu, R.; Dong, W.; Zhang, W.; Gao, Z. CO-releasing materials: an emphasis on therapeutic implications, as release and subsequent cytotoxicity are the part of therapy. *Materials* **2019**, *12*, 1643.

29. Kottelat, E.; Zobi, F. Visible light-activated photoCORMs. *Inorganics* **2017**, *5*, 24.

30. Ford, P. C. Metal complex strategies for photo-uncaging the small molecule bioregulators nitric oxide and carbon monoxide. *Coord. Chem. Rev.* **2018**, *376*, 548-564.

31. Li, Z.; Pierri, A. E.; Huang, P. J.; Wu, G.; Ford, P. C. Dinuclear photoCORMs: dioxygen-assisted carbon monoxide uncaging from long-wavelength-absorbing metal-metal-bonded carbonyl complexes, *Inorg. Chem*. **2017**, *56*, 6094-6104.

32. Ramu, V.; Reddy, G. U.; Liu, J.; Hoffmann, P.; Sollapur, R.; Wyrwa, R.; Kupfer, S.; Spielmann, C.; Bonnet, S.; Neugebauer, U.; Schiller, A. Two-photon-induced CO-releasing molecules as molecular logic systems in solution, polymers, and cells. *Chem. Eur. J.* **2019**, *25*, 8453-8458.

33. Pierri, A. E.; Huang, P.-J.; Garcia, J. V.; Stanfill, J. G.; Chui, M.; Wu, G.; Zheng, N.; Ford, P. C. A photoCORM nanocarrier for CO release using NIR light. *Chem. Commun.* **2015**, *51*, 2072-2075.

34. Wang, C.; Li, Y.; Shi, X.; Zhou, J.; Wei, S. Use of a NIR-light-responsive CO nanodonor to improve the EPR effect in photothermal cancer treatment. *Chem. Commun*. **2018**, *54*, 13403-13406.

35. Carrington, S. J.; Chakraborty, I.; Bernard, J. M. L.; Mascharak, P. K. A theranostic two-tone luminescent photoCORM derived from Re(I) and 2-(pyridyl)-benzothiazole: Trackable CO delivery to malignant cells. *Inorg. Chem.* **2016**, *55*, 7852-7858.

36. Soboleva, T.; Esquer, H. J.; Benninghoff, A. D.; Berreau, L. M. Sense and release: a thiol responsive flavonol-based photonically driven carbon

monoxide-releasing molecule that operates via a multiple input AND logic gate. *J. Am. Chem. Soc.* **2017**, *139*, 9435-9438.

37. Carrington, S. J.; Chakraborty, I.; Bernard, J. M. L. Mascharak, P. K. Synthesis and characterization of a "turn-on" photoCORM for trackable CO delivery to biological targets. *ACS Med. Chem. Lett.* **2014**, *4*, 1324-1328.

38. G, U. R.; Axthelm, J.; Hoffmann, P.; Taye, N.; Glaser, S.; Gorls, H.; Hopkins, S. L.; Plass, W.; Neugebauer, U.; Bonnet, S.; Schiller, A. Co-registered molecular logic gate with a CO-releasing molecule triggered by light and peroxide. *J. Am. Chem. Soc.* **2017**, *139*, 4991-4994.

39. Musib, D.; Raza, M. K.; Martina, K.; Roy, M. Mn(I)-based photoCORMs for trackable visible light-induced CO release and phototoxicity to cancer cells. *Polyhedron* **2019**, In Press, Corrected Proof.

40. Jimenez, J.; Chakraborty, I.; Dominguez, A.; Martinez-Gonzalez, J.; Sameera, W. M. C.; Mascharak, P. K. A luminescent manganese photoCORM for CO delivery to cellular targets under the control of visible light. *Inorg. Chem.* **2018**, *57*, 1766-1773.

41. Jimenez, J.; Pinto, M. N.; Martinez-Gonzalez, J.; Mascharak, P. K. Photo-induced eradication of human colorectal adenocarcinoma HT-29 cells by carbon monoxide (CO) delivery from a Mn-based green luminescent photoCORM. *Inorg. Chim. Acta* **2019**, *485*, 113-117.

42. Romanski, S.; Rucker, H.; Stamellou, E.; Guttentag, M.; Neudorfl, J.-M.; Alberto, R.; Amslinger, S.; Yard, B.; Schmalz, H.-G. Iron dienylphosphate

tricarbonyl complexes as water-soluble enzyme-triggered CO-releasing molecules (ET-CORMs). *Organometallics* **2012**, *31*, 5800-5809.

43. Poh, H. T.; Sim, B. T.; Chwee, T. S.; Leong, W. K.; Fan, W. Y. The dithiolate-bridged diiron hexacarbonyl complex $Na_2[(\mu\text{-}SCH_2CH_2COO)Fe(CO)_3]_2$ as a water-soluble photoCORM. *Organometallics* **2014**, *33*, 959-963.

44. Mede, R.; Klein, M.; Claus, R. A.; Krieck, S.; Quickert, S.; Gorls, H.; Neugebauer, U.; Schmitt, M.; Gessner, G.; Heinemann, S. H.; Popp, J.; Bauer, M.; Westerhausen, M. CORM-EDE1: A highly water soluble and nontoxic manganese-based photoCORM with a biogenic ligand sphere. *Inorg. Chem.* **2016**, *55*, 104-113.

45. Jimenez, J.; Chakraborty, I.; Carrington, S. J.; Mascharak, P. K. Light-triggered CO delivery by a water-soluble and biocompatible manganese photoCORM. *Dalton Trans.* **2016**, *45*, 13204-13213.

46. Marker, S. C.; MacMillan, S. N.; Zipfel, W. R.; Li, Z.; Ford, P. C.; Wilson, J. J. Photoactivated in vitro anticancer activity of Rhenium(I) tricarbonyl complexes bearing water-soluble phosphines. *Inorg. Chem.* **2018**, *57*, 1311-1331.

47. Sheldrick, G. M. SHELXT – Integrated space-group and crystal-structure determination. *Acta Cryst.* **2015**, *A71*, 3–8.

48. Dolomanov, O. V.; Bourhis, L. J.; Gildea, R. J.; Howard, J. A. K.; Puschmann, H. OLEX2: A complete structure solution, refinement and analysis program. *J. Appl. Cryst.* **2009**, *42,* 339–341.

49. Sheldrick, G. M. Crystal structure refinement with SHELXL. *Acta Crystallogr. C, Struct. Chem*. **2015**, *71*, 3–8.

50. Chen, X.; Femia, F. J.; Babich, J. W.; Zubieta, J. Synthesis, characterization and crystal structures of mono-, di-, and trinuclear rhenium(I) tricarbonyl complexes with 2,3,5,6-tetra(2-pyridyl)pyrazine. *Inorg. Chim. Acta*. **2001**, *315,* 66-72.

51. Stenger-Smith, J.; Chakraborty, I.; Mascharak, P. K. Synthesis and structures of photoactive manganese carbonyl complexes derived from 2-(pyridin-2-yl)-1,3-benzothiazole and 2-(quinoline-2-yl)-1,3-benzothiazole. *Acta Cryst.* **2017**, *C73*, 357-361.

2.I.6 Reprints of Publications and Permissions.

Reprinted with permissions from Pinto, M. N.; Chakraborty, I.; Martinez-Gonzalez; Mascharak, P. K. Synthesis and Structures of Photoactive Rhenium Carbonyl Complexes Derived from 2-(pyridin-2-yl)-1,3-benzothiazole, 2-(quinoline-2-yl)-1,3-benzothiazole and 1,10-Phenanthroline. *Acta Cryst*. **2017**, *C73*, 923-929.

Synthesis and structures of photoactive rhenium carbonyl complexes derived from 2-(pyridin-2-yl)-1,3-benzothiazole, 2-(quinolin-2-yl)-1,3-benzothiazole and 1,10-phenanthroline

Miguel Pinto, Indranil Chakraborty, Jorge Martinez-Gonzalez and Pradip Mascharak*

Department of Chemistry & Biochemistry, Univeristy of California Santa Cruz, CA 95064, USA. *Correspondence e-mail: pradip@ucsc.edu

Carbon monoxide (CO) has recently been identified as a gaseous signaling molecule that exerts various salutary effects in mammalian pathophysiology. Photoactive metal carbonyl complexes (photoCORMs) are ideal exogenous candidates for more controllable and site-specific CO delivery compared to gaseous CO. Along this line, our group has been engaged for the past few years in developing group-7-based photoCORMs towards the efficient eradication of various malignant cells. Moreover, several such complexes can be tracked within cancerous cells by virtue of their luminescence. The inherent luminescent nature of some photoCORMs and the change in emission wavelength upon CO release also provide a covenient means to track the entry of the prodrug and, in some cases, both the entry and CO release from the prodrug. In continuation of the research circumscribing the development of trackable photoCORMs and also to graft such molecules covalently to conventional delivery vehicles, we report herein the synthesis and structures of three rhenium carbonyl complexes, namely, fac-tricarbonyl[2-(pyridin-2-yl)-1,3-benzothiazole-κ^2N,N'](4-vinylpyridine-κN)rhenium(I) trifluoromethanesulfonate, [Re(C_7H_7N)($C_{12}H_8N_2S$)($CO)_3$](CF_3SO_3), (1), fac-tricarbonyl[2-(quinolin-2-yl)-1,3-benzothiazole-κ^2N,N']-(4-vinylpyridine-κN)rhenium(I) trifluoromethanesulfonate, [Re(C_7H_7N)($C_{16}H_{10}N_2S$)($CO)_3$](CF_3SO_3), (2), and fac-tricarbonyl[1,10-phenanthroline-κ^2N,N'](4-vinylpyridine-κN)rhenium(I) trifluoromethanesulfonate, [Re(C_7H_7N)($C_{12}H_8N_2$)($CO)_3$](CF_3SO_3), (3). In all three complexes, the Re^I center resides in a distorted octahedral coordination environment. These complexes exhibit CO release upon exposure to low-power UV light. The apparent CO release rates of the complexes have been measured to assess their comparative CO-donating capacity. The three complexes are highly luminescent and this in turn provides a convenient way to track the entry of the prodrug molecules within biological targets.

1. Introduction

Carbon monoxide (CO), widely known for its toxicity, has recently been recognized as a gaseous signaling molecule (gasotransmitter) responsible for a variety of physiological responses in mammalian physiology and pathology (Motterlini & Otterbein, 2010). CO is endogenously produced through heme catabolism (Yoshida & Migita, 2000) and, unlike other gasotransmitters, it does not undergo chemical alterations within cells. CO primarily binds low-valent metal centers of heme proteins (Motterlini & Otterbein, 2010), blocking (Zuckerbraun et al., 2003) or enhancing their functions (Chin et al., 2007). This interaction results in signaling cascades responsible for the modulation of several processes, such as inflammation (Otterbein et al., 2000; Haschemi et al., 2007),

200
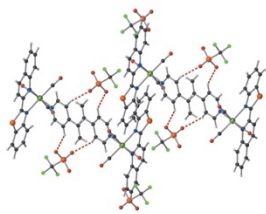
oxidative stress (Pintadosi, 2008), and hypertension (Stec *et al.*, 2008). Interestingly, moderate doses of CO (∼200 ppm) have been shown to sensitize cancer cells to conventional chemotherapeutics (Wegiel *et al.*, 2013), as well as induce apoptosis in malignant cells (Chakraborty *et al.*, 2017). The main challenge regarding the use of CO as a direct or adjuvant chemotherapeutic is to deliver this gaseous molecule in a site-specific manner. Direct inhalation of this gasotransmitter requires continuous exposure to relatively high levels of CO, which lacks specificity and may cause negative effects. Carbon-monoxide-releasing molecules (CORMs) offer an alternative way to deliver controlled amounts of CO to a specific site of interest (Garcia-Gallego & Bernardes, 2014). The difficulty in using first-generation CORMs in clinical settings arises from their short half-life, low solubility, and the requirement of organic solvents to trigger CO release (Motterlini *et al.*, 2002). Photoactivated carbon monoxide releasing molecules (photoCORMs) present a relatively facile way to trigger CO release with temporal and spatial control (Chakraborty *et al.*, 2014a; Garcia-Gallego & Bernardes, 2014). Enhancing the concentration of a therapeutic to the desired area is an effective way to increase its efficiency and to minimize the side effects due to global exposure. To achieve this, a logical design strategy is to couple the prodrug/drug (in this case, the photoCORM) to an appropriate drug-delivery vehicle. In order to fullfil this goal, suitable chemical functionalization within the photoCORM is necessary that can be subsequently utilized to couple the delivery vehicle. In such pursuits, we have synthesized three photoCORMs, see (**1**)–(**3**) in Scheme 1, bearing a vinylpyridine (4-vpy) group which can be potentially used to crosslink the metal complex into a polymeric drug delivery vehicle. Three fluorogenic ligands, namely 2-(pyridin-2-yl)-1,3-benzothiazole (pbt), 2-(quinolin-2-yl)-1,3-benzothiazole (qbt), and 1,10-phenanthroline (phen) have also been employed as bidenate ligands to derive luminescent rhenium photoCORMs, namely [Re(4-vpy)(pbt)(CO)₃](CF₃SO₃), (**1**), [Re(4-vpy)(qbt)(CO)₃](CF₃SO₃), (**2**), and [Re(4-vpy)(phen)-(CO)₃](CF₃SO₃), (**3**) (see Scheme 1), that can be tracked within the cellular matrices. All three complexes have been characterized with conventional analytical techniques and single-crystal X-ray crystallography. These rhenium-based photoCORMs reveal variable CO release rates upon increasing the degree of conjugation within the bidentate ligand frame. Moreover, this alteration also leads to moderate red shifts in their emission profile. The photobehavior of all three complexes will also be discussed in this article.

2. Experimental

All reagents were of commercial grade and were used without further purification unless stated otherwise. 2-(Pyridin-2-yl)-1,3-benzothiazole (pbt) (Chen *et al.*, 2001) and 2-(quinolin-2-yl)-1,3-benzothiazole (qbt) (Stenger-Smith *et al.*, 2017) were synthesized following reported procedures. 1,10-Phenanthroline (phen) was purchased from Sigma–Aldrich Inc. and was used as received. A PerkinElmer Spectrum-One FT–IR spectrometer was used to record the IR spectra of the ligands

and complexes. UV–Vis spectra were obtained using a Varian Cary 50 UV–Vis spectrophotometer. Luminescence data were recorded using a Cary-Eclipse Fluorescence Spectrophotometer. Microanalyses were obtained using a PerkinElmer Series II 2400 Elemental Analyzer. The ¹H NMR spectra of the complexes were recorded at 298 K on a Varian Unity Inova 500 MHz instrument.

Scheme 1
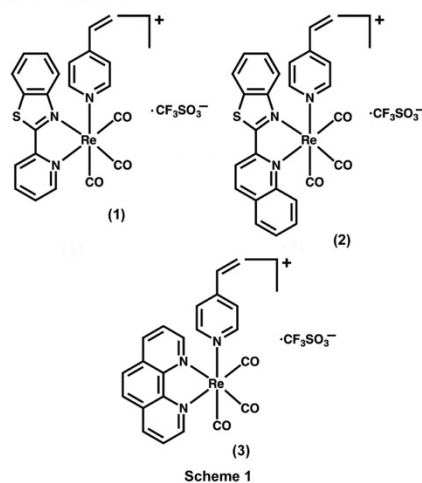
2.1. Synthesis and crystallization

2.1.1. Synthesis of complex (1). A solution of 2-(pyridin-2-yl)-1,3-benzothiazole (0.100 g, 0.47 mmol, 1 equiv.) in chloroform (10 ml) was added to [ReCl(CO)₅] (0.170 g, 0.47 mmol, 1 equiv.) in methanol (20 ml). The mixture was refluxed overnight, resulting in a bright-orange–red solution. The volume of the mixture was then reduced under low pressure until microcrystals of [ReCl(pbt)(CO)₃] were observed. The reaction flask was then stored at 273 K for 1 h. The micro-crystalline material was collected by vacuum filtration, washed with 3–5 ml of hexanes and dried under vacuum to obtain [ReCl(pbt)(CO)₃] as an orange–red powder (yield 0.214 g, 88%). Next, a solution of silver trifluoromethanesulfonate (AgCF₃SO₃, 0.100 g, 0.39 mmol, 1.2 equiv.) in dichloromethane (30 ml) was added to [ReCl(pbt)(CO)₃] (0.168 g, 0.32 mmol, 1 equiv.) and the mixture was refluxed overnight. The solution was filtered using a fritted funnel packed with Celite to remove unreacted silver trifluoromethanesulfonate and silver chloride (AgCl) precipitate. The resulting bright-red filtrate was collected and the solvent volume reduced under vacuum, resulting in a bright-red precipitate. The precipitate was then collected by vacuum filtration and washed with 3–5 ml portions of hexanes, furnishing 0.160 g (79% yield) of [Re(CF₃SO₃)(pbt)(CO)₃] as a red–orange powder. The complex [Re(CF₃SO₃)(pbt)(CO)₃] (0.100 g, 0.16 mmol, 1 equiv.) was dissolved in chloroform (20 ml), followed by the addition

201

Table 1
Experimental details **[Should diffractometers all be the same?]**.

	(1)	(2)	(3)
Crystal data			
Chemical formula	$[Re(C_7H_7N)(C_{12}H_8N_2S)(CO)_3]$-$(CF_3SO_3)\cdot CH_2Cl_2$	$[Re(C_7H_7N)(C_{16}H_{10}N_2S)(CO)_3]$-$(CF_3SO_3)\cdot 0.28H_2O$	$[Re(C_7H_7N)(C_{12}H_8N_2)(CO)_3]$-$(CF_3SO_3)$
M_r	821.62	791.20	704.64
Crystal system, space group	Triclinic, $P\bar{1}$	Monoclinic, $P2_1/n$	Monoclinic, $P2_1/n$
Temperature (K)	293	273	296
a, b, c (Å)	8.596, 11.217, 15.161	12.814 (3), 12.088 (2), 18.248 (4)	12.398 (2), 12.878 (3), 15.393 (3)
α, β, γ (°)	92.88, 104.12, 91.19	90, 96.56 (3), 90	90.00 (3), 91.83 (3), 90.00 (3)
V (Å^3)	1415.1	2808.0 (10)	2456.5 (8)
Z	2	4	4
Radiation type	Mo $K\alpha$	Mo $K\alpha$	Mo $K\alpha$
μ (mm^{-1})	4.70	4.55	5.10
Crystal size (mm)	$0.20 \times 0.18 \times 0.15$	$0.15 \times 0.12 \times 0.10$	$0.18 \times 0.15 \times 0.12$
Data collection			
Diffractometer	Bruker APEXII	Bruker APEXII	Bruker APEXII CCD
Absorption correction	Multi-scan (*SADABS*; Krause *et al.*, 2015)	Multi-scan (*SADABS*; Krause *et al.*, 2015)	Multi-scan (*SADABS*; Krause *et al.*, 2015)
T_{min}, T_{max}	0.635, 0.746	0.611, 0.746	0.490, 0.746
No. of measured, independent and observed [$I > 2\sigma(I)$] reflections	13569, 5706, 5462	25681, 7054, 5250	23150, 5011, 4517
R_{int}	0.017	0.040	0.019
$(\sin\theta/\lambda)_{max}$ (Å^{-1})	0.626	0.684	0.626
Refinement			
$R[F^2 > 2\sigma(F^2)], wR(F^2), S$	0.020, 0.051, 1.04	0.042, 0.104, 1.04	0.019, 0.046, 1.06
No. of reflections	5706	7054	5011
No. of parameters	370	608	481
No. of restraints	0	3097	913
H-atom treatment	H-atom parameters constrained	H-atom parameters constrained	H-atom parameters constrained
$\Delta\rho_{max}, \Delta\rho_{min}$ (e Å^{-3})	0.91, −0.73	1.22, −0.71	1.23, −0.58

Computer programs: *APEX* (Bruker, 2015), *SAINT* (Bruker, 2015), *SHELXT2014* (Sheldrick, 2015*a*), *SHELXL2016* (Sheldrick, 2015*b*), *OLEX2* (Dolomanov *et al.*, 2009) and *publCIF* (Westrip, 2010).

of 4-vinylpyridine (0.173 ml, 1.6 mmol, 10 equiv.). The reaction mixture was refluxed overnight, resulting in a cloudy orange solution. After this time, the reaction mixture was filtered using a fritted funnel and Celite bed to remove a brown residue. The filtrate was collected and the solvent was completely removed under reduced pressure. The resulting solid was recrystallized by layering hexanes over a solution of the complex in dichloromethane to afford 109 mg (93% yield) of [Re(4-vpy)(pbt)(CO)$_3$](CF$_3$SO$_3$), (**1**), as light-orange crystals. Elemental analysis (%) found: C 37.54, H 2.08, N 5.67; calculated for C$_{23}$H$_{15}$F$_3$N$_3$O$_6$ReS$_2$: C 37.50, H 2.05, N 5.70. IR (KBr, cm^{-1}): 3078 (*w*), 2031 (*s*), 1918 (*s*), 1617 (*w*), 1487 (*w*), 1418 (*w*), 1263 (*s*), 1223 (*w*), 1152 (*s*), 1030 (*s*), 944 (*w*), 847 (*w*), 763 (*w*), 724 (*w*), 637 (*s*), 517 (*w*); ^{1}H NMR (CDCl$_3$): δ 9.16 (*d*, 1H), 8.60 (*d*, 1H), 8.44 (*d*, 1H), 8.36 (*t*, 1H), 8.13 (*d*, 1H), 7.98 (*d*, 2H), 7.83 (*m*, 2H), 7.71 (*t*, 1H), 7.18 (*d*, 2H), 6.45 (*m*, 1H), 5.91 (*d*, 1H), 5.52 (*d*, 1H).

2.1.2. Synthesis of complex (2). This complex was prepared following the same procedure used for the preparation of complex (**1**), while employing 2-(quinolin-2-yl)-1,3-benzothiazole (0.125 g, 0.48 mmol) as the ligand (yield 0.105 g, 91%). Elemental analysis (%) found: C 41.25, H 2.21, N 5.38; calculated for C$_{27}$H$_{17}$F$_3$N$_3$O$_6$ReS$_2$: C 41.22, H 2.18, N 5.34. IR (KBr, cm^{-1}): 3066 (*w*), 2033 (*s*), 1934 (*s*), 1913 (*s*), 1616 (*w*), 1590 (*w*), 1518 (*w*), 1427 (*w*), 1260 (*s*), 1148 (*s*), 1093 (*w*), 1029 (*s*), 999 (*w*), 930 (*w*), 853 (*w*), 762 (*w*), 727 (*w*), 636 (*s*), 517 (*w*); ^{1}H NMR (CDCl$_3$): δ 8.90 (*d*, 1H), 8.85 (*d*, 1H), 8.65 (*d*, 1H),

8.57 (*d*, 1H), 8.22 (*d*, 1H), 8.16 (*d*, 1H), 8.11 (*t*, 1H), 8.87 (*t*, 2H), 7.75 (*t*, 1H), 7.52 (*d*, 2H), 7.01 (*d*, 2H), 6.41 (*m*, 1H), 5.86 (*d*, 1H), 5.51 (*d*, 1H).

2.1.3. Synthesis of complex (3). This complex was prepared following the same procedure used for the preparation of complex (**1**), while employing 1,10-phenanthroline (0.090 g, 0.50 mmol) as the ligand (yield 0.112 g, 95%). Elemental analysis (%) found: C 39.24, H 2.17, N 5.92; calculated for C$_{23}$H$_{15}$F$_3$N$_3$O$_6$ReS: C 39.20, H 2.15, N 5.96. IR (KBr, cm^{-1}): 3065 (*w*), 2029 (*s*), 1910 (*s*), 1619 (*w*), 1520 (*w*), 1430 (*w*), 1276 (*s*), 1223 (*w*), 1154 (*s*), 1137 (*s*), 1032 (*s*), 998 (*w*), 944 (*w*), 844 (*w*), 724 (*w*), 636 (*s*); ^{1}H NMR (CDCl$_3$): δ 9.48 (*d*, 2H), 8.76 (*d*, 2H), 8.11 (*m*, 6H), 7.18 (*d*, 2H), 6.39 (*m*, 1H), 5.87 (*d*, 1H), 5.46 (*d*, 1H).

2.1.4. Isolation of single crystals of (1), (2) and (3). Single crystals of all three complexes were obtained by layering hexanes over their dichloromethane solutions. One crystal of each complex was selected and fixed on top of a MiTeGen MicroMounts using Paratone Oil.

2.2. Refinement

Crystal data, data collection and structure refinement details are summarized in Table 1. The non-H atoms were located through instrinsic phasing using *SHELXT* (Sheldrick, 2015*a*) integrated in the *OLEX2* graphical user interface (Dolomanov *et al.*, 2009). H atoms were included in calculated

202

positions riding on the C atoms to which they are bonded, with C—H = 0.93 Å and $U_{iso}(H) = 1.2U_{eq}(C)$. In (2) and (3), the highest residual electron-density peak is located near the Re atom. No satisfactory disorder model could be found to resolve this. In complexes (2) and (3), the triflate counter-anions exhibit disorder.

The triflate anion in complex (2) is disordered over four positions. Two of the positions, with occupancies of 37.5 and 22.2%, have the same orientation of the anion, while the third position contains the anion rotated by 180° so that the –CF$_3$ group is disordered with the –SO$_3$ groups of the anions from the first two domains (12.5%) (Sheldrick, 2015b). The fourth position of the anion is almost perpendicular to the first three and, in this case, the free volume is filled by a partially occupied water molecule. Due to the low occupancy of the water molecule (27.8%) and the extensive disorder of the anion, the H atoms could not be located and are thus not included either in the model or within the sum formula.

The triflate anion in complex (3) is disordered over three positions and the disorder was refined using geometry and U^{ij} similarity restraints (Sheldrick, 2015b). Two of the poisions, with occupancies of 33.8 and 31.8%, have the same orientation of the anion, while the third position contains the anion rotated by 180° so that the –CF$_3$ group is disordered with the –SO$_3$ groups of the anions from the first two domains. The sum of the occupancies of the three refined positions of the triflate anion was restrained to be 1.

3. Results and discussion

In all three title complexes, (1)–(3), the cordination geometry around the Re^I center is distorted octahedral (Tables 2, 3 and 4). In all the structures, the equatorial planes are composed of two cis CO ligands and two N atoms from the bidentate

Figure 2
A perspective view of complex (2), showing the atom-labeling scheme. The minor components of the disordered trifluoromethanesulfonate anion have been omitted for clarity. Displacement ellipsoids are drawn at the 50% probability level.

ligands (pbt, qbt or phen), while the axial positions are occupied by the third CO ligand and the N atom of the vinylpyridine group (Figs. 1, 2 and 3). In (1), the equatorial plane, comprising atoms Re1, C2, C3, N1, and N2, is almost planar, with a mean deviation of 0.018 (3) Å; the corresponding planes in (2) deviate appreciably from planarity [mean deviation = 0.080 (5) Å] and the planarity of the same plane in (3) lies between that of the other two compounds [mean deviation = 0.040 (3) Å]. In complex (1), the chelate ring composed of atoms Re1, N1, C8, C9, and N2 is highly planar, with a mean deviation of 0.020 (5) Å. In contrast, in

Figure 1
A perspective view of complex (1), showing the atom-labeling scheme. Displacement ellipsoids are drawn at the 50% probability level. The chloroform of crystallization has been omitted for clarity.
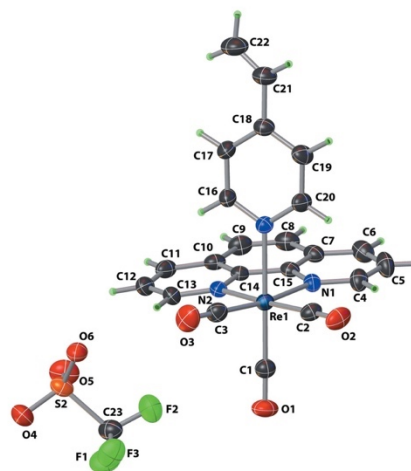
Figure 3
A perspective view of complex (3), showing the atom-labeling scheme. The minor components of the disordered trifluoromethanesulfonate anion have been omitted for clarity. Displacement ellipsoids are drawn at the 50% probability level.

Table 2
Selected geometric parameters (Å, °) for (**1**).

Re1—C2	1.900 (3)	Re1—N2	2.189 (2)
Re1—C1	1.923 (3)	Re1—N1	2.193 (2)
Re1—C3	1.924 (3)	Re1—N3	2.207 (2)
C2—Re1—C1	87.73 (14)	C3—Re1—N1	96.70 (11)
C2—Re1—C3	87.46 (14)	N2—Re1—N1	74.58 (9)
C1—Re1—C3	87.51 (14)	C2—Re1—N3	90.44 (12)
C2—Re1—N2	101.15 (11)	C1—Re1—N3	177.94 (11)
C1—Re1—N2	95.57 (12)	C3—Re1—N3	91.46 (12)
C3—Re1—N2	170.94 (11)	N2—Re1—N3	85.71 (9)
C2—Re1—N1	175.15 (11)	N1—Re1—N3	86.98 (9)
C1—Re1—N1	94.91 (12)		

Table 4
Selected geometric parameters (Å, °) for (**3**).

Re1—C1	1.917 (3)	Re1—N2	2.174 (2)
Re1—C3	1.918 (3)	Re1—N1	2.185 (2)
Re1—C2	1.923 (3)	Re1—N3	2.218 (2)
C1—Re1—C3	88.35 (14)	C2—Re1—N1	98.81 (11)
C1—Re1—C2	88.70 (13)	N2—Re1—N1	75.59 (8)
C3—Re1—C2	88.39 (14)	C1—Re1—N3	178.44 (11)
C1—Re1—N2	91.89 (11)	C3—Re1—N3	92.69 (12)
C3—Re1—N2	97.18 (12)	C2—Re1—N3	92.49 (11)
C2—Re1—N2	174.41 (11)	N2—Re1—N3	86.83 (8)
C1—Re1—N1	96.48 (11)	N1—Re1—N3	82.34 (8)
C3—Re1—N1	171.39 (11)		

Table 3
Selected geometric parameters (Å, °) for (**2**).

Re1—C3	1.909 (5)	Re1—N2	2.176 (4)
Re1—C1	1.910 (6)	Re1—N3	2.214 (4)
Re1—C2	1.924 (6)	Re1—N1	2.222 (4)
C3—Re1—C1	87.9 (2)	C2—Re1—N3	89.5 (2)
C3—Re1—C2	85.7 (2)	N2—Re1—N3	81.63 (14)
C1—Re1—C2	91.2 (2)	C3—Re1—N1	174.73 (18)
C3—Re1—N2	100.42 (18)	C1—Re1—N1	94.45 (18)
C1—Re1—N2	97.63 (19)	C2—Re1—N1	98.97 (18)
C2—Re1—N2	169.40 (18)	N2—Re1—N1	74.63 (14)
C3—Re1—N3	91.92 (19)	N3—Re1—N1	85.63 (13)
C1—Re1—N3	179.21 (19)		

complex (**2**), the chelate ring composed of atoms Re1, N1, C12, C13, and N2 deviates appreciably from planarity [mean deviation = 0.080 (5) Å]. In the case of complex (**3**), the chelate ring composed of atoms Re1, N1, C14, C15, and N2

exhibits a small deviation from planarity [mean deviation = 0.029 (3) Å]. The dihedral angles between the planes of the pyridine ring and the benzothiazole moiety in (**1**) and (**2**) are 7.0 (5) and 10.1 (7)°, respectively. In both cases, the benzothiazole frame is planar, with mean deviations of 0.013 (3) and 0.007 (3) Å for complexes (**1**) and (**2**), respectively. The average Re—C bond lengths in complexes (**1**) and (**2**) are statistically identical [1.915 (3) and 1.912 (7) Å, respectively] (Tables 2 and 3). The average Re—N bond lengths in complexes (**1**) and (**2**) display a similar trend [2.191 (2) and 2.195 (5) Å, respectively]. The average Re—C bond length in complex (**3**) (Table 4) is 1.921 (3) Å, while the average Re—N bond length is marginally shorter [2.179 (2) Å] compared to complexes (**1**) and (**2**). In a structurally similar complex, namely [Re(phen)(pyAl)(CO)$_3$](CF$_3$SO$_3$) (pyAl is pyridine-4-carbaldehyde), the average Re—C [1.919 (6) Å] and Re—N [2.178 (4) Å] bond lengths are statistically identical as those of complex (**3**) (Chakraborty *et al.*, 2017).

The crystal packing of complex (**1**) reveals no intermolecular π–π stacking interactions. However, such interactions have been observed for complexes (**2**) and (**3**). In complex (**2**), offset π–π stacking interactions have been noticed between the quinoline rings of two adjacent molecules

Figure 4
Crystal packing diagram for complex (**1**), showing nonclassical contacts between the aromatic ligand and the triflate anion.
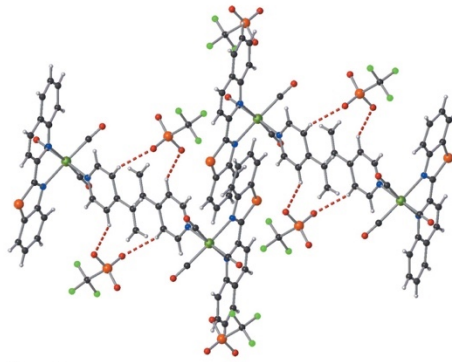
Figure 5
Crystal packing diagram for complex (**2**), showing nonclassical hydrogen-bonding interactions.

204

Table 5
Hydrogen-bond geometry (Å, °) for (**1**).

$D-\mathrm{H}\cdots A$	$D-\mathrm{H}$	$\mathrm{H}\cdots A$	$D\cdots A$	$D-\mathrm{H}\cdots A$
C4—H4···O6^{i}	0.93	2.65	3.333 (5)	131
C5—H5···O5^{i}	0.93	2.65	3.278 (5)	125
C20—H20···O6^{i}	0.93	2.50	3.336 (4)	150
C11—H11···Cl1^{ii}	0.93	2.98	3.640 (4)	129
C24—H24B···O2^{iii}	0.97	2.28	3.189 (6)	156

Symmetry codes: (i) $x, y-1, z$; (ii) $-x+2, -y+1, -z+1$; (iii) $x+1, y, z$.

Table 6
Hydrogen-bond geometry (Å, °) for (**2**).

$D-\mathrm{H}\cdots A$	$D-\mathrm{H}$	$\mathrm{H}\cdots A$	$D\cdots A$	$D-\mathrm{H}\cdots A$
C5—H5···F1B^{i}	0.93	2.33	3.045 (17)	134
C11—H11···O5^{ii}	0.93	2.53	3.459 (16)	178
C11—H11···O4A^{ii}	0.93	2.62	3.48 (3)	154
C11—H11···F3A^{ii}	0.93	2.62	3.199 (19)	121
C11—H11···O4B^{ii}	0.93	2.39	3.31 (3)	168
C11—H11···O6C^{ii}	0.93	2.50	3.27 (3)	140
C21—H21···O4A^{iii}	0.93	2.52	3.35 (3)	150
C21—H21···O4B^{iii}	0.93	2.53	3.26 (3)	136
C21—H21···F2C^{iii}	0.93	2.41	3.27 (3)	154
C23—H23···O6A^{iv}	0.93	2.46	3.23 (2)	141
C23—H23···F3C^{iv}	0.93	2.61	3.44 (3)	150
C24—H24···O7^{v}	0.93	2.18	2.96 (2)	141

Symmetry codes: (i) $-x+\frac{1}{2}, y-\frac{1}{2}, -z+\frac{1}{2}$; (ii) $x-\frac{1}{2}, -y+\frac{3}{2}, z+\frac{1}{2}$; (iii) $-x+\frac{3}{2}, y-\frac{1}{2}, -z+\frac{1}{2}$; (iv) $x-\frac{1}{2}, -y+\frac{1}{2}, z+\frac{1}{2}$; (v) $-x+1, -y+1, -z+1$.

Table 7
Hydrogen-bond geometry (Å, °) for (**3**).

$D-\mathrm{H}\cdots A$	$D-\mathrm{H}$	$\mathrm{H}\cdots A$	$D\cdots A$	$D-\mathrm{H}\cdots A$
C20—H20···F2A^{i}	0.93	2.40	3.24 (2)	149
C20—H20···O4B^{i}	0.93	2.57	3.42 (2)	152
C13—H13···O6B	0.93	2.41	3.15 (3)	136
C12—H12···O5B	0.93	2.58	3.30 (2)	135
C17—H17···F3B^{ii}	0.93	2.56	3.42 (3)	154
C16—H16···N2	0.93	2.61	3.116 (4)	115
C16—H16···F1^{ii}	0.93	2.63	3.34 (3)	133
C16—H16···O4A^{ii}	0.93	2.58	3.23 (3)	127
C16—H16···F1B^{ii}	0.93	2.57	3.22 (2)	127
C4—H4···O4^{i}	0.93	2.44	3.19 (3)	139
C4—H4···O4B^{i}	0.93	2.56	3.24 (3)	130
C5—H5···O6A^{i}	0.93	2.59	3.27 (2)	130

Symmetry codes: (i) $x-1, y, z$; (ii) $-x+\frac{3}{2}, y-\frac{1}{2}, -z+\frac{1}{2}$.

As seen in complexes (**1**) and (**2**), these interactions also result in a three-dimensional hydrogen-bonded network connected through the triflate anions.

The IR spectra of the reported complexes display strong CO stretches indicative of a *facial* disposition of the three carbonyl groups. All the complexes exhibit well-resolved ^{1}H NMR spectra, with no line broadening. This is consistent with the complexes being diamagnetic, as would be expected for low-spin Re^{I} ions d^{6} in an octahedral ligand field. Complexes (**1**), (**2**), and (**3**) display strong absorption bands centered around 340, 386, and 277 nm, respectively. These complexes are indefinitely stable in dichloromethane solutions under dark conditions. Moreover, upon exposure to UV-A irradiation (λ = 365 nm), these complexes exhibit no changes in their electronic absorption spectra. However, upon exposure to UV-B irradiation (λ = 302 nm), the absorption bands of the complexes showed systematic changes (a representative case is shown in Fig. 7). These changes are associated with CO photorelease, as was also evidenced by a standard myoglobin assay (Chakraborty *et al.*, 2014*b*). The apparent rate of CO release (κ_{CO}) have been determined spectrophotometrically by monitoring the changes in spectral traces upon UV-light irradiation at regular time intervals (2 min). The κ_{CO} values, obtained from the plots of $\ln(C)$ *versus* time (t), are 0.05±0.02, 0.13±0.02, and 0.08±0.02 min^{-1} for complexes (**1**), (**2**), and

[centroid-to-centroid distance = 3.852 (5) Å]. In complex (**3**), considerable π–π stacking interactions were apparent between the two phenanthroline rings of two adjacent molecules [centroid-to-centroid distance between the two central phenanthroline rings = 3.579 (5) Å]. In complex (**1**), examination of the extended structure revealed a few nonclassical hydrogen-bonding contacts (Fig. 4 and Table 5). These interactions result in a three-dimensional network of hydrogen-bonded molecules within the lattice. In complex (**2**), analysis of the packing pattern revealed three nonclassical hydrogen-bonding interactions (Fig. 5 and Table 6). Primarily, these interactions are from the aromatic ligands to the triflate anions. Inspection of these contacts reveals that the ensemble is a three-dimensional hydrogen-bonded network. The extended lattice of complex (**3**) was consolidated by several nonclassical hydrogen-bonding contacts (Fig. 6 and Table 7).

Figure 6
Crystal packing diagram for complex (**3**), showing nonclassical hydrogen-bonding contacts.

Figure 7
Spectral changes of complex (**2**) in dichloromethane solution upon exposure to UV-B light (5 mW cm^{-2}).

205

(**3**), respectively (concentration of 5×10^{-5} *M*). Upon excitation of dichloromethane solutions of the complexes at 350 nm, (**1**), (**2**), and (**3**) exhibit strong luminescence centered around 611, 652, and 542 nm, respectively (Fig. 8). The change in luminescence upon CO release can be potentially utilized to track the delivery of CO to specific targets.

In summary, three photoactive Re^{I}–carbonyl complexes derived from three fluorogenic ligands have been synthesized and structurally characterized. These complexes could potentially be employed as trackable CO-donating prodrugs towards biological targets. Additionally, the vinylpyridine ancillary ligand could be used to facilitate anchoring of the complexes covalently into a host polymeric drug carrier by conventional radical-initiated polymerization reactions.

Figure 8
Emission spectrum of complexes (**1**) (orange trace), (**2**) (red trace), and (**3**) (yellow trace) in dichloromethane solutions at 298 K.

References

Bruker (2015). *APEX* and *SAINT*. Bruker AXS Inc., Madison, Wisconsin, USA.
Chakraborty, I., Carrington, S. J. & Mascharak, P. K. (2014*a*). *Acc. Chem. Res.* **47**, 2603–2611.
Chakraborty, I., Carrington, S. J. & Mascharak, P. K. (2014*b*). *ChemMedChem*, **9**, 1266–1274.
Chakraborty, I., Jimenez, J. & Mascharak, P. K. (2017). *Chem. Commun.* **53**, 5519–5522.
Chen, X., Femia, F. J., Babich, J. W. & Zubieta, J. (2001). *Inorg. Chim. Acta*, **314**, 91–96.
Chin, B. Y., Jiang, G., Wegiel, B., Wang, H. J., MacDonald, T., Zhang, X. C., Gallo, D., Cszimadia, E., Bach, F. H., Lee, P. J. & Otterbein, L. E. (2007). *Proc. Natl Acad. Sci.* **104**, 5109–5114.
Dolomanov, O. V., Bourhis, L. J., Gildea, R. J., Howard, J. A. K. & Puschmann, H. (2009). *J. Appl. Cryst.* **42**, 339–341.
Garcia-Gallego, S. & Bernardes, G. J. L. (2014). *Angew. Chem. Int. Ed.* **53**, 9712–9721.
Haschemi, A., Wagner, O., Marculescu, R., Wegiel, B., Robson, S. C., Gagliani, N., Gallo, D., Chen, J. F., Bach, F. H. & Otterbein, L. E. (2007). *J. Immunol.* **178**, 5921–5929.
Krause, L., Herbst-Irmer, R., Sheldrick, G. M. & Stalke, D. (2015). *J. Appl. Cryst.* **48**, 3–10.
Motterlini, R., Clark, J. E., Foresti, R., Sarathchandra, P., Mann, B. E. & Green, C. J. (2002). *Circ. Res.* **90**, e17–e24.
Motterlini, R. & Otterbein, L. E. (2010). *Nat. Rev. Drug Discov.* **9**, 728–743.
Otterbein, L. E., Bach, F. H., Alam, J., Soares, M., Lu, H. T., Wysk, M., Davis, R. J., Flavell, R. A. & Choi, A. M. K. (2000). *Nat. Med.* **6**, 422–428.
Pintadosi, C. A. (2008). *Free Radic. Biol. Med.* **45**, 562–569.
Sheldrick, G. M. (2015*a*). *Acta Cryst.* A**71**, 3–8.
Sheldrick, G. M. (2015*b*). *Acta Cryst.* C**71**, 3–8.
Stec, D. E., Drummond, H. A. & Vera, T. (2008). *Hypertension*, **51**, 597–604.
Stenger-Smith, J., Chakraborty, I., Carrington, S. & Mascharak, P. (2017). *Acta Cryst.* C**73**, 357–361.
Wegiel, B., Gallo, D., Csizmadia, E., Harris, C., Belcher, J., Vercellotti, G. M., Penacho, N., Seth, P., Sukhatme, V., Ahmed, A., Pandolfi, P. P., Helczynski, L., Bjartell, A., Persson, J. L. & Otterbein, L. E. (2013). *Cancer Res.* **73**, 7009–7021.
Westrip, S. P. (2010). *J. Appl. Cryst.* **43**, 920–925.
Yoshida, T. & Migita, C. T. (2000). *J. Inorg. Biochem.* **82**, 33–41.
Zuckerbraun, B. S., Billiar, T. R., Otterbein, S. L., Kim, P. K., Liu, F., Choi, A. M. K. & Otterbein, L. E. (2003). *J. Exp. Med.* **198**, 1707–1716.

206

supporting information

Synthesis and structures of photoactive rhenium carbonyl complexes derived from 2-(pyridin-2-yl)-1,3-benzothiazole, 2-(quinolin-2-yl)-1,3-benzothiazole and 1,10-phenanthroline

Miguel Pinto, Indranil Chakraborty, Jorge Martinez-Gonzalez and Pradip Mascharak

Computing details

For all structures, data collection: *APEX* (Bruker, 2015); cell refinement: *SAINT* (Bruker, 2015); data reduction: *SAINT* (Bruker, 2015); program(s) used to solve structure: SHELXT2014 (Sheldrick, 2015*a*); program(s) used to refine structure: *SHELXL2016* (Sheldrick, 2015*b*); molecular graphics: *OLEX2* (Dolomanov *et al.*, 2009); software used to prepare material for publication: *OLEX2* (Dolomanov *et al.*, 2009) and *publCIF* (Westrip, 2010).

fac-Tricarbonyl[2-(pyridin-2-yl)-1,3-benzothiazole-$\kappa^2 N,N'$](4-vinylpyridine-κN)rhenium(I) trifluoromethanesulfonate (1)

Crystal data

[Re(C$_7$H$_7$N)(C$_{12}$H$_8$N$_2$S)(CO)$_3$](CF$_3$SO$_3$)·CH$_2$Cl$_2$	$Z = 2$
$M_r = 821.62$	$F(000) = 796$
Triclinic, $P\bar{1}$	$D_x = 1.928$ Mg m^{-3}
$a = 8.596$ Å	Mo $K\alpha$ radiation, $\lambda = 0.71073$ Å
$b = 11.217$ Å	Cell parameters from 9893 reflections
$c = 15.161$ Å	$\theta = 2.2–28.9°$
$\alpha = 92.88°$	$\mu = 4.70$ mm^{-1}
$\beta = 104.12°$	$T = 293$ K
$\gamma = 91.19°$	Yellow, block
$V = 1415.1$ Å^3	$0.20 \times 0.18 \times 0.15$ mm

Data collection

Bruker APEXII diffractometer	13569 measured reflections
Radiation source: fine-focus sealed tube	5706 independent reflections
Graphite monochromator	5462 reflections with $I > 2\sigma(I)$
Detector resolution: 8.33 pixels mm^{-1}	$R_{int} = 0.017$
ω–scans	$\theta_{max} = 26.4°$, $\theta_{min} = 2.2°$
Absorption correction: multi-scan (SADABS; Krause *et al.*, 2015)	$h = -10 \rightarrow 10$
	$k = -14 \rightarrow 14$
$T_{min} = 0.635$, $T_{max} = 0.746$	$l = -18 \rightarrow 18$

Refinement

Refinement on F^2	$S = 1.04$
Least-squares matrix: full	5706 reflections
$R[F^2 > 2\sigma(F^2)] = 0.020$	370 parameters
$wR(F^2) = 0.051$	0 restraints

207

Chapter 3.I: Photo-Induced Eradication of Human Colorectal Adenocarcinoma HT-29 Cells by Carbon Monoxide (CO) Delivery from a Mn-Based Luminescent PhotoCORM

3.I.1 Background.

The surprising discovery of salutary effects of carbon monoxide (CO) in mammalian pathophysiology has spurred intense research activity in establishing the therapeutic potential of this noxious gas.[1-5] CO, endogenously produced during the catabolism of heme by the enzyme heme oxygenase (HO), has been identified as an important signaling molecule that participates in various physiological pathways.[6-13] Modulation of these pathways could be selectively achieved by exogenous delivery of CO to specific targets. The noxious nature of this unusual signaling molecule however presents a challenge for its controlled delivery in a hospital setting. CO-releasing molecules (CORMs) provide an alternative means to deliver of CO to biological targets. Among these CO-donors, photoactivated CORMs (photoCORMs) prove advantageous due to their ability to release CO upon exposure to light of various wavelengths.[14-23]

A great majority of photoCORMs has been derived from groups 7 and 8 transition metals.[24-44] Some of the group 7 metal carbonyl complexes have inherent luminescence and have been used as bioimaging agents.[21,33-35,40-43] Although many of these luminescent complexes have been used as CO donors, they require the use of ultraviolet light to release CO and therefore not suitable for biological applications.

Mn(I)-based photoCORMs can be activated with low- power visible light and are therefore preferred for CO delivery to biological targets.[15,21,29,32,36,43] A majority of these complexes has been employed to eradicate selected cancer cell lines in a concentration dependent manner upon visible light excitation. Unfortunately, the Mn(I)-based photoCORMs are inherently non-luminescent despite the use of highly luminescent chelating ligands.[33-35,44] Such quenching of the fluorophore imparted by the Mn(I) center makes it difficult to follow the internalization and localization of the prodrug (photoCORM) before the drug (CO) is delivered. Clearly, different design principles must be implemented toward isolation of Mn(I)-based photoCORMs to circumvent the fluorescence quenching imparted by the Mn(I) center.

In a recent paper, Schiller and coworkers have reported a visible-light active photoCORM [Mn(CO)₃(L)](CF₃SO₃) (**1,** Scheme 1) in which the ligand L is a tridentate aminopyridine ligand with the highly fluorescent dansyl moiety *directly attached* to the central N atom of L through a eSO2e link.[35] The direct binding of the N atom to the Mn (I) center in this photoCORM resulted in almost complete quenching of the fluorescence of the dansyl group. We have utilized the same dansyl moiety in our previous work to isolate a Mn(I)-based photoCORM [Mn(CO)₃(phen)(Imdansyl)](CF₃SO₃) (**2,** Imdansyl = a fluorescent ligand imidazoledansyl, Scheme 1) in which the dansyl unit is connected to the Mn(I) center through an intervening imidazole group.[43] The imidazole linker in **2** separates the fluorophore from the Mn(I) center and retains most of its emissive properties. In this case, the imidazole linker contains two N donor centers one of which is coordinated

directly to the Mn(I) center while the second N atom is attached to the dansyl moiety through the same -SO2- link. Interestingly **2** is a moderately luminescent photoCORM that allowed us, for the first time, to track the prodrug within cellular matrix. The imidazole moiety in **2** provides partial separation between the Mn(I) center and the dansyl moiety leading to ~10% quenching of its fluorescence.[12]

In this chapter we will discuss the complex [Mn(CO)$_3$(phen)(Pipdansyl)] (CF$_3$SO$_3$) **3** which makes use of a different dansyl derivative namely, 1-dansylpiperazine (Pipdansyl), coordinated to an axial position of the Mn(I) center. The Pipdansyl ligand is highly luminescent and displays a bright green emission in acetonitrile (MeCN) and in aqueous media. This piperazine linker has two nitrogens serving different functions analogous to the imidazole moiety of Imdansyl. However,
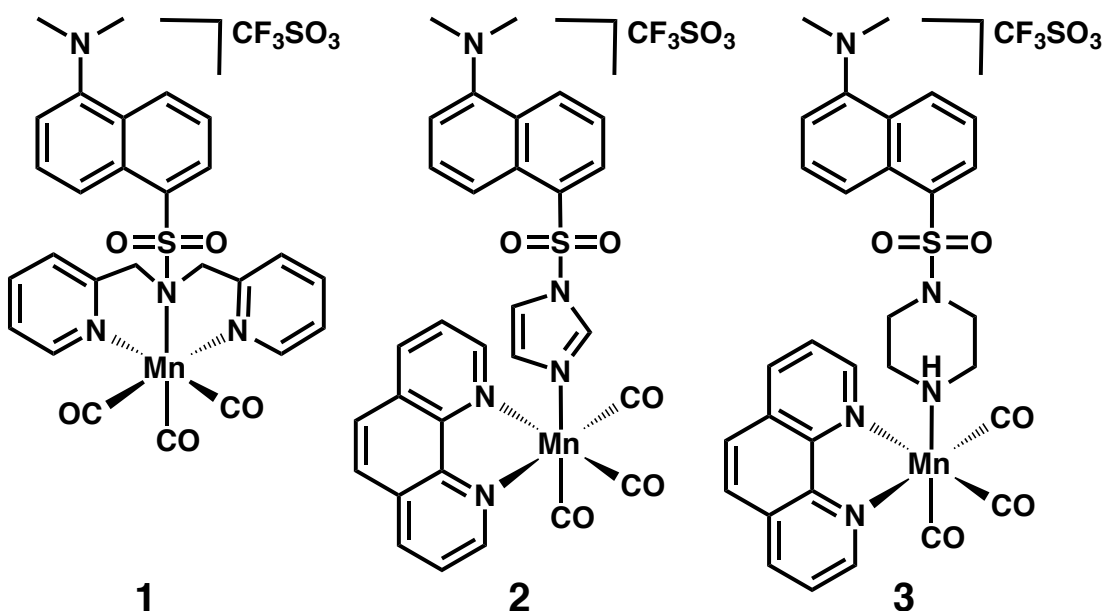
Figure 3.I.1. Schematic representation of Mn(I)-based photoCORMs **1** (reported by the Schiller group),[35] **2** (reported by our group),[43] **3** present work.

the N donors of Pipdansyl are separated by two saturated carbons and thus the Pip group is not in conjugation with the dansyl fluorophore (as it is in Imdansyl). Such separation leads to minimum fluorescence quenching when Pipdansyl is coordinated to the Mn(I) center in **3**. As a consequence, **3** is strongly luminescent and allows trackability of this photoCORM in cellular media. Much like other reported Mn(I)-based photoCORMs, complex **3** is able to release all three CO molecules upon exposure to low-power visible light. In addition, confocal microscopy images show rapid internalization of complex **3** to human colorectal cancer (HT-29) cells and the photoCORM leads to a concentration dependent reduction in the viability of HT-29 cells upon exposure to visible light. Taken together, the mode of conjugation of the fluorophore to the Mn(I) centers of this kind of photoCORMs appears to be an important determinant of their final luminescence characteristics.

3.I.2 Results and Discussion.

*3.I.2.1 Synthesis, Characterization, and Stability of **3**.*

The manganese complex **3** was synthesized by reacting $[Mn(CO)_3(phen)(CF_3SO_3)]$ (previously reported by us)[44] with 1-dansylpiperazine (Pipdansyl) under dark condition. The reaction mixture was allowed to stir for 48 h to ensure completion. The excess/unreacted ligand 1-dansylpiperazine was washed away using diethyl ether. The complex was obtained as a yellow microcrystalline powder after recrystallization from dichloromethane and hexanes. The isolated solid afforded satisfactory elemental analysis. The identity of the complex was also confirmed

through high-resolution mass spectrometry using positive ionization mode. The major

peak at $m/z = 638.12$ corresponded to complex **3** without the trifluoromethane sulfonate

counter anion. The counter anion did travel with the complex as indicated by a

moderate signal at $m/z = 786.93$. Interestingly, a small peak corresponding to two

cations of **3** and one trifluoromethane sulfonate counter ion was also observed at $m/z =$

1425.20 (Figure 3.I.2).
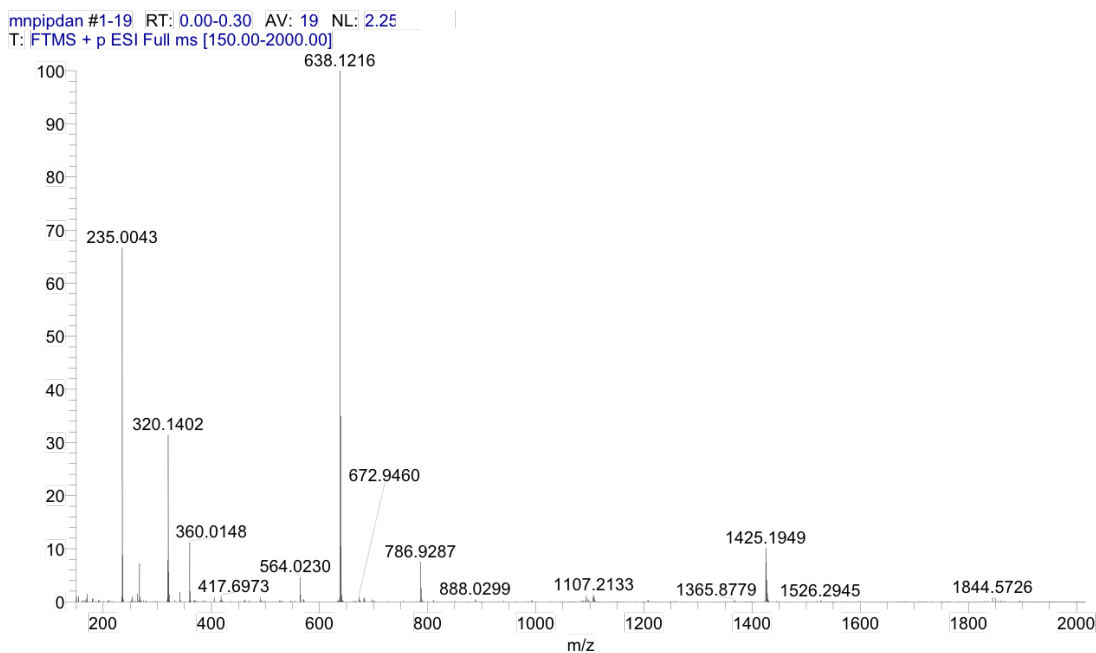
Figure 3.I.2. HR-MS (Electron Spray Ionization) of complex **3** ([Mn(CO)$_3$(phen)

(PipDan)]CF$_3$SO$_3$**)**. Fragmentation pattern: m/z 235.0043 = (5-(dimethylamino)

naphthalene-1-sulfonyl)$^+$ fragment; m/z 320.1402 = [Mn(CO)$_3$(phen)]$^+$ fragment; m/z

638.1216 = [Mn(CO)$_3$(phen)(PipDan)]$^+$ fragment; m/z 786.9287 = ([Mn(CO)$_3$(phen)

(PipDan)]CF$_3$SO$_3$)$^+$; m/z 638.1216 = ([Mn(CO)$_3$(phen)(PipDan)]$_2$CF$_3$SO$_3$)$^+$ fragment.

Complex **3** is soluble in common organic solvents and such solutions are stable when kept in the dark. Stability of **3** in a 2% MeCN in PBS (v/ v) solution was checked by recording the absorption spectrum periodically for a 24 h period when no significant decomposition of the complex was observed when the solution was kept in the dark (Figure 2.I.3). However, such a solution exhibit systematic changes in the electronic absorption spectra upon exposure to low power (15 mW/cm2) broad- band visible light (vide infra).
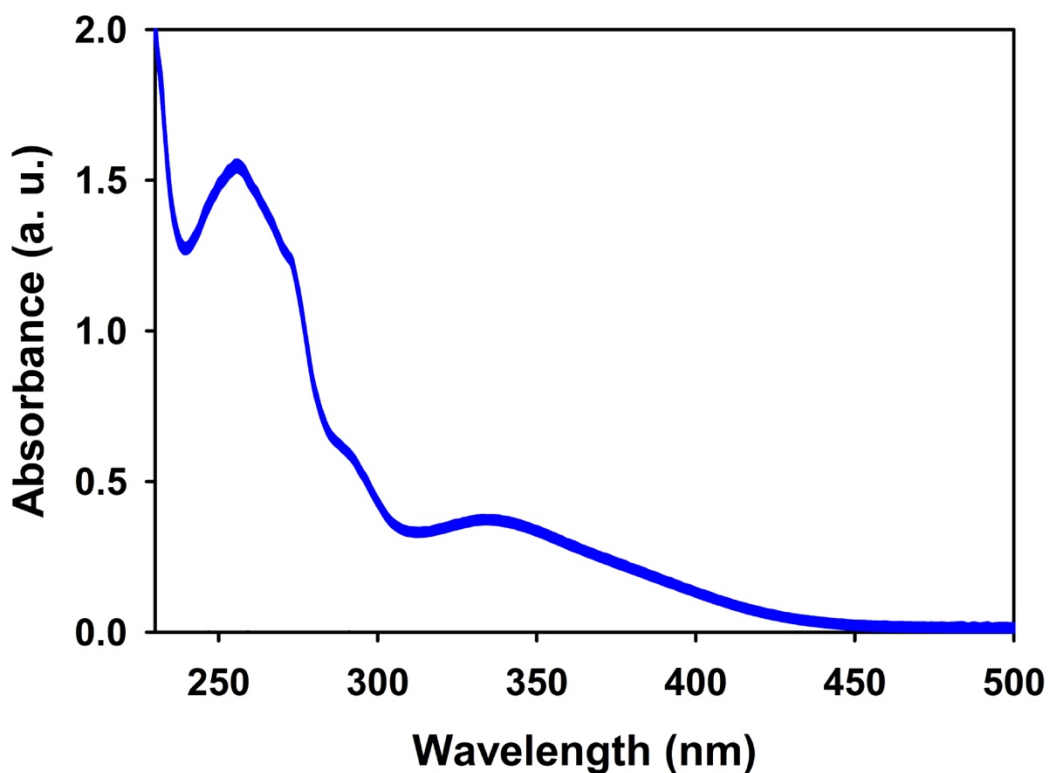
Figure 3.I.3. Stability of complex **3** in PBS solutions containing 2% MeCN (v/v) over a period of 24 h.

3.I.2.2 CO Release Rate of Complex 3.

The rate of CO-release (k_{CO}) from **3** (0.13min^{-1}) was calculated from the changes in electronic absorption spectra upon exposure of **3** in MeCN to visible light (15 mW cm^{-2}) at regular time intervals (Figure 3.I.4). Quantum yield measurement with potassium ferrioxalate as the actinometer yielded a value of 0.39 ± 0.03 for this photoCORM. A myoglobin assay was also carried out to further confirm the release of CO from complex **3** upon exposure to visible light.
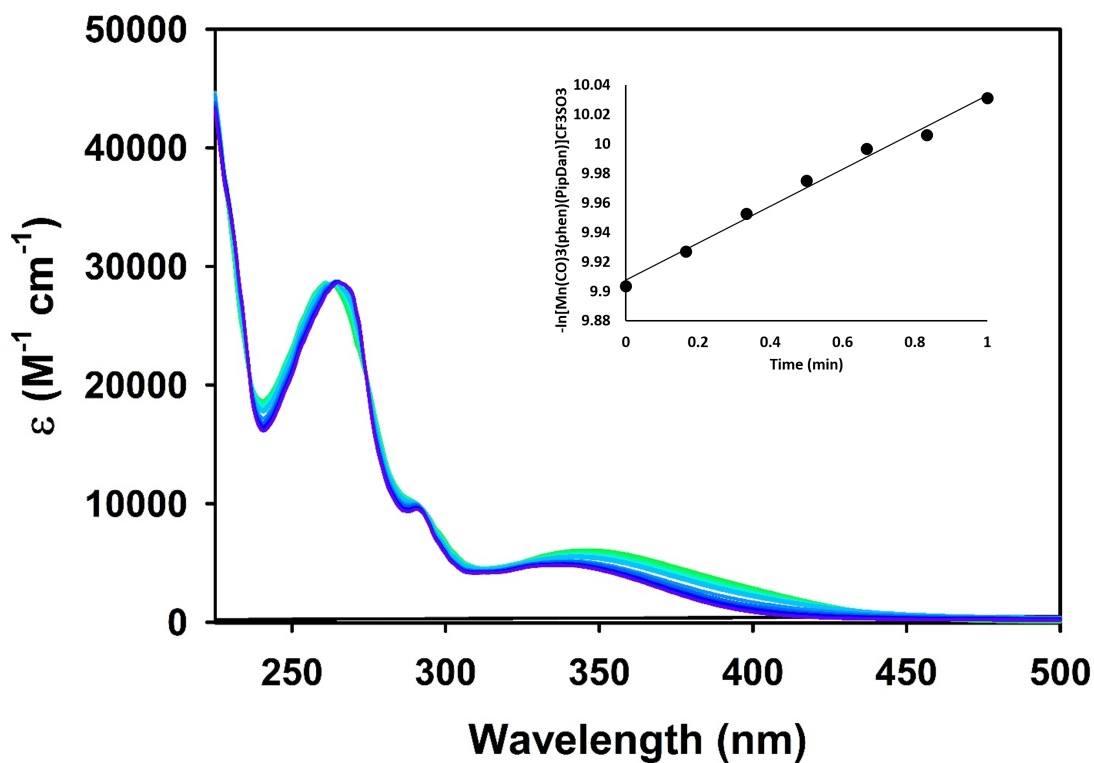
Figure 3.I.4. Systematic changes in the electronic absorption spectrum of **3** upon exposure to small intervals of visible light (15 mW cm^{-2}, 10 s intervals, 298 K) due to CO photorelease.

3.I.2.3 Myoglobin Assay.

The myoglobin assay was carried out in a two-cuvette system to circumvent possible interference from the reducing agent. The first cuvette containing **3** in MeCN was exposed to the same low-power visible light for 5 min and CO released upon such exposure was transferred via canula to a second cuvette containing the reduced myoglobin. The formation of carboxy myoglobin was confirmed by shift of the Soret band of reduced myoglobin from 435 to 424 (Figure 3.I.5).
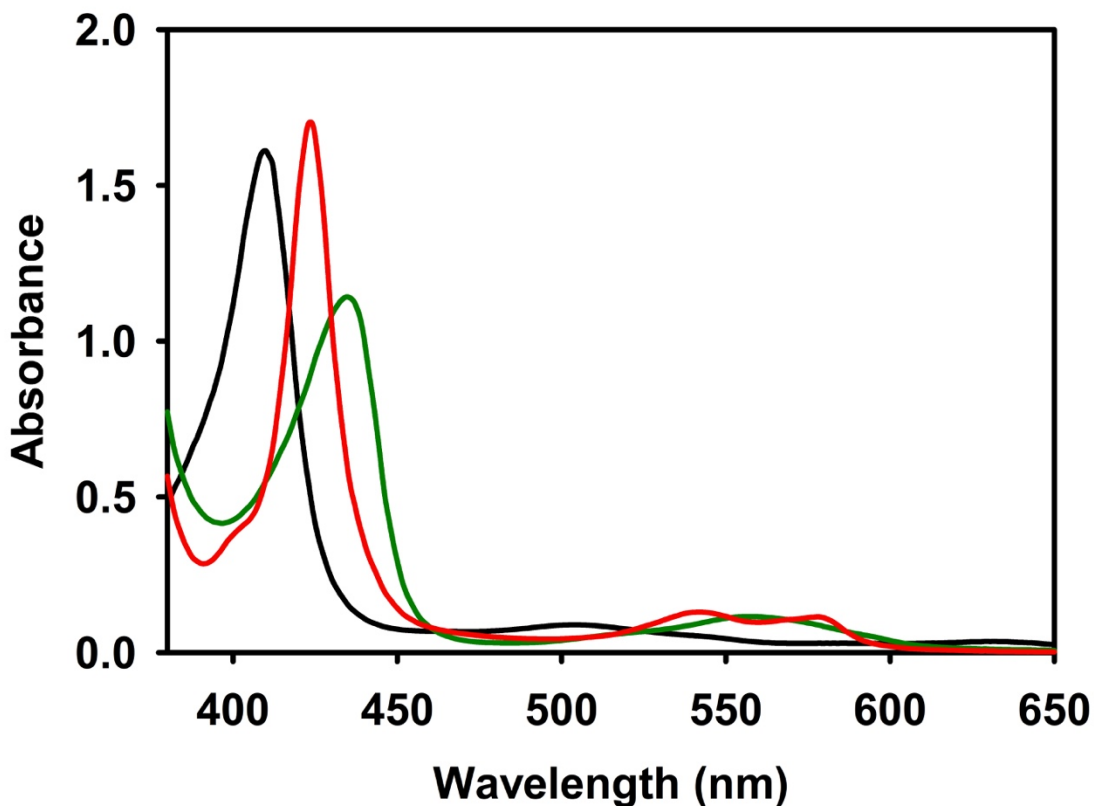
Figure 3.I.5. Myoglobin assay performed using complex **3** triggered by visible light (15 mW cm^{-2}) for 5 min. Shift of the Soret band from 435 nm to 424 nm indicates the formation of Mb$_{CO}$. The black trace represents the absorbance of oxidized myoglobin.

3.I.2.4 Infrared Spectroscopy Studies.

Infrared spectroscopy was employed to assess the number of CO molecules released from **3** upon photolysis. Complex **3** exhibits a set of two strong IR bands at 2036 and 1944 cm^{-1} arising from 3 CO ligands in facial disposition (Figure 3.I.6, blue trace). A batch solution of **3** in MeCN was photolyzed using visible light in a glass petri dish for 40 min, dried under vacuum, and the resulting residue was analyzed by IR spectroscopy. Exhaustive photolysis of complex **3** resulted in complete loss of CO as indicated by the disappearance of the CO bands (Figure 3.I.6, black trace). Similar loss
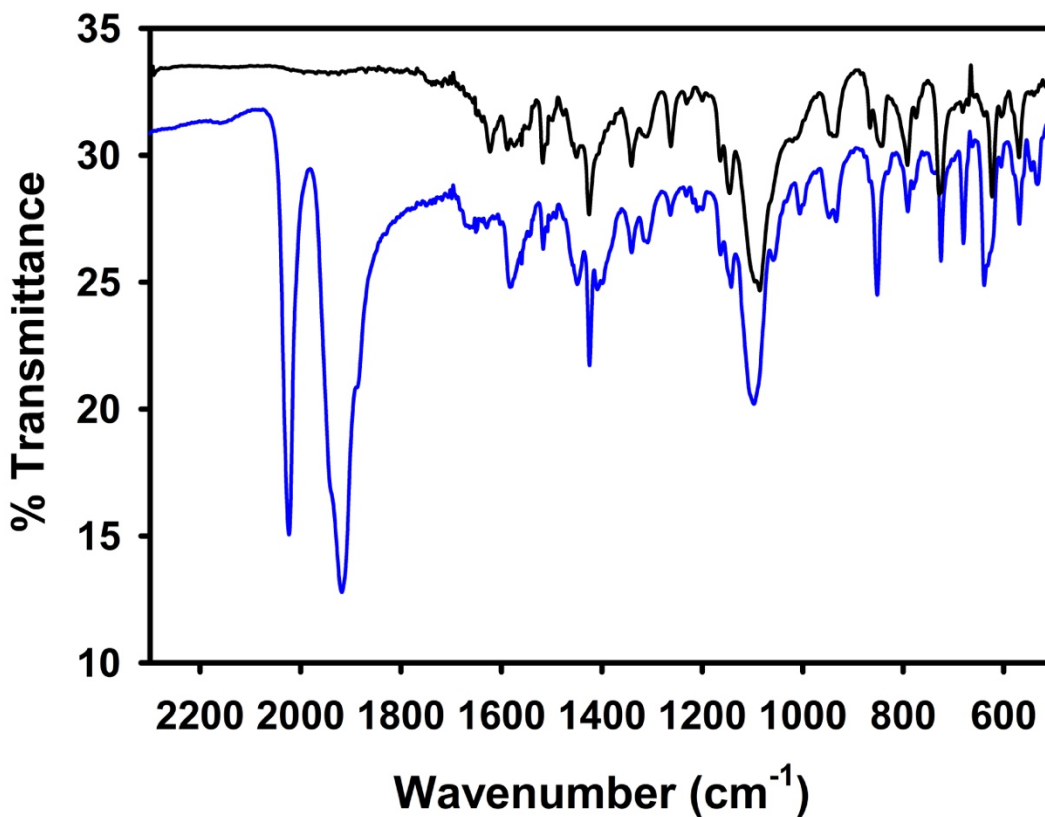
Figure 3.I.6. IR spectra of **3** (blue trace) and its photoproduct (black trace).

of all 3 CO molecules has been observed with other Mn(I)-derived photoCORMs in previous studies.[33,43,45] In case of photo-CORM **2**, loss of three CO molecules led to formation of [Mn(phen)$_2$(H2O)$_2$](CF$_3$SO$_3$)$_2$ and [Mn(phen)$_3$](CF$_3$SO$_3$)$_2$ in a photolyzed solution in addition to free Imdansyl ligand.[46] In the present study high-resolution ESI-MS data on the photolyzed solution of **3** indicated the presence of [Mn(MeOH)$_4$(CF$_3$SO$_3$)]$^+$ and [Mn(phen)$_2$(CF$_3$SO$_3$)]$^+$ species in addition to free phen and Pipdansyl ligands.

3.1.2.5 Luminescence Studies.

The majority of Mn(I)-based photoCORMs derived from fluorescent ligands exhibit no luminescence and hence their accumulation within target cells can hardly be noted. The luminescence of the ligands is quenched upon coordination to the manganese center. In case of photoCORM **1**, reported by Schiller and coworkers, the luminescence of the aminopyridine-dansyl ligand L was completely quenched upon coordination of the N donors to the Mn(I) center.[35] In the case of this ligand L, the dansyl moiety is directly connected to the central N donor which in turn is directly coordinated to the Mn(I) center. In this photoCORM, the PET arising from excitation of the N electron(s) to the dansyl π system is quenched due to the electron-withdrawing effect of the [Mn(CO)$_3$] unit. When the 3 CO molecules are released (upon illumination), the fluorescence of L is observed. In our previous account, the dansyl moiety of the Imdansyl ligand retains most of its luminescence in photoCORM **2** because the intervening imidazole ring partially disconnects the dansyl group from the

electron withdrawing effects of the [Mn(CO)₃] unit. The two distinct N atoms of the imidazole linker in **2** serve different functions. One N is bonded to the dansyl moiety (allowing PET to occur) while the second N is coordinated to the Mn(I) center. The aromaticity of the imidazole linker however allows some mixing of the PET process with the electron withdrawing effects of the [Mn(CO)₃] unit giving rise to *partial quenching*. In **3**, the aromaticity is absent in the piperazine linker and hence the luminescence of the Pipdansyl ligand is *barely* (> 5%) *quenched* when coordinated to the metal center (Figure 3.I.7). The luminescence intensity of the ligand is fully restored after photolysis of a solution of **3** (Figure 3.I.7).
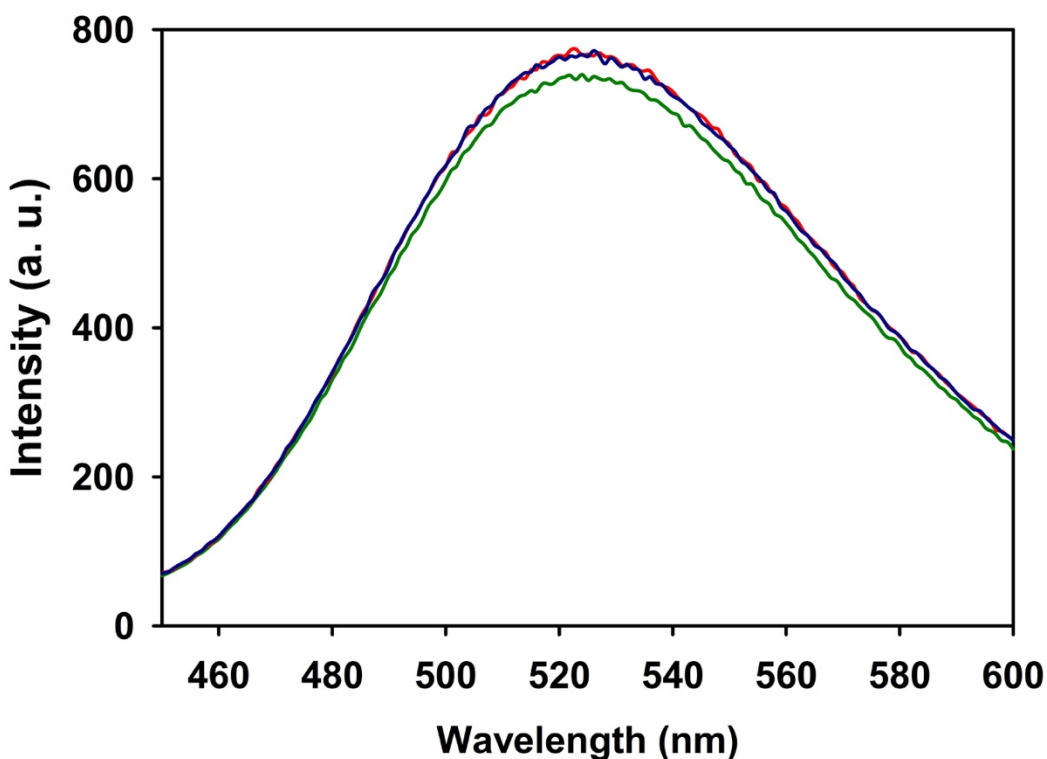
Figure 3.I.7. Emission spectra of **3** (dark green trace), photolyzed solution of **3** (blue trace), and free Pipdansyl ligand (red trace) in MeCN at 298 K.

The change of the linker from imidazole (in photoCORM **2**) to piperazine (in photoCORM **3**) also leads to a *higher luminescence intensity of **3** compared to **2*** under identical concentrations (Figure 3.I.8). This property of **3** could be conveniently exploited in cellular confocal microscopy studies. Furthermore, the emission of **3** (520nm) lies in the green channel which is somewhat preferable in studies where the prodrug is tracked in the green channel and its target (like mitochondria or membrane proteins) is imaged in the red channel.
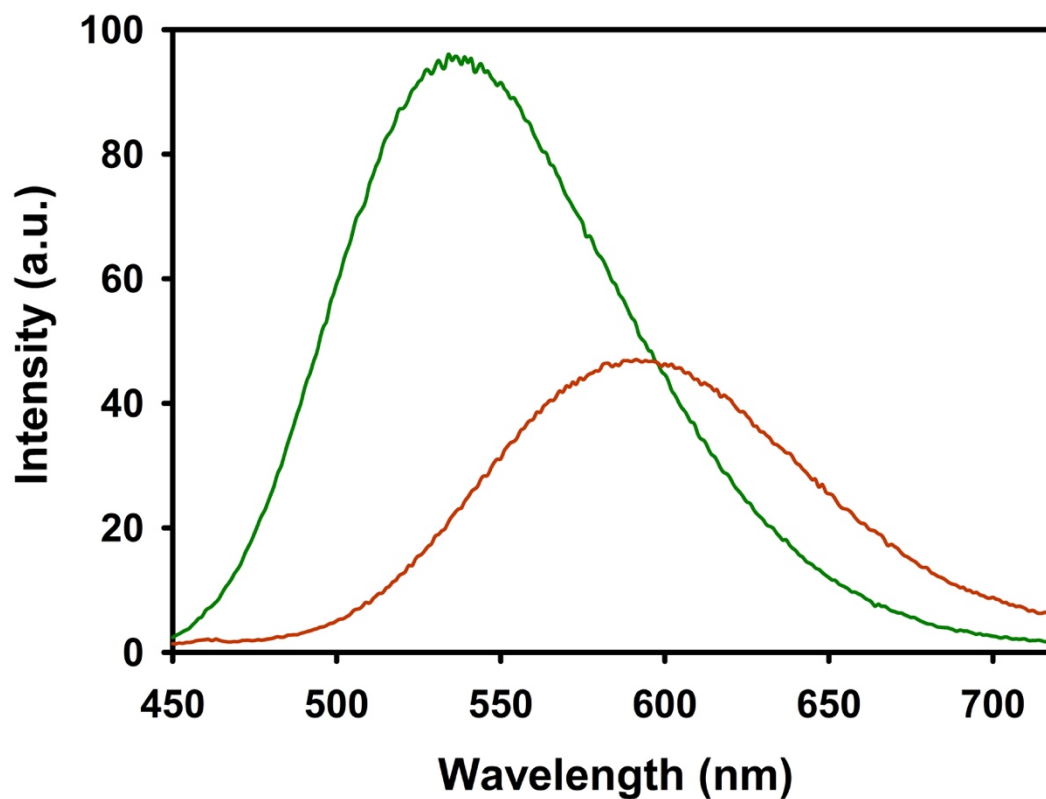
Figure 3.I.8. Emission spectra of **3** (green trace) and **2** (orange-red trace) in MeCN (same concentration).

3.I.2.6 HT-29 Cellular Internalization of Complex 3 and Confocal Microscopy Imaging.

The excellent luminescent properties of **3** prompted us to study its cellular uptake in HT-29 colorectal adenocarcinoma cells. The cells were plated onto imaging disks and allowed to grow for 24 h. Next, they were incubated with 25 μM of **3** for 1 h. The medium was then aspirated, and the cells were washed with PBS. Fresh media free of phenol red and FBS was added to the cells and the images were captured using a confocal microscope to reveal the cellular uptake of **3** into HT-29 cells (Figure 3.I.9). Complex **3** is the second example of a Mn-based photo-CORM that can be tracked inside cancer cells before the CO is released from the complex. The intense luminescence of **3** allows the cells to be imaged at a lower concentration than the previously reported complex **2**.[43]
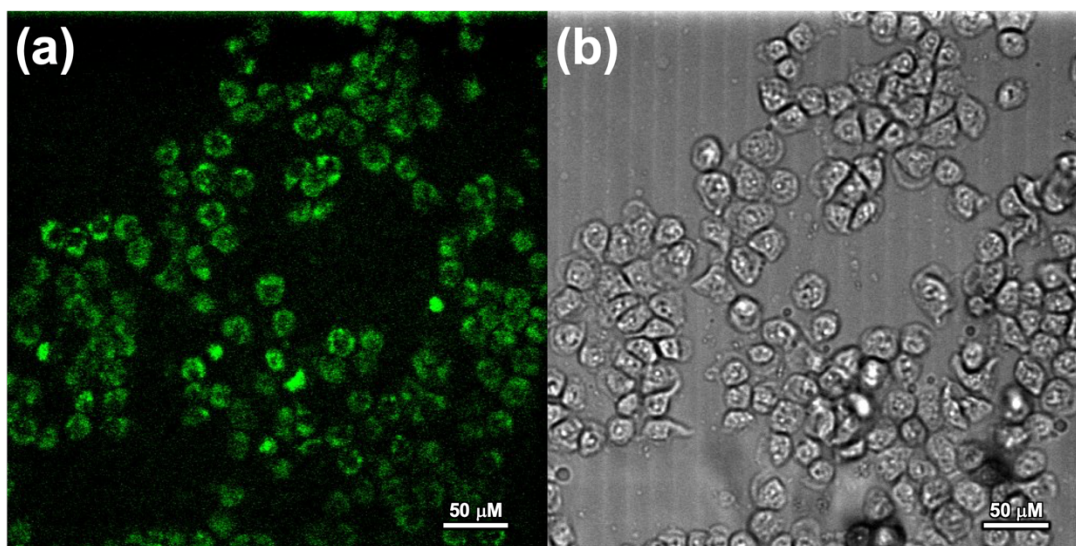
Figure 3.I.9. Fluorescence (left) and bright field (right) images obtained after incubation of HT-29 cells with **3** in media containing 2% MeCN.

3.I.2.7 MTT Viability Assay.

Cell viability of HT-29 colorectal adenocarcinoma cells was investigated upon treatment of the cells with complex **3** under light and dark conditions. The HT-29 cells were treated with a range of concentrations of **3** and the viability was assessed by the reduction of the MTT tetrazolium dye. The assay demonstrated a concentration dependent reduction in viability of HT-29 cells treated with **3** after low-power (15mW
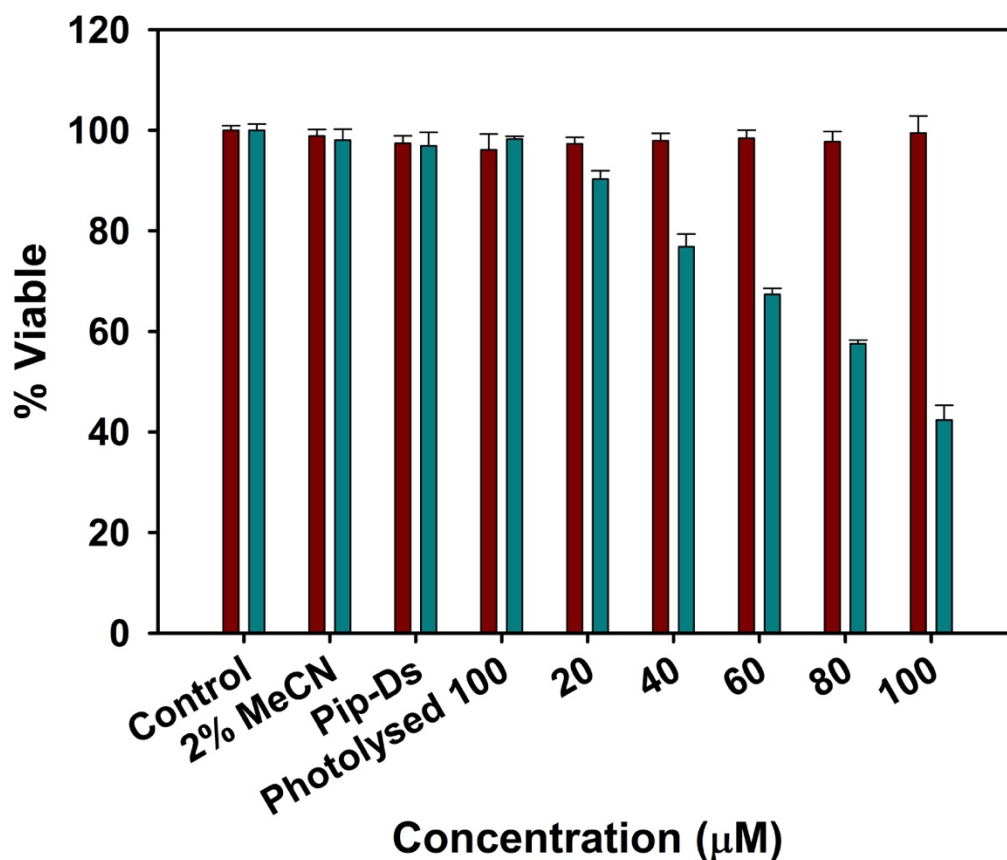
Figure 3.I.10. Reduction in viability of colorectal adenocarcinoma (HT-29) cells by CO photorelease from complex **3** in the dark (red) and under low power visible light (blue, 15 mW cm^{-2}).

cm^{-2}) visible light irradiation for 40min (Figure 3.I.10, green bars). The cells treated with **3** shows 10% – 48% reduction in viability upon exposure to visible light, while control groups that were kept in the dark did not display significant reduction in viability. Other controls including the 2% MeCN solution, the Pipdansyl ligand, or the photolyzed solution of **3** also displayed negligible reduction in viability of HT- 29 cells
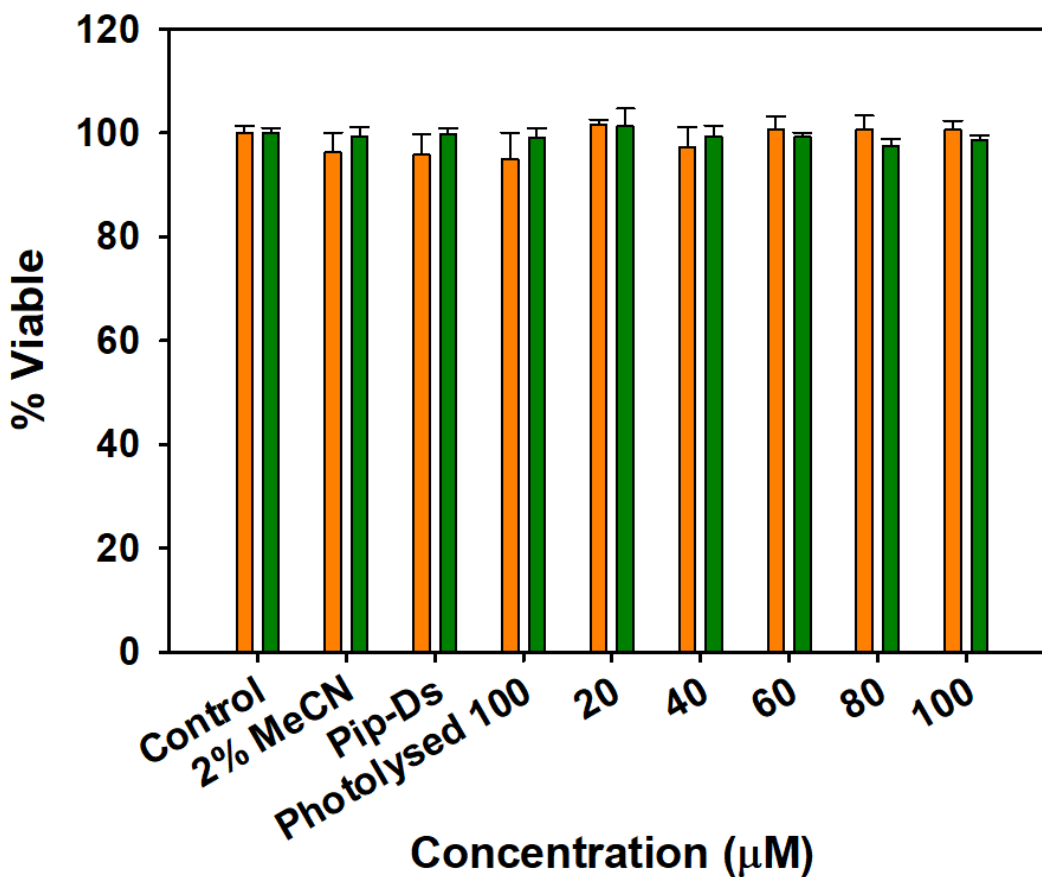
Figure 3.I.11. Reduction in viability of Human Embryonic Kidney (HEK-293) cells by CO photorelease from complex **3** in the dark (red) and under low power visible light (blue, 15 mW cm^{-2}).

under light or dark conditions. These results confirm that the reduction in viability was a direct consequence of exposure of the cells to CO released from photoCORM **3**. No cytotoxicity was observed when human embryonic kidney cells HEK-293 were used in cellular viability study. As shown in Figure 3.I.12, the normal cell line displayed no reduction in viability even with 100 μM of complex **3** in the incubation medium under illumination. This is quite expected since normal healthy cells are known to tolerate low levels of CO without any impairment.

3.I.3 Conclusions.

Prior to our previous report on complex **2**, Mn(I)-based photoCORMs were not inherently luminescent and could not be tracked inside cellular systems prior to CO-release, despite the highly emissive nature of the ligands used. Originally, the intracellular uptake of manganese photoCORMs was indirectly studied by using analogous luminescent Re(I) counterparts or by observing the luminescence obtained from the fluorescent ligands after being released from the complex.[43] However, the entry of the intact manganese photoCORM into the cellular target was never directly demonstrated. In this account, we report the synthesis and characterization of **3**, a luminescent manganese photoCORM which retains its luminescence before and after CO-release. This photoCORM utilizes the Pipdansyl ligand which contains two nitrogens separated by sp^3 carbons. The non-aromaticity of piperazine allows most of the luminescence of the fluorophore to be retained, even after coordination to the metal center. The results of this systematic investigation on the linkers in complexes **1**–**3** open

up the opportunity for the design and synthesis of new luminescent Mn(I) photoCORMs with different ranges of luminescence.

3.I.4 Experimental.

3.I.4.1 General Materials and Methods.

All chemicals, solvents and reagents were purchased from commercial suppliers and were used without further purification unless stated otherwise. All syntheses were carried out using standard Schlenk techniques. The complex [Mn(CO)$_3$(phen)(CF$_3$SO$_3$)],[44] and 1-dansylpiperazine ligand (Pipdansyl)[47] were synthesized in high yield and purity following literature procedures. All manipulations involving Mn(I) species were performed under dark conditions to avoid the decomposition of the complex. IR spectra were obtained using a PerkinElmer Spectrum One FT-IR Spectrometer. UV-Vis spectra were recorded using a Varian Cary 50 UV-vis spectrophotometer. Fluorescence spectra were obtained with an Agilent Cary Eclipse fluorescence spectrophotometer. ^{1}H NMR spectra were recorded at 298 K with a Varian 500 (500MHz) spectrometer. High-resolution ESI-MS data were recorded on an LTQ-Orbitrap Velos Pro MS instrument.

*3.I.4.2 Synthesis of [Mn(CO)$_3$(phen)(Pipdansyl)](CF$_3$SO$_3$) **1**.*

A dichloromethane solution containing [Mn(CO)$_5$Br] (80mg, 0.29mmol) and 1,10-phenanthroline (53mg, 0.30mmol) was stirred for overnight at room temperature, observing a change in the color of the solution to orange. The volume of the solvent

was reduced under vacuum and a yellow powder was obtained upon addition of diethyl ether and subsequent cooling at 5 °C. The solid thus obtained was filtered and washed with dichloromethane, yield 98 mg (80%). Then a solution of 121 mg (0.47 mmol) of $AgCF_3SO_3$ was added to an MeCN solution of $[Mn(CO)_3(pbt)Cl]$ (161 mg, 0.451 mmol) and stirred for 4 h. The light-yellow solution was subsequently filtered through a wet Celite pad, and the filtrate was evaporated to dryness. The resulting $[Mn(CO)_3(pbt)(MeCN)](CF_3SO_3)$ adduct (200 mg, 0.43 mmol) was then dissolved in DCM (25 mL) and a batch of 136.5 mg (0.43 mmol) of Pipdansyl was added. The mixture was magnetically stirred at room temperature under dark conditions for 48 h. The solvent of the mixture was evaporated under low pressure yielding a yellow precipitate. The crude yellow precipitate was washed several times with diethyl ether and then recrystallized from a dichloromethane:hexane (1:1) mixture to afford **1** in 93% yield (312.9 mg, 0.39 mmol) as a bright yellow microcrystalline solid. Anal. Calcd. (%) for $C_{32}H_{29}F_3MnN_5O_6S_2$ (787.66): C, 48.80; H, 3.71; N, 8.89; found: C, 48.67; H 3.69; N, 8.91. Selected IR (KBr disk, cm^{-1}): 3197 (w), 2943 (w), 2036 (s), 1944 (s), 1929 (s), 1573 (w), 1430 (w), 1280 (m), 1252 (m), 1161 (m), 1147 (m), 1030 (m), 947 (w), 848 (w), 726 (w), 637 (m), 569 (w). UV–vis (MeCN), λ_{max} (ε, M^{-1} cm^{-1}): 350 (6 200), 260 (28 750). ^{1}H NMR (500 MHz, MeOD): δ 9.52 (d, 2H), 9.44 (d, 1H), 8.85 (m, 3H), 8.54 (d, 1H), 8.06 (m, 4H), 7.50 (t, 1H), 7.44 (t, 1H), 7.22 (d, 1H), 2.82 (s, 6H), 2.65 (m, 4H), 2.43 (m, 2H), 2.25 (m, 2H). ESI-MS (m/z): 638.1216 (corresponds to $[Mn(CO)3(phen) (Pipdansyl)]^+$).

3.1.4.3 Photolysis Experiments.

An acetonitrile solution of complex **3** with a known concentration (5×10^{-5} M, 298 K) was prepared under dark condition. The rates of CO release (k_{CO}) for **3** at 298K were obtained using a low-power broadband visible light originated from an IL 410 illumination system (Electro Fiber Optics Corp.). The power of the incident visible light (15 mW cm^{-2}) were measured with a Field MaxII- TO laser power meter (Coherent, Portland, OR). The k_{CO} value of **1** was measured by recording the electronic absorption spectra of the solution using a quartz cuvette (1 cm × 1 cm) and monitoring changes in the absorption spectra after exposing the solution in the cuvette to the visible light source at regular time intervals. The k_{CO} value of **1** was then calculated from a ln(C) versus time (t) plot.

3.1.4.4 Luminescence and Stability of Complex 3.

Solutions of complex **3**, complex **2**,[43] [12], and Pipdansyl were prepared at equimolar concentrations (5×10^{-4} M, 298 K) in MeCN under dark condition. The emission spectra were recorded with excitation at 405 nm using a quartz cuvette (1 cm × 1 cm). After recording the luminescence of complex **3**, the solution in the cuvette was exposed to visible light for 1 h and the luminescence spectrum was subsequently recorded (to match the final spectrum with that of free Pipdansyl). The stability of **3** was measured by diluting a concentrated solution of the complex in MeCN with phosphate buffer saline (PBS) until the MeCN content reached 2% (v/v). The electronic

absorption spectrum of **3** in such buffer solution was then recorded every hour for a total period of 24 h.

3.1.4.5 Myoglobin Assay.

Horse heart myoglobin was dissolved in PBS (100 mM, pH 7.4) and reduced with sodium dithionite. The concentration of the resulting deoxymyoglobin (Mb) was calculated from the absorbance of the Soret band at 435 nm ($\varepsilon = 121$ mM^{-1} cm^{-1}). An apparatus with two identical quartz cuvettes was constructed, since sodium dithionate is known to facilitate the release of CO. Both cuvettes were manipulated under anaerobic conditions to avoid oxidation of the reduced myoglobin solution by the atmospheric oxygen. In the first cuvette, a solution of **3** in 2% MeCN in PBS (v/v) was exposed to visible light, releasing CO into the headspace. The photogenerated CO was transferred via cannula using positive pressure of $N_2(g)$ from the headspace of the first cuvette into the solution of the second cuvette containing the reduced Mb solution. The absorbance spectrum of the newly formed carbonmonoxy-myoglobin was subsequently recorded. The formation of carbonmonoxy-myoglobin was observed from the shift of the λ_{max} of the Soret band from 435 to 424 nm.

3.1.4.6 Cellular Culture and Imaging.

The human colorectal adenocarcinoma cell line (HT-29, ATCC no. HTB-38TM) was purchased from American Type Culture Collection (ATCC) and cultured in McCoy's 5A media supplemented with 20% fetal bovine serum (FBS). The cells

were plated on to 35 mm imaging dishes (purchased from ibidi®) and allowed to grow for 24 h. The cells were then incubated with a 25 μM solution of **3** in 2:98 MeCN:media at 37 °C with 5% $CO_2(g)$ for 1h. The cells were then washed with PBS under dark conditions. Fresh McCoy's 5A media (without phenol red and FBS) was then added to the treated cells and confocal microscopy images were recorded. The cellular images were captured with an Inverted Nikon Eclipse TE2000-E spinning disk (CSLI-X1) confocal microscope equipped with a Hamamatsu EM-CCD camera (ImageE MX2) utilizing 405 nm illumination at 50 mW. The gain and offset were set to adjust the brightest pixels below saturation, and there were only a few zero-intensity pixels. The detection gate was set to 500–550 nm. The zoom and the frame size were set to give the pixels that were approximately 111 nm (just below the Nyquist criterion). Images were collected at 340 nm intervals for Z- stacks. Micro-Manager 1.4 software was used to acquire the initial images and the bright-field images were acquired in phase-contrast mode. The images were further processed with *Fiji-ImageJ*, version 1.52c, and *ImageJ* (micromanager), version 1.49 h software.

3.1.4.7 MTT Viability Assay.

Human colorectal adenocarcinoma cells (HT-29, ATCC no. HTB- 38TM) were plated in two independent 96-well plates at a density of 100,000 cells mL^{-1} and incubated for 24 h prior to the experiment. Unless otherwise stated the rest of the MTT assay was performed entirely under dark conditions to avoid decomposition of the manganese complex. A stock solution of **3** was prepared by dissolving 19.7 mg of the

complex in 5 mL of MeCN. A 600 μL aliquot of the stock solution was then diluted to 30.0 mL using McCoy's 5A media supplemented with 20% FBS, resulting in a stock solution of 100 μM with respect to **3**. Stock solutions of 80, 60, 40, and 20 μM were prepared by diluting the initial 100 μM stock solution using fresh media containing 2% MeCN (v/v). The initial incubation media was aspirated from the plates and the cells were incubated with the previously described 100, 80, 60, 40 and 20 μM solutions of **3**. Controls used in the experiment included 100 μM solutions of photolyzed complex **3** and free Pipdansyl ligand in culture media containing 2% MeCN. Other controls included fresh media and 2% MeCN in media (v/v). Once treated, both plates were incubated for 2 h at 37 °C and 5% $CO_2(g)$ to allow internalization of the compounds. After incubation, the media was aspirated, and cells were washed with PBS. Fresh culture media was added to the plates and the cells were incubated for an additional h. Afterwards, one plate was kept incubating under strict dark condition, while the other plate was treated with light from a low-power LED light source (15 mW cm^{-2}) at 1.5 cm for 40 min. After photolysis, the plates were incubated for an additional 2 h under dark condition. Following the incubation time, the old media was aspirated, the cells were washed with PBS and fresh media was introduced to allow the cells to recover while incubating them for 2 h. Lastly, the MTT was added to both plates according to the manufacturer's protocol (Life Technologies), and the viability of the cells was assessed using a microplate reader (Molecular Devises VersaMax®). Control experiments were also performed with human embryonic kidney cells HEK-293 to evaluate the effects of CO on normal healthy cells.

3.I.5 References.

1. Motterlini, R.; Foresti, R. Biological signaling by carbon monoxide and carbon monoxide-releasing molecules. *J. Physiol. Cell Physiol.* **2017**, *312*, C302-313.

2. Motterlini, R.; Otterbein, L. E. The therapeutic potential of carbon monoxide. *Nat. Rev. Drug Discov.* **2010**, *9*, 422-428.

3. Motterlini, R.; Clark, J. E.; Foresti, R.; Saratchandra, P.; Mann, B. E.; Green, C. J. Carbon monoxide-releasing molecules characterization of biochemical and vascular activities. *Circ. Res.* **2002**, *90*, e17-e24.

4. Wu, L.; Wang, R. Carbon monoxide: Endogenous production, physiological functions, and pharmacological applications. *Pharmacol. Rev.* **2005**, *57*, 585-630.

5. Kikuchi, G.; Yoshida, T.; Noguchi, M. Heme oxygenase and heme degradation. *Biochem. Biophys. Res. Commun.* **2005**, *338*, 558-567.

6. Otterbein, L. E.; Bach, F. H.; Alam, J.; Soares, M.; Lu, H. T.; Wysk, M.; Davis, R. J.; Flavell, R. A.; Choi, A. M. K. Carbon monoxide ha anti-inflammatory effects involving the mitogen-activated protein kinase pathway. *Nat. Med.* **2000**, *6*, 422-428.

7. Wu, L.; Wang, R. Carbon monoxide: Endogenous production, physiological functions, and pharmacological applications. *Pharmacol. Rev.* **2005**, *57*, 585-630.

8. Yamamoto, T.; Takano, N.; Ishiwata, K.; Ohmura, M.; Nagahata, Y.; Matsuura, T.; Kamata, A.; Sakamoto, K.; Nakanishi, T.; Kubo, A.; Hishiki, T.; Suematsu, M. Reduced methylation of PFKFB3 in cancer cells shunts glucose towards the pentose phosphate pathway. *Nat. Commun.* **2014**, *5*, 3480.

9. Kawahara, B.; Ramadoss, S.; Chaudhuri, G.; Janzen, C.; Sen, S.; Mascharak, P. K. Carbon monoxide sensitizes cisplatin-resistant ovarian cancer cell lines toward cisplatin via attenuation of levels of glutathione and nuclear metallothionein. *J. Inorg. Biochem.* **2019**, *191*, 29-39.

10. Kawahara, B.; Moller, T.; Hu-Moore, K.; Carrington, S.; Faull, K. F.; Sen, S.; Mascharak, P. K. Attenuation of antioxidant capacity in human breast cancer cells by carbon monoxide through inhibition of cystathionine b-synthase activity: Implications in chemotherapeutic drug sensitivity. *J. Med. Chem.* **2017**, *60*, 8000-8010.

11. Wegiel, B.; Gallo, D.; Csizmadia, E.; Harris, C.; Belcher, J.; Vercellotti, G. M.; Penacho, N.; Seth, P.; Sukatme, V.; Ahmed, A.; Pandolfi, P. P.; Helczynski, L.; Bjartell, A.; Persson, J. L.; Otterbein, L. E. Carbon monoxide expedites metabolic exhaustion to inhibit tumor growth. *Cancer Res.* **2013**, *73*, 7009-7021.

12. Vitek, L.; Gbelcova, H.; Muchova, L.; Vanova, K.; Zelenka, J.; Konickova, R.; Suk, J.; Zadinova, M.; Knejzlik, Z.; Ahmad, S.; Fujisawa, T.; Ahmed, A.; Ruml, T. Antiproliferative effects of carbon monoxide on pancreatic cancer. *Dig. Liver Dis.* **2014**, *46*, 369-375.

13. Motterlini, R.; Clark, J. E.; Foresti, R.; Saratchandra, P.; Mann, B. E.; Green, C. J. Carbon monoxide-releasing molecules characterization of biochemical and vascular activities. *Circ. Res.* **2002**, *90*, e17-e24.

14. Faizan, M.; Muhammad, N.; Niazi, K. U. K.; Hu, Y.; Wang, Y.; Wu, Y.; Sun, H.; Liu, R.; Dong, W.; Zhang, W.; Gao, Z. CO-releasing materials: an emphasis on

therapeutic implications, as release and subsequent cytotoxicity are the part of therapy. *Materials* **2019**, *12*, 1643.

15. Kottelat, E.; Zobi, F. Visible light-activated photoCORMs. *Inorganics* **2017**, *5*, 24.

16. Ford, P. C. Metal complex strategies for photo-uncaging the small molecule bioregulators nitric oxide and carbon monoxide. *Coord. Chem. Rev.* **2018**, *376*, 548-564.

17. Zheng, Y.; Ji, X.; Yu, B.; Ji, K.; Gallo, D.; Csizmadia, E.; Zhu, M.; Choudhury, M. R.; De La Cruz, L. K. C.; Chittavong, V.; Pan, Z.; Yuan, Z.; Otterbein, L. E.; Wang, B. Enrichment-triggered prodrug activation demonstrated through mitochondria-targeted delivery of doxorubicin and carbon monoxide. *Nat. Chem.* **2018**, *10*, 787-794.

18. Ji, X.; De La Cruz, L. K. C.; Pan, Z.; Chittavong, V.; Wang, B. pH-sensitive metal free carbon monoxide prodrugs with tunable and predictable release rates. *Chem. Commun.* **2017**, *53*, 9628-9631.

19. Ji, X.; Pan, Z.; Li, C.; Kang, T.; De La Cruz, L. K. C.; Yang, L.; Yuan, Z.; Ke, B.; Wang, B. Esterase-sensitive and pH-controlled carbon monoxide prodrugs for treating systemic inflammation. *J. Med. Chem*. **2019**, *62*, 3163-3168.

20. Ji, X.; Wang, B. Strategies toward organic carbon monoxide prodrugs. *Acc. Chem. Res.* **2018**, *51*, 1377-1385.

21. Chakraborty, I.; Carrington, S. J.; Mascharak, P. K. Design strategies to improve sensitivity of photoactive metal carbonyl complexes (photoCORMs) to visible light

and their potential as CO-donors to biological targets. *Acc. Chem. Res.* **2014**, *47*, 2603-2611.

22. Garcia-Gallego, S.; Bernardes, G. J. L. Carbon monoxide-releasing molecules for the delivery of therapeutic CO in vivo. *Angew. Chem. Int. Ed*. **2014**, *53*, 9712-9721.

23. Romao, C. C.; Blatter, W. A.; Seixas, J. D.; Bernardes, G. J. Developing drug molecules for therapy with carbon monoxide. *Chem. Soc. Rev.* **2012**, *41*, 3571-3583.

24. Jackson, C. S.; Schmitt, S.; Dou, Q. P.; Kodanko, J. J. Synthesis, characterization, and reactivity of the stable iron carbonyl complex $[Fe(CO)(N4Py)](ClO_4)_2$: Photoactivated carbon monoxide release, growth inhibitory activity, and peptide ligation. *Inorg. Chem*. **2011**, *50*, 5336-5338.

25. Kumar, C. A.; Nagarajaprakash, R.; Victoria, W.; Veena, V.; Sakthivel, N.; Manimaran, B. Synthesis, characterization and cytotoxicity studies on Manganese(I) and Rhenium(I) based metallacrown ethers. *Inorg. Chem. Commun*. **2016**, *64*, 39-44.

26. Kumar, C. A.; Divya, D.; Nagarajaprakash, R.; Veena, V.; Vidhyapriya, P.; Sakthivel, N.; Manimaran, B. Self-assembly of manganese(I) and rhenium(I) based semi-rigid ester functionalized M2L2-type metallacyclophanes: synthesis, characterization, and cytotoxicity evaluation. *J. Organomet. Chem.* **2017**, *846*, 152-160.

27. Vidhyapriya, P.; Divya, D.; Manimara, B.; Sakthivel, N. Photoactivated [Mn(CO)₃(Br(μ-bpcpd)]₂ induces apoptosis in cancer cells via intrinsic pathway. *J. Photochem. Photobiol. B, Biol.* **2018**, *188*, 28-41.

28. Kumar, U.; Roy, S.; Jha, R. K.; Vidhyapriya, P.; Sakthivel, N.; Manimaran, B. Selenolato-bridged manganese(I)-based dinuclear metallacycles as potential anticancer agents and photo-CORMs. *ACS Omega* **2019**, *4*, 1923-1930.

29. Divya, D.; Nagarajaprakash, R.; Vidhyapriya, P.; Sakthivel, N.; Manimaran, B. Single-pot self-assembly of heteroleptic Mn(I)-based aminoquinonato-bridged ester/amide-functionalized dinuclear metallastirrups: potential anticancer and visible light triggered CORMs. *ACS Omega* **2019**, *4*, 12790-12802.

30. Ramakrishna, B.; Nagarajaprakash, R.; Veena, V.; Sakthivel, N.; Manimaran B. Self-assembly of oxamidato bridged ester functionalized dirhenium metallastirrups: synthesis, characterization and cytotoxicity studies. *Dalton Trans.* **2015**, *44*, 17629-17638.

31. Pierri, A. E.; Pallaoro, A.; Wu, G.; Ford, P. C. A luminescent and biocompatible photoCORM. *J. Am. Chem. Soc.* **2012**, *134*, 18197-181200.

32. Anderson, S. N.; Richards, J. M.; Esquer, H. J.; Benninghoff, A. D.; Arif, A. M.; Berreau, L. M. A structurally-tunable 3-hydroxyflavone motif for visible light-induced carbon monoxide-releasing molecules (CORMs). *ChemistryOpen* **2015**, *4*, 590-594.

33. Carrington, S. J.; Chakraborty, I.; Bernard, J. M. L.; Mascharak, P. K. A theranostic two-tone luminescent photoCORM derived from Re(I) and 2-(pyridyl)-

benzothiazole: Trackable CO delivery to malignant cells. *Inorg. Chem.* **2016**, *55*, 7852-7858.

34. Carrington, S. J.; Chakraborty, I.; Bernard, J. M. L. Mascharak, P. K. Synthesis and characterization of a "turn-on" photoCORM for trackable CO delivery to biological targets. *ACS Med. Chem. Lett.* **2014**, *4*, 1324-1328.

35. G, U. R.; Axthelm, J.; Hoffmann, P.; Taye, N.; Glaser, S.; Gorls, H.; Hopkins, S. L.; Plass, W.; Neugebauer, U.; Bonnet, S.; Schiller, A. Co-registered molecular logic gate with a CO-releasing molecule triggered by light and peroxide. *J. Am. Chem. Soc.* **2017**, *139*, 4991-4994.

36. Musib, D.; Raza, M. K.; Martina, K.; Roy, M. Mn(I)-based photoCORMs for trackable visible light-induced CO release and phototoxicity to cancer cells. *Polyhedron* **2019**, In Press, Corrected Proof.

37. Romanski, S.; Rucker, H.; Stamellou, E.; Guttentag, M.; Neudorfl, J.-M.; Alberto, R.; Amslinger, S.; Yard, B.; Schmalz, H.-G. Iron dienylphosphate tricarbonyl complexes as water-soluble enzyme-triggered CO-releasing molecules (ET-CORMs). *Organometallics* **2012**, *31*, 5800-5809.

38. Poh, H. T.; Sim, B. T.; Chwee, T. S.; Leong, W. K.; Fan, W. Y. The dithiolate-bridged diiron hexacarbonyl complex $Na_2[(\mu-SCH_2CH_2COO)Fe(CO)_3]_2$ as a water-soluble photoCORM. *Organometallics* **2014**, *33*, 959-963.

39. Mede, R.; Klein, M.; Claus, R. A.; Krieck, S.; Quickert, S.; Gorls, H.; Neugebauer, U.; Schmitt, M.; Gessner, G.; Heinemann, S. H.; Popp, J.; Bauer, M.;

Westerhausen, M. CORM-EDE1: A highly water soluble and nontoxic manganese-based photoCORM with a biogenic ligand sphere. *Inorg. Chem.* **2016**, *55*, 104-113.

40. Jimenez, J.; Chakraborty, I.; Carrington, S. J.; Mascharak, P. K. Light-triggered CO delivery by a water-soluble and biocompatible manganese photoCORM. *Dalton Trans.* **2016**, *45*, 13204-13213.

41. Marker, S. C.; MacMillan, S. N.; Zipfel, W. R.; Li, Z.; Ford, P. C.; Wilson, J. J. Photoactivated in vitro anticancer activity of Rhenium(I) tricarbonyl complexes bearing water-soluble phosphines. *Inorg. Chem.* **2018**, *57*, 1311-1331.

42. Carrington, S. J.; Chakraborty, I.; Mascharak, P. K. Rapid CO release from a Mn(I) carbonyl complex derived from azopyridine upon exposure to visible light and its phototoxicity toward malignant cells. *Chem. Commun.* **2013**, *49*, 11254-11256.

43. Jimenez, J.; Chakraborty, I.; Dominguez, A.; Martinez-Gonzalez, J.; Sameera, W. M. C.; Mascharak, P. K. A luminescent manganese photoCORM for CO delivery to cellular targets under the control of visible light. *Inorg. Chem.* **2018**, *57*, 1766-1773.

44. Chakraborty, I.; Carrington, S. J.; Roseman, G.; Mascharak, P. K. Synthesis, structures, and CO release capacity of a family of water soluble photoCORMs: assessment of the biocompatibility and their phototoxicity toward human breast cancer cells. *Inorg. Chem.* **2017**, *56*, 1534-1545.

45. Pinto, M. N.; Chakraborty, I.; Sandoval, C.; Mascharak, P. K.; Eradication of HT-29 colorectal adenocarcinoma cells by controlled photorelease of CO from a CO-

releasing polymer (photoCORP-1) triggered by visible light through an optical fiber-based device. *J. Control. Release* **2017**, *264*, 192-202.

46. Rimmer, R. D.; Pierri, A. E.; Ford, P. C. Photochemically activated carbon monoxide release for biological targets. Toward developing air-stable photoCORMs labilized by visible light. *Coord. Chem. Rev*. **2012**, *256*, 1509–1519.

47. Zhang, Y.; Chen, H.; Chen, D.; Wu, D.; Chen, X.; Liu, S. H.; Yin, J. A fluorescent turn-on H_2S-responsive probe: design, synthesis and application. *Org. Biomol. Chem*. **2015**, *13*, 9760-9766.

3.I.6 Reprints of Publications and Permissions.

Reprinted with permissions from Jimenez, J.; Pinto, M. N.; Chakraborty, I.; Martinez-Gonzalez; Mascharak, P. K. Photo-induced eradication of human colorectal adenocarcinoma HT-29 cells by carbon monoxide (CO) from a Mn-Based green luminescent photoCORM. *Inorg. Chim. Acta* **2019**, *485*, 112-117.

Research paper

Photo-induced eradication of human colorectal adenocarcinoma HT-29 cells by carbon monoxide (CO) delivery from a Mn-based green luminescent photoCORM

Jorge Jimenez, Miguel N. Pinto, Jorge Martinez-Gonzalez, Pradip K. Mascharak*

Department of Chemistry and Biochemistry, University of California, Santa Cruz, CA 95064, USA

A B S T R A C T

Exogenous CO delivery to cellular targets for salutary purposes can be readily achieved with photoactive metal carbonyl complexes (photoCORMs). Mn(I)-based photoCORMs are often favored for their ability to release CO upon triggering with visible light (suitable for phototherapy of cancer). To date, the reported Mn(I)-based photoCORMs are all non-luminescent and hence the entry of these CO donors cannot be tracked within the targeted sites. A new luminescent Mn(I) photoCORM namely [Mn(CO)$_3$(phen)(Pipdansyl)](CF$_3$SO$_3$) (3) has been reported. Synthetic strategy to isolate photoCORM 3 and its previous analogue [Mn(CO)$_3$(phen)(Imdansyl)](CF$_3$SO$_3$) (2) has been highlighted to establish protocols for the future isolation of luminescent Mn(I)-based photoCORMs that could be employed as trackable photoCORMs for CO delivery. The entrance of 3 into human colorectal adenocarcinoma HT-29 cells has been visualized by confocal microscopic studies. Eradication of the cancer cells by CO delivery from 3 under visible light illumination has also been demonstrated.

1. Introduction

The surprising discovery of salutary effects of carbon monoxide (CO) in mammalian pathophysiology has spurred intense research activity in establishing the therapeutic potential of this so-called toxic gas [1–3]. CO, endogenously produced during the catabolism of heme by the enzyme heme oxygenase (HO), has been identified as an important signaling molecule that participates in various physiological pathways [4]. Modulation of these pathways could be selectively achieved by exogenous delivery of CO to specific targets. The noxious nature of this unusual signaling molecule however presents a challenge for its controlled delivery in a hospital setting. CO-releasing molecules (CORMs) provide an alternative means to deliver of CO to biological targets. Among these CO-donors, photoactivated CORMs (photoCORMs) prove advantageous due to their ability to release CO upon exposure to light of various wavelengths [5–11].

A great majority of photoCORMs has been derived from groups 7 and 8 transition metals [7,12–26]. Some of the group 7 metal carbonyl complexes have inherent luminescence and have been used as bioimaging agents.[16,17,27–31] Although many of these luminescent complexes have been used as CO donors, they require the use of ultraviolet light to release CO and therefore not suitable for biological applications. Mn(I)-based photoCORMs can be activated with low-power visible light, and are therefore preferred for CO delivery to biological targets [7,13,20,21]. A majority of these complexes has been

employed to eradicate selected cancer cell lines in a concentration dependent manner upon visible light excitation [12–14,19,20]. Unfortunately, the Mn(I)-based photoCORMs are inherently non-luminescent despite the use of highly luminescent chelating ligands [13,19,20,21,32]. Such quenching of the fluorophore imparted by the Mn(I) center makes it difficult to follow the internalization and localization of the prodrug (photoCORM) before the drug (CO) is delivered. Clearly, different design principles must be implemented toward isolation of Mn(I)-based photoCORMs to circumvent the fluorescence quenching imparted by the Mn(I) center.

In a recent paper, Schiller and coworkers have reported a visible-light active photoCORM [Mn(CO)$_3$(L)](CF$_3$SO$_3$) (1, Scheme 1) in which the ligand L is a tridentate aminopyridine ligand with the highly fluorescent dansyl moiety *directly attached* to the central N atom of L through a −SO$_2$− link [32]. The direct binding of the N atom to the Mn(I) center in this photoCORM resulted in almost complete quenching of the fluorescence of the dansyl group. We have utilized the same dansyl moiety in our previous work to isolate a Mn(I)-based photoCORM [Mn(CO)$_3$(phen)(Imdansyl)](CF$_3$SO$_3$) (2, Imdansyl = a fluorescent ligand imidazoledansyl, Scheme 1) in which the dansyl unit is connected to the Mn(I) center through an intervening imidazole group [12]. The imidazole linker in 2 separates the fluorophore from the Mn(I) center and retains most of its emissive properties. In this case, the imidazole linker contains two N donor centers one of which is coordinated directly to the Mn(I) center while the second N atom is attached to the dansyl moiety
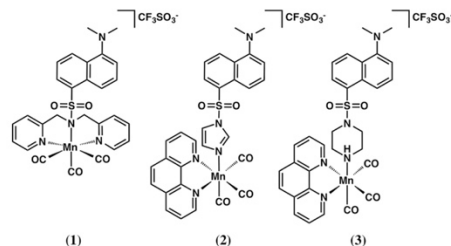
Scheme 1. Molecular structures of complex **1** (the Mn(I)-based photoCORM reported by Schiller and coworkers [32], **2** [12], and **3** (present work).

through the same –SO$_2$– link. Interestingly **2** is a moderately luminescent photoCORM that allowed us, for the first time, to track the prodrug within cellular matrix. The imidazole moiety in **2** provides partial separation between the Mn(I) center and the dansyl moiety leading to ~10% quenching of its fluoresence [12].

In this account we report the complex [Mn(CO)$_3$(phen)(Pipdansyl)] (CF$_3$SO$_3$) (**3**) which makes use of a different dansyl derivative namely, 1-dansylpiperazine (Pipdansyl), coordinated to an axial position of the Mn(I) center. The Pipdansyl ligand is highly luminescent and displays a bright green emission in acetonitrile (MeCN) and in aqueous media. This piperazine linker has two nitrogens serving different functions analogous to the imidazole moiety of Imdansyl. However, the N donors of Pipdansyl are separated by two saturated carbons and thus the Pip group is not in conjugation with the dansyl fluorophore (as it is in Imdansyl). Such separation leads to minimum fluorescence quenching when Pipdansyl is coordinated to the Mn(I) center in **3**. As a consequence, **3** is strongly luminescent and allows trackability of this photoCORM in cellular media. Much like other reported Mn(I)-based photoCORMs, complex **3** is able to release all three CO molecules upon exposure to low-power visible light. In addition, confocal microscopy images show rapid internalization of complex **3** to human colorectal cancer (HT-29) cells and the photoCORM leads to a concentration dependent reduction in the viability of HT-29 cells upon exposure to visible light. Taken together, the mode of conjugation of the fluorophore to the Mn(I) centers of this kind of photoCORMs appears to be an important determinant of their final luminescence characteristics.

2. Experimental

2.1. Materials and methods

All chemicals, solvents and reagents were purchased from commercial suppliers and were used without further purification unless stated otherwise. All syntheses were carried out using standard Schlenk techniques. The complex [Mn(CO)$_3$(phen)(CF$_3$SO$_3$)] [13], and 1-dansylpiperazine ligand (Pipdansyl) [33] were synthesized in high yield and purity following literature procedures. All manipulations involving Mn(I) species were performed under dark conditions to avoid the decomposition of the complex. IR spectra were obtained using a PerkinElmer Spectrum One FT-IR Spectrometer. UV–Vis spectra were recorded using a Varian Cary 50 UV–vis spectrophotometer. Fluorescence spectra were obtained with an Agilent Cary Eclipse fluorescence spectrophotometer. ^{1}H NMR spectra were recorded at 298 K with a Varian 500 (500 MHz) spectrometer. High-resolution ESI-MS data were recorded on an LTQ-Orbitrap Velos Pro MS instrument.

2.2. [Mn(CO)$_3$(phen)(Pipdansyl)](CF$_3$SO$_3$) (1)

A batch of 136.5 mg (0.43 mmol) of Pipdansyl was added to a dichloromethane (25 mL) solution of [Mn(CO)$_3$(phen)(CF$_3$SO$_3$)] (200 mg,

0.43 mmol). The mixture was magnetically stirred at room temperature under dark conditions for 48 h. The solvent of the mixture was evaporated under low pressure yielding a yellow precipitate. The crude yellow precipitate was then recrystallized from a dichloromethane:hexane (1:1) mixture to afford **1** in 93% yield (312.9 mg, 0.39 mmol) as a bright yellow microcrystalline solid. Anal. Calcd. (%) for C$_{32}$H$_{29}$F$_3$MnN$_5$O$_6$S$_2$ (787.66): C, 48.80; H, 3.71; N, 8.89; found: C, 48.67; H 3.69; N, 8.91. Selected IR (KBr disk, cm^{-1}): 3197 (w), 2943 (w), 2036 (s), 1944 (s), 1929 (s), 1573 (w), 1430 (w), 1280 (m), 1252 (m), 1161 (m), 1147 (m), 1030 (m), 947 (w), 848 (w), 726 (w), 637 (m), 569 (w). UV–vis (MeCN), λ_{max} (ε, M^{-1} cm^{-1}): 350 (6 200), 260 (28 750). ^{1}H NMR (500 MHz, MeOD): δ 9.52 (d, 2H), 9.44 (d, 1H), 8.85 (m, 3H), 8.54 (d, 1H), 8.06 (m, 4H), 7.50 (t, 1H), 7.44 (t, 1H), 7.22 (d, 1H), 2.82 (s, 6H), 2.65 (m, 4H), 2.43 (m, 2H), 2.25 (m, 2H). ESI-MS (m/z): 638.1216 (corresponds to [Mn(CO)$_3$(phen) (Pipdansyl)]$^+$).

2.3. Photolysis experiments

An acetonitrile solution of complex **3** with a known concentration (5 × 10^{-5} M, 298 K) was prepared under dark condition. The rates of CO release (k$_{CO}$) for **3** at 298 K were obtained using a low-power broadband visible light originated from an IL 410 illumination system (Electro Fiber Optics Corp.). The power of the incident visible light (15 mW/cm^2) were measured with a Field MaxII- TO laser power meter (Coherent, Portland, OR). The k$_{CO}$ value of **1** was measured by recording the electronic absorption spectra of the solution using a quartz cuvette (1 cm × 1 cm) and monitoring changes in the absorption spectra after exposing the solution in the cuvette to the visible light source at regular time intervals. The k$_{CO}$ value of **1** was then calculated from a ln(C) versus time (t) plot.

2.4. Luminescence and stability of complex 3

Solutions of complex **3**, complex **2** [12], and Pipdansyl were prepared at equimolar concentrations (5 × 10^{-4} M, 298 K) in MeCN under dark condition. The emission spectra were recorded with excitation at 405 nm using a quartz cuvette (1 cm × 1 cm). After recording the luminescence of complex **3**, the solution in the cuvette was exposed to visible light for 1 h and the luminescence spectrum was subsequently recorded (to match the final spectrum with that of free Pipdansyl. The stability of **3** was measured by diluting a concentrated solution of the complex in MeCN with phosphate buffer saline (PBS) until the MeCN content reached 2% (v/v). The electronic absorption spectrum of **3** in such buffer solution was then recorded every hour for a total period of 24 h.

2.5. Myoglobin assay

Horse heart myoglobin was dissolved in PBS (100 mM, pH 7.4) and reduced with sodium dithionite. The concentration of the resulting deoxymyoglobin (Mb) was calculated from the absorbance of the Soret band at 435 nm (ε = 121 mM^{-1} cm^{-1}). An apparatus with two identical quartz cuvettes was constructed, since sodium dithionate is known to facilitate the release of CO. Both cuvettes were manipulated under anaerobic conditions to avoid oxidation of the reduced myoglobin solution by the atmospheric oxygen. In the first cuvette, a solution of **3** in 2% MeCN in PBS (v/v) was exposed to visible light, releasing CO into the headspace. The photogenerated CO was transferred via cannula using positive pressure of N$_2$(g) from the headspace of the first cuvette into the solution of the second cuvette containing the reduced Mb solution. The absorbance spectrum of the newly formed carboxy-myoglobin was subsequently recorded. The formation of carboxy-myoglobin was observed from the shift of the λ_{max} of the Soret band from 435 to 424 nm.

2.6. Cellular culture and imaging

The human colorectal adenocarcinoma cell line (HT-29, ATCC no. HTB-38TM) was purchased from American Type Culture Collection (ATCC) and cultured in McCoy's 5A media supplemented with 20% fetal bovine serum (FBS). The cells were plated on to 35 mm imaging dishes (purchased from ibidi®) and allowed to grow for 24 h. The cells were then incubated with a 25 μM solution of **3** in 2:98 MeCN:media at 37 °C with 5% $CO_2(g)$ for 1 h. The cells were then washed with PBS under dark conditions. Fresh McCoy's 5A media (without phenol red and FBS) was then added to the treated cells and confocal microscopy images were recorded. The cellular images were captured with an Inverted Nikon Eclipse TE2000-E spinning disk (CSLI-X1) confocal microscope equipped with a Hamamatsu EM-CCD camera (ImageE MX2) utilizing 405 nm illumination at 50 mW. The gain and offset were set to adjust the brightest pixels below saturation, and there were only a few zero-intensity pixels. The detection gate was set to 500–550 nm. The zoom and the frame size were set to give the pixels that were approximately 111 nm (just below the Nyquist criterion). Images were collected at 340 nm intervals for Z-stacks. Micro-Manager 1.4 software was used to acquire the initial images and the bright-field images were acquired in phase-contrast mode. The images were further processed with *Fiji-ImageJ*, version 1.52c, and *ImageJ* (micromanager), version 1.49 h software.

2.7. MTT viability assay

Human colorectal adenocarcinoma cells (HT-29, ATCC no. HTB-38TM) were plated in two independent 96-well plates at a density of $100{,}000$ cells mL^{-1} and incubated for 24 h prior to the experiment. Unless otherwise stated the rest of the MTT assay was performed entirely under dark conditions to avoid decomposition of the manganese complex. A stock solution of **3** was prepared by dissolving 19.7 mg of the complex in 5 mL of MeCN. A 600 μL aliquot of the stock solution was then diluted to 30.0 mL using McCoy's 5A media supplemented with 20% FBS, resulting in a stock solution of 100 μM with respect to **3**. Stock solutions of 80, 60, 40, and 20 μM were prepared by diluting the initial 100 μM stock solution using fresh media containing 2% MeCN (v/v). The initial incubation media was aspirated from the plates and the cells were incubated with the previously described 100, 80, 60, 40 and 20 μM solutions of **3**. Controls used in the experiment included 100 μM solutions of photolyzed complex **3** and free Pipdansyl ligand in culture media containing 2% MeCN. Other controls included fresh media and 2% MeCN in media (v/v). Once treated, both plates were incubated for 2 h at 37 °C and 5% $CO_2(g)$ to allow internalization of the compounds. After incubation, the media was aspirated, and cells were washed with PBS. Fresh culture media was added to the plates and the cells were incubated for an additional h. Afterwards, one plate was kept incubating under strict dark condition, while the other plate was treated with light from a low-power LED light source (15 mW/cm²) at 1.5 cm for 40 min. After photolysis, the plates were incubated for an additional 2 h under dark condition. Following the incubation time, the old media was aspirated, the cells were washed with PBS and fresh media was introduced to allow the cells to recover while incubating them for 2 h. Lastly, the MTT was added to both plates according to the manufacturer's protocol (Life Technologies), and the viability of the cells was assessed using a microplate reader (Molecular Devises VersaMax®). Control experiments were also performed with human embryonic kidney cells HEK-293 to evaluate the effects of CO on normal healthy cells.

3. Results and discussion

3.1. Synthesis, characterization and stability of 3

The manganese complex **3** was synthesized by reacting [Mn $(CO)_3$(phen)(CF_3SO_3)] (previously reported by us, [13]) with 1-
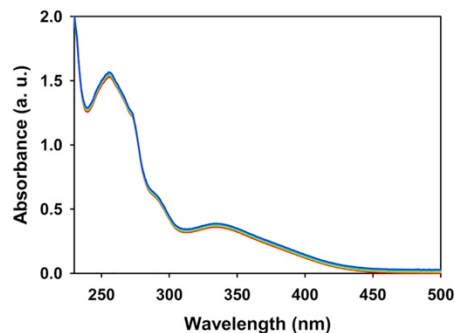
Fig. 1. Stability of complex **3** in PBS containing 2% MeCN over a period of 24 h.

dansylpiperazine (Pipdansyl) under dark condition. The reaction mixture was allowed to stir for 48 h to ensure completion. The complex was obtained as a yellow microcrystalline powder after recrystallization from dichloromethane and hexanes. The isolated solid afforded satisfactory elemental analysis. The identity of the complex was also confirmed through high-resolution mass spectrometry using positive ionization mode. The major peak at $m/z = 638.12$ corresponded to complex **3** without the trifluoromethane sulfonate counter anion. The counter anion did travel with the complex as indicated by a moderate signal at $m/z = 786.93$. Interestingly, a small peak corresponding to two cations of **3** and one trifluoromethane sulfonate counter ion was also observed at $m/z = 1425.20$ (Supporting Information, Fig. S1).

Complex **3** is soluble in common organic solvents and such solutions are stable when kept in the dark. Stability of **3** in a 2% MeCN in PBS (v/v) solution was checked by recording the absorption spectrum periodically for a 24 h period when no significant decomposition of the complex was observed when the solution was kept in the dark (Fig. 1). However, such a solution exhibit systematic changes in the electronic absorption spectra upon exposure to low power (15 mW/cm²) broadband visible light (vide infra).

3.2. CO photorelease studies

The rate of CO-release (k_{CO}) from **3** ($0.13\,min^{-1}$) was calculated from the changes in electronic absorption spectra upon exposure of **3** in MeCN to visible light (power = 15 mW/cm²) at regular time intervals (Fig. 2). Quantum yield measurement with potassium ferrioxalate as the actinometer yielded a value of 0.39 ± 0.03 for this photoCORM. A myoglobin assay was also carried out to further confirm the release of CO from complex **3** upon exposure to visible light. The assay was carried out in a two-cuvette system to circumvent possible interference from the reducing agent. The first cuvette containing **3** in MeCN was exposed to the same low-power visible light for 5 min and CO released upon such exposure was transferred via canula to a second cuvette containing the reduced myoglobin. The formation of carboxy myoglobin was confirmed by shift of the Soret band of reduced myoglobin from 435 to 424 (Fig. 3).

3.3. Infrared spectroscopy studies

Infrared spectroscopy was employed to assess the number of CO molecules released from **3** upon photolysis. Complex **3** exhibits a set of two strong IR bands at 2036 and 1944 cm⁻¹ arising from 3 CO ligands in facial disposition (Fig. 4, blue trace). A batch of MeCN solution of **3** was photolyzed with visible light in a glass petri dish for 40 min, dried
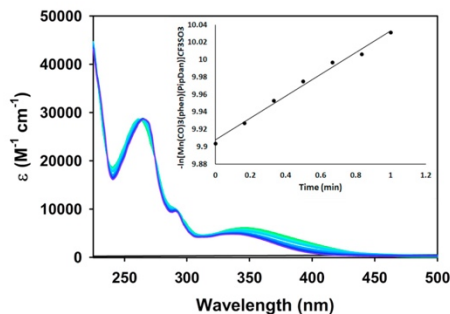
Fig. 2. Spectral changes in the electronic absorption of **3** in MeCN upon exposure to low power visible light (15 mW/cm²) at periodic time intervals.
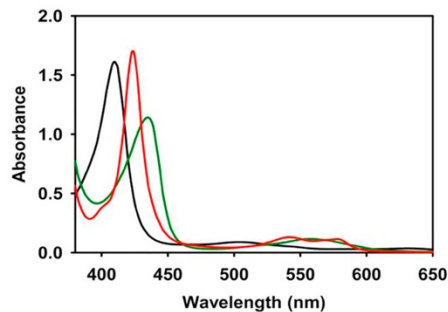
Fig. 3. UV–vis absorption traces from the myoglobin assay using complex **3** in PBS/MeCN solution at 298 K; Oxidized myoglobin (black trace), reduced myoglobin (green trace) and carboxy myoglobin (red trace). (For interpretation of the references to colour in this figure legend, the reader is referred to the web version of this article.)
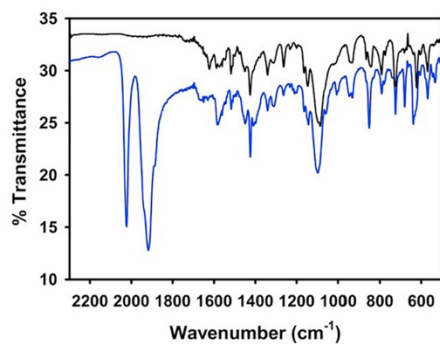
Fig. 4. IR spectra of **3** (blue trace) and its photoproduct (black trace). (For interpretation of the references to colour in this figure legend, the reader is referred to the web version of this article.)

under vacuum, and the resulting residue was analyzed by IR spectroscopy. The exhaustive photolysis resulted in complete loss of CO from **3** as indicated by the disappearance of the CO bands (Fig. 4, black trace). Similar loss of all 3 CO molecules has been observed with other Mn(I)-derived photoCORMs in previous studies [12,13,17]. In case of photoCORM **2**, loss of three CO molecules led to formation of [Mn(phen)$_2$(H$_2$O)$_2$](CF$_3$SO$_3$)$_2$ and [Mn(phen)$_3$](CF$_3$SO$_3$)$_2$ in a photolyzed solution in addition to free Imdansyl ligand [12]. In the present study high-resolution ESI-MS data on the photolyzed solution of **3** indicated the presence of [Mn(MeOH)$_4$(CF$_3$SO$_3$)]$^+$ and [Mn(phen)$_2$(CF$_3$SO$_3$)]$^+$ species in addition to free phen and Pipdansyl ligands (Supporting Information, Fig. S2).

3.4. Luminescence studies

The majority of Mn(I)-based photoCORMs derived from fluorescent ligands exhibit no luminescence and hence their accumulation within target cells can hardly be noted. The luminescence of the ligands is quenched upon coordination to the manganese center. In case of photoCORM **1**, reported by Schiller and coworkers, the luminescence of the aminopyridine-dansyl ligand L was completely quenched upon coordination of the N donors to the Mn(I) center [32]. In L, the dansyl moiety is directly connected to the central N donor which in turn is directly coordinated to the Mn(I) center. In this photoCORM, the PET arising from excitation of the N electron(s) to the dansyl π system is quenched due to the electron-withdrawing effect of the [Mn(CO)$_3$] unit. When the 3 CO molecules are released (upon illumination), the fluorescence of L is observed. In our previous account, the dansyl moiety of the Imdansyl ligand retains most of its luminescence in photoCORM **2** because the intervening imidazole ring partially protects the dansyl group from the electron withdrawing effects of the [Mn(CO)$_3$] unit. The two distinct N atoms of the imidazole linker in **2** serve different functions. One N is bonded to the dansyl moiety (allowing PET to occur) while the second N is coordinated to the Mn(I) center. The aromaticity of the imidazole linker however allows some mixing of the PET process with the electron withdrawing effects of the [Mn(CO)$_3$] unit giving rise to *partial quenching*. In **3**, the aromaticity is absent in the piperazine linker and hence the luminescence of the Pipdansyl ligand is *barely* (> 5%) *quenched* when coordinated to the metal center (Fig. 5). The luminescence intensity of the ligand is fully restored after photolysis of a solution of **3** (Fig. 5).

The change of the linker from imidazole (in photoCORM **2**) to piperazine (in photoCORM **3**) also leads to a *higher luminescence intensity*
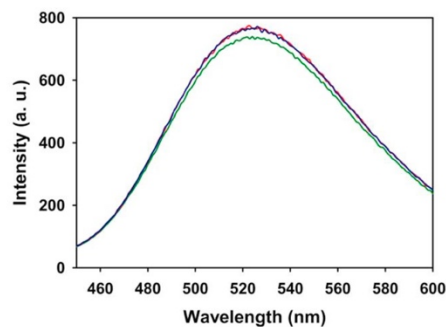
Fig. 5. Emission spectra of **3** (dark green trace), photolized solution of **3** (blue trace), and Pipdansyl (red trace) in MeCN at 298 K. (For interpretation of the references to colour in this figure legend, the reader is referred to the web version of this article.)

243
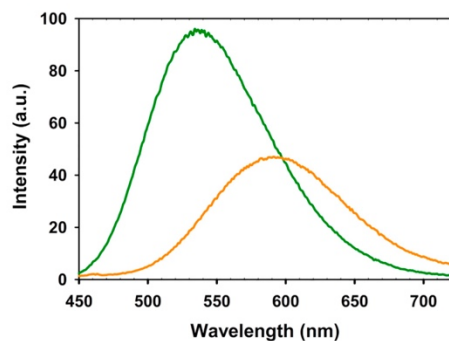
Fig. 6. Emission spectra of **3** (green trace) and **2** (orange-red trace) in MeCN (same concentration). (For interpretation of the references to colour in this figure legend, the reader is referred to the web version of this article.)

Fig. 8. Reduction in viability of colorectal adenocarcinoma (HT-29) cells by CO photorelease from complex **3** in the dark (red) and under low power visible light (blue). (For interpretation of the references to colour in this figure legend, the reader is referred to the web version of this article.)

*of **3** compared to **2*** under identical concentrations (Fig. 6). This property of **3** could be conveniently explotied in cellular confocal microscopy studies. Furthermore, the emission of **3** (520 nm) lies in the green channel which is somewhat preferable in studies where the prodrug is tracked in the green channel and its target (like mitochondria or membrane proteins) is imaged in the red channel.

3.5. Cellular imaging

The excellent luminescent properties of **3** prompted us to study its cellular uptake in HT-29 colorectal adenocarcinoma cells. The cells were plated onto imaging disks and allowed to grow for 24 h. Next, they were incubated with 25 μM of **3** for 1 h. The medium was then aspirated, and the cells were washed with PBS. Fresh media free of phenol red and FBS was added to the cells and the images were captured using a confocal microscope to reveal the cellular uptake of **3** in to HT-29 cells (Fig. 7). Complex **3** is the second example of a Mn-based photo-CORM that can be tracked inside cancer cells before the CO is released from the complex. The intense luminescence of **3** allows the cells to be imaged at a lower concentration than the previously reported complex **2** [12].

3.6. MTT viability assay

Cell viability of HT-29 colorectal adenocarcinoma cells was investigated upon treatment of the cells with complex **3** under light and dark conditions. The HT-29 cells were treated with a range of concentrations of **3** and the viability was assessed by the reduction of the MTT tetrazolium dye. The assay demonstrated a concentration dependent reduction in viability of HT-29 cells treated with **3** after low-power (15 mW/cm^2) visible light irradiaton for 40 min (Fig. 8, green bars). The cells treated with **3** shows 10% – 48% reduction in viability upon exposure to visible light, while control groups that were kept in the dark did not display significant reduction in viability. Other controls including the 2% MeCN solution, the Pipdansyl ligand, or the photolized solution of **3** also displayed negligible reduction in viability of HT-29 cells under light or dark conditions. These results confirm that the reduction in viability was a direct consequence of exposure of the cells to CO released from photoCORM **3**. No cytotoxicity was observed when human embryonic kidney cells HEK-293 were used in cellular viability study. As shown in Fig. S3 (Supporting Information), the normal cell line displayed no reduction in viability even with 100 μM of complex **3** in the incubation medium under illumination. This is quite expected

Fig. 7. Fluorescence (left) and bright field (right) images obtained after incubation of HT-29 cells with **3** in media containing 2% MeCN.

116

244

since normal healthy cells are known to tolerate low levels of CO without any impairment [3].

4. Conclusion

Prior to our previous report on complex **2**, Mn(I)-based photoCORMs were not inherently luminescent and could not be tracked inside cellular systems prior to CO-release, despite the highly emissive nature of the ligands used. Originally, the intracellular uptake of manganese photoCORMs was indirecly studied by using analogous luminescent Re(I) counterparts or by observing the luminesence obtained from the fluoresecent ligands after being released from the complex [13]. However, the entry of the intact manganese photoCORM into the cellular target was never directly demonstrated. In this account, we report the synthesis and characterization of **3**, a luminescent manganese photoCORM which retains its luminescence before and after CO-release. This photoCORM utilizes the Pipdansyl ligand which contains two nitrogens separated by sp³ carbons. The non-aromaticity of piperazine allows most of the luminescence of the fluorophore to be retained, even after coordination to the metal center. The results of this systematic investigation on the linkers in complexes **1–3** open up the opportunity for the design and synthesis of new luminescent Mn(I) photoCORMs with different ranges of luminescence.

Appendix A. Supplementary data

ESI-MS for complex **3** (Fig. S1) and its photoproduct(s) (Fig. S2), and HEK-293 cell viability results (Fig. S3) can be found in the online version at https://doi.org/10.1016/j.ica.2018.09.088.

References

[1] R. Motterlini, R. Foresti, Am. J. Physiol. Cell Physiol. 312 (2017) C302–313.
[2] R. Motterlini, L.E. Otterbein, Nat. Rev. Drug Discovery 9 (2010) 727–734.
[3] L. Wu, R. Wang, Pharmacol. Rev. 57 (2005) 585–630.
[4] G. Kikuchi, T. Yoshida, M. Noguchi, Biochem. Biophys. Res. Commun. 338 (2005) 558–567.
[5] E. Kottelat, F. Zobi, Inorganics 5 (2017) 24.
[6] U. Schatzschneider, Br. J. Pharmacol. 272 (2015) 1638–1650.
[7] I. Chakraborty, S.J. Carrington, P.K. Mascharak, Acc. Chem. Res. 47 (2014) 2603–2611.
[8] S. Heinemann, T. Hoshi, M. Westernhausen, A. Schiller, Chem. Commun. 50 (2014) 3644–3660.
[9] S. Garcia-Gallego, G.J.L. Bernardes, Angew. Chem. Int. Ed. 53 (2014) 9712–9721.
[10] C.C. Romao, W.A. Blatter, J.D. Seixas, G.J.L. Bernardes, Chem. Soc. Rev. 41 (2012) 3571–3583.
[11] R.D. Rimmer, A.E. Pierri, P.C. Ford, Coord. Chem. Rev. 256 (2010) 1509–1519.
[12] J. Jimenez, I. Chakraborty, A. Dominguez, J. Martinez-Gonzalez, W.M.C. Sameera, P.K. Mascharak, Inorg. Chem. 57 (2018) 1766–1773.
[13] I. Chakraborty, S.J. Carrington, G. Roseman, P.K. Mascharak, Inorg. Chem. 56 (2017) 1534–1545.
[14] M.N. Pinto, I. Chakraborty, C. Sandoval, P.K. Mascharak, J. Control. Release 264 (2017) 192–202.
[15] I. Chakraborty, J. Jimenez, P.K. Mascharak, Chem. Commun. 53 (2017) 5519–5522.
[16] I. Chakraborty, J. Jimenez, W.M.C. Sameera, M. Kato, P.K. Mascharak, Inorg. Chem. 56 (2017) 2863–2873.
[17] S.J. Carrington, I. Chakraborty, J. Bernard, P.K. Mascharak, Inorg. Chem. 55 (2016) 7852–7858.
[18] S.J. Carrington, I. Chakraborty, P.K. Mascharak, Dalton Trans. 44 (2015) 13828–13834.
[19] S.J. Carrington, I. Chakraborty, J.M.L. Bernard, P.K. Mascahrak, A.C.S. Med. Chem. Lett. 5 (2014) 1324–1328.
[20] S.J. Carrington, I. Chakraborty, P.K. Mascharak, Chem. Commun. 49 (2013) 11254–11256.
[21] M.J. Rose, P.K. Mascharak, Coord. Chem. Rev. 252 (2008) 2093–2114.
[22] M.A. Wright, J.A. Wright, Dalton Trans. 45 (2016) 6801–6811.
[23] H. Pfeiffer, A. Rojas, J. Niesel, U. Schatzschneider, Dalton Trans. (2009) 4292–4298.
[24] J. Niesel, A. Pinto, H.W.P. NDongo, K. Merz, I. Ott, R. Gust, U. Schatzschneider, Chem. Commun. (2008) 1798–1800.
[25] E. Kottelat, A. Ruggi, F. Zobi, Dalton Trans. 45 (2016) 6920–6927.
[26] A.E. Pierri, P.J. Huang, J.V. Garcia, J.G. Stanfill, M. Chui, G. Wu, N. Zheng, P.C. Ford, Chem. Commun. 51 (2015) 2072–2075.
[27] L.C.-C. Lee, K.-K. Leung, K.K.-W. Lo, Dalton Trans. 46 (2017) 16357–16380.
[28] K. Ranasinghe, S. Handunnetti, I.C. Perera, T. Perera, Chem. Central J. 10 (2016) 71.
[29] E.E. Langdon-Jones, N.O. Symonds, S.E. Yates, A.J. Hayes, D. Lloyd, R. Willams, S.J. Coles, P.N. Horton, S.J.A. Pope, Inorg. Chem. 53 (2014) 3788–3797.
[30] A.E. Pierri, A. Pallaoro, G. Wu, P.C. Ford, J. Am. Chem. Soc. 134 (2012) 18197–18200.
[31] F.L. Thorp-Greenwood, M.P. Coogan, L. Mishra, N. Kumari, G. Rai, S. Saripella, New J. Chem. 36 (2012) 64–72.
[32] R.G. Upendar, J. Axthelm, P. Hoffmann, N. Taye, S. Glaser, H. Gorls, S.L. Hopkins, W. Plass, U. Neugebauer, S. Bonnet, A. Schiller, J. Am. Chem. Soc. 139 (2017) 4991–4994.
[33] Y. Zhang, H. Chen, D. Chen, D. Wu, X. Chen, S.H. Liu, J. Yin, Org. Biomol. Chem. 13 (2015) 9760.

Chapter 3.II: Therapeutic Potential of Two Visible Light Responsive Luminescent photoCORMs: Enhanced Cellular Internalization Driven by Lipophilicity.

3.II.1 Background.

The pathophysiological roles of carbon monoxide (CO) as a signaling molecule in mammalian cells are now well *established*.[1-4] The homeodynamic nature of CO has recently ushered the potential of this small gaseous molecule in therapeutic applications despite its widespread implication as a toxic pollutant.[1,2] In mammals, heme oxygenase-catalyzed degradation of heme proteins leads to generation of endogenous CO.[5,6] Among other salutary effects, CO provides cytoprotection[2,7] (pro-proliferative) to cellular milieu and has also been shown to exert vasoregulatory actions.[8,9] However, in certain malignant cells CO induces an anti-Warburg effect ultimately resulting in metabolic exhaustion and cellular apoptosis.[10] This mechanism is exclusively operational only within malignant cells due to their metabolic acquisition of a glycolytic phenotype. It is now apparent that a more controlled and sustainable application of CO from an external source can impart selective pro-apoptotic action in malignant cells without causing any noticeable damage to normal (primary) cells. Furthermore, CO has recently been shown to play active role in sensitization of conventional chemotherapeutics and thereby could be utilized as adjuvant therapeutics.[10-12]

Among various external CO sources (including gaseous CO), the photoactivated CO-releasing molecules (photoCORMs) have shown significant

promise as superior CO donors in terms of more controlled and sustainable delivery.[13-19] Several research groups including ours have exploited the therapeutic potential of photo-triggered CO from photoCORMs against selected malignancies.[14,19-27] Despite such capacity of the photoCORMs to induce apoptosis in certain malignant cells under the control of light,[27] the efficacy of cellular penetration of these prodrugs are debatable. The light-triggered CO from photoCORM prodrugs can diffuse into the cell and exert its activity, even if the prodrug shows moderate to poor cellular internalization. However, this may result in undesirable loss of CO before reaching the target of interest and could mitigate the extent of its salutary benefit. Poor internalization of the photoCORM results in the use of higher concentration of the prodrug to exert the therapeutic effect. In contrast, a strategically designed photoCORM with optimal lipophilicity could be internalized more efficiently into cells and in such scenario the uncaged CO molecules are likely to display a more pronounced effect at a relatively lower dose of the prodrug. Lipophilicity plays critical role in medicinal chemistry.[28,29] Uptake of drug molecules is a function of solubility and cell permeability. Although for a given drug molecule aqueous solubility is important for its physiological acceptability, low lipophilicity can contribute to poor cell membrane permeability. The bioavailability of the drug is crucial and generally high lipophilicity contributes in maintaining a favorable metabolic stability through circumventing its first pass clearance. Overall, optimal lipophilicity could be a major factor in achieving a modular drug/prodrug system, which will be effective towards desired action on a

cellular target (in our case towards eradication of certain malignancies) at a relatively lower dosage by virtue of its superior cell penetration capacity.

In this account we report a luminescent photoCORM [Mn(CO)$_3$(**L1**)(Imdansyl)](CF$_3$SO$_3$) **1** (Figure 3.II.1) derived from a diazabutadiene-based ligand **L1** containing two *highly lipophilic* adamantyl motifs (Imdansyl = dansylimidazole) as shown in Figure 3.II.2. Adamantane derivatives are excellent pharmacophores with enhanced lipophilicity, stability, and often exhibit improved pharmacokinetic profiles.[29] Aminoadamantanes such as amantadine and rimantadine
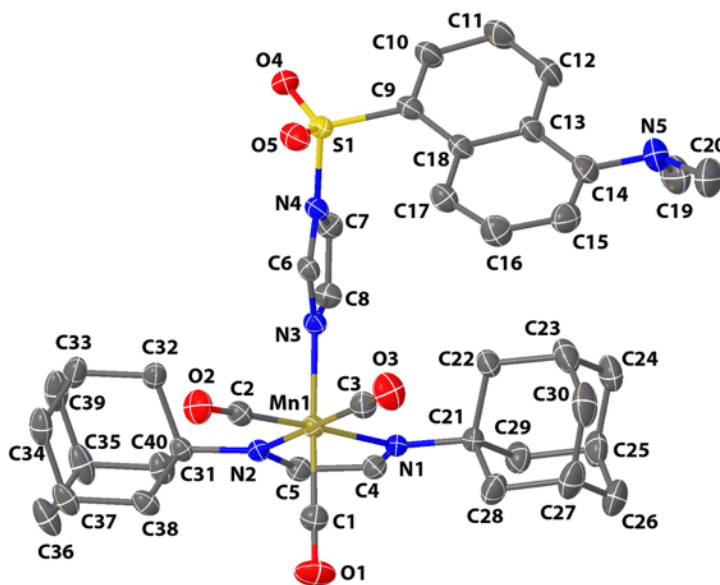
Figure 3.II.1. Thermal ellipsoid plot with atom labeling scheme of the cation of complex **1** shown with 50% probability ellipsoids. Hydrogen atoms and the counter anion are omitted for the sake of clarity. Selected bond distances (Å): Mn1−N1, 2.108(3); Mn1−N2, 2.096(2); Mn1−N3, 2.079(3); Mn1−C1, 1.823(4); Mn1−C2, 1.800(4); Mn1−C3, 1.803(4).
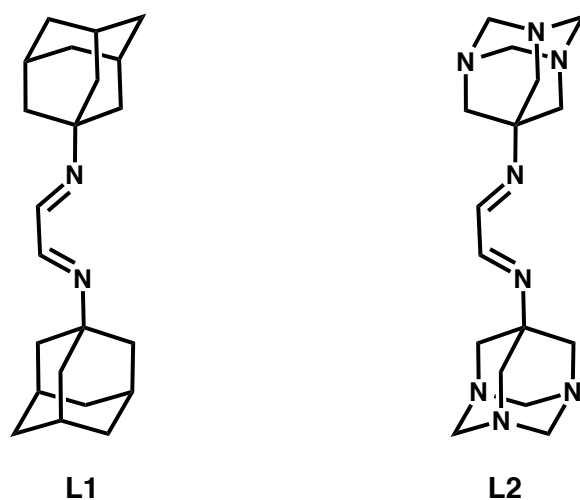
Figure 3.II.2. Lipophilic ligand **L1** and hydrophilic ligand **L2** employed in the present work.

are amongst the first successful drug candidates bearing the "lipophilic bullets" and are still in pharmaceutical markets to date.[30,31] There has been a significant development in the area of adamantane-based pharmaceuticals to treat critical viral infections such as, *Influenza A*, *Herplex simplex*, *Hepatitis C* and *HIV*.[29] Herein, for the first time, we report the successful synthesis and characterization of a highly lipophilic photoCORM derived from a diazabutadiene ligand bearing a clinically approved lipophilic pharmacophore. The efficacy of this photoCORM towards CO-induced cellular apoptosis has been assessed with human colon adenocarcinoma (HT-29) cells. Furthermore, for sake of comparison of cellular permeability, an analogous complex derived from a diazabutadiene ligand bearing the *hydrophilic* 1,3,5-triazaadamantyl group (**L2**, Figure 3.II.2) namely, [Mn(CO)₃)(**L2**)(Imdansyl](CF₃SO₃) **2** has been synthesized and studied. The hydrophilicity of azaadamantane and its derivatives arises

from good hydrogen acceptor capabilities of the tertiary nitrogen groups.[32-34] To date, triazaadamantyl-bearing complexes have been shown to possess excellent antimetastatic and antiangiogenic properties. This motif constitutes part of certain anticancer drugs that are currently undergoing phase II clinical trials.[35,36] The sixth position in both complexes **1** and **2** is occupied by one of the N-centers of a known fluorophore, namely Imidazoledansyl (Imdansyl). This ligand has been incorporated in the design to provide an easy handle for monitoring the internalization of various CO-prodrugs through confocal microscopy.[20,37] Complexes **1** and **2** have been characterized by analytical and spectroscopic techniques, including X-ray crystallography. Finally, biological studies employing these two photoCORMs with different lipophilicity have been completed to clearly demonstrate that proper ligand design could afford photoCORMs which avert unwanted CO loss outside the membrane before reaching the target of interest and thus exhibit superior proapoptotic effects.

3.II.2 Results and Discussion.

*3.II.2.1 Synthesis of Complexes **1** and **2**.*

Both **L1** and **L2** were found to react slowly with $[Mn(CO)_5Br]$ and required extended (48 h) reaction time for coordination. Subsequent reaction of $[Mn(CO)_3(\textbf{L1})Br]$ with $AgCF_3SO_3$ was however complete within 6 h in CH_2Cl_2 without any problems. In contrast, reaction of $[Mn(CO)_3(\textbf{L2})Br]$ with the silver salt required the use of anhydrous MeOH as the solvent since the resulting complex $[Mn(CO)_3(\textbf{L2})(CF_3SO_3)]$ exhibited poor solubility in CH_2Cl_2. This reaction was also

carefully carried out in absence of air and moisture to avoid unwanted side reactions between $[Mn(CO)_3(\textbf{L2})(CF_3SO_3)]$ and H_2O. The complex $[Mn(CO)_3(\textbf{L1})(CF_3SO_3)]$ reacted with 2-fold excess of Imdansyl for 48 h to ensure complete formation of **1**. Although complex **1** is considerably stable under dark conditions, presence of moisture in the last step of its synthesis interferes with the coordination of Imdansyl and facilitates the substitution of CF_3SO_3 by a H_2O molecule, resulting in the partial formation of the aqua complex $[Mn(CO)_3(\textbf{L1})(H_2O)](CF_3SO_3)$ (Figure 3.II.3) However, under strict anaerobic and anhydrous conditions, the reaction of the triflate adduct with Imdansyl proceeds smoothly to afford complex **1** of high purity. In case of $[Mn(CO)_3(\textbf{L2})(CF_3SO_3)]$, the synthesis required the use of strictly anhydrous MeOH and exactly 1 equiv. of Imdansyl with a reaction time of 6 h to avoid the formation of any aqua complex $[Mn(CO)_3(\textbf{L2})(H_2O)]CF_3SO_3$. The isolated crude mixture was composed mainly of complex **2**, and unreacted starting materials were removed by recrystallization from CH_2Cl_2/hexanes. Careful studies were carried out to determine if the presence of water in the solvent results in the displacement of the Imdansyl ligand. Complexes **1** and **2** were stirred in wet MeOH (MeOH:H_2O 9:1) for 48 h. The solvent was removed under reduced pressure and the resulting crude powder was analyzed through ^{1}H-NMR. The results indicated that neither complex undergoes decomposition. This observation confirms that water does not displace the Imdansyl ligand within at least 48 h.

Figure 3.II.3. Thermal ellipsoid plot with atom labeling scheme of the cation of [Mn(CO)$_3$(**L1**)(H$_2$O)]CF$_3$SO$_3$ shown with 50% probability ellipsoids. Hydrogen atoms and the counter anion are omitted for the sake of clarity. Selected bond distances (Å): Mn1−N1, 2.098(3); Mn1−N2, 2.111(2); Mn1−O7, 2.071(3); Mn1−C1, 1.800(3); Mn1−C2, 1.813(2); Mn1−C3, 1.805(2).

3.II.2.2 Structure and X-Ray Crystallography.

The molecular structure of **1** and [Mn(CO)$_3$(**L1**)(H$_2$O)]CF$_3$SO$_3$ have been determined by single crystal X-ray crystallography. The coordination geometry of the Mn centers in both complexes (**1** and [Mn(CO)$_3$(**L1**)(H$_2$O)]CF$_3$SO$_3$) is distorted octahedral with three facially disposed CO ligands (Figures 3.II.1 and 3.II.3). In both structures the asymmetric unit consists of one full molecule of the cationic **1**$^+$ or Mn(CO)$_3$(**L1**)(H$_2$O)]$^+$ along with CF$_3$SO$_3$ counter anion. The two N atoms of the ligand **L1** and two C atoms from two CO constitute the equatorial planes, while the third CO occupies one of the axial positions. The second axial position is occupied by the N atom of Imdansyl group in complex **1** and O atom of the coordinated water molecule in [Mn(CO)$_3$(**L1**)(H$_2$O)]CF$_3$SO$_3$. The equatorial planes composed of N1, N2, C2 and C3

atoms for complexes **1** and $[Mn(CO)_3(\textbf{L1})(H_2O)]CF_3SO_3$ are satisfactorily planar with mean deviations of 0.019(3) and 0.020(3) Å respectively. The Mn atoms are slightly displaced by 0.006 and 0.009 Å for complexes **1** and $[Mn(CO)_3(\textbf{L1})(H_2O)]CF_3SO_3$ respectively from the equatorial planes toward the C1 atom of the axial CO group. The chelate rings for **1** and $[Mn(CO)_3(\textbf{L1})(H_2O)]CF_3SO_3$ (composed of Mn1, N1, N2, C4 and C5 atoms) fairly deviate from planarity with mean deviations of 0.030(3) and 0.021(3) Å respectively. In **1**, the dihedral angle between the imidazole and the dansyl group is 85.6°. Analysis of crystal packing of **1** (Figure 3.II.4), reveals few non classical hydrogen bonding interactions which consolidates its solid state structure [C8-H8---O8[i], with H8---O8, 2.28 Å; C10-H10---O4, with H10---O4, 2.36 Å; C11- H11---O7[ii], with H11---O7, 2.54 Å; C12-H12---N5, with H12---N5, 2.47 Å; C17-H17---O5, with H17---O5, 2.46 Å; and C34-H34A---O7[iii], with H34A---O7, 2.59 Å; symmetry codes: (i) -x+1, - y+2, -z+1; (ii) x+1, y, z-1; (iii) x+1, y, z]. In addition, moderate π-π stacking
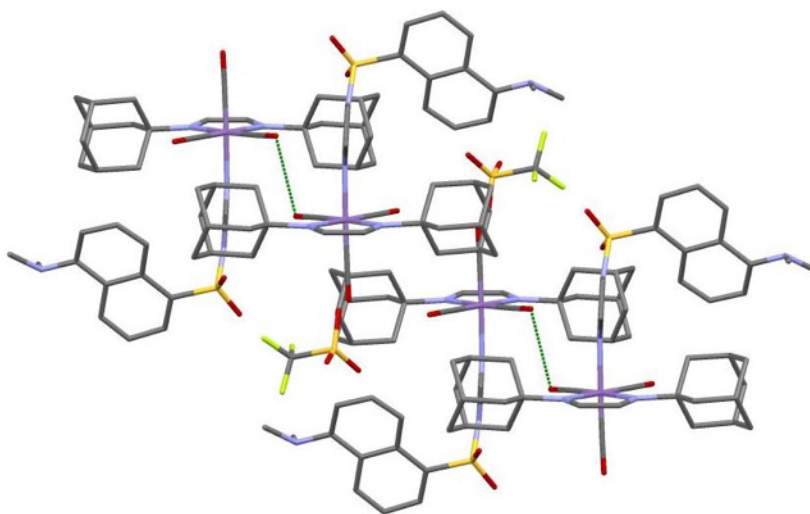
Figure 3.II.4. Packing pattern of **1** along b axis.

interactions have been noticed between the quinoline rings of the dansyl moieties of two adjacent molecules (centroid-to-centroid distance, 3.825 Å, Figure 3.II.5). Careful inspection of the packing patterns of $[Mn(CO)_3(\mathbf{L1})(H_2O)]CF_3SO_3$, revealed two classical hydrogen-bonding interactions [O7-H7A---O5^i, with H7A---O5, 1.90 Å; and O7-H7B---O6, with H7B---O6, 1.89 Å; symmetry code: (i) –x+1, y-1/2, -z+1/2]. In this case no intermolecular π-π interactions have been realized (Figure 3.II.6).
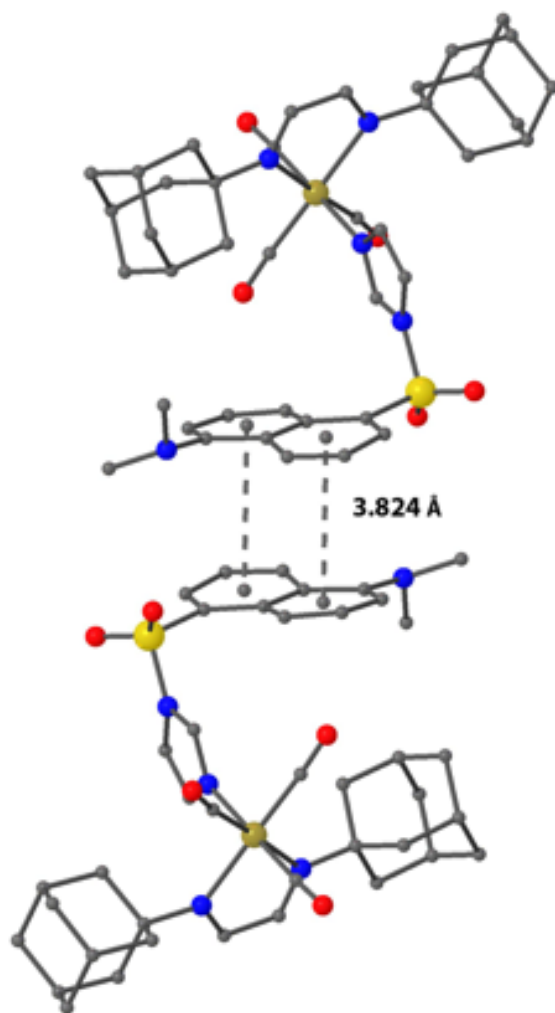
Figure 3.II.5. Intermolecular π-π stacking interactions in complex **1**.
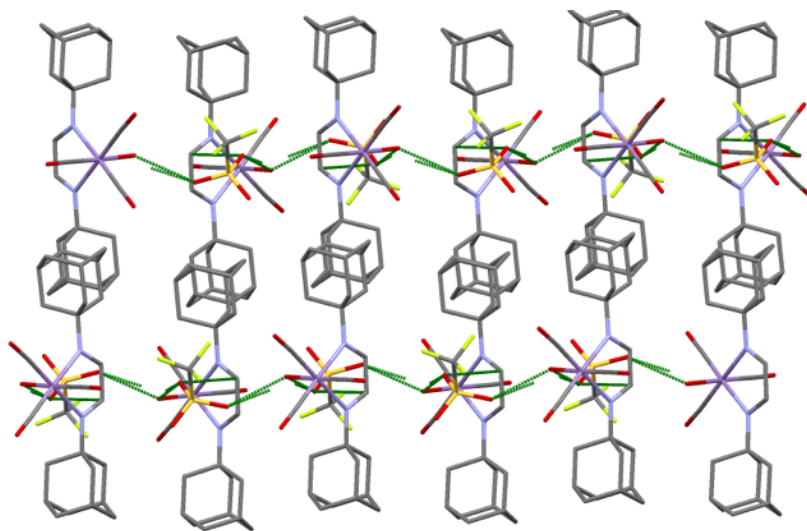
Figure 3.II.6. Packing pattern of $[Mn(CO)_3(\textbf{L1})(H_2O)](CF_3SO_3)$ along a axis, the green dotted line indicate weak intermolecular interactions involving, the O atom of the coordinated water molecule and one of the O atoms of the triflate anion.

3.II.2.3 Solubility and Stability of Complexes 1 and 2.

      Complex **1** is highly soluble in organic solvents and MeCN/H_2O mixtures but insoluble in pure H_2O. In contrast, complex **2** is highly soluble in H_2O and MeOH, but partially soluble in ethanol and organic solvents. The solubility of **2** in H_2O was obtained by fully dissolving a known amount of the complex in water and serially diluting the solution to prepare a standard curve. A saturated solution of **2** was prepared separately, volumetrically diluted (10-fold), and its absorbance recorded. The concentration of the dilution prepared from the saturated solution was determined using the linear regression obtained from the standard curve (red dot Figure 3.II.7). After correcting for the 10-fold dilution factor, the saturated solution was calculated to
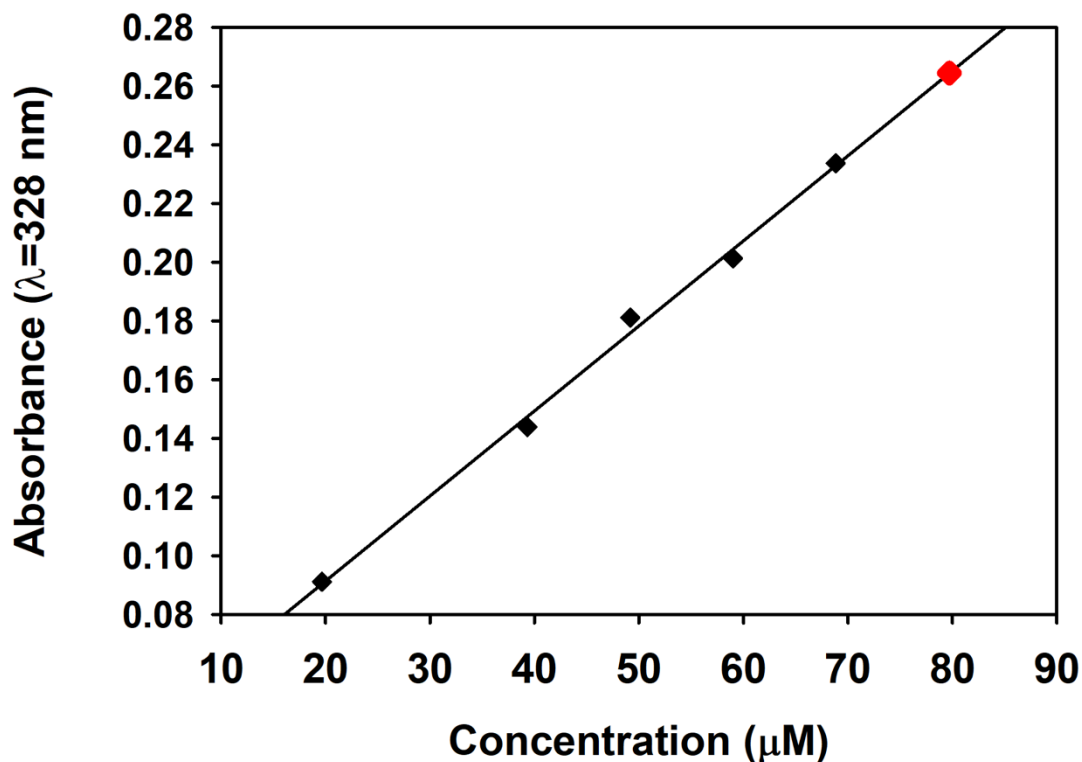
Figure 3.II.7. Standard curve prepared by serial dilution of a solution with known concentration of complex **2** in H_2O and linear regression (black line) used to calculate the concentration of a saturated solution of complex **2** diluted by a factor of 10 (red dot).

contain a concentration of 0.73 mg mL^{-1} (797 μM). In absence of light, both complexes are indefinitely stable as solids. Solutions of complex **1** or **2** containing 2% MeCN, the solvent pair employed in the biological experiments (*vide infra*), are stable for at least 24 h, as indicated by its absorption spectrum (Figure 3.II.8 3.II.9). Furthermore, solutions of both complexes are very stable in CH_2Cl_2 and $CHCl_3$.
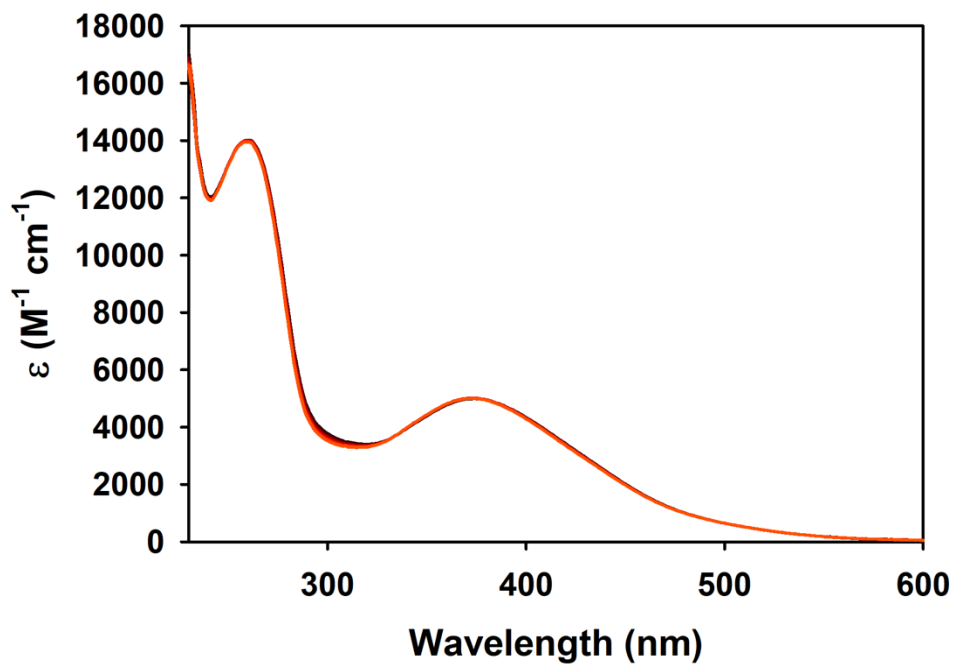
Figure 3.II.8. Changes in UV-Vis traces of **1** in 2% MeCN in PBS at 298 K over 24 h.
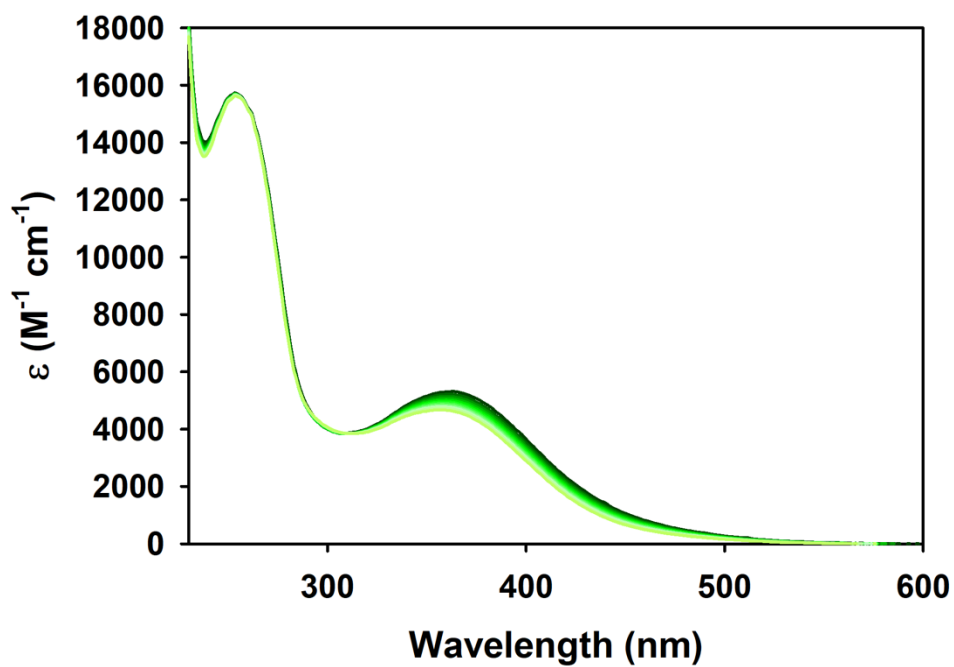
Figure 3.II.9. Changes in UV-is traces of **2** in 2% MeCN in PBS at 298K over 24 h.

3.II.2.4 Carbon Monoxide Photorelease.

Upon exposure to broadband low power visible light (15 mW cm^{-2}) both complexes exhibit systematic changes in the electronic absorption spectra (Figures 3.II.10 and 3.II.11). These changes are associated with uncaging of CO from the respective complexes as confirmed by standard Myoglobin assay[38] (Figure 3.II.12). Because sodium dithionite is known to facilitate the release of CO from carbonyl complexes, a dual quartz cuvette system[22] was utilized in these experiments. The apparent CO release rates (k_{CO}) from both complexes have been determined by
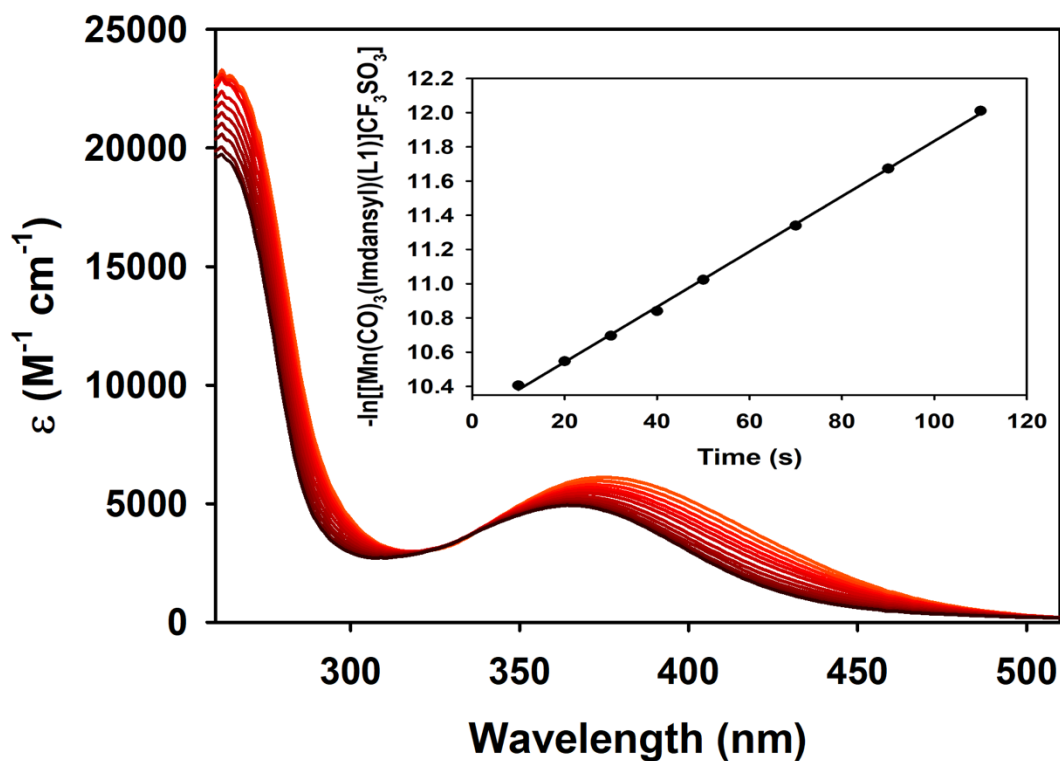
Figure 3.II.10. Changes in UV-Vis spectrum of **1** (conc. 2.0 x 10^{-4} M) in CH$_2$Cl$_2$ solution upon exposure to low power visible light (15 mW cm^{-2}) at 298 K.
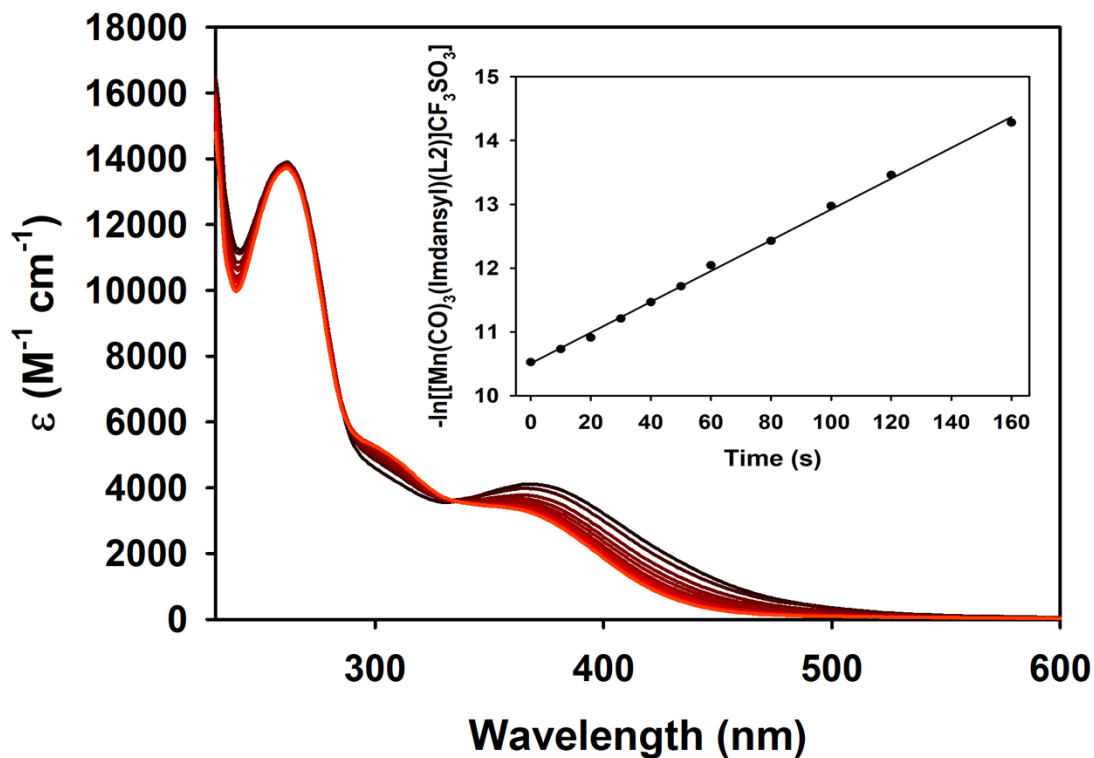
Figure 3.II.11. Changes in UV-Vis spectrum of **2** (conc. 2.0 x 10^{-4} M) in CH_2Cl_2 solution upon exposure to low power visible light (15 mW cm^{-2}) at 298 K.

recording the electronic absorption spectra and monitoring changes of the spectral traces at 410 nm upon exposure to light at 10 s intervals. The k_{CO} values were calculated from ln(C) vs t plot (Figure 3.II.10 and 3.II.11) and were found to be 1.03 and 0.66 min^{-1} for complexes **1** (ϕ_{380} = 0.35+0.02) and **2** (ϕ_{380} = 0.23+0.02) respectively. That exposure to light released all 3 CO molecules from both complexes were confirmed by IR studies performed on the extensively photolysed solutions of the complexes **1** and **2** (Figures 3.II.13-3.II.16).
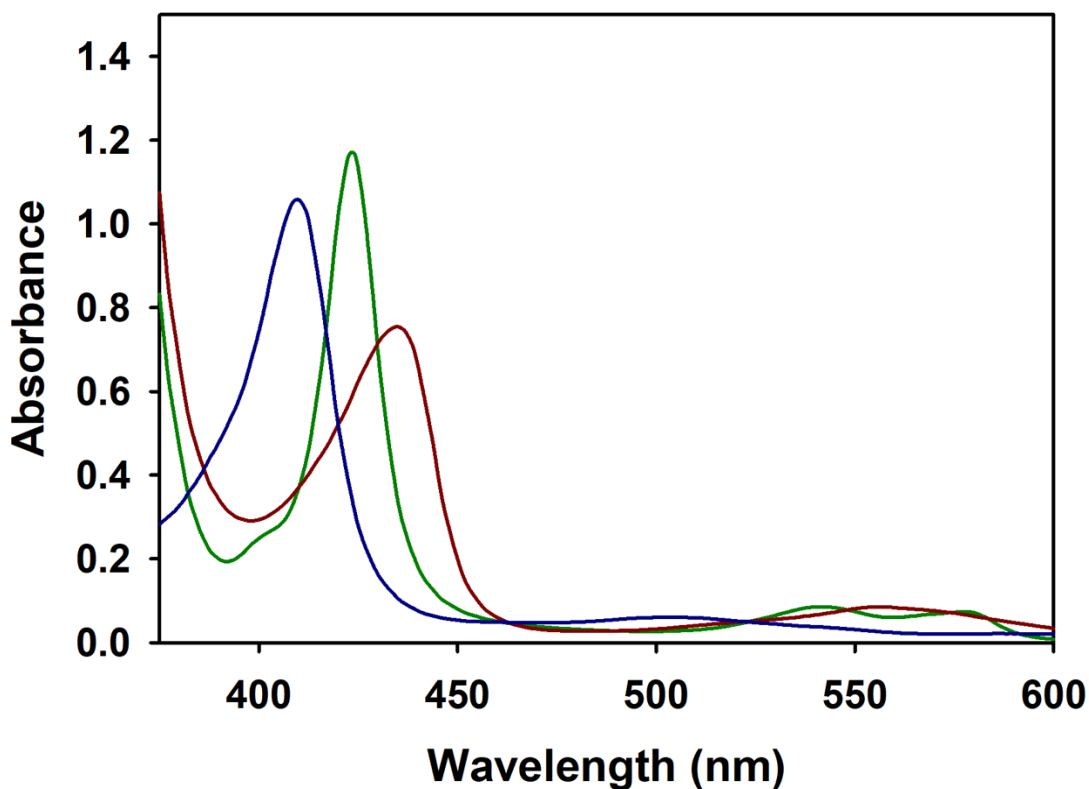
Figure 3.II.12. UV-Vis traces from the Mb assay for **1** in PBS solution at 298 K; blue trace, oxidized-Mb; green trace, reduced-Mb; red trace, CO-Mb.

3.II.2.5 Spectroscopic Properties of Complexes 1 and 2.

Infrared studies revealed the C-O stretching bands of both CO complexes in the region of 1900-2050 cm^{-1}, typical of the *fac*-Mn(CO)$_3$ unit.[20,22] Evaporation of the photolysed solutions of both complexes and subsequent recording of the IR spectra showed complete disappearance of the C-O stretching bands. This finding clearly suggests uncaging of all three coordinated CO ligands from these complexes upon illumination. Furthermore, the photolysed solutions of the respective complexes
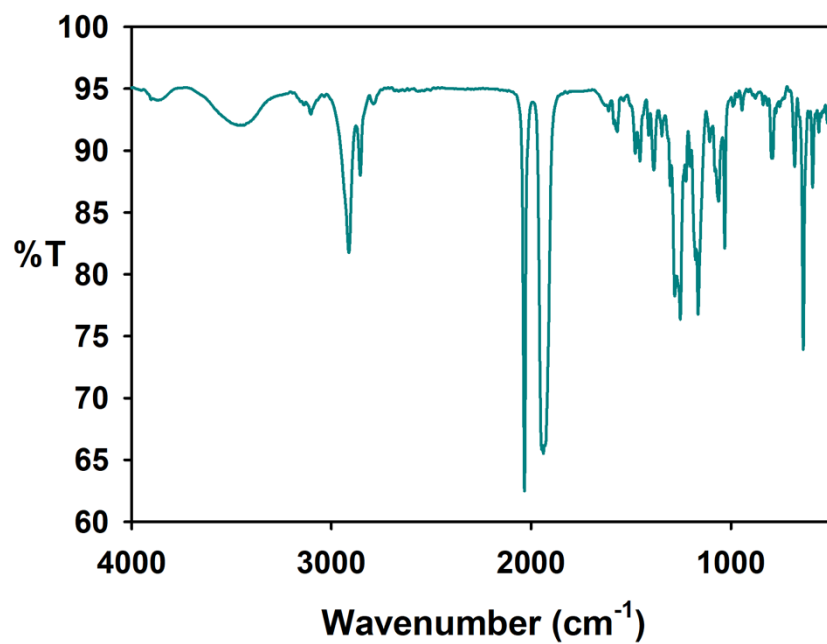
Figure 3.II.13. IR spectrum of complex **1** (KBr disk).
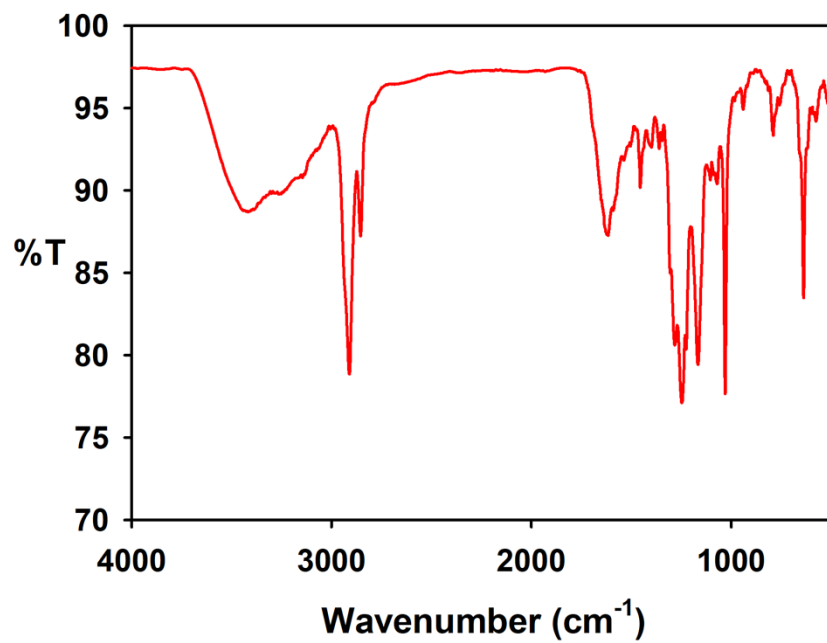
Figure 3.II.14. IR spectrum of complex **1** after photolysis (KBr disk).
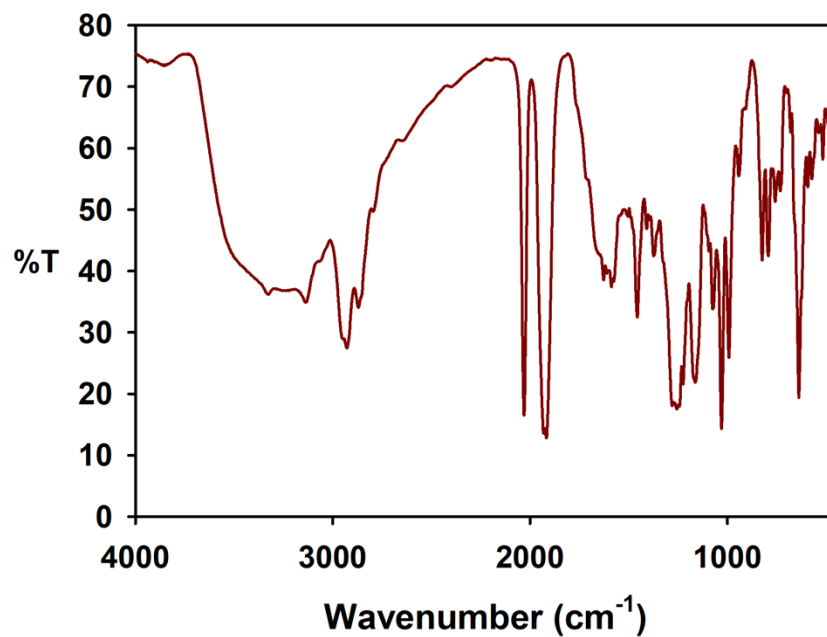
Figure 3.II.15. IR spectrum of complex **2** (KBr disk).
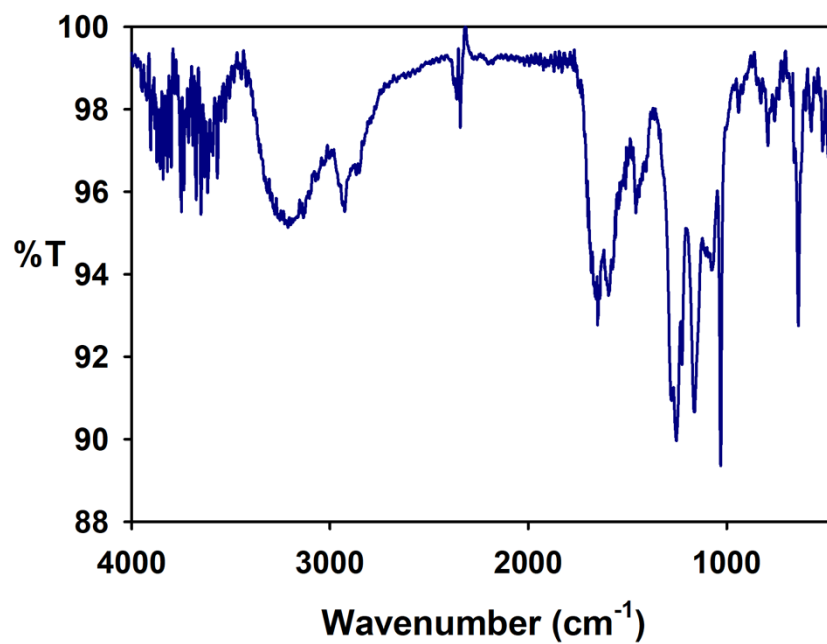
Figure 3.II.16. IR spectrum of complex **2** after photolysis (KBr disk).

display well-defined 6-line EPR spectra (X-band) consistent with the presence of Mn(II) (Figures 3.II.17 and 3.II.18). Comments must be made here about the photoproduct(s) in case a deligation process is associated with the photoinduced CO-release. Our current design ensures minimal or no toxicity in the event of such deligation through utilization of biocompatible or clinically relevant ligands/co-ligands. For example, glyoxal (the carbonyl precursor used for the synthesis both **L1** and **L2**), has been shown to form endogenously in humans through pathways linked
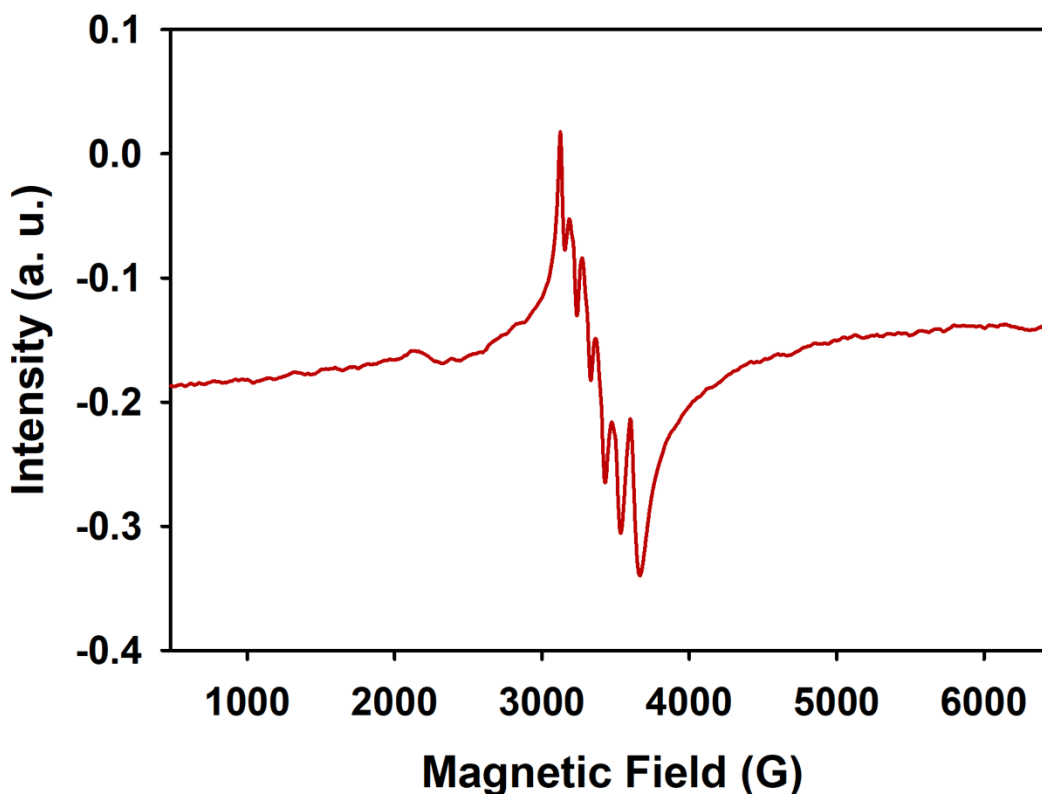
Figure 3.II.17. X-band EPR spectrum of complex **1** at 77K. Microwave frequency, 9.4 GHz; modulation amplitude 2 G; modulation frequency, 100 KHz.
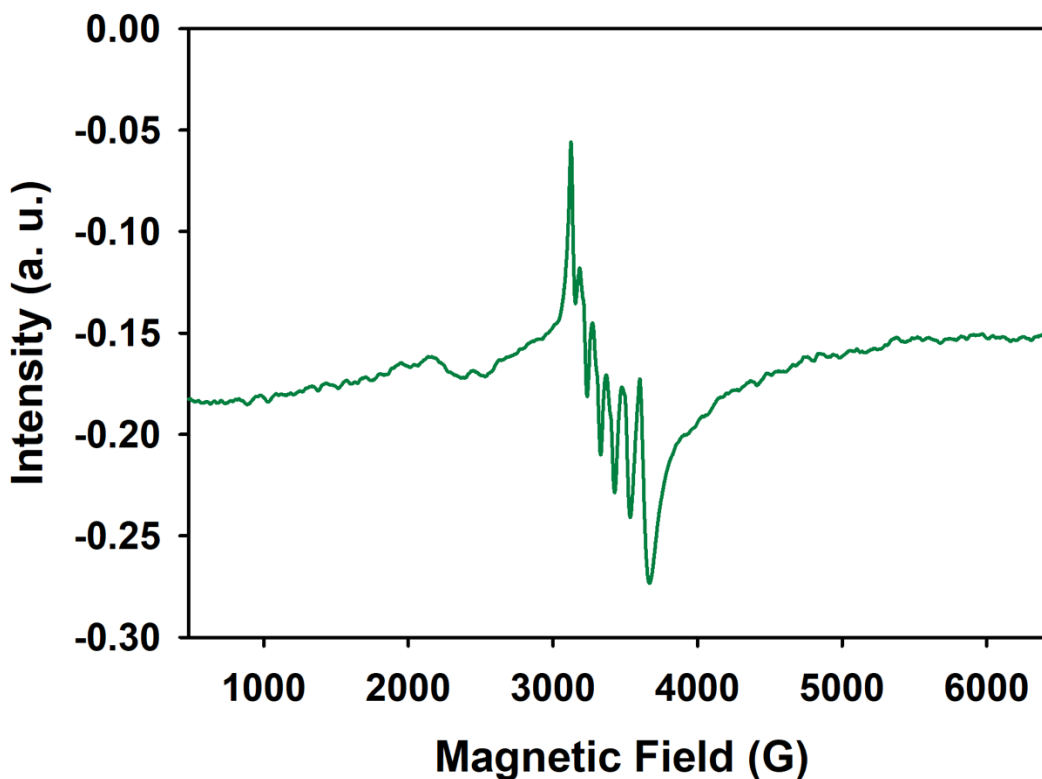
Figure 3.II.18. X-band EPR spectrum of complex **2** at 77K. Microwave frequency, 9.4 GHz; modulation amplitude 2 G; modulation frequency, 100 KHz.

with oxidative stress. There are mechanisms in place for detoxification of glyoxal in humans and animals by the glyoxalase system present in the cells.[47] As mentioned earlier, both adamantyl and triazaadamantyl derivatives serve as active pharmacophores for several known or potential therapeutics. Moreover, dansyl-based fluorogenic chemo-sensors have been widely employed in cellular imaging due to their known biocompatibility.[48] Thus the present lipophilic photoCORM **1** comprises all biocompatible/clinically acceptable constituents. At room temperature upon excitation

at 370 nm, solutions of complexes **1** and **2** in CH$_3$CN display broad emission bands centred at 590 nm. The quenching of the fluorescence is similar to what was observed with previous complexes, and in this report the quenching was observed to be higher for complex **1** than complex **2** (Figure 3.II.19). Upon photolysis, the luminescence of the complexes increases as the Imdansyl ligand is released (Figures 3.II.20 and 3.II.21). Such luminescence properties provided a convenient means to track the prodrug molecules within cellular targets through "turn-on" luminescence.
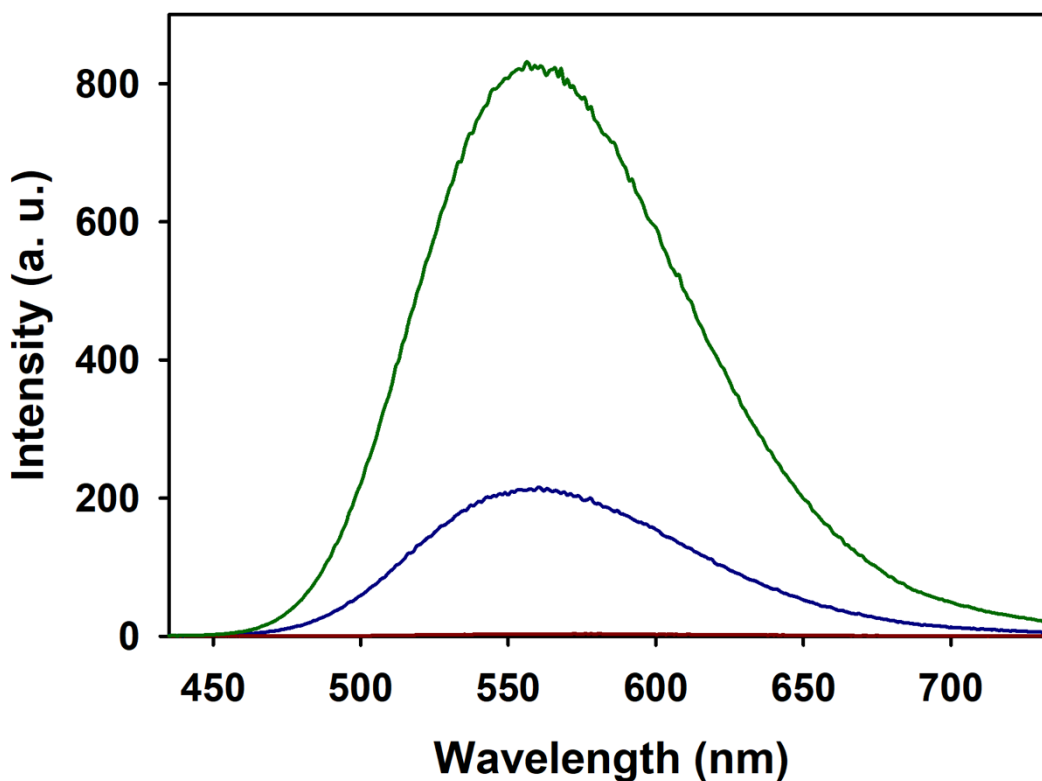
Figure 3.II.19. Fluorescence intensity comparison of complex **1** (red trace), complex **2** (blue trace), and free Imidazole dansyl (green trace) at identical molar concentration in DCM (λ_{ex} = 375nm; Excitation/Emission slit width = 2.5 nm).
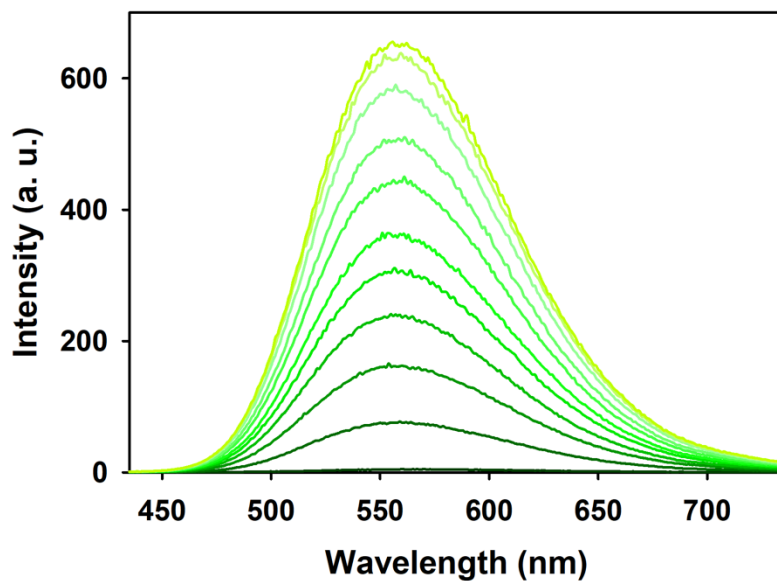
Figure 3.II.20. Luminescence increase of **1** upon irradiation with visible light (15 mW cm^{-2}) in 10 s intervals (λ_{ex} = 375nm; Excitation/Emission slit width = 2.5 nm).
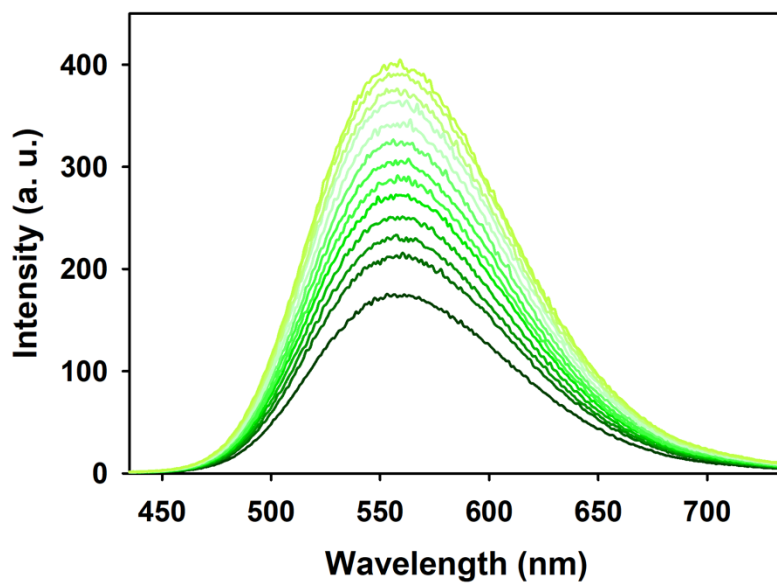
Figure 3.II.21. Luminescence increase of **2** upon irradiation with visible light (15 mW cm^{-2}) in 10 s intervals (λ_{ex} = 375nm; Excitation/Emission slit width = 2.5 nm).

3.II.2.6 Cellular Internalization Experiments.

In order to evaluate and qualitatively compare the cellular uptake properties of the two complexes (**1** and **2**) confocal imaging experiments were performed (Figure 3.II.22). In these studies, the human colorectal cancer HT-29 cells were first plated on the imaging disks at a density of 250,000 cells mL^{-1}. The plating of the HT-29 cells to achieve optimal confluency was performed according to standard protocols and details can be found in the experimental section. The cells were then treated with complexes **1** or **2** in McCoy's 5A medium (devoid of fetal bovine serum and phenol red) for 10,
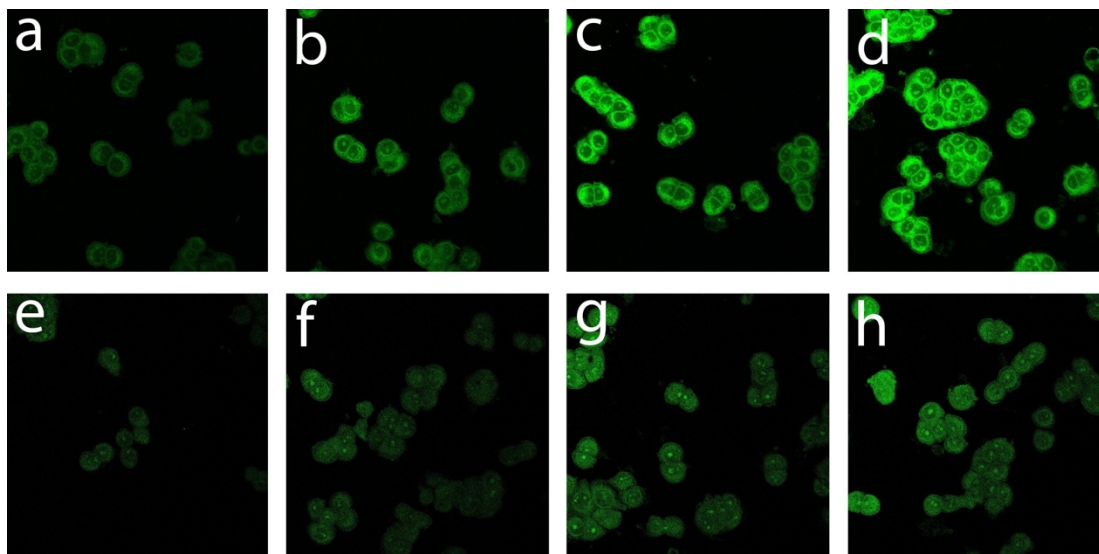
Figure 3.II.22. Confocal images of HT-29 cells showing the extent of internalization of the two complexes (**1** and **2**) with increasing incubation time (λ_{ex} – 405 nm). Upper panel, micrographs, a-d display cell images recorded upon treatment with complex **1** with 10, 20, 30, and 40 min incubation (left to right). Lower panel depicts same experiments with complex **2** as in case of the upper panel.

20, 30 or 40 min. After each round of incubation, the media were aspirated, and cells were washed three times with PBS very carefully. Trypan blue was added prior to recording each image to quench any extracellular fluorescence. The images of cells with increasing incubation time (10 - 40 min) were then captured separately with the aid of a confocal microscope. The cellular images (acquired using the same instrument settings and processed as one batch) suggest internalization of the luminescent complexes and apparently some nuclear localization. The image collage shown in Figure 3.II.22 clearly reveals the preferential cellular uptake of complex **1** under same experimental conditions. This is consistent with the superior lipophilicity of complex **1** compared to complex **2**, which in turn would facilitate an improved membrane penetration.

3.II.2.7 Co-Localization Experiments of Complexes 1 and 2 with Cell-Membrane and Nuclear Stains.

Close inspection of figures 3.II.22d and 3.II.22h suggests that complex **1** appears to accumulate preferentially along the cellular membrane due to its lipophilicity, whereas complex **2** appears to primarily accumulate in the cytoplasm due to its hydrophilicity. This prompted us to investigate the cellular colocalization of these complexes by treating the cells with a cell membrane (Vybrant^{TM} DiD) labelling reagent (red fluorescence). The confocal micrographs indicate that complex **1** (appearing green in Figure 3.II.23b) indeed co-localizes primarily in the cell membrane (Figure 3.II.23c) producing an orange color in merge image (Figure 3.II.23d).
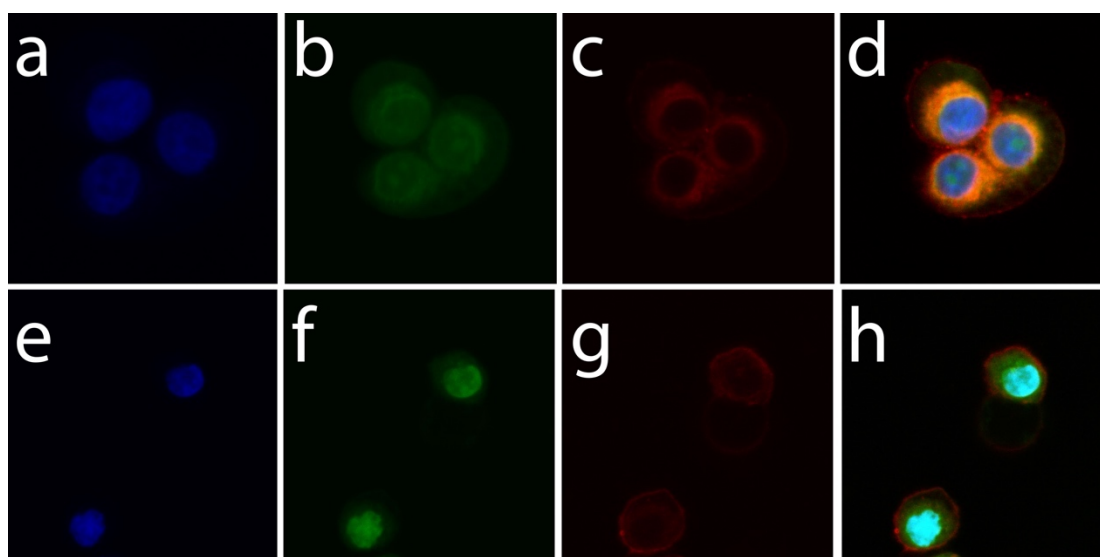
Figure 3.II.23. Colocalization experiments of complexes **1** (top row) and **2** (bottom row) within the cellular matrix; (a) HOECHST nuclear stain; (b) complex **1**; (c) DiD cell membrane stain; (d) merge of images a-c. (e) HOECHST nuclear stain; (f) complex **2;** (g) DiD cell membrane stain; and (h) merge of images e-g.

Additionally, complex **1** appear to co-localize slightly within the nucleus stained blue (3.II.23a). Confocal micrographs of the colocalization experiments using **1** exhibited two green signals (corresponding to **1**) within the blue stained nucleus (Figure 3.II.23d). In contrast, complex **2** primarily localizes inside the cytoplasm and its green signal does not overlap with the red cell membrane stain (Figure 3.II.23h). To the best of our knowledge, this work for the first time reports a comparative assessment of cellular internalization capacity and localization of two structurally similar photoCORMs merely differentiated by their distinct lipophilicities. Also, it is important to note that such differentiation in lipophilicity has been achieved through subtle modification of

otherwise two identical diazabutadiene-based ligand frames. Unlike the previously reported fluorescent Re carbonyl-based photoCORMs which unfailingly require UV light for uncaging the coordinated CO,[49-51] the present Mn carbonyl-based complexes (**1** and **2**) rapidly release CO under low power *visible* light illumination. This could be advantageous to evade any potential harmful effects towards the target tissues arising from the UV radiation. Also, incorporation of a known fluorophore (dansylimidazole) allows both luminescent complexes to be conveniently tracked within the biological targets.

3.II.2.8 MTT Viability Assay.

After ascertaining the cellular uptake properties through confocal imaging studies, we assessed the viability of HT-29 cells *in vitro* upon visible light-triggered CO delivery from both complexes via standard MTT assay. Results of the MTT assay show a clear dose-dependent reduction in cell viability upon treatment of the malignant cells with both complexes **1** (Figure 3.II.24) and **2** (Figure 3.II.25) under visible light illumination. Similar experiments when performed under strict absence of light showed no noticeable reduction of cell viability. These findings suggest no apparent cytotoxicity from the pro-drugs. One representative The CO released from **1** resulted in an IC_{50} value bellow 40 μM under illumination using broadband visible light. The IC_{50} value for **1** is amongst the lowest reported to date for HT-29 colorectal adenocarcinoma cells using a metal-containing photoCORM.[23] It is important to note that the free ligands (**L1** or **L2**) as well as the fully photolyzed solution of the complexes

271
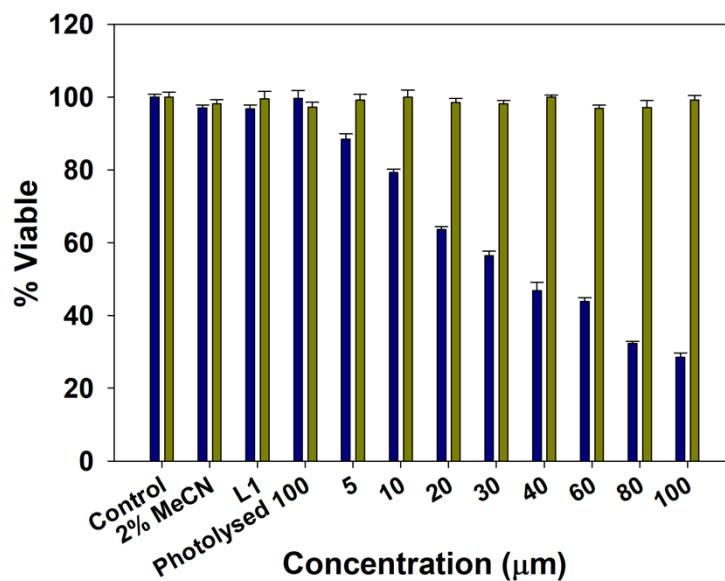
Figure 3.II.24. MTT assay results (HT-29) using complex **1**. Cell viability upon exposure to visible light (blue bars), cell viability under dark conditions (green bars).
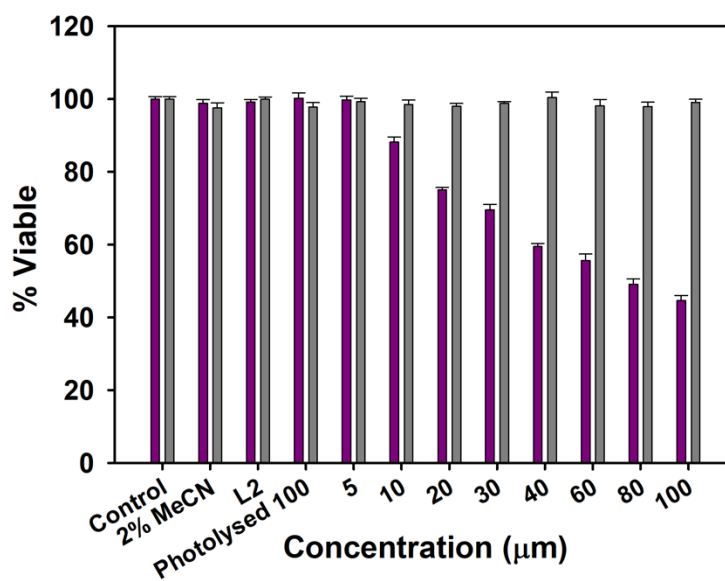
Figure 3.II.25. MTT assay results (HT-29) using complex **2**. Cell viability upon exposure to visible light (pink bars), cell viability under dark conditions (gray bars).

1 or **2** (at highest concentration 100 µM) caused no significant cytotoxicity both under dark and illuminated conditions. Taken together, these results demonstrate that the dose-dependent eradication of HT-29 cells is a direct consequence of intracellular CO-release. The hydrophilic complex **2** required a dose of 70 µM to reduce cell viability by 50%, a fact supporting the hypothesis that the enhanced internalization of the lipophilic complex **1** result in more efficient eradication of the target cells.

3.II.2.9 Cellular Imaging for Caspase Activation.

The reduction in cancer cell viability induced from photoreleased-CO is often primarily investigated using MTT or other similar tetrazolium reduction assays. Tetrazolium reduction assays give insights to the number of viable cells and their metabolic activity. Upon treatment with MTT, live cells reduce the tetrazolium dye and hence the formazan product accumulates linearly. The absorbance of formazan can therefore be correlated to cell viability. When MTT is used in excess or for prolonged periods of time, it exerts toxicity (continuously reducing equivalents of NADH) resulting in misrepresentation of the results.[52] Additionally, the signals generated from MTT tests are highly dependent on culture conditions,[52] which may vary largely between investigators. Since these tests have yet to be standardized, it is advisable to investigate the viability of cells and/or nature of cell death through alternative and complementary methods. Caspase activity detection is an attractive method for

determining the process of cell death. In a previous account we investigated caspase-3/7 activation upon CO delivery to colorectal adenocarcinoma cells using a UV-light active rhenium carbonyl complex grafted into a carboxymethyl chitosan carrier.[27] Caspase-3, -6, and -7 coordinate the execution of apoptosis, promoting membrane blebbing and controlled disassembly of cellular components. In particular, caspase-3 is the primary executioner of apoptosis, and is responsible for DNA fragmentation and nuclear collapse in some systems.[53] In this account, we report the activation and detection of caspase-3/7 upon delivery of photoreleased CO to HT-29 cells using a photoCORM irradiated with broadband visible light. HT-29 cells were incubated with 50 μM of complex **1** for 30 min, washed, and exposed to low-power (15 mW cm^{-2}) broadband visible light for 40 min. The cells were subsequently incubated with CellEvent^{TM} caspase detection agent and the activation of caspase-3/7 was visualized through confocal microscopy (Figure 3.II.26). No activation of caspase-3/-7 was detected on control experiments where the cells were incubated with the complex and kept under strict dark conditions (Figure 3.II.26a). However, cells treated with **1** and subsequently exposed to visible light clearly showed onset of apoptosis (Figures 3.II.26b and 3.II.26c). The fluorescent signal coming from the Caspase-3/7 activation appears to localize primarily in the nucleus of the cell (Figure 3.II.26c). It is expected that the caspase activation signal should originate from the nucleus due to the involvement of caspase-3 in DNA fragmentation and nuclear collapse.[53]
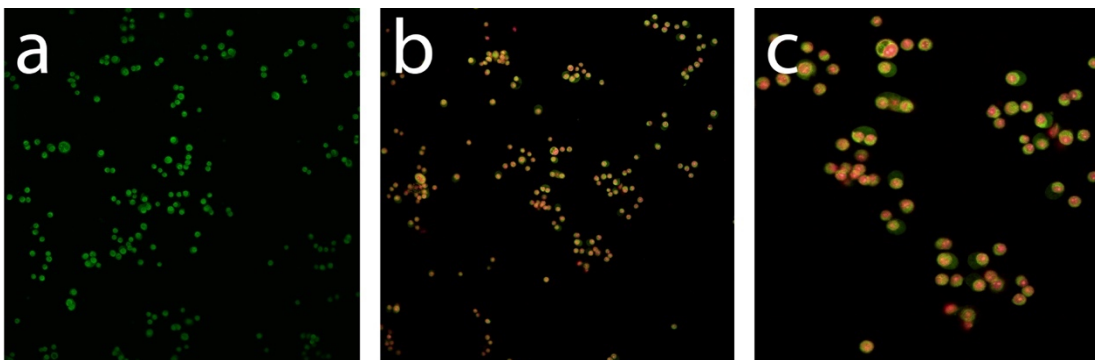
Figure 3.II.26. Confocal micrograph results of caspase-3/-7 activation induced CO-photoreleased from complex **1**. (a) Treated cells kept under strict dark conditions; (b) Treated cells after 30 min exposure to low-power (15 mW cm^{-2}) broadband visible light; (c) Figure 3.II.26b zoomed in.

3.II.3 Conclusions.

In conclusion, we have synthesised and characterised two biocompatible photoCORMs that readily deliver CO upon exposure to visible light. By virtue of their luminescence properties, both complexes could easily be tracked within cellular matrices through confocal fluorescence imaging. For the first time, we have compared the extent of cellular internalization of two structurally similar photoCORMs differentiated by their distinct lipophilicity. Indeed, under same experimental conditions, the more lipophilic photoCORM prodrug **1** showed enhanced cellular uptake by human colon adenocarcinoma HT-29 cells due to its lipophilicity. Colocalization experiments confirmed that the lipophilic photoCORM **1** preferentially accumulates in the membrane, whereas the hydrophilic photoCORM **2** preferentially accumulates in the cytoplasm. Both complexes exhibited dose-dependent eradication

of the HT-29 cells under illumination. CO-induced apoptotic cell death of the cancer cells was confirmed through detection of caspase-3/7 activation. Since, optimal lipophilicity is of pivotal importance in pharmaceutical industry, the present work is expected to provide a credible guideline to develop highly lipophilic organometallic pro-drugs with biocompatible constituents for facile cellular membrane penetration.

3.II.4 Experimental.

3.II.4.1 General Materials and Methods.

All chemicals, and reagents were purchased from Sigma-Aldrich and used without further purification unless otherwise specified. MTT (3-(4,5-dimethylthiazol-2-yl)-2,5-diphenyltetrazolium bromide), CellEvent™ Caspase 3/7 detection reagent, and Vybrant™ DiD cell labeling solution were acquired from Life Technologies. The precursor 7-amino-1,3,5-triazaadamantane was purchased from Combi-Blocks Inc. All solvents were purified according to standard procedures. All manipulations involving Mn species were carefully performed under strictly dark conditions. The human colorectal adenocarcinoma cell line HT-29 was purchased from American Type Culture Collection (ATCC). Cellular imaging experiments were carried out in 35 mm imaging dishes purchased from ibidi™. Unless otherwise stated, the cells were cultured in McCoy's 5A supplemented with 20% fetal bovine serum (FBS).

3.II.4.2 Physical Measurements and Instrumentation.

IR spectra were obtained using a Perkin-Elmer Spectrum One FT-IR spectrometer. UV-Vis data was recorded using a Varian Cary 50 UV-Vis spectrophotometer. Fluorescence spectra were collected using an Agilent Cary-Eclipse fluorescence spectrophotometer. The ^{1}H-NMR spectra were obtained at 298K using a Bruker 500 MHz instrument. Microanalyses (C, H, N) were carried out with a PerkinElmer 2400 Series II elemental analyzer. An Electro Fiber Optics Corp. IL410 illumination system was used as a broadband visible light source for UV-Vis spectroscopic studies. A Husky[TM] portable work-light LED panel (15 mW cm^{-2}) was used for the biological experiments. The power of the incident visible light used during the experiments was measured with a Field MaxII-TO laser power meter (Coherent, Portland, OR). Myoglobin assays were performed with **1** and **2** by following a previously reported literature procedure.[38] The MTT assays absorbances were recorded using a Molecular Devices VersaMax[TM] tunable microplate reader. The confocal images were acquired using an Inverted Nikon Eclipse TE2000-E spinning disk (CSLI-X1) confocal microscope equipped with a Hamamatsu EM-CCD camera (ImageE MX2) utilizing 405 nm, 488 nm, or 635 nm illumination at 50 mW. The gain and offset were adjusted to set the brightest pixels below saturation. The detection gates were set to 490-540 nm for the complexes, 580-700 nm for Caspase-3/7 detection agent, and 650-700 nm for DiD cell labeling dye. The raw confocal microscopy images were further processed using Fiji-ImageJ version 1.52e.

*3.II.4.3 Synthesis of N,N′-bis-1-(adamantly)-1,4-diazabutadiene (**L1**).*

Adamantan-1-amine (532 mg, 3.52 mmol) was dissolved in 15 mL of MeOH. Next, 202 µL (1.76 mmol) of glyoxal (40% in H_2O) was added to this solution and the reaction mixture was stirred overnight. A white precipitate formed after the solvent was reduced under vacuum. The product thus obtained was collected via vacuum filtration and recrystallized three times from MeOH yielding **L1** as microcrystalline white solid (506 mg, 89%). IR (KBr, cm^{-1}) 3423(w), 2904(s), 2844(s), 2656(s), 1628(m), 1450(m), 1343(w), 1313(w), 1185(w), 1118(w), 1091(m), 983(w), 907(w), 811(w), 721(w), 646(w), 471(w). ^{1}H-NMR (CDCl$_3$, δ ppm) 7.93 (s, 2H), 2.14 (s, 6H), 1.72 (m, 24H). ESI-MS (*m/z*): M + H$^+$ 325.32 (Calc. 325.26).

*3.II.4.4 Synthesis of N,N′-bis-1-(3,5,7-triazaadamantly)-1,4-diazabutadiene (**L2**).*

A batch of 93 µL (0.81 mmol) of Glyoxal (40% in H_2O) was added to a solution of 250 mg (1.62 mmol) of 7-amino-1,3,5-triazaadamantane in 10 mL of MeOH and the reaction mixture was stirred overnight at room temperature. The resulting brownish-white precipitate was collected via vacuum filtration. The powder was recrystallized three times from DCM/MeOH yielding 228 mg (85%) of **L2** as microcrystalline white solid. IR (KBr, cm^{-1}) 3435(m), 2933(w), 2860(w), 1621(w), 1451(w), 1365(w), 1319(w), 1243(w), 1031(m), 995(s), 822(m), 640(w). ^{1}H-NMR (MeOD, δ ppm) 7.84 (s, 2H), 4.55 (d, 6H), 4.15 (d, 6H), 3.46 (s, 12H). ESI-MS (*m/z*): M + H$^+$ 331.30 (Calc. 331.24).

*3.II.4.5 Synthesis of [Mn(CO)$_3$(Imdansyl)(**L1**)]CF$_3$SO$_3$ (**1**).*

A batch of **L1** (200 mg, 0.62 mmol) was dissolved in 10 mL of CHCl$_3$. Then [Mn(CO)$_5$Br] (171 mg, 0.62 mmol) was dissolved in 30 mL of MeOH and added to the **L1** solution. The reaction mixture was stirred at room temperature for 48 h. The orange precipitate thus obtained was collected via vacuum filtration. The powder was washed with 3 x 10 mL portions of hexanes and dried under vacuum, yielding 276 mg (82%) of [Mn(CO)$_3$(**L1**)Br] as a red-orange microcrystalline powder. IR (KBr, cm^{-1}) 3455(w) 2921(w), 2854(w), 2017(s), 1919(s), 1908(s), 1650(w), 1452(w), 1385(w), 1085(w), 868(w), 626(w). ^{1}H-NMR (CDCl$_3$, δ ppm) 8.28 (s, 2H), 2.32 (s, 6H), 2.19 (m, 12H), 1.78 (m, 12H). Next, a solution of AgCF$_3$SO$_3$ (80 mg, 0.31 mmol) in 40 mL of DCM was added to [Mn(CO)$_3$(**L1**)Br] (150 mg, 0.28 mmol). The reaction mixture was stirred at room temperature for 6 h. The resulting cloudy light-orange solution was filtered over a Celite bed to remove excess AgCF$_3$SO$_3$ and the newly formed AgBr. The clear-orange filtrate was collected, and the solvent was removed under reduced pressure. The product [Mn(CO)$_3$(**L1**)(CF$_3$SO$_3$)] was isolated as a light orange powder (123 mg, 72%). IR (KBr, cm^{-1}) 3450(m), 2911(w), 2854(w), 2036(s), 1940(s), 1923(s), 1637(w), 1455(m), 1345(m), 1293(w), 1233(m), 1207(m), 1173(w), 1085(w), 1029(w), 1020(m), 637(m), 520(w). ^{1}H-NMR (CDCl$_3$, δ ppm) 8.36 (m, 2H), 2.35 (s, 6H), 2.15 (m, 12H), 1.78 (m, 12H). The ligand dansylimidazole (98 mg, 0.32 mmol) was added to a solution of [Mn(CO)$_3$(**L1**)(CF$_3$SO$_3$)] (100 mg, 0.16 mmol) in 20 mL of distilled DCM. The reaction mixture was stirred for 48 h at room temperature under anaerobic conditions. The solvent was then removed under reduced pressure resulting in an oily

orange residue. This residue converted to a light orange precipitate upon addition of 10 mL of anhydrous diethyl ether (Et$_2$O). The precipitate was collected through vacuum filtration and washed with 3 x 10 mL portions of anhydrous Et$_2$O. Finally, the product was recrystallized from DCM/hexanes yielding 103 mg of complex **1** (69%) as a light yellow-orange solid. Anal. Calcd. (%) for C$_{41}$H$_{47}$F$_3$MnN$_5$O$_8$S$_2$ (913.89): C, 53.88; H, 5.18; N, 7.66. Found: C, 53.82; H, 5.21; N, 7.72. Selected IR (KBr, cm^{-1}) 3441(m), 3148(w), 2913(s), 2855(m), 2036(s), 1949(s), 1920(s), 1906(s), 1614(w), 1568(w), 1481(w), 1455(w), 1409(w), 1384(m), 1347(w), 1304(m), 1252(s), 1224(m), 1203(w), 1166(s), 1105(w), 1059(m), 1027(m), 941(w), 783(m), 679(w), 638(s), 558(w). UV-Vis (DCM) λ_{max}: 375 nm (ε = 6400). ^{1}H NMR (CDCl$_3$, δ ppm) 8.68 (m, 4H), 8.18 (s, 1H), 8.12 (d, 1H), 7.73 (t, 1H), 7.62 (t, 1H), 7.42 (s, 1H), 7.17 (d, 1H), 6.93 (s, 1H), 2.86 (s, 6H), 1.62 (m, 30H). ESI-MS (m/z): M$^+$ 764.29 (Calc. 764.27).

3.II.4.6 Synthesis of [Mn(CO)$_3$(Imdansyl)(L2)]CF$_3$SO$_3$ (2).

A batch of 200 mg **(**0.72 mmol) of **[**Mn(CO)$_5$Br] was dissolved in 30 mL of anhydrous MeOH and added to a CHCl$_3$ solution of **L2** (166 mg, 0.72 mmol). The reaction mixture was stirred at room temperature for 48 h and the resulting precipitate was collected using vacuum filtration. The powder was washed with 3 x 10 mL portions of hexanes and dried under vacuum, yielding 281 mg (71%) of [Mn(CO)$_3$(**L2**)Br] as dark-red microcrystalline powder. IR (KBr, cm^{-1}) 3468(w) 2912(w), 2029(s), 1933(s), 1916(s), 1456(w), 1242(w), 1212(w), 1030(m), 992(m), 821(w), 632(w). The following reactions were carried out carefully to exclude air and moisture. Anhydrous

MeOH (20 mL) was added to a N_2-purged reaction flask containing [Mn(CO)$_3$(**L2**)Br] (200 mg, 0.36 mmol) forming a fine suspension. An anhydrous methanolic solution (20 mL) containing AgCF$_3$SO$_3$ (94 mg, 0.36 mmol) was then added to the reaction flask. The mixture was stirred at room temperature for 5 h resulting in a cloudy red-orange solution. This solution was filtered under nitrogen using a Celite bed to remove the newly formed AgBr. The resulting clear red filtrate was collected, and the solvent removed under reduced pressure. Portions of distilled DCM (3 x 10 mL) were added to the resulting oily residue and subsequently removed under vacuum. Finally, anhydrous Et$_2$O (5 mL) was added to the residue forming a precipitate. The product was collected under nitrogen via vacuum filtration and washed with 3 x 5 mL of anhydrous Et$_2$O to afford [Mn(CO)$_3$(**L2**)(CF$_3$SO$_3$)] as a light red powder (137 mg, 61%). IR (KBr, cm^{-1}) 3475(w), 2872(w), 2039(s), 1953(s), 1921(s), 1649(w), 1456(w), 1282(m), 1241(m), 1220(m), 1165(w), 1094(w), 1029(m), 994(m), 820(w), 633(w), 503(w). ^{1}H-NMR (MeOD, δ ppm) 8.39 (s, 2H), 4.68 (d, 6H), 4.20 (d, 6H), 3.86 (s, 12H). The complex [Mn(CO)$_3$(**L2**)(CF$_3$SO$_3$)] (100 mg, 0.16 mmol) was dissolved in 10 mL of anhydrous MeOH in an N_2-purged reaction flask. Dansylimidazole (49 mg, 0.16 mmol) was dissolved in 10 mL of anhydrous MeOH and added to this solution. The reaction mixture was stirred for 5 h at room temperature. The solvent was removed under reduced pressure resulting in an oily red-orange film. Distilled DCM (5 mL) was then added to the flask and subsequently removed under reduced pressure. Next, anhydrous Et$_2$O was added to the residue resulting in the formation of a light red-orange precipitate. The solution was vacuum filtered under N_2 atmosphere and washed with 3

x 10 mL portions of anhydrous Et$_2$O. Finally, the product was recrystallized from DCM/hexanes yielding 60 mg of complex **2** (40%) as a light red-orange solid. Anal. Calcd. (%) for C$_{35}$H$_{41}$F$_3$MnN$_{11}$O$_8$S$_2$ (919.84): C, 45.70; H, 4.49; N, 16.75. Found: C, 45.66; H, 4.40; N, 16.66. Selected IR (KBr, cm^{-1}) 345.54(s), 2924(m), 2036(s), 1931(s),m 1917(s), 1637(w), 1575(w), 1461(w), 1412(w), 1383(w), 1259(s), 1163(s), 1059(m) 1029(s), 993(s), 822(m), 791(m), 635(s), 588(w). UV-Vis (DCM) λ_{max}: 370 nm (ε = 4300). ^{1}H NMR (MeOD, δ ppm) 8.75 (d, 1H), 8.53 (d, 1H), 8.41 (s, 2H), 8.37 (s, 1H), 8.33 (d, 1H), 7.72 (t, 1H), 7.66 (t, 1H), 7.56 (s, 1H), 7.32 (d, 1H), 7.04 (s, 1H), 4.68 (d, 6H), 4.19 (d, 6H), 3.84 (m, 12H), 2.89 (s, 6H). ESI-MS (*m/z*): M$^+$ 770.24 (Calcd. 770.24).

3.II.4.7 X-Ray Crystallography, Structure Determination and Refinement.

Orange block-shaped crystals of **1** and [Mn(CO)$_3$(**L1**)(H$_2$O)](CF$_3$SO$_3$) were obtained by layering hexanes on top of a solution of the respective complex in toluene. In both cases, a suitable crystal was selected and mounted on a Bruker D8 Quest diffractometer equipped with PHOTON II detector operating at T = 298 K. Data were collected with ω shutterless scan technique using graphite monochromated Mo-Kα radiation (λ = 0.71073 Å). The total number of runs and images for both data collections was based on the strategy calculation from the program *APEX3* (Bruker).[39] Cell parameters were retrieved using the *SAINT* (Bruker) software[40] and refined using *SAINT* (Bruker) on 5340 reflections for **1** and on 9305 reflections for [Mn(CO)$_3$(**L1**)(H$_2$O)](CF$_3$SO$_3$). Data reduction was performed using the *SAINT*

(Bruker) software, which corrects for Lorentz and polarization effects. The final completeness was 99.5% for **1** and 99.2% for [Mn(CO)$_3$(**L1**)(H$_2$O)](CF$_3$SO$_3$). Multi-scan absorption corrections were performed with both data sets using *SADABS* 2016/2.[41] The absorption coefficients for **1** and [Mn(CO)$_3$(**L1**)(H$_2$O)](CF$_3$SO$_3$) were 0.44 mm^{-1} and 0.60 mm^{-1} respectively. Minimum and maximum transmissions for **1** were 0.660 and 0.745 while the corresponding values for [Mn(CO)$_3$(**L1**)(H$_2$O)](CF$_3$SO$_3$) were 0.707 and 0.745. The structures for **1** and [Mn(CO)$_3$(**L1**)(H$_2$O)](CF$_3$SO$_3$) were solved in the space group *P-1* (No. 2) and *P2$_1$/c* (No. 14) respectively by *intrinsic phasing* using the *ShelXT*[42] structure solution program and refined by full matrix least squares on F^2 using version 2016/6 of *ShelXL*.[43] All non-hydrogen atoms were refined anisotropically in both cases. Hydrogen atom positions were calculated geometrically and refined using the riding model. To alleviate the complications related to solvent accessible voids within the extended lattice in cases of **1**, *SQUEEZE* operation (included in the *PLATON* program) was performed with the raw data set and the structure was refined form the data obtained upon *SQUEEZE* operation.[44] Calculations and molecular graphics were preformed using *SHELXTL* 2014 and *Olex2*[45] programs. Crystal data and structure refinement parameters are listed in Tables 3.II.1 and 3.II.2.

3.II.4.8 Photolysis, Luminescence and Stability Experiments.

Solutions of **1** and **2** (concentration: of 2.0 x 10^{-4} M) were prepared in DCM. The CO release rates (k$_{co}$) for **1** and **2** were performed in a quartz cuvette (1 cm x 1 cm)

Table 3.II.1. Crystal data and structure refinements for complex **1**.

	1
Empirical formula	$C_{40}H_{47}MnN_5O_5S.CF_3O_3S$
T(K)	298
λ (Å)	0.71073
Crystal system	Triclinic
Space group	P-1
a (Å)	11.272(3)
b (Å)	14.302(3)
c (Å)	16.252(4)
α (°)	72.026(3)
β (°)	71.438(3)
γ (°)	74.745(4)
V (Å^3)	2322.7(9)
Z	2
D_{calc} (Mg m^{-3})	1.307
Absorption Coeff (mm^{-1})	4.342
No. of unique reflections	8107
Goodness-of-fit[a] on F^2	1.020
R_1[b]	0.053
wR_2[c]	0.141

using a 15 mW cm^{-2} broadband visible light (IL 410 illumination system Electro Fiber Optics Corp). Changes in the electronic absorption spectra were recorded after exposing the solution in the cuvette to visible light at regular time intervals. The k_{co} value was then calculated from a ln(C) versus time (t) plot. Equimolar solutions of Imdansyl, **1**, and **2** (2.0 x 10^{-4} M) were prepared and the emission spectra were recorded

Table 3.II.2. Crystal data and structure refinements for complex [Mn(CO)$_3$(**L1**)(H$_2$O)](CF$_3$SO$_3$).

	[Mn(CO)$_3$(**L1**)(H$_2$O)](CF$_3$SO$_3$)
Empirical formula	C$_{25}$H$_{34}$MnN$_2$O$_4$.CF$_3$O$_3$S
T(K)	298
λ (Å)	0.71073
Crystal system	Monoclinic
Space group	$P2_1/c$
a (Å)	12.0192(16)
b (Å)	10.8282(15)
c (Å)	22.633(3)
α (°)	90
β (°)	102.230(2)
γ (°)	90
V (Å^3)	2878.8(7)
Z	4
D_{calc} (Mg m^{-3})	1.455
Absorption Coeff (mm^{-1})	4.355
No. of unique reflections	4903
Goodness-of-fit[a] on F^2	1.060
R_1[b]	0.037
wR_2[c]	0.105

using an excitation wavelength of 375 nm. The stability of the complexes was determined by preparing concentrated solutions of the complexes in MeCN and diluting PBS until the MeCN concentration reached 2%. Changes in the absorbance spectrum of the solutions was then recorded once every h for 24 h. For quantum yield (ϕ)

determination, solutions of **1** and **2** in MeCN were used to ensure sufficient absorbance (>99%) at the incident wavelength (380 nm); no more than 10% photolysis occurred in each measurement. Standard actinometry using potassium ferrioxalate was employed to calibrate the light source (Newport Oriel Apex Illuminator; 380 nm, 10 mW at 1 cm distance).

*3.II.4.9 Aqueous Solubility of **2**.*

Deionized water (1.5 mL) was volumetrically added to a vial containing 20.0 mg of **2** and the solution was stirred magnetically overnight. The following day, the resulting aqueous suspension was spun down at 13,000 rpm and the supernatant was carefully placed into a separate container. This saturated solution was volumetrically diluted by a factor of 10 and its absorbance was recorded. A 196.7 μM stock solution of **2** was prepared by dissolving 18.1 mg of the complex in 100 mL of deionized water in a volumetric flask. From this stock solution, a series of standards of concentrations 19.7, 39.3, 49.2, 59.0, and 68.8 μM were prepared in 10 mL volumetric flasks and their absorbances (λ = 328 nm) were recorded. A standard curve relating absorbance to concentration was obtained and its linear regression was used to relate the absorbance to the concentration of the saturated solution of **2**.

3.II.4.10 Cellular Internalization Experiments.

All manipulations were performed under strict dark conditions to avoid exposure to any ambient light. Fresh medium devoid of phenol red and FBS was used

to prepare the treatment solutions containing complexes **1**, and **2**. The human colorectal adenocarcinoma HT-29 cells were plated in 35 mm imaging disks at a density of 250,000 cells mL^{-1} (2 mL) and incubated at 37 °C for 24 h with 5% CO_2. The following day, the culture media was aspirated, and cells were washed with 2 mL PBS. The cells were then treated with 2 mL of fresh media containing 50 μM of **1**, or **2**, and incubated for 10, 20, 30, or 40 min. At the end of each incubation period, the media was aspirated, and the cells were washed with 3 x 1 mL portions of PBS buffer. Fresh McCoy's 5A medium (devoid of phenol red, FBS, or complex) was added to the imaging disks and the cells were incubated for 2 h and the confocal microscopy images were recorded.

3.II.4.11 Colocalization Experiments.

All manipulations were performed under strict dark conditions to avoid accidental exposure to any ambient light. Human adenocarcinoma (HT-29) cells were plated on 35 mm imaging disks at a density of 250,000 cells mL^{-1} (2 mL) and incubated at 37 °C and 5% CO_2 for 24 h. The media was aspirated, and the imaging disks were washed with PBS 3 x 1 mL portions. Then the cells were treated with 2 mL of fresh media containing 50 μM of complex **1** or **2**, and further incubated for 40 min. At the end of the incubation period, the media containing the complexes was removed and the cells were washed with 3 x 1 mL portions of PBS. The cells were then incubated with the Vybrant DiD cell-labeling solution according to manufacturer protocol. After incubation the dye was aspirated, and the cells were washed with 3 x 1 mL portions of

PBS. Following incubation of these cells in fresh cell growth media (devoid of phenol-red, FBS, or complex) for 1 h, the confocal microscopy images were recorded.

3.II.4.12 Cellular Imaging Experiments for Caspase Activation.

Two imaging disks were plated with HT-29 cells at a cell density of 250,000 cell mL^{-1} (2 mL) in 35 mm imaging disks and incubated for 24 h at 37 °C and 5% CO_2. The media was aspirated, then the cells were washed with 3 x 1 mL of PBS and incubated for 40 min with 2 mL of fresh media containing 50 μM of complex **1**. After this incubation period the media was removed and replaced with phenol-red free media. One imaging disk was kept under strict dark conditions and the second imaging disk was irradiated with broadband visible light (15 mW cm^{-2}) for 30 min. The CellEvent™ Caspase-3/7 detection reagent was added to each of the imaging disks according to the manufacturer's protocol. The cells were then incubated for an additional h at 37 °C with 5% CO_2 and the confocal microscopy images were recorded.

3.II.4.13 MTT Viability Assay.

Unless otherwise stated all manipulations were carried out under strict dark conditions to avoid premature decomposition of the manganese complexes. A stock solution of complex **1** was prepared by dissolving it in MeCN and diluting it to 2% with fresh cell culture media to reach a concentration of 100 μM. Stock solutions of 5, 10, 20, 30, 40, 60, and 80 μM were subsequently prepared by diluting the initial 100 μM stock solution using fresh cell culture media containing 2% MeCN. Control

solutions of the ligand and photoproducts were prepared with concentrations of 100 µM in fresh media containing 2% MeCN. Other control solutions included fresh media and 2% MeCN in media (v/v). Two separate 96-well plates were plated with human colorectal adenocarcinoma cells at a density of 100,000 cells mL^{-1} (200 µL) and incubated for 24 h. After the initial incubation period the growth media was aspirated, and the cells were incubated for 2 h at 37 °C and 5% CO_2 with the above-mentioned stock solutions. After this incubation period the media was removed, and the cells were washed using PBS. Fresh cell culture media was then added to the plates and incubated for 1 h. Afterwards, one plate was kept under dark conditions, while the other plate was photolysed with broadband visible light from a low power LED light source (15 mW cm^{-2}) for 40 min. After treatment, the plates were incubated for 2 h at 37 °C with 5% CO_2. The MTT was added to both plates following the manufacturer's protocol and the viability of the cells was assessed using a microplate reader (VersaMax™). The viability assay was repeated using complex **2**, its ligand **L2**, and its photoproducts following the same procedure described above. Cell viability studies were performed in triplicate.

3.II.5 References.

1. Motterlini, R.; Otterbein, L. E. The therapeutic potential of carbon monoxide. *Nat. Rev. Drug Discov*. **2010**, *9*, 728-743.

2. Motterlini, R.; Foresti, R. Biological signalling by carbon monoxide and carbon monoxide-releasing molecules. *Am. J. Physiol. Cell Physiol*. **2012**, *312*, C302-313.

3. Mustafa, A. K.; Gadalla, M. M.; Snyder, S. H. Signalling by gasotransmitters. *Sci. Signal*. **2009**, *2*, re2.

4. Wu, L.; Wang, R. Carbon monoxide: endogenous production, physiological functions, and pharmacological applications. *Pharmacol. Rev*. **2005**, *57*, 585-630.

5. Levitt, D. G.; Levitt, M. Carbon monoxide: a critical quantitative analysis and review of the extent and limitations of its second messenger function. *Clinical Pharmacol*. **2015**, *7*, 37-56.

6. Kikuchi, G.; Yoshida, T.; Noguchi, M. Heme oxygenase and heme degradation. *Biochem. Biophys. Res. Commun*. **2005**, *338*, 558-567.

7. Takahashi, T.; Shimizu, H.; Morimatsu, H.; Maeshima, K.; Inoue, K.; Akagi, R.; Matsumi, M.; Katayama, H.; Morita, K. Heme oxygenase-1 is an essential cytoprotective component in oxidative tissue injury induced by hemorrhagic shock. *J. Clin. Biochem. Nutr*. **2009**, *44*, 28-40.

8. Lamon, B. D.; Zhang, F. F.; Puri, N.; Brodsky, S. V.; Goligorsky, M. S.; Nasjletti, A. Dual pathways of carbon monoxide-mediated vasoregulation: modulation by redox mechanisms. *Circ. Res*. **2009**, *105*, 775-783.

9. Ryter, S. W.; Choi, A. M. K. Targeting heme oxygenase-1 and carbon monoxide for therapeutic modulation of inflammation. *Transl. Res*. **2016**, *167*, 7-34.

10. Weigel, B.; Gallo, D.; Csizmadia, E.; Harris, C.; Belcher, J.; Vercellotti, G. M.; Penacho, N.; Seth, P.; Sukhatme, V.; Ahmed, A.; Pandolfi, P. P.; Helczynski, L.; Bjartell, A.; Persson, J. L.; Otterbein, L. E. Carbon monoxide expedites metabolic exhaustion to inhibit tumor growth. *Cancer. Res*. **2013**, *73*, 7009-7021.

11. Kawahara, B.; Ramadoss, S.; Chaudhuri, G.; Janzen, C.; Sen, S.; Mascharak, P. K. Carbon monoxide sensitizes cisplatin-resistant ovarian cancer cell lines towards cisplatin via attenuation of levels of glutathione and nuclear metallothionein. *J. Inorg. Biochem.* **2019**, *191*, 29-39.

12. Kawahara, B.; Moller, T.; Hu-Moore, K.; Carrington, S.; Faull, K. F.; Sen, S.; Mascharak, P. K. Attenuation of antioxidant capacity in human breast cancer cells by carbon monoxide through inhibition of cystathionine -synthase activity: implications in chemotherapeutic drug delivery. *J. Med. Chem*. **2017**, *60*, 8000-8010.

13. Kottelat, E.; Zobi, F. Visible light-activated photoCORMs. *Inorganics*, **2017**, *5*, 24. doi:10.3390/inorganics5020024.

14. Popova, M.; Soboleva, T.; Ayad, S.; Benninghoff, A. D.; Berreau, L. M. Visible-light activate quinolone carbon-monoxide-releasing molecule: prodrug and albumin-assisted delivery enables anticancer and potent anti-inflammatory effects. *J. Am. Chem. Soc*. **2018**, *140*, 9721-9729.

15. Wright, M.; Wright, J. A. PhotoCORMs: CO release moves into the visible. *Dalton. Trans*. **2016**, *45*, 6801-6811.

16. Palao, E.; Slanina, T.; Muchova, L.; Solomek, T.; Vitek, L.; Klan, P. Transition-metal-free CO-releasing BODIPY derivatives activatable by visible to NIR light as promising bioactive molecules. *J. Am. Chem. Soc.* **2016**, *138*, 126-133.

17. Chakraborty, I.; Carrington, S. J.; Mascharak, P. K. Design strategies to improve sensitivity of photoactive metal carbonyl complexes (photoCORMs) to visible light and their potential as CO-donors to biological targets. *Acc. Chem. Res*. **2014**, *47*, 2603-2611.

18. Rimmer, R. D.; Pierri, A. E.; Ford, P. C. Photochemically activated carbon monoxide release for biological targets. Toward developing air stable photoCORMs liabilized by visible light. *Coord. Chem. Rev*. **2012**, *256*, 1509-1519.

19. Pinto, M. N.; Chakraborty, I.; Sandoval, C.; Mascharak, P. K. Eradication of HT-29 colorectal adenocarcinoma cells by controlled photorelease of CO from a CO-releasing polymer (photoCORP-1) triggered by visible light through an optical fiber-based device. *J. Control. Release* **2017**, *264*, 192-202.

20. Jimenez, J.; Chakraborty, I.; Dominguez, A.; Martinez-Gonzalez, J.; Sameera, W. M. C.; Mascharak, P. K. A luminescent manganese photoCORM for CO delivery to cellular targets under the control of visible light. *Inorg. Chem.* **2018**, *57*, 1766-1733.

21. Soboleva, T.; Esquer, H. J.; Benninghoff, A. B.; Berreau, L. M. Sense and release: a thiol-responsive flavonol-based photonically driven carbon monoxide-releasing molecule that operates via multiple-input AND logic gate. *J. Am. Chem. Soc*. **2017**, *139*, 9435-9438.

22. Chakraborty, I.; Carrington, S. J.; Roseman, G.; Mascharak, P. K. Synthesis, structures and CO release capacity of a family of water-soluble photoCORMs: assessment of the biocompatibility and their phototoxicity toward human breast cancer cells. *Inorg. Chem*. **2017**, *56*, 1534-1545.

23. Kourti, M.; Jiang, W. G.; Cai, J. Aspects of carbon monoxide in form of CO-releasing molecules used in cancer treatment: More light on the way. *Oxidative Med. Cell. Longevity* **2017**, 9326454. doi:10.1155/2017/9326454.

24. Heinemann, S.; Hoshi, T.; Westerhausen, M.; Schiller, A. Carbon monoxide – physiology, detection and controlled release. *Chem. Commun*. **2014**, *50*, 3644-3660.

25. Carrington, S. J.; Chakraborty, I.; Mascharak, P. K. Rapid CO release from a Mn(I) carbonyl complex derived from azopyridine upon exposure to visible light and its phototoxicity toward malignant cells. *Chem. Commun.* **2013**, *49*, 11254-11256.

26. Schatzschneider, U. Novel lead structures and activation mechanisms for CO-releasing molecules (CORMs). *Br. J. Pharmacol*. **2015**, *172*, 1638-1650.

27. Chakraborty, I.; Jimenez, J.; Mascharak, P. K. CO-induced apoptotic cell death of colorectal cancer cells by a luminescent photoCORM grafted on biocompatible carboxymethyl chitosan. *Chem. Commun*. **2017**, *53*, 5519-5522.

28. Arnott, J. A.; Planey, S. L. The influence of lipophilicity in drug discovery and design. *Expert Opin. Drug Discov*. **2010**, *7*, 863-875.

29. Waring, M. J. Lipophilicity in drug discovery. *Expert Opin. Drug Discov*. **2010**, 5, 235-248.

30. Wanka, L.; Iqbal, K.; Schreiner, P. R. The lipophilic bullet hits the targets: mericinal chemistry of adamantane derivatives. *Chem. Rev*. **2013**, *113*, 3516-3604.

31. Davies, W. L.; Grunert, R. R.; Haff, R. F.; McGahen, J. W.; Neumayer, E. M.; Paulshock, M.; Watts, J. C.; Wood, T. R.; Hermann, E. C.; Hoffmann, C. E. Antiviral activity of 1-adamantanamine (adamantadine). *Science* **1964**, *144*, 862-863.

32. Kirillov, A. M. Hexamethylenetetramine: an old new building block for design of coordination polymers. *Coord. Chem. Rev*. **2011**, *255*, 1603-1622.

33. Balija, A. M.; Kohman, R. E.; Zimmerman, S. C. Substituted 1,3,5-triazaadamantanes: biocompatible and degradable building blocks. *Angew. Chem. Int. Ed*. **2008**, *47*, 8072-8074.

34. Zheng, S. -L.; Tong, M. -L.; Chen, X. -M. Silver(I)-hexamethylenetetramine molecular architectures: from self-assembly to design assembly. *Coord. Chem. Rev.* **2003**, *246*, 185-202.

35. Tsunoda, A.; Maassab, H. F.; Cochran, K. W.; Eveland, W. C. Antiviral activity of α-methyl-1-adamantanemethylamine hydrochloride. *Antimicrob. Agents Chemother.* **1965**, *5*, 553-560.

36. Guerriero, A.; Oberhauser, W.; Riedel, T.; Peruzzini, M.; Dyson, P. J.; Gonsalvi, L. New class of half-sandwich ruthenium(II) arene complexes bearing the water-soluble CAP ligand as an in vitro anticancer agent. *Inorg. Chem.* **2017**, *56*, 5514-5518.

37. Jimenez, J.; Pinto, M. N.; Martinez-Gonzalez, J.; Mascharak, P. K. Photo-induced eradication of colorectal adenocarcinoma cells by carbon monoxide (CO) delivery from a Mn-based green luminescent photoCORM. *Inorganica Chim. Acta* **2019**, *485*, 112-117.

38. McLean, S.; Mann, B. E.; Poole, R. K. Sulfite species enhance carbon monoxide release from CO-releasing molecules: implications for deoxymyoglobin assay of activity. *Anal. Biochem.* **2012**, *427*, 36-40.

39. Bruker APEX3, Bruker AXS Inc. Madison, Wisconsin, USA, 2014.

40. Bruker SAINT, Bruker AXS Inc., Madison, Wisconsin, USA, 2012.

41. Bruker SADABS, Bruker AXS Inc., Madison, Wisconsin, USA, 2016.

42. Sheldrick. G. M. SHELXT – Integrated space-group and crystal-structure determination. *Acta Crystallogr.* **2015**, *A71*, 3-8.
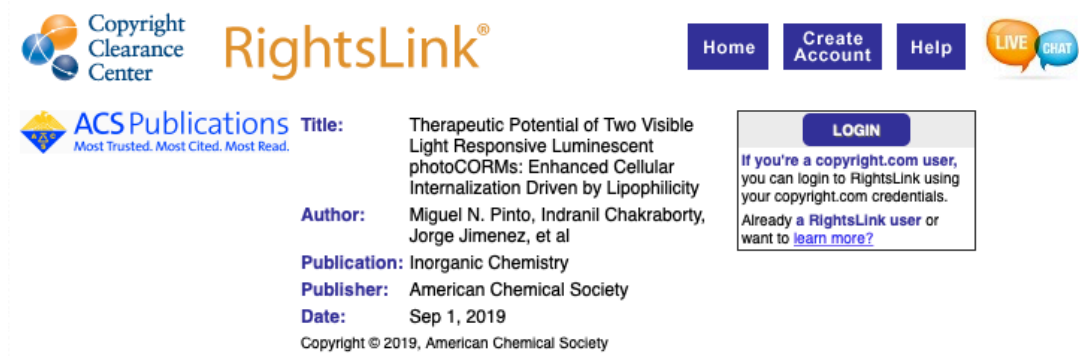
43. Sheldrick. G. M. Crystal structure refinement with SHELXL. *Acta Crystallogr.* **2015**, *C71*, 3-8.

44. Spek. A. L. PLATON SQUEEZE: a tool for the calculation of the disordered solvent contribution to the calculated structure factors. *Acta Crystallogr.* **2015**, *C71*, 9-18.

45. Dolomanov, O. V.; Bourhis, L. J.; Gildea, R. J.; Howard, J. A. K.; Puschmann. H. OLEX2: a complete structure solution, refinement and analysis program. *J Appl. Crystallogr.* **2009**, *42*, 339-341.

46. Jimenez, J.; Chakraborty, I.; Carrington, S. J.; Mascharak, P. K. Light-triggered CO delivery by a water-soluble and biocompatible manganese photoCORM. *Dalton. Trans.* **2016**, *33*, 13204-13213.

47. Thornalley, P. J. The glyoxalase system in health and disease. *Mol. Aspects Med.* **1993**, *14*, 287-371.

48. Wang, P.; Zhou, D.; Chen, B. Highly selective and sensitive detection of Zn(II) using tetrapeptide-based dansyl fluorescent chemosensor and its application in cell imaging. *SpectroChim. Acta A* **2018**, *204*, 735-742.

49. Chakraborty, I.; Jimenez, J.; Sameera, W, M. C.; Kato, M.; Mascharak, P. K. Luminescent Re(I) carbonyl complexes as trackable photoCORMs for CO delivery to cellular targets. *Inorg. Chem*. **2017**, *56*, 2863-2873.

50. Pierri, A. E.; Pallaoro, A.; Wu, G.; Ford, P. C. A luminescent and biocompatible photoCORM. *J. Am. Chem. Soc*. **2012**, *134*, 18197-18200.

51. Pinto, M.; Chakraborty, I.; Martinez-Gonzalez, J.; Mascharak P. Synthesis and structures of photoactive rhenium carbonyl complexes derived from 2-pyridin-2-yl)-1,3-benzothiazole, 2-(quinoline-2-yl)-1,3-benzothiazole and 1,10-phenanthroline. *Acta Crystallogr.* **2017**, *C73*, 923-929.

52. Riss, T. L.; Moravec, R. A.; Niles, A. L.; Duellman, S.; Benik, H. A.; Worzella, T. J.; Minor, L. Assay Guidance Manual. [Online]. Eli Lilly & Company and the National Center for Advancing Translational Sciences. 2004.

53. Slee, E. A.; Adrain, C.; Martin, S. J. Executioner caspase-3, -6, and -7 perform distinct, non-redundant roles during the demolition phase of apoptosis. *J. Biol. Chem.* **2001**, *276*, 7320-7326.

3.II.6 Reprints of Publications and Permissions.

Reprinted with permissions from Pinto, M. N.; Chakraborty, I.; Jimenez, J.; Murphy, K.; Wenger, J.; Mascharak, P. K. Therapeutic potential of two visible light responsive luminescent photoCORMs: Enhanced cellular internalization driven by lipophilicity. *Inorg. Chem.* **2019**, XX, XX-XX.

Therapeutic Potential of Two Visible Light Responsive Luminescent photoCORMs: Enhanced Cellular Internalization Driven by Lipophilicity

Miguel N. Pinto,[†] Indranil Chakraborty,[‡] Jorge Jimenez,[†] Katelyn Murphy,[†] John Wenger,[†] and Pradip K. Mascharak*,[†]

[†]Department of Chemistry and Biochemistry, University of California, Santa Cruz, 1156 High Street, Santa Cruz, California 95064, United States

[‡]Department of Chemistry and Biochemistry, Florida International University, 11200 SW Eighth Street, Miami, Florida 33199, United States

Ⓢ *Supporting Information*

ABSTRACT: Herein we report the synthesis, characterization, and cellular internalization properties of two visible-light active luminescent Mn-based photoCORMs. The enhanced membrane permeability of the photoactive Mn carbonyl complex (photo-CORM) derived from a designed lipophilic ligand namely, $[Mn(CO)_3(Imdansyl)(L1)](CF_3SO_3)$ (**1**) (where **L1** = a diazabutadiene-based ligand containing two highly lipophilic adamantyl motifs, Imdansyl = dansylimidazole) promoted rapid internalization within human colorectal adenocarcinoma (HT-29) cells compared to $[Mn(CO)_3(Imdansyl)(L2)](CF_3SO_3)$ (**2**) (where **L2** = a diazabutadiene ligand bearing two hydrophilic 1,3,5-triazaadamantyl group). Colocalization experiments using membrane stain indicate different extents of localization of the two CO complexes within the cellular matrix. Visible-light triggered CO release from the lipophilic photoCORM induced caspase-3/7 activation on HT-29 cells, which was detected using confocal microscopy. The rapid accumulation of the lipophilic photoCORM **1** in the cellular membrane resulted in more efficient CO-induced cell death compared to the hydrophilic analogue **2**.
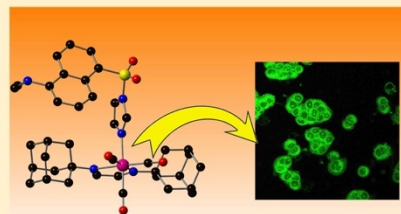
■ INTRODUCTION

The pathophysiological roles of carbon monoxide (CO) as a signaling molecule in mammalian cells are now well established.[1–4] The homeodynamic nature of CO has recently ushered the potential of this small gaseous molecule in therapeutic applications despite its widespread implication as a toxic pollutant.[1,2] In mammals, heme oxygenase-catalyzed degradation of heme proteins leads to generation of endogenous CO.[5,6] Among other salutary effects, CO provides cytoprotection[2,7] (pro-proliferative) to cellular milieu and has also been shown to exert vasoregulatory actions.[8,9] However, in certain malignant cells CO induces an anti-Warburg effect, ultimately resulting in metabolic exhaustion and cellular apoptosis.[10] This mechanism is exclusively operational only within malignant cells due to their metabolic acquisition of a glycolytic phenotype. It is now apparent that a more controlled and sustainable application of CO from an external source can impart selective pro-apoptotic action in malignant cells without causing any noticeable damage to normal (primary) cells. Furthermore, CO has recently been shown to play active role in sensitization of conventional chemotherapeutics and thereby could be utilized as adjuvant therapeutics.[10–12]

Among various external CO sources (including gaseous CO), the photoactivatable CO-releasing molecules (photo-CORMs) have shown significant promise as superior CO donors in terms of more controlled and sustainable delivery.[13–19] Several research groups including ours have exploited the therapeutic potential of phototriggered CO from photoCORMs against selected malignancies.[14,19–27] Despite such capacity of the photoCORMs to induce apoptosis in certain malignant cells under the control of light,[27] the efficacy of cellular penetration of these prodrugs are debatable. The light-triggered CO from photoCORM prodrugs can diffuse into the cell and exert its activity, even if the prodrug shows moderate to poor cellular internalization. However, this may result in undesirable loss of CO before reaching the target of interest and could mitigate the extent of its salutary benefit. Poor internalization of the photoCORM results in the use of higher concentration of the prodrug to exert the therapeutic effect. In contrast, a strategically designed photoCORM with optimal lipophilicity could be internalized more efficiently into

300

cells and in such scenario the uncaged CO molecules are likely to display a more pronounced effect at a relatively lower dose of the prodrug. Lipophilicity plays critical role in medicinal chemistry.[28,29] Uptake of drug molecules is a function of solubility and cell permeability. Although for a given drug molecule aqueous solubility is important for its physiological acceptability, low lipophilicity can contribute to poor cell membrane permeability. The bioavailability of the drug is crucial and generally high lipophilicity contributes in maintaining a favorable metabolic stability through circumventing its first pass clearance. Overall, optimal lipophilicity could be a major factor in achieving a modular drug/prodrug system, which will be effective toward desired action on a cellular target (in our case toward eradication of certain malignancies) at a relatively lower dosage by virtue of its superior cell penetration capacity.

In this account, we report a luminescent photoCORM $[Mn(CO)_3(Imdansyl)(\mathbf{L1})](CF_3SO_3)$ (**1**) derived from a diazabutadiene-based ligand containing two *highly lipophilic* adamantyl motifs (Imdansyl = dansylimidazole) as shown in Scheme 1. Adamantane derivatives are excellent pharmaco-

Scheme 1. Lipophilic Ligand L1 and Hydrophilic Ligand L2 Employed in the Present Work
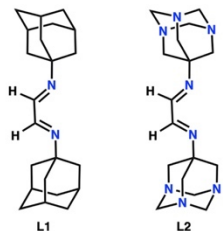
phores with enhanced lipophilicity, stability, and often exhibit improved pharmacokinetic profiles.[29] Aminoadamantanes such as amantadine and rimantadine are among the first successful drug candidates bearing the "lipophilic bullets" and are still in pharmaceutical markets to date.[30,31] There has been a significant development in the area of adamantane-based pharmaceuticals to treat critical viral infections such as influenza A, herplex simplex, hepatitis C, and HIV.[29] Herein, for the first time, we report the successful synthesis and characterization of a highly lipophilic photoCORM derived from a diazabutadiene ligand bearing a clinically approved lipophilic pharmacophore. The efficacy of this photoCORM toward CO-induced cellular apoptosis has been assessed with human colon adenocarcinoma (HT-29) cells. Furthermore, for sake of comparison of cellular permeability, an analogous complex derived from a diazabutadiene ligand bearing the *hydrophilic* 1,3,5-triazaadamantyl group (**L2**, Scheme 1), namely $[Mn(CO)_3(Imdansyl)(\mathbf{L2})](CF_3SO_3)$ (**2**), has been synthesized and studied. The hydrophilicity of azaadamantane and its derivatives arises from good hydrogen acceptor capabilities of the tertiary nitrogen groups.[32−34] To date, triazaadamantyl-bearing complexes have been shown to possess excellent antimetastatic and antiangiogenic properties. This motif constitutes part of certain anticancer drugs that are currently undergoing phase II clinical trials.[35,36] The sixth

position in both complexes **1** and **2** is occupied by one of the N-centers of a known fluorophore, namely, imidazoledansyl (Imdansyl). This ligand has been incorporated in the design to provide an easy handle for monitoring the internalization of the prodrugs through confocal microscopy.[20,37] Complexes **1** and **2** have been characterized by analytical and spectroscopic techniques, including X-ray crystallography. Finally, biological studies employing these two photoCORMs with different lipophilicity have been completed to clearly demonstrate that proper ligand design could afford photoCORMs which avert unwanted CO loss outside the membrane before reaching the target of interest and thus exhibit superior proapoptotic effects.

■ EXPERIMENTAL SECTION

Materials and Methods. $[Mn(CO)_5Br]$ and all the required chemicals were purchased from Sigma-Aldrich and used without further purification unless otherwise specified. MTT (3-(4,5-dimethylthiazol-2-yl)-2,5-diphenyltetrazolium bromide), CellEvent Caspase 3/7 detection reagent, and Vybrant DiD cell labeling solution were acquired from Life Technologies. The precursor 7-amino-1,3,5-triazaadamantane was purchased from Combi-Blocks Inc. All solvents were purified according to standard procedures. All manipulations involving Mn species were carefully performed under strictly dark conditions. The human colorectal adenocarcinoma cell line HT-29 was purchased from American Type Culture Collection (ATCC). Cellular imaging experiments were carried out in 35 mm imaging dishes purchased from ibidi. Unless otherwise stated, the cells were cultured in McCoy's 5A supplemented with 20% fetal bovine serum (FBS).

Physical Measurements. IR spectra were obtained using a PerkinElmer Spectrum One FT-IR spectrometer. UV−vis data was recorded using a Varian Cary 50 UV−vis spectrophotometer. Fluorescence spectra were collected using an Agilent Cary-Eclipse fluorescence spectrophotometer. The ^{1}H NMR spectra were obtained at 298 K using a Bruker 500 MHz instrument. Microanalyses (C, H, N) were carried out with a PerkinElmer 2400 Series II elemental analyzer. An Electro Fiber Optics Corp. IL410 illumination system was used as a broadband visible light source for UV−vis spectroscopic studies. A Husky portable work-light LED panel (15 mW cm^{-2}) was used for the biological experiments. The power of the incident visible light used during the experiments was measured with a Field MaxII-TO laser power meter (Coherent, Portland, OR). Myoglobin assays were performed with **1** and **2** by following a previously reported literature procedure.[38] The MTT assays absorbances were recorded using a Molecular Devices VersaMax tunable microplate reader. The confocal images were acquired using an Inverted Nikon Eclipse TE2000-E spinning disk (CSLI-X1) confocal microscope equipped with a Hamamatsu EM-CCD camera (ImageE MX2) utilizing 405, 488, or 635 nm illumination at 50 mW. The gain and offset were adjusted to set the brightest pixels below saturation. The detection gates were set to 490−540 nm for the complexes, 580−700 nm for the Caspase-3/7 detection agent, and 650−700 nm for the DiD cell labeling dye. The raw confocal microscopy images were further processed using Fiji-ImageJ version 1.52e.

*Synthesis of N,N′-Bis-1-(adamantly)-1,4-diazabutadiene (**L1**).* Adamantan-1-amine (532 mg, 3.52 mmol) was dissolved in 15 mL of MeOH. Next, 202 μL (1.76 mmol) of glyoxal (40% in H$_2$O) was added to this solution, and the reaction mixture was stirred overnight. A white precipitate formed after the solvent was reduced under vacuum. The product thus obtained was collected via vacuum filtration and recrystallized three times from MeOH, yielding **L1** as microcrystalline white solid (506 mg, 89%). IR (KBr, cm^{-1}): 3423 (w), 2904 (s), 2844 (s), 2656 (s), 1628 (m), 1450 (m), 1343 (w), 1313 (w), 1185 (w), 1118 (w), 1091 (m), 983 (w), 907 (w), 811 (w), 721 (w), 646 (w), 471 (w). ^{1}H NMR (CDCl$_3$, δ, ppm): 7.93 (s, 2H), 2.14 (s, 6H), 1.72 (m, 24H). ESI-MS (*m/z*): M + H$^+$325.32 (calcd 325.26).

301

Synthesis of N,N′-Bis-1-(3,5,7-triazaadamantly)-1,4-diazabuta-diene (L2). A batch of 93 μL (0.81 mmol) of Glyoxal (40% in H$_2$O) was added to a solution of 250 mg (1.62 mmol) of 7-amino-1,3,5-triazaadamantane in 10 mL of MeOH, and the reaction mixture was stirred overnight at room temperature. The resulting brownish white precipitate was collected via vacuum filtration. The powder was recrystallized three times from CH$_2$Cl$_2$/MeOH, yielding 228 mg (85%) of **L2** as microcrystalline white solid. IR (KBr, cm^{-1}): 3435 (m), 2933 (w), 2860 (w), 1621 (w), 1451 (w), 1365 (w), 1319 (w), 1243 (w), 1031 (m), 995 (s), 822 (m), 640 (w). ^{1}H NMR (MeOD, δ, ppm): 7.84 (s, 2H), 4.55 (d, 6H), 4.15 (d, 6H), 3.46 (s, 12H). ESI-MS (m/z): M + H$^+$ 331.30 (calcd 331.24).

Synthesis of [Mn(CO)$_3$(Imdansyl)(L1)]CF$_3$SO$_3$ (1). A batch of **L1** (200 mg, 0.62 mmol) was dissolved in 10 mL of CHCl$_3$. Then [Mn(CO)$_5$Br] (171 mg, 0.62 mmol) was dissolved in 30 mL of MeOH and added to the **L1** solution. The reaction mixture was stirred at room temperature for 48 h. The orange precipitate thus obtained was collected via vacuum filtration. The powder was washed with 3 × 10 mL portions of hexanes and dried under vacuum, yielding 276 mg (82%) of [Mn(CO)$_3$(**L1**)Br] as a red-orange microcrystalline powder. IR (KBr, cm^{-1}): 3455 (w) 2921 (w), 2854 (w), 2017 (s), 1919 (s), 1908 (s), 1650 (w), 1452 (w), 1385 (w), 1085 (w), 868 (w), 626 (w). ^{1}H NMR (CDCl$_3$, δ, ppm): 8.28 (s, 2H), 2.32 (s, 6H), 2.19 (m, 12H), 1.78 (m, 12H). Next, a solution of AgCF$_3$SO$_3$ (80 mg, 0.31 mmol) in 40 mL of CH$_2$Cl$_2$ was added to [Mn(CO)$_3$(**L1**)Br] (150 mg, 0.28 mmol). The reaction mixture was stirred at room temperature for 6 h. The resulting cloudy light-orange solution was filtered over a Celite bed to remove excess AgCF$_3$SO$_3$ and the newly formed AgBr. The clear-orange filtrate was collected, and the solvent was removed under reduced pressure. The product [Mn(CO)$_3$(**L1**)(CF$_3$SO$_3$)] was isolated as a light orange powder (123 mg, 72%). IR (KBr, cm^{-1}): 3450 (m), 2911 (w), 2854 (w), 2036 (s), 1940 (s), 1923 (s), 1637 (w), 1455 (m), 1345 (m), 1293 (w), 1233 (m), 1207 (m), 1173 (w), 1085 (w), 1029 (w), 1020 (m), 637 (m), 520 (w). ^{1}H NMR (CDCl$_3$, δ, ppm): 8.36 (m, 2H), 2.35 (s, 6H), 2.15 (m, 12H), 1.78 (m, 12H). The ligand dansylimidazole (98 mg, 0.32 mmol) was added to a solution of [Mn(CO)$_3$(**L1**)(CF$_3$SO$_3$)] (100 mg, 0.16 mmol) in 20 mL of distilled CH$_2$Cl$_2$. The reaction mixture was stirred for 48 h at room temperature under anaerobic conditions. The solvent was then removed under reduced pressure resulting in an oily orange residue. This residue converted to a light orange precipitate upon addition of 10 mL of anhydrous diethyl ether (Et$_2$O). The precipitate was collected through vacuum filtration and washed with 3 × 10 mL portions of anhydrous Et$_2$O. Finally, the product was recrystallized from CH$_2$Cl$_2$/hexanes yielding 103 mg of complex **1** (69%) as a light yellow-orange solid. Anal. Calcd (%) for C$_{41}$H$_{47}$F$_3$MnN$_5$O$_8$S$_2$ (913.89): C, 53.88; H, 5.18; N, 7.66. Found: C, 53.82; H, 5.21; N, 7.72. Selected IR (KBr, cm^{-1}): 3441 (m), 3148 (w), 2913 (w), 2855 (m), 2036 (w), 1949 (s), 1920 (s), 1906 (s), 1614 (w), 1568 (w), 1481 (w), 1455 (w), 1409 (w), 1384 (m), 1347 (w), 1304 (m), 1252 (s), 1224 (m), 1203 (w), 1166 (s), 1105 (w), 1059 (m), 1027 (m), 941 (w), 783 (m), 679 (s), 638 (s), 558 (w). UV−vis (CH$_2$Cl$_2$), λ$_{max}$= 375 nm (ε = 6400). ^{1}H NMR (CDCl$_3$, δ, ppm): 8.68 (m, 4H), 8.18 (s, 1H), 8.12 (d, 1H), 7.73 (t, 1H), 7.62 (t, 1H), 7.42 (s, 1H), 7.17 (d, 1H), 6.93 (s, 1H), 2.86 (s, 6H), 1.62 (m, 30H). ESI-MS (m/z): M$^+$ 764.29 (calcd 764.27).

Synthesis of [Mn(CO)$_3$(Imdansyl)(L2)]CF$_3$SO$_3$ (2). A batch of 200 mg (0.72 mmol) of [Mn(CO)$_5$Br] was dissolved in 30 mL of anhydrous MeOH and added to a CHCl$_3$ solution of **L2** (166 mg, 0.72 mmol). The reaction mixture was stirred at room temperature for 48 h and the resulting precipitate was collected using vacuum filtration. The powder was washed with 3 × 10 mL portions of hexanes and dried under vacuum, yielding 281 mg (71%) of [Mn(CO)$_3$(**L2**)Br] as dark-red microcrystalline powder. IR (KBr, cm^{-1}): 3468 (w) 2912 (w), 2029 (s), 1933 (s), 1916 (s), 1456 (w), 1242 (w), 1212 (w), 1030 (m), 992 (m), 821 (w), 632 (w). The following reactions were carried out carefully to exclude air and moisture. Anhydrous MeOH (20 mL) was added to a N$_2$-purged reaction flask containing [Mn(CO)$_3$(**L2**)Br] (200 mg, 0.36 mmol) forming a fine suspension. An anhydrous methanolic solution (20

mL) containing AgCF$_3$SO$_3$ (94 mg, 0.36 mmol) was then added to the reaction flask. The mixture was stirred at room temperature for 5 h resulting in a cloudy red-orange solution. This solution was filtered under nitrogen using a Celite bed to remove the newly formed AgBr. The resulting clear red filtrate was collected, and the solvent removed under reduced pressure. Portions of distilled CH$_2$Cl$_2$ (3 × 10 mL) were added to the resulting oily residue and subsequently removed under vacuum. Finally, anhydrous Et$_2$O (5 mL) was added to the residue forming a precipitate. The product was collected under nitrogen via vacuum filtration and washed with 3 × 5 mL of anhydrous Et$_2$O to afford [Mn(CO)$_3$(**L2**)(CF$_3$SO$_3$)] as a light red powder (137 mg, 61%). IR (KBr, cm^{-1}): 3475 (w), 2872 (w), 2039 (s), 1953 (s), 1921 (s), 1649 (w), 1456 (w), 1282 (m), 1241 (m), 1220 (m), 1165 (w), 1094 (w), 1029 (m), 994 (m), 820 (w), 633 (w), 503 (w). ^{1}H NMR (MeOD, δ, ppm): 8.39 (s, 2H), 4.68 (d, 6H), 4.20 (d, 6H), 3.86 (s, 12H). The complex [Mn(CO)$_3$(**L2**)(CF$_3$SO$_3$)] (100 mg, 0.16 mmol) was dissolved in 10 mL of anhydrous MeOH in an N$_2$-purged reaction flask. Dansylimidazole (49 mg, 0.16 mmol) was dissolved in 10 mL of anhydrous MeOH and added to this solution. The reaction mixture was stirred for 5 h at room temperature. The solvent was removed under reduced pressure resulting in an oily red-orange film. Distilled CH$_2$Cl$_2$ (5 mL) was then added to the flask and subsequently removed under reduced pressure. Next, anhydrous Et$_2$O was added to the residue, resulting in the formation of a light red-orange precipitate. The solution was vacuum filtered under N$_2$ atmosphere and washed with 3 × 10 mL portions of anhydrous Et$_2$O. Finally, the product was recrystallized from CH$_2$Cl$_2$/hexanes yielding 60 mg of complex **2** (40%) as a light red-orange solid. Anal. Calcd (%) for C$_{35}$H$_{41}$F$_3$MnN$_{11}$O$_8$S$_2$ (919.84): C, 45.70; H, 4.49; N, 16.75. Found: C, 45.66; H, 4.40; N, 16.66. Selected IR (KBr, cm^{-1}): 345.54 (s), 2924 (m), 2036 (s), 1931 (s), m 1917 (s), 1637 (w), 1575 (w), 1461 (w), 1412 (w), 1383 (w), 1259 (s), 1163 (s), 1059 (m) 1029 (s), 993 (s), 822 (m), 791 (m), 635 (s), 588 (w). UV−vis (CH$_2$Cl$_2$), λ$_{max}$= 370 nm (ε = 4300). ^{1}H NMR (MeOD, δ, ppm): 8.75 (d, 1H), 8.53 (d, 1H), 8.41 (s, 1H), 8.37 (s, 1H), 8.33 (d, 1H), 7.72 (t, 1H), 7.66 (t, 1H), 7.56 (s, 1H), 7.32 (d, 1H), 7.04 (s, 1H), 4.68 (d, 6H), 4.19 (d, 6H), 3.84 (m, 12H), 2.89 (s, 6H). ESI-MS (m/z): M$^+$ 770.24 (calcd 770.24).

X-ray Crystallography. Orange block-shaped crystals of **1** and [Mn(CO)$_3$(**L1**)(H$_2$O)](CF$_3$SO$_3$) were obtained by layering hexanes on top of a solution of the respective complex in toluene. In both cases, a suitable crystal was selected and mounted on a Bruker D8 Quest diffractometer equipped with PHOTON II detector operating at T = 298 K. Data were collected with ω shutterless scan technique using graphite monochromated Mo Kα radiation (λ = 0.71073 Å). The total number of runs and images for both data collections was based on the strategy calculation from the program *APEX3* (Bruker).[39] Cell parameters were retrieved using the *SAINT* software[40] and refined using *SAINT* (Bruker) on 5340 reflections for **1** and on 9305 reflections for [Mn(CO)$_3$(**L1**)(H$_2$O)](CF$_3$SO$_3$). Data reduction was performed using the *SAINT* (Bruker) software, which corrects for Lorentz and polarization effects. The final completeness was 99.5% for **1** and 99.2% for [Mn(CO)$_3$(**L1**)(H$_2$O)](CF$_3$SO$_3$). Multiscan absorption corrections were performed with both data sets using *SADABS* 2016/2.[41] The absorption coefficients for **1** and [Mn(CO)$_3$(**L1**)-(H$_2$O)](CF$_3$SO$_3$) were 0.44 and 0.60 mm^{-1}, respectively. Minimum and maximum transmissions for **1** were 0.660 and 0.745 while the corresponding values for [Mn(CO)$_3$(**L1**)-(H$_2$O)](CF$_3$SO$_3$) were 0.707 and 0.745. The structures for **1** and [Mn(CO)$_3$(**L1**)(H$_2$O)](CF$_3$SO$_3$) were solved in the space group $P\bar{1}$ (No. 2) and P2$_1$/c (No. 14) respectively by *intrinsic phasing* using the *ShelXT*[42] structure solution program and refined by full matrix least-squares on F^2 using version 2016/6 of *ShelXL*.[43] All non-hydrogen atoms were refined anisotropically in both cases. Hydrogen atom positions were calculated geometrically and refined using the riding model. To alleviate the complications related to solvent accessible voids within the extended lattice in cases of **1**, *SQUEEZE* operation (included in the *PLATON* program) was performed with the raw data set and the structure was refined form the data obtained upon *SQUEEZE* operation.[44] Calculations and molecular graphics were

preformed using *SHELXTL* 2014 and *Olex2*[45] programs. Crystal data and structure refinement parameters are listed in Table S1.

Photolysis, Luminescence, and Stability Experiments. Solutions of **1** and **2** (concentration of 2.0×10^{-4} M) were prepared in CH_2Cl_2. The CO release rates (k_{co}) for **1** and **2** were performed in a quartz cuvette (1 cm × 1 cm) using a 15 mW cm^{-2} broadband visible light (IL 410 illumination system Electro Fiber Optics Corp). Changes in the electronic absorption spectra were recorded after exposing the solution in the cuvette to visible light at regular time intervals. The k_{co} value was then calculated from a $\ln(C)$ versus time (*t*) plot. Equimolar solutions of Imdansyl, **1**, and **2** (2.0×10^{-4} M) were prepared and the emission spectra were recorded using an excitation wavelength of 375 nm. The stability of the complexes was determined by preparing concentrated solutions of the complexes in acetonitrile (MeCN) and diluting PBS until the MeCN concentration reached 2%. Changes in the absorbance spectrum of the solutions was then recorded once every h for 24 h. For quantum yield (φ) measurements, solutions of **1** and **2** in MeCN were used to ensure sufficient absorbance (≥99%) at the incident wavelength (380 nm); no more than 10% photolysis occurred in each measurement. Standard actinometry using potassium ferrioxalate was employed to calibrate the light source (Newport Oriel Apex illuminator, 10 mW at 1 cm distance at 380 nm).

Aqueous Solubility of 2. Deionized water (1.5 mL) was volumetrically added to a vial containing 20.0 mg of **2** and the solution was stirred magnetically overnight. The following day, the resulting aqueous suspension was spun down at 13 000 rpm and the supernatant was carefully placed into a separate container. This saturated solution was volumetrically diluted by a factor of 10 and its absorbance was recorded. A 196.7 μM stock solution of **2** was prepared by dissolving 18.1 mg of the complex in 100 mL of deionized water in a volumetric flask. From this stock solution, a series of standards of concentrations 19.7, 39.3, 49.2, 59.0, and 68.8 μM were prepared in 10 mL volumetric flasks and their absorbances ($\lambda = 328$ nm) were recorded. A standard curve relating absorbance to concentration was obtained and its linear regression was used to relate the absorbance to the concentration of **2**.

Cellular Internalization Experiments. All manipulations were performed under strict dark conditions to avoid exposure to any ambient light. Fresh medium devoid of phenol red and FBS was used to prepare the treatment solutions containing complexes **1**, and **2**. The human colorectal adenocarcinoma HT-29 cells were plated in 35 mm imaging disks at a density of 250 000 cells mL^{-1} (2 mL) and incubated at 37 °C for 24 h with 5% CO_2. The following day, the culture media was aspirated, and cells were washed with 2 mL PBS. The cells were then treated with 2 mL of fresh media containing 50 μM of **1**, or **2**, and incubated for 10, 20, 30, or 40 min. At the end of each incubation period, the media was aspirated, and the cells were washed with 3 × 1 mL portions of PBS buffer. Fresh McCoy's 5A medium (devoid of phenol red, FBS, or complex) was added to the imaging disks, the cells were incubated for 2 h, and the confocal microscopy images were recorded.

Colocalization Experiments. All manipulations were performed under strict dark conditions to avoid accidental exposure to any ambient light. Human adenocarcinoma (HT-29) cells were plated on 35 mm imaging disks at a density of 250 000 cells mL^{-1} (2 mL) and incubated at 37 °C and 5% CO_2 for 24 h. The media was aspirated, and the imaging disks were washed with PBS 3 × 1 mL portions. Then the cells were treated with 2 mL of fresh media containing 50 μM of complex **1** or **2**, and further incubated for 40 min. At the end of the incubation period, the media containing the complexes was removed and the cells were washed with 3 × 1 mL portions of PBS. The cells were then incubated with the Vybrant DiD cell-labeling solution according to manufacturer protocol. After incubation the dye was aspirated, and the cells were washed with 3 × 1 mL portions of PBS. Following incubation of these cells in fresh cell growth media (devoid of phenol-red, FBS, or complex) for 1 h, the confocal microscopy images were recorded.

Cellular Imaging Experiments for Caspase Activation. Two imaging disks were plated with HT-29 cells at a cell density of 250 000 cell mL^{-1} (2 mL) in 35 mm imaging disks and incubated for 24 h at 37 °C and 5% CO_2. The media was aspirated, then the cells were washed with 3 × 1 mL of PBS and incubated for 40 min with 2 mL of fresh media containing 50 μM of complex **1**. After this incubation period, the media was removed and replaced with phenol-red free media. One imaging disk was kept under strict dark conditions and the second imaging disk was irradiated with broadband visible light (15 mW cm^{-2}) for 30 min. The CellEvent Caspase-3/7 detection reagent was added to each of the imaging disks according to the manufacturer's protocol. The cells were then incubated for an additional h at 37 °C with 5% CO_2 and the confocal microscopy images were recorded.

MTT Assays. Unless otherwise stated all manipulations were carried out under strict dark conditions to avoid premature decomposition of the manganese complexes. A stock solution of complex **1** was prepared by dissolving it in MeCN and diluting it to 2% with fresh cell culture media to reach a concentration of 100 μM. Stock solutions of 5, 10, 20, 30, 40, 60, and 80 μM were subsequently prepared by diluting the initial 100 μM stock solution using fresh cell culture media containing 2% MeCN. Control solutions of the ligand and photoproducts were prepared with concentrations of 100 μM in fresh media containing 2% MeCN. Other control solutions included fresh media and 2% MeCN in media (v/v). Two separate 96-well plates were plated with human colorectal adenocarcinoma cells at a density of 100 000 cells mL^{-1} (200 μL) and incubated for 24 h. After the initial incubation period the growth media was aspirated, and the cells were incubated for 2 h at 37 °C and 5% CO_2 with the above-mentioned stock solutions. After this incubation period the media was removed, and the cells were washed using PBS. Fresh cell culture media was then added to the plates and incubated for 1 h. Afterward, one plate was kept under dark conditions, while the other plate was photolyzed with broadband visible light from a low power LED light source (15 mW cm^{-2}) for 40 min. After treatment, the plates were incubated for 2 h at 37 °C with 5% CO_2. The MTT was added to both plates following the manufacturer's protocol and the viability of the cells was assessed using a microplate reader (VersaMax). The viability assay was repeated using complex **2**, its ligand **L2**, and its photoproducts following the same procedure described above. Cell viability studies were performed in triplicate.

■ RESULTS AND DISCUSSION

Synthesis, Structure, and X-ray crystallography. Both **L1** and **L2** were found to react slowly with $[Mn(CO)_5Br]$ and required extended (48 h) reaction time for coordination. Subsequent reaction of $[Mn(CO)_3(L1)Br]$ with $AgCF_3SO_3$ was however complete within 6 h in CH_2Cl_2 without any problems. In contrast, reaction of $[Mn(CO)_3(L2)Br]$ with the silver salt required the use of anhydrous MeOH as the solvent since the resulting complex $[Mn(CO)_3(L2)(CF_3SO_3)]$ exhibited poor solubility in CH_2Cl_2. This reaction was also carefully carried out in absence of air and moisture to avoid unwanted side reactions between $[Mn(CO)_3(L2)(CF_3SO_3)]$ and H_2O. The complex $[Mn(CO)_3(L1)(CF_3SO_3)]$ reacted with 2-fold excess of Imdansyl for 48 h to ensure complete formation of **1**. Although complex **1** is considerably stable under dark conditions, presence of moisture in the last step of its synthesis interferes with the coordination of Imdansyl and facilitates the substitution of CF_3SO_3 by a H_2O molecule, resulting in the partial formation of the aqua complex $[Mn(CO)_3(L1)(H_2O)](CF_3SO_3)$ (X-ray structure determination and details are included in the Supporting Information). However, under strict anaerobic and anhydrous conditions, the reaction of the triflate adduct with Imdansyl proceeds smoothly to afford complex **1** of high purity. In case of $[Mn(CO)_3(L2)(CF_3SO_3)]$, the synthesis required the use of strictly anhydrous MeOH and exactly 1 equiv of Imdansyl with a reaction time of 6 h to avoid the formation of any aqua

complex $[Mn(CO)_3(\mathbf{L2})(H_2O)]CF_3SO_3$. The isolated crude mixture was composed mainly of complex **2**, and unreacted starting materials were removed by recrystallization from CH_2Cl_2/hexanes. Careful studies were carried out to determine if the presence of water in the solvent results in the displacement of the Imdansyl ligand. Complexes **1** and **2** were stirred in wet MeOH (MeOH:H_2O 9:1) for 48 h. The solvent was removed under reduced pressure and the resulting crude powder was analyzed through ^1H NMR. The results indicated that neither complex undergoes decomposition. This observation confirms that water does not displace the Imdansyl ligand within at least 48 h.

The molecular structure of **1** and $[Mn(CO)_3(\mathbf{L1})(H_2O)]$-$CF_3SO_3$ have been determined by single crystal X-ray crystallography. The coordination geometry of the Mn centers in both complexes (**1** and $[Mn(CO)_3(\mathbf{L1})(H_2O)]CF_3SO_3$) is distorted octahedral with three facially disposed CO ligands (Figures 1 and S1). In both structures the asymmetric unit
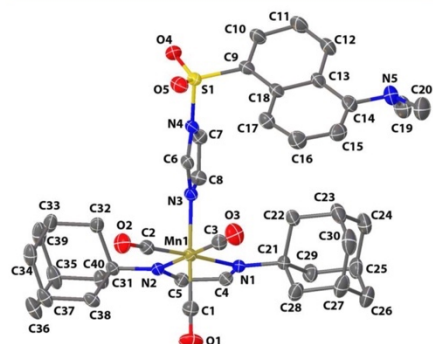
Figure 1. Thermal ellipsoid plot with atom labeling scheme of the cation of complex **1** shown with 50% probability ellipsoids. Hydrogen atoms and the counteranion are omitted for the sake of clarity. Selected bond distances (Å): Mn1–N1, 2.108(3); Mn1–N2, 2.096(2); Mn1–N3, 2.079(3); Mn1–C1, 1.823(4); Mn1–C2, 1.800(4); Mn1–C3, 1.803(4).

consists of one full molecule of the cationic $\mathbf{1}^+$ or $[Mn(CO)_3(\mathbf{L1})(H_2O)]^+$ along with $CF_3SO_3^-$ counteranion. The two N atoms of the ligand **L1** and two C atoms from two CO constitute the equatorial planes, while the third CO occupies one of the axial positions. The second axial position is occupied by the N atom of Imdansyl group in complex **1** and O atom of the coordinated water molecule in $[Mn(CO)_3(\mathbf{L1})(H_2O)]CF_3SO_3$. The equatorial planes composed of N1, N2, C2 and C3 atoms for complexes **1** and $[Mn(CO)_3(\mathbf{L1})(H_2O)]CF_3SO_3$ are satisfactorily planar with mean deviations of 0.019(3) and 0.020(3) Å, respectively. The Mn atoms are slightly displaced by 0.006 and 0.009 Å for complexes **1** and $[Mn(CO)_3(\mathbf{L1})(H_2O)]CF_3SO_3$ respectively from the equatorial planes toward the C1 atom of the axial CO group. The chelate rings for **1** and $[Mn(CO)_3(\mathbf{L1})(H_2O)]CF_3SO_3$ (composed of Mn1, N1, N2, C4, and C5 atoms) fairly deviate from planarity with mean deviations of 0.030(3) and 0.021(3) Å respectively. In **1**, the dihedral angle between the imidazole and the dansyl group is 85.6°. Analysis of crystal packing of **1**

(Figure S2), reveals few non classical hydrogen bonding interactions which consolidates its solid state structure [C8–H8···O8^i, with H8···O8, 2.28 Å; C10–H10···O4, with H10···O4, 2.36 Å; C11–H11···O7^{ii}, with H11···O7, 2.54 Å; C12–H12···N5, with H12···N5, 2.47 Å; C17–H17···O5, with H17···O5, 2.46 Å; and C34–H34A···O7^{iii}, with H34A···O7, 2.59 Å; symmetry codes: (i) $-x + 1, -y + 2, -z + 1$; (ii) $x + 1, y, z - 1$; (iii) $x + 1, y, z$]. In addition, moderate π–π stacking interactions have been noticed between the quinoline rings of the dansyl moieties of two adjacent molecules (centroid-to-centroid distance, 3.825 Å, Figure S3 left panel). Careful inspection of the packing patterns of $[Mn(CO)_3(\mathbf{L1})$-$(H_2O)]CF_3SO_3$, revealed two classical hydrogen-bonding interactions [O7–H7A···O5^i, with H7A···O5, 1.90 Å; and O7–H7B···O6, with H7B···O6, 1.89 Å; symmetry code: (i) $-x + 1, y - \frac{1}{2}, -z + \frac{1}{2}$]. In this case, no intermolecular π–π interactions have been realized (Figure S3, right panel).

The trans influence of the dansyl imidazole group in **1** (as opposed to the axially coordinated water molecule in $[Mn(CO)_3(\mathbf{L1})(H_2O)]CF_3SO_3$) is evident from a slight increase of the Mn1–C1 bond distance in **1** (1.823 Å) compared to the two equatorial Mn–C distances (average, 1.802 Å). In both complexes, the average Mn–C (equatorial) distances (1.802 and 1.809 Å for complexes **1** and $[Mn(CO)_3(\mathbf{L1})(H_2O)]CF_3SO_3$, respectively) are comparable. The average Mn–N distances are also quite similar in both complexes (2.102 and 2.105 Å for complexes **1** and $[Mn(CO)_3(\mathbf{L1})(H_2O)]CF_3SO_3$ respectively). Comparison of the metric parameters of the present structures with another structurally similar complex derived from bidentate ligand bearing adamantyl group, namely $[MnBr(CO)_3(pyAm)]$[46] (where pyAm = 2(pyridyl)iminoadamantane) showed subtle difference. Although the average equatorial Mn–C distance (1.807 Å) in $[MnBr(CO)_3(pyAm)]$ is comparable with both complexes **1** and $[Mn(CO)_3(\mathbf{L1})(H_2O)]CF_3SO_3$, the axial Mn–C length in $[MnBr(CO)_3(pyAm)]$ (1.959 Å) is noticeably longer compared to the corresponding distances in complexes **1** and $[Mn(CO)_3(\mathbf{L1})(H_2O)]CF_3SO_3$ (1.823 and 1.800 Å, respectively).

Solubility and Stability of Complexes 1 and 2. Complex **1** is highly soluble in organic solvents and MeCN/H_2O mixtures but insoluble in pure H_2O. In contrast, complex **2** is highly soluble in H_2O and MeOH, and partially soluble in ethanol and organic solvents. The solubility of **2** in H_2O was obtained by fully dissolving a known amount of the complex in water and serially diluting the solution to prepare a standard curve. A saturated solution of **2** was prepared separately, volumetrically diluted (10-fold), and its absorbance recorded. The concentration of the dilution prepared from the saturated solution was determined using the linear regression obtained from the standard curve (red dot in Figure S6). After correcting for the 10-fold dilution factor, the saturated solution was calculated to contain a concentration of 0.73 mg mL^{-1} (797 μM). In absence of light, both complexes are indefinitely stable as solids. Complex **1** in aqueous solution containing 2% MeCN, the solvent pair employed in the biological experiments (*vide infra*), is stable for at least 24 h, as indicated by its absorption spectrum (Figure S7). Furthermore, solutions of both complexes are very stable in CH_2Cl_2 and CHCl$_3$.

CO Photorelease. Upon exposure to broadband low power visible light (15 mW cm^{-2}) both complexes exhibit systematic changes in the electronic absorption spectra. These changes are associated with uncaging of CO from the
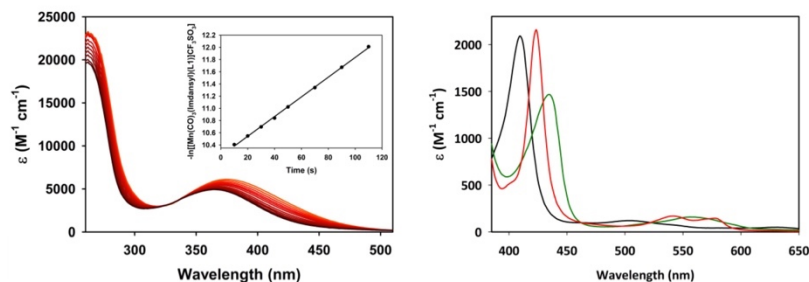
Figure 2. Changes in UV−vis spectrum of **1** (concentration 2.0×10^{-4} M) in CH_2Cl_2 solution upon exposure to low power visible light (15 mW cm^{-2}) at 298 K (left panel). UV−vis traces from the Mb assay for **1** in PBS solution at 298 K (right panel): blue trace, oxidized-Mb; green trace, reduced-Mb; red trace, CO-Mb.
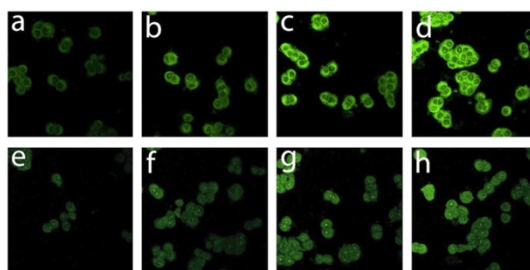
Figure 3. Confocal images of HT-29 cells showing the extent of internalization of the two complexes (**1** and **2**) with increasing incubation time (λ_{ex} = 405 nm). Upper panel: micrographs (parts a−d) display cell images recorded upon treatment with complex **1** with 10, 20, 30, and 40 min incubation (left to right). Lower panel: same experiments with complex **2** as in case of the upper panel.

respective complexes as confirmed by standard Myoglobin assay[37,38] (Figure 2 and see the Supporting Information). Because sodium dithionite is known to facilitate the release of CO from carbonyl complexes, a dual quartz cuvette system[22] was utilized in these experiments. The apparent CO release rates (k_{CO}) from both complexes have been determined by recording the electronic absorption spectra and monitoring the changes of the spectral traces at 410 nm upon exposure to light at 10 s intervals. The k_{CO} values were calculated from $\ln(C)$ vs t plot (left panel inset Figure 2) and were found to be 1.03 and 0.66 min^{-1} for complexes **1** (φ_{380}= 0.35 ± 0.02) and **2** (φ_{380}= 0.23 ± 0.02) respectively. That exposure to light released all three CO molecules from both complexes was confirmed by IR studies performed on the photoproducts (Figures S9−S12; see Supporting Information).[17,20]

Spectroscopic Properties. Infrared studies revealed the C−O stretching bands of both CO complexes in the region of 1900−2050 cm^{-1}, typical of the fac-Mn(CO)$_3$ unit.[20,22] Evaporation of the photolyzed solutions of both complexes and subsequent recording of the IR spectra showed complete disappearance of the C−O stretching bands. This finding clearly suggests uncaging of all three coordinated CO ligands from these complexes upon illumination. Furthermore, the photolyzed solutions of the respective complexes display well-defined 6-line EPR spectra (X-band) consistent with the presence of Mn(II) (See Supporting Information). Comments

must be made here about the photoproduct(s) in case a deligation process is associated with the photoinduced CO-release. Our current design ensures minimal or no toxicity in the event of such deligation through utilization of biocompatible or clinically relevant ligands/coligands. For example, glyoxal (the carbonyl precursor used for the synthesis both **L1** and **L2**), has been shown to form endogenously in humans through pathways linked with oxidative stress. There are mechanisms in place for detoxification of glyoxal in humans and animals by the glyoxalase system present in the cells.[47] As mentioned earlier, both adamantyl and triazaadamantyl derivatives serve as active pharmacophores for several known or potential therapeutics. Moreover, dansyl-based fluorogenic chemo-sensors have been widely employed in cellular imaging due to their known biocompatibility.[48] Thus, the present lipophilic photoCORM **1** comprises all biocompatible/clinically acceptable constituents. At room temperature upon excitation at 370 nm, solutions of complexes **1** and **2** in CH_3CN display broad emission bands (centered at 590 nm, see Supporting Information). Such luminescence properties provided a convenient means to track the prodrug molecules within cellular targets.

Cellular Internalization Experiments. In order to evaluate and qualitatively compare the cellular uptake properties of the two complexes (**1** and **2**) confocal imaging experiments were performed. In these studies, the human

F
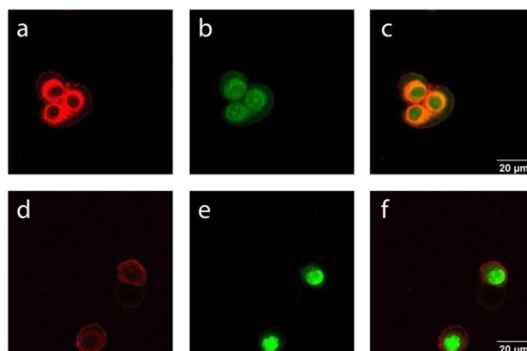
Figure 4. Colocalization experiments of complexes **1** (top row) and **2** (bottom row) within the cellular matrix: (a) DiD cell membrane stain, (b) complex **1** and (c) merge of images a and b; (d) DiD cell membrane stain, (e) complex **2**, and (f) merge of images d and e.

colorectal cancer HT-29 cells were first plated on the imaging disks at a density of 250,000 cells mL^{-1}. The plating of the HT-29 cells to achieve optimal confluency was performed according to standard protocols, and details can be found in the Experimental Section. The cells were then treated with complexes **1** or **2** in McCoy's 5A medium (devoid of fetal bovine serum and phenol red) for 10, 20, 30, and 40 min. After each round of incubation, the media were aspirated, and cells were washed three times with PBS very carefully. Trypan blue was added prior to recording each image to quench any extracellular fluorescence. The images of cells with increasing incubation time (10−40 min) were then captured separately with the aid of a confocal microscope. The cellular images (acquired using the same instrument settings and processed as one batch) suggest internalization of the luminescent complexes and apparently some nuclear localization. The image collage shown in Figure 3 clearly reveals the preferential cellular uptake of complex **1** under same experimental conditions. This is consistent with the superior lipophilicity of complex **1** compared to complex **2**, which in turn would facilitate an improved membrane penetration.

Colocalization Experiments. Close inspection of parts d and h of Figure 3 suggests that complex **1** appears to accumulate preferentially along the cellular membrane due to its lipophilicity, whereas complex **2** appears to primarily accumulate in the cytoplasm due to its hydrophilicity. This prompted us to investigate the cellular colocalization of these complexes by treating the cells with a cell membrane (Vybrant DiD) labeling reagent (red fluorescence). The confocal micrographs indicate that complex **1** (appearing green in Figure 4b) indeed colocalizes primarily in the cell membrane (Figure 4a) producing an orange color in the merged image (Figure 4c). In comparison, complex **2** primarily localizes inside the cytoplasm and its green signal does not overlap with the red cell membrane stain (Figure 4f). To the best of our knowledge, this work for the first time reports a comparative assessment of cellular internalization capacity and localization of two structurally similar photoCORMs merely differentiated by their distinct lipophilicities. Also, it is important to note that such differentiation in lipophilicity has been achieved through subtle modification of otherwise two identical diazabutadiene-

based ligand frames. Unlike the previously reported fluorescent Re carbonyl-based photoCORMs which unfailingly require UV light for uncaging the coordinated CO,[49−51] the present Mn carbonyl-based complexes (**1** and **2**) rapidly release CO under low power *visible* light illumination. This could be advantageous to evade any potential harmful effects toward the target tissues arising from the UV radiation. Also, incorporation of a known fluorophore (dansylimidazole) allows both luminescent complexes to be conveniently tracked within the biological targets.

Viability Assay. After ascertaining the cellular uptake properties through confocal imaging studies, we assessed the viability of HT-29 cells *in vitro* upon visible light-triggered CO delivery from both complexes via standard MTT assay. Results of the MTT assay show a clear dose-dependent reduction in cell viability upon treatment of the malignant cells with both complexes **1** and **2** under visible light illumination. Similar experiments when performed under strict absence of light showed no noticeable reduction of cell viability. These findings suggest no apparent cytotoxicity from the pro-drugs. One representative MTT assay plot is shown in Figure 5 (MTT
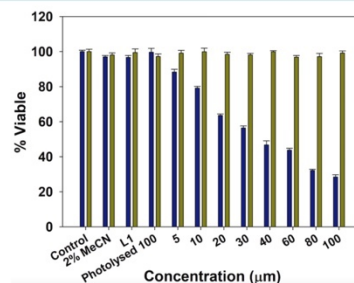
Figure 5. Results of MTT assay with HT-29 cells and complex **1**. Blue bars represent cell viability upon exposure to low power broadband visible light (Husky LED panel,15 mw cm^{-1}) while green bars represent cell viability under strict dark conditions.

assay plot with complex **2** is included in the Supporting Information). The CO released from **1** resulted in an IC$_{50}$ value bellow 40 μM under illumination using broadband visible light. The IC$_{50}$ value for **1** is among the lowest reported to date for HT-29 colorectal adenocarcinoma cells using a metal-containing photoCORM.[23] It is important to note that the free ligands (**L1** or **L2**) as well as the fully photolyzed solution of the complexes **1** or **2** (at highest concentration 100 μM) caused no significant cytotoxicity both under dark and illuminated conditions as evident from Figure 5. Taken together, these results demonstrate that the dose-dependent eradication of HT-29 cells is a direct consequence of intracellular CO-release. The hydrophilic complex **2** required a dose of 70 μM to reduce cell viability by 50%, a fact supporting the hypothesis that the enhanced internalization of the lipophilic complex **1** result in more efficient eradication of the target cells.

Cellular Imaging Experiments for Caspase-3/7 Activation. The reduction in cancer cell viability induced from photoreleased-CO has been primarily investigated using MTT or other similar tetrazolium reduction assays. Tetrazolium reduction assays give insights to the number of viable cells and their metabolic activity. Upon treatment with MTT, live cells reduce the tetrazolium dye and hence the formazan product accumulates linearly. The absorbance of formazan can therefore be correlated to cell viability. When MTT is used in excess or for prolonged periods of time, it exerts toxicity (continuously reducing equivalents of NADH) resulting in misrepresentation of the results.[52] Additionally, the signals generated from MTT tests are highly dependent on culture conditions,[52] which may vary largely between investigators. Since these tests have yet to be standardized, it is advisable to investigate the viability of cells and/or nature of cell death through alternative and complementary methods. Caspase activity detection is an attractive method for determining the process of cell death. In a previous account, we investigated caspase-3/7 activation upon CO delivery to colorectal adenocarcinoma cells using a UV-light active rhenium carbonyl complex grafted into a carboxymethyl chitosan carrier.[27] Caspase-3, -6, and -7 coordinate the execution of apoptosis, promoting membrane blebbing and controlled disassembly of cellular components. In particular, caspase-3 is the primary executioner of apoptosis, and is responsible for DNA fragmentation and nuclear collapse in some systems.[53] In this account, we report the activation and detection of caspase-3/7 upon delivery of photoreleased CO to HT-29 cells using a photoCORM irradiated with broadband visible light. HT-29 cells were incubated with 50 μM of complex **1** for 30 min, washed, and exposed to low-power (15 mW cm^{-2}) broadband visible light for 40 min. The cells were subsequently incubated with CellEvent caspase detection agent and the activation of caspase-3/7 was visualized through confocal microscopy (Figure 6). No activation of caspase-3/-7 was detected on control experiments where the cells were incubated with the complex and kept under strict dark conditions (Figure 6a). However, cells treated with **1** and subsequently exposed to visible light clearly showed onset of apoptosis (Figures 6b and 6c). The fluorescent signal coming from the caspase-3/7 activation appears to localize primarily in the nucleus of the cell (Figure 6c). It is expected that the caspase activation signal should originate from the nucleus due to the involvement of caspase-3 in DNA fragmentation and nuclear collapse.[53]
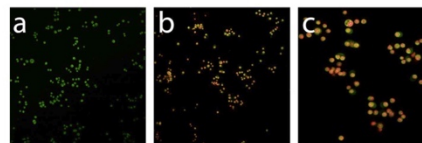
Figure 6. Confocal micrograph results of caspase-3/-7 activation induced CO-photoreleased from complex **1**. (a) Treated cells kept under strict dark conditions. (b) Treated cells after 30 min exposure to low-power (15 mW cm^{-2}) broadband visible light. (c) Figure 6b zoomed in.

■ CONCLUSIONS

In conclusion, we have synthesized and characterized two biocompatible photoCORMs that readily deliver CO upon exposure to visible light. By virtue of their luminescence properties, both complexes could easily be tracked within cellular matrices through confocal fluorescence imaging. For the first time, we have compared the extent of cellular internalization of two structurally similar photoCORMs differentiated by their distinct lipophilicity. Indeed, under same experimental conditions, the more lipophilic photoCORM prodrug **1** showed preferential cellular uptake by human colon adenocarcinoma HT-29 cells. Colocalization experiments confirmed that the lipophilic photoCORM preferentially accumulates in the membrane, whereas the hydrophilic photoCORM preferentially accumulates in the cytoplasm. Both complexes exhibited dose-dependent eradication of the HT-29 cells under illumination. CO-induced apoptotic cell death of the cancer cells was confirmed through detection of caspase-3/7 activation. Since optimal lipophilicity is of pivotal importance in the pharmaceutical industry, the present work is expected to provide a credible guideline to develop highly lipophilic organometallic pro-drugs with biocompatible constituents for facile cellular membrane penetration.

■ ASSOCIATED CONTENT

ⓢ Supporting Information

The Supporting Information is available free of charge on the ACS Publications website at DOI: 10.1021/acs.inorg-chem.9b02121.

Table containing crystal data and structure refinement parameters for **1** and [Mn(CO)$_3$(Imdansyl)(**L1**)-(H$_2$O)](CF$_3$SO$_3$) (Table S1), MTT assay result with **2** and ellipsoid plot with atom labeling scheme of the cation of the aqua complex [Mn(CO)$_3$(Imdansyl)(**L1**)-(H$_2$O)] (Figure S1), crystal packing pattern (along b axis) and intermolecular $\pi-\pi$ stacking interactions in **1** (Figures S2 and S3), ^{1}H NMR spectrum of **1** in CDCl$_3$ (Figure S4), myoglobin assay result with **2** (Figure S5), standard curve for the determination of the solubility of **2** in H$_2$O (Figure S6), stability data of **1** and **2** in PBS containing 2% MeCN (Figure S7 and S8), FTIR spectra of **1** and **2** before and after photolysis (Figures S9−S12), absorption spectral changes of **2** in CH$_2$Cl$_2$ upon exposure to visible light (15 mW cm^{-2}) at periodic time intervals (Figure S13), fluorescence intensity comparison of **1** and free imidazole dansyl in CH$_2$Cl$_2$ and in a H$_2$O/MeCN mixture (Figures S14 and S15), luminescence increase of **1** and **2** upon irradiation with

broadband visible light (Figures S16 and S17), X-band EPR spectra of irradiated samples of **1** and **2** (Figures S18 and S19), and HT-29 cell viability results with **2** under dark and light conditions (Figure S20). (PDF)

Accession Codes

CCDC 1912936−1912937 contain the supplementary crystallographic data for this paper. These data can be obtained free of charge via www.ccdc.cam.ac.uk/data_request/cif, or by emailing data_request@ccdc.cam.ac.uk, or by contacting The Cambridge Crystallographic Data Centre, 12 Union Road, Cambridge CB2 1EZ, UK; fax: +44 1223 336033.

■ AUTHOR INFORMATION

Corresponding Author

*(P.K.M.) Fax: +1 831 459 2935. Telephone: +1 831 459 4251. E-mail: pradip@ucsc.edu.

ORCID

Indranil Chakraborty: 0000-0003-2842-211X
Pradip K. Mascharak: 0000-0002-7044-944X

Notes

The authors declare no competing financial interest.

■ REFERENCES

(1) Motterlini, R.; Otterbein, L. E. The Therapeutic Potential of Carbon Monoxide. *Nat. Rev. Drug Discovery* **2010**, *9*, 728−743.
(2) Motterlini, R.; Foresti, R. Biological Signalling by Carbon Monoxide and Carbon Monoxide-releasing molecules. *Am. J. Physiol. Cell Physiol.* **2017**, *312*, C302−C313.
(3) Mustafa, A. K.; Gadalla, M. M.; Snyder, S. H. Signalling by Gasotransmitters. *Sci. Signaling* **2009**, *2*, No. re2.
(4) Wu, L.; Wang, R. Carbon Monoxide: Endogenous Production, Physiological Functions, and Pharmacological Applications. *Pharmacol. Rev.* **2005**, *57*, 585−630.
(5) Levitt, D. G.; Levitt, M. Carbon Monoxide: A Critical Quantitative Analysis and Review of the Extent and Limitations of its Second Messenger Function. *Clin. Pharmacol.: Adv. Appl.* **2015**, *7*, 37−56.
(6) Kikuchi, G.; Yoshida, T.; Noguchi, M. Heme Oxygenase and Heme Degradation. *Biochem. Biophys. Res. Commun.* **2005**, *338*, 558−567.
(7) Takahashi, T.; Shimizu, H.; Morimatsu, H.; Maeshima, K.; Inoue, K.; Akagi, R.; Matsumi, M.; Katayama, H.; Morita, K. Heme oxygenase-1 is an Essential Cytoprotective Component in Oxidative Tissue Injury Induced by Hemorrhagic Shock. *J. Clin. Biochem. Nutr.* **2009**, *44*, 28−40.
(8) Lamon, B. D.; Zhang, F. F.; Puri, N.; Brodsky, S. V.; Goligorsky, M. S.; Nasjletti, A. Dual Pathways of Carbon Monoxide-mediated Vasoregulation: Modulation by Redox Mechanisms. *Circ. Res.* **2009**, *105*, 775−783.
(9) Ryter, S. W.; Choi, A. M. K. Targeting Heme oxygenase-1 and Carbon Monoxide for Therapeutic Modulation of Inflammation. *Transl. Res.* **2016**, *167*, 7−34.
(10) Wegiel, B.; Gallo, D.; Csizmadia, E.; Harris, C.; Belcher, J.; Vercellotti, G. M.; Penacho, N.; Seth, P.; Sukhatme, V.; Ahmed, A.; Pandolfi, P. P.; Helczynski, L.; Bjartell, A.; Persson, J. L.; Otterbein, L.

E. Carbon Monoxide Expedites Metabolic Exhaustion to Inhibit Tumor Growth. *Cancer Res.* **2013**, *73*, 7009−7021.
(11) Kawahara, B.; Ramadoss, S.; Chaudhuri, G.; Janzen, C.; Sen, S.; Mascharak, P. K. Carbon Monoxide Sensitizes Cisplatin-resistant Ovarian Cancer Cell Lines Towards Cisplatin via Attenuation of Levels of Glutathione and Nuclear Metallothionein. *J. Inorg. Biochem.* **2019**, *191*, 29−39.
(12) Kawahara, B.; Moller, T.; Hu-Moore, K.; Carrington, S.; Faull, K. F.; Sen, S.; Mascharak, P. K. Attenuation of Antioxidant Capacity in Human Breast Cancer Cells by Carbon Monoxide Through Inhibition of Cystathionine γ-synthase Activity: Implications in Chemotherapeutic Drug Delivery. *J. Med. Chem.* **2017**, *60*, 8000−8010.
(13) Kottelat, E.; Fabio, Z. Visible Light-activated photoCORMs. *Inorganics* **2017**, *5*, 24.
(14) Popova, M.; Soboleva, T.; Ayad, S.; Benninghoff, A. D.; Berreau, L. M. Visible-light Activate Quinolone Carbon-monoxide-releasing Molecule: Prodrug and Albumin-assisted Delivery Enables Anticancer and Potent Anti-inflammatory Effects. *J. Am. Chem. Soc.* **2018**, *140*, 9721−9729.
(15) Wright, M.; Wright, J. A. PhotoCORMs: CO Release Moves into the Visible. *Dalton. Trans.* **2016**, *45*, 6801−6811.
(16) Palao, E.; Slanina, T.; Muchova, L.; Solomek, T.; Vitek, L.; Klan, P. Transition-metal-free CO-releasing BODIPY Derivatives Activatable by Visible to NIR Light as Promising Bioactive Molecules. *J. Am. Chem. Soc.* **2016**, *138*, 126−133.
(17) Chakraborty, I.; Carrington, S. J.; Mascharak, P. K. Design Strategies to Improve Sensitivity of Photoactive Metal Carbonyl Complexes (photoCORMs) to Visible Light and Their Potential as CO-donors to Biological Targets. *Acc. Chem. Res.* **2014**, *47*, 2603−2611.
(18) Rimmer, R. D.; Pierri, A. E.; Ford, P. C. Photochemically Activated Carbon Monoxide Release for Biological Targets. Toward Developing Air Stable photoCORMs Labilized by Visible Light. *Coord. Chem. Rev.* **2012**, *256*, 1509−1519.
(19) Pinto, M. N.; Chakraborty, I.; Sandoval, C.; Mascharak, P. K. Eradication of HT-29 Colorectal Adenocarcinoma Cells by Controlled Photorelease of CO from a CO-releasing polymer (photoCORP-1) Triggered by Visible Light Through an Optical Fiber-based Device. *J. Controlled Release* **2017**, *264*, 192−202.
(20) Jimenez, J.; Chakraborty, I.; Dominguez, A.; Martinez-Gonzalez, J.; Sameera, W. M. C.; Mascharak, P. K. A Luminescent Manganese photoCORM for CO Delivery to Cellular Targets under the Control of Visible Light. *Inorg. Chem.* **2018**, *57*, 1766−1733.
(21) Soboleva, T.; Esquer, H. J.; Benninghoff, A. B.; Berreau, L. M. Sense and Release: A Thiol-responsive Flavonol-based Photonically Driven Carbon Monoxide-releasing Molecule that Operates via Multiple-input AND Logic Gate. *J. Am. Chem. Soc.* **2017**, *139*, 9435−9438.
(22) Chakraborty, I.; Carrington, S. J.; Roseman, G.; Mascharak, P. K. Synthesis, Structures and CO Release Capacity of a Family of Water-soluble photoCORMs: Assessment of the Biocompatibility and Their Phototoxicity Toward Human Breast Cancer Cells. *Inorg. Chem.* **2017**, *56*, 1534−1545.
(23) Kourti, M.; Jiang, W. G.; Cai, J. Aspects of Carbon Monoxide in form of CO-releasing Molecules Used in Cancer Treatment: More Light on the Way. *Oxid. Med. Cell. Longevity* **2017**, *2017*, 9326454.
(24) Heinemann, S.; Hoshi, T.; Westerhausen, M.; Schiller, A. Carbon monoxide - Physiology, Detection and Controlled Release. *Chem. Commun.* **2014**, *50*, 3644−3660.
(25) Carrington, S. J.; Chakraborty, I.; Mascharak, P. K. Rapid CO Release from a Mn(I) Carbonyl Complex Derived from Azopyridine upon Exposure to Visible Light and its Phototoxicity Toward Malignant Cells. *Chem. Commun.* **2013**, *49*, 11254−11256.
(26) Schatzschneider, U. Novel Lead Structures and Activation Mechanisms for CO-releasing Molecules (CORMs). *Br. J. Pharmacol.* **2015**, *172*, 1638−1650.
(27) Chakraborty, I.; Jimenez, J.; Mascharak, P. K. CO-induced Apoptotic Cell Death of Colorectal Cancer Cells by a Luminescent

photoCORM Grafted on Biocompatible Carboxymethyl Chitosan. *Chem. Commun.* **2017**, *53*, 5519−5522.

(28) Arnott, J. A.; Planey, S. L. The Influence of Lipophilicity in Drug Discovery and Design. *Expert Opin. Drug Discovery* **2012**, *7*, 863−875.

(29) Waring, M. J. Lipophilicity in Drug Discovery. *Expert Opin. Drug Discovery* **2010**, *5*, 235−248.

(30) Wanka, L.; Iqbal, K.; Schreiner, P. R. The Lipophilic Bullet Hits the Targets: Medicinal Chemistry of Adamantane Derivatives. *Chem. Rev.* **2013**, *113*, 3516−3604.

(31) Davies, W. L.; Grunert, R. R.; Haff, R. F.; McGahen, J. W.; Neumayer, E. M.; Paulshock, M.; Watts, J. C.; Wood, T. R.; Hermann, E. C.; Hoffmann, C. E. Antiviral Activity of 1-adamantanamine (amantadine). *Science* **1964**, *144*, 862−863.

(32) Kirillov, A. M. Hexamethylenetetramine: An Old New Building Block for Design of Coordination Polymers. *Coord. Chem. Rev.* **2011**, *255*, 1603−1622.

(33) Balija, A. M.; Kohman, R. E.; Zimmerman, S. C. Substituted 1,3,5-triazaadamantanes: Biocompatible and Degradable Building Blocks. *Angew. Chem., Int. Ed.* **2008**, *47*, 8072−8074.

(34) Zheng, S.-L.; Tong, M.-L.; Chen, X.-M. Silver(I)-hexamethylenetetramine Molecular Architectures: From Self-assembly to Design Assembly. *Coord. Chem. Rev.* **2003**, *246*, 185−202.

(35) Tsunoda, A.; Maassab, H. F.; Cochran, K. W.; Eveland, W. C. Antiviral Activity of c-methyl-1-adamantanemethylamine Hydrochloride. *Antimicrob. Agents Chemother.* **1965**, *5*, 553−560.

(36) Guerriero, A.; Oberhauser, W.; Riedel, T.; Peruzzini, M.; Dyson, P. J.; Gonsalvi, L. New Class of Half-sandwich Ruthenium(II) Arene Complexes Bearing the Water-soluble CAP Ligand as an in vitro Anticancer Agent. *Inorg. Chem.* **2017**, *56*, 5514−5518.

(37) Jimenez, J.; Pinto, M. N.; Martinez-Gonzalez, J.; Mascharak, P. K. Photo-induced Eradication of Colorectal Adenocarcinoma Cells by Carbon Monoxide (CO) Delivery from a Mn-based Green Luminescent photoCORM. *Inorg. Chim. Acta* **2019**, *485*, 112−117.

(38) McLean, S.; Mann, B. E.; Poole, R. K. Sulfite Species Enhance Carbon Monoxide Release from CO-releasing Molecules: Implications for Deoxymyoglobin Assay of Activity. *Anal. Biochem.* **2012**, *427*, 36−40.

(39) *Bruker APEX3*; Bruker AXS Inc.: Madison, WI, 2014.

(40) *Bruker SAINT*; Bruker AXS Inc.: Madison, WI, 2012.

(41) *Bruker SADABS*; Bruker AXS Inc.: Madison, WI, 2016.

(42) Sheldrick, G. M. SHELXT - Integrated Space-group and Crystal-structure Determination. *Acta Crystallogr., Sect. A: Found. Adv.* **2015**, *A71*, 3−8.

(43) Sheldrick, G. M. Crystal Structure Refinement with SHELXL. *Acta Crystallogr., Sect. C: Struct. Chem.* **2015**, *C71*, 3−8.

(44) Spek, A. L. PLATON SQUEEZE: A Tool for the Calculation of the Disordered Solvent Contribution to the Calculated Structure Factors. *Acta Crystallogr., Sect. C: Struct. Chem.* **2015**, *C71*, 9−18.

(45) Dolomanov, O. V.; Bourhis, L. J.; Gildea, R. J.; Howard, J. A. K.; Puschmann, H. OLEX2: A Complete Structure Solution, Refinement and Analysis Program. *J. Appl. Crystallogr.* **2009**, *42*, 339−341.

(46) Jimenez, J.; Chakraborty, I.; Carrington, S. J.; Mascharak, P. K. Light-triggered CO Delivery by a Water-soluble and Biocompatible Manganese photoCORM. *Dalton. Trans.* **2016**, *45*, 13204−13213.

(47) Thornalley, P. J. The Glyoxalase System in Health and Disease. *Mol. Aspects Med.* **1993**, *14*, 287−371.

(48) Wang, P.; Zhou, D.; Chen, B. Highly Selective and Sensitive Detection of Zn(II) Using Tetrapeptide-based dansyl Fluorescent Chemosensor and its Application in Cell Imaging. *Spectrochim. Acta, Part A* **2018**, *204*, 735−742.

(49) Chakraborty, I.; Jimenez, J.; Sameera, W. M. C.; Kato, M.; Mascharak, P. K. Luminescent Re(I) Carbonyl Complexes as Trackable photoCORMs for CO Delivery to Cellular Targets. *Inorg. Chem.* **2017**, *56*, 2863−2873.

(50) Pierri, A. E.; Pallaoro, A.; Wu, G.; Ford, P. C. A Luminescent and Biocompatible photoCORM. *J. Am. Chem. Soc.* **2012**, *134*, 18197−18200.

(51) Pinto, M.; Chakraborty, I.; Martinez-Gonzalez, J.; Mascharak, P. Synthesis and Structures of Photoactive Rhenium Carbonyl Complexes Derived from 2-pyridin-2-yl)-1,3-benzothiazole, 2-(quinoline-2-yl)-1,3-benzothiazole and 1,10-phenanthroline. *Acta Crystallogr., Sect. C: Struct. Chem.* **2017**, *C73*, 923−929.

(52) Riss, T. L.; Moravec, R. A.; Niles, A. L.; Duellman, S.; Benik, H. A.; Worzella, T. J.; Minor, L. *Assay Guidance Manual.* [Online]. Eli Lilly & Company and the National Center for Advancing Translational Sciences: 2004.

(53) Slee, E. A.; Adrain, C.; Martin, S. J. Executioner Caspase-3, −6, and −7 Perform Distinct, Non-redundant Roles During the Demolition Phase of Apoptosis. *J. Biol. Chem.* **2001**, *276*, 7320−7326.

Chapter 4.I: Tracking Silver Delivery to Bacteria Using Turn-On Fluorescence.

4.I.1 Background.

The treatment and prevention of infections caused by multidrug resistant organisms (MDROs) continue to be a challenge to the pharmaceutical industry[1] and a serious threat to global health.[2] The misuse and overuse of antibiotics combined with rising population densities and increased international travel expedite bacterial resistance to our current antimicrobial arsenal.[2] Recently, bacterial resistance to a ''last resort'' antibiotic, namely colistin (polymyxin E), has been reported in China[3] and the United States.[4]

Metals, particularly silver, have been used as antimicrobial agents since ancient times due to their high toxicity towards microorganisms and low toxicity towards mammalian cells.[5] Although the use of silver diminished with the introduction of b-lactam antibiotic chemotherapy in the 1940s, silver salts continue to be used for the treatment and prevention of infections of burns and difficult-to-treat wounds.[6] Currently, the application of silver in the form of nanoparticles, salts, and complexes, has gained interest due to its bactericidal properties against MDROs that can withstand conventional antibiotic chemotherapy. Silver exerts its bactericidal activity by continuously releasing trace amounts of cations (Ag^+), which are toxic to microorganisms.[7] Silver ions generate their toxicity by producing reactive oxygen species, as well as disrupting biochemical processes by interacting with thiol and amino groups on proteins, nucleic acids, and cell membranes.[8] Silver-killed microorganisms

can serve as a reservoir of silver and slowly release Ag^+ cations which can then again exert their bactericidal activity, known as the ''zombies effect''.[9,10]

Ingestion of large amounts of silver can produce adverse effects such as argyria.[11] Therefore most silver based therapies are applied topically for the treatment of burn wound infections. Since Ag^+ is highly reactive, it tends to precipitate as an insoluble AgCl salt in the presence of chloride ions, which are abundant in blood plasma ($[Cl] = 95-110$ mM).[8] For this reason, wound treatments require multiple irrigations with silver salts (up to 12 times per day) to keep the wound sterile.[11] Having a way to follow the extent of active silver released to the wound would be advantageous in determining how regularly the topical antibiotic should be administered to keep the wound free of infection. Our group previously developed a florescent silver complex which was used to track its migration from a bandage onto a skin and soft tissue infection model.[12] However, the fluorescence only indicated that the ligand/complex was transferred from the bandage to the skin and had no indication of the extent of Ag^+ (actual drug) delivered to the wound site.

In this chapter we discuss the synthesis of several silver complexes with fluorescence tracking properties. The synthesis and characterization of a silver complex, $[Ag(qPyr)_2]CF_3SO_3$ (where the ligand qPyr is 1-(quinoline-2-ylmethylene) aminopyrene) (**1**, Figure 4.I.1), that exhibits a change in luminescence upon silver release is discussed in detail. In the design of this compound, qPyr was included due to its characteristic absorption and emission profile, which could allow tracking of the ligand and silver within the cell membrane of the bacteria.[13] The second silver complex
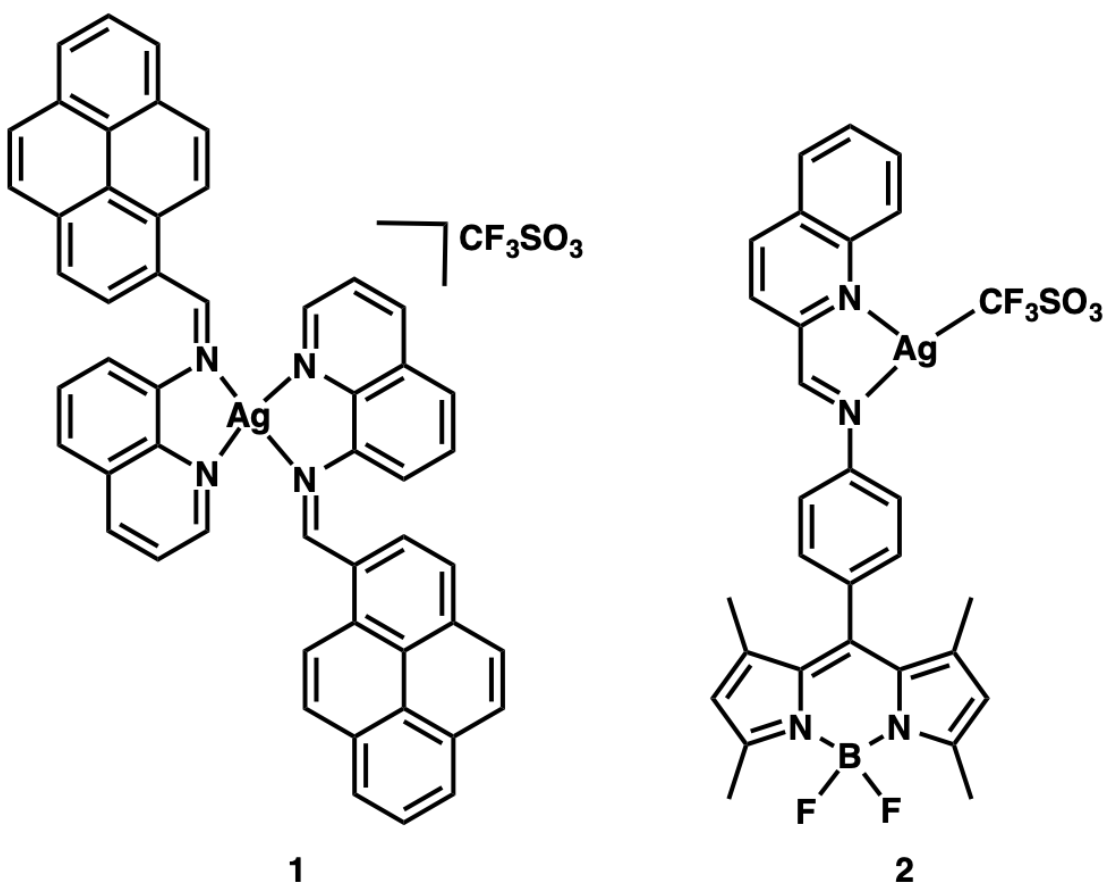
Figure 4.I.1. Schematic representation of $[Ag(qPyr)_2]CF_3SO_3$ **1**, and $[Ag(qBODIPY)(CF_3SO_3)]$ **2**.

is derived from a Schiff base ligand tethered with a boron-dipyrromethene (BODIPY) fragment. In a similar fashion to the ligand of complex **1**, qBODIPY was obtained by the condensation of quinoline-2-aldehyde and an aniline derivative of the ligand (in this case BODIPY), affording $[Ag(qBODIPY)(CF_3SO_3)]$ (**2**, Figure 4.I.1) upon reaction with $Ag(CF_3SO_3)$. BODIPY-based fluorophores have raised great interest in the bioimaging community due to their high molar extinction coefficient, high fluorescence quantum yield, sharp absorption and emission spectra, high lipophilicity,

low toxicity, and excellent chemical/photochemical stability.[14,15] The BODIPY fluorophore is known to penetrate cell membranes and eventually accumulate within subcellular membranes due to its high lipophilicity.[15] A problem with BODIPY-based dyes is the small Stokes' shift, which makes it difficult to use in flow cytometry and fluorescence microscopy.[14] In order to circumvent the small Stokes' shift, ancillary ligands can be used to capture light of shorter wavelength, forming a "fluorescence resonance energy transfer cassette".[13] The absorbed energy is channeled to the BODIPY emitter effectively increasing the Stokes shift.[14,16] An important feature of these compounds is the electronic isolation of the two chromophores, preventing the donor-acceptor molecule from acting as a single ''supermolecule'' with an extended LUMO.[16] This is achieved by arranging the connecting linkage in an ''orthogonal'' manner so that the donor and acceptor moieties are no longer coplanar.[15] In our design this is achieved by inserting two methyl substituents on C19 and C23 of the BODIPY moiety. Although the absorption spectrum of the qBODIPY ligand contains features from both subunits, the fluorescence emission occurs only from the BODIPY unit.[14]

4.I.2 Results and Discussion.

4.I.2.1 Synthesis of [Ag(qPyr)₂]CF₃SO₃ 1, and [Ag(qBODIPY)(CF₃SO₃)] 2.

The synthesis of both complexes **1** and **2** was carried out by a condensation reaction between an aldehyde and a free primary amine resulting in an α-imino moiety. For complex **1**, the aldehyde was localized on the pyrene fluorophore and the amine was located in the quinoline ring. In complex **2**, the BODIPY fluorophore contained

the free amine which reacted with the aldehyde of a quinoline fragment. The condensation reaction was carried out in anhydrous methanol by refluxing. It was necessary to use anhydrous methanol since the condensation reaction produces one equivalent of H_2O, and therefore excessive water in the solvent would drive the reaction to starting materials and lower the yield. It was found necessary to isolate and purify extensively both of the ligands prior to reaction with the silver center. Silver reactions were carried out under low levels of light due to the sensitivity of the silver complexes towards light. Upon reaction the complexes were isolated and purified several times through recrystallization before growing single crystals for X-ray structure determination. Single crystals of both complexes were obtained by layering hexanes on top of a dichloromethane solution of the respective complex.

4.1.2.2 X-Ray Structure Determination and Refinement.

The molecular structure of complex **1** is shown in Figure 4.I.2. The coordination environment of the Ag(I) atom in the cationic complex is distorted tetrahedral (Table 4.I.1). The qPyr ligand binds to the metal in a bidentate fashion. In this complex, the chelate rings composed of atoms Ag1, N2, C8, C9, N1 and Ag1, N4, C34, C35, N3 are reasonably planar, with mean deviations of 0.054 (3) and 0.059 (3) Å, respectively. The dihedral angle between these two chelate planes is 69.0 (4)°. The two quinoline fragments within the qPyr ligand in the title complex are satisfactorily planar, with mean deviations of 0.031 (4) and 0.035 (4) Å. The dihedral angles between the quinoline moieties and the pyrene rings are quite similar [73.5 (4) and 73.8 (3)°].
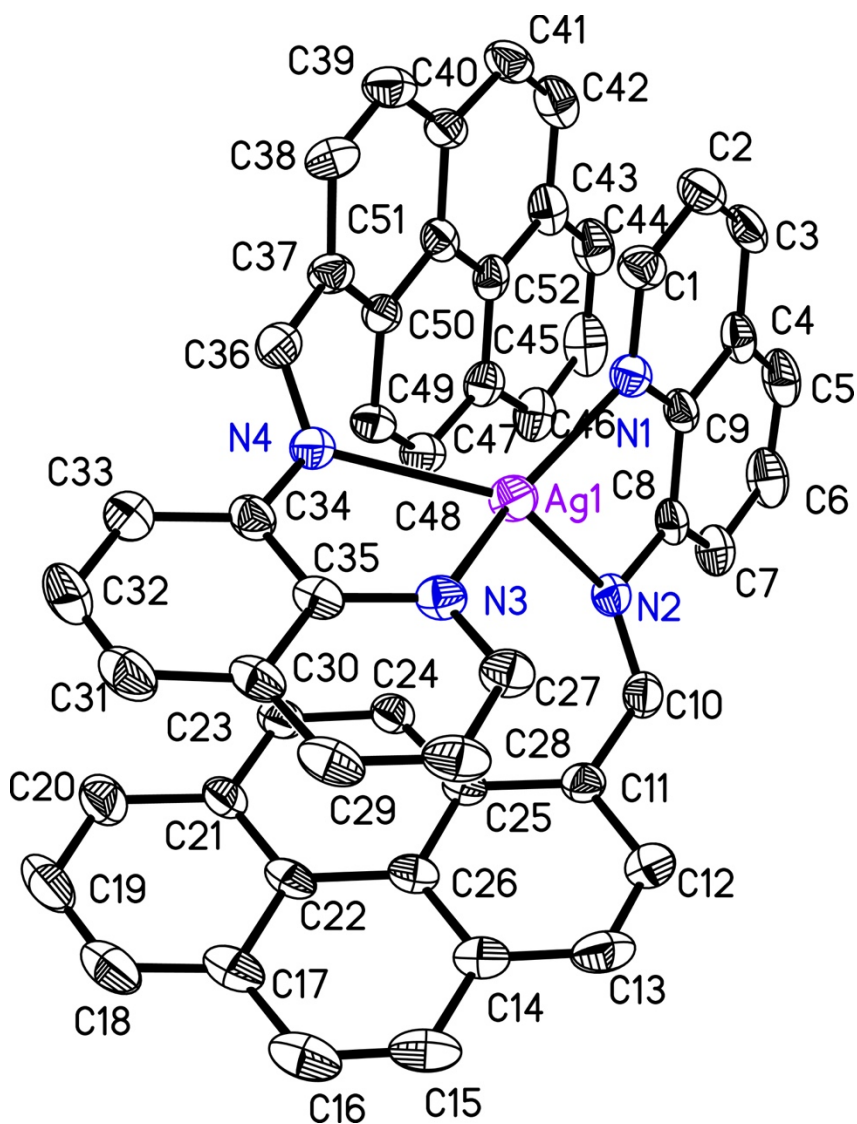
Figure 4.I.2. Molecular structure of the cation [Ag(qPyr)$_2$]$^+$. Displacement ellipsoids correspond to the 50 % probability level; the counter-anion is not shown.

The packing pattern exhibits the presence of both intra- and intermolecular offset π- π stacking interactions (Figures 4.I.3 and 4.I.4). The extent of the intermolecular π- π interaction is found to be relatively stronger [3.543 (5) Å] compared to the intra-molecular π- π stacking interactions [3.642 (5) and 3.617 (5) Å]. In both cases, the

Table 4.I.1. Selected geometric parameters (Å, °) for complex **1**.

	1
Ag1-N3	2.249 (4)
Ag1-N1	2.228 (4)
Ag1-N4	2.411 (4)
Ag1-N2	2.399 (4)
N3-Ag1-N4	72.24 (15)
N3-Ag1-N2	120.45 (15)
N3-Ag1-N1	151.52 (16)
N1-Ag1-N4	119.33 (15)
N1-Ag1-N2	73.09 (15)
N2-Ag1-N4	131,88 (14)

angle between the ring normal and the vector between the ring centroids is close to 20° and centroid-to-centroid distances are within the upper limit of 3.8 Å.[17] The crystal packing of the complex reveals also a non-classical hydrogen-bonding interaction[18] of the type C-H $\cdots$ O between the cation and the triflate anion (Figure 4.I.5). The arrangement of the two types of molecules along the c axis is shown in Figure 4.I.6.

A search of Cambridge Structural Database[19] revealed that molecular systems where Ag(I) resides in a distorted tetrahedral coordination environment are primarily of a supramolecular nature. In a relatively recent report, two discrete Ag complexes, namely $[Ag(HL^1)_2](PF_6)$ and $[Ag(HL^1)_2](NO_3)(H_2O)$ (where HL^1 = (n-Py)-CH=N-$C_{10}H_6$-COOH) are reported[20] which are structurally similar to complex **1**.
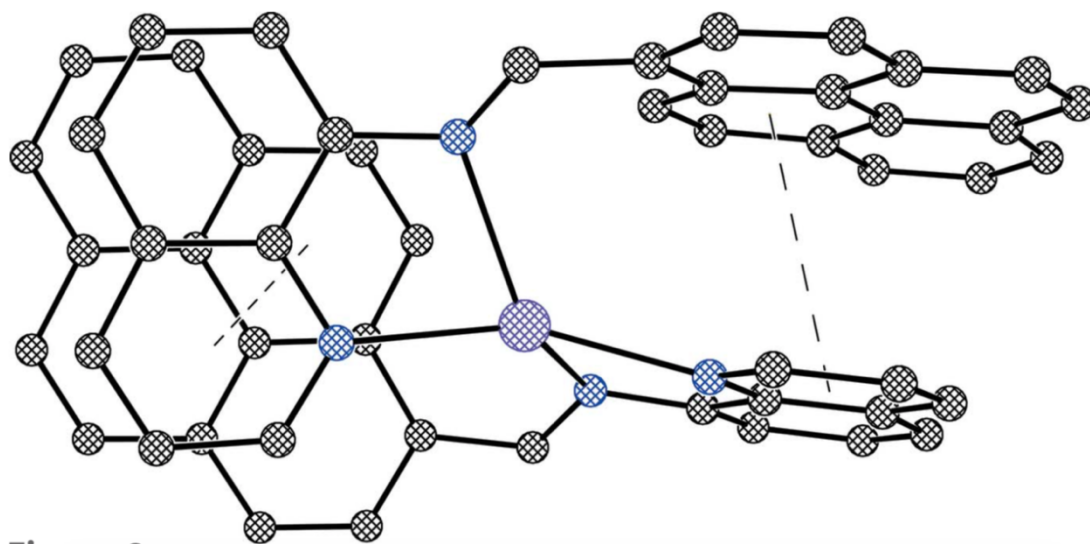
Figure 4.I.3. Schematic representation of intramolecular π-π stacking within **1**.
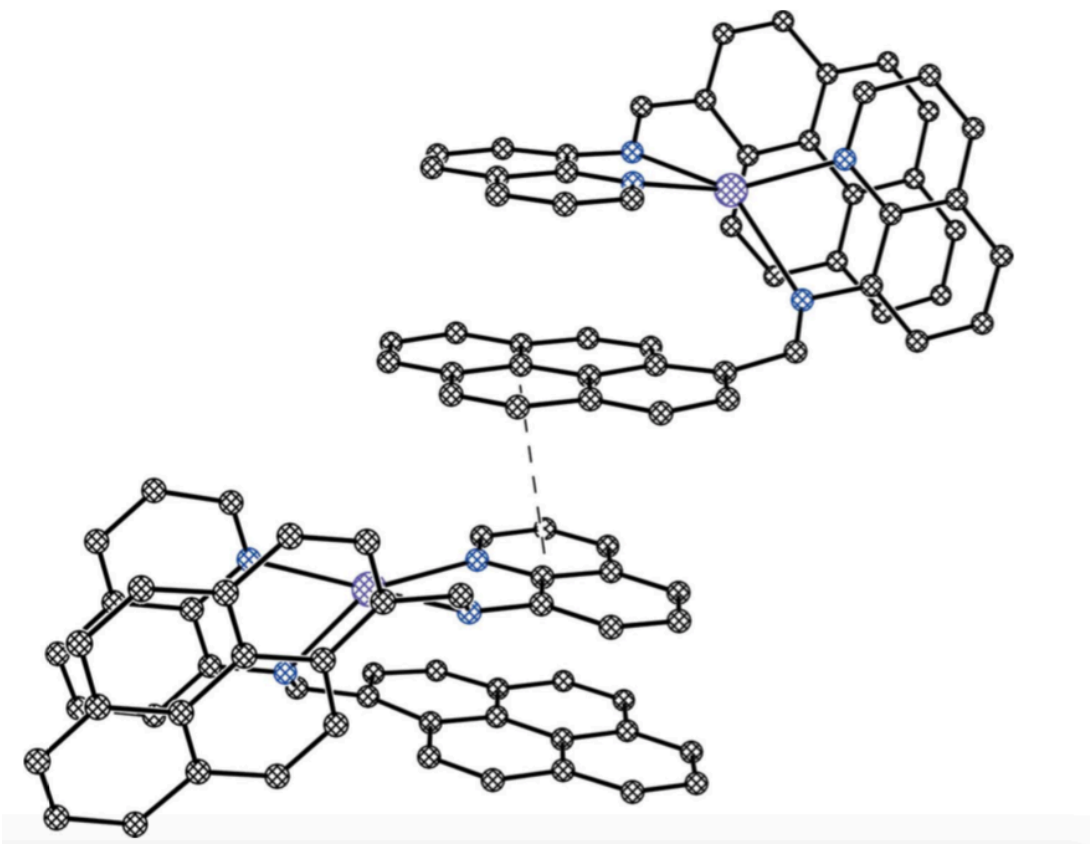
Figure 4.I.4. Schematic representation of intermolecular π-π stacking within **1**.
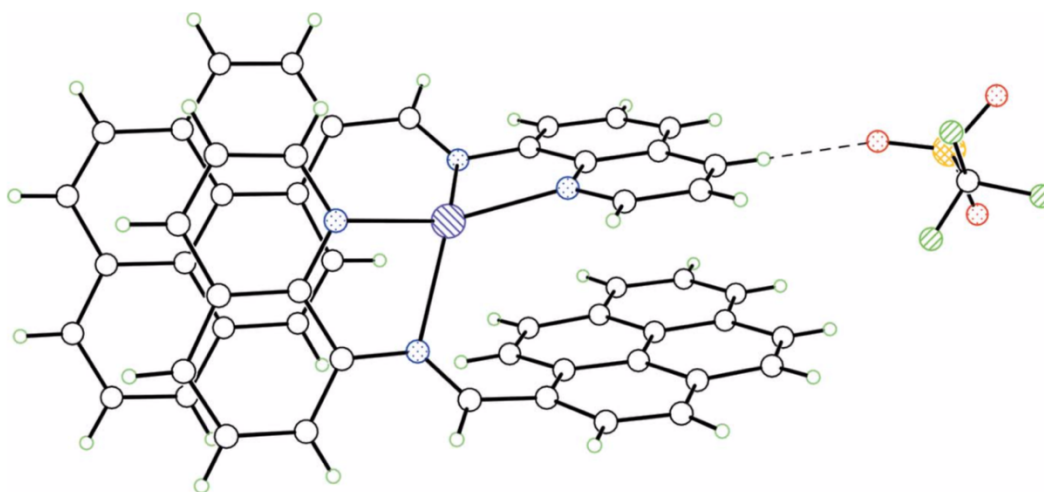
Figure 4.I.5. Packing pattern of **1** showing the C-H$\cdots$O interactions between the cation and its anion.

Both these molecules adopt triclinic symmetry in space group *P1*. The average Ag-N distances for these complexes are slightly longer (2.349 and 2.346 Å) than that of the title complex (2.322 Å). Unlike the present complex, these two Ag complexes are characterized by significant intramolecular O-H$\cdots$F and O-H$\cdots$O hydrogen-bonding interactions with the PF_6^- and NO_3^- counter-ions. In another report, three Ag complexes, namely [Ag(**L**)$_2$](NO$_3$), [Ag(**L**)$_2$](PF$_6$) and [Ag(**L**)$_2$](CF$_3$SO$_3$) [where **L** = (R)-2-(pyridin-2-ylmethylimino)-20-(dimethylamino)-1,10-binapthyl] are described with similar structural features.[21] In this study, [Ag(**L**)$_2$](NO$_3$) and [Ag(**L**)$_2$](PF$_6$) crystallize in space group *P2$_1$2$_1$2$_1$* while [Ag(**L**)$_2$](CF$_3$SO$_3$) crystallizes in *P2$_1$*. Here the Ag-N distances span the range 2.354-2.376 Å, noticeably longer than that of complex **1**.
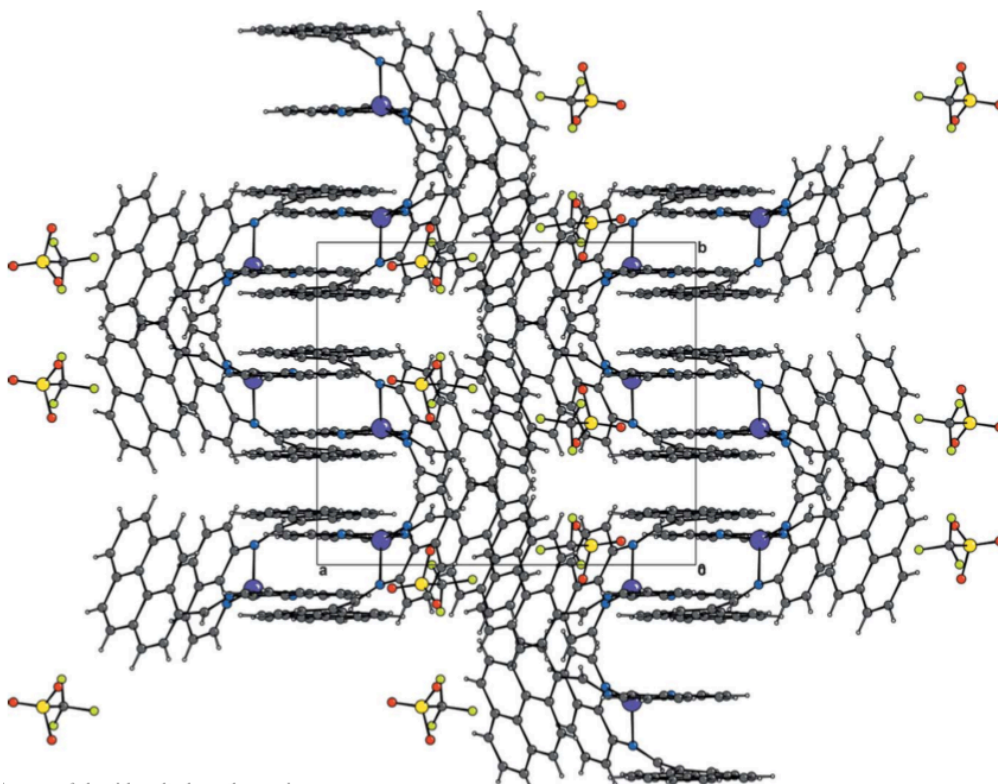
Figure 4.I.6. Packing diagram of complex **1** along the *c* axis.

Crystal data, data collection, and structure refinement details for complex **1** are summarized in Table 4.I.2. Hydrogen atoms were included in calculated positions on the C atoms to which they are bonded with C-H – 0.93 Å and $U_{iso}(H) = 1.2\ U_{eq}(C)$.

The molecular structure of **2** was authenticated by single crystal X-ray crystallography. The thermal ellipsoid plot of the complex is shown in Figure 4.I.7 while the extended structure is presented in Figure 4.I.8. Careful examination of the extended lattice of this complex reveals the presence of two types of Ag centers with different coordination environments. One of the Ag centers resides in a highly distorted square planar environment (mean deviation of the plane: 0.110 Å). In this case the

Table 4.I.2. Experimental details for complex **1**.

	1
Empirical formula	$[Ag(C_{26}H_{16}N_2)_2]CF_3SO_3$
T(K)	298
λ (Å)	0.71073
Crystal system	Monoclinic
Space group	$P2_1/c$
a (Å)	17.132 (1)
b (Å)	13.6108 (8)
c (Å)	18.9712 (11)
α (°)	90
β (°)	110.887 (1)
γ (°)	90
V (Å^3)	4133 (4)
Z	4
D_{calc} (Mg m^{-3})	1.534
Absorption Coeff (mm^{-1})	0.61
No. of unique reflections	4227
Goodness-of-fit[a] on F^2	1.03
R_1[b]	0.058
wR_2[c]	0.181
largest diff peak and hole	0.60, -0.54

metal atom forms a five-membered chelate ring with the qBODIPY ligand (the chelate ring composed of Ag1, N2, C10, C9 and N1 is satisfactorily planar with a mean deviation of 0.083 Å). The O atoms from the two triflate anions occupy the other two sites of this Ag center. Another Ag center resides in a distorted octahedral coordination
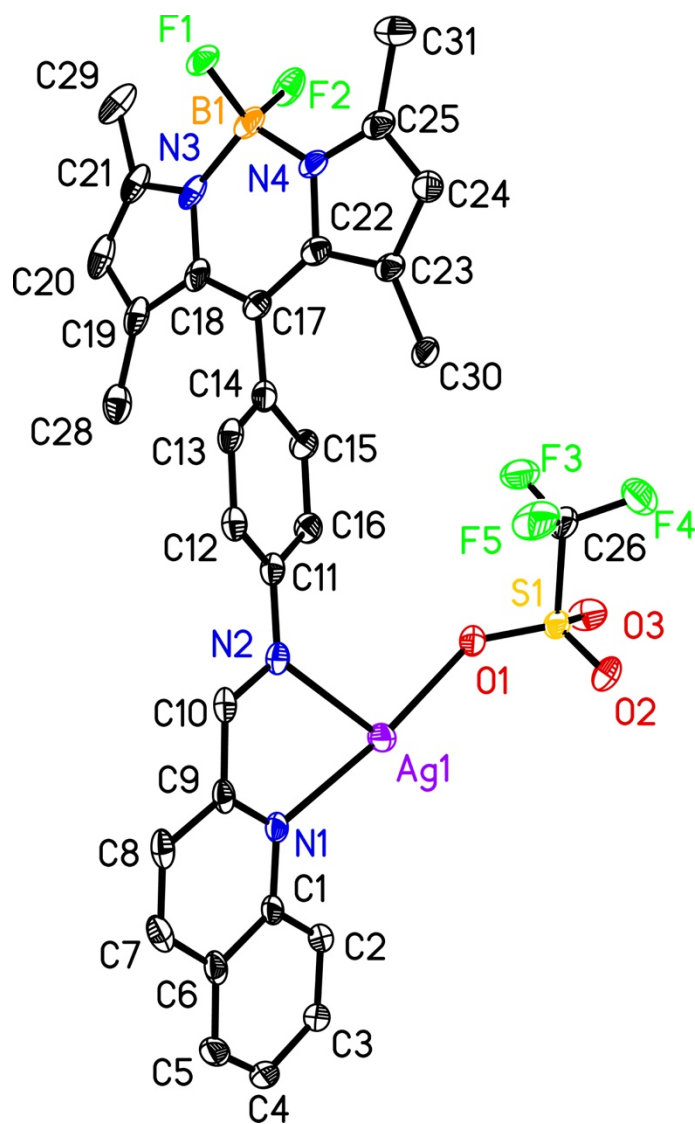
Figure 4.I.7. Molecular structure of complex **2** with atom numbering scheme (thermal ellipsoids are shown at the 50% thermal probability level; the hydrogen atoms are omitted for clarity).

environment with the equatorial plane comprised of the four O atoms from the triflates (mean deviation: 0.024 Å). Two such six-coordinated Ag centers formed a paddle-wheel framework in the extended structure with four m-2 bridging triflate ligands
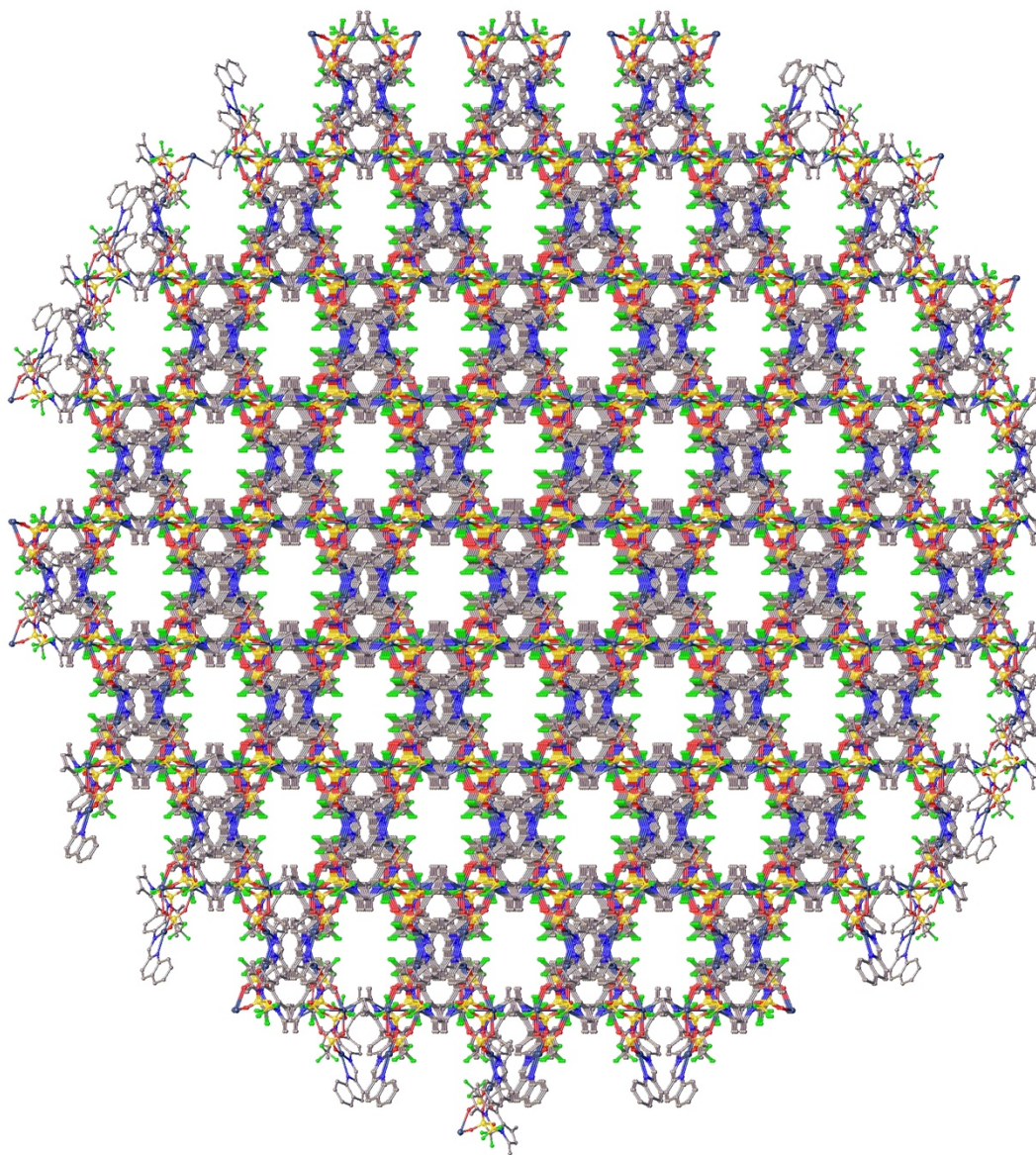
Figure 4.I.8. Packing pattern of complex **2** along *c* axis (generated with the aid pro the program Olex2).

(Figure 4.I.9). This arrangement results in considerable argentophilic inter- actions between the two Ag centers (Ag–Ag, 3.2175(12) Å). No noticeable π-π stacking
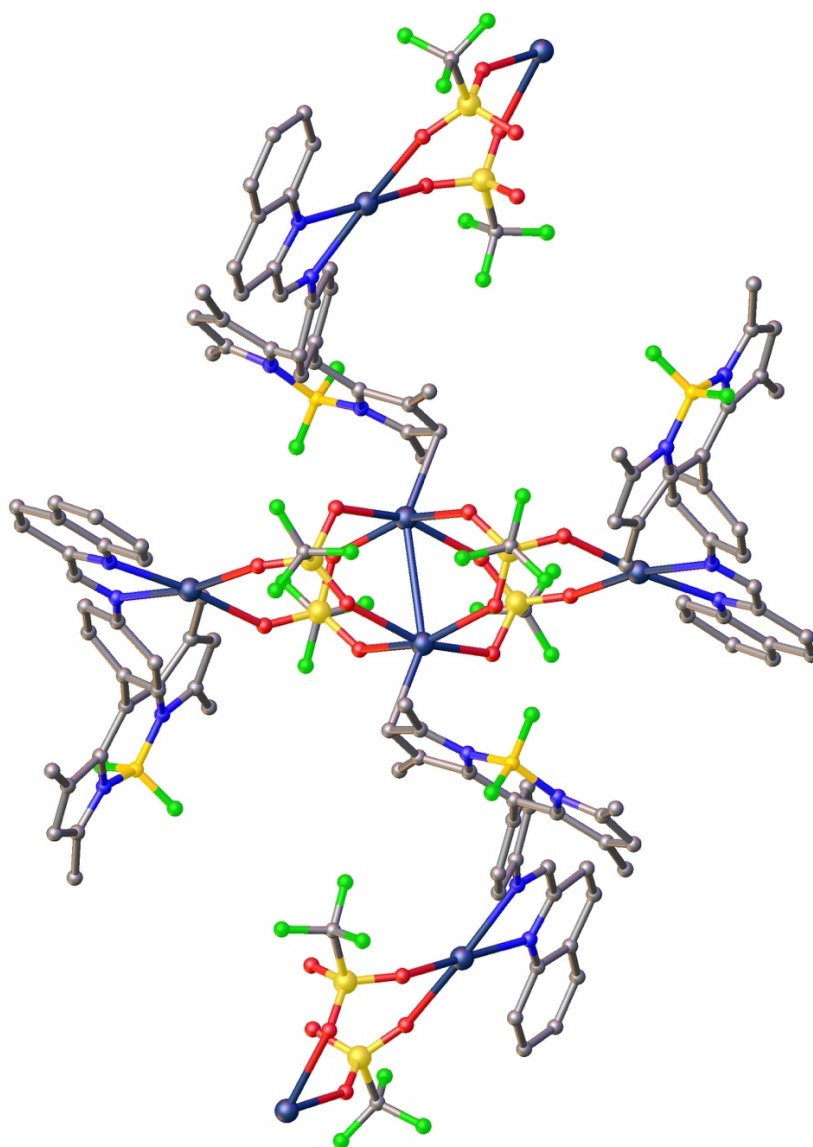
Figure 4.I.9. Ball-stick representation of a partial extended pattern of complex **2** showing two different Ag coordination environments. The hydrogen atoms are omitted for clarity.

interactions have been noted in the crystal packing. The dihedral angle between the C17–C25 moiety and the C11–C16 aryl ring is 821 and the dihedral angle between the

quinoline ring and the C11–C16 aryl ring is 19.41°. Crystal data, data collection, and structure refinement details for complex **2** are summarized in Table 4.I.3.

Table 4.I.3. Crystal data and structure refinement parameters for complex **2**.

	2
Empirical formula	$C_{31}H_{25}N_4O_6BF_8S_2Ag_2$
T(K)	293
λ (Å)	0.71073
Crystal system	Monoclinic
Space group	C_2/c
a (Å)	26.8250 (13)
b (Å)	14.8903 (7)
c (Å)	22.4731 (11)
α (°)	90
β (°)	115.102 (2)
γ (°)	90
V (Å^3)	8128.7 (7)
Z	8
D_{calc} (Mg m^{-3})	1.622
Absorption Coeff (mm^{-1})	1.146
No. of unique reflections	7509
Goodness-of-fit[a] on F^2	1.137
R_1[b]	0.0742
wR_2[c]	0.3462
largest diff peak and hole	1.231, -0.523

4.I.2.3 Stability, Luminescence, and Luminescence Quenching Properties.

Solutions of complexes **1** and **2** in DCM, 1:9 DMSO:H$_2$O and 1:99 DMSO:H$_2$O are stable for up to two months at room temperature in the dark and over three months at 0 °C in the dark. However, both complexes exhibit mild decomposition in neat DMSO after 48 hours, and full decomposition after 14 days. Pyrene and its derivatives are relatively toxic and carcinogenic due to their ability to intercalate between the base pairs of DNA. This led to the discontinuation of complex **1** for use as in antimicrobial studies. The absorption spectrum of complex **2** is centered at ~505 nm with high extinction coefficient (ε = 46000 M^{-1} cm^{-1} in DCM) along with a less intense band at
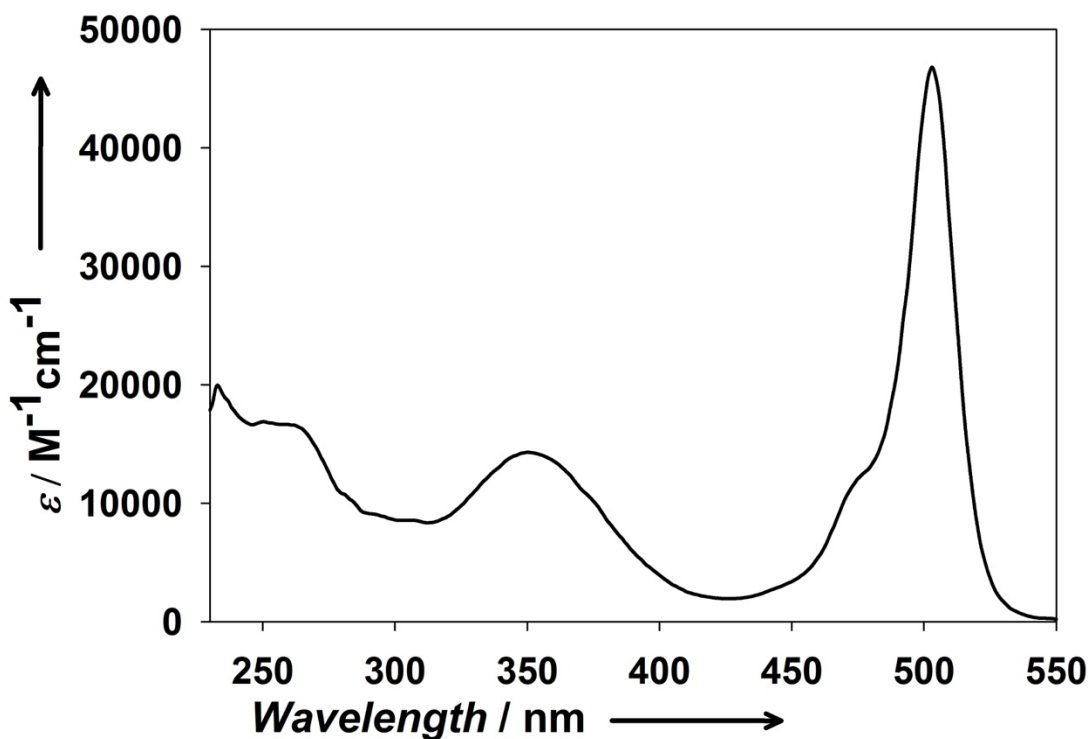
Figure 3.I.10. Absorbance spectrum of complex **2** in DCM.

326

around 350 nm (Figure 3.I.10). The fluorescence emission for qBODIPY is centered at ~520 nm in DCM and at ~511 (Figure 4.I.11) resulting in a bright green color. The excitation wavelength maximum is centered at 505 nm, but a wide range of wavelengths from 230 nm to 500 nm can be used to excite the ligand.[23] The fluorescence emitted by the qBODIPY ligand is quenched dramatically upon coordination to silver (Figures 4.I.12 and 4.I.13). In order to study the release profile of silver from the complex, a solution of **2** in DCM was titrated with increasing concentrations of tetrabutylammonium chloride (Figure 4.I.14). The chloride ions bind silver, effectively releasing it from the qBODIPY complex. It was observed that
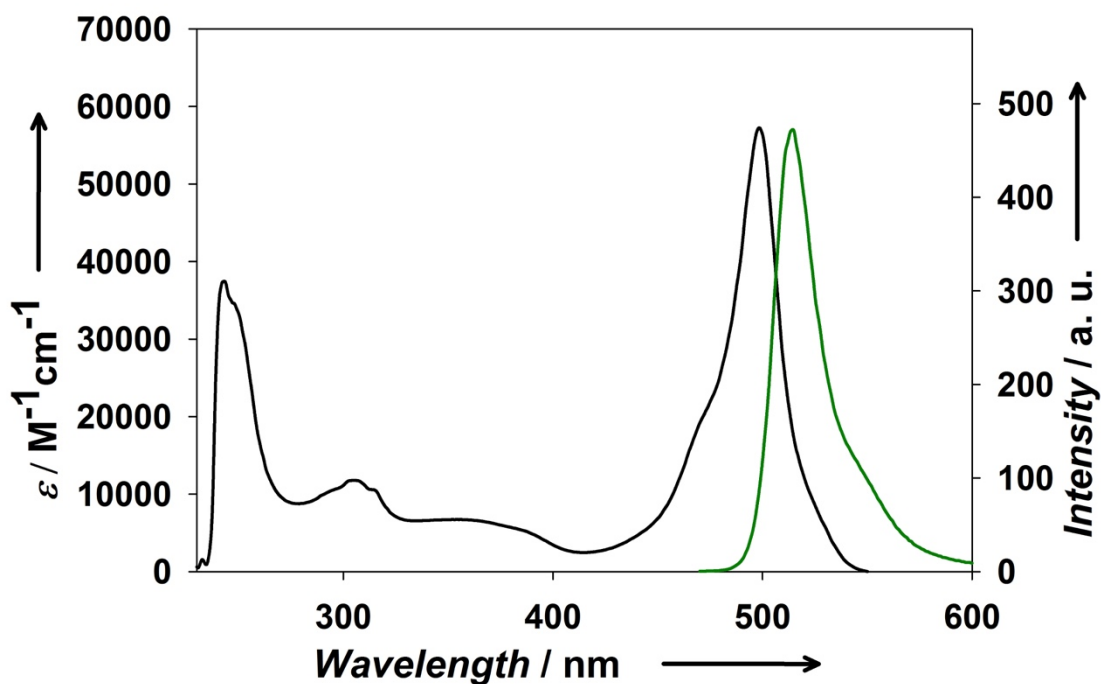
Figure 4.I.11. Absorbance (black trace) and emission (green trace) of the free ligand qBODIPY in DCM.
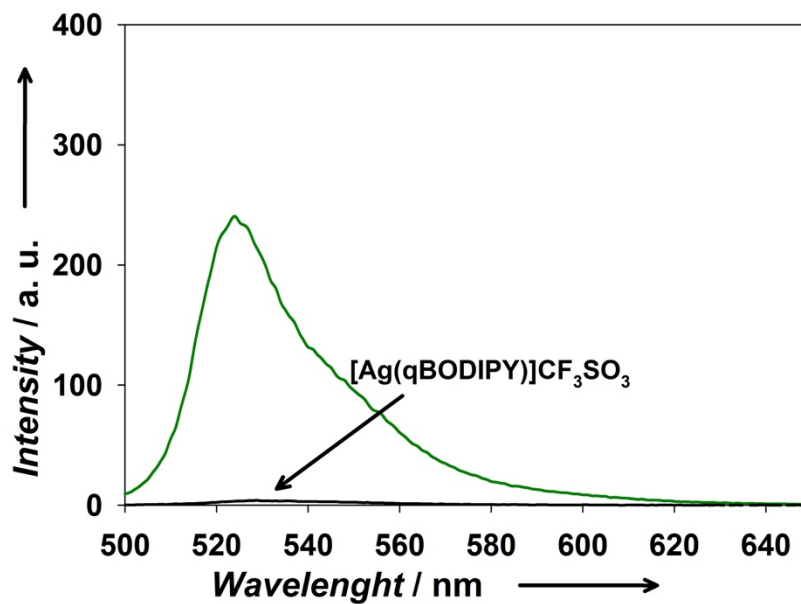
Figure 4.I.12. Luminescence of the free qBODIPY ligand (green trace) and complex **2** (black trace) in DCM.
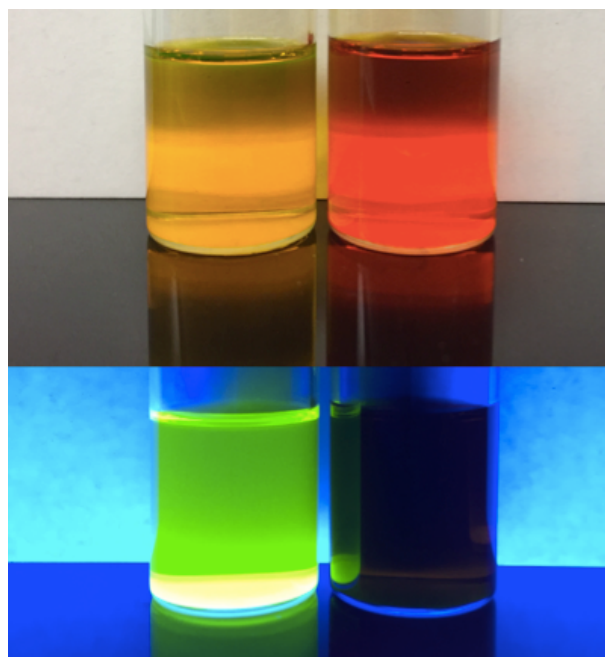
Figure 4.I.13. Solutions of qBODIPY (left) and **2** (right) in DCM under visible (top) and UV light (bottom)
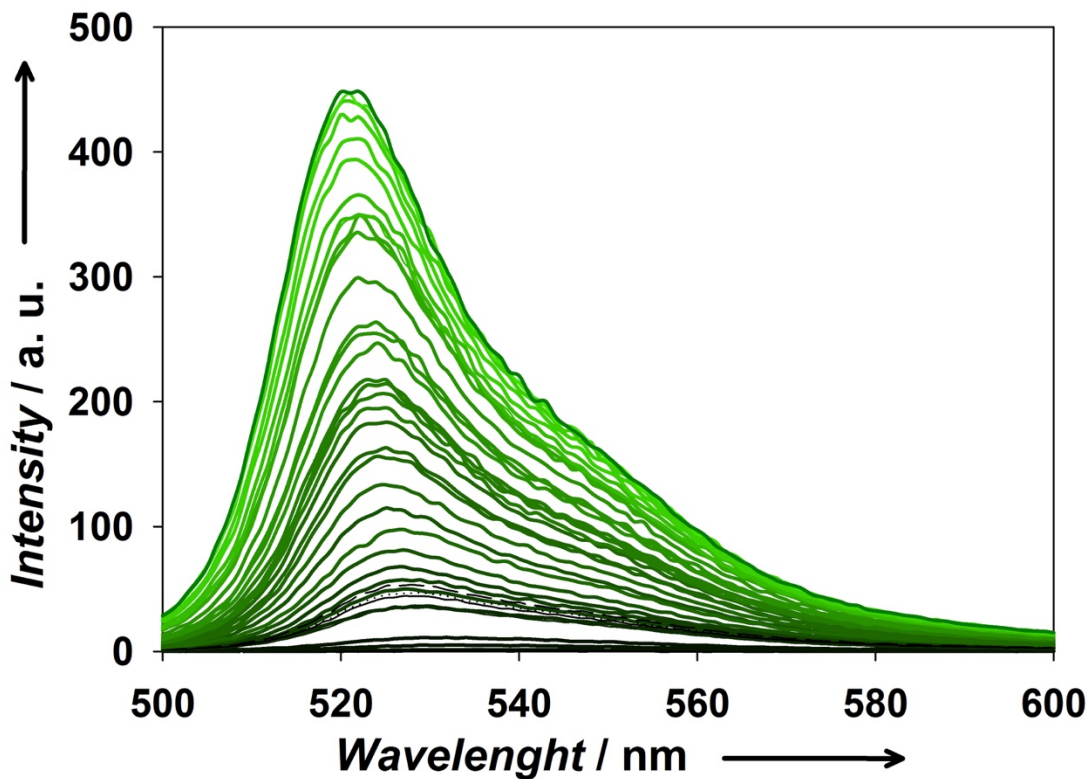
Figure 4.I.14. Luminescence increase through subsequent addition of tetrabutylammonium chloride to a solution of **2** in DCM, slit width = 2.5 nm.

fluorescence was restored almost immediately upon the addition of chloride and the fluorescence intensity of the ligand was fully restored after the addition of 38 equiv. of chloride (Figure 4.I.14). The stability of complex **2** was then studied under conditions that resemble the environment used for the bacterial growth studies to determine how much silver is released by the bacterial growth medium. A solution of complex **2** in 1:99 DMSO:H_2O was titrated with aqueous solutions of 10, 20, 30, and 50% of Mueller Hinton broth (MHB). Such studies indicated that only 4% of the silver is released when

329
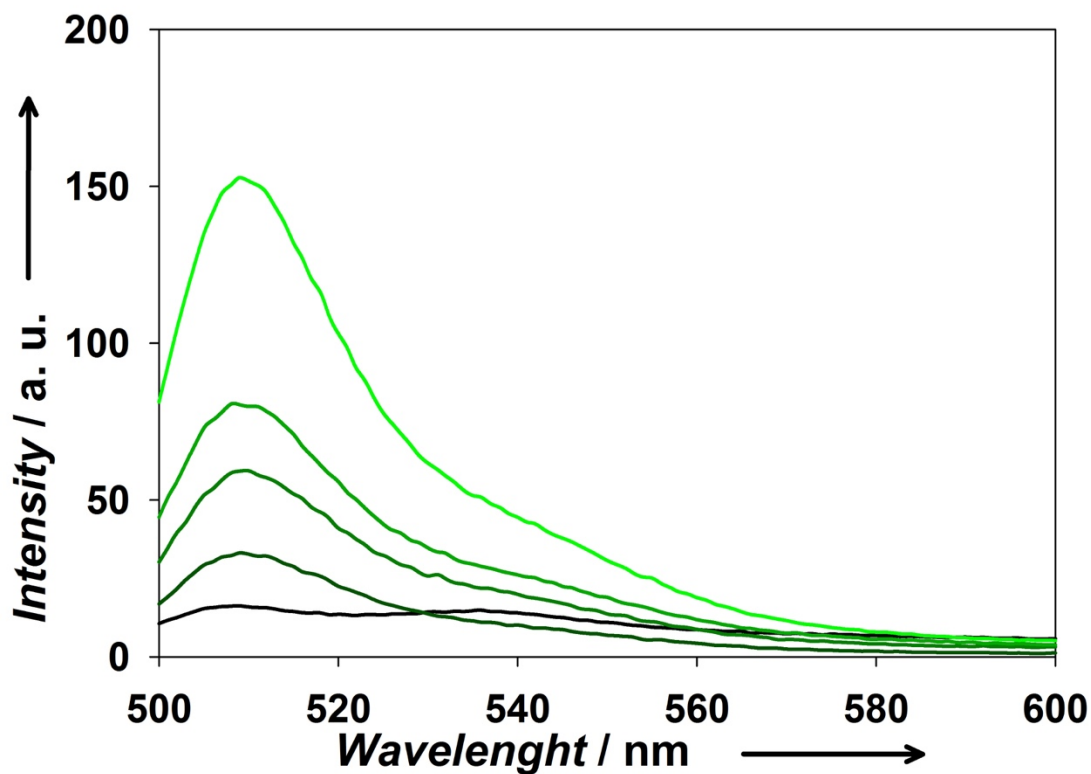
Figure 4.I.15. Luminescence increase through subsequent addition of Mueller-Hinton Broth to a solution of **2** in 1:99 DMSO:H2O, sit width = 10 nm. (because of the quenching of luminescence by water, the slit width was increased to record the low luminescence intensity increase),

exposed to 20% of MHB (Figure 4.I.16). This is presumably attributed to interactions between **2** and the amino acids present in the growth medium as well as residual chloride.

4.I.2.4 Luminescence Tracking of Silver Delivery to Bacterial Cells Using Complex 2.

The dramatic luminescence quenching combined with the restoration of fluorescence upon silver release from **2** raised the possibility of convenient tracking of the process of silver delivery to the wound. In order to check whether silver delivery can indeed be tracked in live cells, we added 2 mL of a 10 mM solution of **2** (in 1:99 DMSO:H2O) to a 2 mL *E. coli* suspension in water on the stage of a confocal microscope and recorded the emergence of the fluorescence of qBODIPY upon the release of silver within the cellular matrix. As shown in Figure 4.I.16., the green
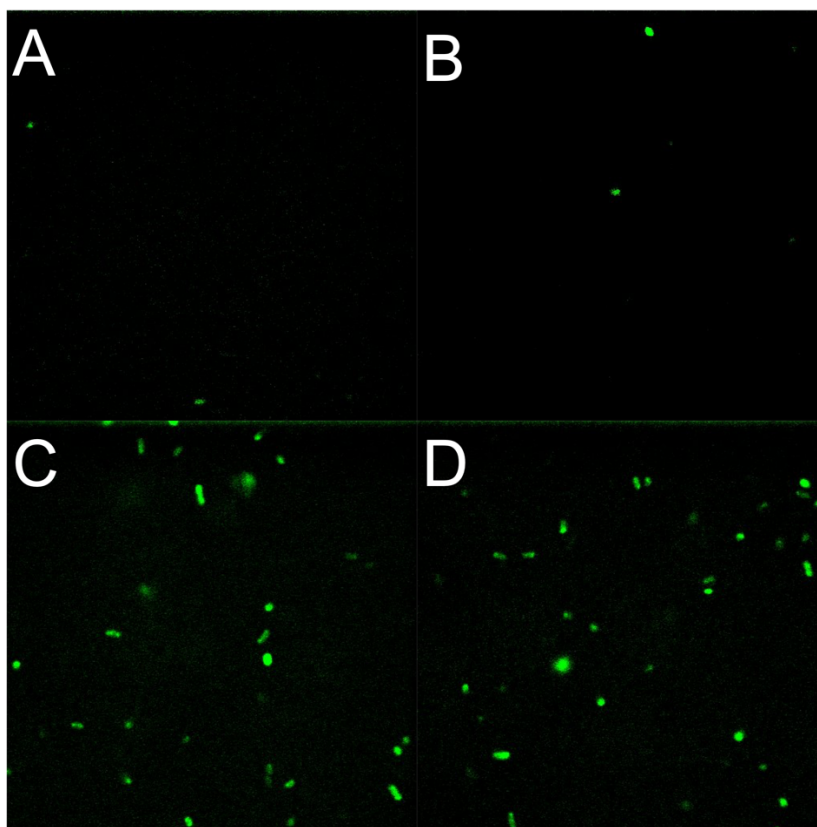
Figure 4.I.16. Representative confocal micrographs of *E. coli* cells suspended in water after the addition of a (1:99 DMSO:H$_2$O) solution of **2**: (A) 1 min, (B) 3 min, (C) 6 min, and (D) 9 min.

331

fluorescence of qBODIPY emerged from the initial dim background after 1 minute (Figure 4.I.16A) and continued to increase in intensity with time Figure 4.I.16B-4.I.16D). These time- dependent frames clearly indicated that the entrance of **2** into the *E. coli* cells leads to deligation of the qBODIPY ligand, releasing the Ag^+ ion in the membrane as well as in the intracellular matrix. A blank experiment with the qBODIPY ligand itself confirmed that the emergence of the green fluorescence in Figure 4.I.17A

\
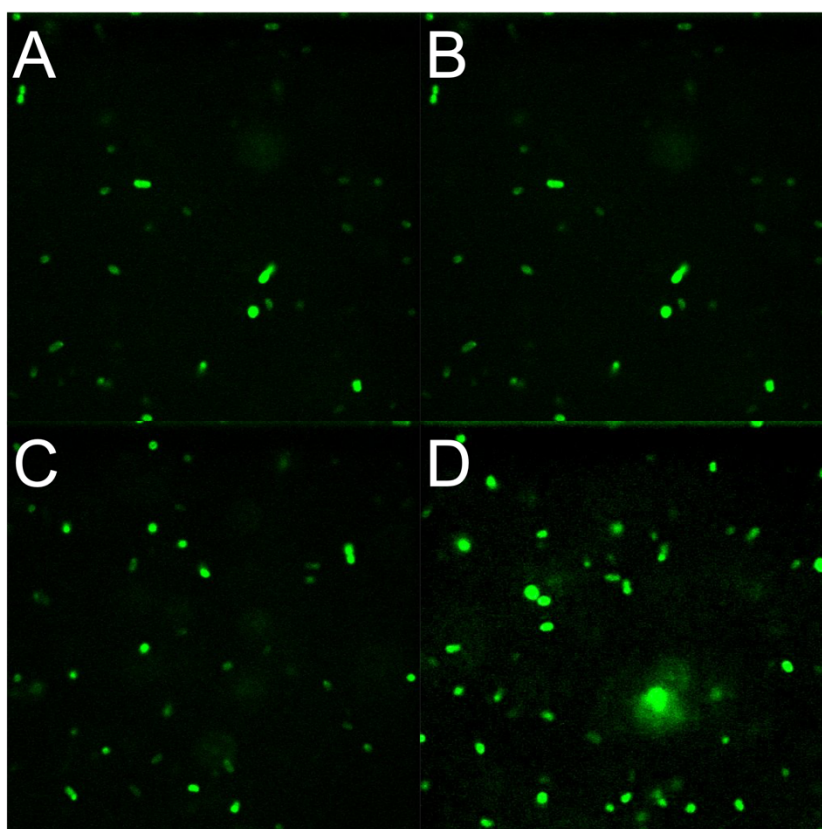
Figure 4.I.17. Representative confocal micrographs of *E. coli* cells suspended in water after the addition of a (1:99 DMSO:H_2O) solution of qBODIPY: (A) 1 min, (B) 3 min, (C) 6 min, and (D) 9 min.

through Figure 4.I.17 is indeed connected to the presence of the free ligand either on the membrane of the bacterial wall(s) or within the intracellular space. It is important to note that the increase of fluorescence upon the addition of **2** was much less pronounced compared to the frames with an equivalent concentration of qBODIPY (compare Figure 4.I.16D and 4.I.17D). This is expected as the silver complex **2** is stabilized by the chelation of the qBODIPY ligand, a fact that effectively decelerates the rate of dissociation of the Ag^+ ion from the complex. The delayed release of silver ions thus allows for a significant fraction of complex **2** to accumulate inside the bacterial cells before releasing the cytotoxic Ag^+ ions.

4.I.2.5 Antibacterial Effects of Complex 2.

The antibacterial effects of Ag+ released within the bacterial cells have also been evaluated in the present work. We studied the antibacterial effects of **2** and qBODIPY on *E. coli*, *P. aeruginosa*, and *S. aureus* at various concentrations to determine the minimum inhibitory concentration (MIC). In the case of *E. coli*, complex **2** showed a MIC value of 1 µM, a value comparable to silver nitrate (Figure 4.I.18). For *P. aeruginosa*, complex **2** had a MIC of 2 µM while silver nitrate exhibited a MIC of 1 µM (Figure 4.I.19). Finally, for *S. aureus*, complex **2** exhibited a MIC of 7 µM while silver nitrate had a MIC of 6 µM (Figure 4.I.20). No effect on bacterial growth was observed with qBODIPY with concentration as high as 50 mM on all three bacterial strains (Figure 4.I.21). It is thus apparent that the antibacterial effect arises solely from the Ag^+ released from **2** within the cell and not the qBODIPY ligand.
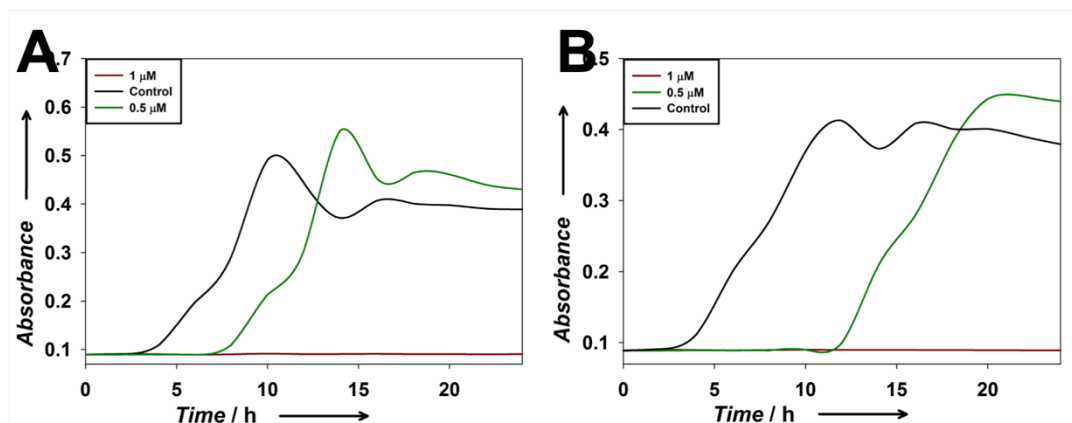
Figure 4.I.18. *E. coli* growth kinetics in the presence of **2** (A) and AgNO$_3$ (B).
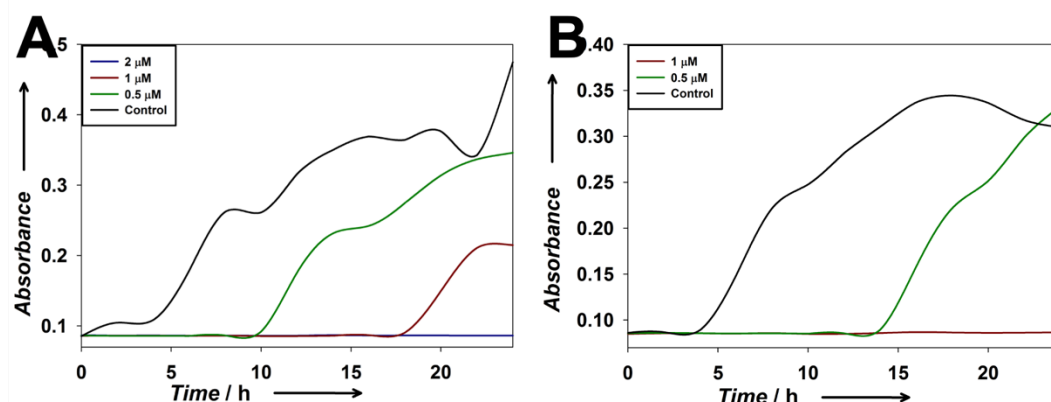
Figure 4.I.19. *P. aeruginosa* growth kinetics in the presence of **2** (A) and AgNO$_3$ (B).
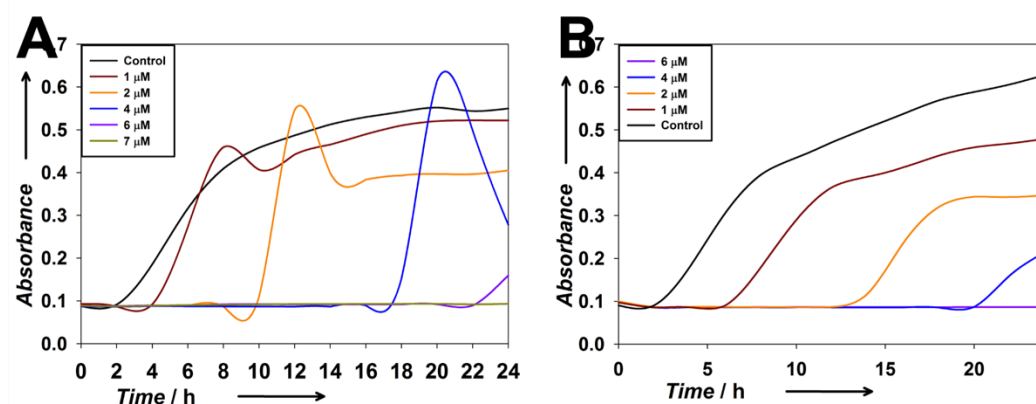
Figure 4.I.20. *S. aureus* growth kinetics in the presence of **2** (A) and AgNO$_3$ (B).
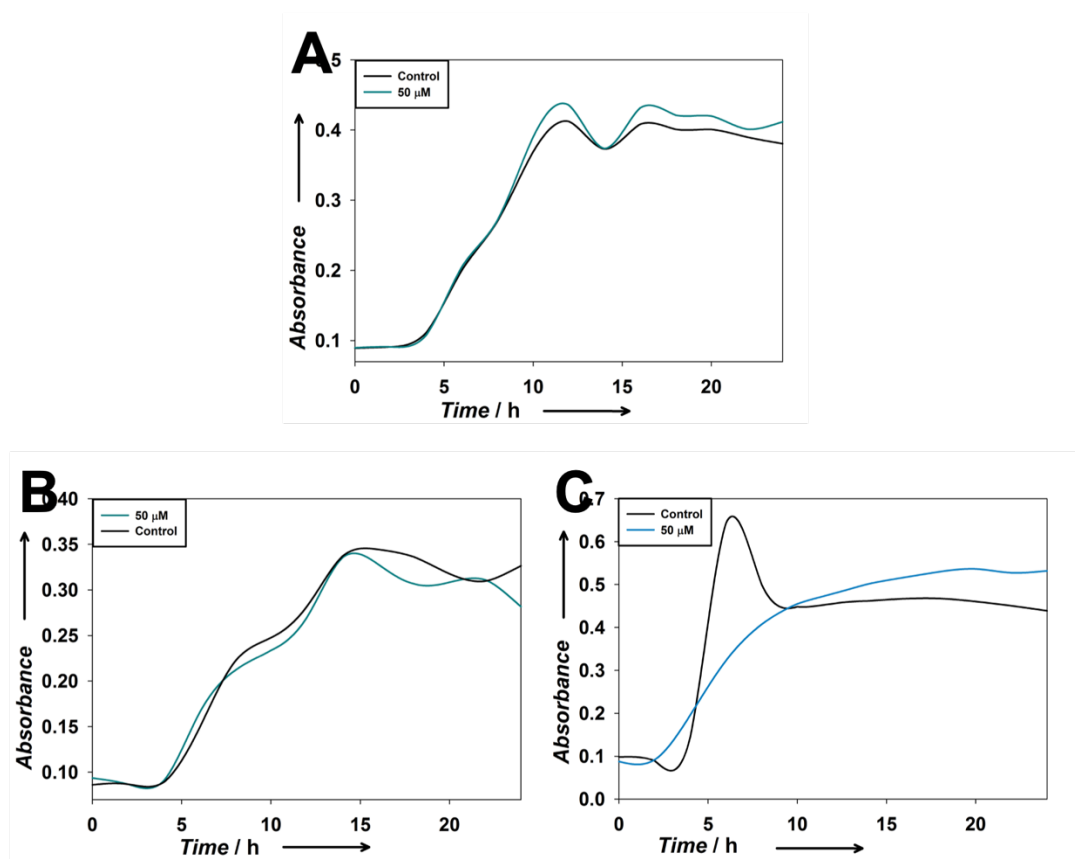
Figure 4.I.21. Bacterial growth kinetics in the presence of qBODIPY for (A) *E. coli,* (B) *P. aeruginosa*, and (C) *S. aureus*.

4.I.3 Conclusions.

In conclusion, we have synthesized a silver complex 1 that exhibits strong fluorescence upon silver release. The strong fluorescence arising from the free ligand is almost completely quenched upon complexation to silver. This novel complex was used to track the delivery of silver to bacteria through "turn-on" luminescence. Intracellular chloride and/or thiols appear to be responsible for the release of silver within the bacteria. The extent of eradication of *E. coli, P. aeruginosa*, and *S. aureus*

by such silver delivery by complex **2** compares well with the antibacterial efficacy of silver nitrate, indicating that the release of silver from the complex is relatively quick and therefore potent. We anticipate that this novel complex can potentially be incorporated into a bandage material to treat burn wound infections with the advantage of real time tracking of silver release.

4.I.4 Experimental.

4.I.4.1 General Materials and Methods.

All chemicals, solvents and reagents were purchased from Sigma-Aldrich and used without further purification unless otherwise specified. The BODIPY derivative 8-(4-amino)-4,4-difluoro-1,3,5,7-tetramethyl-4-bora-3a,4a-diaza-a-indacene was synthesized by following a previously reported procedure.[22] UV-Vis spectra were obtained using a Varian Cary 50 UV-Vis spectrophotometer. IR spectra were acquired using a Perkin-Elmer Spectrum One FT-IR spectrometer. Fluorescence spectra were recorded using an Agilent Cary-Eclipse florescence spectrophotometer. Bacterial growth curves were obtained using a Versa max microplate reader. Confocal microscopy images were acquired on a Solamere Spinning disk confocal microscope equipped with a Nikon TE2000 inverted stand, a CSU-X1 spinning disk, and a Hamamatsu ImageEMX2 camera. A 488 nm laser with a 500-550 nm band-pass emission filter was utilized as the excitation source, and a 100x (1.4 NA) Nikon Plan Apo utilized as the objective lens. *E. coli* suspensions were imaged at 1 frame per second for a total of 9.5 minutes with a 100 ms exposure time.

4.I.4.2 Synthesis of qPyr.

A solution of 1-pyrenecarboxaldehyde (115 mg, 0.50 mmol) in 10 ml of dichloromethane was added drop wise to a solution of 8-aminoquinoline (72 mg, 0.50 mmol) in 10 ml of methanol. The mixture was heated to reflux for 16 h and then concentrated under reduced pressure. The precipitate thus formed was collected by vacuum filtration affording 162 mg (91% yield) of N-(1-pyrene)-1-quinolin-2-ylmethanimine (qPyr) as a light-brown powder.

*4.I.4.3 Synthesis of [Ag(qPyr)$_2$](CF$_3$SO$_3$) **1**.*

Two equivalents of qPyr (100 mg, 0.28 mmol) were dissolved in 20 ml of 1:1 methanol:dichloromethane along with one equivalent of silver trifluoromethane sulfonate (36 mg, 0.14 mmol). The reaction mixture was then stirred for 12 h. After this time, the solution was concentrated under reduced pressure. The resulting precipitate was collected through vacuum filtration affording a light-yellow powder. This powder was recrystallized from methanol to obtain [Ag(qPyr)$_2$]CF$_3$SO$_3$ **1** as a light yellow-brown powder (124 mg, 91%). Single crystals were obtained by vapor diffusion of ethyl ether into a solution of [Ag(qPyr)$_2$]CF$_3$SO$_3$ in methanol.

4.I.4.4 Synthesis of qBODIPY.

The amino BODIPY starting material 8-(4-amino)-4,4-difluoro-1,3,5,7-tetramethyl-4-bora-3a,4a-diaza-a-indacene (170 mg, 0.50mmol) and 2-quinolinecarboxaldehyde (79 mg, 0.50 mmol) were dissolved in 25 mL of MeOH. The

orange mixture was refluxed for 48 h forming a red/orange precipitate. The volume of solvent was reduced under low pressure and the precipitate was collected through vacuum filtration using a fritted funnel. The crude compound was recrystallized from MeOH to afford qBODIPY (82%, 196 mg, 0.41 mmol) as a bright orange powder.

*4.I.4.5 Synthesis of [Ag(qBODIPY)(CF$_3$SO$_3$)]$_2$ **2**.*

The ligand qBODIPY (100 mg, 0.21 mmol) was dissolved in 20 mL of DCM. A solution of silver trifluoromethane sulfonate (107.5 mg, 0.42 mmol) in 20 mL of MeOH was added dropwise into this solution. The mixture was magnetically stirred at room temperature for 24 hours yielding a dark red precipitate. The volume of the solvent was decreased under reduced pressure and the precipitate was collected through vacuum filtration using a fritted funnel. The obtained powder was recrystallized twice from MeOH to afford complex **2** (91%, 189 mg, 0.19 mmol) as a dark red microcrystalline powder.

4.I.4.6 X-Ray Data Collection and Structure Refinement.

Single crystals of the complexes were obtained by layering hexanes over its dichloromethane solution. Suitable crystals were mounted on a MitiGen loop with Paratone-N oil (Hampton Research) and transferred to the diffractometer. Data were collected on a Bruker APEX II single crystal X-ray diffractometer equipped with PHOTON 100 detector with synchrotron radiation source by the ϕ and ω-scan technique in the range $3 \leq 2\theta \leq 51$. The data integration and reduction were done with

SAINT[24] module. The multi scan semi-empirical absorption correction was applied to the collected reflections using SADABS. The structure was generated using ShelXT (intrinsic phasing)[25] using Olex2[26] graphical user interface and subsequently refined by full-matrix least squares procedure on F^2 using ShelXL refinement package.[27] All non-hydrogen atoms were refined anisotropically. All hydrogen atoms were included in calculated positions. Calculations were also performed using the SHELXTL 2014 program package.[28] The SQUEEZE[29] module within the PLATON[30] program was used to alleviate the Alert As emerged due to solvent accessible voids in the structure.

4.I.4.7 Fluorescence Tracking of Silver Delivery to Bacterial Cells.

Escherichia coli (ATCC 25922) cells were prepared by first spreading frozen liquid cultures (20% v/v glycerol, -72 °C) on Luria broth (LB) agar plates and incubating them at 37 °C overnight. From these plates, an individual colony was selected and used to inoculate 3 mL of sterile, liquid LB and subsequently incubated at 37 °C for 18 h with constant shaking at 250 rpm. Upon completion of this growth period, a 1 mL aliquot of this bacterial suspension was washed by centrifuging a 1 mL aliquot at 5000 rpm for 5 min, discarding the supernatant, and re-suspending the pellet in 1 mL sterile nanopure water. This process was repeated once, and a 2 μL drop of the washed suspension was placed onto a 1.5 microscope cover slip (0.17 mm thickness) and used for fluorescence imaging. *E. coli* suspensions were imaged at 1 frame per second for a total of 9.5 minutes with a 100 ms exposure time. After 30 seconds, a 2 μL aliquot of a 5 μM complex **1** or qBODIPY solution (1:99 DMSO:H2O) was added

to the 2 μL drop of the *E. coli* suspension being imaged, and the increase in qBODIPY fluorescence was noted over the remaining time.

4.I.4.8 Bacterial Growth Kinetics.

Escherichia coli, *Pseudomonas aeuroginosa*, and *Staphylococcus aureus* cells were first grown by spreading frozen liquid cultures (20% glycerol, -72 °C) on Luria broth (LB) agar plates and incubating them at 37 °C overnight. From these plates, one individual colony was selected and used to inoculate a 3 mL aliquot of sterile liquid Mueller-Hinton broth (MHB) which was then incubated at 37 °C for 18 h with constant shaking at 250 rpm. Upon completion of this growth period, the bacterial cells were washed by centrifuging a 1 mL aliquot of each bacterial suspension at 5000 rpm for 5 min, discarding the supernatant, and re-suspending the pellet in 1 mL sterile MHB. This process was repeated once, with enough of the second re-suspension added to a 5 mL volume of sterile Mueller-Hinton Broth to bring the optical density at 600 nm to 0.100. This new suspension with 0.100 optical density was subsequently used for all inoculations. A 96-well plate (Costar) was utilized to obtain bacterial growth profiles, with each well having 20 μL of this bacterial inoculation suspension, 20 μL fresh MHB, varying volumes (2-100 μL) of complex **1** solution, and enough 1:99 DMSO:H_2O to bring the final volume to 200 μL. Upon addition of all components, the wells were mixed by pipetting, then the 96-well plate was immediately placed into a Molecular Devices VERSAmax microplate reader maintained at a constant temperature of 37 °C with measurements of each well's optical density at 600 nm taken every 3 minutes over

a 24 h period with a 15 s mixing period between each acquisition. The concentrations at which no bacterial growth was observed in the plate after the incubation period was determined to be the minimum inhibitory concentration (MIC) for that compound.

4.I.5 References.

1. Kresse, H.; Beasley M. J.; Rovini, H. The antibacterial drugs market. *Nat. Rev. Drug Discovery* **2007**, *6*, 19-20.

2. Wright, P. M.; Seiple I. B.; Myers, A. G. The evolving role of chemical synthesis in antibacterial drug discovery. *Angew. Chem. Int. Ed.* **2014**, *53*, 8840-8869.

3. Liu, Y. Y.; Wang, Y.; Walsh, T. R.; Yi, L. X.; Zhang, R.; Spencer, J.; Doi, Y.; Tian, G.; Dong, B.; Huang, X.; Yu, L. F.; Gu, D.; Ren, H.; Chen, X.; Lv, L.; He, D.; Zhou, H.; Liang, Z.; Liu J. H.; Shen, J. Emergence of plasmid-mediated colistin resistance mechanism MCR-1 in animals and human beings in China: a microbiological and molecular biological study. *Lancet Infect. Dis.* **2016**, *16*, 161-168.

4. McGann, P.; Snesrud, E.; Maybank, R.; Corey, B.; Ong, A. C.; Clifford, R.; Hinkle, M.; Whitman, T.; Lesho E.; Schaecher, K. E. *Escherichia coli* harboring MCR-1 and blaCTX-M on a novel IncF plasmid: first report of MCR-1 in the united states. *Antimicrob. Agents Chemother*. **2016**, *60*, 4420-4421.

5. Lemire, J. A.; Harrison J. J.; Turner, R. J. Antimicrobial activity of metals: mechanisms, molecular targets and applications. *Nat. Rev. Microbiol*. **2013**, *11*, 371-384.

6. Chopra, I. The increasing use of silver-based products as antimicrobial agents: a useful development or a cause for concern? *J. Antimicrob. Chemother.* **2007**, *59*, 587-590.

7. Liu, J.; Sonshine, D. A.; Shervani S.; Hurt, R. H. Controlled release of biologically active silver from nanosilver surfaces. *ACS Nano* **2010**, *11*, 6930-6913.

8. Chernousova S.; Epple, M. Silver as antibacterial agent: Ion, nanoparticle, and metal. *Angew. Chem. Int. Ed.* **2013**, *52*, 1636-1653.

9. Wakshlak, R. B. K.; Pedahzur R.; Avnir, D. Antibacterial activity of silver-killed bacteria: the "zombies" effect. *Sci. Rep.* **2015**, *5*, 9555. DOI: 10.1038/srep09555.

10. Glisic, B. D.; Senerovic, L.; Comba, P.; Wadepohl, H.; Veselinovic, A.; Milivojevic, D. R.; Djuran M. I.; Nikodinovic-Runic, J. Silver(I) complexes with phthalazine and quinazoline as effective agents against pathogenic *Pseudomonas aeruginosa* strains. *J. Inorg. Biochem*. **2016**, *155*, 115-128.

11. Klasen, H. J. Historical review of the use of silver in the treatment of burns. Early uses. *Burns* **2000**, *26*, 117-130.

12. deBoer, T. R.; Chakraborty I.; Mascharak, P. K. Design and construction of a silver(I)-loaded cellulose-based wound dressing: trackable and sustained

release of silver for controlled therapeutic delivery to wound sites. *J. Mater. Sci. Mater. Med.* **2015**, *26*, 243.

13. Basu Ray, G. B.; Chakraborty, I.; Moulik, S. P. Pyrene absorption can be a convenient method for probing critical micellar concentration and indexing micellar polarity. *J. Colloid Interface Sci.* **2006**, *294*, 248-254.

14. Ulrich, G.; Ziessel, R.; Harriman, A. The chemistry of fluorescent bodipy dyes: versatility unsurpassed. *Angew. Chem. Int. Ed*. **2008**, *47*, 1184-1201.

15. Kowada, T.; Maeda, H.; Kikuchi K. BODIPY-based probes for the fluorescence imaging of biomolecules in living cells. *Chem. Soc. Rev*. **2015**, *44*, 4953-4972.

16. Ziessel, R.; Goze, C.; Ulrich, G.; Cesario, M.; Retailleau, P.; Harriman, A.; Rostron, J. P. Intramolecular energy transfer in pyrene-bodipy molecular dyads and triads. *Chem. Eur. J.* **2005**, *11*, 7366.

17. Janiak, C. J. A critical account on π-π stacking in metal complexes with aromatic nitrogen-containing ligands. *Chem. Soc Dalton Trans.* **2000**, 3885-3896.

18. Steiner, T. C-H-O Hydrogen Bonding in Crystals. *Crystallogr. Rev.* **1996**, *6*, 1-51.

19. Groom, C. R.; Bruno, I. J. Lightfoot, M. P.; Ward, S. C. The Cambridge structural database. *Acta Cryst.* **2016**, *B72*, 171-179.

20. Lee, Y. J.; Lee, S. W. Ligands containing pyridyl-carboxylate terminals and their discrete silver and polymeric cadmium compounds (n-py)-CH=N-$C_{10}H_6$-

COOH (N = 2 (HL^1)), 3 (HL^2)), [Ag(HL^1)$_2$](PF$_6$), Ag(HL^1)$_2$](NO$_3$)(H$_2$O), and [Cd(L^2)$_2$]. *Polyhedron* **2013**, *53*, 103-112.

21. Zhang, H.; Chen, L.; Song, H.; Zi, G. Synthesis, structure, and catalytic activity of chiral silver(I) and copper(II) complexes with biaryl-based nitrogen-containing ligands. *Inorg. Chim. Acta* **2011**, *366*, 320-336.

22. Lu, H.; Zhang, S. S.; Liu, H. Z.; Wang, Y. W.; Shen, Z.; Liu, C. G.; You, X. Z. Experimentation and theoretical calculation of a BODIPY sensor based on photoinduced electron transfer for ions detection. *J. Phys. Chem. A* **2009**, *113*, 14081-14086.

23. Singha, S.; Kim, D.; Seo, H.; Cho, S. W.; Ahn, K. H. Fluorescence sensing systems for gold and silver species. *Chem. Soc. Rev*. **2015**, *44*, 4367.

24. *SAINT Plus*, version 7.03; Bruker AXS Inc.: Madison, WI, **2004**.

25. Sheldrick, G. M. SHELXT – Integrated space-group and crystal-structure determination. *Acta Cryst.* **2015**, *A71*, 3–8.

26. Dolomanov, O. V.; Bourhis, L. J.; Gildea, R. J.; Howard, J. A. K.; Puschmann, H. OLEX2: a complete structure solution, refinement and analysis program. *J. Appl. Crystallogr*. **2009**, *42*, 339–341.

27. Sheldrick, G. M. A short history of SHELX. *Acta Crystallogr*. **2008**, *A64*, 112-122.

28. Sheldrick, G. M. Crystal structure refinement with SHELXL. *Acta Crystallogr., Struct. Chem*. **2015**, *C71*, 3–8.

29. Spek. A. L. PLATON SQUEEZE: a tool for the calculation of the disordered solvent contribution to the calculated structure factors. *Acta Crystallogr.* **2015**, *C71*, 9-18.

30. Spek, A. L. PLATON, a Multipurpose Crystallographic Tool; Utrecht University: Utrecht, The Netherlands, **2005**.

4.I.6 Reprints of Publications and Permissions.

Reprinted with permissions from Pinto, M. N.; Chakraborty, I.; Mascharak, P. K. Synthesis and crystal structure of bis(1-{[(quinoline-8-yl)imino]methyl}pyrene-K2N,N')silver(I) trifluoromethanesulfonate. Acta Crystallogr. 2016, E72, 1495-1498.

And

Reprinted with permissions from Pinto, M. N.; Chakraborty, I.; Schultz-Simonton. W.; Rojas-Andrade, M.; Braslau, R.; Mascharak, P. K. Tracking silver delivery to bacteria using turn-on fluorescence. Chem. Commun. 2017, 53, 1459-1462.

Tracking silver delivery to bacteria using turn-on fluorescence

M. N. Pinto, I. Chakraborty, W. Schultz-Simonton, M. Rojas-Andrade, R. Braslau and P. K. Mascharak, *Chem. Commun.*, 2017, **53**, 1459

Synthesis and crystal structure of bis(1-{[(quinolin-8-yl)imino]methyl}pyrene-$\kappa^2 N,N'$)silver(I) trifluoromethanesulfonate

Miguel Pinto, Indranil Chakraborty and Pradip Mascharak*

Department of Chemistry, University of California Santa Cruz, CA 95064. *Correspondence e-mail: pradip@ucsc.edu

The title compound, [Ag(qPyr)$_2$]CF$_3$SO$_3$ where qPyr = 1-(quinoline-2-ylmethylene)aminopyrene, C$_{26}$H$_{16}$N$_2$, was synthesized from a reaction of silver trifluoromethanesulfonate and qPyr in dichloromethane–methanol mixed media. In this design, the qPyr ligand was chosen for its characteristic excitation and emission profiles, which could enable the tracking of the silver complex within biological targets. The Ag^I atom resides in a distorted tetrahedral N$_4$ coordination sphere. Analysis of the packing pattern revealed significant intra- and intermolecular π–π stacking interactions between the [Ag(qPyr)$_2$]$^+$ cations. In addition, a weak C—H···O hydrogen bond consolidates the packing between cations and anions.

1. Chemical context

Silver metal and its salts have been used for their well known antimicrobial properties since ancient times (Chernousova & Epple, 2013). In recent years, the use of silver has regained interest due to the emergence of multidrug-resistant organisms (MDROs) (Kresse *et al.*, 2007; Liu *et al.*, 2010; Thornton *et al.*, 2016). Silver is primarily used topically to treat chronic infections in burn wounds (deBoer *et al.*, 2015). The metal exerts its microbial toxicity by slowly releasing Ag^I ions that inflict damage on cell walls, produce reactive oxygen species and bind to DNA base pairs as well as proteins, impeding normal cellular functions (Liu *et al.*, 2010; Thornton *et al.*, 2016). As silver ions tend to precipitate as AgCl in the presence of blood plasma chloride (Chernousova & Epple, 2013), there is a need for stable silver complexes that can slowly and sustainably release silver ions into biological matrices. Herein we report the synthesis and characterization of a novel silver complex, [Ag(qPyr)$_2$]CF$_3$SO$_3$ [where qPyr = 1-(quinoline-2-ylmethylene)aminopyrene] which could serve as a stable complex for the delivery of silver. In the design of this compound, qPyr was included due to its characteristic absorption and emission profile, which could allow tracking of the ligand and silver within the cell membrane of the bacteria (Ray *et al.*, 2006).

2. Structural commentary

The molecular structure of the cation in the title complex is shown in Fig. 1. The coordination environment of the Ag^I atom in the cationic complex is distorted tetrahedral (Table 1). The qPyr ligand binds to the metal in a bidentate fashion. In this complex, the chelate rings composed of atoms Ag1, N2, C8, C9, N1 and Ag1, N4, C34, C35, N3 are reasonably planar,

348
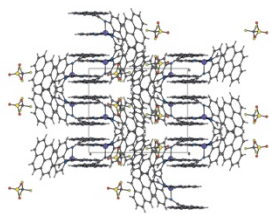
research communications

Ag1—N3	2.249 (4)	Ag1—N4	2.411 (4)
Ag1—N1	2.228 (4)	Ag1—N2	2.399 (4)
N3—Ag1—N4	72.24 (15)	N1—Ag1—N4	119.33 (15)
N3—Ag1—N2	120.45 (15)	N1—Ag1—N2	73.09 (15)
N1—Ag1—N3	151.52 (16)	N2—Ag1—N4	131.88 (14)

with mean deviations of 0.054 (3) and 0.059 (3) Å, respectively. The dihedral angle between these two chelate planes is 69.0 (4)°. The two quinoline fragments within the qPyr ligand in the title complex are satisfactorily planar, with mean deviations of 0.031 (4) and 0.035 (4) Å. The dihedral angles between the quinoline moieties and the pyrene rings are quite similar [73.5 (4) and 73.8 (3)°].

CF$_3$SO$_3$
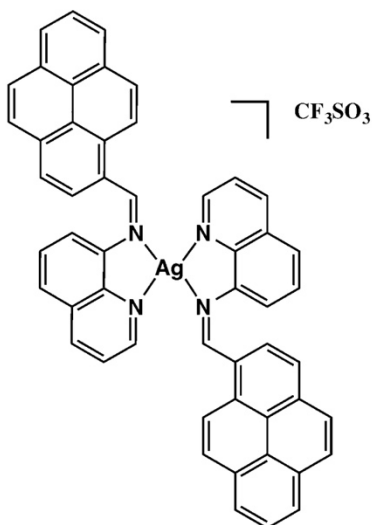
3. Supramolecular features

The packing pattern exhibits the presence of both intra- and intermolecular offset π–π stacking interactions (Figs. 2 and 3). The extent of the intermolecular π–π interaction is found to be relatively stronger [3.543 (5) Å] compared to the intramolecular π–π stacking interactions [3.642 (5) and 3.617 (5) Å]. In both cases, the angle between the ring normal and the vector between the ring centroids is close to 20° and centroid-to-centroid distances are within the upper limit of 3.8 Å (Janiak, 2000). The crystal packing of the complex reveals also a non-classical hydrogen-bonding interaction (Steiner, 1996) of the type C—H···O between the cation and
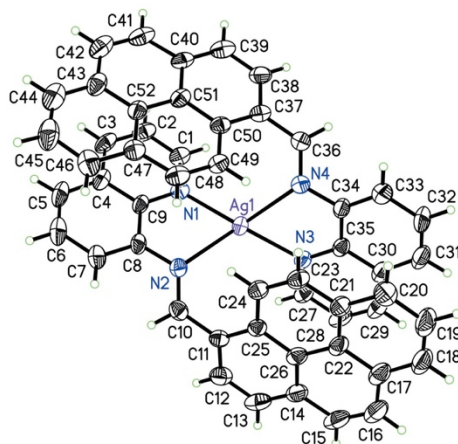
Figure 1
The molecular structure of the cation in the title salt. Displacement ellipsoids correspond to the 50% probability level; the counter-anion is not shown.
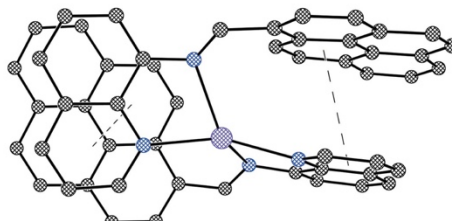
Figure 2
Representation of intramolecular π–π stacking within the title complex.
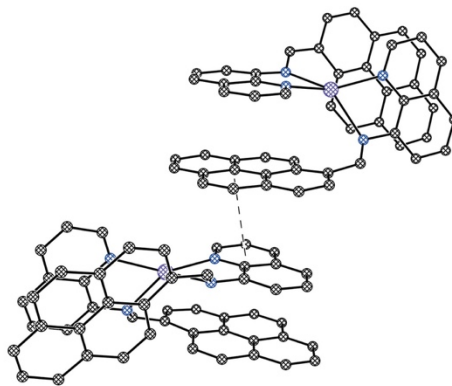
Figure 3
Representation of intermolecular π–π stacking within the title complex.

349
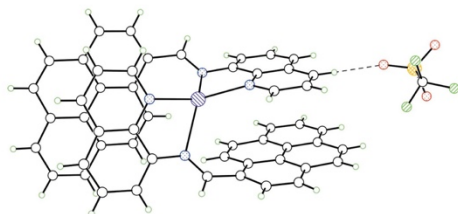
Figure 4
Packing pattern of the title salt showing the C—H⋯O interaction between cation and anion.

Table 2
Hydrogen-bond geometry (Å, °).

D—H⋯A	D—H	H⋯A	D⋯A	D—H⋯A
C3—H3⋯O3^i	0.93	2.44	3.359 (10)	140

Symmetry code: (i) $x - 1, -y + \frac{3}{2}, z - \frac{1}{2}$.

the triflate anion (Table 2, Fig. 4). The arrangement of the two types of molecules along the c axis is shown in Fig. 5.

4. Database survey

A search of Cambridge Structural Database (Groom *et al.*, 2016) revealed that molecular systems where Ag^I resides in a distorted tetrahedral coordination environment are primarily of a supramolecular nature. In a relatively recent report, two discrete Ag complexes, namely [Ag(HL^1)$_2$](PF$_6$) and [Ag(HL^1)$_2$](NO$_3$)(H$_2$O) (where HL^1 = (*n*-Py)—CH=N—

C$_{10}$H$_6$—COOH) are reported (Lee & Lee, 2013) which are structurally similar to the title complex. Both these molecules adopt triclinic symmetry in space group $P\bar{1}$. The average Ag—N distances for these complexes are slightly longer (2.349 and 2.346 Å) than that of the title complex (2.322 Å). Unlike the present complex, these two Ag complexes are characterized by significant intramolecular O—H⋯F and O—H⋯O hydrogen-bonding interactions with the PF$_6^-$ and NO$_3^-$ counter-ions. In another report, three Ag complexes, namely [Ag(**1**)$_2$](NO$_3$), [Ag(**1**)$_2$](PF$_6$) and [Ag(**1**)$_2$](OTf) [where **1** = (*R*)-2-(pyridin-2-ylmethylimino)-2'-(dimethylamino)-1,1'-binapthyl] are described with similar structural features (Zhang *et al.*, 2011). In this study, [Ag(**1**)$_2$](NO$_3$) and [Ag(**1**)$_2$](PF$_6$) crystallize in space group $P2_12_12_1$ while [Ag(**1**)$_2$](OTf) crystallizes in $P2_1$. Here the Ag—N distances span the range 2.354–2.376 Å, noticeably longer than that of the title complex.
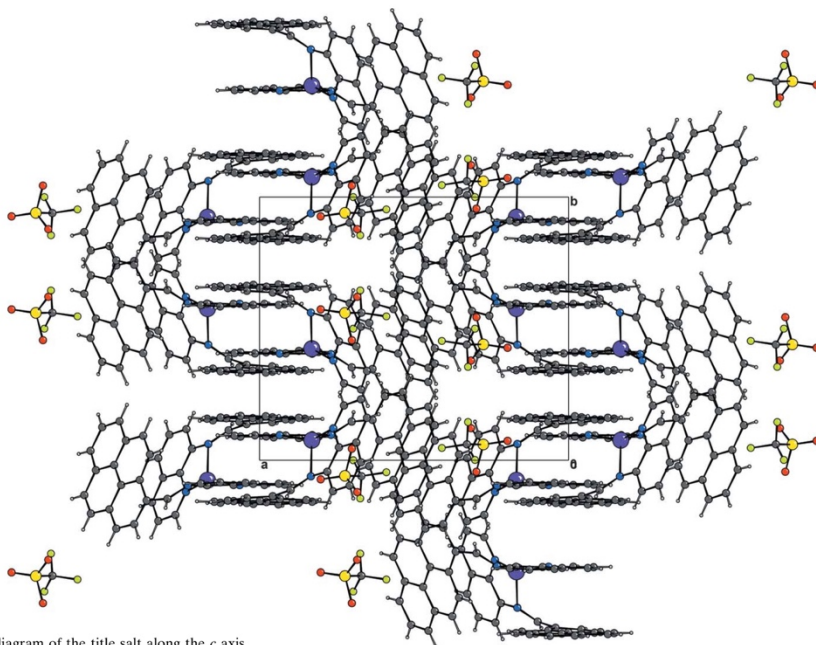
Figure 5
Packing diagram of the title salt along the c axis.

350

research communications

Table 3
Experimental details.

Crystal data

Chemical formula	$[Ag(C_{26}H_{16}N_2)_2]CF_3SO_3$
M_r	969.75
Crystal system, space group	Monoclinic, $P2_1/c$
Temperature (K)	273
a, b, c (Å)	17.132 (1), 13.6108 (8), 18.9712 (11)
β (°)	110.887 (1)
V (Å^3)	4133.0 (4)
Z	4
Radiation type	Mo $K\alpha$
μ (mm^{-1})	0.61
Crystal size (mm)	$0.15 \times 0.07 \times 0.03$

Data collection

Diffractometer	Bruker APEXII CCD
Absorption correction	Multi-scan (*SADABS*; Bruker, 2012)
T_{min}, T_{max}	0.627, 0.745
No. of measured, independent and observed [$I > 2\sigma(I)$] reflections	35302, 7406, 4227
R_{int}	0.084
$(\sin \theta/\lambda)_{max}$ (Å^{-1})	0.602

Refinement

$R[F^2 > 2\sigma(F^2)]$, $wR(F^2)$, S	0.058, 0.181, 1.03
No. of reflections	7406
No. of parameters	587
No. of restraints	598
H-atom treatment	H-atom parameters constrained
$\Delta\rho_{max}, \Delta\rho_{min}$ (e Å^{-3})	0.60, −0.54

Computer programs: *APEX2* and *SAINT* (Bruker, 2012), *SHELXT2014* (Sheldrick, 2015*a*), *SHELXL2014* (Sheldrick, 2015*b*), *XP* in *SHELXTL* (Sheldrick, 2008), *CrystalMaker* (Palmer, 2014) and *OLEX2* (Dolomanov *et al.*, 2009).

5. Synthesis and crystallization

Synthesis of the qPyr ligand

A solution of 1-pyrenecarboxaldehyde (115 mg, 0.50 mmol) in 10 ml of dichloromethane was added drop wise to a solution of 8-aminoquinoline (72 mg, 0.50 mmol) in 10 ml of methanol. The mixture was heated to reflux for 16 h and then concentrated under reduced pressure. The precipitate thus formed was collected by vacuum filtration affording 162 mg (91% yield) of *N*-(1-pyrene)-1-quinolin-2-ylmethanimine (qPyr) as a light-brown powder.

Synthesis of the title complex

Two equivalents of qPyr (100 mg, 0.28 mmol) were dissolved in 20 ml of 1:1 methanol:dichloromethane along with one equivalent of silver trifluoromethanesulfonate (36 mg, 0.14 mmol). The reaction mixture was then stirred for 12 h. After this time, the solution was concentrated under reduced

pressure. The resulting precipitate was collected through vacuum filtration affording a light-yellow powder. This powder was recrystallized from methanol to obtain $[Ag(qPyr)_2]CF_3SO_3$ as a light yellow–brown powder (124 mg, 91%). Single crystals were obtained by vapor diffusion of ethyl ether into a solution of $[Ag(qPyr)_2]CF_3SO_3$ in methanol.

6. Refinement

Crystal data, data collection and structure refinement details are summarized in Table 3. Hydrogen atoms were included in calculated positions on the C atoms to which they are bonded, with C—H = 0.93 Å and $U_{iso}(H) = 1.2U_{eq}(C)$.

References

Bruker (2012). *APEX2*, *SAINT* and *SADABS*. Bruker AXS Inc., Madison, Wisconsin, USA.
Chernousova, S. & Epple, M. (2013). *Angew. Chem. Int. Ed.* **52**, 1636–1653.
deBoer, T. R., Chakraborty, I. & Mascharak, P. K. (2015). *J. Mater. Sci. Mater. Med.* **26**, 243.
Dolomanov, O. V., Bourhis, L. J., Gildea, R. J., Howard, J. A. K. & Puschmann, H. (2009). *J. Appl. Cryst.* **42**, 339–341.
Groom, C. R., Bruno, I. J., Lightfoot, M. P. & Ward, S. C. (2016). *Acta Cryst.* B**72**, 171–179.
Janiak, C. (2000). *J. Chem. Soc. Dalton Trans.* pp. 3885–3896.
Kresse, H., Belsey, M. J. & Rovini, H. (2007). *Nat. Rev. Drug Discov.* **6**, 19–20.
Lee, Y. J. & Lee, S. W. (2013). *Polyhedron*, **53**, 103–112.
Liu, J., Sonshine, D. A., Shervani, S. & Hurt, R. H. (2010). *ACS Nano*, **4**, 6903–6913.
Palmer, D. C. (2014). *CrystalMaker.* CrystalMaker Software Ltd, Begbroke, England.
Ray, G. B., Chakraborty, I. & Moulik, S. P. (2006). *J. Colloid Interface Sci.* **294**, 248–254.
Sheldrick, G. M. (2008). *Acta Cryst.* A**64**, 112–122.
Sheldrick, G. M. (2015*a*). *Acta Cryst.* A**71**, 3–8.
Sheldrick, G. M. (2015*b*). *Acta Cryst.* C**71**, 3–8.
Steiner, T. (1996). *Crystallogr. Rev.* **6**, 1–51.
Thornton, L., Dixit, V., Assad, L. O. N., Ribeiro, T. P., Queiroz, D. D., Kellett, A., Casey, A., Colleran, J., Pereira, M. D., Rochford, G., McCann, M., O'Shea, D., Dempsey, R., McClean, S., Kia, A. F. A., Walsh, M., Creaven, B., Howe, O. & Devereux, M. (2016). *J. Inorg. Biochem.* **159**, 120–132.
Zhang, H., Chen, L., Song, H. & Zi, G. (2011). *Inorg. Chim. Acta*, **366**, 320–336.

351

supporting information

Synthesis and crystal structure of bis(1-{[(quinolin-8-yl)imino]methyl}pyrene-κ²*N,N′*)silver(I) trifluoromethanesulfonate

Miguel Pinto, Indranil Chakraborty and Pradip Mascharak

Computing details

Data collection: *APEX2* (Bruker, 2012); cell refinement: *SAINT* (Bruker, 2012); data reduction: *SAINT* (Bruker, 2012); program(s) used to solve structure: *SHELXT2014* (Sheldrick, 2015*a*); program(s) used to refine structure: *SHELXL2014* (Sheldrick, 2015*b*); molecular graphics: *XP* in *SHELXTL* (Sheldrick, 2008) and *CrystalMaker* (Palmer, 2014); software used to prepare material for publication: *OLEX2* (Dolomanov *et al.*, 2009).

Bis(1-{[(quinolin-8-yl)imino]methyl}pyrene-κ²*N,N′*)silver(I) trifluoromethanesulfonate

Crystal data

$[Ag(C_{26}H_{16}N_2)_2]CF_3SO_3$	$F(000) = 1968$
$M_r = 969.75$	$D_x = 1.558$ Mg m^{-3}
Monoclinic, $P2_1/c$	Mo $K\alpha$ radiation, $\lambda = 0.71073$ Å
$a = 17.132$ (1) Å	Cell parameters from 3637 reflections
$b = 13.6108$ (8) Å	$\theta = 2.5–18.3°$
$c = 18.9712$ (11) Å	$\mu = 0.61$ mm^{-1}
$\beta = 110.887$ (1)°	$T = 273$ K
$V = 4133.0$ (4) Å^3	Block, yellow
$Z = 4$	$0.15 \times 0.07 \times 0.03$ mm

Data collection

Bruker APEXII CCD diffractometer	7406 independent reflections
	4227 reflections with $I > 2\sigma(I)$
ω scans	$R_{int} = 0.084$
Absorption correction: multi-scan (*SADABS*; Bruker, 2012)	$\theta_{max} = 25.3°$, $\theta_{min} = 2.5°$
	$h = -20\rightarrow20$
$T_{min} = 0.627$, $T_{max} = 0.745$	$k = -16\rightarrow16$
35302 measured reflections	$l = -22\rightarrow22$

Refinement

Refinement on F^2	Hydrogen site location: inferred from neighbouring sites
Least-squares matrix: full	
$R[F^2 > 2\sigma(F^2)] = 0.058$	H-atom parameters constrained
$wR(F^2) = 0.181$	$w = 1/[\sigma^2(F_o^2) + (0.0931P)^2]$
$S = 1.03$	where $P = (F_o^2 + 2F_c^2)/3$
7406 reflections	$(\Delta/\sigma)_{max} = 0.001$
587 parameters	$\Delta\rho_{max} = 0.60$ e Å^{-3}
598 restraints	$\Delta\rho_{min} = -0.54$ e Å^{-3}
Primary atom site location: structure-invariant direct methods	

ChemComm

Chemical Communications

rsc.li/chemcomm

ROYAL SOCIETY
OF CHEMISTRY
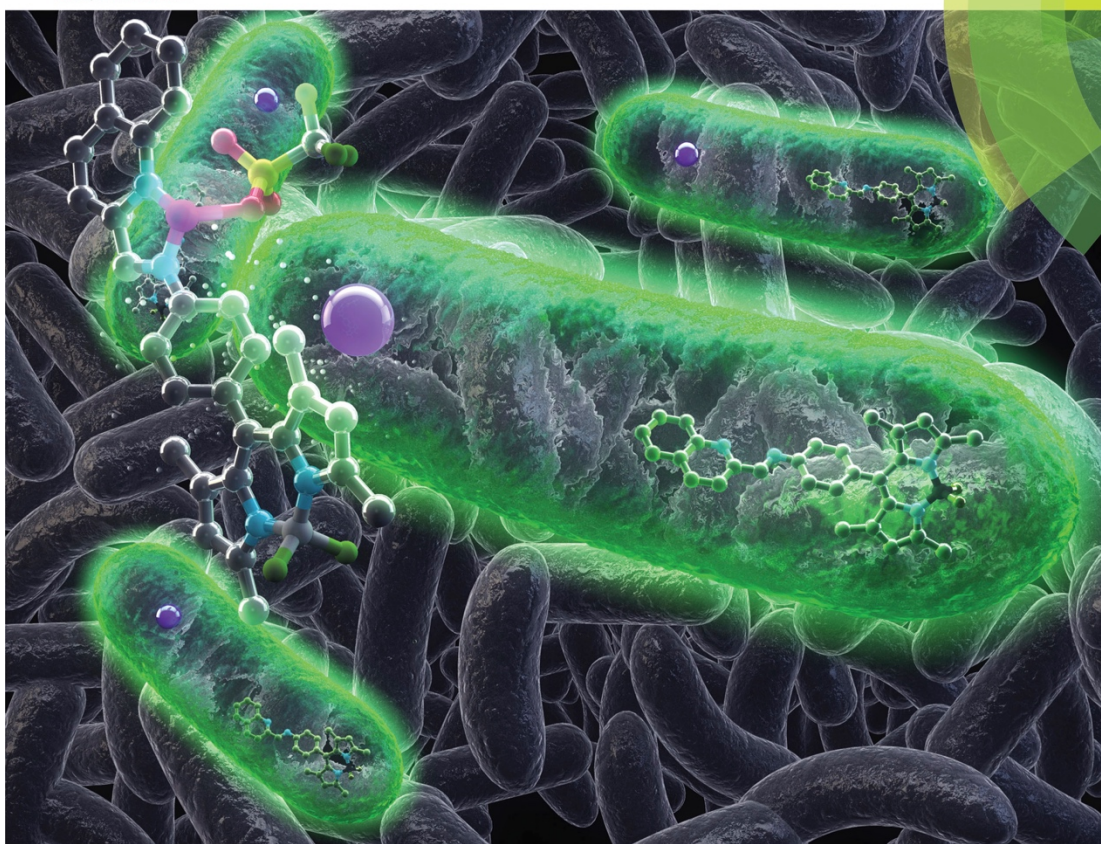
COMMUNICATION
Pradip K. Mascharak *et al.*
Tracking silver delivery to bacteria using turn-on fluorescence

ChemComm

ROYAL SOCIETY OF CHEMISTRY

COMMUNICATION

Tracking silver delivery to bacteria using turn-on fluorescence†

Miguel N. Pinto, Indranil Chakraborty, Wiley Schultz-Simonton, Mauricio Rojas-Andrade, Rebecca Braslau and Pradip K. Mascharak*

Herein we present a novel silver complex [Ag(qBODIPY)(CF₃SO₃)] (1) that exhibits dramatic increase in fluorescence upon silver release. Complex 1 has a minimum inhibitory concentration comparable to that of silver nitrate. Confocal microscopy was used to track the delivery of silver to bacterial targets.

The treatment and prevention of infections caused by multi-drug resistant organisms (MDROs) continue to be a challenge to the pharmaceutical industry[1] and a serious threat to global health.[2] The misuse and overuse of antibiotics combined with rising population densities and increased international travel expedite bacterial resistance to our current antimicrobial arsenal.[2] Recently, bacterial resistance to a "last resort" antibiotic, namely colistin (polymyxin E), has been reported in China[3] and the United States.[4]

Metals, particularly silver, have been used as antimicrobial agents since ancient times due to their high toxicity towards microorganisms and low toxicity towards mammalian cells.[5] Although the use of silver diminished with the introduction of β-lactam antibiotic chemotherapy in the 1940s, silver salts continue to be used for the treatment and prevention of infections of burns and difficult-to-treat wounds.[6] Currently, the application of silver in the form of nanoparticles, salts, and complexes, has gained interest due to its bactericidal properties against MDROs that can withstand conventional antibiotic chemotherapy. Silver exerts its bactericidal activity by continuously releasing trace amounts of cations (Ag⁺), which are toxic to microorganisms.[7] Silver ions generate their toxicity by producing reactive oxygen species, as well as disrupting biochemical processes by interacting with thiol and amino groups on proteins,

nucleic acids, and cell membranes.[8] Silver-killed microorganisms can serve as a reservoir of silver and slowly release Ag⁺ cations which can then again exert their bactericidal activity, known as the "zombie effect".[9,10]

Ingestion of large amounts of silver can produce adverse effects such as argyria.[11] Therefore most silver based therapies are applied topically for the treatment of burn wound infections. Since Ag⁺ is highly reactive, it tends to precipitate as an insoluble AgCl salt in the presence of chloride ions, which are abundant in blood plasma ([Cl] = 95–110 mM).[8] For this reason, wound treatments require multiple irrigations with silver salts (up to 12 times per day) to keep the wound sterile.[11] Having a way to follow the extent of active silver released to the wound would be advantageous in determining how regularly the topical antibiotic should be administered to keep the wound free of infection. Our group previously developed a florescent silver complex which was used to track its migration from a bandage onto a skin and soft tissue infection model.[12] However, the fluorescence only indicated that the ligand/complex was transferred from the bandage to the skin and had no indication of the extent of Ag⁺ (actual drug) delivered to the wound site.

In this study, we report a novel silver complex derived from a Schiff base ligand tethered with a boron-dipyrromethene (BODIPY) fragment. The ligand qBODIPY, obtained by the condensation of quinoline-2-aldehyde and an aniline derivative of BODIPY, affords [Ag(qBODIPY)(CF₃SO₃)] (1, Fig. 1A) upon reaction with Ag(CF₃SO₃). BODIPY-based fluorophores have raised great interest in the bioimaging community due to their high molar extinction coefficient, high fluorescence quantum yield, sharp absorption and emission spectra, high lipophilicity, low toxicity, and excellent chemical/photochemical stability.[13,14] The BODIPY fluorophore is known to penetrate cell membranes and eventually accumulate within subcellular membranes due to its high lipophilicity.[14] A problem with BODIPY-based dyes is the small Stokes' shift, which makes it difficult to use in flow cytometry and fluorescence microscopy.[13] In order to circumvent the small Stokes' shift, ancillary ligands can be used to capture

Department of Chemistry and Biochemistry, University of California, Santa Cruz, CA 95064, USA. E-mail: pradip@ucsc.edu; Fax: +1 831 459 4251; Tel: +1 831 459 2935

354
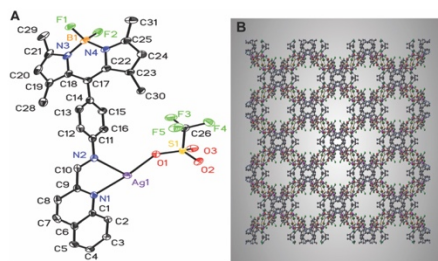
Fig. 1 (A) Molecular structure of **1** with atom numbering scheme (thermal ellipsoids are shown at the 50% thermal probability level; the hydrogen atoms are omitted for clarity). (B) Extended structure of complex **1** along the *c*-axis. Selected bond distances [Å]: Ag1–O1 2.343(6), Ag1–O4 2.482(6), Ag1–N1 2.342(6), Ag1–N2 2.404(6), Ag2–O3 2.475(6), and Ag2–O5 2.428(6).

light of shorter wavelength, forming a "fluorescence resonance energy transfer cassette".[13] The absorbed energy is channelled to the BODIPY emitter effectively increasing the Stokes shift.[13,15] An important feature of these compounds is the electronic isolation of the two chromophores, preventing the donor–acceptor molecule from acting as a single "supermolecule" with an extended LUMO.[15] This is achieved by arranging the connecting linkage in an "orthogonal" manner so that the donor and acceptor moieties are no longer coplanar.[15] In our design this is achieved by inserting two methyl substituents on C19 and C23 of the BODIPY moiety (Fig. 1A). Although the absorption spectrum of the qBODIPY ligand contains features from both subunits, the fluorescence emission occurs only from the BODIPY unit.[13]

In complex **1**, we employed a quinoline ancillary ligand as the donor molecule (Fig. 1A). The BODIPY acceptor and the quinoline donor are coupled through a "twisted" aniline linker and thus electronically isolated from each other. The aniline derivative of BODIPY was obtained according to the literature procedure[16] and was handled under an inert atmosphere since it is relatively sensitive to oxidation. The aniline-BODIPY was then refluxed in MeOH with quinoline-2-aldehyde for 48 h under an inert atmosphere yielding the orange Schiff base ligand (qBODIPY). Stirring of ∼2 equiv. of Ag(CF₃SO₃) with 1 equiv. of ligand at room temperature in 1 : 1 MeOH : DCM afforded the silver complex **1**. The crude complex was purified by recrystallization from MeOH and single crystals were obtained from layering hexanes over a solution of **1** in DCM.

The molecular structure of **1** was authenticated by single crystal X-ray crystallography.‡ The thermal ellipsoid plot of the complex is shown in Fig. 1A while the extended structure is presented in Fig. 1B. Careful examination of the extended lattice of this complex reveals the presence of two types of Ag centers with different coordination environments. One of the Ag centers resides in a highly distorted square planar environment (mean deviation of the plane: 0.110 Å). In this case the metal atom forms a five-membered chelate ring with the qBODIPY ligand (the chelate ring composed of Ag1, N2, C10, C9 and N1 is satisfactorily planar with a mean deviation of

0.083 Å). The O atoms from the two triflate anions occupy the other two sites of this Ag center. Another Ag center resides in a distorted octahedral coordination environment with the equatorial plane comprised of the four O atoms from the triflates (mean deviation: 0.024 Å). Two such six-coordinated Ag centers formed a paddle-wheel framework in the extended structure with four μ-2 bridging triflate ligands (see the ESI†). This arrangement results in considerable argentophilic interactions between the two Ag centers (Ag–Ag, 3.2175(12) Å). No noticeable π–π stacking interactions have been noted in the crystal packing. The dihedral angle between the C17–C25 moiety and the C11–C16 aryl ring is 82° and the dihedral angle between the quinoline ring and the C11–C16 aryl ring is 19.4°.

Solutions of complex **1** in DCM, 1 : 9 DMSO : H₂O and 1 : 99 DMSO : H₂O are stable for up to two months at room temperature in the dark and over three months at 0 °C in the dark. However, complex **1** shows mild decomposition in neat DMSO after 48 hours, and full decomposition after 14 days. The absorption spectrum of **1** is centered at ∼505 nm with high extinction coefficient ($\varepsilon = 46\,000$ M⁻¹ cm⁻¹ in DCM, $\varepsilon = 107\,000$ M⁻¹ cm⁻¹ in DMSO, and $\varepsilon = 62\,000$ M⁻¹ cm⁻¹ in 1 : 10 DMSO : H₂O; Fig. S2, ESI†) along with a less intense band at around 350 nm.

The fluorescence emission for the qBODIPY ligand is centered at ∼520 nm in DCM and at ∼511 nm in 1 : 99 DMSO : H₂O resulting in a bright green color. The excitation wavelength maximum is centered at ∼505 nm, but a wide range of wavelengths from 230 nm to 500 nm can be used to excite the ligand.[17] The fluorescence emitted by the qBODIPY ligand is quenched dramatically upon coordination to silver (Fig. 2). In order to study the release profile of silver from the complex, a solution of **1** in DCM was titrated with increasing concentrations of tetrabutylammonium chloride (Fig. 3A). The chloride ions bind silver, effectively releasing it from the qBODIPY complex. It was observed that fluorescence was restored almost immediately upon the addition of chloride and the fluorescence intensity of the ligand was fully restored after the addition of 38 equiv. of chloride (Fig. 3A). The stability of complex **1** was then studied under conditions that resemble the environment used for the bacterial growth studies to determine how much silver is released by the bacterial growth medium. A solution of complex **1** in 1 : 99 DMSO : H₂O was titrated with aqueous solutions of 10, 20, 30, and 50% of Mueller Hinton broth (MHB). Such studies indicated
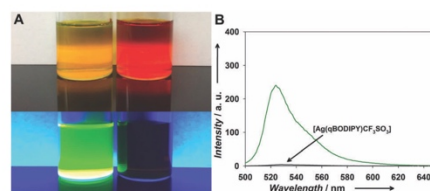
Fig. 2 (A) Solutions of qBODIPY (left) and [Ag(qBODIPY)(CF₃SO₃)] **1** (right) in DCM under visible (top) and UV light (bottom). (B) Fluorescence of qBODIPY (green trace) *vs.* **1** (black trace) in DCM; slit width = 2.5 nm.

355
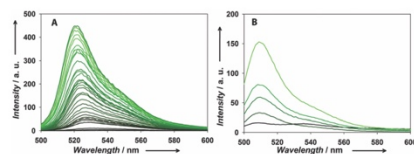
Fig. 3 (A) Fluorescence increase through subsequent addition of tetra-butylammonium chloride to a solution of **1** in DCM, slit width = 2.5 nm; (B) fluorescence increase through subsequent addition of Mueller-Hinton broth to a solution of **1** in 1 : 99 DMSO : H$_2$O, slit width = 10 nm (because of quenching of fluorescence by water, the slit width was increased to record the low fluorescence intensity in this case).

that only 4% of the silver is released when exposed to 20% of MHB (Fig. 3B). This is presumably attributed to interactions between **1** and the amino acids present in the growth medium as well as residual chloride.

The dramatic fluorescence quenching combined with the restoration of fluorescence upon silver release from **1** raised the possibility of convenient tracking of the process of silver delivery to the wound. In order to check whether silver delivery can indeed be tracked in live cells, we added 2 μL of a 10 μM solution of **1** (in 1 : 99 DMSO : H$_2$O) to a 2 μL *E. coli* suspension in water on the stage of a confocal microscope and recorded the emergence of the fluorescence of qBODIPY upon the release of silver within the cellular matrix (Video S1, ESI†). As shown in Fig. 4, the green fluorescence of qBODIPY emerged from the initial dim background after 1 minute (Fig. 4A), and continued to increase in intensity with time (Fig. 4B–D§). These time-dependent frames clearly indicated that the entrance of **1** into the *E. coli* cells leads to deligation of the qBODIPY ligand, releasing the Ag$^+$ ion in the membrane as well as in the intracellular matrix. A blank experiment with the qBODIPY ligand itself (Video S2, ESI†) confirmed that the emergence of the green fluorescence in Fig. 4E through Fig. 4H is indeed connected to the presence of the free ligand either on the membrane of the bacterial wall(s) or within the intracellular space. It is important to note that the increase of fluorescence upon the addition of **1** was much less pronounced compared to the frames with an equivalent concentration of qBODIPY (compare Fig. 4D and H). This is expected as the silver complex **1** is stabilized by the chelation of the qBODIPY ligand, a fact that effectively decelerates the rate of dissociation of the Ag$^+$ ion from the complex. The delayed release of silver ions thus allows for a significant fraction of complex **1** to accumulate inside the bacterial cells before releasing the cytotoxic Ag$^+$ ions.

The antibacterial effects of Ag$^+$ released within the bacterial cells have also been evaluated in the present work. We studied the antibacterial effects of **1** and qBODIPY on *E. coli*, *P. aeruginosa*, and *S. aureus* at various concentrations to determine the minimum inhibitory concentration (MIC). In the case of *E. coli*, complex **1** showed a MIC value of 1 μM, a value comparable to silver nitrate (Fig. S3B and C, ESI†). For *P. aeruginosa*, complex **1** had a MIC of 2 μM while silver nitrate exhibited a MIC of 1 μM (Fig. S3E and F, ESI†). Finally for
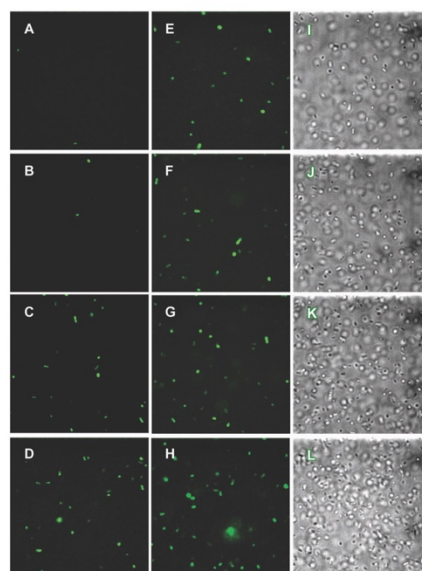
Fig. 4 Representative confocal micrographs (frames) of *E. coli* cells suspended in water after the addition of a (1 : 99 DMSO : H$_2$O) solution of **1**: (A) 1 min, (B) 3 min, (C) 6 min, and (D) 9 min. Corresponding confocal micrographs of *E. coli* cells suspended in water after the addition of an equivalent amount of qBODIPY: (E) 1 min, (F) 3 min, (G) 6 min, and (H) 9 min. Confocal bright field micrographs of *E. coli* cells suspended in water after the addition of **1**: (I) 1 min, (J) 3 min, (K) 6 min, and (L) 9 min.

S. aureus, complex **1** exhibited a MIC of 7 μM while silver nitrate had a MIC of 6 μM (Fig. S3H and I, ESI†). No effect on bacterial growth was observed with qBODIPY with concentration as high as 50 μM on all three bacterial strains (Fig. S3A, D and G, ESI†). It is thus apparent that the antibacterial effect arises solely from the Ag$^+$ released from **1** within the cell and not the qBODIPY ligand.

In conclusion, we have synthesized a silver complex **1** that exhibits strong fluorescence upon silver release (Video S4, ESI†). The strong fluorescence arising from the free ligand is almost completely quenched upon complexation to silver. This novel complex was used to track the delivery of silver to bacteria through turn-on fluorescence. Intracellular chloride and/or thiols appear to be responsible for the release of silver within the bacteria. The extent of eradication of *E. coli*, *P. aeruginosa*, and *S. aureus* by such silver delivery by **1** compares well with the antibacterial efficacy of silver nitrate. We anticipate that this novel complex can potentially be incorporated into a bandage material to treat burn wound infections with the advantage of real time tracking of silver release.

356

Notes and references

‡ Crystal data for **1**: $C_{31}H_{25}N_4O_6BF_8S_2Ag_2$, M_r = 992.22, monoclinic, $C2/c$, a = 26.8250(13) Å, b = 14.8903(7) Å, c = 22.4731(11) Å, β = 115.102(2), V = 8128.7(7) Å^3, T = 293 K, Z = 8, ρ_{calc} = 1.622 g cm^{-3}, μ(Mo-Kα) = 1.146 mm^{-1}, a total of 46 665 reflections in the range of $1.99 < \theta < 25.454$ were collected, of which 7509 were unique, final R indices ($I < 2\sigma(I)$) R_1 = 0.0471 mm^{-1}, wR_2 = 0.2462, GOF = 1.137. CCDC 1491751.
§ Confocal microscopy videos: https://drive.google.com/open?id=0B4D-uRVc73VvMVhZMXA2aXZZZUU.

1 H. Kresse, M. J. Beasley and H. Rovini, *Nat. Rev. Drug Discovery*, 2007, **6**, 19.
2 P. M. Wright, I. B. Seiple and A. G. Myers, *Angew. Chem., Int. Ed.*, 2014, **53**, 8850.
3 Y. Y. Liu, Y. Wang, T. R. Walsh, L. X. Yi, R. Zhang, J. Spencer, Y. Doi, G. Tian, B. Dong, X. Huang, L. F. Yu, D. Gu, H. Ren, X. Chen, L. Lv, D. He, H. Zhou, Z. Liang, J. H. Liu and J. Shen, *Lancet Infect. Dis.*, 2016, **16**, 161.

4 P. McGann, E. Snesrud, R. Maybank, B. Corey, A. C. Ong, R. Clifford, M. Hinkle, T. Whitman, E. Lesho and K. E. Schaecher, *Antimicrob. Agents Chemother.*, 2016, **60**, 4420.
5 J. A. Lemire, J. J. Harrison and R. J. Turner, *Nat. Rev. Microbiol.*, 2013, **11**, 371.
6 I. Chopra, *J. Antimicrob. Chemother.*, 2007, **59**, 587.
7 J. Liu, D. A. Sonshine, S. Shervani and R. H. Hurt, *ACS Nano*, 2010, **11**, 371.
8 S. Chernousova and M. Epple, *Angew. Chem., Int. Ed.*, 2013, **52**, 1636.
9 R. B. K. Wakshlak, R. Pedahzur and D. Avnir, *Sci. Rep.*, 2015, **5**, DOI: 10.1038/srep09555.
10 B. D. Glisic, L. Senerovic, P. Comba, H. Wadepohl, A. Veselinovic, D. R. Milivojevic, M. I. Djuran and J. Nikodinovic-Runic, *J. Inorg. Biochem.*, 2016, **155**, 115.
11 H. J. Klasen, *Burns*, 2000, **26**, 117.
12 T. R. deBoer, I. Chakraborty and P. K. Mascharak, *J. Mater. Sci.: Mater. Med.*, 2015, **26**, 242.
13 G. Ulrich, R. Ziessel and A. Harriman, *Angew. Chem., Int. Ed.*, 2008, **47**, 1184.
14 T. Kowada, H. Maeda and K. Kikuchi, *Chem. Soc. Rev.*, 2015, **44**, 4953.
15 R. Ziessel, C. Goze, G. Ulrich, M. Cesario, P. Retailleau, A. Harriman and J. P. Rostron, *Chem. – Eur. J.*, 2005, **11**, 7366.
16 H. Lu, S. S. Zhang, H. Z. Liu, Y. W. Wang, Z. Shen and C. G. J. Liu, *J. Phys. Chem. A*, 2009, **113**, 14081.
17 S. Singha, D. Kim, H. Seo, S. W. Cho and K. H. Ahn, *Chem. Soc. Rev.*, 2015, **44**, 4367.

357

Chapter 4.II: Incorporation of a Theranostic "Two-Tone" Luminescent Silver Complex into Biocompatible Agar Hydrogel Composite for the Eradication of ESKAPE Pathogens in a Skin and Soft Tissue Infection Model.

4.II.1 Background.

In recent years, infections caused by drug-resistant pathogens are a considerable cause of global morbidity and mortality, leading to major clinical and economic burden.[1–3] In particular, nosocomial infections caused by the notoriously pathogenic *Enterococcus faecium, Staphylococcus aureus, Klebsiella pneumoniae, Acinetobacter baumannii, Pseudomonas aeruginosa,* and *Enterobacter spp.* (*ESKAPE*) bacteria present a major therapeutic challenge due to their resistance to conventional antibiotics.[4–6] Skin and soft tissue infections (SSTIs) are among the most common type of concern with increasing rates of hospitalization and severities ranging from mild to lethal.[7,8] Although skin serves as a structural barrier, damage and breaks in the skin allow for the infection and colonization by a variety of pathogens.[8,9] Microbial invasion of the skin and underlying soft tissues are caused predominantly by *S. aureus*, and to a lesser yet considerable extent by *A. Baumannii* and *P. aeuroginosa*. Treatment of SSTIs caused by these pathogens is becoming increasingly difficult due to the emergence and rapid dissemination of drug-resistant strains in hospital settings.[9–13] *S. aureus* is a Gram-positive bacteria that breaks down tissue for nutrition during the course of infection by employing a variety of extracellular proteins such as hemolysins, proteases, and collagenases.[5] Over 95% of clinical isolates of *S. aureus* are resistant to

penicillin, and more than 50% are resistant to methicillin.[12,14] Infections caused by *P. aeruginosa* and *A. baumannii* are becoming increasingly prevalent, particularly in hospitals,[1,5–7,15] and are the principal pathogens responsible for chronic wound infections.[4,15] *P. aeuroginosa* is one of the most common Gram- negative drug-resistant pathogens encountered in SSTIs.[16] Strains of *P. aeruginosa* can be highly resistant against most or almost all current antibiotic chemotherapeutics and are often classified as "panresistant".[17] *A. baumannii* is another opportunistic and problematic Gram-negative bacteria found in hospital environments affecting immunocompromised individuals.[18] Resistant *A. baumannii* infections have also been reported by military service members injured in combat in Iraq and Afghanistan[19–21] exemplifying its persistence in dry inanimate environments for extended periods of time.[22] *A. baumannii* is of particular interest due to its inherent resistance to some Gram-negative antibiotics as well as rapid development of drug resistance to others.[23]

Systemic therapeutic options for SSTIs caused by resistant strains of bacteria are becoming extremely limited.[6,24] Accounts of resistance toward toxic "last-resort" antibiotics such as Carbapanem and Colistin (polymixin E) have already been reported globally.[3,25–27] Thus, development of new, safe, and effective antibiotic treatments for SSTIs is of paramount importance. Topical antimicrobial therapy provides an attractive route for the treatment of SSTIs compared to systemic antibiotic therapy.[7] High antimicrobial doses can be delivered directly to the site of infection, which avoids metabolic and enzymatic degradation (with associated side effects) and clearance by

the gastrointestinal tract. Topical delivery of antibiotics also increases patient compliance, convenience, and reduces treatment costs.

Silver has been used for the treatment of infections since ancient times, and it is currently utilized in a variety of consumer products, healthcare applications, and medical devices. Silver (metal, salts, nanoparticles, complexes) has gained interest as an antimicrobial agent due to its low toxicity to mammalian cells and its broad-spectrum activity against multidrug-resistant organisms.[28] Although the underlying bactericidal mechanisms of silver are poorly understood, silver cations (Ag^+) are known to disrupt biochemical processes in bacterial cells by interacting with thiol and amino groups on amino acid residues, proteins, nucleic acids, and cell membranes.[29,30] Because systemic administration of silver often produces adverse effects in humans, most silver therapies are confined to topical applications including prophylactic treatment for burn wounds and antimicrobial therapy for SSTIs.[29,31−33] Because of its reactive nature, silver tends to precipitate as an insoluble salt (AgCl) in the presence of chloride ions (blood plasma chloride concentration: 95−110 mM).[29] Thus, silver therapies require multiple applications and irrigations to maintain the infected area sterile. Topical application of silver sulfadiazine (Ag-SD) cream is an attractive way to treat SSTIs and burn wound infections. However, it also tends to adhere to the wound and leads to damage to newly epithelized surfaces during dressings and delay in wound healing.[32,34] Excessive topical use of silver may result in hypersensitivity, allergic contact dermatitis, erythema multiforme, and permanent undesirable aesthetic outcomes such as localized argyria.[35] A desirable wound dressing therefore needs to

deliver the minimum yet effective dose of silver to an affected area while allowing painless application and easy removal of the bandage.

In this chapter we discuss two fluorescent silver complexes [Ag$_2$(DSX)$_2$(NO$_3$)$_2$] **1** and [Ag$_2$(DSX)$_2$](CF$_3$SO$_3$)$_2$ **2** (DSX = 5-(dimethylamino)-N,N- bis(pyridin-2-ylmethyl) naphthalene-1-sulfonamide) suspended in a soft agar hydrogel for the topical delivery of silver to selected members of *ESKAPE* bacteria that account for the majority of SSTIs. The complex **1**−agar composite material can be cast into any shape or form and has a strong luminescence with a considerable hypsochromic shift (50 nm) upon the release of Ag$^+$. The "two-tone" luminescence displayed by the free ligand and the silver complex allows one to determine the antimicrobial effect of silver ions combined with a visual signal that indicates the extent of drug (Ag$^+$) delivered and pro-drug (the metal complex) remaining in the bandage. As a consequence, the complex **1**−agar composite material is a "theranostic" agent for convenient use in SSTI infection. The qualitative fluorescence beacon of the composite that notifies the need for a bandage change is a special advantage; such a signal notifies the exact time to change the wound dressing, thus eliminating arbitrary replacement of bandages, reducing exposure of open wounds, and minimizing patient discomfort. The complex **1**−agar composite hydrogel has been tested for its antibacterial efficiency in "bacterial suspension" SSTI models and shown to be very effective against two strains of multidrug-resistant *P. aeruginosa*, one strain of *S. aureus*, and one strain of *A. baumannii*. The material demonstrated prolonged antimicrobial inhibition zones superior to ampicillin and silver

nitrate controls. Additionally, because of the softness and malleability of the hydrogel, this material can be used as a prophylactic for burn wound infections.

4.II.2 Results and Discussion.

*4.II.2.1   Synthesis   and   Characterization   of   [Ag$_2$(DSX)$_2$(NO$_3$)$_2$]   **1**   and [Ag$_2$(DSX)$_2$](CF$_3$SO$_3$)$_2$ **2**.*

The synthesis of the ligand DSX was performed according to literature procedures and obtained in high yield and purity.[36] The microcrystalline powder was mixed with equimolar amounts of silver nitrate (complex **1**) or silver trifluoromethane sulfonate (complex **2**) in a 1:4 methanol/chloroform mixture. The solvent system was chosen such that, upon reduction of solvent volume at decreased pressure, the complex would remain in a mixture of mostly chloroform for ease of isolation. All reactions were performed under low levels of light to avoid potential decomposition of the precursor silver salts. Both complexes were isolated as microcrystalline yellow powders after recrystallization, which were analyzed satisfactorily. Single crystals were obtained by layering hexanes over a solution of the complex in dichloromethane (DCM). The resulting yellow-green single crystals were then characterized by conventional spectroscopy and X-ray diffraction (XRD). Infrared (IR) spectroscopy was used to confirm the presence of the nitrate or trifluoromethane sulfonate counterion in the respective complex (Figures 4.II.1 and 4.II.2).
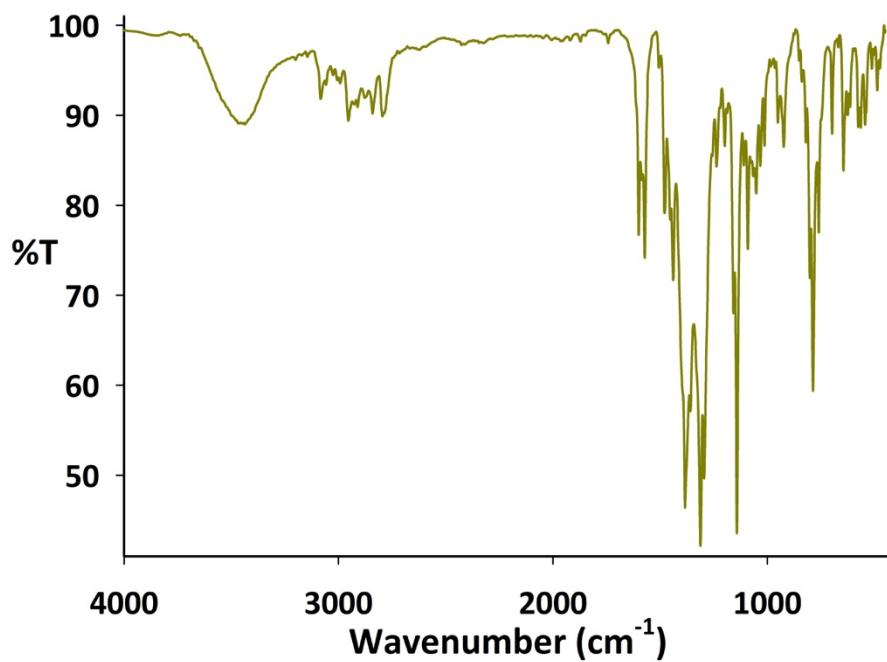
Figure 4.II.1. Infrared spectrum of $[Ag_2(DSX)_2(NO_3)_2]$ **1**.
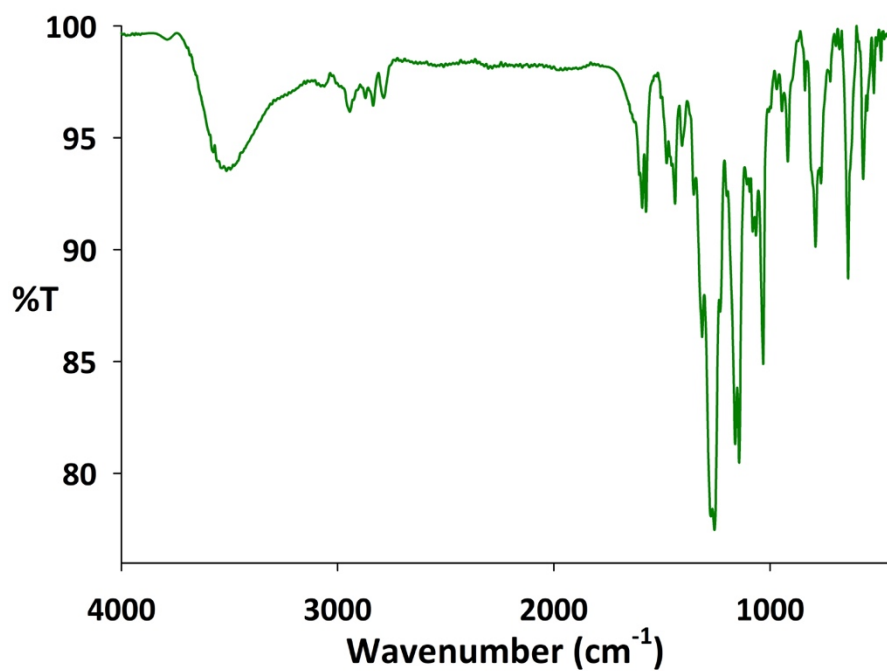
Figure 4.II.2. Infrared spectrum of $[Ag_2(DSX)_2](CF_3SO_3)_2$ **2**.

4.II.2.2 X-Ray Structure Determination and Refinement.

Single-crystal analysis revealed the molecular structures for both complexes. The perspective view with atom labeling scheme for the two structures is shown in Figures 4.II.3 and 4.II.4. Selected bond parameters are also listed in the figure captions. For both structures, only half of the formula unit is present in the asymmetric unit, with
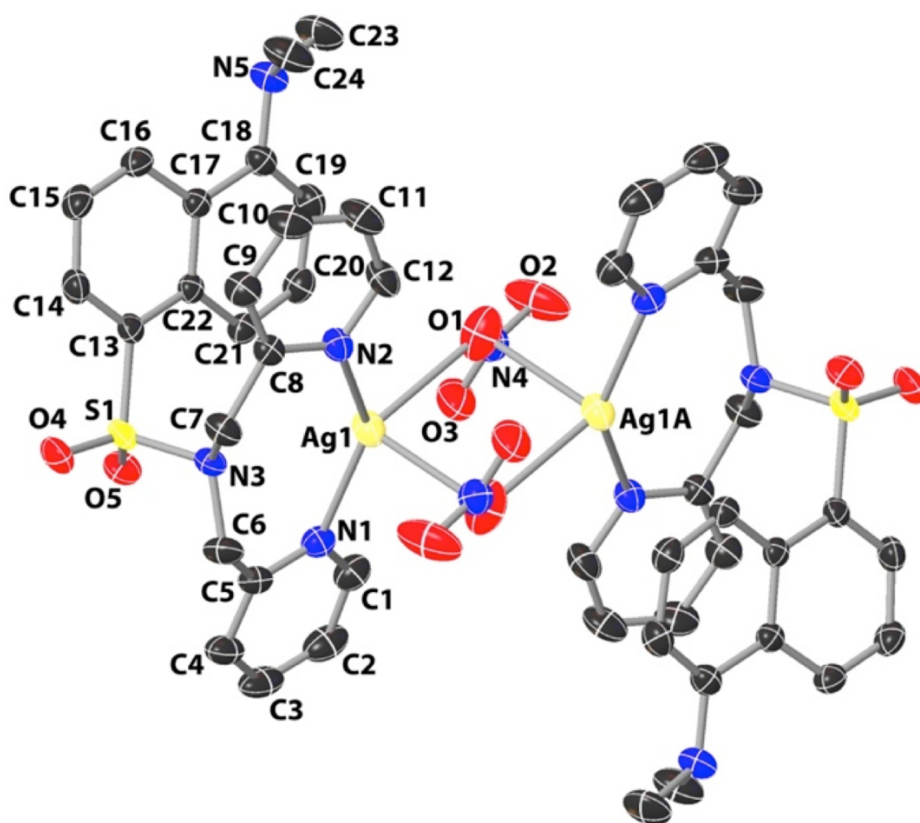
Figure 4.II.3. Perspective view of the molecular structure of complex **1**. The thermal ellipsoids are shown at 50% probability level (H atoms are omitted). Selected bond distances (Å): Ag1−N1, 2.259(2); Ag1−N2, 2.2922(2); Ag1−O1, 2.542(2); Ag1···Ag1A, 3.853(3) and angles (deg): N1−Ag1−N2, 137.31(7); N1−Ag1−O1, 132.33(8); N2−Ag1−O1, 90.08(8).
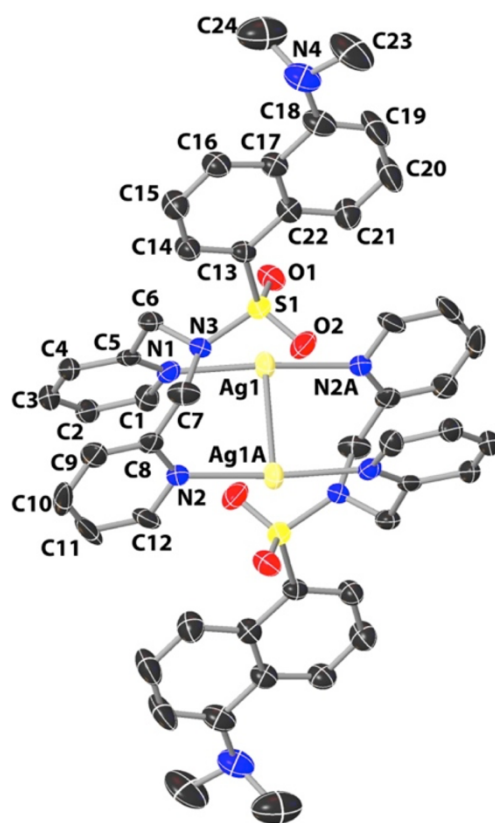
Figure 4.II.4. Perspective view of the molecular structure of the cation of complex **2**. The thermal ellipsoids are shown at 50% probability level (H atoms are omitted). Selected bond distances (Å): Ag1−N1, 2.171(6); Ag1A−N2, 2.180(6); Ag1−Ag1A, 3.2151(13); and angles (deg): N1−Ag1−N2A, 170.1(2); N1−Ag1−Ag1A, 90.79(16); N2A−Ag1−Ag1A, 91.65(16).

the other half consisting of symmetry equivalent atoms. The geometry around the metal centers in complexes **1** and **2** is quite distinctive. In case of **1**, each Ag(I) center resides in a distorted tetrahedral coordination environment, where the metal center is coordinated to two pyridine N atoms from the DSX ligand and two O atoms from the two shared μ_2-NO$_3$ ligands. In case of **2**, each Ag(I) center resides in a quasi linear

coordination environment, where each metal center is coordinated to two pyridine N atoms from two different DSX ligands.

Inspection of the metric parameters of the two structures clearly indicated that average Ag-N bond length (2.276 (3) Å) in complex **1** is noticeably longer compared to that in complex **2** (2.176 (6) Å). In complex **1**, Ag⋯Ag distance suggested moderate argentophilic interaction between the Ag(I) centers, while in complex **2**, the Ag⋯Ag distance (3.2151 Å) is considerably below the sum of van der Waals radii of the two Ag ions (3.40 Å) indicating strong interaction between the metal centers. In **1**, the two μ_2-nitrate ligands act as bridges between the two Ag(I) centers forming the central O_2NO- Ag⋯Ag$-ONO_2$ motif. Careful scrutiny of the Cambridge Structural Database (CSD) indicated that this motif is quite sparse in Ag(I) chemistry with few exceptions that are mostly limited to multinuclear Ag clusters.[37] Although there are reported examples of dinuclear Ag complexes with similar coordination sphere as complex **2**, in majority of those system the stronger Ag⋯Ag interactions have been forced by the ligand structure. In those cases, pyrolidintate,[38] formamidinate,[39] and similar types of ligand frames are employed with suitable geometry that favors metal-metal bond formation. There are only a few examples that are analogous with ligand type utilized for synthesizing complex **2**. For example, few Ag_2 complexes isolated from a family of triazole-based flexible ligands have similar structures as **2**. However, in those cases, the intramolecular Ag⋯Ag distances are quite long (spanning the range of 5.76-7.36 Å).[40] A simple dinuclear complex, namely, $[Ag_2(Pic)_4]^{2+}$ (where Pic = β-picoline) has also been found to comprise coordination geometry much like **2**.[41] In this case Ag-Ag

interaction is much stronger (Ag-Ag bond length, 3.1226 (13) Å), while the Ag-N distances and N-Ag-N angle are fairly comparable to those in **2**.

Examination of the packing pattern of **1** shows several nonclassical hydrogen nonbonding contacts, which consolidated the extended structure (Figure 4.II.5 and 4.II.6). These interactions mainly comprised of C−H···O hydrogen bonding involving the pyridine ring and the bridging nitrate ligand (C2−H2···O2, with C···O, 3.358(4) Å[i]; C2−H2···O3, with C···O, 3.431(4) Å[i]; C3−H3···O2, with C···O, 3.464(4) Å[ii], C7−H7···O4, with C··· O, 3.028(4) Å; C12−H12···O1, with C···O, 3.226(4) Å, C14−H14···O4, with C···O, 2.818(3) Å; C20−H20···O3, with C···O, 3.248(4) Å, C21−H21···O5, with C···O, 3.082 (3) Å. Symmetry codes: (i) −x + 2, −y + 1, −z and (ii) x + 1, y − 1, z).
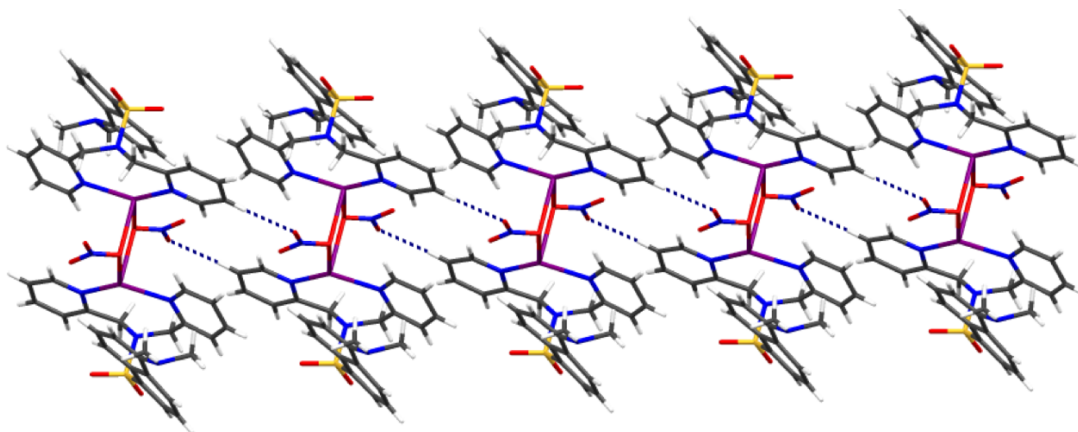
Figure 4.II.5. Packing pattern of **1** along *b* axis displaying the C-H···O intermolecular interactions.
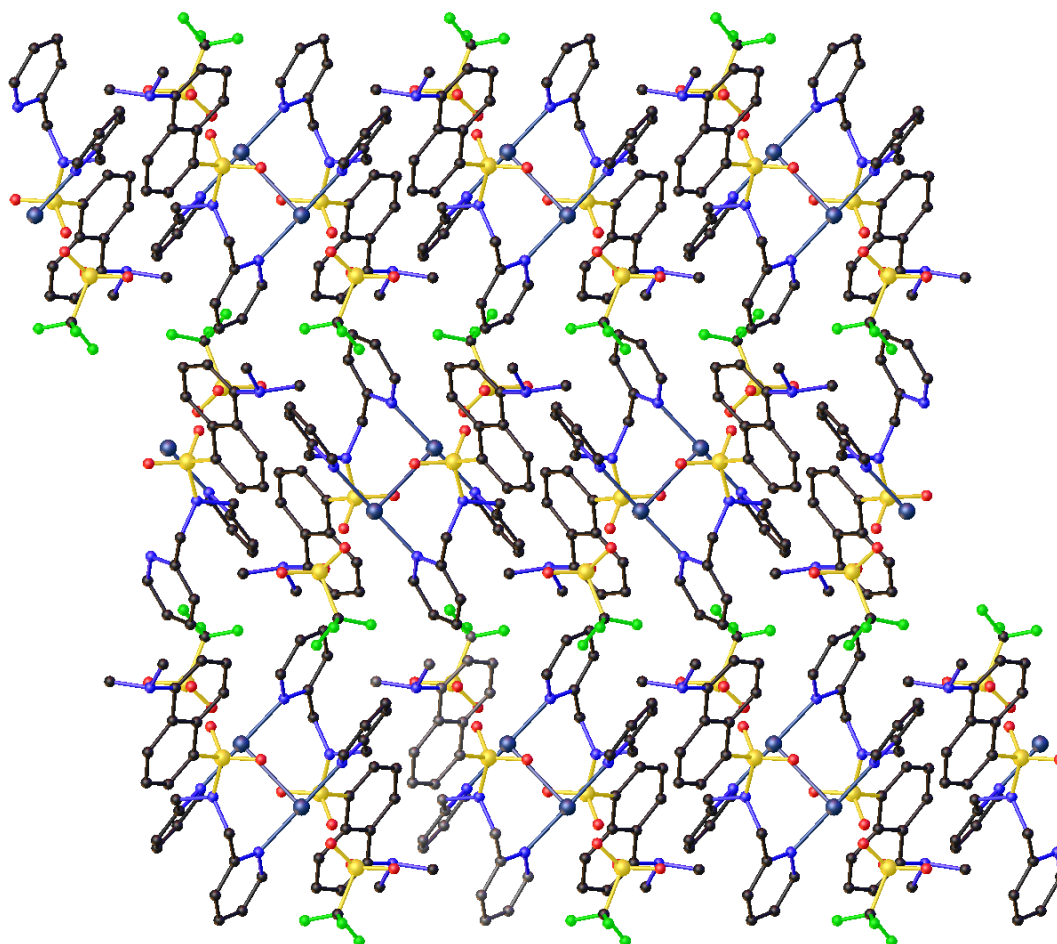
Figure 4.II.6. Packing pattern of **1** along *c* axis.

In case of **2**, C−H···O, C−H···N, and C−H···F hydrogen bonding involving the pyridine rings and the triflate anions and Ag···O(triflate) nonbonding interactions consolidated the extended network (Figure 4.II.7 and 4.II.8). Several C−H···O and C−H···N nonbonding contacts are found from the analysis of the extended structure of **2** (C1− H1···O2, with C···O, 3.012(10) Å[i]; C4−H4···O3, with C···O, 3.348(12) Å[ii]; C6−H6···O1, with C···O, 2.899(9) Å; C6−H6··· O2, with C···O, 3.548(12) Å[ii];
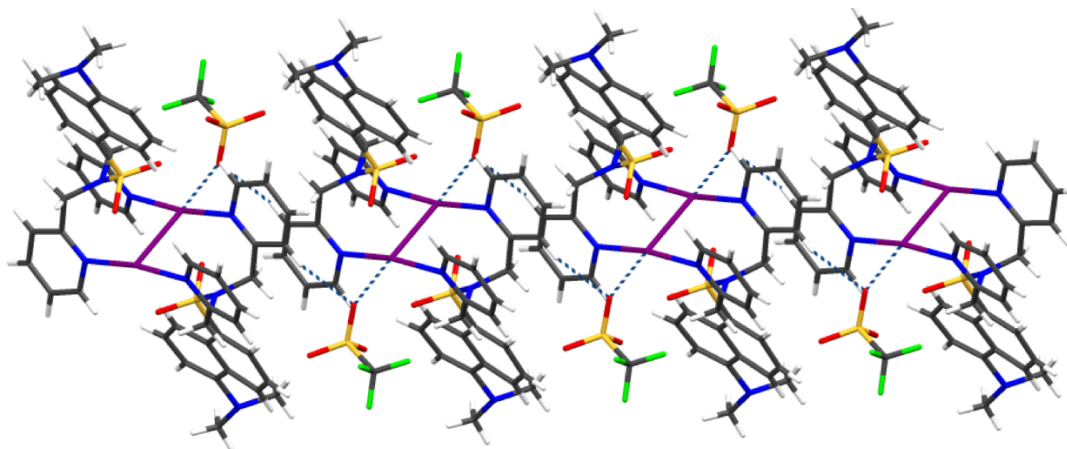
Figure 4.II.7. Packing pattern of **2** along *c* axis displaying the relatively stronger C-H···O and Ag···O intermolecular interactions (only very crucial nonbonding contacts are shown for the sake of clarity).

C7−H7···O2, with C···O, 2.908(10) Å; C11−H11···O3, with C···O, 3.362(12) Å^{iii}; C12−H12···O1, with C···O, 3.309(10) Å^{i}; C14−H14···N3, with C···N, 3.010(11) Å; C16−H16···N4, with C···N, 2.845(12); C24−H24···F3, with C···F, 3.163(16) Å^{iv}; symmetry codes: (i) −x + 1,−y,−z+1,(ii)−x+1,−y+1,−z+1,(iii)x,−y+1/2,z+ 1/2, (iv) −x + 1, y + 1/2, −z + 1/2). The triflate anions are in appropriate position to exhibit moderate Ag···O nonbonding interactions (2.792(5) Å), and they also contributed toward particular arrangements of the molecules within the lattice. Structural analysis also revealed significant face-to-face intermolecular and intramolecular π−π stacking interactions in **1** and **2**, respectively (Figures 4.II.7 and 4.II.8).
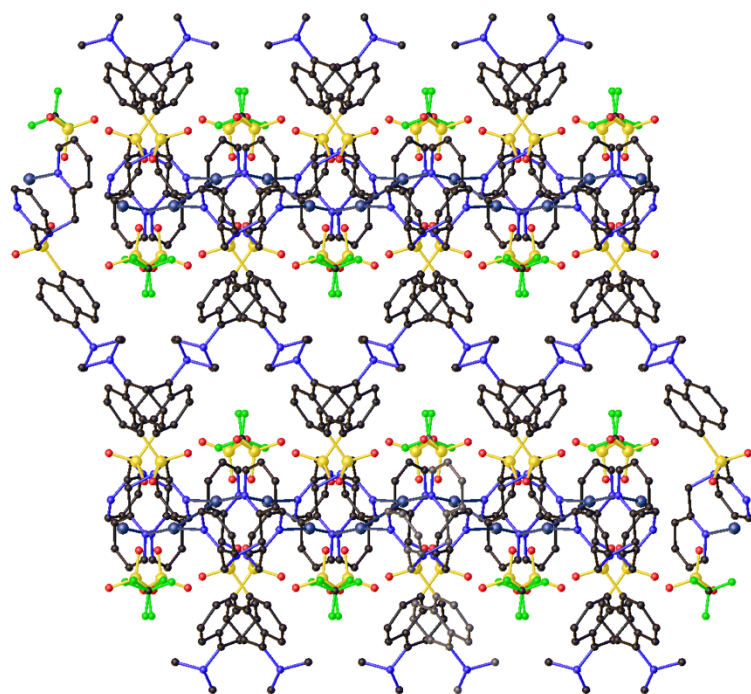
Figure 4.II.8. Packing pattern of **2** along *b* axis.
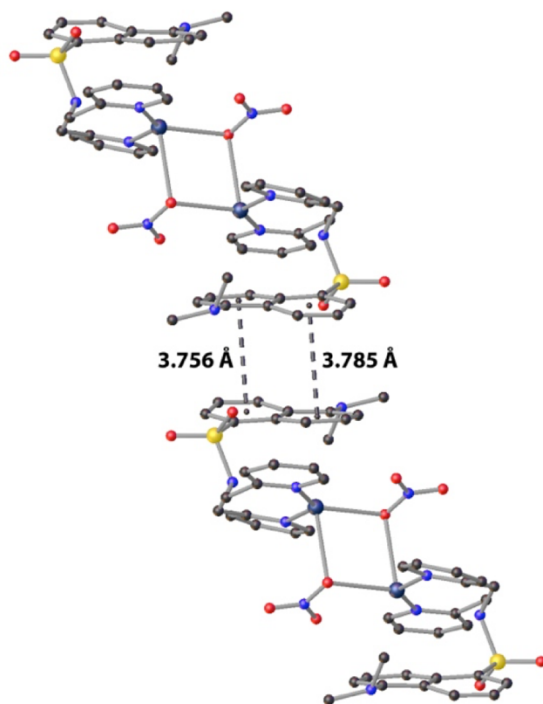
Figure 4.II.9. Intermolecular π -π stacking interactions in **1**.
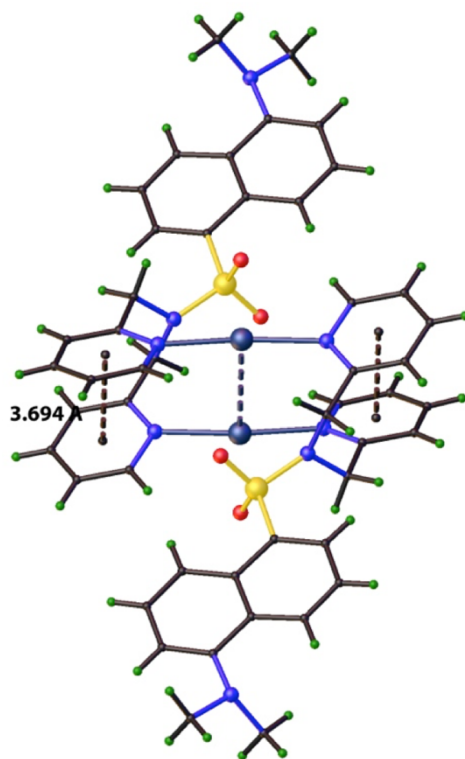
Figure 4.II.10. Intramolecular π -π stacking interactions in **2**.

4.II.2.3 Luminescence Characteristics of DSX, Complex 1, and Complex 2.

The dansyl-appended ligand DSX was selected for the present study primarily because of its excellent luminescence and biocompatibility. Additionally, this ligand with (dimethylamino)naphthalene sulfonamide moiety is known to exert relatively low toxicity in LX-2 and HepaRG hepatic cell lines (EC_{50} of 114 ± 4.6 and 73 ± 5.7 μM, respectively).[36] Finally, the pyridine N atoms are expected to readily coordinate to silver. The luminescence of DSX is centered at 505 nm in DCM. Upon complexation to silver, the fluorescence exhibits a bathochromic shift of 20 nm for **1** (λ max = 525 nm; Figure 4.II.11). The luminescence of DSX also exhibits modest quenching upon
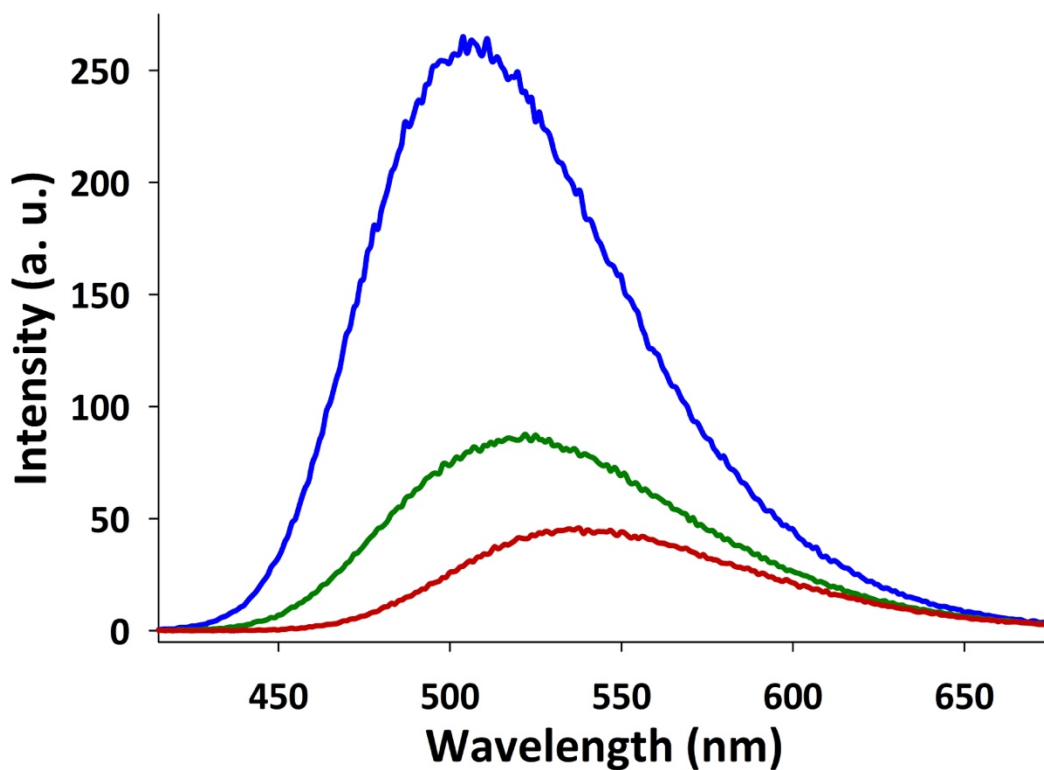
Figure 4.II.11. Fluorescence spectra of DSX (blue), [Ag$_2$(DSX)$_2$(NO$_3$)$_2$] **1** (green), and [Ag$_2$(DSX)$_2$](CF$_3$SO$_3$)$_2$ **2** (red) in DCM.

coordination, similar to its manganese analogue.[36] When suspended in water, DSX exhibits a hypsochromic shift of 50 nm (λ_{max} = 455 nm) relative to its fluorescence in DCM. Complex **1** also exhibits a hypsochromic shift of 20 nm (λ_{max} = 505 nm) in aqueous suspension (Figure 4.II.12). Therefore, a total of 70 nm shift is observed between complex **1** and free DSX ligand. The increase in fluorescence intensity of **1** in aqueous media and the hypsochromic shift most possibly arise from breakdown of the

\
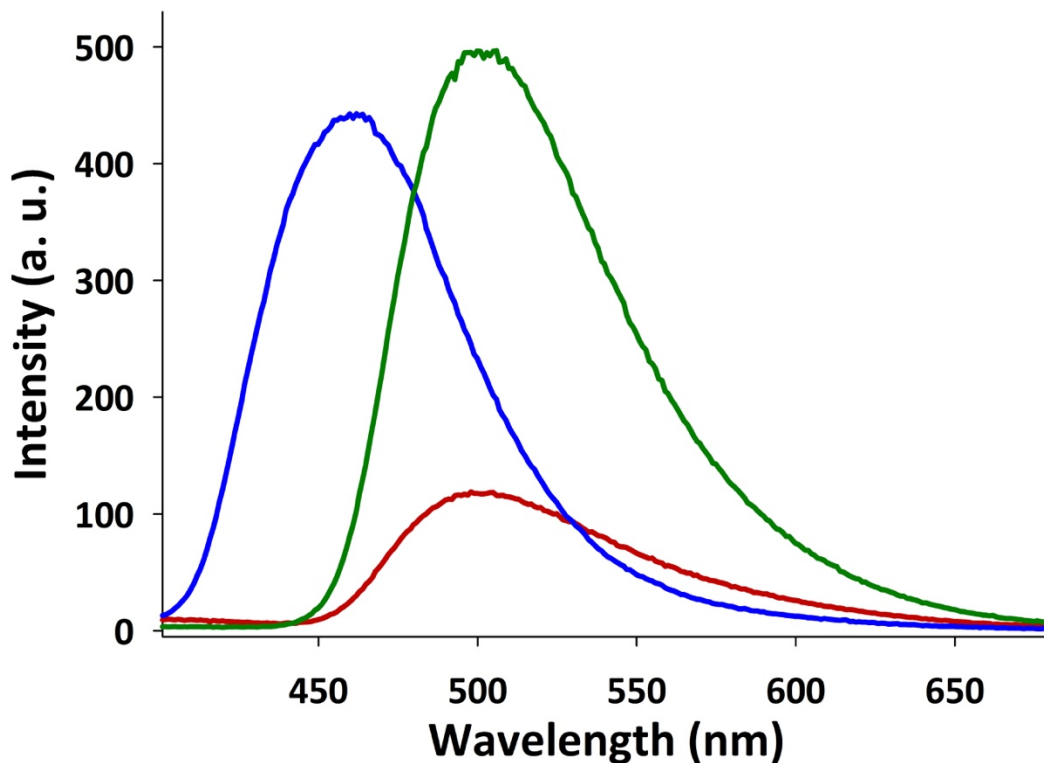
Figure 4.II.12. Luminescence spectra of DSX (blue), $[Ag_2(DSX)_2(NO_3)_2]$ **1** (green), and $[Ag_2(DSX)_2](CF_3SO_3)_2$ **2** (red) in aqueous suspension.

nitrate bridge in highly dissociative medium. Indeed, the electrospray ionization-mass spectrometry (ESI-MS) spectra of both complexes (run in methanol) exhibit the $[Ag(DSX)]^+$ ion as the prominent one. Because complex **2** did not afford a good suspension in aqueous solution, we did not study its fluorescence behavior further.

*4.II.2.4 Stability of Complexes **1** and **2** in Chloride Containing Solutions.*

The stability of complexes **1** and **2** was investigated in solution as well as in solid state. Because chloride ions are abundant in human blood and tissue (blood plasma $[Cl^-] = 95-110$ mM, tissue $[Cl^-] \approx 10$ mM) use of silver as antimicrobial could result in the precipitation of the Ag^+ as AgCl. To investigate the stability of the complexes in the presence of chloride ions, **1** and **2** were dissolved in DCM and were treated with tetra-n-butylammonium chloride (n-Bu$_4$N$^+$Cl$^-$). DCM was chosen as the solvent, since both complexes are insoluble in water. The solutions were prepared individually from concentrated stocks to maintain identical concentrations of the complex under investigation. Addition of 0.1 equiv increments of $^\wedge$-Bu$_4$N$^+$Cl$^-$ to 1 equiv of complex **1** resulted in an increase and hypsochromic shift of fluorescence (Figure 4.II.13). This is attributed to the release of the free ligand. Upon addition of 1 equiv of chloride to complex, the luminescence reached a maximum intensity that matched the fluorescence of the free ligand at identical concentration (Figure 4.II.13, black trace). This indicates that, in solution, complex **1** readily releases Ag^+ ions in the presence of chloride. In a similar manner, complex **2** releases silver at the same rate as complex **1** in the presence of chloride (Figure 4.II.14).

To improve the release rate of Ag^+ from the complexes in the presence of chloride ions, we decided to estimate the release rate of Ag^+ from powdered samples suspended in aqueous solutions. Since complex **1** exhibits the largest bathochromic shift in aqueous suspensions (50 nm, Figure 4.II.12), its stability in an aqueous
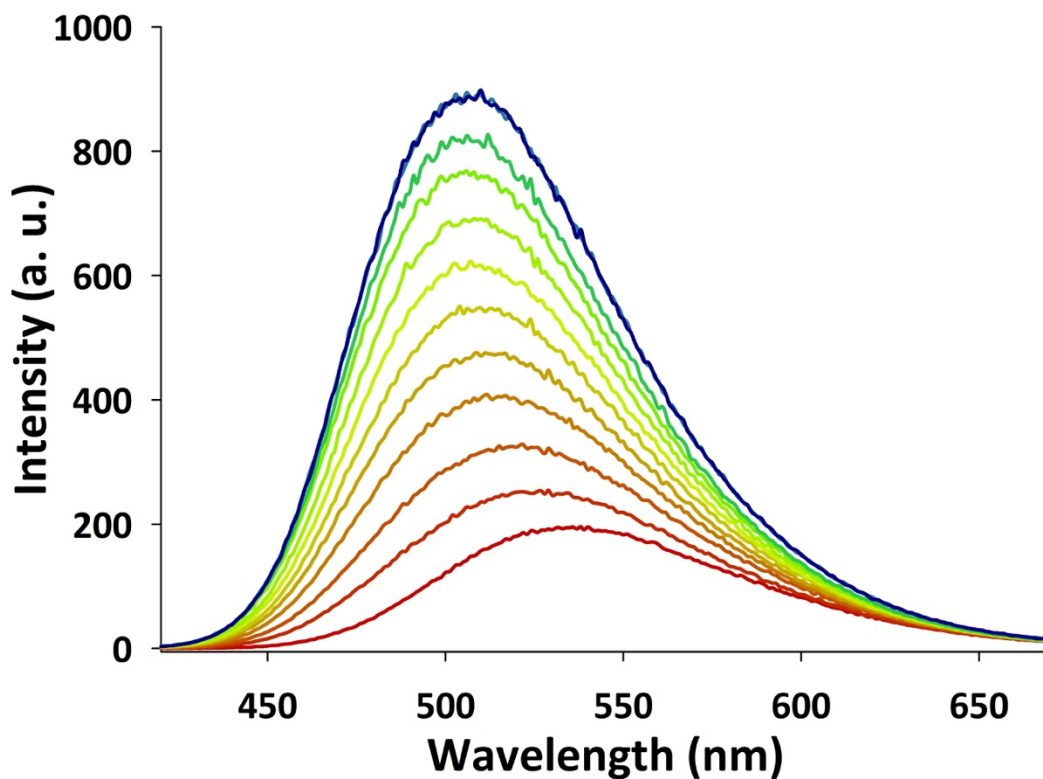
Figure 4.II.13. Fluorescence increase through subsequent addition of 0.1 mol equiv of *n*-Bu$_4$N$^+$Cl$^-$ to a DCM solution of [Ag$_2$(DSX)$_2$(NO$_3$)$_2$] **1**.

suspension was checked in the presence of chloride. Interestingly, 1 molar equiv of chloride produced negligible loss of silver when **1** was suspended in water, even after a few hours. This can be attributed to the fact that Ag$^+$ can only be released from the surface of the powdered sample in such cases. The stability of **1** was investigated against an isotonic saline solution containing [NaCl] = 154 mM. A decrease in fluorescence was observed immediately upon addition of aqueous chloride to the
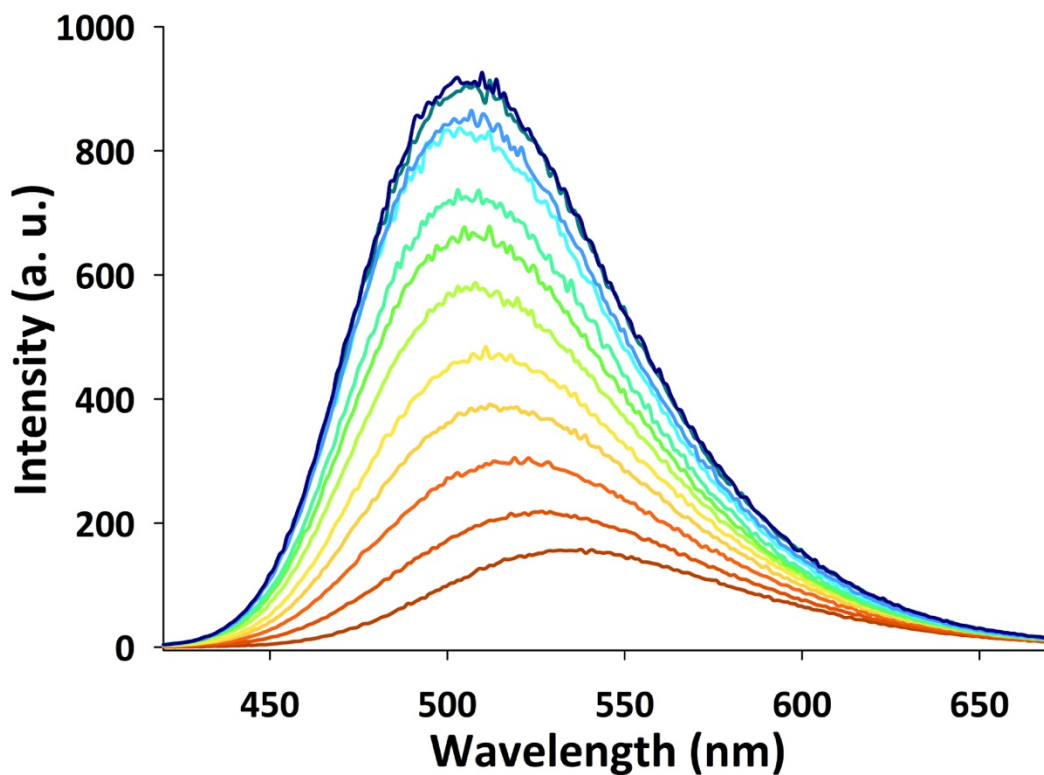
Figure 4.II.14. Fluorescence increase through subsequent addition of 0.1 mol equiv of *n*-Bu$_4$N$^+$Cl$^-$ to a DCM solution of [Ag$_2$(DSX)$_2$](CF$_3$SO$_3$)$_2$ **2**.

suspension of complex **1** (Figure 4.II.15) presumably due to initial coagulation of the fine particles. The sample was then stored at room temperature in the dark, and its fluorescence was measured after 2, 4, 8, 12, and 24 h (Figure 4.II.15) following sonication (to obtain a homogeneous suspension). The high chloride concentration led to precipitation of both AgCl and some free DSX on the side of the cuvette. Nevertheless, a clear green to blue color change was observed (Figure 4.II.15, compare
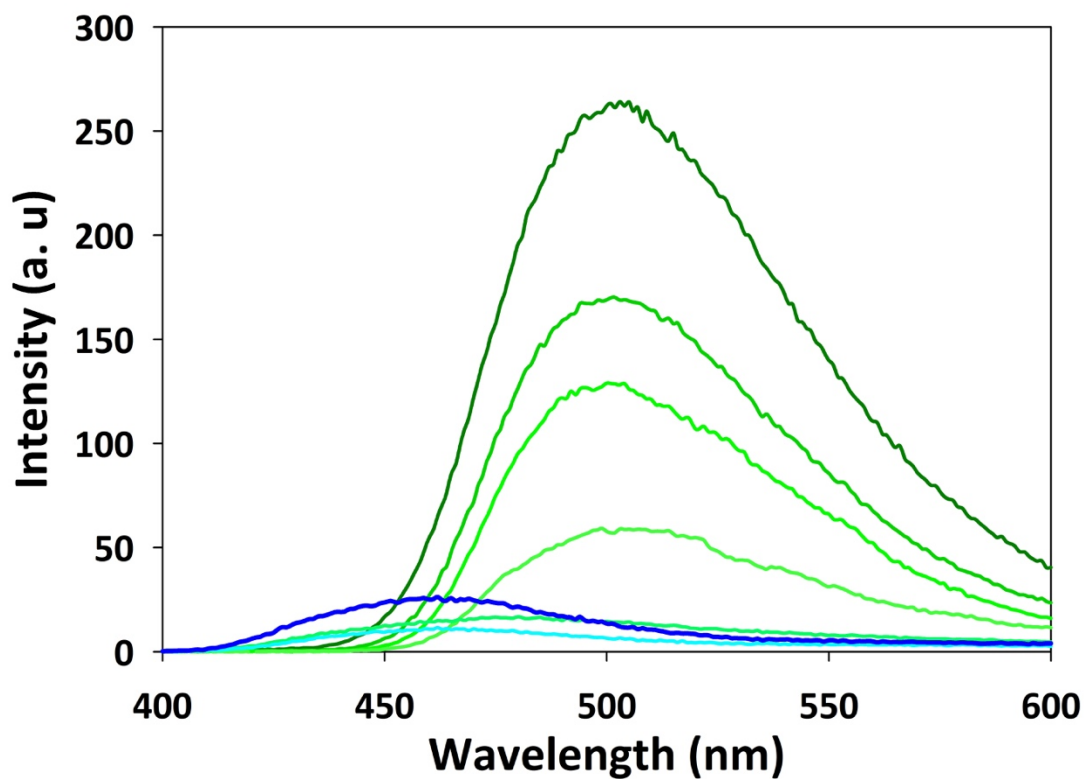
Figure 4.II.15. Silver release profile from a suspension of complex **1** incubated in an isotonic aqueous chloride solution ([Cl$^-$] = 154 mM) for 0, 2, 4, 8, 12, and 24 h.

the blue and the green traces). This experiment confirmed that Ag$^+$ releases slowly from solid particles of **1** in the presence of high chloride concentration and that a green-to-blue color change can be observed as an indicator of the silver release. The stability of **2** as a suspension was not investigated, because **2** does not exhibit such a distinct color change in suspension.

*4.II.2.5 Complex **1**-Agar ([Ag$_2$(DSX)$_2$(NO$_3$)$_2$]-Agar) Hydrogel Composite Material.*

A variety of polymeric hydrogels were considered as delivery vehicles. Since silver salts and complexes are sensitive to both light and oxidation, it was necessary to use a material that could be easily constructed under mild conditions. The use of radical initiators, high temperatures, or materials that contained functional groups interacting strongly with silver were avoided. It is important to note that the wound dressing material needs to be relatively inert toward the complex and have minimal affinity for Ag$^+$. In principle, a slowdown of Ag$^+$ by material may help to deliver the therapeutic for extended periods of time to the infected area. Rapid release of Ag$^+$ may help clear proximal bacterial loads but will also result in quick depletion of the antimicrobial from the bandage material and therefore requiring multiple changes. Conversely, if the hydrogel interacts too strongly with Ag$^+$, enough therapeutic will not be released to elicit the bactericidal effect. The application and removal of the bandage must also be taken into consideration, since some antibiotics, such as silver sulfadiazine, may stick to the newly epithelized skin layer. Removal of these dressings may reopen the wound, delaying the healing process.[32,34]

Bacteriological-grade agarose gel was selected as the drug carrier for the present antimicrobial experiments due to its well-known biocompatibility, softness, mechanical strength, stability, moisture retention, and cost effectiveness. [Ag$_2$(DSX)$_2$(NO$_3$)$_2$] **1** was selected for the antimicrobial experiments due to its moderate silver release profile and an excellent color change upon silver loss. We decided to incorporate the complex into the hydrogel matrix as a suspension, to take

advantage of the significant hypsochromic shift in fluorescence upon silver release as shown in Figure 4.II.15. Using the complex in the solid state also results in a relatively slow and sustained release of Ag^+. The percentage of agar used was optimized to produce a low gelling temperature (40-45 °C); the use of high temperatures (<60 °C) results in the decomposition of complex **1** as well as other silver salts and antibiotics used as controls. The resulting complex **1**-agar composite material contained 0.01% (w/v) **1** and exhibited yellow-green fluorescence (Figure 4.II.16a and 4.II.16b). This material is stable for over one month at 4 °C, and upon silver release, its blue fluorescence is identical to an agar disk containing the free ligand (Figure 4.II.16c). This appearance of the blue fluorescence thus indicates an expended material (time for
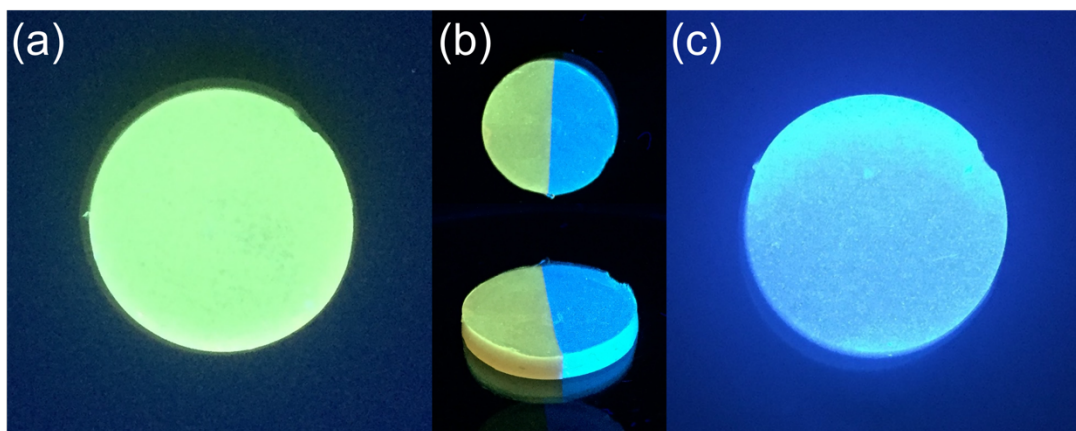
Figure 4.II.16. Composite material containing (a) $[Ag_2(DSX)_2(NO_3)_2)]$ **1**, (b) two half disks of complex **1** and DSX joined together for contrast and clarity, and (c) free DSX ligand (after silver release).

change). A color change in the bandage material will definitely minimize untimely and repeated changes of wound dressings and patient discomfort, while keeping the wound free of opportunistic microbes. The spent complex **1**−agar can be easily removed from an infected area by pouring fresh water over it. This occlusive material can also absorb moisture from wound exudate and can be cast, cut, or molded into any shape or form. The resulting complex **1**-agar composite material was tested for its silver release profile in water using flame atomic absorption spectrophotometry (Figure 4.II.17). Small
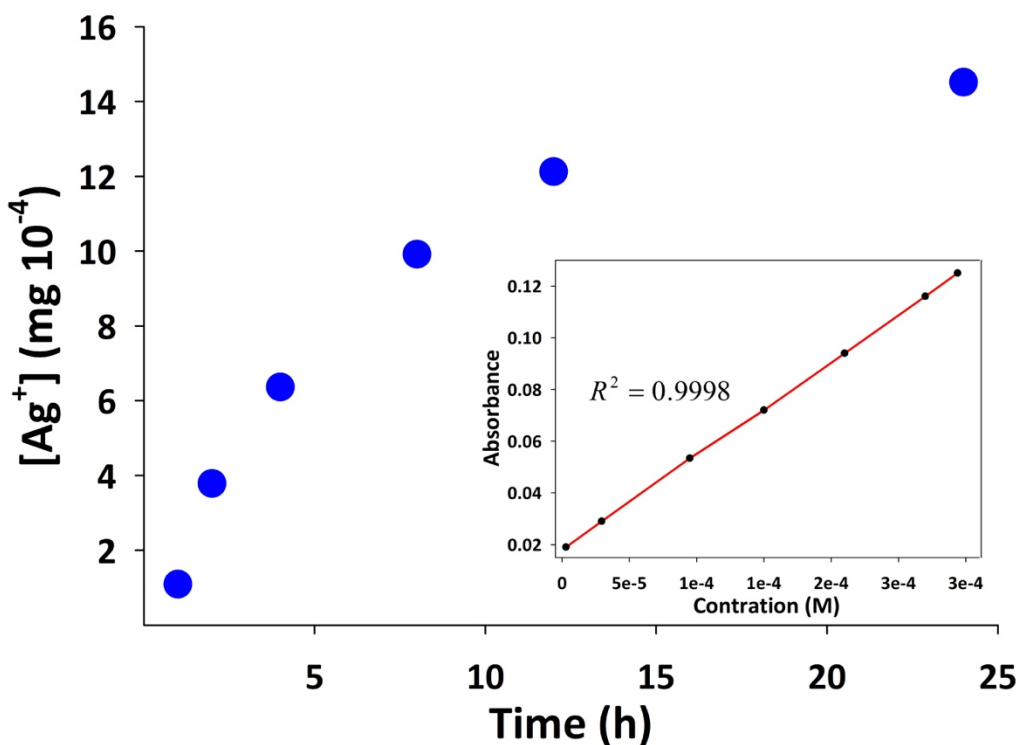
Figure 4.II.17. Leaching of Ag$^+$ from the Complex **1**-agar composite material in water analyzed by flame atomic absorption spectrophotometry.

381

pieces (100 mg each) of the silver (0.01% Ag) containing disks were individually incubated for 0, 1, 2, 4, 8, 12, or 24 h in 1 mL of water. After the incubation time was reached, the material was removed, and the solution was analyzed for silver content using flame atomic absorption spectrophotometry. The results indicated that the release of silver into solution occurs faster at the beginning of the incubation period. It was observed that the release rate of Ag^+ ions decreased as time progressed, and the total amount of Ag^+ released into water in 24 h was 81%. This may be attributed to partitioning of Ag^+ between the solution and the material at equilibrium. The complex **1**−agar composite material that was used for the 24 h incubation was digested in nitric acid, and optical analysis revealed that the remaining 19% of the Ag^+ remained in the material. The leftover silver can help keep the dressing sterile after the main therapeutic load is released, preventing the spread of infection from handling the discarded bandage material.

4.II.2.6 Skin and Soft Tissue Infection(SSTI) Model.

The "bacterial suspension" SSTI model that was used in the present work was fabricated by using procedure reported by this laboratory.[42,43] In short, the SSTI model is composed of a soft brine agar layer inoculated with the microbe of interest ($>1 \times 10^5$ CFU mL^{-1}) plated over a modified nutrition-rich agar layer. The soft agar allows for mobility, growth, and colonization of the microbes similar to a human SSTI. The nutrition gradient of the model promotes bacterial penetration into the modified nutrient agar, resulting in gradients of oxygen availability and metabolic activity of the

microbes similar to what is observed in SSTI. The SSTI model addresses some of the limitations of standard antibiotic susceptibility tests that are normally performed under ambient oxygen conditions.[44] Pathogens responsible for SSTIs infect the dermis and epidermis9 and not the surface of the skin, which is primarily composed of dead cells. Standardized methods test the antimicrobial efficacy of a drug on surface-exposed bacteria and do not account for effects in deeper tissues. SSTIs have a wide range of clinical manifestations and severity.[4,8] Uncomplicated SSTIs are normally superficial (dermis), often resolve on their own, and can be treated with systemic antibiotic therapy.[4,8] If left untreated, some SSTIs can spread to subcutaneous tissue, fascia, and muscle.[4,9] Neglected SSTIs may lead to the formation of metastatic abscesses, bacteremia, necrotizing fasciitis, or sepsis, which often require surgical intervention and thus are limb- and life-threatening.[4,8,9] Additionally, standardized antimicrobial tests do not take into account oxygen availability in deeper tissues, which may impact the efficacy of certain antibiotics.[44] Studies have shown that low oxygen levels decrease the susceptibility of *S. aureus* and *P. aeruginosa* to certain antibiotics such as *β*-lactams.[44] Since oxygen is an essential nutrient to aerobic bacteria, decreased oxygen availability results in attenuated growth, which reduces antimicrobial susceptibility to drugs that target metabolic and/ or other processes during growth.[45-48]

4.II.2.7 Bactericidal Assays Using Complex 1-Agar.

The antimicrobial efficiency of the complex **1**–agar composite material was tested against one clinical isolate of *S. aureus*, two clinical isolates of multi drug-

resistant (MDR) *P. aeruginosa*, and one *A. baumannii* (NCIMB 12457) strain. These microbes are the predominant species that account for the majority of SSTIs.[1,5−7,15] The soft agar was inoculated with a specific microbe (>1 × 10^5 CFU mL^{-1}), plated over a nutrient-rich agar, and incubated for 1 h to allow the bacteria to adhere and form cell-to-cell contacts. The complex **1**–agar hydrogel wound dressings were fabricated fresh and placed on top of the SSTI model after the initial incubation period. Air bubbles trapped between the SSTI and the agar disks were carefully removed to ensure full contact of both materials. Control agar-composite materials containing no compound, free ligand, and ampicillin were constructed under identical conditions and molar equivalency to silver. Freshly prepared agar disks (3 × 25 mm) and individual SSTI plates (100 mm) were used for each of the experiments. The SSTI models together with the agar disk were incubated for 18 h at 37 °C to allow the bacteria to grow. All bacterial experiments were performed in triplicate at the minimum to ensure consistent and reproducible results.

The experimental results are presented in Figures 4.II.18 through 4.II.21. A full and uniform bacterial lawn was produced in all plates. All of the materials tested, with the exception of the composites containing complex **1**, exhibit growth of bacteria leading up to the border of the agar disk. The bacteria penetrate deep into the SSTI model to reach the subsurface source of nutrients. The delivery of silver from the agar composite material could be easily tracked qualitatively through fluorescence (Figure 4.II.22). This feature allowed to determine the end point of the incubation period, and consistently indicated the presence and delivery of Ag$^+$ to the SSTI model.
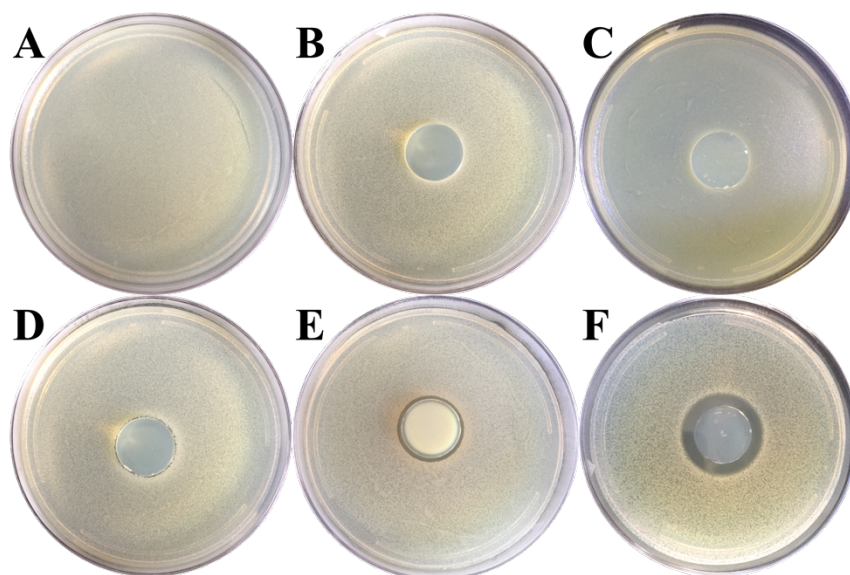
Figure 4.II.18. Results obtained from bactericidal tests against *A. baumannii* using composite materials. (a) blank, (b) blank agar, (c) DSX ligand, (d) ampicillin, (e) AgNO$_3$, (f) complex **1**.
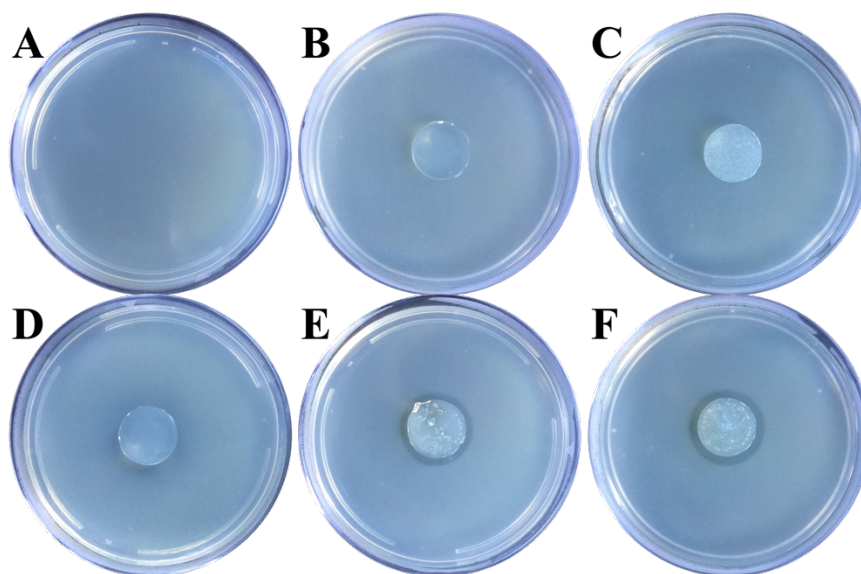
Figure 4.II.19. Results obtained from bactericidal tests against *P. aeruginosa* 1 using composite materials. (a) blank, (b) blank agar, (c) DSX ligand, (d) ampicillin, (e) AgNO$_3$, (f) complex **1**.
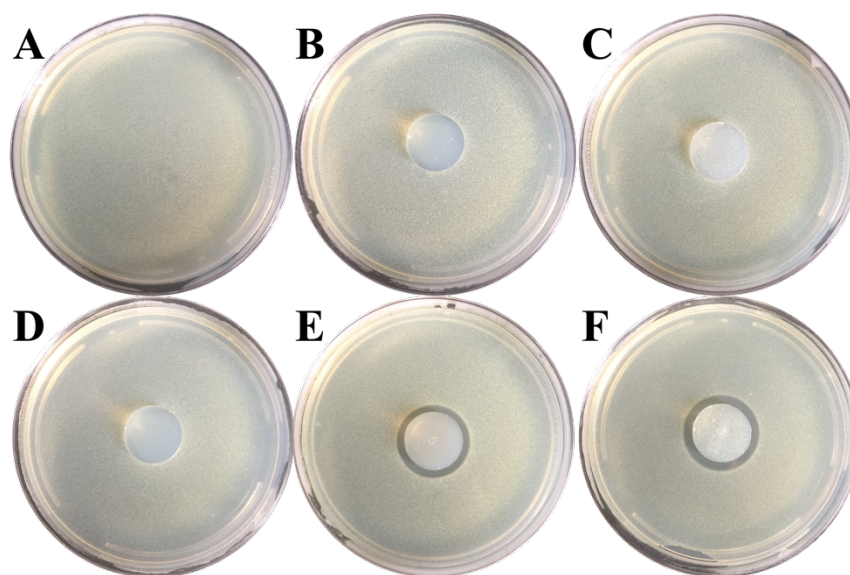
Figure 4.II.20. Results obtained from bactericidal tests against *P. aeruginosa* 2 using composite materials. (a) blank, (b) blank agar, (c) DSX ligand, (d) ampicillin, (e) AgNO₃, (f) complex **1**.
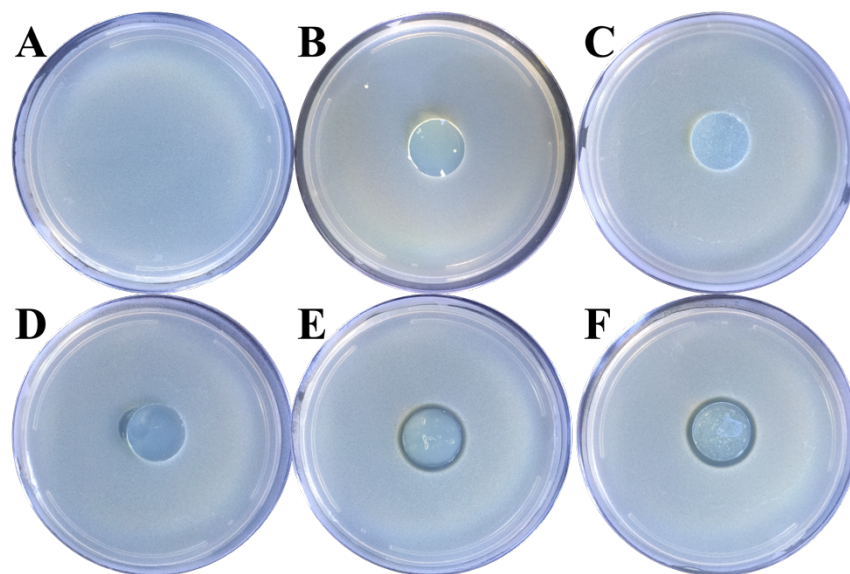
Figure 4.II.21. Results obtained from bactericidal tests against *S aureus* using composite materials. (a) blank, (b) blank agar, (c) DSX ligand, (d) ampicillin, (e) AgNO₃, (f) complex **1**.
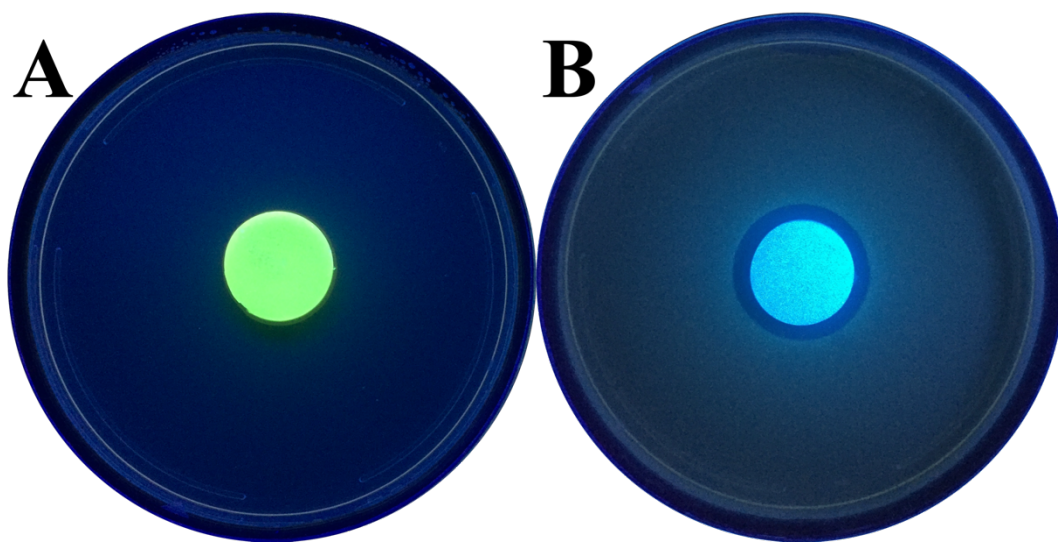
Figure 4.II.22. Representative example of luminescence tracking of silver delivery. The release of Ag$^+$ from the Complex **1**-agar composite material can be qualitatively followed through fluorescence. (a) Composite material loaded with complex **1**, (b) composite material after Ag$^+$ release (exhibiting zone of inhibition).

In all bacterial strains, the complex **1**−agar composite material exhibited a clear zone of inhibition of bacterial growth. The size of the inhibition zone is relatively compact due to the slow/sustained release of Ag$^+$ ions from the powder encapsulated inside the agar hydrogel. After overnight incubation, the complex **1**−agar composites were removed from the SSTI models, and the zones of inhibition were individually tested for viable bacteria. Silver delivery by the complex **1**−agar composite disks afforded zones of inhibition that are clear of bacteria throughout the entire depth of the SSTI models. No growth was observed upon inoculation of fresh media with the agar located throughout the entire depth of the zone of inhibition. The complex **1**−agar

composite material yielded zones of inhibition of 29.8 ± 0.3, 30.8 ± 0.3, 31.4 ± 0.2, and 37.0 ± 0.3 mm for *S. aureus*, *P. aeruginosa* 1 (*P*1), *P. aeruginosa* 2 (*P*2), and *A. baumannii*, respectively (Figures 4.II.18F through 4.II.21F). Bacterial strains of *P. aeruginosa* 1 (*P*1) and *P. aeruginosa* 2 (*P*2) exhibited similar zones of inhibition produced by the complex **1**−agar disk (Figures 4.II.19F and 4.II.20F, respectively). This is an interesting finding, since both these Gram-negative pathogens have similar patterns of resistance toward antibiotics. Finally, the largest zones of inhibition were observed for *A. baumannii* NCIMB 12457. Collectively, these results suggest that silver is an effective treatment for drug-susceptible and drug-resistant infections caused by the Gram-positive and Gram-negative SSTI *ESKAPE* pathogens.

In the present study, *S. aureus* exhibited no zone of inhibition when an ampicillin-loaded agar disk was used as a control. This was not surprising, since the majority of clinical isolates of *S. aureus* are resistant to penicillin and its derivatives. Both clinical isolates of *P. aeruginosa* (*P*1 and *P*2) were also resistant to ampicillin. In each case, presence of bacteria was confirmed upon inoculation of fresh media with agar located beneath the ampicillin disk. Interestingly, a small zone of partial inhibition (<25.8 mm) was observed for *A. baumannii* strain (Figures 4.II.18D through 4.II.21D). Nevertheless, bacterial growth was observed after inoculation of fresh growth media with material from the resulting zone of inhibition of *A. baumannii* in this experiment.

When the $AgNO_3$-agar and control disks were removed after the initial incubation period (24 h) and the SSTI model was further incubated for another 24 h, not surprisingly, all bacterial strains were able to resume growth in the zones previously

covered by the control hydrogel material (Figure 4.II.23). As expected, the density of

the bacterial load inside this area appeared visually lower, relative to areas that were
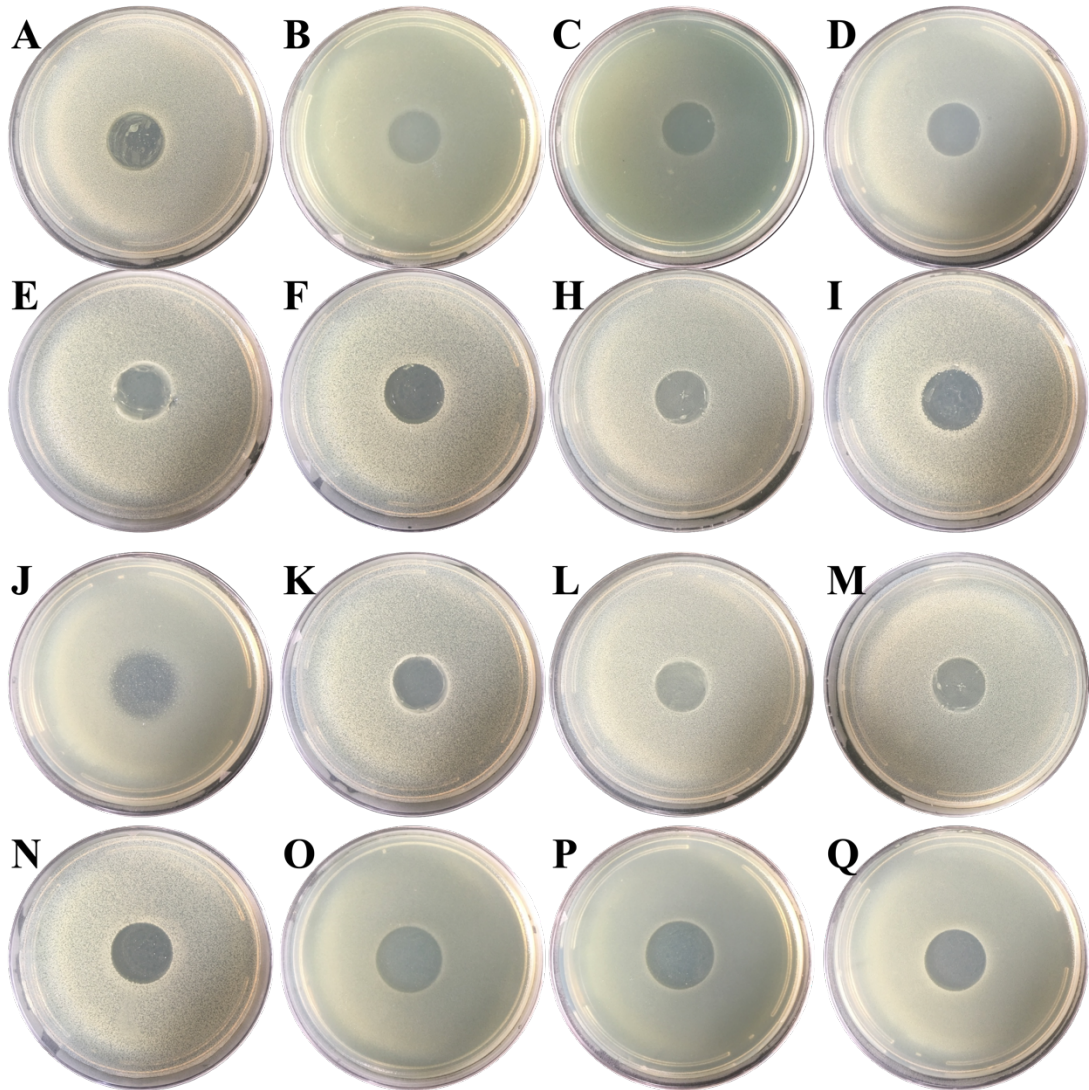
Figure 4.II.23. Zones of inhibition after removal of composite materials and incubation

for an additional 48 h. (A row) blank agar, (E row) DSX ligand, (J row) ampicillin, (N

row) complex **1**-agar, (A column) *A. baumannii*, (B column) *P. aeruginosa* 1, (C

column) *P. aeruginosa* 2, (D column) *S. aureus*.

not previously covered. However, no bacterial growth was observed in the zone of clearance exerted by the complex **1**−agar composite material (containing complex **1**), even after 48 h (Figure 4.II.12N-Q). This suggests that enough Ag^+ was delivered to the SSTI model to maintain the zone of inhibition sterile for an extended period of time. It is known that silver-killed microbes can become a reservoir of silver. The slow release of Ag^+ from dead bacteria can then exert bactericidal activity on viable bacteria, known as the "zombies effect,"[49] and can account for the prolonged antibacterial activity observed (Figure 4.II.23 N-Q).

Control experiments using $AgNO_3$-agar hydrogels were performed to compare the efficiency of complex **1**. Incorporation of $AgNO_3$ into the material was in fact quite challenging. Solutions of $AgNO_3$ exhibited low tolerance for heated agar relative to the suspension of **1**. The silver salt exhibited signs of decomposition if the agar solution was not cooled below 45 °C prior to mixing, whereas complex **1** was able to tolerate temperatures greater than 50 °C. Prolonged exposure to light also resulted in the decomposition of the $AgNO_3$ composite. Antibacterial experiments performed with silver nitrate disks produced small zones of inhibition (26.8 ± 0.2 mm) relative to complex **1** (Figure 4.II.18E and 4.II.18F). Upon overnight incubation on top of the SSTI model the $AgNO_3$−agar disk turned greyish-white, indicative of AgCl formation (Figure 4.II.18E). The results indicate that such precipitation interferes with the Ag^+ ion-induced killing resulting in smaller zones of inhibition. Contrary to this behavior,

the material fabricated with complex **1** is more stable and efficient in sustained release of Ag+ with minimum interference from chloride (Figure 4.II.18F). Incorporation of **1** as a powdered solid suspended in agar clearly makes the composite an excellent source for slow and sustained silver release.

4.II.3 Conclusions.

Development of new and advanced therapies for the treatment and prevention of SSTIs by drug-resistant bacteria is of paramount importance. Traditional silver antibiotic therapies have proved effective toward eradication of drug-resistant pathogens. However, most of these therapies require the excessive use of silver salts, as well as arbitrary/periodic bandage changes. The present complex 1−agar composite material described above performs exceptionally well against the predominant ESKAPE pathogens responsible for SSTIs. In addition to its bactericidal efficacy, the material also bears a fluorescent beacon that indicates the amount of drug (Ag+) or prodrug (complex 1) present in the material. Apart from excellent antibacterial effects, this composite can be fabricated easily, and it is both biocompatible and cost-effective. Besides treatment of SSTIs, the reported material can find useful applications in the treatment of chronic wound infections and as prophylactic treatment for burn wound infections.

4.II.4 Experimental.

4.II.4.1 General Materials and Methods.

All chemicals, solvents, and reagents were obtained from commercial suppliers and were used without further purification unless stated otherwise. All syntheses were performed using standard Schlenk techniques. Preparations involving precursor silver salts were performed under dim light to avoid decomposition. All organic solvents used were distilled in triplicate. The ligand 5-(dimethylamino)-N,N-bis(pyridin-2-ylmethyl) naphthalene-1-sulfonamide (DSX) was synthesized in high yield as a white powder following the literature procedure.[36] IR spectra were obtained using a PerkinElmer Spectrum One FT-IR Spectrometer. UV−Vis spectra were recorded using a Varian Cary 50 UV−vis spectrophotometer. Fluorescence spectra were obtained with an Agilent Cary Eclipse Fluorescence spectrophotometer. ^{1}H NMR spectra were recorded using a Varian 500 (500 MHz) spectrometer. Atomic absorption data was recorded using a PerkinElmer AAnalyst 100 Flame Atomic Absorption Spectrometer. Ultrapure water (Milli-Q, 18.2 MΩ cm) was obtained from a NANOpure Diamond water purification system. High- resolution ESI-MS data were recorded on an LTQ-Orbitrap Velos Pro MS instrument. Two multidrug-resistant clinical strains of *P. aeruginosa* (identified by sensitivity testing performed by drug dilution using Gram-negatives panels on the BD Phoenix or e-tests; Figures 4.II.24 and 2.II.25) and one clinical strain of *S. aureus* (Figure 4.II.26) were obtained from the Microbiology Laboratory of UCSD Health. The strain of *A. baumannii* (NCIMB 12457) was obtained from the UCSC Chemical Screening Center.

P. aeruginosa #1

		Pseudomonas aeruginosa Not Specified	
Amikacin	>32 mcg/mL	Resistant [1]	
Aztreonam	>16 mcg/mL	Resistant [1]	
Cefepime	>16 mcg/mL	Resistant [2]	
Ceftazidime	>16 mcg/mL	Resistant [2]	
Ciprofloxacin	>2 mcg/mL	Resistant [2]	
Colistin	1 mcg/mL	Susceptible [1]	
Doripenem	>2 mcg/mL	Resistant [2]	
Gentamicin	>8 mcg/mL	Resistant [1]	
Meropenem	>8 mcg/mL	Resistant [2]	
Piperacillin/Tazobactam	>64 mcg/mL	Resistant [3]	
Tobramycin	>8 mcg/mL	Resistant [1]	
Trimethoprim/Sulfamethoxazole	>2/38 mcg/mL	Resistant [3]	

[1] Low risk of C. diff infection
[2] HIGH risk of C. diff infection
[3] MODERATE risk of C. diff infection

Susceptibility

Figure 4.II.24. Sensitivity pattern for *P. aeruginosa* 1 (*P*1) clinical isolate obtained from UCSD Health.

Pseudo #2

Ph.D.   San Diego CA 92121

		Pseudomonas aeruginosa (mucoid) Not Specified	
Amikacin	>32 mcg/mL	Resistant [1]	
Aztreonam	>16 mcg/mL	Resistant [1]	
Cefepime	>16 mcg/mL	Resistant [2]	
Ceftazidime	>16 mcg/mL	Resistant [2]	
Ciprofloxacin	2 mcg/mL	Intermediate [2]	
Doripenem	>2 mcg/mL	Resistant [2]	
Gentamicin	>8 mcg/mL	Resistant [1]	
Meropenem	>8 mcg/mL	Resistant [2]	
Piperacillin/Tazobactam	>64 mcg/mL	Resistant [3]	
Tobramycin	8 mcg/mL	Intermediate [1]	

[1] Low risk of C. diff infection
[2] HIGH risk of C. diff infection
[3] MODERATE risk of C. diff infection

Figure 4.II.25. Sensitivity pattern for *P. aeruginosa* 1 (*P*2) clinical isolate obtained from UCSD Health.

Amp / Pcu		Not Specified	
Cefazolin		<=2 mcg/mL	Susceptible [1]
Clindamycin		<=0.5 mcg/mL	Susceptible [1]
Daptomycin		<=1 mcg/mL	Susceptible [2]
Erythromycin		<=0.5 mcg/mL	Susceptible [3]
Linezolid		2 mcg/mL	Susceptible [2]
Minocycline		<=1 mcg/mL	Susceptible [2]
Oxacillin		0.5 mcg/mL	Susceptible [3]
Rifampin		<=0.5 mcg/mL	Susceptible [2]
Tetracycline		<=0.5 mcg/mL	Susceptible [2]
Trimethoprim/Sulfamethoxazole		<=0.5/9.5 m...	Susceptible [3]
Vancomycin		1 mcg/mL	Susceptible [2]

[1] HIGH risk of C. diff infection
[2] Low risk of C. diff infection
[3] MODERATE risk of C. diff infection

) and Collection

Figure 4.II.26. Sensitivity pattern for *S. aureus* clinical isolate obtained from UCSD Health.

*4.II.4.2 Synthesis of [Ag$_2$(DSX)$_2$(NO$_3$)$_2$] **1**.*

The ligand DSX (100 mg, 0.23 mmol) was dissolved in chloroform (40 mL), followed by the dropwise addition of a methanolic solution (10 mL) of silver nitrate (39 mg, 0.23 mmol). The mixture was stirred magnetically at room temperature overnight under dark conditions. The volume of the resulting clear yellow solution was reduced under low pressure until a yellow precipitate was formed. The mixture was then cooled at 0 °C for 2 h, and the resulting product was collected through vacuum filtration. The yellow powder was recrystallized from DCM/hexanes (1:1) to afford **1** in 95% yield (151 mg, 0.22 mmol) as a microcrystalline yellow-green powder. Anal. Calcd for C$_{48}$H$_{48}$Ag$_2$N$_{10}$O$_{10}$S$_2$: C, 47.85; H, 4.02; N, 11.63. Found: C, 47.49; H, 4.08; N, 11.77%. 1H NMR (500 MHz, CDCl3): δ 8.34 (m, 3H), 8.05 (d, 1H), 7.80 (d, 1H),

7.68 (m, 3H), 7.28 (m, 3H), 7.16 (m, 3H), 4.65 (s, 4H), 2.90 (s, 6H). Selected IR (KBr

disk, cm^{-1}) 1600, 1572, 1479, 1439, 1383, 1312, 1295, 1142, 787.

Figure 4.II.27. Electronic absorption spectrum of [Ag$_2$(DSX)$_2$(NO$_3$)$_2$] **1** in DCM.
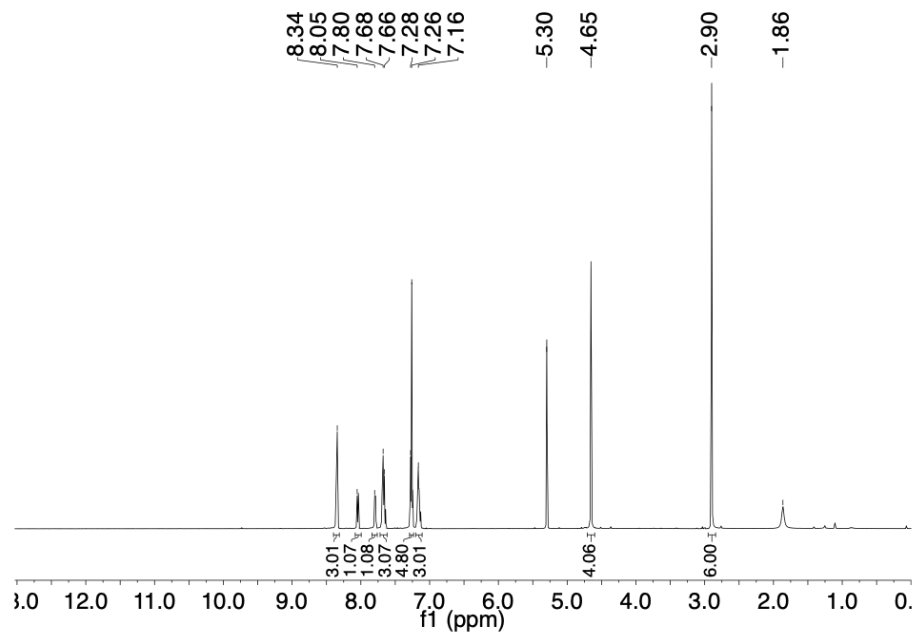
Figure 4.II.28. ^{1}H-NMR (CDCl$_3$) spectrum of [Ag$_2$(DSX)$_2$(NO$_3$)$_2$] **1**.

395

*4.II.4.3 Synthesis of [Ag₂(DSX)₂](CF₃SO₃)₂ **2**.*

The synthesis of **2** was performed using the same procedure used for the preparation of complex **1**, while employing AgCF$_3$SO$_3$ (59 mg, 0.23 mmol) as the silver salt. Yield: 91% (129 mg, 0.21 mmol) of **2** as a microcrystalline yellow powder. Anal. Calc for C$_{50}$H$_{48}$Ag$_2$N$_8$O$_{10}$S$_4$F$_6$: C, 43.55; H, 3.51; N, 8.13. Found: C, 43.59; H, 3.45; N, 8.17%. ^{1}H NMR (500 MHz, CDCl$_3$): δ 8.44 (d, 2H), 8.34 (d, 1H), 8.07 (d, 1H), 7.85 (d, 1H), 7.73 (m, 3H), 7.32 (m, 3H), 7.17 (m, 3H), 4.67 (s, 4H), 2.91 (s, 6H). Selected IR (KBr disk, cm^{-1}) 1591, 1573, 1439, 1314, 1256, 1161, 1142, 1031, 789.

Figure 4.II.29. Electronic absorption spectrum of [Ag₂(DSX)₂](CF₃SO₃)₂ **2** in DCM.
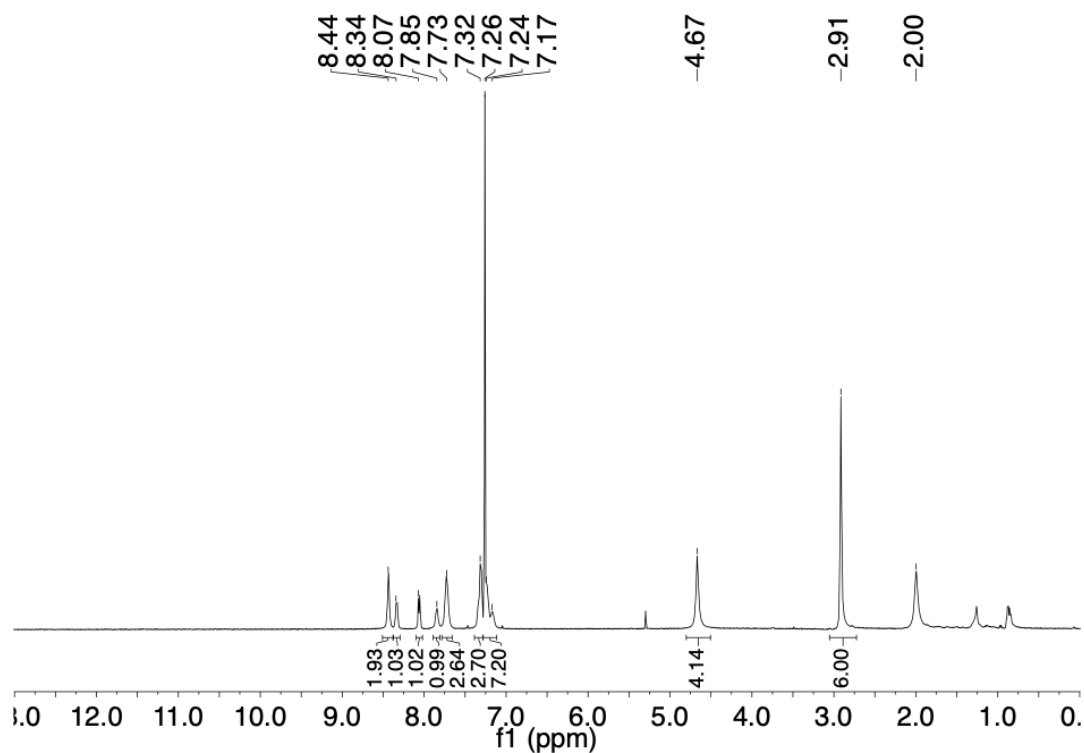
Figure 4.II.30. ^{1}H-NMR (CDCl$_3$) spectrum of [Ag$_2$(DSX)$_2$](CF$_3$SO$_3$)$_2$ **2**.

4.II.4.4 X-Ray Diffraction and Structure Refinement.

Light yellow and colorless block-shaped crystals of complexes [Ag$_2$(DSX)$_2$(NO$_3$)$_2$] **1** and [Ag$_2$(DSX)$_2$](CF$_3$SO$_3$)$_2$ **2**, respectively, were obtained by recrystallization through diffusion of hexanes into their respective DCM solutions. In both cases, a suitable crystal was selected and mounted on a Bruker D8 Quest diffractometer equipped with PHOTON 100 detector operating at T = 298 K. Data were collected with ω shutterless scan technique using graphite monochromated Mo Kα radiation (λ = 0.71073 Å). The total number of runs and images for both data collections was based on the strategy calculation from the program APEX3 (Bruker).[50] The

397

maximum resolution achieved was $\theta = 28.3°$ for **1** and $\theta = 25.1°$ for **2**. Cell parameters were retrieved using the SAINT (Bruker) software[51] and refined using SAINT (Bruker) on 9969 reflections for **1** and on 6594 reflections for **2**. Data reduction was performed using the SAINT (Bruker) software, which corrects for Lorentz polarization. The final completeness is 99.4% out to 28.3° in θ for **1** and 99.7% out to 25.1° in θ for **2**. Multi-scan absorption corrections were performed with both data sets using SADABS 2016/2.52 The absorption coefficient for **1** is 0.98 mm^{-1} and for **2** is 0.84 mm^{-1}; the minimum and maximum transmissions for **1** are 0.677 and 0.746, and the corresponding values for **2** are 0.649 and 0.745. The structures for **1** and **2** were solved in the space group P-*1* (No. 2) and P*21/c* (No. 14), respectively, by intrinsic phasing using the ShelXT (Sheldrick, 2015)[53] structure solution program and refined by full matrix least-squares procedure on F2 using version 2016/6 of ShelXL (Sheldrick, 2015).[54] All non-hydrogen atoms were refined anisotropically in both cases. Hydrogen atom positions were calculated geometrically and refined using the riding model. For both structures, only half of the formula unit is present in the asymmetric unit, with the other half consisting of symmetry equivalent atoms. Despite several attempts, in case of **2**, accurate hydrogen atom positions for the lattice water molecules could not be found. Therefore, no hydrogen is added on those oxygen atoms. Calculations and molecular graphics were preformed using SHELXTL 2014 and Olex2[55] programs. The powder patterns for the two structures are also shown in Figures 4.II.21 and 4.II.22).
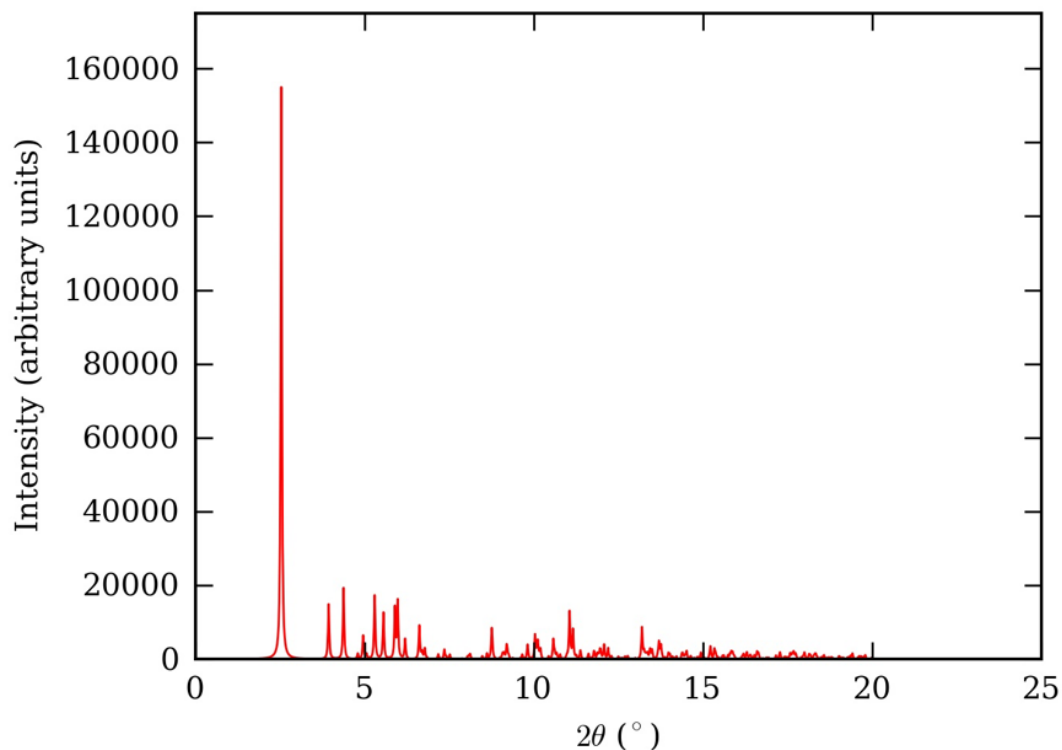
Figure 4.II.31. Powder X-ray diffraction patterns for [Ag$_2$(DSX)$_2$(NO$_3$)$_2$] **1**.

4.II.4.5 Fluorescence and Stability of DSX, Complex 1 and Complex 2.

Solutions of DSX, complex **1**, and complex **2** were prepared at equimolar concentrations with respect to silver in DCM and were manipulated under dim light. The stabilities of complex **1** and complex **2** were determined by addition of 0.1 equiv of tetra-n-butylammonium chloride (*n*-Bu$_4$NCl) in DCM. Briefly, 1 mL of the complex (7.5 × 10^{-4} M) and 1−9 mL of *n*-Bu$_4$NCl (7.5 × 10^{-5} M) were diluted to 10 mL in separate volumetric flasks. The solutions were vortexed for 5 s, and the fluorescence was immediately recorded. The solution containing [Ag$_2$(DSX)$_2$(NO$_3$)$_2$]/*n*-Bu$_4$NCl

Figure 4.II.32. Powder X-ray diffraction patterns for [Ag$_2$(DSX)$_2$](CF$_3$SO$_3$)$_2$ **2**.

(1:1) was prepared by adding equimolar amounts of the complex to the silver salt in a volumetric flask before transferring the solution to the cuvette.

Suspensions of DSX and **1** were prepared by sonication for 3 min. The fluorescence spectra were recorded immediately after sonication. The solid-state stability of 1 was determined by creating a fine suspension of the complex in 1 mL followed by the addition of 3 mL of a 205 mM solution of NaCl. The resulting solution was vortexed for 10 s, and the fluorescence was immediately recorded. The fluorescence of the cuvette was then measured after 0, 2, 4, 8, 12, and 24 h. The solution was sonicated for 5 min before each fluorescence measurement.

*4.II.4.6 Synthesis of Complex **1**-Agar Hydrogel Composite.*

A mixture of 1.3% (w/v) of agar in Milli-Q water was autoclaved and allowed to cool in a 45 °C water bath until the temperature of the solution was stabilized. Once the hydrogel solution reached the desired temperature, 14 mL of this mixture was poured into an aqueous suspension of $[Ag_2(DSX)_2(NO_3)2]$ (**1**, 1.5 mg in 1 mL H_2O) to reach a final concentration of agar of 1.2% (w/v). The suspension of **1** in water was then sonicated for 5 min shortly before the addition of the warm agar solution. The mixture was then quickly vortexed to produce a homogeneous solution, and the liquid complex **1**−agar composite (165 μM, 0.01% w/v of **1**) was then poured into a mold (2.5 mm × 0.3 mm). The resulting composite material was allowed to cool for 20 min under ambient dark conditions.

4.II.4.7 Synthesis of Control Agar Hydrogel Composites.

Control disks containing DSX, $AgNO_3$, and ampicillin were prepared using the same procedure as described above. The DSX ligand was sonicated for a total of 25 min to ensure a homogeneous suspension. Ampicillin almost completely dissolved in water after it was stirred for 5 min and fully dissolved after addition of the warm agar solution. Silver nitrate dissolved readily in water and did not require sonication. All control disks used were prepared using the same molar equivalency to complex **1** (with respect to Ag content). A blank disk was prepared by diluting 14 mL of the autoclaved agar solution to 15 mL and pouring into the mold.

4.II.4.8 Leaching Rate of Silver from the Complex 1-Agar Composite in Water.

Complex **1**-agar composite (0.01% w/v of **1**) disks were prepared fresh as described above. After the material solidified, seven 0.1 g sections were placed into individual Eppendorf tubes followed by the addition of 1 mL of Milli-Q water. The tubes were then sealed and incubated at room temperature in the dark for 0, 1, 2, 4, 8, 12, or 24 h. After incubation period was reached, the material was carefully removed from each tube; 0.5 mL of nitric acid was added, and the resulting solution was finally diluted to 10 mL in a volumetric flask. The complex **1**-agar composite that was incubated for 24 h was analyzed for silver by digesting the material using 0.5 mL of nitric acid, and the resulting solution was diluted to 10 mL. All samples were analyzed by flame atomic absorption spectrophotometry and tested against a set of silver nitrate standard solutions containing 0.5% nitric acid.

4.II.4.9 Growth Conditions for the Bacterial Cultures.

S. aureus, P. aeruginosa (*P*1 and *P*2), and *A. baumannii* cells were fist prepared by spreading frozen liquid cultures (20% glycerol, −72 °C) across Luria broth agar (LBA) plates and incubating at 37 °C for 18 h. One individual colony from each of these plates was used to inoculate 3 mL of sterile Luria broth, which was then incubated at 37 °C for 18 h with constant shaking (250 rpm). Upon completion of this growth period, bacterial cells were washed and resuspended in fresh Luria broth, and the concentration was brought to $OD_{600} = 1.0$. Dilutions of this stock solution were prepared and used for the determination of colony forming unit (CFU) mL^{-1} values.

Conversion factors of 1.2×10^8 CFU mL^{-1}, 2.1×10^8 CFU mL^{-1}, 2.4×10^8 CFU mL^{-1}, and 3.1×10^8 CFU mL^{-1} per unit of OD$_{600}$ were determined for *S. aureus, P. aeruginosa 1, P. aeruginosa 2, and A. baumannii*, respectively.

4.II.4.10 Model of Skin and Soft Tissue Infection.

All bacterial experiments were performed individually on separate plates. Soft brine agar composed of 1.0% NaCl (w/v) and 0.8% agar (w/v) was autoclaved and placed in a 45 °C water bath. After the temperature was stabilized at 40 °C, the soft agar was inoculated with the respective bacteria to reach a concentration of 8.5×10^5 CFU mL^{-1}. The resulting solution was then vortexed gently to produce a homogeneous suspension of bacteria. Then 7 mL of the inoculated agar solution was poured over a modified nutrition "hard" agar. The resulting plates were incubated for 1 h to allow the bacteria to adhere and form cell-to- cell contacts. The modified nutrition agar was composed of starch (0.15% w/v), beef extract (0.4% w/v), tryptone (1.5% w/v), and agar (1.5% w/v).

4.II.4.11 Bactericidal Assays.

The "bacterial suspension" SSTI model and the agar composite materials were fabricated as described above. The bacterial strains were used to inoculate the soft agar and incubated for 1 h. The complex **1**-agar composite disk was constructed during this time, and its bactericidal efficiency was examined individually on all bacterial strains. After the initial incubation period, the agar disks were removed from their mold and

placed directly on top of the inoculated SSTI model. Air bubbles trapped between the composites and the SSTI model were carefully removed to ensure full contact between both materials. All bacterial strains were incubated with the complex **1**-agar composite for 18 h at 37 °C. Control experiments were performed on all strains using the same procedure described above while using composite materials containing water, DSX, or ampicillin. The silver nitrate composite material was tested several times using all the bacterial strains *A. baumannii* strain; however, due to the instability of this material, experiments were not repeated. The zones of inhibition obtained upon treatments were assessed visually and measured manually.

4.II.4.12 Determination of Viable Bacteria in the Zones of Inhibition.

To determine the presence of viable bacteria in the SSTI model, the composite materials were carefully lifted from the SSTI model, and agar samples (1.5 cm × 1.5 cm × 0.5 cm) were carefully removed from the area where the composite material was making contact. The removed sections (containing the entire depth of the SSTI model) were placed inside 3 mL of fresh Luria broth (LB) and incubated at 37 °C for 18 h with constant shaking (250 rpm). The growth of bacteria was assessed visually, and all experiments were performed in triplicate at a minimum. The presence of viable bacteria was additionally confirmed by removing the composite materials and incubating the SSTI model for an additional 24 or 48 h. The growth of the microbes on the area where the composite material was making contact was assessed visually.

4.II.5 References.

1. Kaye, K. S.; Pogue, J. M. Infections Caused by Resistant Gram-Negative Bacteria: Epidemiology and Management. *Pharmacotherapy* **2015**, *35*, 949-962.

2. Barrasa-Villar, J. I.; Aibar-Remon, C.; Prieto-Andres, P.; Mareca-Doñate, R.; Moliner-Lahoz, J. Impact on Morbidity, Mortality, and Length of Stay of Hospital-Acquired Infections by Resistant Microorganisms. *Clin. Infect. Dis.* **2017**, *65*, 644-652.

3. Ventola, C. L. The Antibiotic Resistance Crisis. *P. T.* **2015**, *40*, 277-283.

4. Cardona, A. F.; Wilson, S. E. Skin and Soft-Tissue Infections: A Critical Review and the Role of Telavancin in Their Treatment. *Clin. Infect. Dis*. **2015**, *61*, S69-S78.

5. Pendleton, J. N.; Gorman, S. P.; Gilmore, B. F. Clinical Relevance of the *ESKAPE* Pathogens. *Expert Rev. Anti Infect. Ther.* **2013**, *11*, 297-308.

6. Boucher, H. W.; Talbot, G. H.; Bradley, J. S.; Edwards, J. E.; Gilbert, D.; Rice, L. B.; Scheld, M.; Spellberg, B.; Bartlett, J. Bad Bugs, No Drugs: No *ESKAPE*! An Update from the Infectious Diseases Society of America. *Clin. Infect. Dis*. **2009**, *48*, 1-12.

7. Lam, P. L.; Lee, K. K. H.; Wong, R. S. M.; Cheng, G. Y. M.; Bian, Z. X.; Chui, C. H.; Gambari, R. Recent Advances on Topical Antimicrobials for Skin and Soft Tissue Infections and their Safety Concerns. *Crit. Rev. Microbiol*. **2018**, *44*, 40-78.

8. Eckmann, C.; Dreyden, M. S. Treatment of Complicated Skin and Soft-Tissue Infections Caused by Resistant Bacteria: Value of Linezolid, Tigecycline, Daptomycin and Vancomycin. *Eur. J. Med. Res*. **2010**, *15*, 554-563.

9. Dryden, M. S. Complicated Skin and Soft Tissue Infection. *J. Antimicrob. Chemother*. **2010**, *65*, iii35-44.

10. Ray, G. T.; Suaya, J. A.; Baxter, R. Incidence, Microbiology, and Patient Characteristics of Skin and Soft-Tissue Infections in a U.S. Population: A Retrospective Population-Based Study. *BMC Infect. Dis*. **2013**, *13*, 252.

11. Ki, V.; Rotstein, C. Bacterial Skin and Soft Tissue Infections in Adults: A Review of their Epidemiology, Pathogenesis, Diagnosis, Treatment and Site of Care. *Can. J. Infect. Dis. Microbiol*. **2008**, *19*, 173-184.

12. Gulick, A. M. Nonribosomal Peptide Synthetase Biosynthetic Clusters of ESKAPE pathogens. *Nat. Prod. Rev*. **2017**, *34*, 981-1009.

13. Dryden, M. S. Skin and Soft Tissue Infection: Microbiology and Epidemiology. *Int. J. Antimicrob. Agents* **2009**, *34*, S2-S7.

14. Lyon, B. R.; Skurray, R. Antimicrobial Resistance of *Staphylococcus aureus*: Genetic Basis. *Microbiol. Rev*. **1987**, *51*, 88-134.

15. Sommer, R.; Wagner, S.; Varrot, A.; Nycholat, C. M.; Khaledi, A.; Häussler, S.; Paulson, J. C.; Imberty, A.; Titz, A. The Virulence Factor LecB Varies in Clinical Isolates: Consequences for Ligand Binding and Drug Discovery. *Chem. Sci*. **2016**, *7*, 4990-5001.

16. Viera, A.; Silva, Y. J.; Cunha, A.; Gomes, N. M. C.; Ackermann, H. W.; Almeida, A. Phage Therapy to Control Multidrug-Resistant *Pseudomonas aeruginosa* skin infections: In Vitro and Ex Vivo Experiments. *Eur. J. Clin. Microbiol Infect. Dis*. **2012**, *31*, 3241-3249.

17. Paterson, D. L. The Epidemiological Profile of Infections with Multidrug-Resistant *Pseudomonas aeruginosa* and *Acinetobacter* Species. *Clin. Infect. Dis*. **2006**, *43*, S43-S48.

18. Howard, A.; O'Donoghue, M.; Feeny, A.; Sleator, R. D. *Acinetobacter baumannii*. *Virulence*, **2012**, *3*, 243-250.

19. Calhoun, J. H.; Murray, C. K.; Manring, M. M. Multidrug-Resistant Organisms in Military Wounds from Iraq and Afghanistan. *Clin. Orthop. Relat. Res*. **2008**, *466*, 1356-1362.

20. Scott, P. T. et al. *Acinetobacter baumannii* infections Among Patients at Military Medical Facilities Treating Injured U.S. Service Members, 2002-2004. *MMRW*, **2004**, *292*, 2964-2966.

21. Scott, P.; Deye, G.; Srinivasan, A.; Murray, C.; Moran, K.; Hulten, E.; Fishbain, J.; Craft, D.; Riddell, S.; Lindler, L.; Mancusi, J.; Milstrey, E.; Bautista, C. T.; Patel, J.; Ewel, A.; Hamilton, T.; Gaddy, C.; Tenney, M.; Christopher, G.; Petersen, K.; Endy, T.; Petruccelli, B. An Outbreak of Multidrug-Resistant *Acinetobacter baumannii-calcoaceticus* Complex Infection in the US Military Health Care System Associated with Military Operations in Iraq. *Clin. Infect. Dis*. **2007**, *44*, 1577-1584.

22. Wendt, C.; Dietze, B.; Dietz, E.; Rüden, H. Survival of *Acinetobacter baumannii* on Dry Surfaces. *J. Clin. Microbiol*. **1997**, *35*, 1394-1397.

23. Fair, R. J.; Tor, Y. Antibiotics and Bacterial Resistance in the 21st Century. *Perspect. Medicin. Chem*. **2014**, *6*, 25-64.

24. Falagas, M. E.; Kasiakou, S. K. Colistin: The Revival of Polymyxins for the Management of Multidrug-Resistant Gram-Negative Bacterial Infections. *Clin. Infect. Dis*. **2005**, *40*, 1333-1341.

25. Liu, Y. Y.; Wang, Y.; Walsh, T. R.; Yi, L. X.; Zhang, R.; Spencer, J.; Doi, Y.; Tian, G.; Dong, B.; Huang, X.; Yu, L. F.; Gu, D.; Ren, H.; Chen, X.; Lv, L.; He, D.; Zhou, H.; Liang, Z.; Liu, J. H.; Shen, J. Emergence of Plasmid-Mediated Colistin Resistance Mechanism MCR-1 in Animals and Human Beings in China: A Microbiological and Molecular Biological Study. *Lancet Infect. Dis*. **2016**, *16*, 161-168.

26. McGann, P.; Snesrud, E.; Maybank, R.; Corey, B.; Ong, A. C.; Clifford, R.; Hinkle, M.; Whitman, T.; Lesho, E.; Schaecher, K. E. Escherichia coli Harboring mcr-1 and blaCTX-M on a Novel IncF Plasmid: First Report of mcr-1 in the United States. *Antimicrob. Agents Chemother*. **2016**, *60*, 4420-4421.

27. Davies, M.; Walsh, T. R. A Colistin Crisis in India. *Lancet Infect. Dis*. **2018**, *18*, 256-257.

28. Lemire, J. A.; Harrison, J. J.; Turner, R. J. Antimicrobial Activity of Metals: Mechanism, Molecular Targets and Applications. *Nat. Rev. Microbiol*. **2013**, *11*, 371-384.

29. Chernousova, S.; Epple, M. Silver as Antibacterial Agent: Ion. Nanoparticle, and Metal. *Angew. Chem. Int. Ed.* **2013**, *52*, 1636-1653.

30. Neissa, J.; Perez-Arnaiz, C.; Porto, V.; Busto, N.; Borrajo, E.; Leal, J. M.; Lopez-Quintela, M. A.; Garcia, B.; Dominguez, F. Interaction of Silver Atomic Quantum Clusters with Living Organisms: Bactericidal Effect of Ag_3 Clusters Mediated by Disruption of Topoisomerase-DNA Complexes. *Chem. Sci*. **2015**, *4*, 6717-6724.

31. Lansdown, A. B. G. Silver in Health Care: Antimicrobial Effects and Safety in Use. *Curr. Probl. Dermatol*. **2006**, *33*, 17-34.

32. Aziz, Z.; Abu, S. F.; Chong, N. J. A Systematic Review of Silver-Containing Dressings and Topical Silver Agents (Used with Dressings) for Burn Wounds. *Burns*, **2012**, *38*, 307-318.

33. Nherera, L. M.; Trueman, P.; Roberts, C. D.; Berg, L. A Systematic Review and Meta-Analysis of Clinical Outcomes Associated with Nanocrystalline Silver Use Compared to Alternative Silver Delivery Systems in the Management of Superficial and Deep Partial Thickness Burns. *Burns* **2017**, *43*, 939-948.

34. Thomas, S. S.; Lawrence, J.; Thomas, A. Evaluation of Hydrocolloids and Topical Medication in Minor Burns. *J. Wound Care* **1995**, *4*, 218-220.

35. Fisher, N. M.; Marsh, E.; Lazoca, R. Scar-Localized Argyria Secondary to Silver Sulfadiazine Cream. *J. Am. Acad. Dermatol*. **2003**, *49*, 730-732.

36. G, U. R. ; Axthelm, J.; Hoffmann, P.; Taye, N.; Glaser, S.; Gorls, H.; Hopkins, S. L.; Plass, W.; Neugebauer, U.; Bonnet, S.; Schiller, A. Co-Registered Molecular Logic Gate with a CO-Releasing Molecule Triggered by Light and Peroxide. *J. Am. Chem. Soc*. **2017**, *139*, 4991-4994.

37. Cheng, P.-S.; Hau, S. C. K.; Mak, T. C. W. Layer-Type Organosilver(I) Complexes Assembled with Nitrate and Functionalized Phenylethynide Ligands. *Inorg. Chim. Acta.* **2013**, *403*, 110-119.

38. Coyle, J. P.; Gordon, P. G.; Wells, A. P.; Mandia, D. J.; Sirianni, E. R.; Yap, G. P. A.; Barry, S. T. Thermally Robust Gold and Silver Iminopyrrolidinates for Chemical Vapor Deposition of Metal Films. *Chem. Mater*. **2013**, *25*, 4566-4573.

39. Lane, A. C.; Vollmer, M. V.; Laber, C. H.; Melgarejo, D. Y.; Chiarella, G. M.; Fackler Jr., J. P.; Yang, X.; Baker, G. A.; Walensky, J. R. Multinuclear Copper(I) and Silver(I) Amidinate Complexes: Synthesis, Luminescence, and CS_2 Insertion Reactivity. *Inorg. Chem.* **2014**, *53*, 11357-11366.

40. Du, J.-L.; Hu, T.-L.; Zhang, S.-M.; Zeng, Y.-F.; Bu, X.-H. Tuning Silver(I) Coordination Architectures by Ligands Design: From Dinuclear, Trinuclear, to 1D and 3D Frameworks. *Cryst. Eng. Comm*. **2008**, *10*, 1866-1874.

41. Wu, H. ; Dong, X.-W.; Ma, J.-F. Tetrakis (β-picoline)disilver(I) (Ag-Ag) bis(2-amino-5-chloro-benzenesulfonate) dihydrate. *Acta. Cryst*. **2006**, *E62*, m1227-m1228.

42. Heilman, B. J.; Halpenny, G. M.; Mascharak, P. K. Synthesis, Characterization, and Light-Controlled Antibiotic Application of a Composite Material Derived from Polyurethane and Silica Xerogel with Embedded Photoactive Manganese Nitrosyl. *J. Biomed, Mater. Res. B* **2011**, *99B*, 328-337.

43. Heilman, B. J.; St. John, J.; Oliver, S. R. J.; Mascharak, P. K. Light-Triggered Eradication of *Acinetobacter baumannii* by Means of NO Delivery from a Porous Material with an Entrapped Metal Nitrosyl. *J. Am. Chem. Soc*. **2013**, *134*, 11573-11582.

44. Gupta, S.; Laskar, N.; Kadouri, D. E. Evaluating the Effect of Oxygen Concentrations on Antibiotic Sensitivity, Growth, and Biofilm Formation of Human Pathogenesis. *Microbiol. Insights* **2016**, *9*, 37-46.

45. Flemming, H.-C.; Wingender, J.; Szewyk, U.; Steinberg, P.; Rice, S. A.; Kjelleberg, S. Biofilms: An Emergent Form of Bacterial Life. *Nat. Rev. Microbiol. 2016*, **14**, 563-575.

46. Driffield, K.; Miller, K.; Bostock, J. M.; O'Neill, A. J.; Chopra, I. Increased Mutability of *Pseudomonas aeruginosa* in Biofilms. *J. Antimicrob. Chemother*. **2008**, *61*, 1053-1056.

47. Borriello, G.; Werner, E.; Roe, F.; Kim, A. M.; Ehrlich, G. D.; Stewart, P. S. Oxygen Limitation Contributes to Antibiotic Tolerance of *Pseudomonas aeruginosa* in Biofilms. *Antimicrob. Agents Chemother*. **2004**, *48*, 2659-2664.

48. Walters, M. C.; Roe, F.; Bugnicourt, A.; Franklin, M. J.; Stewart, P. S. Contributions of Antibiotic Penetration, Oxygen Limitation, and Low

Metabolic Activity to Tolerance of Pseudomonas aeruginosa Biofilms to Ciprofloxacin and Tobramycin. *Antimicrob. Agents Chemother*. **2003**, *47*, 317-323.

49. Wakshlak, W. B-K.; Pedahzur, R.; Anvir, D. Antibacterial Activity of Silver-Killed Bacteria: The "Zombies" Effect. *Sci. Rep*. **2015**, *5*, 9555.

50. Bruker APEX 3, Bruker AXS Inc., Madison, Wisconsin, USA, **2014**.

51. Bruker SAINT, Bruker AXS Inc., Madison, Wisconsin, USA, **2012**.

52. Krause, L.; Herbst-Irmer, R.; Sheldrick, G. M.; Stalke, D. Comparison of Silver and Molybdenum Microfocus X-ray Sources for Single-Crystal Structure Determination. *J. Appl. Cryst*. **2015**, *48*, 3-10.

53. Sheldrick, G. M. SHELXT – Integrated Space-Group and Crystal-Structure Determination. *Acta Cryst.* **2015**, A*71*, 3-8.

54. Sheldrick, G. M. Crystal Structure Refinement with SHELXL. *Acta Cryst.* **2015**, C*71*, 3-8.

55. Dolomanov, O. V.; Bourhis, L. J.; Gildea, R. J.; Howard, J. A. K.; Puschmann, H. OLEX2: A Complete Structure Solution, Refinement and Analysis Program. *J. Appl. Cryst*. **2009**, *42*, 339-341.

4.II.6 Reprints of Publications and Permissions.

Reprinted with permissions from Pinto, M. N.; Martinez-Gonzalez, J.; Mascharak, P. K. Incorporation of a theranostic "two-tone" luminescent silver complex into biocompatible agar hydrogel composite for the eradication of ESKAPE pathogens in a Skin and Soft Tissue Infection Model. Inorg. Chem. 2018, 57, 6692-6701.

Incorporation of a Theranostic "Two-Tone" Luminescent Silver Complex into Biocompatible Agar Hydrogel Composite for the Eradication of ESKAPE Pathogens in a Skin and Soft Tissue Infection Model

Miguel N. Pinto, Jorge Martinez-Gonzalez, Indranil Chakraborty, and Pradip K. Mascharak*

Contribution from Department of Chemistry and Biochemistry, University of California, Santa Cruz, California 95064, United States

S Supporting Information

ABSTRACT: Microbial invasion and colonization of the skin and underlying soft tissues are among the most common types of infections, becoming increasingly prevalent in hospital settings. Systemic antibiotic chemotherapies are now extremely limited due to emergence of drug-resistant Gram-positive and multidrug-resistant Gram-negative bacterial strains. Topical administration of antimicrobials provides an effective route for the treatment of skin and soft tissue infections (SSTIs). Therefore, the development of new and effective materials for the delivery of these agents is of paramount importance. Silver is a broad-spectrum antibiotic used for the treatment and prevention of infections since ancient times. However, the high reactivity of silver cation (Ag^+) makes its incorporation in delivery materials quite challenging. Herein we report a novel soft agar hydrogel composite for the delivery of Ag^+ into infected wound sites. This material incorporates a Ag(I) complex $[Ag_2(DSX)_2(NO_3)_2]$ (**1**; DSX = 5-(dimethylamino)-*N,N*-bis(pyridin-2-ylmethyl) naphthalene-1-sulfonamide) that exhibits a change in fluorescence upon Ag^+ release and qualitatively indicates the end point of silver delivery. The antibacterial efficacy of the material was tested against several bacterial strains in an SSTI model. The complex **1**−agar composite proved effective at eradicating the pathogens responsible for the majority of SSTIs. The theranostic (therapeutic/diagnostic) properties coupled with its stability, softness, ease of application, and removal make this material an attractive silver-delivery vehicle for the treatment and prevention of SSTIs.
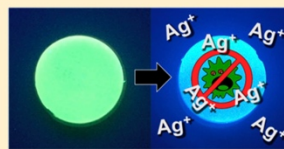
■ INTRODUCTION

In recent years, infections caused by drug-resistant pathogens are a considerable cause of global morbidity and mortality, leading to major clinical and economic burden.[1−3] In particular, nosocomial infections caused by the notoriously pathogenic *Enterococcus faecium, Staphylococcus aureus, Klebsiella pneumoniae, Acinetobacter baumannii, Pseudomonas aeruginosa, and Enterobacter spp.* (ESKAPE) bacteria present a major therapeutic challenge due to their resistance to conventional antibiotics.[4−6] Skin and soft tissue infections (SSTIs) are among the most common type of concern with increasing rates of hospitalization and severities ranging from mild to lethal.[7,8] Although skin serves as a structural barrier, damage and breaks in the skin allow for the infection and colonization by a variety of pathogens.[8,9] Microbial invasion of the skin and underlying soft tissues are caused predominantly by *S. aureus*, and to a lesser yet considerable extent by *A. Baumannii* and *P. aeruginosa*. Treatment of SSTIs caused by these pathogens is becoming increasingly difficult due to the emergence and rapid dissemination of drug-resistant strains in hospital settings.[9−13] *S. aureus* is a Gram-positive bacteria that can break down tissue for nutrition during the course of infection by employing a variety of extracellular proteins such as hemolysins, proteases, and collagenases.[5] Over 95% of *S. aureus* strains are resistant to penicillin, and more than 50% are resistant to methicillin.[12,14]

Infections caused by *P. aeruginosa* and *A. baumannii* are becoming increasingly prevalent, particularly in hospitals,[1,5−7,15] and are the principal pathogens responsible for chronic wound infections.[4,15] *P. aeruginosa* is one of the most common Gram-negative drug-resistant pathogens encountered in SSTIs.[16] Strains of *P. aeruginosa* can be highly resistant against most or almost all current antibiotic chemotherapeutics and are often classified as "panresistant".[17] *A. baumannii* is another opportunistic and problematic Gram-negative bacteria found in hospital environments affecting immunocompromised individuals.[18] Resistant *A. baumannii* infections have also been reported by military service members injured in combat in Iraq and Afghanistan[19−21] exemplifying its persistence in dry inanimate environments for extended periods of time.[22] *A. baumannii* is of particular interest due to its inherent resistance to some Gram-negative antibiotics as well as rapid development of drug resistance to others.[23]

Systemic therapeutic options for SSTIs caused by resistant strains of bacteria are becoming extremely limited.[6,24] Accounts of resistance toward toxic "last-resort" antibiotics such as Carbapanem and Colistin (polymyxin E) have already been reported globally.[3,25−27] Thus, development of new, safe, and

effective antibiotic treatments for SSTIs is of paramount importance. Topical antimicrobial therapy provides an attractive route for the treatment of SSTIs compared to systemic antibiotic therapy.[7] High antimicrobial doses can be delivered directly to the site of infection, which avoids metabolic and enzymatic degradation (with associated side effects) and clearance by the gastrointestinal tract. Topical delivery of antibiotics also increases patient compliance, convenience, and reduces treatment costs.

Silver has been used for the treatment of infections since ancient times, and it is currently utilized in a variety of consumer products, healthcare applications, and medical devices. Silver (metal, salts, nanoparticles, complexes) has gained interest as an antimicrobial agent due to its low toxicity to mammalian cells and its broad-spectrum activity against multidrug-resistant organisms.[28] Although the underlying bactericidal mechanisms of silver are poorly understood, silver cations (Ag^+) are known to disrupt biochemical processes in bacterial cells by interacting with thiol and amino groups on amino acid residues, proteins, nucleic acids, and cell membranes.[29,30] Because systemic administration of silver often produces adverse effects in humans, most silver therapies are confined to topical applications including prophylactic treatment for burn wounds and antimicrobial therapy for SSTIs.[29,31−33] Because of its reactive nature, silver tends to precipitate as an insoluble salt (AgCl) in the presence of chloride ions (blood plasma chloride concentration: 95−110 mM).[29] Thus, silver therapies require multiple applications and irrigations to maintain the infected area sterile. Topical application of silver sulfadiazine (Ag-SD) cream is an attractive way to treat SSTIs and burn wound infections. However, it also tends to adhere to the wound and leads to damage to newly epithelized surfaces during dressings and delay in wound healing.[32,34] Excessive topical use of silver may result in hypersensitivity, allergic contact dermatitis, erythema multiforme, and permanent undesirable aesthetic outcomes such as localized argyria.[35] A desirable wound dressing therefore needs to deliver the minimum yet effective dose of silver to an affected area while allowing painless application and easy removal of the bandage.

Herein we report a fluorescent silver complex $[Ag_2(DSX)_2(NO_3)_2]$ (**1**) (DSX = 5-(dimethylamino)-*N,N*-bis(pyridin-2-ylmethyl) naphthalene-1-sulfonamide) suspended in a soft agar hydrogel for the topical delivery of silver to selected members of ESKAPE bacteria that account for the majority of SSTIs. The complex **1**−agar composite material can be cast into any shape or form and has a strong luminescence with a considerable hypsochromic shift (50 nm) upon the release of Ag^+. The "two-tone" luminescence displayed by the free ligand and the silver complex allows one to determine the antimicrobial effect of silver ions combined with a visual signal that indicates the extent of drug (Ag^+) delivered and pro-drug (the metal complex) remaining in the bandage. As a consequence, the complex **1**−agar composite material is a "theranostic" agent for convenient use in SSTI infection. The qualitative fluorescence beacon of the composite that notifies the need for a bandage change is a special advantage; such a signal notifies the exact time to change the wound dressing, thus eliminating arbitrary replacement of bandages, reducing exposure of open wounds, and minimizing patient discomfort. The complex **1**−agar composite hydrogel has been tested for its antibacterial efficiency in "bacterial suspension" SSTI models and shown to be very effective against two strains of multidrug-

resistant *P. aeruginosa*, one strain of *S. aureus*, and one strain of *A. baumannii*. The material demonstrated prolonged antimicrobial inhibition zones superior to ampicillin and silver nitrate controls. Additionally, because of the softness and malleability of the hydrogel, this material can be used as a prophylactic for burn wound infections.

■ RESULTS AND DISCUSSION

Synthesis and Characterization of $[Ag_2(DSX)_2(NO_3)_2]$ (1) and $[Ag_2(DSX)_2](CF_3SO_3)_2$ (2). The synthesis of the ligand DSX was performed according to literature procedures and obtained in high yield and purity.[36] The microcrystalline powder was mixed with equimolar amounts of silver nitrate (complex **1**) or silver trifluoromethanesulfonate (complex **2**) in a 1:4 methanol/chloroform mixture. The solvent system was chosen such that, upon reduction of solvent volume at decreased pressure, the complex would remain in a mixture of mostly chloroform for ease of isolation. All reactions were performed under low levels of light to avoid potential decomposition of the precursor silver salts. Both complexes were isolated as microcrystalline yellow powders after recrystallization, which were analyzed satisfactorily. Single crystals were obtained by layering hexanes over a solution of the complex in dichloromethane (DCM). The resulting yellow-green single crystals were then characterized by conventional spectroscopy and X-ray diffraction (XRD). Infrared (IR) spectroscopy was used to confirm the presence of the nitrate or trifluoromethanesulfonate counterion in the respective complex (Supporting Information, Figures S1 and S2).

X-ray Structure Analysis. Single-crystal analysis revealed the molecular structures for both complexes. The perspective view with atom labeling scheme for the two structures is shown in Figures 1 and 2. Selected bond parameters are also listed in the figure captions. For both structures, only half of the formula unit is present in the asymmetric unit, with the other half consisting of symmetry equivalent atoms. The geometry around the metal centers in complexes **1** and **2** is quite distinctive. In
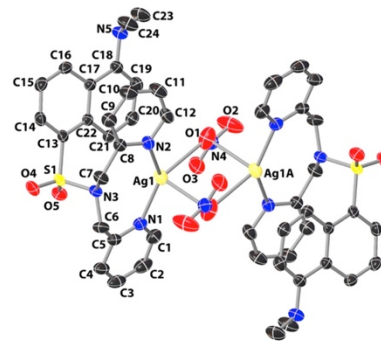

Figure 1. Perspective view of the molecular structure of complex **1**. The thermal ellipsoids are shown at 50% probability level (H atoms are omitted). Selected bond distances (Å): Ag1−N1, 2.259(2); Ag1−N2, 2.2922(2); Ag1−O1, 2.542(2); Ag1···Ag1A, 3.853(3) and angles (deg): N1−Ag1−N2, 137.31(7); N1−Ag1−O1, 132.33(8); N2−Ag1−O1, 90.08(8).
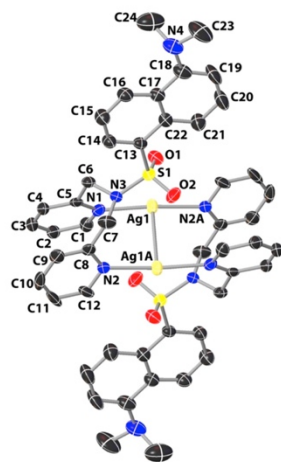
415

Figure 2. Perspective view of the molecular structure of the cation of complex **2**. The thermal ellipsoids are shown at 50% probability level (H atoms are omitted). Selected bond distances (Å): Ag1–N1, 2.171(6); Ag1A–N2, 2.180(6); Ag1–Ag1A, 3.2151(13); and angles (deg): N1–Ag1–N2A, 170.1(2); N1–Ag1–Ag1A, 90.79(16); N2A–Ag1–Ag1A, 91.65(16).

case of **1**, each Ag(I) center resides in a distorted tetrahedral coordination environment, where the metal center is coordinated to two pyridine N atoms from the DSX ligand and two O atoms from the two shared μ_2-NO$_3$ ligands. In case of **2**, each Ag(I) center resides in a quasi linear coordination environment, where each metal center is coordinated to two pyridine N atoms from two different DSX ligands.

Inspection of the metric parameters of the two structures clearly indicated that average Ag–N bond length (2.276(3) Å) in complex **1** is noticeably longer compared to that in complex **2** (2.176(6) Å). In complex **1**, Ag···Ag distance suggested moderate argentophilic interaction between the Ag(I) centers, while in complex **2**, the Ag···Ag distance (3.2151 Å) is considerably below the sum of van der Waals radii of the two Ag ions (3.40 Å) indicating strong interaction between the metal centers. In **1**, the two μ_2-nitrate ligands act as bridges between the two Ag(I) centers forming the central O$_2$NO– Ag···Ag–ONO$_2$ motif. Careful scrutiny of the Cambridge Structural Database (CSD) indicated that this motif is quite sparse in Ag(I) chemistry with few exceptions that are mostly limited to multinuclear Ag clusters.[37] Although there are reported examples of dinuclear Ag complexes with similar coordination sphere as complex **2**, in majority of those system the stronger Ag···Ag interactions have been forced by the ligand structure. In those cases, pyrolidintate,[38] formamidinate,[39] and similar types of ligand frames are employed with suitable geometry that favors metal–metal bond formation. There are only a few examples that are analogous with ligand type utilized for synthesizing complex **2**. For example, few Ag$_2$ complexes isolated from a family of triazole-based flexible ligands have similar structures as **2**. However, in those cases, the intramolecular Ag···Ag distances are quite long (spanning the

range of 5.76−7.36 Å).[40] A simple dinuclear complex, namely, [Ag$_2$(Pic)$_4$]$^{2+}$ (where Pic = β-picoline) has also been found to comprise coordination geometry much like **2**.[41] In this case Ag−Ag interaction is much stronger (Ag−Ag bond length, 3.1226(13) Å), while the Ag−N distances and N−Ag−N angle are fairly comparable to those in **2**.

Examination of the packing pattern of **1** shows several nonclassical hydrogen nonbonding contacts, which consolidated the extended structure (Figure 3). These interactions
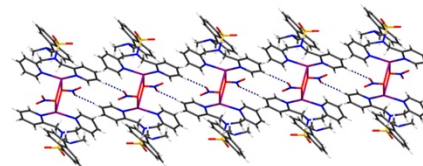
Figure 3. Packing pattern of **1** along b axis displaying the C−H···O intermolecular interactions.

mainly comprised of C−H···O hydrogen bonding involving the pyridine ring and the bridging nitrate ligand (C2−H2···O2, with C···O, 3.358(4) Å^i; C2−H2···O3, with C···O, 3.431(4) Å^i; C3−H3···O2, with C···O, 3.464(4) Å^{ii}, C7−H7···O4, with C···O, 3.028(4) Å; C12−H12···O1, with C···O, 3.226(4) Å, C14−H14···O4, with C···O, 2.818(3) Å; C20−H20···O3, with C···O, 3.248(4) Å, C21−H21···O5, with C···O, 3.082 (3) Å. Symmetry codes: (i) −x + 2, −y + 1, −z and (ii) x + 1, y − 1, z).

In case of **2**, C−H···O, C−H···N, and C−H···F hydrogen bonding involving the pyridine rings and the triflate anions and Ag···O(triflate) nonbonding interactions consolidated the extended network (Figure 4).
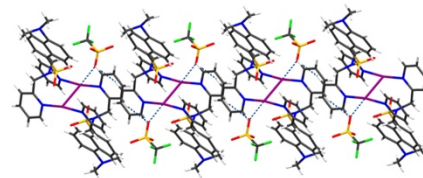
Figure 4. Packing pattern of **2** along c axis displaying the relatively stronger C−H···O and Ag···O intermolecular interactions (only very crucial nonbonding contacts are shown for the sake of clarity).

Several C−H···O and C−H···N nonbonding contacts are found from the analysis of the extended structure of **2** (C1−H1···O2, with C···O, 3.012(10) Å^i; C4−H4···O3, with C···O, 3.348(12) Å^{ii}; C6−H6···O1, with C···O, 2.899(9) Å; C6−H6···O2, with C···O, 3.548(12) Å^{ii}; C7−H7···O2, with C···O, 2.908(10) Å; C11−H11···O3, with C···O, 3.362(12) Å^{iii}; C12−H12···O1, with C···O, 3.309(10) Å^i; C14−H14···N3, with C···N, 3.010(11) Å; C16−H16···N4, with C···N, 2.845(12); C24−H24···F3, with C···F, 3.163(16) Å^{iv}; symmetry codes: (i) −x + 1, −y, −z + 1, (ii) −x + 1, −y + 1, −z + 1, (iii) x, −y + 1/2, z + 1/2, (iv) −x + 1, y + 1/2, −z + 1/2). The triflate anions are in appropriate position to exhibit moderate Ag···O nonbonding
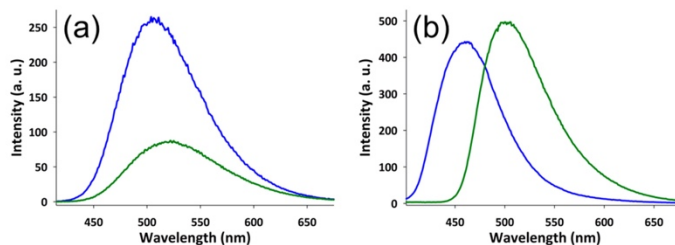
Figure 5. Fluorescence spectra of DSX (blue) and $[Ag_2(DSX)_2(NO_3)_2]$ (**1**, green) in (a) DCM and (b) aqueous suspension.
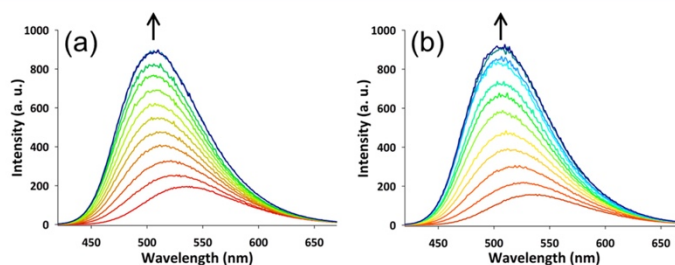
Figure 6. Fluorescence increase through subsequent addition of 0.1 mol equiv of n-Bu$_4$N$^+$Cl$^-$ to a DCM solution of (a) $[Ag_2(DSX)_2(NO_3)_2]$ (**1**) and (b) $[Ag_2(DSX)_2](CF_3SO_3)_2$ (**2**).

interactions (2.792(5) Å), and they also contributed toward particular arrangements of the molecules within the lattice. Structural analysis also revealed significant face-to-face intermolecular and intramolecular $\pi-\pi$ stacking interactions in **1** and **2**, respectively (Figures S3 and S4; Supporting Information).

Luminescence Characteristics of DSX, Complex 1, and Complex 2. The dansyl-appended ligand DSX was selected for the present study primarily because of its excellent luminescence and biocompatibility. Additionally, this ligand with (dimethylamino)naphthalene sulfonamide moiety is known to exert relatively low toxicity in LX-2 and HepaRG hepatic cell lines (EC$_{50}$ of 114 ± 4.6 and 73 ± 5.7 μM, respectively).[36] Finally, the pyridine N atoms are expected to readily coordinate to silver. The luminescence of DSX is centered at 505 nm in DCM. Upon complexation to silver, the fluorescence exhibits a bathochromic shift of 20 nm for **1** (λ_{max} = 525 nm; Figure 5a). The luminescence of DSX also exhibits modest quenching upon coordination, similar to its manganese analogue.[36] When suspended in water, DSX exhibits a hypsochromic shift of 50 nm (λ_{max} = 455 nm) relative to its fluorescence in DCM. Complex **1** also exhibits a hypsochromic shift of 20 nm (λ_{max} = 505 nm) in aqueous suspension (Figure 5b). The increase in fluorescence intensity of **1** in aqueous media (Figure 5) and the hypsochromic shift most possibly arise from breakdown of the nitrate bridge in highly dissociative medium. Indeed, the electrospray ionization-mass spectrometry (ESI-MS) spectra of both complexes (run in methanol) exhibit the $[Ag(DSX)]^+$ ion as the prominent one (Figures S15 and S16, Supporting Information). Because complex **2** did not

afford a good suspension in aqueous solution, we did not study its fluorescence behavior further.

Stability of Complexes 1 and 2 in Chloride-Containing Solutions. The stability of complexes **1** and **2** was investigated in solution as well as in solid state. Because chloride ions are abundant in human blood and tissue (blood plasma $[Cl^-]$ = 95–110 mM, tissue $[Cl^-]$ ≈ 10 mM) use of silver as antimicrobial could result in the precipitation of the Ag$^+$ as AgCl. To investigate the stability of the complexes in the presence of chloride ions, **1** and **2** were dissolved in DCM and were treated with tetra-n-butylammonium chloride (n-Bu$_4$N$^+$Cl$^-$). DCM was chosen as the solvent, since both complexes are insoluble in water. The solutions were prepared individually from concentrated stocks to maintain identical concentrations of the complex under investigation. Addition of 0.1 equiv increments of n-Bu$_4$N$^+$Cl$^-$ to 1 equiv of complex **1** resulted in an increase and hypsochromic shift of fluorescence (Figure 6a). This is attributed to the release of the free ligand. Upon addition of 1 equiv of chloride to complex, the luminescence reached a maximum intensity that matched the fluorescence of the free ligand at identical concentration (Figure 6a, black trace). This indicates that, in solution, complex **1** readily releases Ag$^+$ ions in the presence of chloride. In a similar manner, complex **2** releases silver at the same rate as complex **1** in the presence of chloride (Figure 6b).

To improve the release rate of Ag$^+$ from the complexes in the presence of chloride ions, we decided to estimate the release rate of Ag$^+$ from powdered samples suspended in aqueous solutions. Since complex **1** exhibits the largest bathochromic shift in aqueous suspensions (50 nm, Figure 5b), its stability in an aqueous suspension was checked in the presence of chloride.

417

Interestingly, 1 molar equiv of chloride produced negligible loss of silver when **1** was suspended in water, even after a few hours. This can be attributed to the fact that Ag^+ can only be released from the surface of the powdered sample in such cases. The stability of **1** was investigated against an isotonic saline solution containing $[NaCl] = 154$ mM. A decrease in fluorescence was observed immediately upon addition of aqueous chloride to the suspension of complex **1** (Figure 7) presumably due to initial

Figure 7. Silver release profile from a suspension of complex **1** incubated in an isotonic aqueous chloride solution ($[Cl^-] = 154$ mM) for 0, 2, 4, 8, 12, and 24 h.

coagulation of the fine particles. The sample was then stored at room temperature in the dark, and its fluorescence was measured after 2, 4, 8, 12, and 24 h (Figure 7) following sonication (to obtain a homogeneous suspension). The high chlori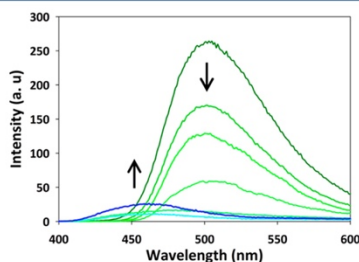de concentration led to precipitation of both AgCl and some free DSX on the side of the cuvette. Nevertheless, *a clear green to blue color change* was observed (Figure 7, compare the blue and the green traces). This experiment confirmed that Ag^+ releases slowly from solid particles of **1** in the presence of high chloride concentration and that a green-to-blue color change can be observed as an indicator of the silver release. The stability of **2** as a suspension was not investigated, because **2** does not exhibit such a distinct color change in suspension.

Agar-[Ag$_2$(DSX)$_2$(NO$_3$)$_2$] Hydrogel Composite Material. A variety of polymeric hydrogels was considered as delivery vehicles. Since silver salts and complexes are sensitive to both light and oxidation, it was necessary to use a material that could be easily constructed under mild conditions. The use of radical initiators, high temperatures, or materials that contained functional groups interacting strongly with silver were avoided. It is important to note that the wound dressing material needs to be relatively inert toward the complex and to have minimal affinity for Ag^+. In principle, a slowdown of Ag^+ by material may help to deliver the therapeutic for extended periods of time to the infected area. Rapid release of Ag^+ may help clear proximal bacterial loads but will also result in quick depletion of the antimicrobial from the bandage material and therefore requiring multiple changes. Conversely, if the hydrogel interacts too strongly with Ag^+, enough therapeutic will not be released to elicit the bactericidal effect. The application and removal of the bandage must also be taken into consideration, since some antibiotics, such as silver sulfadiazine, may stick to the newly epithelized skin layer. Removal of these dressings may reopen the wound, delaying the healing process.[32,34]

Bacteriological-grade agarose gel was selected as the drug carrier for the present antimicrobial experiments due to its well-

known biocompatibility, softness, mechanical strength, stability, moisture retention, and cost effectiveness. $[Ag_2(DSX)_2(NO_3)_2]$ (**1**) was selected for the antimicrobial experiments due to its moderate silver release profile and an excellent color change upon silver loss. We decided to incorporate the complex into the hydrogel matrix as a suspension, to take advantage of the significant hypsochromic shift in fluorescence upon silver release as shown in Figure 7. Using the complex in the solid state also results in a relatively slow and sustained release of Ag^+. The percentage of agar used was optimized to produce a low gelling temperature (40−45 °C); the use of high temperatures (<60 °C) results in the decomposition of complex **1** as well as other silver salts and antibiotics used as controls. The resulting complex **1**−agar composite material contained 0.01% (w/v) **1** and exhibited yellow-green fluorescence (Figure 8a,b). This material is stable for over
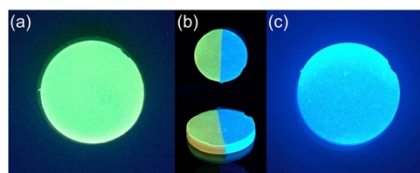
Figure 8. Composite materials containing (a) $[Ag_2(DSX)_2(NO_3)_2]$ **1**, (b) two half disks of complex **1** and DSX joined together for contrast and clarity, and (c) free DSX ligand (after silver release).

one month at 4 °C, and upon silver release, its blue fluorescence is identical to an agar disk containing the free ligand (Figure 8c). This appearance of the blue fluorescence thus indicates an expended material (time for change). A color change in the bandage material will definitely minimize untimely and repeated changes of wound dressings and patient discomfort, while keeping the wound free of opportunistic microbes. The spent complex **1**−agar can be easily removed from an infected area by pouring fresh water over it. This occlusive material can also absorb moisture from wound exudate and can be cast, cut, or molded into any shape or form.

The resulting complex **1**−agar composite material was tested for its silver release profile in water using flame atomic absorption spectrophotometry (Figure S11). Small pieces (100 mg each) of the silver (0.01% Ag) containing disks were individually incubated for 0, 1, 2, 4, 8, 12, or 24 h in 1 mL of water. After the incubation time was reached, the material was removed, and the solution was analyzed for silver content using flame atomic absorption spectrophotometry. The results indicated that the release of silver into solution occurs faster at the beginning of the incubation period. It was observed that the release rate of Ag^+ ions decreased as time progressed, and the total amount of Ag^+ released into water in 24 h was 81%. This may be attributed to partitioning of Ag^+ between the solution and the material at equilibrium. The complex **1**−agar composite material that was used for the 24 h incubation was digested in nitric acid, and optical analysis revealed that the remaining 19% of the Ag^+ remained in the material. The leftover silver can help keep the dressing sterile after the main therapeutic load is released, preventing the spread of infection from handling the discarded bandage material.

Skin and Soft Tissue Infection (SSTI) Model. The "bacterial suspension" SSTI model that was used in the present work was fabricated by using procedure reported by this laboratory.[42,43] In short, the SSTI model is composed of a soft brine agar layer inoculated with the microbe of interest (>1 × 10^5 CFUmL^{-1}) plated over a modified nutrition-rich agar layer. The soft agar allows for mobility, growth, and colonization of the microbes similar to a human SSTI. The nutrition gradient of the model promotes bacterial penetration into the modified nutrient agar, resulting in gradients of oxygen availability and metabolic activity of the microbes similar to what is observed in SSTI. The SSTI model addresses some of the limitations of standard antibiotic susceptibility tests that are normally performed under ambient oxygen conditions.[44] Pathogens responsible for SSTIs infect the dermis and epidermis[9] and not the surface of the skin, which is primarily composed of dead cells. Standardized methods test the antimicrobial efficacy of a drug on surface-exposed bacteria and do not account for effects in deeper tissues. SSTIs have a wide range of clinical manifestations and severity.[4,8] Uncomplicated SSTIs are normally superficial (dermis), often resolve on their own, and can be treated with systemic antibiotic therapy.[4,8] If left untreated, some SSTIs can spread to subcutaneous tissue, fascia, and muscle.[4,9] Neglected SSTIs may lead to the formation of metastatic abscesses, bacteremia, necrotizing fasciitis, or sepsis, which often require surgical intervention and thus are limb- and life-threatening.[4,8,9] Additionally, standardized antimicrobial tests do not take into account oxygen availability in deeper tissues, which may impact the efficacy of certain antibiotics.[44] Studies have shown that low oxygen levels decrease the susceptibility of *S. aureus* and *P. aeruginosa* to certain antibiotics such as β-lactams.[44] Since oxygen is an essential nutrient to aerobic bacteria, decreased oxygen availability results in attenuated growth, which reduces antimicrobial susceptibility to drugs that target metabolic and/or other processes during growth.[45−48]

Bactericidal Assays. The antimicrobial efficiency of the complex **1**−agar composite material was tested against one clinical isolate of *S. aureus*, two clinical isolates of multi drug-resistant (MDR) *P. aeruginosa*, and one *A. baumannii* (NCIMB 12457) strain. These microbes are the predominant species that account for the majority of SSTIs.[1,5−7,15] The soft agar was inoculated with a specific microbe (>1 × 10^5 CFUmL^{-1}), plated over a nutrient-rich agar, and incubated for 1 h to allow the bacteria to adhere and form cell-to-cell contacts. The complex **1**−agar hydrogel wound dressings were fabricated fresh and placed on top of the SSTI model after the initial incubation period. Air bubbles trapped between the SSTI and the agar disks were carefully removed to ensure full contact of both materials. Control agar-composite materials containing no compound, free ligand, and ampicillin were constructed under identical conditions and molar equivalency to silver. Freshly prepared agar disks (3 × 25 mm) and individual SSTI plates (100 mm) were used for each of the experiments. The SSTI models together with the agar disk were incubated for 18 h at 37 °C to allow the bacteria to grow. All bacterial experiments were performed in triplicate at the minimum to ensure consistent and reproducible results.

A representative example of the experimental results is presented in Figure 9. A full and uniform bacterial lawn was produced in all plates. All of the materials tested, with the exception of the composites containing complex **1**, exhibit growth of bacteria leading up to the border of the agar disk.
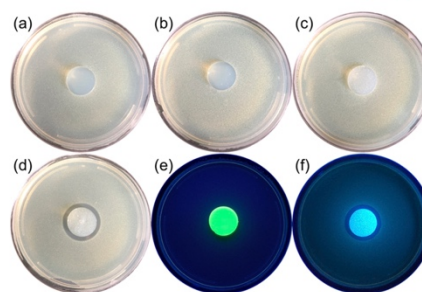
Figure 9. Representative example of results obtained from bactericidal tests against MDR *P. aeruginosa* 2 (P2) using agar-composite materials. (a) Blank agar, (b) DSX ligand, (c) ampicillin, (d) [Ag$_2$(DSX)$_2$(NO$_3$)$_2$] (**1**) after 24 h of incubation; (e) **1** under UV light before incubation, (f) **1** under UV light after incubation.

The bacteria penetrate deep into the SSTI model to reach the subsurface source of nutrients.

In all bacterial strains, the complex **1**−agar composite material exhibited a clear zone of inhibition of bacterial growth. The size of the inhibition zone is relatively compact due to the slow/sustained release of Ag$^+$ ions from the powder encapsulated inside the agar hydrogel. After overnight incubation, the complex **1**−agar composites were removed from the SSTI models, and the zones of inhibition were *individually tested for viable bacteria.* Silver delivery by the complex **1**−agar composite disks afforded zones of inhibition that are clear of bacteria throughout the entire depth of the SSTI models. No growth was observed upon inoculation of fresh media with the agar located throughout the entire depth of the zone of inhibition. The complex **1**−agar composite material yielded zones of inhibition of 29.8 ± 0.3, 30.8 ± 0.3, 31.4 ± 0.2, and 37.0 ± 0.3 mm for *S. aureus, P. aeruginosa* 1 (*P1*), *P. aeruginosa* 2 (*P2*), and *A. baumannii,* respectively (Figure 10). Bacterial strains of *P. aeruginosa* 1 (*P1*) and *P. aeruginosa* 2 (*P2*) exhibited similar zones of inhibition produced by the complex **1**−agar disk (Figure 10b,c, respectively). This is an interesting finding, since both these Gram-negative pathogens have similar patterns of resistance toward antibiotics. Finally, the largest zones of inhibition were observed for *A. baumannii* NCIMB 12457. Collectively, these results suggest that silver is an effective treatment for drug-susceptible and drug-resistant infections caused by the Gram-positive and Gram-negative SSTI ESKAPE pathogens.

In the present study, *S. aureus* exhibited no zone of inhibition when an ampicillin-loaded agar disk was used as a control. This was not surprising, since the majority of clinical isolates of *S. aureus* are resistant to penicillin and its derivatives. Both clinical isolates of *P. aeruginosa* (*P1* and *P2*) were also resistant to ampicillin. In each case, presence of bacteria was confirmed upon inoculation of fresh media with agar located beneath the ampicillin disk. Interestingly, a small zone of partial inhibition (<25.8 mm) was observed for *A. baumannii* strain (Figure S17, Supporting Information). Nevertheless, bacterial growth was observed after inoculation of fresh growth media with material from the resulting zone of inhibition of *A. baumannii* in this experiment.
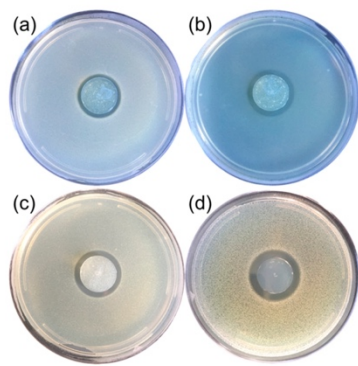
Figure 10. Zones of inhibition produced by $[Ag_2(DSX)_2(NO_3)_2]$ (**1**) on bacterial strains of (a) *S. aureus*, (b) MDR *P. aeruginosa* 1 (*P1*), (c) MDR *P. aeruginosa* 2 (*P2*), and (d) *A. baumannii*.

When the $AgNO_3$–agar and control disks were removed after the initial incubation period (24 h) and the SSTI model was further incubated for another 24 h, not surprisingly, all bacterial strains were able to resume growth in the zones previously covered by the control hydrogel material. As expected, the density of the bacterial load inside this area appeared visually lower, relative to areas that were not previously covered. However, no bacterial growth was observed in the zone of clearance exerted by the complex **1**–agar composite material (containing complex **1**), even after 48 h. This suggests that enough Ag^+ was delivered to the SSTI model *to maintain the zone of inhibition sterile for an extended period of time*. It is known that silver-killed microbes can become a reservoir of silver. The slow release of Ag^+ from dead bacteria can then exert bactericidal activity on viable bacteria, known as the "zombies effect,"[49] and can account for the prolonged antibacterial activity observed.

Control experiments using $AgNO_3$–agar hydrogels were performed to compare the efficiency of complex **1**. Incorporation of $AgNO_3$ into the material was in fact quite challenging. Solutions of $AgNO_3$ exhibited low tolerance for heated agar relative to the suspension of **1**. The silver salt exhibited signs of decomposition if the agar solution was not cooled below 45 °C prior to mixing, whereas complex **1** was able to tolerate temperatures greater than 50 °C. Prolonged exposure to light also resulted in the decomposition of the $AgNO_3$ composite. Antibacterial experiments performed with silver nitrate disks produced small zones of inhibition (26.8 ± 0.2 mm) relative to complex **1** (Figure S18). Upon overnight incubation on top of the SSTI model the $AgNO_3$–agar disk turned greyish-white, indicative of AgCl formation (Figure S18a). The results indicate that such precipitation interferes with the Ag^+ ion-induced killing resulting in smaller zones of inhibition. Contrary to this behavior, the material fabricated with complex **1** is more stable and efficient in sustained release of Ag^+ with minimum interference from chloride (Figure S18b). Incorporation of **1** as a powdered solid suspended in agar clearly makes the composite an excellent source for slow and sustained silver release.

■ CONCLUSIONS

Development of new and advanced therapies for the treatment and prevention of SSTIs by drug-resistant bacteria is of paramount importance. Traditional silver antibiotic therapies have proved effective toward eradication of drug-resistant pathogens. However, most of these therapies require the excessive use of silver salts, as well as arbitrary/periodic bandage changes. The present complex **1**–agar composite material described above performs exceptionally well against the predominant ESKAPE pathogens responsible for SSTIs. In addition to its bactericidal efficacy, the material also bears a fluorescent beacon that indicates the amount of drug (Ag^+) or prodrug (complex **1**) present in the material. Apart from excellent antibacterial effects, this composite can be fabricated easily, and it is both biocompatible and cost-effective. Besides treatment of SSTIs, the reported material can find useful applications in the treatment of chronic wound infections and as prophylactic treatment for burn wound infections.

■ EXPERIMENTAL SECTION

Materials. All chemicals, solvents, and reagents were obtained from commercial suppliers and were used without further purification unless stated otherwise. All syntheses were performed using standard Schlenk techniques. Preparations involving precursor silver salts were performed under dim light to avoid decomposition. All organic solvents used were distilled in triplicate. The ligand 5-(dimethylamino)-*N*,*N*-bis(pyridin-2-ylmethyl) naphthalene-1-sulfonamide (DSX) was synthesized in high yield as a white powder following the literature procedure.[36] IR spectra were obtained using a PerkinElmer Spectrum One FT-IR Spectrometer. UV–Vis spectra were recorded using a Varian Cary 50 UV–vis spectrophotometer. Fluorescence spectra were obtained with an Agilent Cary Eclipse Fluorescence spectrophotometer. ^{1}H NMR spectra were recorded using a Varian 500 (500 MHz) spectrometer. Atomic absorption data was recorded using a PerkinElmer AAnalyst 100 Flame Atomic Absorption Spectrometer. Ultrapure water (Milli-Q, 18.2 MΩ cm) was obtained from a NANOpure Diamond water purification system. High-resolution ESI-MS data were recorded on an LTQ-Orbitrap Velos Pro MS instrument. Two multidrug-resistant clinical strains of *P. aeruginosa* (identified by sensitivity testing performed by drug dilution using Gram-negatives panels on the BD Phoenix or e-tests; Figures S12–S14) and one clinical strain of *S. aureus* were obtained from the Microbiology Laboratory of UCSD Health. The strain of *A. baumannii* (NCIMB 12457) was obtained from the UCSC Chemical Screening Center.

Synthesis of [Ag$_2$(DSX)$_2$(NO$_3$)$_2$] (**1**). The ligand DSX (100 mg, 0.23 mmol) was dissolved in chloroform (40 mL), followed by the dropwise addition of a methanolic solution (10 mL) of silver nitrate (39 mg, 0.23 mmol). The mixture was stirred magnetically at room temperature overnight under dark conditions. The volume of the resulting clear yellow solution was reduced under low pressure until a yellow precipitate was formed. The mixture was then cooled at 0 °C for 2 h, and the resulting product was collected through vacuum filtration. The yellow powder was recrystallized from DCM/hexanes (1:1) to afford **1** in 95% yield (151 mg, 0.22 mmol) as a microcrystalline yellow-green powder. Anal. Calcd for $C_{48}H_{48}Ag_2N_{10}O_{10}S_2$: C, 47.85; H, 4.02; N, 11.63. Found: C, 47.49; H, 4.08; N, 11.77%. ^{1}H NMR (500 MHz, CDCl$_3$): δ 8.34 (m, 3H), 8.05 (d, 1H), 7.80 (d, 1H), 7.68 (m, 3H), 7.28 (m, 3H), 7.16 (m, 3H), 4.65 (s, 4H), 2.90 (s, 6H). Selected IR (KBr disk, cm^{-1}) 1600, 1572, 1479, 1439, 1383, 1312, 1295, 1142, 787.

Synthesis of [Ag$_2$(DSX)$_2$](CF$_3$SO$_3$)$_2$ (**2**). The synthesis of **2** was performed using the same procedure used for the preparation of complex **1**, while employing AgCF$_3$SO$_3$ (59 mg, 0.23 mmol) as the silver salt. Yield: 91% (129 mg, 0.21 mmol) of **2** as a microcrystalline yellow powder. Anal. Calc for $C_{50}H_{48}Ag_2N_8O_{10}S_4F_6$: C, 43.55; H, 3.51; N, 8.13. Found: C, 43.59; H, 3.45; N, 8.17%. ^{1}H NMR (500 MHz,

420

CDCl$_3$): δ 8.44 (d, 2H), 8.34 (d, 1H), 8.07 (d, 1H), 7.85 (d, 1H), 7.73 (m, 3H), 7.32 (m, 3H), 7.17 (m, 3H), 4.67 (s, 4H), 2.91 (s, 6H). Selected IR (KBr disk, cm^{-1}) 1591, 1573, 1439, 1314, 1256, 1161, 1142, 1031, 789.

X-ray Diffraction Analysis. Light yellow and colorless block-shaped crystals of complexes $[Ag_2(DSX)_2(NO_3)_2]$ (**1**) and $[Ag_2(DSX)_2](CF_3SO_3)_2$ (**2**), respectively, were obtained by recrystallization through diffusion of hexanes into their respective DCM solutions. In both cases, a suitable crystal was selected and mounted on a Bruker D8 Quest diffractometer equipped with PHOTON 100 detector operating at T = 298 K. Data were collected with ω shutterless scan technique using graphite monochromated Mo Kα radiation (λ = 0.710 73 Å). The total number of runs and images for both data collections was based on the strategy calculation from the program APEX3 (Bruker).[50] The maximum resolution achieved was θ = 28.3° for **1** and θ = 25.1° for **2**. Cell parameters were retrieved using the SAINT (Bruker) software[51] and refined using SAINT (Bruker) on 9969 reflections for **1** and on 6594 reflections for **2**. Data reduction was performed using the SAINT (Bruker) software, which corrects for Lorentz polarization. The final completeness is 99.4% out to 28.3° in θ for **1** and 99.7% out to 25.1° in θ for **2**. Multiscan absorption corrections were performed with both data sets using SADABS 2016/2.[52] The absorption coefficient for **1** is 0.98 mm^{-1} and for **2** is 0.84 mm^{-1}; the minimum and maximum transmissions for **1** are 0.677 and 0.746, and the corresponding values for **2** are 0.649 and 0.745. The structures for **1** and **2** were solved in the space group $P\bar{1}$ (No. 2) and $P2_1/c$ (No. 14), respectively, by intrinsic phasing using the ShelXT (Sheldrick, 2015)[53] structure solution program and refined by full matrix least-squares procedure on F^2 using version 2016/6 of ShelXL (Sheldrick, 2015).[54] All non-hydrogen atoms were refined anisotropically in both cases. Hydrogen atom positions were calculated geometrically and refined using the riding model. For both structures, only half of the formula unit is present in the asymmetric unit, with the other half consisting of symmetry equivalent atoms. Despite several attempts, in case of **2**, accurate hydrogen atom positions for the lattice water molecules could not be found. Therefore, no hydrogen is added on those oxygen atoms. Calculations and molecular graphics were preformed using SHELXTL 2014 and Olex2[55] programs. The powder patterns for the two structures are also shown in the Supporting Information (Figures S9 and S10).

Fluorescence and Stability of DSX, Complex 1, and Complex 2. Solutions of DSX, complex **1**, and complex **2** were prepared at equimolar concentrations with respect to silver in DCM and were manipulated under dim light. The stabilities of complex **1** and complex **2** were determined by addition of 0.1 equiv of tetra-n-butylammonium chloride (n-Bu$_4$NCl) in DCM. Briefly, 1 mL of the complex (7.5 × 10^{-4} M) and 1–9 mL of n-Bu$_4$NCl (7.5 × 10^{-5} M) were diluted to 10 mL in separate volumetric flasks. The solutions were vortexed for 5 s, and the fluorescence was immediately recorded. The solution containing $[Ag_2(DSX)_2(NO_3)_2]/n$-Bu$_4$NCl (1:1) was prepared by adding equimolar amounts of the complex to the silver salt in a volumetric flask before transferring the solution to the cuvette.

Suspensions of DSX and **1** were prepared by sonication for 3 min. The fluorescence spectra were recorded immediately after sonication. The solid-state stability of **1** was determined by creating a fine suspension of the complex in 1 mL followed by the addition of 3 mL of a 205 mM solution of NaCl. The resulting solution was vortexed for 10 s, and the fluorescence was immediately recorded. The fluorescence of the cuvette was then measured after 0, 2, 4, 8, 12, and 24 h. The solution was sonicated for 5 min before each fluorescence measurement.

Synthesis of Complex 1–Agar Hydrogel Composite. A mixture of 1.3% (w/v) of agar in Milli-Q water was autoclaved and allowed to cool in a 45 °C water bath until the temperature of the solution was stabilized. Once the hydrogel solution reached the desired temperature, 14 mL of this mixture was poured into an aqueous suspension of $[Ag_2(DSX)_2(NO_3)_2]$ (**1**, 1.5 mg in 1 mL H$_2$O) to reach a final concentration of agar of 1.2% (w/v). The suspension of **1** in water was then sonicated for 5 min shortly before the addition of the warm agar solution. The mixture was then quickly vortexed to produce a homogeneous solution, and the liquid complex **1**–agar composite (165 μM, 0.01% w/v of **1**) was then poured into a mold (2.5 mm × 0.3 mm). The resulting composite material was allowed to cool for 20 min under ambient dark conditions.

Synthesis of Control Agar Hydrogel Composites. Control disks containing DSX, AgNO$_3$, and ampicillin were prepared using the same procedure as described above. The DSX ligand was sonicated for a total of 25 min to ensure a homogeneous suspension. Ampicillin almost completely dissolved in water after it was stirred for 5 min and fully dissolved after addition of the warm agar solution. Silver nitrate dissolved readily in water and did not require sonication. All control disks used were prepared using the same molar equivalency to complex **1** (with respect to Ag content). A blank disk was prepared by diluting 14 mL of the autoclaved agar solution to 15 mL and pouring into the mold.

Leaching Rate of Silver from the Complex 1–Agar Composite in Water. Complex **1**–agar composite (0.01% w/v of **1**) disks were prepared fresh as described above. After the material solidified, seven 0.1 g sections were placed into individual Eppendorf tubes followed by the addition of 1 mL of Milli-Q water. The tubes were then sealed and incubated at room temperature in the dark for 0, 1, 2, 4, 8, 12, or 24 h. After incubation period was reached, the material was carefully removed from each tube; 0.5 mL of nitric acid was added, and the resulting solution was finally diluted to 10 mL in a volumetric flask. The complex **1**–agar composite that was incubated for 24 h was analyzed for silver by digesting the material using 0.5 mL of nitric acid, and the resulting solution was diluted to 10 mL. All samples were analyzed by flame atomic absorption spectrophotometry and tested against a set of silver nitrate standard solutions containing 0.5% nitric acid.

Growth Conditions for the Bacterial Cultures. *S. aureus*, *P. aeruginosa* (P1 and P2), and *A. baumannii* cells were fist prepared by spreading frozen liquid cultures (20% glycerol, −72 °C) across Luria broth agar (LBA) plates and incubating at 37 °C for 18 h. One individual colony from each of these plates was used to inoculate 3 mL of sterile Luria broth, which was then incubated at 37 °C for 18 h with constant shaking (250 rpm). Upon completion of this growth period, bacterial cells were washed and resuspended in fresh Luria broth, and the concentration was brought to OD$_{600}$ = 1.0. Dilutions of this stock solution were prepared and used for the determination of colony forming unit (CFU) mL^{-1} values. Conversion factors of 1.2 × 10^8 CFU mL^{-1}, 2.1 × 10^8 CFU mL^{-1}, 2.4 × 10^8 CFU mL^{-1}, and 3.1 × 10^8 CFU mL^{-1} per unit of OD$_{600}$ were determined for *S. aureus*, *P. aeruginosa* 1, *P. aeruginosa* 2, and *A. baumannii*, respectively.

Model of Skin and Soft Tissue Infection. All bacterial experiments were performed individually on separate plates. Soft brine agar composed of 1.0% NaCl (w/v) and 0.8% agar (w/v) was autoclaved and placed in a 45 °C water bath. After the temperature was stabilized, the soft agar was inoculated with the respective bacteria to reach a concentration of 8.5 × 10^5 CFU mL^{-1}. The resulting solution was then vortexed gently to produce a homogeneous suspension of bacteria. Then 7 mL of the inoculated agar solution was poured over a modified nutrition "hard" agar. The resulting plates were incubated for 1 h to allow the bacteria to adhere and form cell-to-cell contacts. The modified nutrition agar was composed of starch (0.15% w/v), beef extract (0.4% w/v), tryptone (1.5% w/v), and agar (1.5% w/v).

Bactericidal Assays. The "bacterial suspension" SSTI model and the agar composite materials were fabricated as described above. The bacterial strains were used to inoculate the soft agar and incubated for 1 h. The complex **1**–agar composite disk was constructed during this time, and its bactericidal efficiency was examined individually on all bacterial strains. After the initial incubation period, the agar disks were removed from their mold and placed directly on top of the inoculated SSTI model. Air bubbles trapped between the composites and the SSTI model were carefully removed to ensure full contact between both materials. All bacterial strains were incubated with the complex **1**–agar composite for 18 h at 37 °C. Control experiments were performed on all strains using the same procedure described above while using composite materials containing water, DSX, or ampicillin.

The silver nitrate composite material was tested several times using *A. baumannii* strain; however, due to the instability of this material, experiments with other strains were not performed. The zones of inhibition were assessed visually and measured manually.

Determination of Viable Bacteria in the Zones of Inhibition. To determine the presence of viable bacteria in the SSTI model, the composite materials were carefully lifted from the SSTI model, and agar samples (1.5 cm × 1.5 cm × 0.5 cm) were carefully removed from the area where the composite material was making contact. The removed sections (containing the entire depth of the SSTI model) were placed inside 3 mL of fresh Luria broth (LB) and incubated at 37 °C for 18 h with constant shaking (250 rpm). The growth of bacteria was assessed visually, and all experiments were performed in triplicate at a minimum. The presence of viable bacteria was additionally confirmed by removing the composite materials and incubating the SSTI model for an additional 24 or 48 h. The growth of the microbes on the area where the composite material was making contact was assessed visually.

■ ASSOCIATED CONTENT

⑤ Supporting Information

The Supporting Information is available free of charge on the ACS Publications website at DOI: 10.1021/acs.inorgchem.8b00901.

> Crystal data and structure refinement parameters, FTIR spectra, intramolecular $\pi-\pi$ stacking interactions, other spectral characterizations, powder X-ray diffraction analysis and flame atomic absorption data, sensitivity patterns of the bacteria, ESI-MS data, and agar gel pictures (PDF)

Accession Codes

CCDC 1827285 (complex **1**) and CCDC 1827286 (complex **2**) contain the supplementary crystallographic data for this paper. These data can be obtained free of charge from The Cambridge Crystallographic Data Center via www.ccdc.cam.ac.uk/data_request.cif.

■ AUTHOR INFORMATION

Corresponding Author

*E-mail: Pradip@ucsc.edu. Fax: (831) 459-2935.

ORCID ⊙

Pradip K. Mascharak: 0000-0002-7044-944X

Notes

The authors declare no competing financial interest.

■ REFERENCES

(1) Kaye, K. S.; Pogue, J. M. Infections Caused by Resistant Gram-Negative Bacteria: Epidemiology and Management. *Pharmacotherapy* **2015**, *35*, 949−962.

(2) Barrasa-Villar, J. I.; Aibar-Remon, C.; Prieto-Andres, P.; Mareca-Doñate, R.; Moliner-Lahoz, J. Impact on Morbidity, Mortality, and Length of Stay of Hospital-Acquired Infections by Resistant Microorganisms. *Clin. Infect. Dis.* **2017**, *65*, 644−652.

(3) Ventola, C. L. The Antibiotic Resistance Crisis. *Pharm. Ther.* **2015**, *40*, 277−283.

(4) Cardona, A. F.; Wilson, S. E. Skin and Soft-Tissue Infections: A Critical Review and the Role of Telavancin in Their Treatment. *Clin. Infect. Dis.* **2015**, *61*, S69−S78.

(5) Pendleton, J. N.; Gorman, S. P.; Gilmore, B. F. Clinical Relevance of the *ESKAPE* Pathogens. *Expert Rev. Anti-Infect. Ther.* **2013**, *11*, 297−308.

(6) Boucher, H. W.; Talbot, G. H.; Bradley, J. S.; Edwards, J. E.; Gilbert, D.; Rice, L. B.; Scheld, M.; Spellberg, B.; Bartlett, J. Bad Bugs, No Drugs: No *ESKAPE*! An Update from the Infectious Diseases Society of America. *Clin. Infect. Dis.* **2009**, *48*, 1−12.

(7) Lam, P. L.; Lee, K. K. H.; Wong, R. S. M.; Cheng, G. Y. M.; Bian, Z. X.; Chui, C. H.; Gambari, R. Recent Advances on Topical Antimicrobials for Skin and Soft Tissue Infections and their Safety Concerns. *Crit. Rev. Microbiol.* **2018**, *44*, 40−78.

(8) Eckmann, C.; Dreyden, M. S. Treatment of Complicated Skin and Soft-Tissue Infections Caused by Resistant Bacteria: Value of Linezolid, Tigecycline, Daptomycin and Vancomycin. *Eur. J. Med. Res.* **2010**, *15*, 554−563.

(9) Dryden, M. S. Complicated Skin and Soft Tissue Infection. *J. Antimicrob. Chemother.* **2010**, *65*, iii35−44.

(10) Ray, G. T.; Suaya, J. A.; Baxter, R. Incidence, Microbiology, and Patient Characteristics of Skin and Soft-Tissue Infections in a U.S. Population: A Retrospective Population-Based Study. *BMC Infect. Dis.* **2013**, *13*, 252.

(11) Ki, V.; Rotstein, C. Bacterial Skin and Soft Tissue Infections in Adults: A Review of their Epidemiology, Pathogenesis, Diagnosis, Treatment and Site of Care. *Can. J. Infect. Dis. Microbiol.* **2008**, *19*, 173−184.

(12) Gulick, A. M. Nonribosomal Peptide Synthetase Biosynthetic Clusters of ESKAPE pathogens. *Nat. Prod. Rep.* **2017**, *34*, 981−1009.

(13) Dryden, M. S. Skin and Soft Tissue Infection: Microbiology and Epidemiology. *Int. J. Antimicrob. Agents* **2009**, *34*, S2−S7.

(14) Lyon, B. R.; Skurray, R. Antimicrobial Resistance of *Staphylococcus aureus*: Genetic Basis. *Microbiol. Rev.* **1987**, *51*, 88−134.

(15) Sommer, R.; Wagner, S.; Varrot, A.; Nycholat, C. M.; Khaledi, A.; Häussler, S.; Paulson, J. C.; Imberty, A.; Titz, A. The Virulence Factor LecB Varies in Clinical Isolates: Consequences for Ligand Binding and Drug Discovery. *Chem. Sci.* **2016**, *7*, 4990−5001.

(16) Vieira, A.; Silva, Y. J.; Cunha, A.; Gomes, N. M. C.; Ackermann, H. W.; Almeida, A. Phage Therapy to Control Multidrug-Resistant *Pseudomonas aeruginosa* skin infections: In Vitro and Ex Vivo Experiments. *Eur. J. Clin. Microbiol. Infect. Dis.* **2012**, *31*, 3241−3249.

(17) Paterson, D. L. The Epidemiological Profile of Infections with Multidrug-Resistant *Pseudomonas aeruginosa* and *Acinetobacter* Species. *Clin. Infect. Dis.* **2006**, *43*, S43−S48.

(18) Howard, A.; O'Donoghue, M.; Feeney, A.; Sleator, R. D. *Acinetobacter baumannii*: An Emerging Opportunistic Pathogen. *Virulence* **2012**, *3*, 243−250.

(19) Calhoun, J. H.; Murray, C. K.; Manring, M. M. Multidrug-Resistant Organisms in Military Wounds from Iraq and Afghanistan. *Clin. Orthop. Relat. Res.* **2008**, *466*, 1356−1362.

(20) Scott, P. T.; et al. Acinetobacter baumannii infections Among Patients at Military Medical Facilities Treating Injured U.S. Service Members, 2002−2004. *MMWR* **2004**, *53*, 1063−1066.

(21) Scott, P.; Deye, G.; Srinivasan, A.; Murray, C.; Moran, K.; Hulten, E.; Fishbain, J.; Craft, D.; Riddell, S.; Lindler, L.; Mancuso, J.; Milstrey, E.; Bautista, C. T.; Patel, J.; Ewell, A.; Hamilton, T.; Gaddy, C.; Tenney, M.; Christopher, G.; Petersen, K.; Endy, T.; Petruccelli, B. An Outbreak of Multidrug-Resistant *Acinetobacter baumannii-calcoaceticus* Complex Infection in the US Military Health Care System Associated with Military Operations in Iraq. *Clin. Infect. Dis.* **2007**, *44*, 1577−1584.

(22) Wendt, C.; Dietze, B.; Dietz, E.; Rüden, H. Survival of *Acinetobacter baumannii* on Dry Surfaces. *J. Clin. Microbiol.* **1997**, *35*, 1394−1397.

(23) Fair, R. J.; Tor, Y. Antibiotics and Bacterial Resistance in the 21st Century. *Perspect. Med. Chem.* **2014**, *6*, 25−64.

(24) Falagas, M. E.; Kasiakou, S. K.; et al. Colistin: The Revival of Polymyxins for the Management of Multidrug-Resistant Gram-Negative Bacterial Infections. *Clin. Infect. Dis.* **2005**, *40*, 1333–1341.

(25) Liu, Y. Y.; Wang, Y.; Walsh, T. R.; Yi, L. X.; Zhang, R.; Spencer, J.; Doi, Y.; Tian, G.; Dong, B.; Huang, X.; Yu, L. F.; Gu, D.; Ren, H.; Chen, X.; Lv, L.; He, D.; Zhou, H.; Liang, Z.; Liu, J. H.; Shen, J. Emergence of Plasmid-Mediated Colistin Resistance Mechanism MCR-1 in Animals and Human Beings in China: A Microbiological and Molecular Biological Study. *Lancet Infect. Dis.* **2016**, *16*, 161–168.

(26) McGann, P.; Snesrud, E.; Maybank, R.; Corey, B.; Ong, A. C.; Clifford, R.; Hinkle, M.; Whitman, T.; Lesho, E.; Schaecher, K. E. Escherichia coli Harboring mcr-1 and blaCTX-M on a Novel IncF Plasmid: First Report of mcr-1 in the United States. *Antimicrob. Agents Chemother.* **2016**, *60*, 4420–4421.

(27) Davies, M.; Walsh, T. R. A Colistin Crisis in India. *Lancet Infect. Dis.* **2018**, *18*, 256–257.

(28) Lemire, J. A.; Harrison, J. J.; Turner, R. J. Antimicrobial Activity of Metals: Mechanism, Molecular Targets and Applications. *Nat. Rev. Microbiol.* **2013**, *11*, 371–384.

(29) Chernousova, S.; Epple, M. Silver as Antibacterial Agent: Ion. Nanoparticle, and Metal. *Angew. Chem., Int. Ed.* **2013**, *52*, 1636–1653.

(30) Neissa, J.; Perez-Arnaiz, C.; Porto, V.; Busto, N.; Borrajo, E.; Leal, J. M.; Lopez-Quintela, M. A.; Garcia, B.; Dominguez, F. Interaction of Silver Atomic Quantum Clusters with Living Organisms: Bactericidal Effect of Ag$_3$ Clusters Mediated by Disruption of Topoisomerase-DNA Complexes. *Chem. Sci.* **2015**, *6*, 6717–6724.

(31) Lansdown, A. B. G. Silver in Health Care: Antimicrobial Effects and Safety in Use. *Curr. Probl. Dermaol.* **2006**, *33*, 17–34.

(32) Aziz, Z.; Abu, S. F.; Chong, N. J. A Systematic Review of Silver-Containing Dressings and Topical Silver Agents (Used with Dressings) for Burn Wounds. *Burns* **2012**, *38*, 307–318.

(33) Nherera, L. M.; Trueman, P.; Roberts, C. D.; Berg, L. A Systematic Review and Meta-Analysis of Clinical Outcomes Associated with Nanocrystalline Silver Use Compared to Alternative Silver Delivery Systems in the Management of Superficial and Deep Partial Thickness Burns. *Burns* **2017**, *43*, 939–948.

(34) Thomas, S. S.; Lawrence, J.; Thomas, A. Evaluation of Hydrocolloids and Topical Medication in Minor Burns. *J. Wound Care* **1995**, *4*, 218–220.

(35) Fisher, N. M.; Marsh, E.; Lazova, R. Scar-Localized Argyria Secondary to Silver Sulfadiazine Cream. *J. Am. Acad. Dermatol.* **2003**, *49*, 730–732.

(36) G, U. R.; Axthelm, J.; Hoffmann, P.; Taye, N.; Glaser, S.; Gorls, H.; Hopkins, S. L.; Plass, W.; Neugebauer, U.; Bonnet, S.; Schiller, A. Co-Registered Molecular Logic Gate with a CO-Releasing Molecule Triggered by Light and Peroxide. *J. Am. Chem. Soc.* **2017**, *139*, 4991–4994.

(37) Cheng, P.-S.; Hau, S. C. K.; Mak, T. C. W. Layer-Type Organosilver(I) Complexes Assembled with Nitrate and Function-alized Phenylethynide Ligands. *Inorg. Chim. Acta* **2013**, *403*, 110–119.

(38) Coyle, J. P.; Gordon, P. G.; Wells, A. P.; Mandia, D. J.; Sirianni, E. R.; Yap, G. P. A.; Barry, S. T. Thermally Robust Gold and Silver Iminopyrrolidinates for Chemical Vapor Deposition of Metal Films. *Chem. Mater.* **2013**, *25*, 4566–4573.

(39) Lane, A. C.; Vollmer, M. V.; Laber, C. H.; Melgarejo, D. Y.; Chiarella, G. M.; Fackler, J. P., Jr.; Yang, X.; Baker, G. A.; Walensky, J. R. Multinuclear Copper(I) and Silver(I) Amidinate Complexes: Synthesis, Luminesence, and CS$_2$ Insertion Reactivity. *Inorg. Chem.* **2014**, *53*, 11357–11366.

(40) Du, J.-L.; Hu, T.-L.; Zhang, S.-M.; Zeng, Y.-F.; Bu, X.-H. Tuning Silver(I) Coordination Architectures by Ligands Design: From Dinuclear, Trinuclear, to 1D and 3D Frameworks. *CrystEngComm* **2008**, *10*, 1866–1874.

(41) Wu, H.; Dong, X.-W.; Ma, J.-F. Tetrakis (β-picoline)disilver(I) (Ag-Ag) bis(2-amino-5-chloro-benzenesulfonate) dihydrate. *Acta Crystallogr., Sect. E: Struct. Rep. Online* **2006**, *E62*, m1227–m1228.

(42) Heilman, B. J.; Halpenny, G. M.; Mascharak, P. K. Synthesis, Characterization, and Light-Controlled Antibiotic Application of a Composite Material Derived from Polyurethane and Silica Xerogel

with Embedded Photoactive Manganese Nitrosyl. *J. Biomed. Mater. Res., Part B* **2011**, *99B*, 328–337.

(43) Heilman, B. J.; St John, J.; Oliver, S. R. J.; Mascharak, P. K. Light-Triggered Eradication of *Acinetobacter baumannii* by Means of NO Delivery from a Porous Material with an Entrapped Metal Nitrosyl. *J. Am. Chem. Soc.* **2012**, *134*, 11573–11582.

(44) Gupta, S.; Laskar, N.; Kadouri, D. E. Evaluating the Effect of Oxygen Concentrations on Antibiotic Sensitivity, Growth, and Biofilm Formation of Human Pathogenesis. *Microbiol. Insights* **2016**, *9*, 37–46.

(45) Flemming, H.-C.; Wingender, J.; Szewzyk, U.; Steinberg, P.; Rice, S. A.; Kjelleberg, S. Biofilms: An Emergent Form of Bacterial Life. *Nat. Rev. Microbiol.* **2016**, *14*, 563–575.

(46) Driffield, K.; Miller, K.; Bostock, J. M.; O'Neill, A. J.; Chopra, I. Increased Mutability of *Pseudomonas aeruginosa* in Biofilms. *J. Antimicrob. Chemother.* **2008**, *61*, 1053–1056.

(47) Borriello, G.; Werner, E.; Roe, F.; Kim, A. M.; Ehrlich, G. D.; Stewart, P. S. Oxygen Limitation Contributes to Antibiotic Tolerance of *Pseudomonas aeruginosa* in Biofilms. *Antimicrob. Agents Chemother.* **2004**, *48*, 2659–2664.

(48) Walters, M. C.; Roe, F.; Bugnicourt, A.; Franklin, M. J.; Stewart, P. S. Contributions of Antibiotic Penetration, Oxygen Limitation, and Low Metabolic Activity to Tolerance of Pseudomonas aeruginosa Biofilms to Ciprofloxacin and Tobramycin. *Antimicrob. Agents Chemother.* **2003**, *47*, 317–323.

(49) Wakshlak, W. B-K.; Pedahzur, R.; Avnir, D. Antibacterial Activity of Silver-Killed Bacteria: The "Zombies" Effect. *Sci. Rep.* **2015**, *5*, 9555.

(50) Bruker. *APEX 3*; Bruker AXS Inc.: Madison, WI, 2014.

(51) Bruker. *SAINT*; Bruker AXS Inc.: Madison, WI, 2012.

(52) Krause, L.; Herbst-Irmer, R.; Sheldrick, G. M.; Stalke, D. Comparison of Silver and Molybdenum Microfocus X-ray Sources for Single-Crystal Structure Determination. *J. Appl. Crystallogr.* **2015**, *48*, 3–10.

(53) Sheldrick, G. M. SHELXT – Integrated Space-Group and Crystal-Structure Determination. *Acta Crystallogr., Sect. A: Found. Adv.* **2015**, *A71*, 3–8.

(54) Sheldrick, G. M. Crystal Structure Refinement with SHELXL. *Acta Crystallogr., Sect. C: Struct. Chem.* **2015**, *C71*, 3–8.

(55) Dolomanov, O. V.; Bourhis, L. J.; Gildea, R. J.; Howard, J. A. K.; Puschmann, H. OLEX2: A Complete Structure Solution, Refinement and Analysis Program. *J. Appl. Crystallogr.* **2009**, *42*, 339–341.

423

Chapter 4.III: Synthesis, Structures and Antibacterial Properties of Cu(II) and Ag(I) Complexes Derived from 2,6-bis(benzothiazole)-pyridine.

4.III.1 Background.

The persistent emergence of multidrug-resistant (MDR) microbes, triggered by poor prescription and hasty consumption habits, will be a primary concern for human health in the forthcoming decades.[1] The World Health Organization (WHO) has recently published a report listing twelve MDR pathogens that require urgent attention, highlighting the need for developing new effective antibacterial agents.[2] Among others, human burn wound pathogens, especially the nosocomial pathogens, have surfaced as a significant threat.[3-5] These opportunistic microorganisms, including both Gram-positive and Gram-negative pathogens, have gradually developed antimicrobial resistance, rendering several treatment options ineffective. Human skin acts as a crucial layer of first defense against bacterial infections.[6,7] It also controls fluid homeostasis, thermoregulation and specific metabolic functions.[6] By disrupting the skin barriers, burn injuries alter vital physiological functions of skin, one of the most ominous consequences being the loss of ability to thwart infections. Application of topical antimicrobial agents, including silver-based materials, is the most efficient method to reduce the risk of nosocomial infections.[8,9] These agents are often utilized as adjuvant therapeutics concurrently with surgical excision procedures. Presently, silver-based materials are predominantly used as topical antimicrobials. The two most commonly used silver-based antimicrobials are silver nitrate (0.5% solution) and silver

sulfadiazine (SilvodeneTM, FlamazineTM, ThermazineTM, BurnazineTM),[10] the latter available as cream of an oil-in-water emulsion. Silver nitrate reacts rapidly with biological chloride ions and precipitates as silver chloride, thereby diminishing the availability of bioactive silver. This necessitates the continuous application of silver nitrate, which can eventually be harmful through induction of electrolytic imbalance.[11] Although silver sulfadiazine releases bioactive silver by dissociating relatively slowly compared to silver nitrate, poor dermal penetration limits its effectiveness.[12] Moreover, the sulfadiazine component has been linked with an allergic reaction in patients receiving this topical therapy.

These findings have prompted us to develop efficient silver(I)-based antimicrobial agents to treat burn wound infections which are devoid of the above limitations. In our design we attempt to isolate Ag(I) compounds that can release bio-active Ag$^+$ in a slow and sustainable fashion.[13–15] We have also designed and synthesized Ag(I) complexes with fluorogenic ligands/co-ligands towards developing theranostic antibacterial agents.[16,17] In these cases, the delivery of bioactive Ag$^+$ could be tracked within the cellular matrices through a fluorescence ''Turn-On'' event. In several occasions, we employed ligands which themselves can be bactericidal and would impart minimal cytotoxicity. This feature is crucial as upon release of the Ag$^+$ in biological milieu, the dissociated ligand should be non-toxic to the normal cells. Along this line our group has recently reported the synthesis and antibacterial properties of two Ag(I) complexes derived from benzothiazole- based ligands, namely,

Ag(pbt)$_2$](BF$_4$) and [Ag(qbt)$_2$](BF$_4$) (where pbt = 2-(pyridyl)benzothiazole and qbt = 2-(quinolyl)benzothiazole, Figure 4.III.1).[18]

Compounds containing benzothiazole moieties are well known for a range of biological activities, namely, antibacterial,[19] anti-fungal,[20] antitumor,[21] anticonvulsant,[22] and also anti-inflammatory[23] and exert none or minimal cytotoxicity. In our design we achieved the antimicrobial activity of bioactive Ag$^+$ along with additional antibacterial effect from the benzothiazole ligands. In fact, both [Ag(pbt)$_2$](BF$_4$) and [Ag(qbt)$_2$](BF$_4$) complexes exhibit excellent antibacterial activity

[Ag(pbt)$_2$]BF$_4$ **[Ag(qbt)$_2$]BF$_4$**
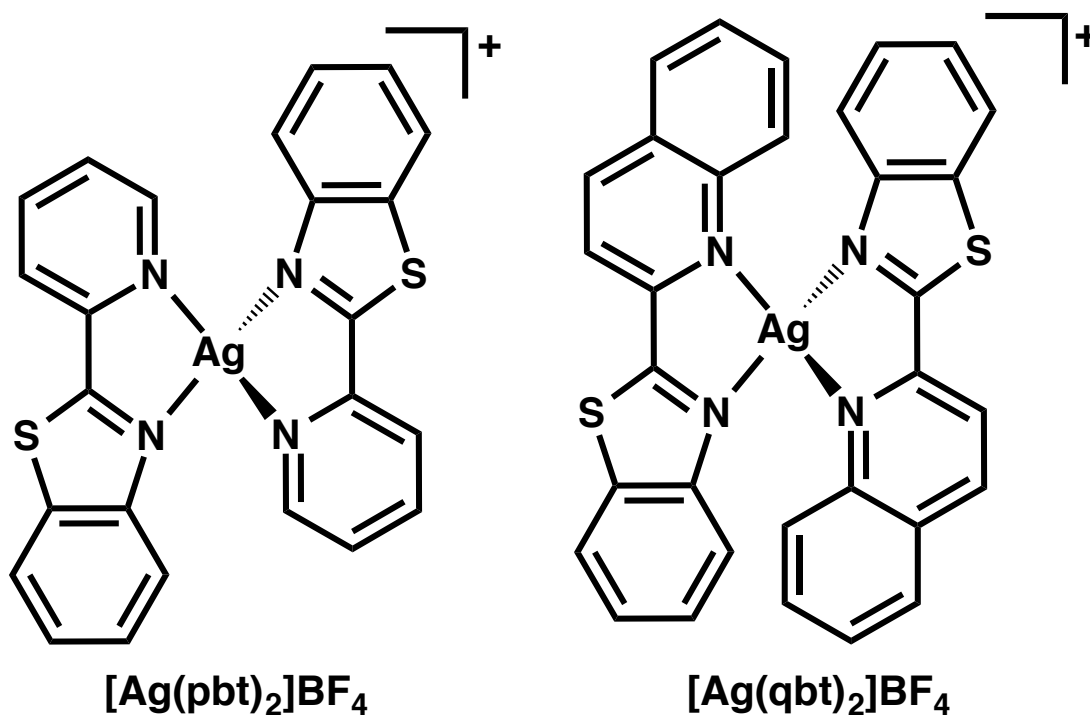
Figure 4.III.1. Schematic representation of the cations of [Ag(pbt)$_2$]BF$_4$ and [Ag(qbt)$_2$]BF$_4$.

against Gram-positive and Gram-negative pathogens. Cu(II) complexes of designed ligands also exhibit antimicrobial effects.[24] For example, Le and coworkers have reported a ternary Cu(II) complex of formula, $[Cu(pbt)(Gly)]ClO_4$ (where Gly = glycinate) and assessed its antimicrobial efficacy against two Gram-positive and two Gram-negative microorganisms,[25] In addition to the assessment of antibacterial efficacy of $[Ag(pbt)_2](BF_4)$ and $[Ag(qbt)_2](BF_4)$ complexes, we were also curious to identify the modes of binding of pbt and qbt ligands with Ag(I) centers. The free rotation of the CAC single bond conjoining the pyridyl(quinolyl) and the benzothiazole moiety presents the possibility of either a N,N or a N,S-coordination. Despite the known preference of silver towards S-donors, in these two complexes, N, N-coordination by the ligands has been realized exclusively (Figure 4.III.1).

In the present work, we sought to explore the possibility of synthesizing complexes of two coinage metals (Cu and Ag) with a closely related ligand, namely, 2,6-bis(benzothiazole)-pyridine (bztpy). This ligand along with its benzimidazole derivative has previously been utilized to develop spin crossover complexes with fascinating properties.[26–28] Our interest in bztpy ligand arose from the fact that the ligand frame consists of two benzothiazole fragment, rendering the ability of this ligand to bind metal centers in a tridentate fashion. In addition, bztpy can adopt three possible binding conformations as shown in Figure 4.III.2. Herein we report the syntheses of two new complexes of coinage metals derived from the bztpy ligand, namely, $[CuCl_2(bztpy)_2]$ **1** and $[Ag_2(bztpy)_2](CF_3SO_3)_2$ **2** (Figure 4.III.3). Single crystal X-ray structure determination has revealed very distinct molecular structure for the two
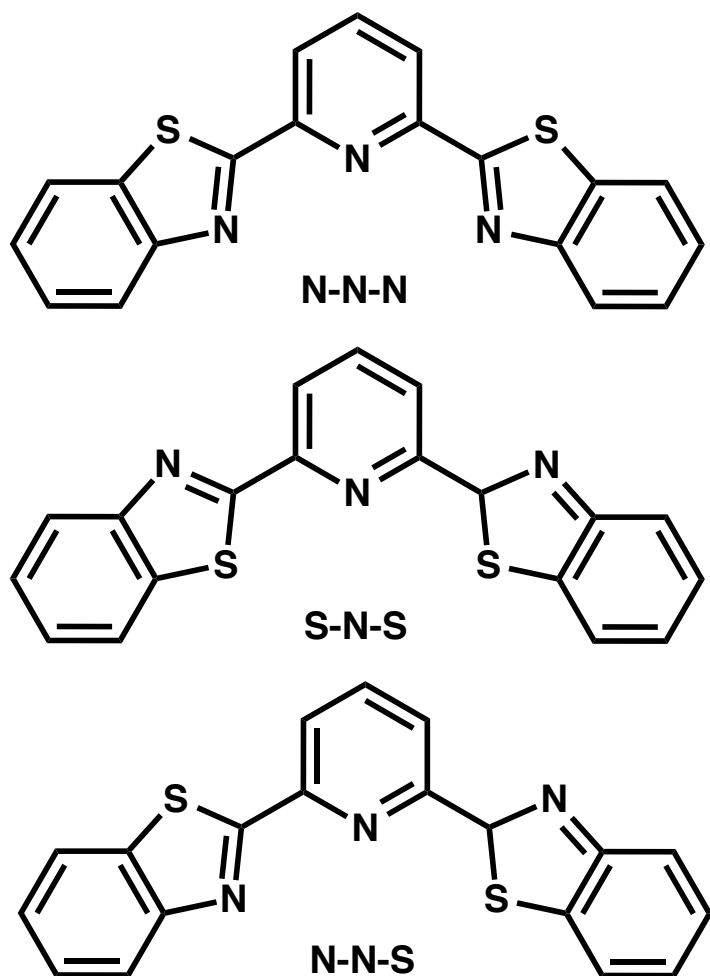
Figure 4.III.2. Possible modes of binding of the bztpy ligand to a metal center.

complexes though the N,N,N-binding mode of the ligand is observed in each case. While the Cu(II) complex has been isolated as a monomer, the Ag(I) complex revealed a unique double helical dimeric structure. Both complexes have been characterized by conventional analytical techniques and their antibacterial efficacy has been assessed against a Gram-positive and a Gram-negative bacterial strain with the aid of a soft tissue and skin infection (SSTI) model.
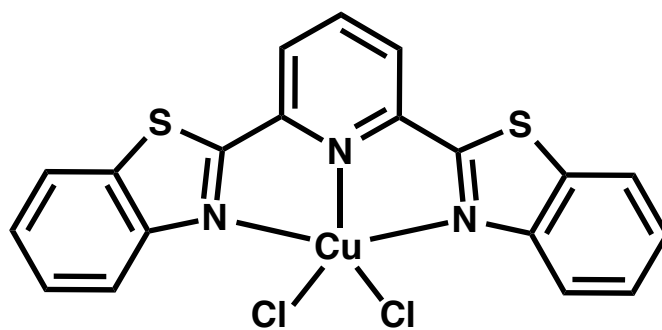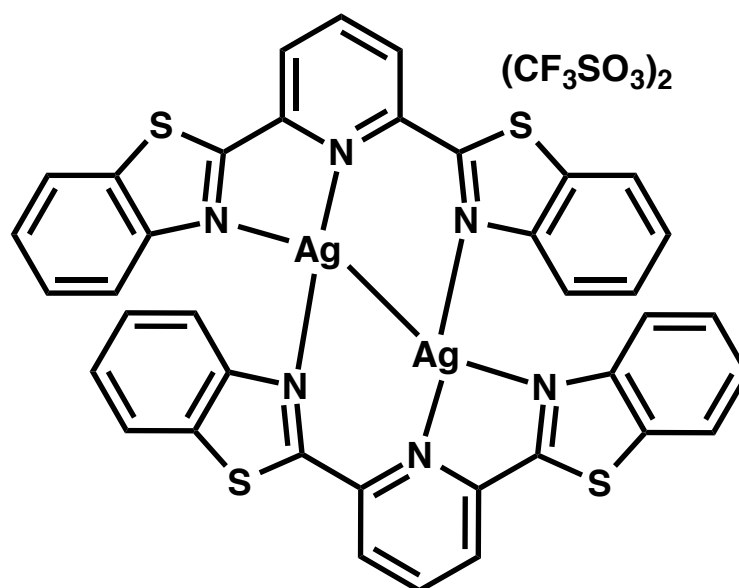
Figure 4.III.3. Schematic representation of the two complexes reported in this work.

4.III.2 Results and Discussion.

4.III.2.1 Synthesis and Spectroscopic Properties.

Syntheses of **1** and **2** were achieved by addition of $CuCl_2$ and $Ag(CF_3SO_3)$ respectively to a methanolic solution of bztpy ligand. Significant quenching of the ligand fluorescence was noted upon addition of the metal salts in both cases (Figure

4.III.4). Both complexes precipitated upon completion of the reactions and pure products were isolated upon filtration and subsequent washing of the residues with cold methanol. Electronic absorption spectra of the two complexes and bztpy uniformly exhibit a band with λ_{max} at 325 nm. In case of complex **1**, a second absorption centered at 365 nm was noted which extends beyond 400 nm (Figure 4.III.5). The X-band EPR spectrum of complex **1** (Figure 4.III.6) is characteristic of a mononuclear Cu(II) system with axial g tensor and the four-line hyperfine splitting on the parallel region
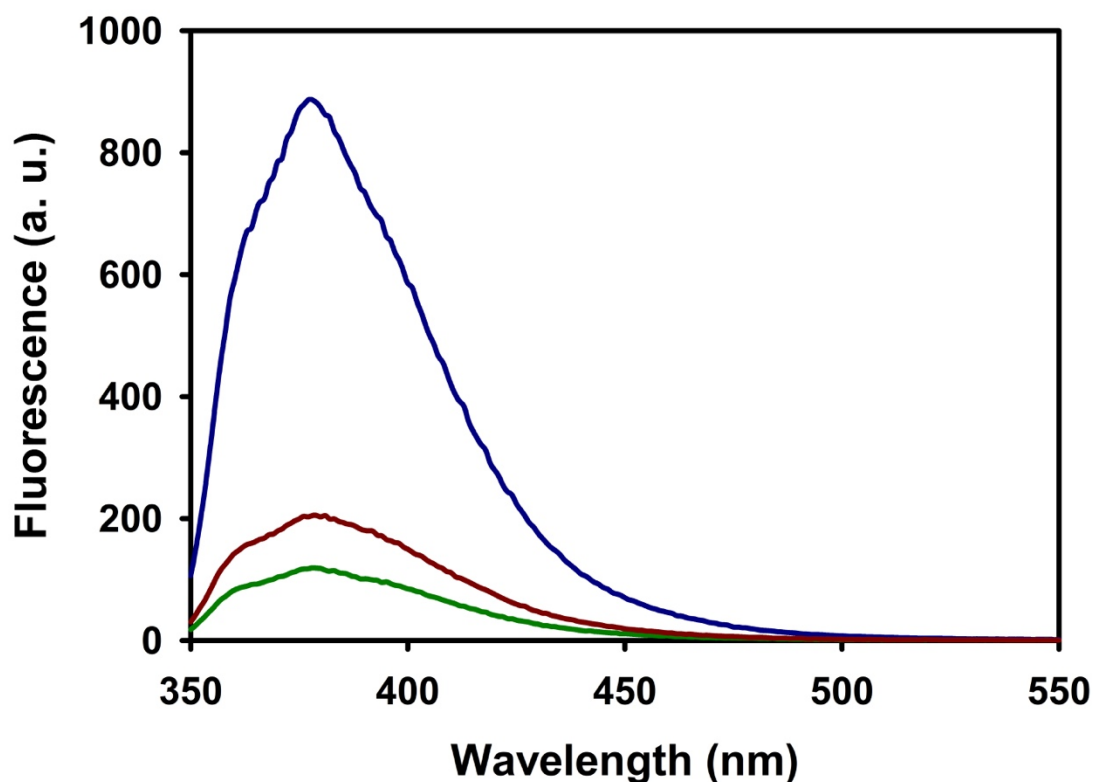
Figure 4.III.4. Fluorescence quenching of the bztpy ligand (blue trace) by Cu in complex **1** (green trace), and by Ag in complex **2** (red trace).

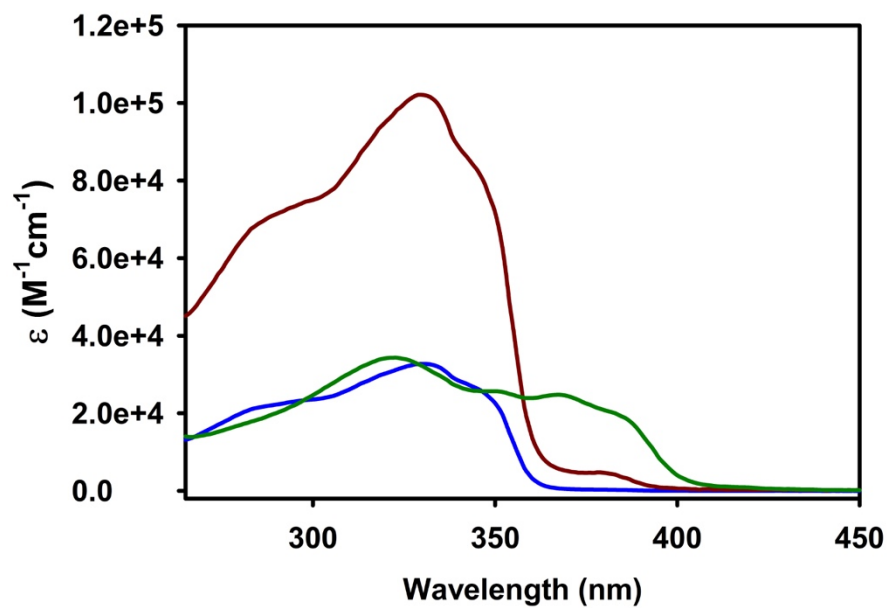**Figure 4.III.5.** Absorbance spectra of free bztpy ligand (blue trace), complex **1** (green trace) and complex **2** (red trace) in dichloromethane.
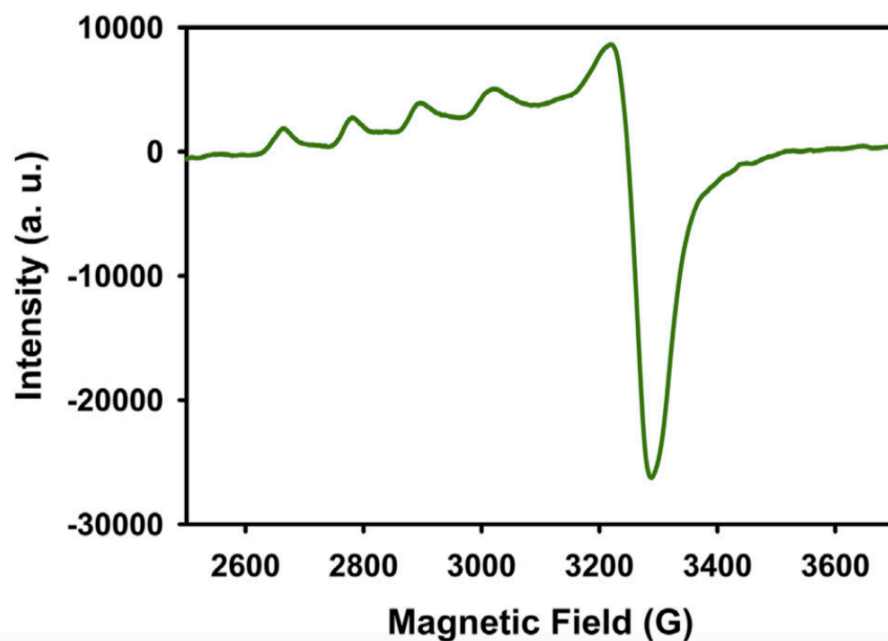
Figure 4.III.6. X-band EPR spectrum of complex **1** at 77 K. Microwave frequency, 9.44 GHz; modulation amplitude, 2.00G; modulation frequency, 100 KHz.

originating from a spin doublet, S = 1/2, interacting with a single I = 3/2 nuclear moment. The calculated g|| and A|| values (2.381 and 117 G) are comparable to a reported distorted pentacoordinate Cu(II) complex derived from a similar ligand containing benzimidazole moieties.[29]

4.III.2.2 X-Ray Structure Description.

Single crystal X-ray crystallographic analyses reveal the molecular structures of the two complexes (**1** and **2**). The perspective views of the structures are shown in Figures 4.III.7 and 4.III.8 selected metric parameters are listed in Tables 4.III.1 and 4.III.2.

Table 4.III.1. Selected bond distances (Å) and angles (°) for **1**.

	1
Cu1-N1	2.010 (3)
Cu1-N2	2.058 (3)
Cu1-N3	2.060 (3)
Cu1-Cl1	2.3987 (13)
Cu1-Cl2	2.2624 (12)
Cl1Cu1-Cl1	109.39 (5)
N1-Cu1-Cl1	112.42 (10)
N1-Cu1-Cl2	138.07 (10)
N1-Cu1-N2	77.58 (14)
N1-Cu1-N3	78.69 (13)
N2-Cu1-Cl1	93.70 (10)
N2-Cu1-Cl2	96.87 (10)
N2-Cu1-N3	156.08 (13)
N3-Cu1-Cl1	98.06 (10)

Table 4.III.2. Selected bond distances (Å) and angles (°) for **2**.

	2
Ag1-N1	2.610 (7)
Ag1-N2	2.214 (6)
Ag1-N3	2.260 (7)
Ag2-N4	2.568 (6)
Ag3-N5	2.211 (7)
Ag2-N6	2.263 (6)
Ag1-Ag2	2.9310 (11)
N1-Ag1-N3	69.9 (2)
N1-Ag1-N5	118.7 (2)
N6-Ag2-N4	69.2 (2)
N2-Ag2-N4	124.7 (2)
N6-Ag2-N2	163.0 (2)

A CSD (accessed on November 18, 2018) survey revealed only three crystal structures of metal complexes of 2,6-bis(benzothiazole)-pyridine (bztpy) ligand reported so far. Two of these mononuclear complexes contain Mn(II) centers and the third one comprises a Fe(III) center. The coordination geometry of the Mn (II) complexes[30] are similar to that of **1**, where the ligand binds the respective metal centers in a tridentate fashion and the central metals reside in a distorted square pyramidal coordination environment (for **1** see Table 4.III.1). In case of the Fe(III) complex the ligand binds the metal center also in a tridentate fashion and the remaining sites are occupied by three chlorides, resulting in a distorted octahedral system.[31]

X-ray structure of complex **2** (Figure 4.III.8) reveals a binuclear com- plex with two chemically equivalent but crystallographically distinct Ag(I) centers and each

Figure 4.III.7. Perspective view of the molecular structure of complex **1**. The thermal ellipsoids are shown at 50% probability level (H atoms are omitted in the labeling scheme are shown only for the hetero atoms for the sake of clarity).

metal center resides in highly distorted trigonal environment. As shown in Figure 4.III.8, the molecular structure of complex **2** is quite interesting. Here each of the bztpy ligand binds two different Ag(I) centers. Despite the potential to form two five-membered chelate rings, each ligand forms one chelate ring with a Ag atom through the pyridyl N and the N atom of one of the benzothiazole moieties, while the remaining N atom of the second benzothiazole fragment of the same ligand binds a different Ag(I) center in a monodentate fashion (Figure 4.III.8). This bonding arrangement results in a
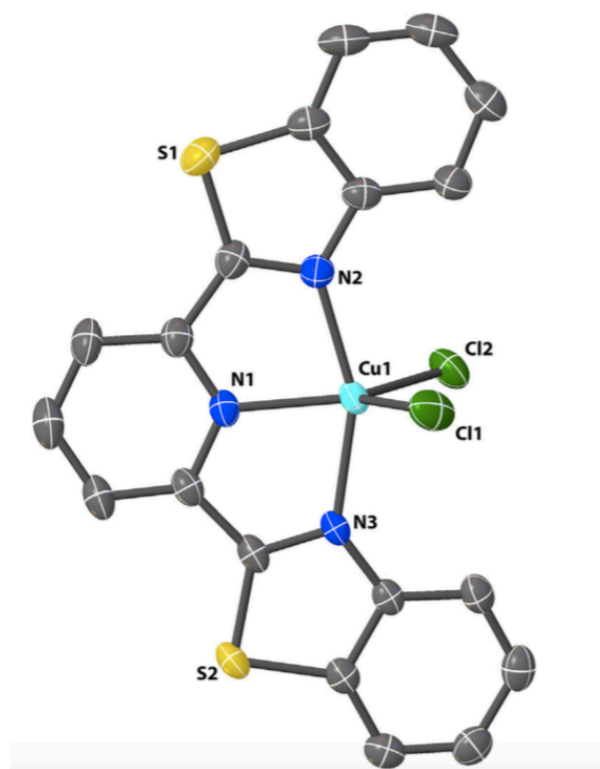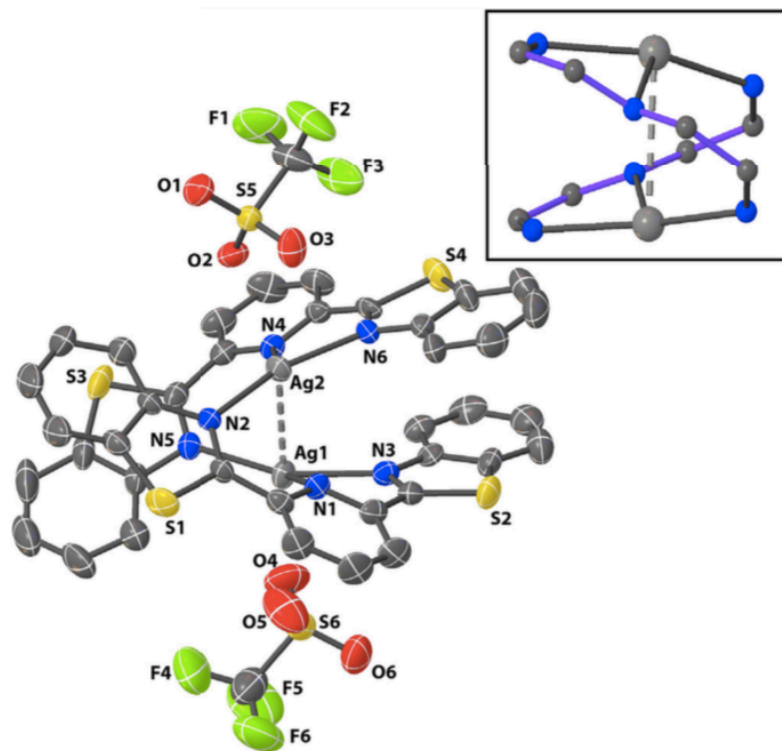
Figure 4.III.8. Perspective view of the molecular structure of the cation of complex **2**. The thermal ellipsoids are shown at 50% probability level (H atoms are omitted, and the labeling scheme are shown only for the hetero atoms for the sake of clarity, dotted line represents Ag ⋯ Ag argentophilic interactions). The inset displays the helical coordination around the two Ag(I) centers.

double-helical coordination pattern around the two metal centers as highlighted in the inset of Figure 4.III.8. Williams and coworkers have reported a double-helical dinculear Cu(I) complex, namely $[Cu_2(L1)_2]^{2+}$ (where L1 = 2,6-bis(methylbenzimidazole-2-yl)pyridine). However, in this structure each L1 ligand

binds the two Cu(I) centers in different fashion giving rise to a quasi-linear coordination geometry.[32]

Complexes **1** and **2** reported in this account represent the first examples of coinage metal complexes derived from bztpy ligands. Moreover, the double helical coordination pattern in complex **2** is noteworthy. In **1**, the two five-membered chelate rings are highly planar with average mean deviations of 0.010 Å. The distorted square pyramidal geometry around the Cu(II) center can be realized from the Cl1–Cu1–Cl2 bond angle (109.39(5)°, Table 4.III.1). In this complex the bztpy ligand also exhibits reasonable planarity with mean deviation of 0.075 Å. In case of **2**, both Ag(I) centers are tri-coordinated and the planes constituted by Ag1, N1, N3, N5 and Ag2, N2, N4, N6 are noticeably deviated from planarity (mean deviations, 0.130 and 0.071 Å respectively). In this complex the two five-membered chelate rings (from two different bztpy ligands) are also severely distorted from planarity (mean deviations, 0.095 and 0.164 Å).

In complex **1**, the Cu–N(pyridyl) bond length and the average Cu–N(benzothiazole) bond distances are 2.010(3) and 2.059(3) Å respectively. These values are comparable (1.972(6) and 2.062 (7) Å respectively) to corresponding bond lengths in another five coordinated Cu(II) complex, namely, [Cu(pbt)$_2$(H$_2$O)](ClO$_4$)$_2$.[34] In case of **2**, the average Ag-N(pyridyl) and Ag-N(benzothiazole) bond distances are 2.589(6) and 2.237(6) Å respectively. The Ag-N(pyridyl) length in **2** is noticeably longer compared to the corresponding distance (2.453(6) Å) observed with the Ag(I) complex [Ag(pbt)$_2$](BF$_4$), previously reported by our group.[18] The Ag-N

(benzothiazole) distances in **2** and [Ag(pbt)$_2$](BF$_4$) are however comparable (2.237(6) and 2.256(6) Å respectively). The two complexes have different coordination geometry, which might have some influence towards the modest differences in the metric parameters. In **2**, a relatively stronger intra dimer Ag ⋯ Ag interaction has been noted (2.9310(11) Å). This is significantly shorter than twice the van der Waals radius of Ag(I) (3.44 Å).[34] This intradimer interaction between two d^{10} metal centers is possible via significant participation of 5s and 5p orbitals in bonding that are close in energy to the 4d orbitals. Though no π– π stacking contributed to reinforce the Ag ⋯ Ag interaction in case of **2**, the double helical pattern of the two ligands might have facilitated bringing the two metal centers sufficiently closer.

The packing pattern of **1** (Fig 4.III.9), reveal no classical hydrogen bonding interactions. However, two moderate non-classical interactions consolidated its extended structure [C20-H20A ⋯ S1, with H ⋯ S, 2.83 Å^i and C20-H20B ⋯ Cl1, with H ⋯ Cl, 2.11 Å; symmetry code: (i) x + 1/2, y + 3/2, z 1/2]. The extended lattice of **2** is consolidated with few non classical hydrogen bonding interactions involving the metal complex cation and the triflate counter anions [C3-H ⋯ O2, with H ⋯ O, 2.59Å^i; C4-H4 ⋯ S1, with H ⋯ S, 2.76Å; C17-H17 ⋯ O4, with H ⋯ O, 2.52Å^{ii}; C21-H21 ⋯ O6, with H ⋯ O, 2.39 Å^{iii}; C22-H22 ⋯ O6, with H ⋯ O, 2,54 Å^{ii}; C23-H23 ⋯ S4, with H ⋯ S, 2.79Å and C35-H35 ⋯ O3, with H ⋯ O, 2.51Å^{iv}; symmetry codes: (i) x+1, y, z; (ii) x+1, y+1, z; (iii) x1, y, z; (iv) x +1, y+1, z+1. The packing pattern is shown in Figure 4.III.10.
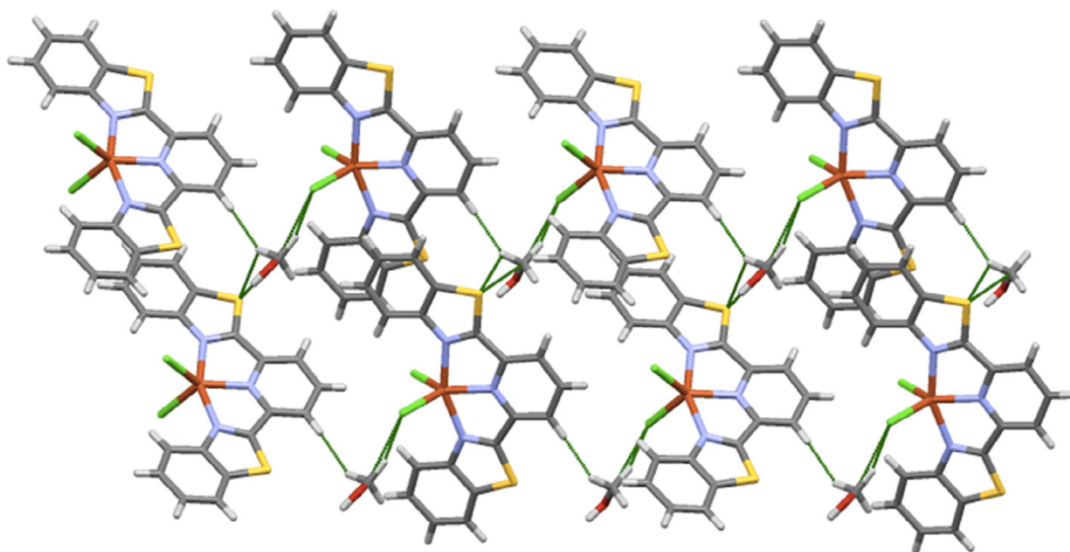
Figure 4.III.9. Packing pattern of complex **1** extending along *b* axis, green lines indicating non-classical hydrogen bonding interactions.
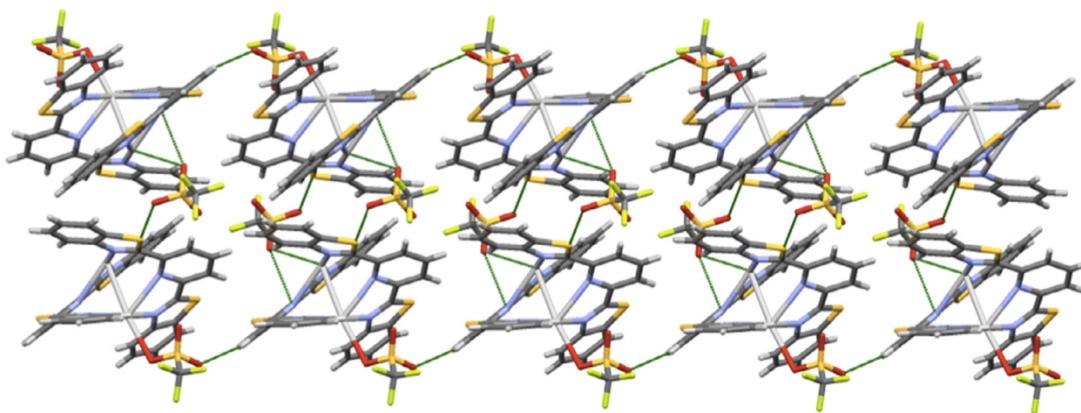

Figure 4.III.10. Packing pattern of complex **2** extending along *b* axis, green lines indicating non-classical hydrogen bonding interactions.

4.III.2.3 Antibacterial Studies Using Skin and Soft Tissue Infection Model.

The antimicrobial efficacies of complexes **1** and **2** were tested using a SSTI model previously developed in this laboratory.[35] This model resembles skin infections by mimicking the gradual penetration of bacteria into the underlying soft tissue. In brief, the system is composed of a soft brine agar layer inoculated with a Gram-positive (Staphylococcus epidermidis) or Gram-negative (Acinetobacter baumannii) bacterium to reach a concentration of 8.0×10^5 CFU mL^{-1}. The inoculated soft agar layer lies on top of a nutrient rich agar. The soft brine agar allows for bacterial mobility, while the nutrient rich bottom agar layer promotes penetration. The SSTI model addresses some of the limitations of standard susceptibility tests discussed in detail elsewhere.[35] The antimicrobial properties of **1** and **2** were tested using 7 mm diameter KBr disks containing 2% w/w of the complexes under investigation. Control KBr disks containing bztpy, AgNO$_3$, or only KBr were also fabricated and tested in a similar manner. All KBr disks were prepared fresh and placed carefully on top of the inoculated agar plates.

The SSTI antibacterial experimental results are presented in Figure 4.III.11. Inoculation of the soft brine agar with the bacteria afforded uniform lawns through the entire agar plate. No zones of inhibition were observed in the cultures when using bztpy or blank KBr disks. However, disks containing **1**, **2**, or AgNO$_3$ displayed well-defined zones of inhibition. In all cases (Figure 4.III.11) the zones of inhibition of **2** and AgNO$_3$ were noticeably larger than the zones of inhibition of **1**. This is in line with the well-established superior antimicrobial efficacy of Ag-based compounds. Unlike other antibiotics, the bioactive silver (Ag$^+$ ions) inflicts damage to bacterial cells through
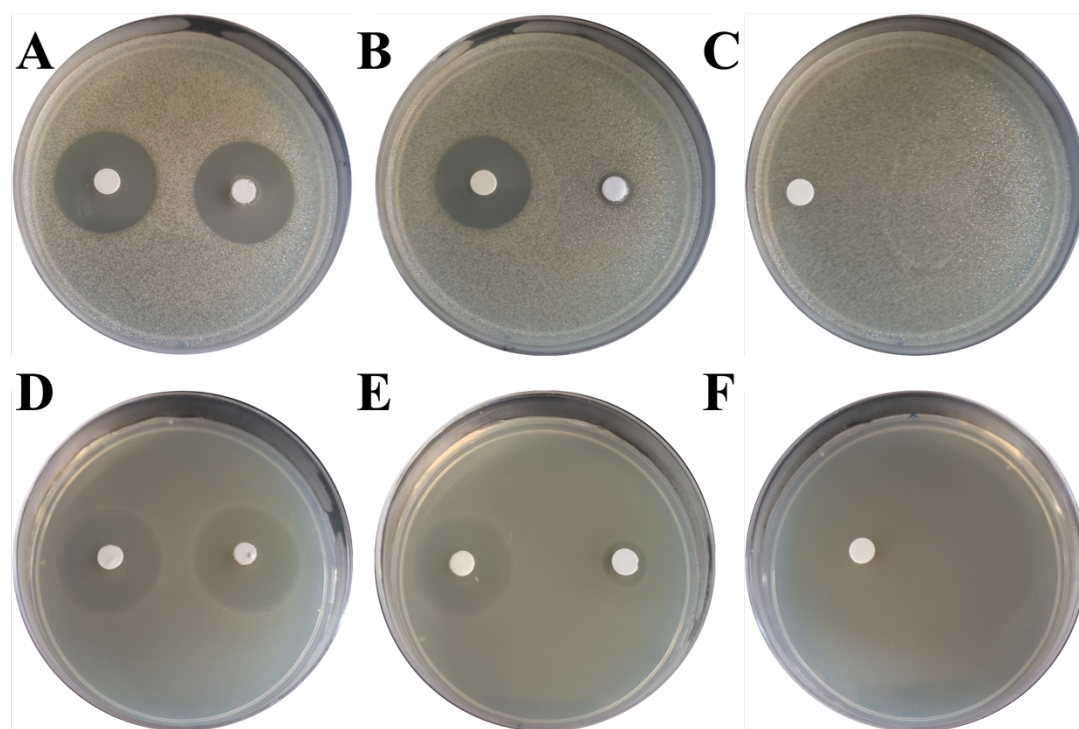
Figure 4.III.11. Clearing of bacterial growth of *Acinetobacter baumannii* (top row): pate (A) KBr pellet 2% (w/w) with complex **2** (left side) and AgNO$_3$ (right side); Plate (B) KBR pellet 2% (w/w) with complex **2** (left side) and complex **1** (right side); Plate (C) KBr pellet 2% (w/w) with bztpy (left side) and blank pellet (right side). *Staphylococcus epidermidis* (bottom row): plate (D) KBr pellet 2% (w/w) with complex **2** (left side) and AgNO$_3$ (right side); Plate (E) KBr pellet 2% (w/w) with complex **2** (left side and complex **1** (right side); Plate (F) KBr Pellet 2% (w/w) with bztpy (left side) and blank pellet (right side).

multiple mechanisms, making it difficult for these microorganisms to develop resistance.[36] For both bacterial strains, AgNO$_3$ and **2** produced zones of inhibition of 25 ± 3 mm and 27 ± 3 mm respectively for *S. epidermidis*. The zones of inhibition for

complex **1** were 8 ± 3 mm and 12 ± 3 mm for *A. baumannii* and *S. epidermidis* respectively. No growth was observed when fresh growth media was inoculated with agar containing the entire depth of the zones of inhibition. It is important to note here that due to insoluble nature of the two complexes in aqueous (biological) media, their antibacterial efficiency is limited by diffusion. Despite this fact, **2** was able to produce relatively large zones of inhibition. Modest electronegative surface potential of bacterial cell walls is known to allow more facile cell penetration in case of cationic complexes compared to their neutral analogues.[37] Thus, the dicationic silver complex **2** in the present work would enjoy the relative ease of cellular internalization into the bacterial cells compared to the neutral copper complex **1**. Additionally, the zones of inhibition of **2** were on average somewhat larger than those produced by $AgNO_3$ salt. Although $AgNO_3$ is soluble in water, the high reactivity of Ag^+ results in the rapid precipitation as AgCl when exposed to high concentration of Cl, as present in the soft brine agar. It is also interesting to note that the zones of inhibition observed were consistently larger for *S. epidermidis* compared to *A. baumannii*. This can be attributed to relatively higher antimicrobial resistance displayed by the *Gram-negative* bacteria.

4.III.3 Conclusions.

In conclusion two complexes of coinage metals (**1** and **2**) derived from 2,6-bis(benzothiazole)-pyridine (bztpy) ligand have been synthesized and structurally characterized. X-ray structure of the dimeric complex **2** reveals a double helical arrangement of the two ligands around two Ag(I) atoms. This pattern might have also

contributed towards reinforcing the strong argentophilic interactions between the Ag(I) centers (Ag $\cdots$ Ag, 2.9310(11) Å). Antibacterial efficacies of both complexes have been assessed against one Gram-positive and one Gram-negative bacterial strains with aid of a SSTI model previously developed in this laboratory. While almost no growth inhibition has been noted with bztpy ligand itself, significant clearance of bacterial lawns has been realized with both complexes (**1** and **2**). Between the two complexes, **2** inflicts considerably more antimicrobial actions uniformly against both types of bacteria. These findings are in accordance with the well-known broad-spectrum antibacterial property of Ag-based compounds. Moreover, the dicationic complex **2** enjoys the advantage of facile cellular internalization compared to the neutral complex **1**. Complexes with few other derivatives of bis (benzothiazole)-based ligand systems and their antimicrobial properties are currently under investigation in this laboratory.

4.III.4 Experimental.

4.III.4.1 General Materials and Methods.

All reagents were of commercial grade and were used without further purification unless stated otherwise. 2,6-bis(benzothiazole)-pyridine (bztpy) was synthesized in high yield following a literature procedure.[38] A PerkinElmer Spectrum-One FT-IR spectrometer was used to record the IR spectra. UV–Vis spectra were obtained with a Varian Cary 50 UV–Vis spectrophotometer. Luminescence measurements were carried out with a Cary-Eclipse Fluorescence Spectrophotometer.

High-resolution ESI-MS data were recorded on an LTQ-Orbitrap VelosPro MS instrument. A Bruker EMX Spectrometer was used to record the EPR spectrum of **1**.

4.III.4.2 Synthesis of [CuCl$_2$(bztpy)] **1**.

A batch of 0.200 g (0.580 mmol) of bztpy was dissolved in 25m L of methanol, followed by the addition of solid CuCl$_2$ (0.078 g, 0.580 mmol). The reaction mixture immediately turned from cloudy white to greenish-yellow. After 4 h, the volume of the reaction mixture was reduced at low pressure and the resulting microcrystalline greenish powder was collected by vacuum filtration. The residue was then washed three times using 10 mL portions of cold methanol to obtain **1** in 94% yield (0.260g, 0.542 mmol) as a microcrystalline greenish-yellow powder. Selected IR (KBr disk, cm^{-1}) 3448 (m), 1600 (w), 1585 (w), 1566 (w), 1558 (w), 1494 (s), 1434, (w), 1409 (w), 1322 (m), 1266 (w), 1248 (w), 1182 (m), 1028 (w), 899 (w), 817 (m), 722 (s), 720 (w). UV– Vis (MeCN:DMF 1:99), λ_{max} (ε, M^{-1} cm^{-1}): 325 nm (34,000); 365 nm (25,000). ESI-MS (m/z): 442.98 [Cu(bzpty)Cl]$^+$.

4.III.4.3 Synthesis of [Ag$_2$(bztpy)$_2$](CF$_3$SO$_3$)$_2$ **2**.

A solution of silver trifluoromethane sulfonate (0.149g, 0.580 mmol) in methanol (5 mL) was added to a solution of bztpy (0.200 g, 0.580 mmol) in 25 mL of methanol. The mixture was stirred magnetically for 16 h at room temperature when an off-white solid separated. The volume of the mixture was then reduced at low pressure and the precipitate was collected via vacuum filtration. The residue was then washed using

three 10 mL portions of cold methanol. Complex 2 was obtained in 92% yield (0.320 g, 0.531 mmol) as an off-white powder. Selected IR (KBr disk, cm1) 3052 (m), 1584 (w), 1566 (m), 1514 (m), 1448 (m), 1434 (m), 1321, (s), 1084 (s), 1072 (s), 1050 (s), 1035 (s), 976 (s), 816 (m), 755 (s), 736 (s), 719 (m), 647 (w). UV–Vis (MeCN:DMF 1:99), λ_{max} (ε, M^{-1} cm^{-1}): 325 nm (102,000). ESI-MS (m/z): 453.94 $[Ag_2(bzpty)_2]^{2+}$; 798.98 $[Ag(bztpy)_2]^+$.

4.III.4.4 Growth Conditions for Bacterial Cultures.

Strains of *S. epidermidis* and *A. baumannii* were prepared by spreading frozen liquid cultures (20 glycerol 72 ℃) on Luria broth agar (LBA) plates and incubating them for 18 h at 37 ℃. Individual colonies from each plate were used to inoculate 5 mL of sterile Luria broth (LB), following incubation for 18 h at 37 ℃ with constant shaking (250 rpm). The bacterial cells were then washed, suspended in fresh LB, and diluted to OD_{600} = 1.0. Dilutions of this stock were used for determination of colony forming units (CFU) mL^{-1}. The conversion factors found for *S. epidermidis* and *A. baumannii* were 1.4 x 10^8 CFU mL^{-1}, and 3.2 x 10^8 CFU mL^{-1}, respectively.

4.III.4.5 Skin and Soft Tissue Infection Model and Bactericidal Assays.

The SSTI model was prepared by following literature procedures[17] with minor adjustments. In brief, soft brine agar (1.0% NaCl w/v, 0.8% agar w/v) was autoclaved and placed in a 45 ℃ water bath. The agar was then inoculated with the respective bacteria to reach a concentration of 8.0 x 10^5 CFU mL^{-1}. The inoculated agar solution

was then vortexed to produce a homogeneous suspension of bacteria and 8 mL were carefully poured over a modified nutrition agar (composition: starch 0.15% w/v, beef extract 0.4% w/v, tryptone 1.5% w/v and agar 1.5% w/v). The resulting plates were incubated for 1 h at 37 ºC to allow the bacteria to adhere and form cell-to-cell contacts. KBr disks containing 2% w/w of $AgNO_3$, bztpy, **1**, or **2** were prepared by grinding each compound individually with KBr to obtain a homogeneous mixture. Then 35 ± 2 mg of each mixture were pressed into disks with a 2-ton load. Blank disks containing only KBr were prepared in a similar manner. The disks were carefully removed from their mold, placed over the SSTI model, and incubated at 37 ºC for 18 h.

4.III.4.6 Determination of Viable Bacteria in the Zones of Inhibition.

The KBr disks were carefully lifted from the SSTI model, and agar samples 0.5 cm x 0.5 cm x 0.5 cm were removed from the zone of inhibition. The removed sections of agar were then placed in 3 mL of sterile LB and incubated for 18 h at 37 ºC with constant shaking (250 rpm). The growth of the bacteria was assessed by spreading 10 µL of this solution on fresh LBA plates and incubating them at 37 ºC for 18 h. All experiments were performed in triplicate at a minimum.

4.III.4.7 X-Ray Data Collection and Structure Refinement.

Block-shaped crystals of the complexes (**1** and **2**) were obtained by recrystallization through diffusion of hexanes into their dichloromethane (CH_2Cl_2) solutions. In both cases a suitable crystal was selected and mounted on a Bruker D8

Quest diffractometer equipped with PHOTON 100 detector operating at T = 298 K. Data were collected with ω shutter less scan technique using graphite monochromated Mo Kα radiation (λ = 0.71073 Å). The total number of runs and images for data collection was based on strategy calculation from the program APEX3 (Bruker).[39] Resolution of θ > 25º was achieved in both cases. Cell parameters were retrieved using the SAINT (Bruker) software.[40] and refined using SAINT (Bruker) on 2449 reflections for **1** and 8794 reflections for **2**. Data reduction was performed using the SAINT (Bruker) software, which corrects for Lorentz and polarization effects. The final completeness is 99.6% and 99.2% for **1** and **2** respectively. Multi-scan absorption corrections were performed on all data sets using SADABS 2016/2.[41] The minimum and maximum transmissions for **1** are 0.644 and 0.745, and for **2** are 0.867 and 0.962. The structures for complexes **1** and **2** were solved in the space group P*21/n* (No. 11) and P-*1* (No. 2) respectively by intrinsic phasing using the SHELXT (Sheldrick, 2015)[42] structure solution program and refined by full matrix least square procedure on F2 using version 2016/6 of SHELXL.[43] The non-hydrogen atoms were refined anisotropically in all cases. Hydrogen atom positions were calculated geometrically and refined using the riding model. To alleviate the complications related to solvent accessible voids within the extended lattice in case of **2**, the SQUEEZE operation (included in the PLATON program) was performed with the raw data set and the structure was refined form the data obtained upon SQUEEZE operation.[43] All calculations and molecular graphics were preformed using either SHELXTL 2014 or

Olex2[44] programs. Crystal data and structure refinement parameters are listed in Table 4.III.3 and Table 4.III.4.

Table 4.II.3. Crystal data and structure refinement parameters for complex **1**.

	1
Empirical formula	$C_{20}H_{15}Cl_2CuN_3S_2O$
T(K)	293
λ (Å)	0.71073
Crystal system	Monoclinic
Space group	$P2_1/n$
a (Å)	9.219 (2)
b (Å)	13.822 (3)
c (Å)	17.227 (4)
α (°)	90
β (°)	96.600 (4)
γ (°)	90
V (Å^3)	2023.0 (8)
Z	4
D_{calc} (Mg m^{-3})	1.681
Absorption Coeff (mm^{-1})	1.57
No. of unique reflections	3694
Goodness-of-fit[a] on F^2	1.130
R_1[b]	0.046
wR_2[c]	0.102

Table 4.II.4. Crystal data and structure refinement parameters for complex **2**.

	2
Empirical formula	$C_{40}H_{22}Ag_2N_6S_6O_7F_6$
T(K)	293
λ (Å)	0.71073
Crystal system	Triclinic
Space group	*P-1*
a (Å)	10.5611 (14)
b (Å)	14.116 (3)
c (Å)	17.388 (3)
α (°)	69.171 (4)
β (°)	82.126 (5)
γ (°)	85.684 (4)
V (Å^3)	2398.9
Z	2
D_{calc} (Mg m^{-3})	1.690
Absorption Coeff (mm^{-1})	1.15
No. of unique reflections	9721
Goodness-of-fit[a] on F^2	1.040
R_1[b]	0.074
wR_2[c]	0.197

4.III.5 References.

1. Klein, E. Y.; Boeckel, T. P.; Martinez, E. M.; Pant, S.; Gandra, S.; Levin, S. A.; Goossens, H.; Laxminarayan, R. Global increase and geographic convergence in antibiotic consumption between 2000 and 2015. *Proc. Natl. Acad. Sci. USA* **2018**, *115*, E3463-E3470.

2. World Health Organization Report http://www.who.int/en/news-room/detail/27-02-2017-who-publishes-list-of-bacteria-for-which-new-antibiotics-are-urgently-needed, 2017.

3. Ponce-de-Leon, A.; Rodriguez-Noriega, E.; Morfin-Otero, R.; Cornejo-Juarez, D. P.; Tonoco, J. C.; Cervantes, J. L. V.; Sifuentes-Osorni, J. Antimicrobial susceptibility of gram negative bacilli isolated from intra-abdominal and urinary-tract infections in Mexico from 2009 to 2015: Results from the Study for Monitoring Antimicrobial Resistance Trends (SMART). *PLoS One* **2018**, *13*, e0198621.

4. Mehrab, B.; Clark, N. M.; Zhanel, G. G.; Lynch, J. P. Antimicrobial resistance in hospital acquired Gram-negative bacterial infections. *Chest* **2015**, *147*, 1413-1421.

5. Altoparlak, U.; Erol, S.; Akcay, M. N.; Celebi, F.; Kadanali, A. The time-related changes of antimicrobial resistance patterns ad predominant bacterial profiles of burn wounds and body flora of burned patients. *Burns* **2004***, 30*, 660-664.

6. Boer, M.; Duchnik, E.; Maleszka, R.; Marchlewicz, M. Structural and biophysical characteristics of human skin in maintaining proper epidermal barrier function. *Postepy. Dermatol. Alergol.* **2016***, 33*, 1-5.

7. DeBoer, S.; O'Connor, Prehospital and emergency department burn care. A. *Crit. Care Nurs. Clin. North Am.* **2004***, 16,* 61-73.

8. Tong, Q. J.; Hammer, K. D. P.; Johnson, E. M.; Zegarra, M.; Goto, M.; Lo, T. S. A systematic review and meta-analysis on the use of prophylactic topical antibiotics for the prevention of uncomplicated wound infections. *Infect. Drug Resist.* **2018***, 11,* 417-425.

9. Banerjee, S.; Argaez. C. Topical Antibiotics for Infection Prevention: A Review of the Clinical Effectiveness and Guidelines. Canadian Agency for Drugs and Technologies in Health, 2017.

10. Politano, A. D.; Campbell, K. T.; Rosenberger, L. H.; Sawyer, R. G. Use of silver in the prevention and treatment of infections: Silver review. *Surg. Infect.* **2013***, 14*, 8-9.

11. Heggers, J. P.; Hawkins, H.; Edgar, P.; Villarreal, C.; Herndon, D. N. Treatment of infections in burns, in: D.N. Herndon (Ed.), Total Burn Care, Saunders, London, England, 2002, 120–169.

12. Fox Jr, C. L.; Modak, S. M. Mechanism of silver sulfadiazine action on burn wound infections. *Antimicrob. Agents Chemother.* **1974***, 5*, 582-588.

13. Jimenez, J.; Chakraborty, I.; Rojas-Andrade, M.; Mascharak, P. K. Silver complexes of ligands derived from adamantylamines: water-soluble silver-donating compounds with antibacterial properties. *J. Inorg. Biochem.* **2017***, 168*, 13-17.

14. Jimenez, J.; Chakraborty, I.; Del Cid, A. M.; Mascharak, P. K. Five- and six-coordinated silver(I) complexes derived from 2,6-(pyridyl)iminodiadamantanes: sustained release of bioactive silver. *Inorg. Chem.* **2017***, 56,* 4784-4787.

15. deBoer, T. R.; Chakraborty, I.; Mascharak, P. K. Design and construction of a silver(I)-loaded cellulose-based wound dressing: trackable and sustained release of silver for controlled therapeutic delivery to wound sites. *J. Mater. Sci: Mater Med.* **2015***, 26*, 243.

16. Pinto, M. N.; Chakraborty, I.; Schultz-Simonton, W.; Rojas-Andrade, M.; Braslau, R.; Mascharak, P. K. Tracking silver delivery to bacteria using turn on fluorescence. *Chem. Commun.* **2017***, 53*, 1459-1462.

17. Pinto, M. N.; Martinez-Gonzalez, J.; Chakraborty, I.; Mascharak, P. K. Incorporation of a theranostic "two-tone" luminescent silver complex into biocompatible agar hydrogel composite for the eradication of *ESKAPE* pathogens in a skin and soft tissue infection model. *Inorg. Chem.* **2018***, 57*, 6692-6701.

18. Stenger-Smith, J.; Chakraborty, I.; Sameera, W. M. C.; Mascharak, P. K. Antimicrobial silver (I) complexes derived from aryl-benzothiazoles as turn-on sensors: syntheses, properties and density functional studies. *Inorg. Chim. Acta* **2018***, 471,* 326-335.

19. Sahu, P. K.; Sahu, P. K.; Gupta, S. K.; Thavaselvam, D.; Agarwal, D. D. Synthesis and evaluation of antimicrobial activity of 4H-pyrimido[2,1-*b*]benzothiazole pyrazole and benzylidene derivatives of curcumin. *Eur. J. Med. Chem.* **2012***, 54*, 366-378.

20. Yamazaki, K.; Kaneko, Y.; Suwa, K.; Ebara, S.; Nakazawa, K.; Yasuno, K. Synthesis of potent and selective inhibitors of Candida albicans N-myristoyltransferase based on the benzothiazole structure. *Bioorg. Med. Chem.* **2005**, *13*, 2509-2522.

21. Weekes, A. A.; Westwell, A. D. 2-Arylbenzotiazoles as privileged scaffold in drug discovery. *Curr. Med. Chem.* **2009**, *16*, 2430-2440.

22. Gagoria, J.; Verma, P. K.; Khatkar, A. Anticonvulsant and neurological profile of benzothiazoles: a mini-review. *Cent. Nerv. Syst. Agents Med. Chem.* **2015**, *15,* 11-16.

23. Kumar, V.; Sharma, S.; Husain, A. Synthesis and in vivo anti-inflammatory and analgesic activities of oxadiazoles clubbed with benzothiazole nucleus. *Int. Cur. Pharm. J.* **2015**, *4*, 457-461.

24. Hossain M. S.; Zakaria, C. M.; Kudrat-E-Zahan, M. Metal complexes as potential antimicrobial agent: a review. *Am. J. Heterocy. Chem.* **2018**, *4*, 1-21.

25. Lu, Y.; Chen, Y.; Ou, Z.; Chen, S.; Zhuang, C.; Le, X. Synthesis, antibacterial activities and nuclease properties of ternary copper(II) complex containing 2-(2'-pyridyl)benzothiazole and glycinate. *Chin. J. Chem.* **2012**, *30*, 303-310.

26. Boca, R.; Boca, M.; Dlhan, L.; Falk, K.; Fuess, H.; Haase, W.; Jarosciak, R.; Papankova, B.; Renz, F.; Vrbova, M.; Werner, R. Strong cooperativeness in the mononuclear iron(II) derivative exhibiting an abrupt spin transition above 400 K. *Inorg. Chem.* **2001**, *40*, 3025-3033.

27. Boca, R.; Baran, P.; Boca, M.; Dlhan, L.; Fuess, H.; Haase, W.; Linert, W.; Papankova, B.; Werner, R. Spin crossover in bis(2,6-bis(benzimidazole-2-yl)pyridine)iron(II) tetraphenylborate. *Inorg. Chim. Acta* **1998**, *278,* 190-196.

28. Linert, W. Konecny, M.; Renz, F. Spin-state equilibria in non-aqueous solution and quantum-mechanical investigation of iron(II) and nickel(II) complexes with 4-substituted 2,6-bis(benzimidazole-2-yl)pyridines. *J. Chem. Soc. Dalton Trans.* **1994**, 1523-1531.

29. Batra, G.; Mathur, P. Antibacterial and antifungal studies of macrocyclic complexes of trivalent transition metal ions with their spectroscopic approach. *Transit. Met. Chem.* **1995**, *20*, 26-33.

30. Thompson, J. R.; Williams, V. E.; Leznoff, D. B. The role of hydrogen bonds in facilitating planar alignment of Mn(II) halide 2,6-bis(benzimidazole)pyridine-based complexes. *Cryst. Growth Des.* **2017**, *17*, 1180-1189.

31. Boca, M.; Boca, R.; Kickelbick, G.; Linert, W.; Svoboda, I.; Fuess, H. Novel complexes of 2,6-bis(benzthiazol-2-yl)pyridine. *Inorg. Chim. Acta* **2002**, *338,* 36-50.

32. Piguet, C.; Bernardinelli, G.; Williams, A. F. Preparation and crystal structure of the unusual double-helical copper(I) comples bis(2,6-bis(1-methylbenzimidazol-2-yl)pyridine)dicoper(I) naphthalene-1,5-disulfonate. *Inorg. Chem.* **1989**, *28*, 2920-2925.

33. Beloglazkina, E. K.; Yudin, I. V.; Majouga, A. G.; Moiseeva, A. A.; Tursina, A. I.; Zyk, N. V. Synthesis and electrochemical study of 2-(2-pyridyl)benzothiazole

complexes with transition metals (Co^{II}, Ni^{II}, and Cu^{II}). Molecular structure of aquabis[2-(2-pyridyl)benzothiazole]copper(II) diperchlorate. *Russ. Chem. Bull. Int. Ed.* **2006***, 55,* 1803-1809.

34. Bondi, A. van der Waals Volumes and Radii. *J. Phys. Chem.* **1964***, 68,* 441-451.

35. Heilman, B. J.; St. John, J.; Oliver, S. R. J.; Mascharak, P. K. Light-triggered eradication of *Acinetobacter baumannii* by means of NO delivery from a porous material with an entrapped metal nitrosyl. *J. Am. Chem. Soc.* **2012***, 134,*11573-11582.

36. Jung, W. K.; Koo, H. C.; Kim, K. W.; Shin, S.; Kim, S. H.; Park, Y. H. Antibacterial activity and mechanisms of action of the silver ion in *Staphylococcus aureus* and *Escherichia coli*. *Appl. Environ. Microbiol.* **2008***, 74*, 2171-2178.

37. van Rijt, S. H.; Sadler, P. J. Current applications and future potential for bioinorganic chemistry in the development of anticancer drugs. *Drug Discov. Today* **2009***, 14,* 1089-1097.

38. Guerriero, P.; Bullita, E.; Vigato, P.; Pietro, A.; Pelli, B.; Traldi, P. Synthesis and unexpected reactions of 2-hydroxy-3-pyridinylacetic hydrazides. Formation of 2H-pyrrolo[2,3-*b*]pyridin-2-ones. *J. Heterocycl. Chem.* **1998***, 25*, 145-149.

39. Bruker APEX3, Bruker AXS Inc. Madison, Wisconsin, USA, 2014.

40. Bruker SAINT, Bruker AXS Inc., Madison, Wisconsin, USA, 2012.

41. Bruker SADABS, Bruker AXS Inc., Madison, Wisconsin, USA, 2016.

42. Sheldrick, G. M. SHELXT – Integrated Space-Group and Crystal-Structure Determination. *Acta Cryst.* **2015**, A*71*, 3-8.

43. Spek. A. L. PLATON SQUEEZE: a tool for the calculation of the disordered solvent contribution to the calculated structure factors. *Acta Crystallogr.* **2015**, *C71*, 9-18.

44. Dolomanov, O. V.; Bourhis, L. J.; Gildea, R. J.; Howard, J. A. K.; Puschmann, H. OLEX2: A Complete Structure Solution, Refinement and Analysis Program. *J. Appl. Cryst.* **2009**, *42*, 339-341.

4.III.6 Reprints of Publications and Permissions.

Reprinted with permissions from Chakraborty, I.; Pinto, M. N.; Stenger-Smith, J.; Martinez-Gonzalez, J.; Mascharak, P. K. Synthesis, structures and antibacterial properties of Cu(II) and Ag(I) complexes derived from 2,6-bis(benzothiazole)-pyridine. Polyhedron **2019**, In Press, Corrected Proof.

Synthesis, structures and antibacterial properties of Cu(II) and Ag(I) complexes derived from 2,6-bis(benzothiazole)-pyridine

Indranil Chakraborty [1], Miguel Pinto, Jenny Stenger-Smith, Jorge Martinez-Gonzalez, Pradip K. Mascharak *

Department of Chemistry and Biochemistry, University of California Santa Cruz, Santa Cruz, CA 95064, United States

A B S T R A C T

Two new coinage metal complexes, namely [Cu(bztpy)Cl$_2$] (**1**) and [Ag$_2$(bztpy)$_2$](CF$_3$SO$_3$) (**2**) (where bztpy = 2,6-bis(benzothiazole)-pyridine) have been synthesized and structurally characterized. The coordination geometry of **1** is distorted square pyramidal, while in case of the dinuclear complex **2**, the two crystallographically distinct Ag centers resides in a highly distorted trigonal coordination environment. In this structure the two ligands bind the metal centers in a way that results in a double helical pattern. Both complexes exert strong antimicrobial actions against *Gram-positive* and *Gram-negative* bacterial strain. The zone of bacterial clearance by complex **2** in SSTI (soft tissue and skin infection) model is found to be comparable to that by silver nitrate. For both types of pathogens, complex **2** inflicts superior growth inhibition compared to complex **1** under same experimental conditions.

Published by Elsevier Ltd.

1. Introduction

The persistent emergence of multidrug-resistant (MDR) microbes, triggered by poor prescription and hasty consumption habits, will be a primary concern for human health in the forthcoming decades [1]. The World Health Organization (WHO) has recently published a report listing twelve MDR pathogens that require urgent attention, highlighting the need for developing new effective antibacterial agents [2]. Among others, human burn wound pathogens, especially the nosocomial pathogens, have surfaced as a significant threat [3–5]. These opportunistic microorganisms, including both *Gram-positive* and *Gram-negative* pathogens, have gradually developed antimicrobial resistance, rendering several treatment options ineffective. Human skin acts as a crucial layer of first defense against bacterial infections [6,7]. It also controls fluid homeostasis, thermoregulation and specific metabolic functions [6]. By disrupting the skin barriers, burn injuries alter vital physiological functions of skin, one of the most ominous consequences being the loss of ability to thwart infections. Application of topical antimicrobial agents, including silver-based materials, is the most efficient method to reduce the risk of nosocomial infections [8,9]. These agents are often utilized as adjuvant therapeutics

concurrently with surgical excision procedures. Presently, silver-based materials are predominantly used as topical antimicrobials.

The two most commonly used silver-based antimicrobials are silver nitrate (0.5% solution) and silver sulfadiazine (Silvodene™, Flamazine™, Thermazine™, Burnazine™) [10], the latter available as cream of an oil-in-water emulsion. Silver nitrate reacts rapidly with biological chloride ions and precipitates as silver chloride, thereby diminishing the availability of bioactive silver. This necessitates the continuous application of silver nitrate, which can eventually be harmful through induction of electrolytic imbalance [11]. Although silver sulfadiazine releases bioactive silver by dissociating relatively slowly compared to silver nitrate, poor dermal penetration limits its effectiveness [12]. Moreover, the sulfadiazine component has been linked with an allergic reaction in patients receiving this topical therapy.

These findings have prompted us to develop efficient silver(I)-based antimicrobial agents to treat burn wound infections which are devoid of the above limitations. In our design we attempt to isolate Ag(I) compounds that can release bio-active Ag$^+$ in a slow and sustainable fashion [13–15]. We have also designed and synthesized Ag(I) complexes with fluorogenic ligands/coligands towards developing theranostic antibacterial agents [16,17]. In these cases the delivery of bioactive Ag$^+$ could be tracked within the cellular matrices through a fluorescence "Turn-On" event. In several occasions, we employed ligands which themselves can be bactericidal and would impart minimal cytotoxicity. This feature is crucial as upon release of the Ag$^+$ in biological milieu, the dissociated ligand should be non-toxic to the normal cells. Along this

---

* Corresponding author. Fax (831) 459 2935.
 E-mail address: deposit@ccdc.cam.ac.uk (P.K. Mascharak).
 [1] Present address: Department of Chemistry and Biochemistry, Florida International University, Miami, FL 33174, United States.

line our group has recently reported the synthesis and antibacterial properties of two Ag(I) complexes derived from benzothiazole-based ligands, namely, [Ag(pbt)₂](BF₄) and [Ag(qbt)₂](BF₄) (where pbt = 2-(pyridyl)benzothiazole and qbt = 2-(quinolyl)benzothiazole, Scheme 1) [18].

Compounds containing benzothiazole moieties are well known for a range of biological activities, namely, antibacterial [19], antifungal [20], antitumor [21], anticonvulsant [22] and also anti-inflammatory [23] and exert none or minimal cytotoxicity. In our design we achieved the antimicrobial activity of bioactive Ag⁺ along with additional antibacterial effect from the benzothiazole ligands. In fact both [Ag(pbt)₂](BF₄) and [Ag(qbt)₂](BF₄) complexes exhibit excellent antibacterial activity against *Gram-positive* and *Gram-negative* pathogens. Cu(II) complexes of designed ligands also exhibit antimicrobial effects [24]. For example, Le and coworkers have reported a ternary Cu(II) complex of formula, [Cu(pbt)(Gly)]ClO₄ (where Gly = glycinate) and assessed its antimicrobial efficacy against two *Gram-positive* and two *Gram-negative* microorganisms [25]. In addition to the assessment of antibacterial efficacy of [Ag(pbt)₂](BF₄) and [Ag(qbt)₂](BF₄) complexes, we were also curious to identify the modes of binding of pbt and qbt ligands with Ag(I) centers. The free rotation of the C—C single bond conjoining the pyridyl(quinolyl) and the benzothiazole moiety presents the possibility of either a N,N or a N,S-coordination. Despite the known preference of silver towards S-donors, in these two complexes, N, N-coordination by the ligands has been realized exclusively (Scheme 1).

In the present work, we sought to explore the possibility of synthesizing complexes of two coinage metals (Cu and Ag) with a closely related ligand, namely, 2,6-bis(benzothiazole)-pyridine (bztpy). This ligand along with its benzimidazole derivative has previously been utilized to develop spin crossover complexes with fascinating properties [26–28]. Our interest in bztpy ligand arose from the fact that the ligand frame consists of two benzothiazole fragment, rendering the ability of this ligand to bind metal centers in a tridentate fashion. In addition, bztpy can adopt three possible binding conformations as shown in Scheme 2. Herein we report the syntheses of two new complexes of coinage metals derived from the bztpy ligand, namely, [CuCl₂(bztpy)₂] (**1**) and [Ag₂(bztpy)₂] (CF₃SO₃)₂ (**2**) (Scheme 3). Single crystal X-ray structure determina-

tion has revealed very distinct molecular structure for the two complexes though the N,N,N-binding mode of the ligand is observed in each case. While the Cu(II) complex has been isolated as a monomer, the Ag(I) complex revealed a unique double helical dimeric structure. Both complexes have been characterized by conventional analytical techniques and their antibacterial efficacy has been assessed against a *Gram-positive* and a *Gram-negative* bacterial strain with the aid of a soft tissue and skin infection (SSTI) model.

2. Experimental

2.1. Materials and methods

All reagents were of commercial grade and were used without further purification unless stated otherwise. 2,6-bis(benzothiazole)-pyridine (bztpy) was synthesized in high yield following a literature procedure [29]. A PerkinElmer Spectrum-One FT-IR spectrometer was used to record the IR spectra. UV–Vis spectra were obtained with a Varian Cary 50 UV–Vis spectrophotometer. Luminescence measurements were carried out with a Cary-Eclipse Fluorescence Spectrophotometer. High-resolution ESI-MS data were recorded on an LTQ-Orbitrap Velos Pro MS instrument. A Bruker EMX Spectrometer was used to record the EPR spectrum of **1**.
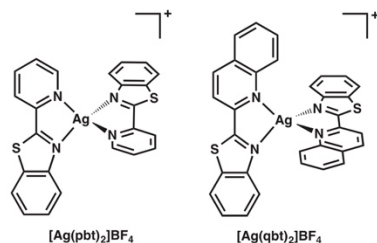
2.2. Synthesis of complexes

2.2.1. Synthesis of [CuCl₂(bztpy)] (**1**)

A batch of 0.200 g (0.580 mmol) of bztpy was dissolved in 25 mL of methanol, followed by the addition of solid CuCl₂ (0.078 g, 0.580 mmol). The reaction mixture immediately turned from cloudy white to greenish-yellow. After 4 h, the volume of the reaction mixture was reduced at low pressure and the resulting microcrystalline greenish powder was collected by vacuum filtration. The residue was then washed three times using 10 mL portions of cold methanol to obtain **1** in 94% yield (0.260 g, 0.542 mmol) as a microcrystalline greenish-yellow powder. Selected IR (KBr disk, cm⁻¹) 3448 (m), 1600 (w), 1585 (w), 1566 (w), 1558 (w), 1494 (s), 1434, (w), 1409 (w), 1322 (m), 1266 (w), 1248 (w), 1182 (m), 1028 (w), 899 (w), 817 (m), 722 (s), 720 (w). UV–Vis (MeCN:DMF 1:99), λ_max (ε, M⁻¹ cm⁻¹): 325 nm (34 000); 365 nm (25,000). ESI-MS (m/z): 442.98 [Cu(bzpty)Cl]⁺.

2.2.2. Synthesis of [Ag₂(bztpy)₂](CF₃SO₃)₂ (**2**)

A solution of silver trifluoromethane sulfonate (0.149 g, 0.580 mmol) in methanol (5 mL) was added to a solution of bztpy (0.200 g, 0.580 mmol) in 25 mL of methanol. The mixture was stirred magnetically for 16 h at room temperature when an off-white solid separated. The volume of the mixture was then reduced at low pressure and the precipitate was collected via vacuum filtration. The residue was then washed using three 10 mL portions of cold methanol. Complex **2** was obtained in 92% yield (0.320 g, 0.531 mmol) as an off-white powder. Selected IR (KBr disk, cm⁻¹) 3052 (m), 1584 (w), 1566 (m), 1514 (m), 1448 (m), 1434 (m), 1321, (s), 1084 (s), 1072 (s), 1050 (s), 1035 (s), 976 (s), 816 (m), 755 (s), 736 (s), 719 (m), 647 (w). UV–Vis (MeCN:DMF 1:99), λ_max
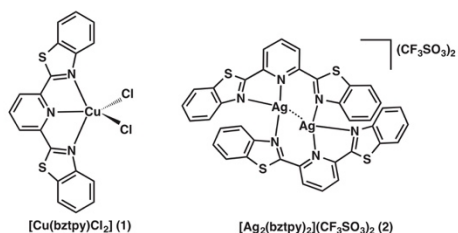

Scheme 1. Schematic representation of the cations of [Ag(pbt)₂]BF₄ and [Ag(qbt)₂] BF₄ complexes.
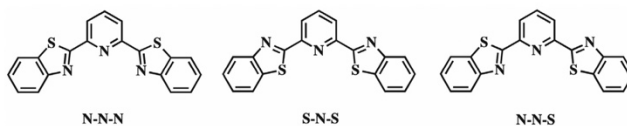
Scheme 2. Possible modes of binding of the bztpy ligand to a metal center.

459

Scheme 3. The two complexes reported in this work.

(ε, M^{-1} cm^{-1}): 325 nm (102 000). ESI-MS (*m/z*): 453.94 [Ag$_2$(bztpy)$_2$]$^{2+}$; 798.98 [Ag(bztpy)$_2$]$^+$.

2.3. Growth conditions for bacterial cultures

Strains of *S. epidermidis* and *A. baumannii* were prepared by spreading frozen liquid cultures (20 glycerol −72 °C) on Luria broth agar (LBA) plates and incubating them for 18 h at 37 °C. Individual colonies from each plate were used to inoculate 5 mL of sterile Luria broth (LB), following incubation for 18 h at 37 °C with constant shaking (250 rpm). The bacterial cells were then washed, suspended in fresh LB, and diluted to OD$_{600}$ = 1.0. Dilutions of this stock were used for determination of colony forming units (CFU) mL^{-1}. The conversion factors found for *S. epidermidis* and *A. baumannii* were 1.4 × 10^8 CFU mL^{-1}, and 3.2 × 10^8 CFU mL^{-1}, respectively.

2.4. Skin and soft tissue infection model and bactericidal assays

The SSTI model was prepared by following literature procedures [17] with minor adjustments. In brief, soft brine agar (1.0% NaCl w/ v, 0.8% agar w/v) was autoclaved and placed in a 45 °C water bath. The agar was then inoculated with the respective bacteria to reach a concentration of 8.0 × 10^5 CFU mL^{-1}. The inoculated agar solution was then vortexed to produce a homogeneous suspension of bacteria and 8 mL were carefully poured over a modified nutrition agar (composition: starch 0.15% w/v, beef extract 0.4% w/v, tryptone 1.5% w/v and agar 1.5% w/v). The resulting plates were incubated for 1 h at 37 °C to allow the bacteria to adhere and form cell-to-cell contacts. KBr disks containing 2% w/w of AgNO$_3$, bztpy, **1**, or **2** were prepared by grinding each compound individually with KBr to obtain a homogeneous mixture. Then 35 ± 2 mg of each mixture were pressed into disks with a 2-ton load. Blank disks containing only KBr were prepared in a similar manner. The disks were carefully removed from their mold, placed over the SSTI model, and incubated at 37 °C for 18 h.

2.5. Determination of viable bacteria in the zones of Inhibition

The KBr disks were carefully lifted from the SSTI model, and agar samples 0.5 cm × 0.5 cm × 0.5 cm were removed from the zone of inhibition. The removed sections of agar were then placed in 3 mL of sterile LB at 37 °C for 18 h with constant shaking (250 rpm). The growth of the bacteria was assessed by spreading 10 μL of this solution on fresh LBA plates and incubating them at 37 °C for 18 h. All experiments were performed in triplicate at a minimum.

2.6. X-ray data collection and structure refinement

Block-shaped crystals of the complexes (**1** and **2**) were obtained by recrystallization through diffusion of hexanes into their dichloromethane (CH$_2$Cl$_2$) solutions. In both cases a suitable crystal was selected and mounted on a Bruker *D8 Quest* diffractometer equipped with PHOTON 100 detector operating at *T* = 298 K. Data were collected with ω shutter less scan technique using graphite monochromated Mo Kα radiation (λ = 0.71073 Å). The total number of runs and images for data collection was based on strategy calculation from the program *APEX3* (Bruker) [30]. Resolution of θ > 25° was achieved in both cases. Cell parameters were retrieved using the SAINT (Bruker) software [31] and refined using SAINT (Bruker) on 2449 reflections for **1** and 8794 reflections for **2**. Data reduction was performed using the SAINT (Bruker) software, which corrects for Lorentz and polarization effects. The final completeness is 99.6% and 99.2% for **1** and **2** respectively. Multi-scan absorption corrections were performed on all data sets using SADABS 2016/2 [32]. The minimum and maximum transmissions for **1** are 0.644 and 0.745, and for **2** are 0.867 and 0.962. The structures for complexes **1** and **2** were solved in the space group *P*2$_1$/*n* (No. 11) and *P-1* (No. 2) respectively by *intrinsic phasing* using the SHELXT (Sheldrick, 2015) [33] structure solution program and refined by full matrix least square procedure on F^2 using version 2016/6 of SHELXL [33]. The non-hydrogen atoms were refined anisotropically in all cases. Hydrogen atom positions were calculated geometrically and refined using the riding model. To alleviate the complications related to solvent accessible voids within the extended lattice in case of **2**, the *SQUEEZE* operation (included in the PLATON program) was performed with the raw data set and the structure was refined form the data obtained upon *SQUEEZE* operation [34]. All calculations and molecular graphics were preformed using

Table 1
Crystal data and structure refinement parameters for the complexes.

	1	**2**
Formula	C$_{20}$H$_{15}$Cl$_2$CuN$_3$S$_2$O	C$_{40}$H$_{22}$Ag$_2$N$_6$S$_6$O$_7$F$_6$
D_{calc} (g cm^{-3})	1.681	1.690
M (mm^{-1})	1.57	1.15
Formula weight	511.91	1220.73
Color	green	yellow
Shape	block	block
T (K)	298(2)	298(2)
Crystal System	monoclinic	triclinic
Space group	*P*2$_1$/*n*	$P\bar{1}$
a (Å)	9.219(2)	10.5611(14)
b (Å)	12.822(3)	14.116(3)
c (Å)	17.227(4)	17.388(3)
α (°)	90	69.171(4)
β (°)	96.600(4)	82.126(5)
γ (°)	90	85.684(4)
V (Å^3)	2023.0(8)	2398.9(7)
Z	4	2
Wavelength (Å)	0.71073	0.71073
Radiation type	Mo Kα	Mo Kα
2θ$_{min}$ (°)	6.20	5.80
2θ$_{max}$ (°)	50.80	52.80
Measured Refl.	18 230	44 254
Independent Refl.	3694	9721
Reflections Used	2886	4918
R_{int}	0.049	0.106
Parameters	264	604
GOF[a]	1.130	1.040
wR$_2$[c]	0.102	0.197
R$_1$[b]	0.046	0.074

[a] GOF = [Σ [ω (F$_o^2$ − F$_c^2$)^2]/(N_o − N_v)]$^{1/2}$ (N_o = number of observations, N_v = number of variables).
[b] R$_1$ = Σ ||F$_o$| − |F$_c$||/Σ |F$_o$|.
[c] wR$_2$ = [(Σ ω (F$_o^2$ − F$_c^2$)^2/ Σ |F$_o$|^2)]$^{1/2}$.

460

either SHELXTL 2014 or *Olex2* [35] programs. Crystal data and structure refinement parameters are listed in Table 1. CCDC 1,874,951 (complex **1**), CCDC 1,874,952 (complex **2**) contains the supplementary crystallographic data for this paper. These data can be obtained free of charge from The Cambridge Crystallographic Data Center via http://www.ccdc.cam.ac.uk/data_request.cif.

3. Results and discussion

3.1. Synthesis and spectroscopic properties

Syntheses of **1** and **2** were achieved by addition of $CuCl_2$ and Ag (CF_3SO_3) respectively to a methanolic solution of bztpy ligand. Significant quenching of the ligand fluorescence was noted upon addition of the metal salts in both cases (Fig. S1). Both complexes precipitated upon completion of the reactions and pure products were isolated upon filtration and subsequent washing of the residues with cold methanol. Electronic absorption spectra of the two complexes and bztpy uniformly exhibit a band with λ_{max} at 325 nm. In case of complex **1**, a second absorption centered at 365 nm was noted which extends beyond 400 nm (Fig. S2). The X-band EPR spectrum of complex **1** (Fig. 1) is characteristic of a mononuclear Cu(II) system with axial g tensor and the four line hyperfine splitting on the parallel region originating from a spin doublet, $S = 1/2$, interacting with a single $I = 3/2$ nuclear moment. The calculated $g_\parallel$ and $A_\parallel$ values (2.381 and 117 G) are comparable to a reported distorted pentacoordinate Cu(II) complex derived from a similar ligand containing benzimidazole moieties [36].

3.2. Description of the X-ray structures

Single crystal X-ray crystallographic analyses reveal the molecular structures of the two complexes (**1** and **2**). The perspective views of the structures are shown in Figs. 2, and 3 and selected metric parameters are listed in Tables 2 and 3.

A CSD (accessed on November 18, 2018) survey revealed only three crystal structures of metal complexes of 2,6-bis(benzothiazole)-pyridine (bztpy) ligand reported so far. Two of these mononuclear complexes contain Mn(II) centers and the third one comprises a Fe(III) center. The coordination geometry of the Mn(II) complexes [37] are similar to that of **1**, where the ligand binds the respective metal centers in a tridentate fashion and the central metals reside in a distorted square pyramidal coordination environment (for **1** see Table 2). In case of the Fe(III) complex the ligand binds 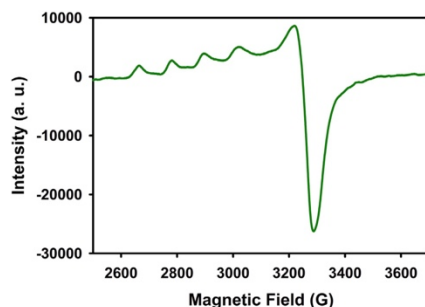the metal center also in a tridentate fashion and the remaining sites are occupied by three chlorides, resulting in a distorted octahedral system [38].
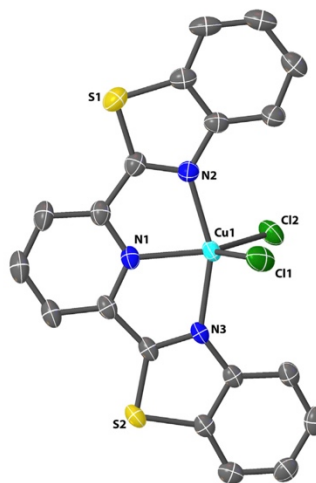

Fig. 2. Perspective view of the molecular structure of complex **1**. The thermal ellipsoids are shown at 50% probability level (H atoms are omitted and the labeling scheme are shown only for the hetero atoms for the sake of clarity).

Fig. 3. Perspective view of the molecular structure of the cation of complex **2**. The thermal ellipsoids are shown at 50% probability level (H atoms are omitted and the labeling scheme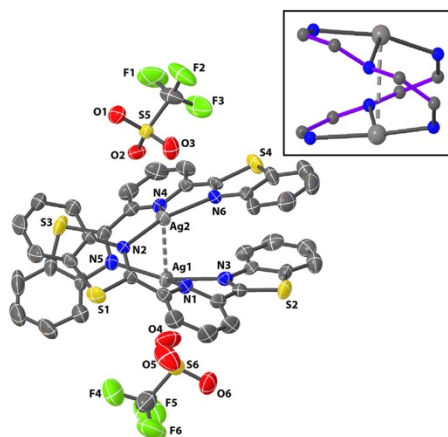 are shown only for the hetero atoms for the sake of clarity, dotted line represents Ag⋯Ag argentophilic interactions). The inset displays the helical coordination around the two Ag(I) centers.

X-ray structure of complex **2** (Fig. 2) reveals a binuclear complex with two chemically equivalent but crystallographically distinct Ag(I) centers and each metal center resides in highly distorted trigonal environment. As shown in Fig. 3, the molecular structure of complex **2** is quite interesting. Here each of the bztpy

Fig. 1. X-band EPR spectrum of complex **1** at 77 K. Microwave frequency, 9.44 GHz; modulation amplitude, 2.00G; modulation frequency, 100 KHz.

Table 2
Selected bond distances (Å) and angles (°) for **1**.

Cu1–N1	2.010(3)
Cu1–N2	2.058(3)
Cu1–N3	2.060(3)
Cu1–Cl1	2.3987(13)
Cu1–Cl2	2.2624(12)
Cl2–Cu1–Cl1	109.39(5)
N1–Cu1–Cl1	112.42(10)
N1–Cu1–Cl2	138.07(10)
N1–Cu1–N2	77.58(14)
N1–Cu1–N3	78.69(13)
N2–Cu1–Cl1	93.70(10)
N2–Cu1–Cl2	96.87(10)
N2–Cu1–N3	156.08(13)
N3–Cu1–Cl1	98.06(10)
N3–Cu1–Cl2	98.74(9)

Table 3
Selected bond distances (Å) and angles (°) for **2**.

Ag1–N1	2.610(7)
Ag1–N2	2.214(6)
Ag1–N3	2.260(7)
Ag2–N4	2.568(6)
Ag2–N5	2.211(7)
Ag2–N5	2.263(6)
Ag1···Ag2	2.9310(11)
N1–Ag1–N3	69.9(2)
N1–Ag1–N5	118.7(2)
N5–Ag1–N3	160.7(2)
N6–Ag2–N4	69.2(2)
N2–Ag2–N4	124.7(2)
N2–Ag2–N6	163.0(2)

ligand binds two different Ag(I) centers. Despite the potential to form two five-membered chelate rings, each ligand forms one chelate ring with a Ag atom through the pyridyl N and the N atom of one of the benzothiazole moieties, while the remaining N atom of the second benzothiazole fragment of the same ligand binds a different Ag(I) center in a monodentate fashion (Fig. 3). This bonding arrangement results in a double-helical coordination pattern around the two metal centers as highlighted in the inset of Fig. 3. Williams and coworkers have reported a double-helical dinuclear Cu(I) complex, namely $[Cu_2(L^1)_2]^{2+}$ (where L^1 = 2,6-bis(methylbenzimidazole-2-yl)pyridine). However in this structure each L^1 ligand binds the two Cu(I) centers in different fashion giving rise to a quasi-linear coordination geometry [39].

Complexes **1** and **2** reported in this account represent the first examples of coinage metal complexes derived from bztpy ligands. Moreover, the double helical coordination pattern in complex **2** is noteworthy. In **1**, the two five-membered chelate rings are highly planar with average mean deviations of 0.010 Å. The distorted square pyramidal geometry around the Cu(II) center can be realized from the Cl1–Cu1–Cl2 bond angle (109.39(5)°, Table 2). In this complex the bztpy ligand also exhibits reasonable planarity with mean deviation of 0.075 Å. In case of **2**, both Ag(I) centers are tricoordinated and the planes constituted by Ag1, N1, N3, N5 and Ag2, N2, N4, N6 are noticeably deviated from planarity (mean deviations, 0.130 and 0.071 Å respectively). In this complex the two five-membered chelate rings (from two different bztpy ligands) are also severely distorted from planarity (mean deviations, 0.095 and 0.164 Å).

In complex **1**, the Cu–N(pyridyl) bond length and the average Cu–N(benzothiazole) bond distances are 2.010(3) and 2.059(3) Å respectively. These values are comparable (1.972(6) and 2.062 (7) Å respectively) to corresponding bond lengths in another five coordinated Cu(II) complex, namely, $[Cu(pbt)_2(H_2O)](ClO_4)_2$ [40].

In case of **2**, the average Ag-N(pyridyl) and Ag-N(benzothiazole) bond distances are 2.589(6) and 2.237(6) Å respectively. The Ag-N(pyridyl) length in **2** is noticeably longer compared to the corresponding distance (2.453(6) Å) observed with the Ag(I) complex $[Ag(pbt)_2](BF_4)$, previously reported by our group [18]. The Ag-N (benzothiazole) distances in **2** and $[Ag(pbt)_2](BF_4)$ are however comparable (2.237(6) and 2.256(6) Å respectively). The two complexes have different coordination geometry, which might have some influence towards the modest differences in the metric parameters. In **2**, a relatively stronger intra dimer Ag···Ag interaction has been noted (2.9310(11) Å). This is significantly shorter than twice the van der Waals radius of Ag(I) (3.44 Å) [41]. This intradimer interaction between two d^{10} metal centers is possible via significant participation of 5s and 5p orbitals in bonding that are close in energy to the 4d orbitals. Though no π–π stacking contributed to reinforce the Ag···Ag interaction in case of **2**, the double helical pattern of the two ligands might have facilitated bringing the two metal centers sufficiently closer.

The packing pattern of **1** (Fig. 4), reveal no classical hydrogen bonding interactions. However, two moderate non-classical interactions consolidated its extended structure [C20-H20A···S1, with H···S, 2.83 Å^i and C20-H20B···Cl1, with H···Cl, 2.11 Å; symmetry code: (i) $x + 1/2, -y + 3/2, z − 1/2$]. The extended lattice of **2** is consolidated with few non classical hydrogen bonding interactions involving the metal complex cation and the triflate counter anions [C3-H···O2, with H···O, 2.59 Å^i; C4-H4···S1, with H···S, 2.76 Å; C17-H17···O4, with H···O, 2.52 Å^{ii}; C21-H21···O6, with H···O, 2.39 Å^{iii}; C22-H22···O6, with H···O, 2,54 Å^{ii}; C23-H23···S4, with H···S, 2.79 Å and C35-H35···O3, with H···O, 2.51 Å^{iv}; symmetry codes: (i) $x + 1, y, z$; (ii) $-x + 1, -y + 1, -z$; (iii) $x − 1, y, z$; (iv) $-x + 1, -y + 1, -z + 1$. The packing pattern is shown in Fig. 5.

3.3. Antibacterial Studies.

The antimicrobial efficacies of complexes **1** and **2** were tested using a SSTI model previously developed in this laboratory [42]. This model resembles skin infections by mimicking the gradual penetration of bacteria into the underlying soft tissue. In brief, the system is composed of a soft brine agar layer inoculated with a *Gram-positive* (*Staphylococcus epidermidis*) or *Gram-negative* bacterium (*Acinetobacter baumannii*) to reach a concentration of 8.0 CFU mL^{-1}. The inoculated soft agar layer lies on top of a nutrient rich agar. The soft brine agar allows for bacterial mobility, while the nutrient rich bottom agar layer promotes penetration. The SSTI model addresses some of the limitations of standard susceptibility tests discussed in detail elsewhere [42]. The antimicrobial properties of **1** and **2** were tested using 7 mm diameter KBr disks containing 2% w/w of the complexes under investigation. Control KBr disks containing bztpy, AgNO$_3$, or only KBr were also fabricated and tested in a similar manner. All KBr disks were prepared fresh and placed carefully on top of the inoculated agar plates.

The SSTI antibacterial experimental results are presented in Fig. 6. Inoculation of the soft brine agar with the bacteria afforded uniform lawns through the entire agar plate. No zones of inhibition were observed in the cultures when using bztpy or blank KBr disks. However, disks containing **1**, **2**, or AgNO$_3$ displayed well-defined zones of inhibition. In all cases (Fig. 6) the zones of inhibition of **2** and AgNO$_3$ were noticeably larger than the zones of inhibition of **1**. This is in line with the well-established superior antimicrobial efficacy of Ag-based compounds. Unlike other antibiotics, the bioactive silver (Ag$^+$ ions) inflicts damage to bacterial cells through multiple mechanisms, making it difficult for these microorganisms to develop resistance [43]. For both bacterial strains, AgNO$_3$ and **2** produced zones of inhibition of 25 ± 3 mm and 27 ± 3 mm respectively for *S. epidermidis*. The zones of inhibition for complex
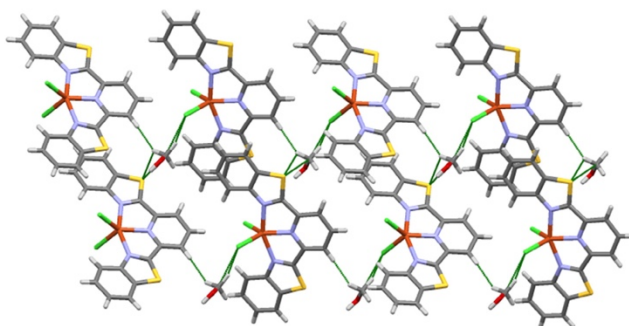
Fig. 4. Packing pattern of complex **1** extending along *b* axis, green lines indicating non-classical hydrogen bonding interactions. (Color online.)
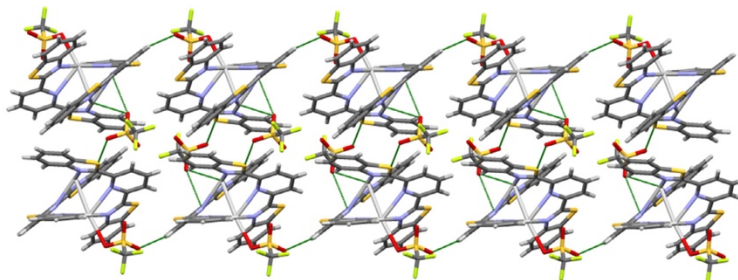

Fig. 5. Packing pattern of complex **2** extending along *b* axis, green lines indicating non-classical hydrogen bonding interactions. (Color online.)
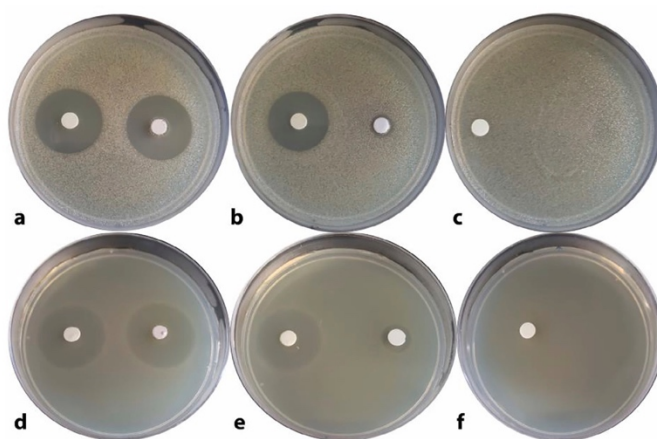

Fig. 6. Clearing of bacterial growth of *Acinetobacter baumannii* (top row): plate (a) KBr pellet 2% (w/w) with complex **2** (left side) and AgNO$_3$ (right side); plate (b) KBr pellet 2% (w/w) with complex **2** (left side) and complex **1** (right side); plate (c) KBr pellet 2% (w/w) with bztpy (left side) and blank pellet (right side). *Staphylococcus epidermidis* (bottom row): plate (a) KBr pellet 2% (w/w) with complex **2** (left side) and AgNO$_3$ (right side); plate (b) KBr pellet 2% (w/w) with complex **2** (left side) and complex **1** (right side); plate (c) KBr pellet 2% (w/w) with bztpy (left side) and blank pellet (right side).

1 were 8 ± 3 mm and 12 ± 3 mm for *A. baumannii* and *S. epidermidis* respectively. No growth was observed when fresh growth media was inoculated with agar containing the entire depth of the zones of inhibition. It is important to note here that due to insoluble nature of the two complexes in aqueous (biological) media, their antibacterial efficiency is limited by diffusion. Despite this fact, **2** was able to produce relatively large zones of inhibition. Modest electronegative surface potential of bacterial cell walls is known to allow more facile cell penetration in case of cationic complexes compared to their neutral analogues [44]. Thus the dicationic silver complex **2** in the present work would enjoy the relative ease of cellular internalization into the bacterial cells compared to the neutral copper complex **1**. Additionally, the zones of inhibition of **2** were on average somewhat larger than those produced by AgNO₃ salt. Although AgNO₃ is soluble in water, the high reactivity of Ag⁺ results in the rapid precipitation as AgCl when exposed to high concentration of Cl⁻, as present in the soft brine agar. It is also interesting to note that the zones of inhibition observed were consistently larger for *S. epidermidis* compared to *A. baumannii*. This can be attributed to relatively higher antimicrobial resistance displayed by the *Gram-negative* bacteria.

4. Conclusion

In conclusion two complexes of coinage metals (**1** and **2**) derived from 2,6-bis(benzothiazole)-pyridine (bztpy) ligand have been synthesized and structurally characterized. X-ray structure of the dimeric complex **2** reveals a double helical arrangement of the two ligands around two Ag(I) atoms. This pattern might have also contributed towards reinforcing the strong argentophilic interactions between the Ag(I) centers (Ag···Ag, 2.9310(11) Å). Antibacterial efficacies of both complexes have been assessed against one *Gram-positive* and one *Gram-negative* bacterial strains with aid of a SSTI model previously developed in this laboratory. While almost no growth inhibition has been noted with bztpy ligand itself, significant clearance of bacterial lawns has been realized with both complexes (**1** and **2**). Between the two complexes, **2** inflicts considerably more antimicrobial actions uniformly against both types of bacteria. These findings are in accordance with the well-known broad-spectrum antibacterial property of Ag-based compounds. Moreover, the dicationic complex **2** enjoys the advantage of facile cellular internalization compared to the neutral complex **1**. Complexes with few other derivatives of bis (benzothiazole)-based ligand systems and their antimicrobial properties are currently under investigation in this laboratory.

Acknowledgement

Appendix A. Supplementary data

CCDC 1874951 and 1874952 contains the supplementary crystallographic data for complex **1** and **2**. These data can be obtained free of charge via http://www.ccdc.cam.ac.uk/conts/retrieving.html, or from the Cambridge Crystallographic Data Centre, 12 Union Road, Cambridge CB2 1EZ, UK; fax: (+44) 1223-336-033; or e-mail: deposit@ccdc.cam.ac.uk. Supplementary data to this article can be found online at https://doi.org/10.1016/j.poly.2019.02.001.

References

[1] E.Y. Klein, T.P. Boeckel, E.M. Martinez, S. Pant, S. Gandra, S.A. Levin, H. Goossens, R. Laxminarayan, Proc. Natl. Acad. Sci. USA 115 (2018) E3463.
[2] World Health Organization Report http://www.who.int/en/news-room/detail/27-02-2017-who-publishes-list-of-bacteria-for-which-new-antibiotics-are-urgently-needed, 2017.
[3] A. Ponce-de-Leon, E. Rodriguez-Noriega, R. Morfin-Otero, D.P. Cornejo-Juarez, J. C. Tonoco, J.L.V. Cervantes, J. Sifuentes-Osorni, PLoS One 13 (2018) e0198621.
[4] B. Mehrab, N.M. Clark, G.G. Zhanel, J.P. Lynch, Chest 147 (2015) 1413.
[5] U. Altoparlak, S. Erol, M.N. Akcay, F. Celebi, A. Kadanali, Burns 30 (2004) 660.
[6] M. Boer, E. Duchnik, R. Maleszka, M. Marchlewicz, Postepy. Dermatol. Alergol. 33 (2016) 1.
[7] S. DeBoer, A. O'Connor, Crit. Care Nurs. Clin. North Am. 16 (2004) 61.
[8] Q.J. Tong, K.D.P. Hammer, E.M. Johnson, M. Zegarra, M. Goto, T.S. Lo, Infect. Drug Resist. 11 (2018) 417.
[9] S. Banerjee, C. Argaez. Topical Antibiotics for Infection Prevention: A Review of the Clinical Effectiveness and Guidelines. Canadian Agency for Drugs and Technologies in Health, 2017.
[10] A.D. Politano, K.T. Campbell, L.H. Rosenberger, R.G. Sawyer, Surg. Infect. (Larchmt). 14 (2013) 8.
[11] J.P. Heggers, H. Hawkins, P. Edgar, C. Villarreal, D.N. Herndon, Treatment of infections in burns, in: D.N. Herndon (Ed.), Total Burn Care, Saunders, London, England, 2002, pp. 120–169.
[12] C.L. Fox Jr, S.M. Modak, Antimicrob. Agents Chemother. 5 (1974) 582.
[13] J. Jimenez, I. Chakraborty, M. Rojas-Andrade, P.K. Mascharak, J Inorg. Biochem. 168 (2017) 13.
[14] J. Jimenez, I. Chakraborty, A.M. Del Cid, P.K. Mascharak, Inorg. Chem. 56 (2017) 4784.
[15] T.R. deBoer, I. Chakraborty, P.K. Mascharak, J. Mater. Sci: Mater Med. 26 (2015) 243.
[16] M.N. Pinto, I. Chakraborty, W. Schultz-Simonton, M. Rojas-Andrade, R. Braslau, P.K. Mascharak, Chem. Commun. 53 (2017) 1459.
[17] M.N. Pinto, J. Martinez-Gonzalez, I. Chakraborty, P.K. Mascharak, Inorg. Chem. 57 (2018) 6692.
[18] J. Stenger-Smith, I. Charaborty, W.M.C. Sameera, P.K. Mascharak, Inorg. Chim. Acta 471 (2018) 326.
[19] P.K. Sahu, S.K. Gupta, D. Thavaselvam, D.D. Agarwal, Eur. J. Med. Chem. 54 (2012) 366.
[20] K. Yamazaki, Y. Kaneko, K. Suwa, S. Ebara, K. Nakazawa, K. Yasuno, Bioorg. Med. Chem. 13 (2005) 2509.
[21] A.A. Weekes, A.D. Westwell, Curr. Med. Chem. 16 (2009) 2430.
[22] J. Gagoria, P.K. Verma, A. Khatkar, Cent. Nerv. Syst. Agents Med. Chem. 15 (2015) 11.
[23] V. Kumar, S. Sharma, A. Husain, Int. Cur. Pharm. J. 4 (2015) 457.
[24] Md.S. Hossain, C.M. Zakaria, Md. Kudrat-E-Zahan, Am. J. Heterocy. Chem. 4 (2018) 1.
[25] Y. Lu, Y. Chen, Z. Ou, S. Chen, C. Zhuang, X. Le, Chin. J. Chem. 30 (2012) 303.
[26] R. Boca, M. Boca, L. Dlháń, K. Falk, H. Fuess, W. Haase, R. Jarosciak, B. Papánková, F. Renz, M. Vrbová, R. Werner, Inorg. Chem. 40 (2001) 3025.
[27] R. Boca, P. Baran, M. Boca, L'. Dlháń, H. Fuess, W. Linert, B. Papánková, R. Werner, Inorg. Chim. Acta 278 (1998) 190.
[28] W. Linert, M. Konecny, F. Renz, J. Chem. Soc., Dalton Trans. (1994) 1523.
[29] P. Guerriero, E. Bullita, P. Vigato, A. Pietro, B. Pelli, P. Traldi, J. Heterocycl. Chem. 25 (1998) 145.
[30] Bruker APEX3, Bruker AXS Inc. Madison, Wisconsin, USA, 2014.
[31] Bruker SAINT, Bruker AXS Inc., Madison, Wisconsin, USA, 2012.
[32] Bruker SADABS, Bruker AXS Inc., Madison, Wisconsin, USA, 2016.
[33] G.M. Sheldrick, Acta Crystallogr. Sect A Found. Adv. 71 (2015) 3.
[34] A.L. Spek, Acta Crystallogr. Sect. C 71 (2015) 9.
[35] O.V. Dolomanov, L.J. Bourhis, R.J. Gildea, J.A.K. Howard, H. Puschmann, J Appl. Crystallogr. 42 (2009) 339.
[36] G. Batra, P. Mathur, Transit. Met. Chem. 20 (1995) 26.
[37] J.R. Thompson, V.E. Williams, D.B. Leznoff, Cryst. Growth Des. 17 (2017) 1180.
[38] M. Boca, R. Boca, G. Kickelbick, W. Linert, I. Svoboda, H. Fuess, Inorg. Chim. Acta 338 (2002) 36.
[39] C. Piguet, G. Bernardinelli, A.F. Williams, Inorg. Chem. 28 (1989) 2920.
[40] E.K. Beloglazkina, I.V. Yudin, A.G. Majouga, A.A. Moiseeva, A.I. Tursina, N.V. Zyk, Russ. Chem. Bull. Int. Ed. 55 (2006) 1803.
[41] A. Bondi, J. Phys. Chem. 68 (1964) 441.
[42] B.J. Heilman, J. St, John, S.R.J. Oliver, P.K. Mascharak, J. Am. Chem. Soc 134 (2012) 11573.
[43] W.K. Jung, H.C. Koo, K.W. Kim, S. Shin, S.H. Kim, Y.H. Park, Appl. Environ. Microbiol. 74 (2008) 2171.
[44] S.H. van Rijt, P.J. Sadler, Drug Discov. Today 14 (2009) 1089.

Fin.